SOLAR POWER

Edited by **Radu D. Rugescu**

INTECHWEB.ORG

Solar Power
Edited by Radu D. Rugescu

Published by InTech
Janeza Trdine 9, 51000 Rijeka, Croatia

Publishing Process Manager Igor Babic
Technical Editor Teodora Smiljanic
Cover Designer InTech Design Team

First published February, 2012
Printed in Croatia

A free online edition of this book is available at www.intechopen.com
Additional hard copies can be obtained from orders@intechweb.org

Solar Power, Edited by Radu D. Rugescu
p. cm.
ISBN 978-953-51-0014-0

Contents

Preface

The new book substantially updates the key topic of "Solar Energy" and the existing reference sources in this area of knowledge. Several of the latest concepts and research results are presented by fifty-two top-qualified authors from seventeen countries. Progress extending from new theoretical ways of understanding the photo-voltaic phenomenon, to new means of exploiting biological resources for solar energy extraction are presented. The reader will find that even the harshest topics on solar energy are presented in an attractive and animated manner, drawing attention to various and promising means of extracting solar power. The enlargement of solar technology types described adds value to the new book against our previous, successful work on the topic.

New boundaries are revealed and ways of extending the present technologies in the solar energy extraction are suggested, which will bolster the interested reader for new developments in the field. The editors will be pleased to see that the present book is analysed and debated. They wait for the readers' critical reaction with active interest and welcome positive proposals.

The editor addresses thanks to the contributors for their work and dedication, to InTech for presenting the text in a pleasant presentation, and waits for new, top level contributions in the future.

Radu D. Rugescu PhD
University Politehnica of Bucharest, Bucharest
Romania

Part 1

Solar Radiation

1

Prediction of Solar Radiation Intensity for Cost-Effective PV Sizing and Intelligent Energy Buildings

Eleni Kaplani and Socrates Kaplanis
Technological Educational Institute of Patras
Greece

1. Introduction

The solar radiation in the form of electromagnetic waves emitted by the sun, travels the extraterrestrial space without any essential interaction with matter, and reaches the earth's atmosphere. Therein, the beam solar radiation undergoes physic-chemical processes and experiences scattering by (macro) molecules, dust, or other tiny particles in the air. This process creates the solar radiation component called diffuse radiation. Thus, the solar radiation on any surface on the earth consists of the beam solar radiation, the diffuse radiation and the one reflected by the surroundings.

On the other hand, the length of the path of the solar beam till it reaches the horizontal surface differs both during the day and during the year. It is high during morning and sunset hours and shorter during noon hours. Also, due to the sun's altitude which is low, i.e. closer to the horizontal in winter months for the North Hemisphere, the length of the path of the solar beam is longer and, therefore, the intensity of the solar radiation is essentially affected by the higher air mass it penetrates both on a daily and seasonally basis. Hence, solar radiation finally reaches the earth surface substantially decreased and dissipated compared to the extraterrestrial values. Table 1 and Figure 1 show the extraterrestrial solar

cities	φ	JAN	FEB	MAR	APR	MAY	JUN	JUL	AUG	SEP	OCT	NOV
Cairo	30.05	5.863	7.201	8.843	10.265	11.158	11.460	11.261	10.536	9.316	7.681	6.187
Iraklio	35.32	5.029	6.465	8.307	10.000	11.152	11.582	11.320	10.376	8.889	7.015	5.383
Athens	37.97	4.690	6.158	8.076	9.874	11.130	11.614	11.325	10.292	8.699	6.734	5.054
Thessaloniki	40.52	4.178	5.687	7.708	9.663	11.078	11.642	11.314	10.146	8.395	6.299	4.554
Firenze	43.78	3.664	5.204	7.321	9.429	11.003	11.648	11.281	9.976	8.067	5.848	4.050
Zagreb	45.80	3.322	4.876	7.051	9.259	10.941	11.645	11.248	9.850	7.837	5.540	3.712
Paris	48.87	2.811	4.377	6.631	8.986	10.832	11.624	11.184	9.642	7.474	5.066	3.204
London	51.50	2.309	3.870	6.192	8.691	10.704	11.588	11.104	9.413	7.090	4.581	2.700
Hamburg	53.55	1.980	3.530	5.890	8.484	10.611	11.561	11.045	9.250	6.824	4.252	2.367
Copenhagen	55.72	1.659	3.190	5.581	8.266	10.513	11.531	10.982	9.080	6.549	3.920	2.039
Stockholm	59.35	1.049	2.508	4.943	7.810	10.307	11.479	10.852	8.719	5.977	3.247	1.403
Helsinki	60.22	0.905	2.339	4.780	7.692	10.255	11.470	10.821	8.625	5.829	3.077	1.251

Table 1. Average top-of-atmosphere insolation incident (kWh/m^2) for major cities with latitude spanning from 30^o to 60^o.

radiation data for various latitudes. Calculations and analysis was performed on the daily average solar radiation on top-of-atmosphere data obtained from NASA's online database (NASA Surface meteorology and Solar Energy, 2011). It is evident for the North Hemisphere that, as the latitude increases the top-of-atmosphere solar radiation decreases especially during the winter months, while during Summer the differences are very small. This is due to the position of the earth with respect to the sun.

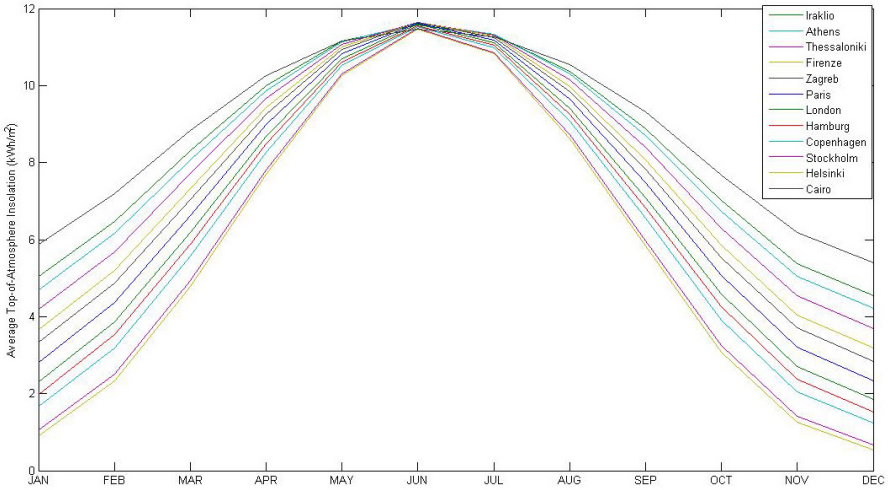

Fig. 1. Average top-of-atmosphere insolation incident (kWh/m²) for major cities with latitude spanning from 30° to 60°.

The intensity of the solar radiation which reaches the earth outside its atmosphere in hour h in a day n_j is the extraterrestrial radiation, represented by $I_{ext}(h;n_j)$, and can be accurately estimated by the following equation.

$$I_{ext}\left(h;n_j\right)=I_{sc}\cdot\left[1+0.033\cdot\cos\left(\frac{360\cdot n_j}{365}\right)\right]\cdot\left[\cos(\varphi)\cos(\delta)\cos(\omega_s)+\sin(\delta)\right] \tag{1}$$

where, I_{sc} is the solar constant, about 1365 W/m², and n_j is the incremental number of the day, with a value range [1, 365], where 1 corresponds to the 1st of January and 365 to the 31st of December. ω_s is the sunset hour angle, φ is the latitude of the site and δ is the angle of declination of the sun. The daily extraterrestrial solar radiation is determined by eq.(2) (Duffie & Beckman, 1991).

$$\begin{aligned}H_{ext}\left(n_j\right)&=\int I_{ext}\left(h;n_j\right)dh=\\&=\frac{24\cdot3600}{\pi}I_{sc}\left[1+0.033\cos\left(\frac{360\mathrm{n_j}}{365}\right)\right]\cdot\left[\cos(\varphi)\cos(\delta)\cos(\omega_s)+\frac{\pi\omega_s}{180}\sin(\varphi)\sin(\delta)\right]\end{aligned} \tag{2}$$

where, ω_s is expressed in degrees. If ω_s is in radians, then the factor π/180 should be omitted. The angle ω_s is determined by the following equation.

$$\omega_s = \cos^{-1}(-\tan(\varphi)\tan(\delta)) \quad (3)$$

Thus, the extraterrestrial solar radiation can be accurately estimated. However, the local weather conditions characterized by the Atmospheric Pressure, P_a, the Ambient Temperature, T_a, the wind velocity, v_w, the relative humidity, RH , and the cloudiness associated to the Clearness Index, K_T, (Collares-Pereira & Rabl, 1979; Kaplanis et al., 2002), may change hour by hour stochastically. Thus, the solar radiation on the horizontal of the earth's surface cannot be accurately pre-determined. All this implies that the solar radiation in a day at a place may not be the same for the same day the year after, as the weather conditions may not be the same for those two days, see for example Figure 2, where it is evident that for the same day in consecutive years the pattern differs, while the insolation in the top-of-atmosphere is always the same.

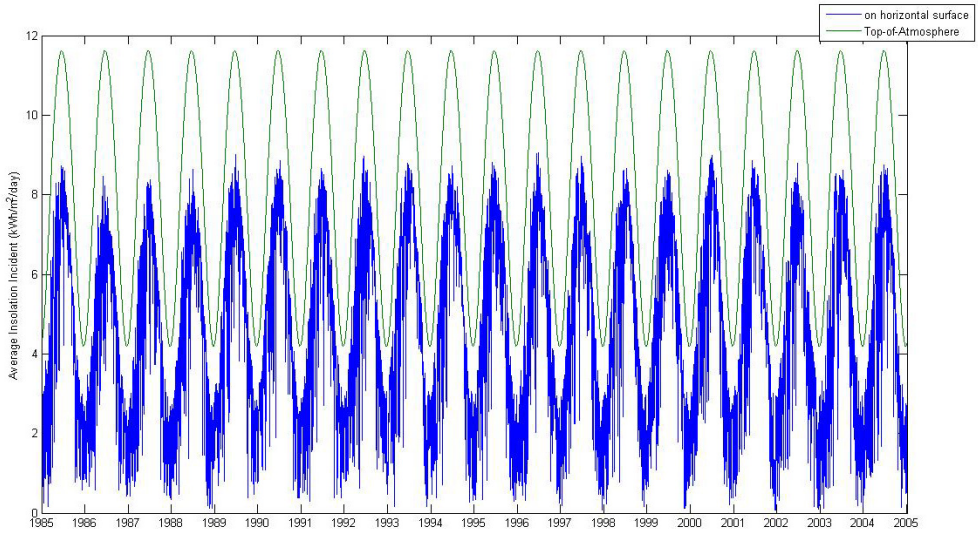

Fig. 2. Average insolation incident on horizontal and on top-of-atmosphere per day for the years 1985-2004 in Athens, Greece.

2. Solar radiation data analysis and the in-built stochastic nature

A large amount of solar radiation data is stored and provided by national databases from local meteorological stations, such as HNMS's (Hellenic National Meteorological Service, 2011), and global databases such as NASA's (NASA Surface meteorology and Solar Energy, 2011), JRC's PVGIS (Photovoltaic Geographical Information System, 2008), SoDa (Solar Radiation Data, 2011), etc. Thus previous years' data for a site of interest may be retrieved and analysed in order to serve as an appropriate input to PV sizing or other applications.

As previously discussed, the solar radiation data exhibit a dispersion, larger or smaller depending on the latitude and the microclimate of the site. Figures 3 and 4 show the fluctuations of the daily solar radiation on the horizontal as it appears around the representative day of each month for the years 1985-2004 for the city of Athens, Greece and

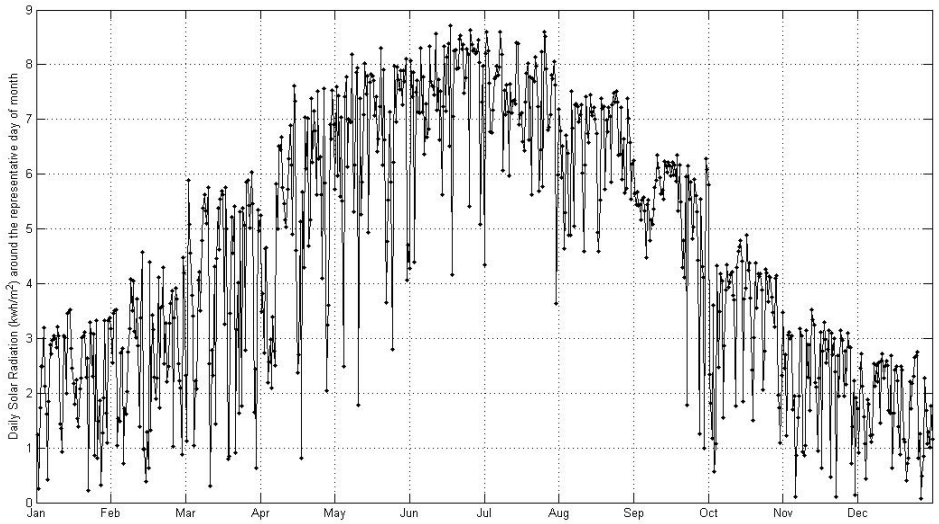

Fig. 3. Daily solar radiation (kwh/m²) around the representative day of each month for the 20 year period (1985-2004), in the city of Athens, Greece.

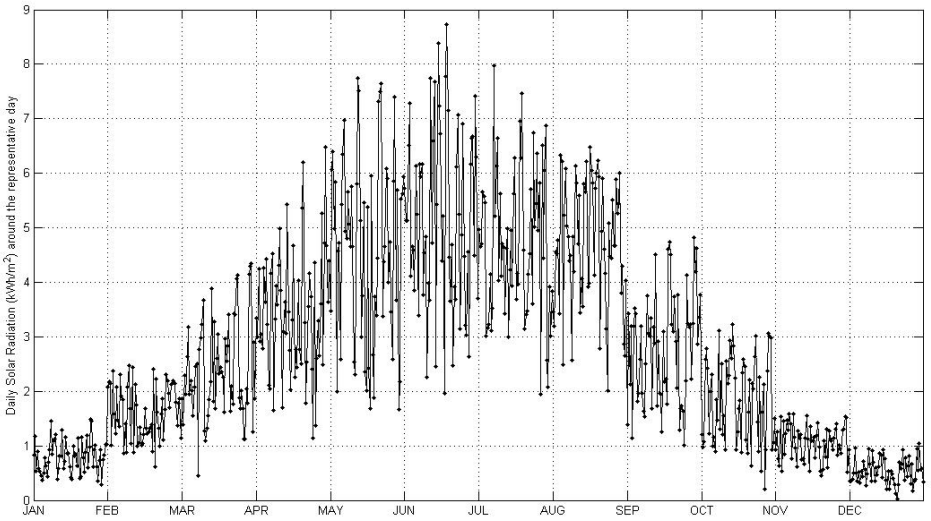

Fig. 4. Daily solar radiation (kwh/m²) around the representative day of each month for the 20 year period (1985-2004), in the city of London, UK.

the city of London, UK, respectively. Calculations and analysis was performed on the daily global solar radiation data obtained from NASA's online database (NASA Surface meteorology and Solar Energy, 2011). It is obvious that the profile of the solar radiation and the degree of the inherent solar radiation stochastic fluctuations in the two cities differ substantially. Figure 5 shows the average global solar radiation on horizontal per month for the same years and for major cities with latitude spanning from 30° to 60°.

As the daily solar radiation exhibits different degree of fluctuations both during the day and throughout the year on different sites, it is important that the past years data available for the site of interest are thoroughly analysed before a solar radiation prediction methodology or PV sizing methodology is employed.

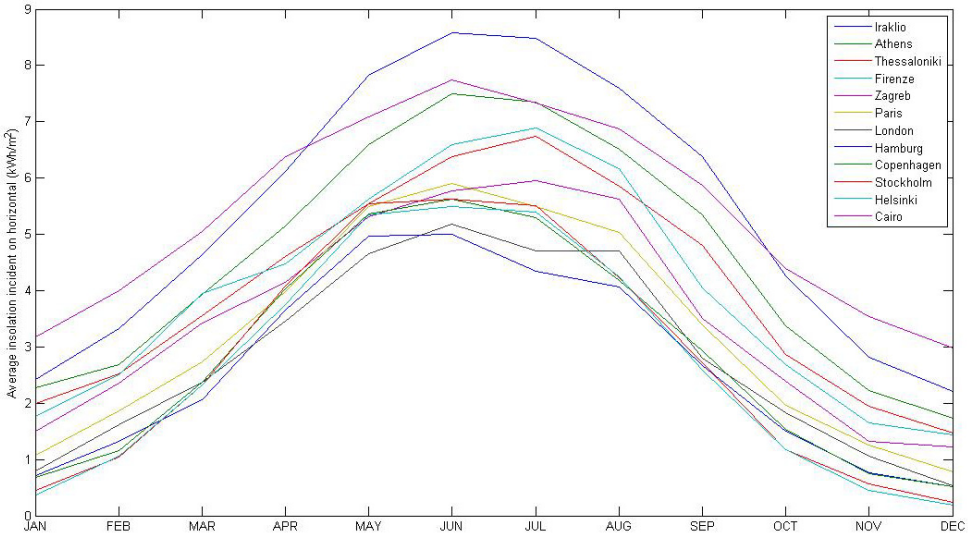

Fig. 5. Average solar radiation around the representative day of each month for the 20 year period (1985-2004), for major cities with latitude from 30° to 60°.

An in-depth analysis of past years data for the site of interest may be carried out to provide the probability density function (pdf) the data obey. Research studies have reported on the use of the Gaussian distribution or modified Gaussian (Jain et al. 1988), the Weibull distribution (Balouktsis et al., 2006), and the Extreme Value (Type I) distribution (Kaplani & Kaplanis, 2011). However, due to the inherent stochastic character of the solar radiation fluctuations, the differences in the location of the various sites, and the differences in the databases used, an argument upon the preference of one pdf over the other is avoided. Instead, the designer may analyse the data of the site of interest, extract the pdfs and assess the best fit provided by the various distributions. The proposed pdfs of the Normal, Weibull, and Extreme Value (Type I) distribution are given by eqs. (4) to (6), respectively.

$$f(x;\mu,\sigma) = \frac{1}{\sigma\sqrt{2\pi}} e^{\frac{-(x-\mu)^2}{2\sigma^2}} \tag{4}$$

$$f(x;a,b) = ba^{-b}x^{b-1}e^{-\left(\frac{x}{a}\right)^b}, \qquad x \geq 0 \tag{5}$$

$$f(x;\mu,\sigma) = \sigma^{-1} \cdot e^{\left(\frac{x-\mu}{\sigma}\right)} \cdot e^{-e^{\left(\frac{x-\mu}{\sigma}\right)}} \tag{6}$$

An example of the fitting of the 3 distributions on the pdf of January's data for Athens, Greece is provided in Figure 6. It is obvious that the Extreme Value distribution in this case provides a more accurate fit on the data.

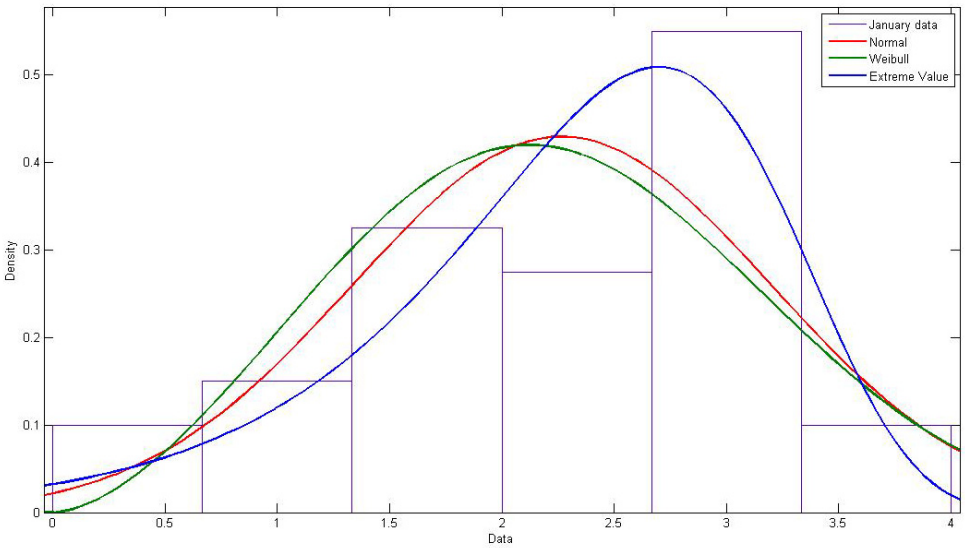

Fig. 6. Normal, Weibull, and Gaussian distributions fitted on the pdf of January's data for Athens, Greece, drawn around the representative day for the period 1985-2004.

Using the maximum Likelihood criterion for assessing the best fitted distribution, the Extreme Value distribution proved to best fit the data for all months (Kaplani & Kaplanis, 2011). A more detailed statistical analysis may be performed, using the Kolmogorov-Smirnov test in order to test the null hypothesis that the data come from a specified Normal distribution, or the Lilliefors test to test the null hypothesis that the data come from a Normal or an Extreme Value distribution, etc. It is recommended that a large sample of data is used for the fitting.

3. Hourly and daily solar radiation prediction

Having performed an in-depth statistical analysis on the past years data, it may be said that future daily solar radiation data may be anticipated to fall within the specific distribution which best fitted the previous years' monthly data. However, several solar radiation prediction models have been proposed in the literature some of which may be more globally applied.

Kaplanis in (Kaplanis, 2006) has proposed the model provided by eq.(7) to estimate the daily solar radiation for any day n_j. Parameters A, B, C are estimated by fitting an equation of this form on average monthly past years'data. An example of the fitting produced by this equation on monthly average data for Athens and Stockholm are displayed in Figures 7, 8. Table 2 shows the estimated A, B, C parameters for different cities and the correlation coefficient r showing the goodness of fit of eq.(7) on the data. Parameters A and B follow a function with argument φ, as it is evident from the profile of the data in Table 2.

$$H(n_j) = A + B \cdot \cos(2\pi n_j/365 + C) \tag{7}$$

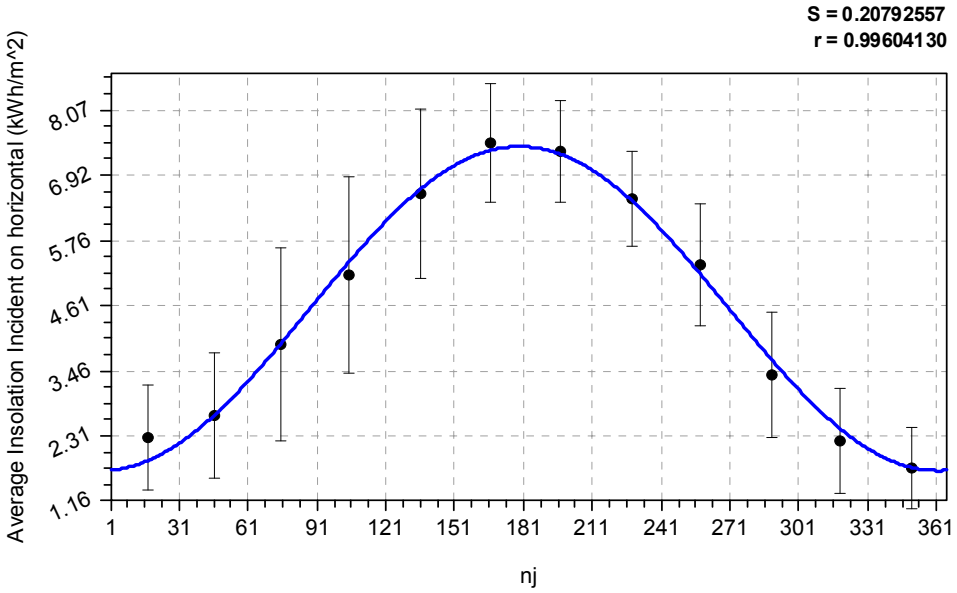

Fig. 7. Fitting results of eq.(7) on monthly data for Athens (period 1985-2004)

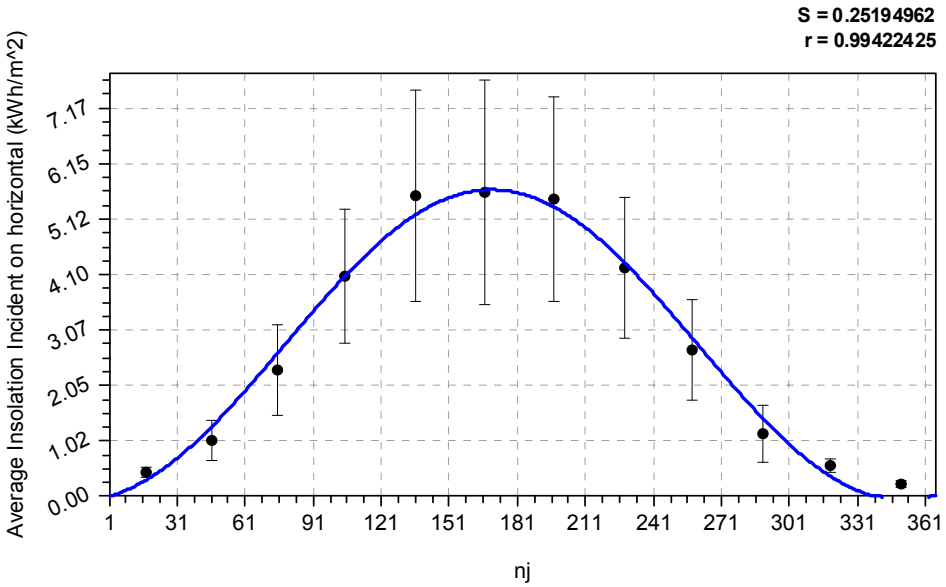

Fig. 8. Fitting results of eq.(7) on monthly data for Stockholm (period 1985-2004)

city	A	B	C	r
Iraklio	5.39	3.26	3.18	0.999
Athens	4.56	2.86	3.21	0.996
Thessaloniki	3.92	2.71	3.19	0.976
Paris	3.20	2.66	3.29	0.992
London	2.77	2.35	-3.01	0.990
Stockholm	2.79	2.87	-2.90	0.995

Table 2. Estimated parameters A, B, C for the various cities

Hourly based prediction models, based on similar functions, have also been proposed such as the model proposed by Kaplanis in eq.(8) (Kaplanis, 2006), where $a(n_j)$ and $b(n_j)$ are estimated through 2 boundary conditions and depend on the site and day n_j. The model proposed by the authors in eq.(9) (Kaplanis & Kaplani, 2007) proved to give much better results compared to other known models.

$$I(h;n_j) = a(n_j) + b(n_j)\cdot\cos(2\pi h/24) \tag{8}$$

$$I(h;n_j) = A + B\frac{e^{-\mu(n_j)x(h)}\cdot\cos(2\pi h/24)}{e^{-\mu(n_j)x(h=12)}} \tag{9}$$

Figure 9, shows an example of the hourly predicted curve obtained by this model using eq. (9) for the 17th January and the city of Patras, Greece. The past years hourly data and average data for the same day are also displayed for comparison. The national database (Hellenic National Meteorological Service, 2011) was used for the hourly solar radiation data for Patras, Greece for the period 1995-2000. For the summer data, where smaller hourly fluctuations occur, the proposed model gives even better results, see Figure 10.

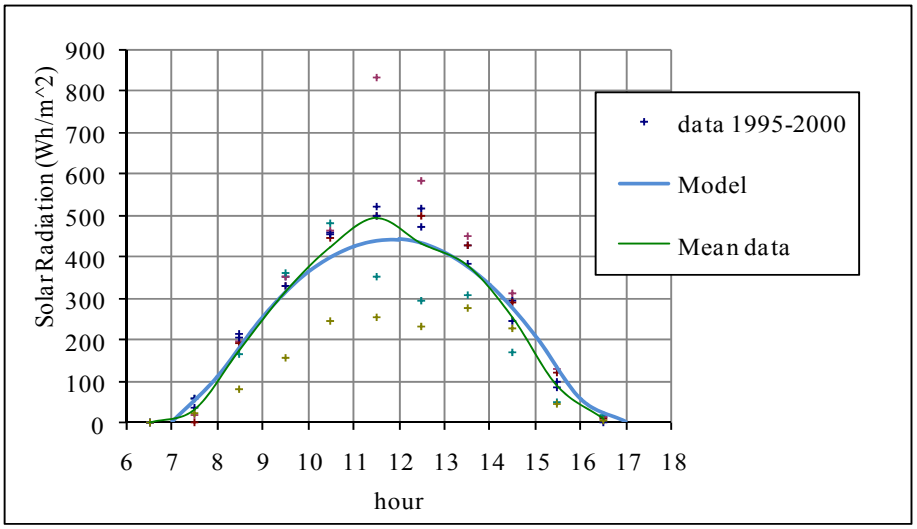

Fig. 9. Hourly data for January 17, for the city of Patras, Greece, and the hourly prediction model.

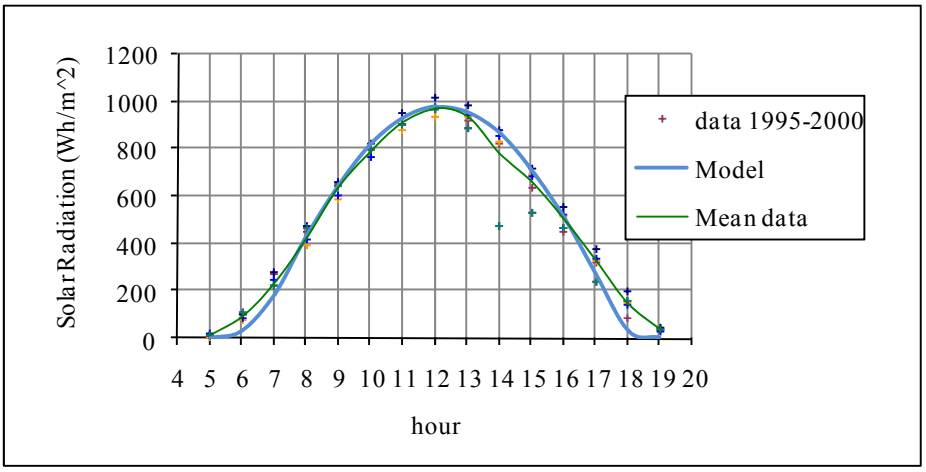

Fig. 10. Hourly data for July 17, for the city of Patras, Greece, and the hourly prediction model.

Several research studies have been published on various aspects in the modeling of solar radiation dealing with mean and stochastic values. For a global perspective the reader is advised to see also (Aguiar et al., 1988; Aguiar & Collares-Pereira, 1992; Festa et al., 1992; Gueymard, 1993; Gueymard, 2000; Jain et al., 1988).

The hourly solar intensity provided by eq.(9), denoted by the authors as mean predicted value $I_{m,pr}$, or mean expected $I_{m,exp}$, is used in a more dynamic stochastic model which uses one morning measurement as an input and based on the statistical difference of this measurement from the mean predicted and the assumption of a Gaussian profile, predicts the hourly solar radiation values for the remaining hours of the day (Kaplanis & Kaplani, 2007). This is a very challenging attempt considering that the model predicts a dynamic hourly profile depending on only one early morning measurement. The authors improved that model to take into account either 1, or 2, or 3 morning measurements, predicting the hourly solar radiation profile for the remaining hours of the day with increased accuracy (Kaplanis & Kaplani, 2010). In case that a rich database of past years data exist, it is proposed also the use of average hourly data instead of the mean expected. Thus, according to this model, the prediction of the solar radiation at hour h in a day n_j is based on the following expression.

$$I_{pr}(h;n_j) = I_{av}(h;n_j) + R \cdot \sigma_{I(h;n_j)} \tag{10}$$

where R is a random number drawn from a Gaussian distribution (μ=0, σ=1) , however, it is confined within the interval [t_1 ±1], where t_1 is determined for the previous hour h_1 by eq.(11). For the estimation of t_1 it is assumed that the difference between the one morning measured value $I_{meas}(h_1;n_j)$ value at hour h_1 from the average $I_{av}(h_1;n_j)$ value at the same hour h_1 from the past years' data, follows a Gaussian probability density function. For the predicted value $I_{pr}(h;n_j)$ only positive values, values less than the extraterrestrial $I_{ext}(h;n_j)$, and less than $I_{av}(h;n_j) + 3\sigma_{I(h;nj)}$ are accepted, which is necessary to cut off the Gaussian tail for high values above the average.

$$t_1 = \frac{I_{meas}(h_1;n_j) - I_{av}(h_1;n_j)}{\sigma_{I(h_1;n_j)}} \tag{11}$$

For the hourly solar radiation prediction profile based on two morning measurements at hours h_1 and h_2, eq.(12) is proposed, which now uses two stochastic terms, one term as in eq.(10), which stands for the stochastic fluctuations at hour h_3, and a second term to stand for the rate of change of the $I(h;n_j)$, within the time interval [h_1, h_2]. t_2 is determined here similarly to t_1 in eq.(11) but now for hour h_2.

$$I_{pr}(h_3;n_j) = I_{av}(h_3;n_j) + R \cdot \sigma_{I(h_3;n_j)} + \frac{1}{4} \cdot \left(t_2 \cdot \sigma_{I(h_2;n_j)} - t_1 \cdot \sigma_{I(h_1;n_j)} \right) \cdot R_1 \tag{12}$$

The hourly solar radiation prediction based on three morning measurements at hours h_1, h_2, h_3 is given by eq.(13), where the use of an extra stochastic term is proposed, which provides the contribution of the second derivative of $[I_{meas}(h;n_j) - I_{av}(h;n_j)]$, with respect to h, to the $I(h;n_j)$ prediction.

$$I_{pr}(h_4;n_j) = I_{av}(h_4;n_j) + R\cdot\sigma_{I(h_4;n_j)} + \frac{1}{4}\cdot\left(t_3\cdot\sigma_{I(h_3;n_j)} - t_2\cdot\sigma_{I(h_2;n_j)}\right)\cdot R1 + \\ + \frac{1}{9}\cdot\left(t_3\cdot\sigma_{I(h_3;n_j)} - 2\cdot t_2\cdot\sigma_{I(h_2;n_j)} + t_1\cdot\sigma_{I(h_1;n_j)}\right)\cdot R2 \quad (13)$$

The model continues to predict the solar radiation at next hour based on the predicted values for the previous hours. For more details on this hourly solar radiation predictive model see (Kaplanis & Kaplani, 2010). Figures 11, 12 show the predicted hourly profile by this dynamic model using a national database for the city of Patras, Greece and the period 1995-2000 (Hellenic National Meteorological Service, 2011). By entering one, two or three morning measurements, the model predicts the hourly solar radiation profile for the remaining hours of the day. It is evident from the figures that the model based on the three morning measurements gives the best results and a prediction very close to the true measured data, even for these cases where the true data lie far away from the average years' data. Due to the random factors that appear in the eqs.(10), (12), (13), the generated hourly predicted profile is never exactly the same but fluctuates stochastically within a small range of values.

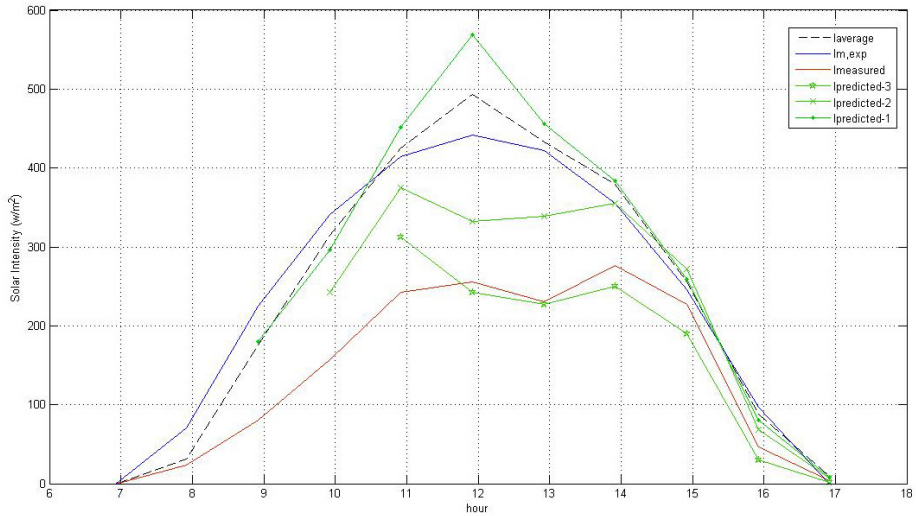

Fig. 11. Hourly predicted profiles based on one (Ipredicted-1), two (Ipredicted-2) and three (Ipredicted-3) morning measurements. Plotted against the average data profile (Iaverage), the mean expected (Im,exp) calculated by eq.(9), and the true measured data (Imeasured) on 17th January 2000, in Patras, Greece.

Other research studies have proposed methodologies for prediction of sets of hourly profiles based on Neural Networks (Kalogirou, 2000), Markov chains (Aguiar et al., 1988) and Fuzzy Logic (Iqdour & Zeroual, 2007).

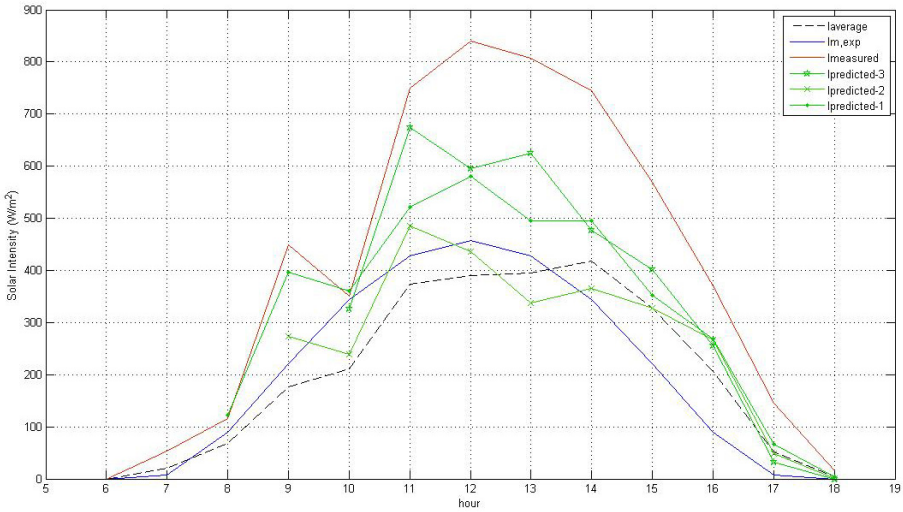

Fig. 12. Hourly predicted profiles based on one (Ipredicted-1), two (Ipredicted-2) and three (Ipredicted-3) morning measurements. Plotted against the average data profile (Iaverage), the mean expected (Im,exp) calculated by eq.(9), and the true measured data (Imeasured) on 16th March 1995, in Patras, Greece.

4. PV sizing methodologies

The previous sections have dealt with the analysis of the in-built stochastic nature of solar radiation data and the challenging issue of predicting daily and hourly solar radiation profiles with a high level of reliability. This would be most useful in problems dealing with the effective and reliable sizing of solar power systems, PV generators, and the predictive management of a complete system of solar energy sources in conjunction with the power demand by the loads, since the output of PV systems is highly affected by stochastic meteo-conditions.

Apart from the requirement for maximizing the Yield Y_f (kWhe/kWp) for a PV plant on an annual basis, there is also an increased concern about the reliability of the PV performance, i.e. to meet the loads with a pre-determined confidence level, at the minimum possible installed Peak power. The design of a PV plant should aim at installing a plant able enough to produce and deliver the right output at the minimum cost, with a small Pay-Back Period (PBP) and a high Performance Ratio (PR), (RETScreen, 2011).

In any PV sizing task all potential power losses related to the PV system elements, i.e. the inverter, charger, battery storage system, cables, etc, and effects due to PV cell ageing, battery ageing, matching effects, shadowing, etc., need to be thoroughly investigated and analysed in order to reach the required Peak Power to be installed. Furthermore, a statistical analysis of the daily solar radiation and hourly solar radiation fluctuations is essential within the scope of the PV sizing, as the inherent statistical fluctuation lead to an uncertainty with respect to the installed Peak Power, a major consideration when a reliable Stand-Alone PV system (SAPV) is to be installed. The issue of reliability has driven sizing

methodologies to the introduction of the concept of energy autonomy period of a PV plant, expressed using the autonomy factor d. The autonomy factor d was introduced for critical and non-critical loads, given by eqs. (14) and (15) respectively, to provide energy autonomy when using non-critical loads, requiring power at least 95% of the time, and when using critical loads, requiring power at least 99% of the time (Messenger & Ventre, 2000).

$$d_{cr} = -1.9 \cdot PSH_{min} + 18.3 \tag{14}$$

$$d_{n-cr} = -0.48 \cdot PSH_{min} + 4.58 \tag{15}$$

where PSH is the Peak Solar Hour, defined and estimated as in (Messenger & Ventre, 2000) for any day, and PSH_{min} is its minimum value. It is evident that the smaller the minimum PSH value, as derived from the past years solar radiation data for a region, the higher the value of d. The drawback of the conventional sizing approach is its high cost, as both the Peak power (P_m) to be installed, given by eq.(16), and the Capacity of the Battery Storage System (C_L), given by eq.(17), increase linearly with the value of d for energy autonomy.

$$P_m = \frac{d \cdot Q_L \cdot F}{PSH_m \cdot R_m} \tag{16}$$

$$C_L = \frac{d \cdot Q_L \cdot F'}{V \cdot DOD} \tag{17}$$

where Q_L is the daily load (Wh), F and F′ are correction factors due to transfer power losses, V is the transfer voltage and DOD the depth of discharge of the battery. The mean PSH is denoted by PSH_m, and R_m is used for the conversion of the solar intensity from the horizontal to the PV array inclined plane, see (Duffie & Beckman, 1991; RETScreen, 2001). R depends on the day of the month, the latitude of the place and the microclimate of the region.

This conventional PV sizing methodology gives reliable results providing energy autonomy to the system through the use of the autonomy factor d in the estimation of P_m and C_L, considering the statistical properties of the solar radiation data as introduced through PSH_{min}. However, with the increase of d to accommodate fluctuations in the solar radiation data, the estimated P_m and C_L to be installed increase substantially, leading to a requirement for a larger PV array and a larger battery storage system.

A more cost-effective approach has been proposed in (Kaplanis & Kaplani, 2006), whereby a different approach to the estimation of the autonomy factor is used, leading to a reliable system with the need for lower installed P_m and C_L. In this approach it is assumed that $H(n_j)$ values follow a Gaussian probability density function, and, thus, the expected $H(n_j)$ value will lie with a 95% confidence level, in the domain:

$$H(n_j) \in \left[H_m(n_j) \pm 2 \cdot \sigma_{H(n_j)}\right] \tag{18}$$

where $H_m(n_j)$ is the mean daily solar radiation on the horizontal for the representative day of the month, for which the PV plant is to be sized, through a period of N years and $\sigma_{H(nj)}$ is the standard deviation of $H(n_j)$.

According to this model if the system is to be sized to guarantee a number of d days of system autonomy to accommodate any possible solar radiation fluctuation, the total uncertainty introduced in the determination of P_m through the estimation of PSH, whose

value (h/day) is numerically equal to the value of $H(n_j)$ measured in kWh/m², would be given by the following expressions.

$$\sigma_{H_d}^2 = \sigma_{H(n_j)_1}^2 + \sigma_{H(n_j)_2}^2 + \cdots + \sigma_{H(n_j)_d}^2 \approx d \cdot \sigma_{H(n_j)}^2 \tag{19}$$

$$\sigma_{H_d} = \sqrt{d} \cdot \sigma_{H(n_j)} \tag{20}$$

The relative change in the P_m to accommodate an energy deficit for d days with a confidence level of 95%, may be given by eq.(21). Thus, a correction factor is introduced in the determination of $P_{m,}$ provided by eq.(22). This correction factor is also included in the determination of C_L, see eq.(23).

$$\frac{\delta P_m}{P_m} = \frac{\delta(PSH)}{PSH_m} = \frac{\sigma_{H_d}}{H_m(n_j)} = \frac{2 \cdot \sqrt{d} \cdot \sigma_{H(n_j)}}{H_m(n_j)} \tag{21}$$

$$P_{m,d} = P_m \cdot \left(1 + \frac{2 \cdot \sqrt{d} \cdot \sigma_{H(n_j)}}{H_m(n_j)}\right) \tag{22}$$

$$C_{L,d} = C_L \cdot \left(1 + \frac{2 \cdot \sqrt{d} \cdot \sigma_{H(n_j)}}{H_m(n_j)}\right) \tag{23}$$

The introduction of this correction factor has been evaluated in (Kaplanis & Kaplani, 2006) using the solar radiation data for January and the period 1995-2000 in Patras, Greece, and concluded in a significant reduction in P_m, and C_L with a system reliability level of 95%.

Recent research studies have proposed new developments of stochastic modeling (Balouktsis et al., 2006; Kaplani & Kaplanis, 2011; Markvart et al., 2006; Tan et al., 2010), the use of Hidden Markov Models (Hogaoglu, 2010), and Neural Networks (Kalogirou, 2001; Mellit et al., 2008), for the sizing of SAPV systems. Several of these approaches are iterative approaches based on the concept of energy balance and Loss of Load Probability. The objective being, a search for the minimum required installed P_m and C_L that would cover the energy needs required by the loads for a number of days so that the system remains autonomous. Some configurations may use, in addition, a diesel generator for SAPV system support in autonomous functionality. A SAPV system configuration is displayed in Figure 13.

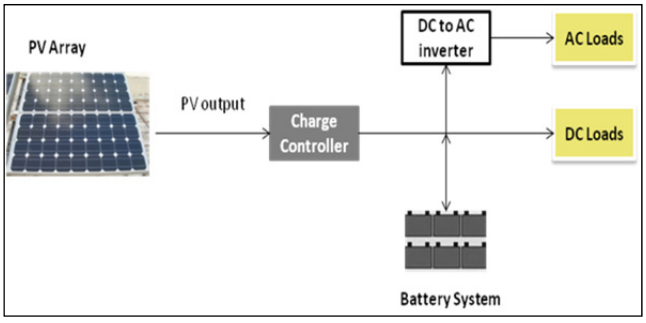

Fig. 13. SAPV system configuration

According to the energy balance concept, eq.(24), the energy offered by the PV array will be used by the loads Q_L, an amount will be dissipated throughout the pathway from the PV array to the loads, i.e. being power losses in cables, in the charge controller, the DC/AC inverter, the battery system, etc., and, finally, the remaining energy will be stored in the batteries.

$$Energy_{offer} - Energy_{demand} - Energy_{losses} = Energy_{stored} \tag{24}$$

Considering a daily description the energy balance equation may take the following form.

$$\sum_{h=hsr}^{hss} A_{PV} I_T\left(h;n_j\right)\eta_{pv}\delta h - \sum_{h=1}^{24} q_L\left(h;n_j\right)\delta h - \sum_{h=1}^{24} power_{losses}\delta h = Energy_{stored} per\ day \tag{25}$$

where A_{PV} is the size of the PV array, $I_T(h;n_j)$ the hourly solar radiation intensity on the inclined plane of the PV array at hour h for a day n_j, and η_{PV} the efficiency of the PV generator. By $q_L(h;n_j)$ we refer to the hourly power demand by the loads. Thus, the energy stored during the day would be the energy remaining from the energy provided by the PV generator, from sunrise to sunset, after it is used up on the loads and an amount 'burnt' due to power transmission and operation losses. During the night, the load power demand is met by the battery storage system, while some power losses from the battery to the loads occur. The remaining energy in the batteries will be carried on to the following day. The battery storage capacity is finite, and, thus, any excess energy after the battery is fully charged will be burnt. Also, the depth of discharge of the batteries, for deep cycle batteries, is about 80%, and, therefore, during a dark period of days when the energy in the batteries has been used up, up to the point where the state of charge (SOC) of the batteries has been reduced to 1-DOD (20%), the batteries will not be able to supply the loads with any more energy and the system will fail.

The energy provided by the PV generator during the day is given by eq. (26), and the remaining energy that will be used to charge the battery is given by eq.(27). The state of charge of the battery after the end of the day is provided in eq.(28). The SOC of the battery will result from the previous SOC with the addition of the remaining energy during the day. The SOC of the battery has an upper limit of 1. Any excess energy will be burnt. The SOC of the battery after the end of the night will be the SOC after the battery is discharged by the power required by the night loads, as given by eq.(29). F and F′ are correction factors due to all power losses from the PV generator to the loads, and from the batteries to the loads respectively. These factors should also accommodate any temperature effects or PV ageing and battery ageing effects that reduce the power output.

$$E_{PV} = P_m \cdot PSH \cdot R \tag{26}$$

$$DE = E_{PV} - F \cdot Q_{Lday} \tag{27}$$

$$SOC = SOC + DE/(C_L \cdot V) \tag{28}$$

$$SOC = SOC - Q_{Lnight} \cdot F'/(C_L \cdot V) \tag{29}$$

Thus, for an effective sizing of a PV system the following need to be thoroughly considered:

- the optimum angle of inclination and the azimuth of the PV arrays, and the other geometrical factors concerning the PV arrays, such as possible lay-outs and array dimensions, especially when there are cases of shadowing by nearby buildings or objects.
- the minimum power losses in cables, chargers, due to the margin in their operation and in the inverter(s), especially, when a group of inverters is used. The effect is crucial if the DC/AC inverter operating domain does not match the i-V characteristic of the PV array connected to it. In such cases, the efficiency of the inverter drops much below 90%.
- the sizing of the battery bank, introducing realistic corrections to the system's total Capacity, C_L (Ah), as otherwise the system might be either oversized or undersized.
- the sizing of the PV generator which has to take into consideration the daily load profile, the solar energy fluctuations during the daytime and if possible the pragmatic solar irradiance on a PV generator in any day. The latter requirement has lead, as earlier mentioned, to the introduction of the concept of d days of energy independence of an SAPV installation.

Finally, a dynamic simulation model which provides the daily and/or hourly profile of the energy expected to be delivered by the PV generator, the energy used by the loads and the state of charge of the battery, such as the one presented in (Kaplani & Kaplanis, 2011), may be found very useful not only for the optimum sizing of the PV generator and battery storage system, but also for the precise evaluation of the forecasted entire system performance and the possibility for application of more efficient controls.

5. Predictive management of PV systems

As several attempts have been recently initiated worldwide towards the development of intelligent buildings with the integration of renewable energy systems, the introduction of predictive PV system management in conjunction with effective load management is of great importance in photovoltaic applications.

A predictive management PV system may be described to have the following modules:

- An inbuilt intelligence for the management of the PV system. This is achieved when the PV system is equipped with the ability to predict the daily global solar radiation profile. Section 3 has presented a dynamic prediction model of the hourly solar radiation profile. This leads to the determination of the pragmatic power to be delivered in a day by the PV plant.
- A data acquisition system, which is tailored to the model management parameters opted for, as for instance the global solar radiation intensity, indoor and outdoor temperature, relative humidity, wind velocity, etc., which is consisted of all the required sensors, such as pyranometer, thermocouples, anemometers, etc.
- A micro-processor control unit, with an analysis and control module.

The configuration of a predictive management PV & Loads system for an intelligent building is provided in Figure 14. It is consisted of the sensors network, the load network

and the control network. The sensors signal output are fed to the data logger, which in turn communicates with the Analysis and Control Module in the PC. Given the information acquired from the sensors the Analysis Module predicts the energy to be delivered during all hours of the day, communicates with the Control module, which manages the loads through priority handling. The Control Module through the Interface to the Loads may then serve the immediate loads and shift flexible low priority loads to the following days, in order to efficiently meet the energy demand. The Control Module could have an additional functionality for remote control, i.e. web-based or via mobile.

A predictive management PV system will be seen to succeed in cases where conventional design methodologies or even more dynamic stochastic models may fail to meet the daily energy requirements. An effective PV sizing installation in conjunction with a predictive management PV system will serve as a long term cost-effective solution for energy saving and efficient energy use.

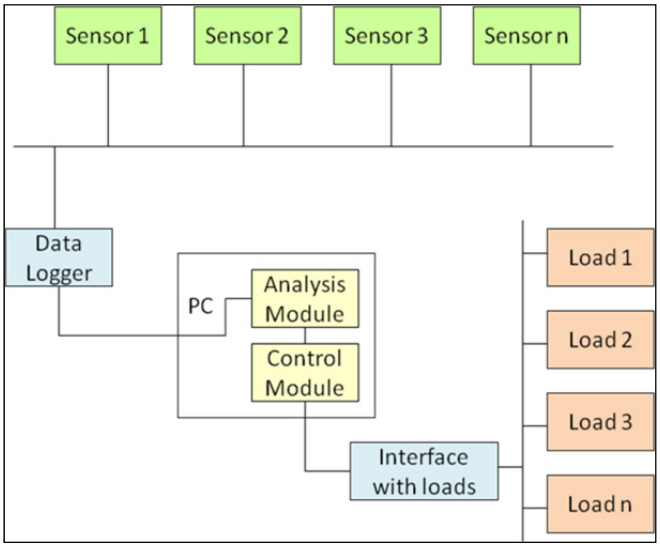

Fig. 14. Configuration of predictive management system for an intelligent building with solar radiation prediction and load management functions.

6. Conclusions

Due to the stochastic nature of the weather conditions, the intensity of the global solar radiation for any hour in any day at any place on the ground cannot be absolutely determined, while this is possible for the extraterrestrial radiation. The stochastic nature of the solar radiation on the ground surface is the weak point in the cost-effective design of solar engineering plants, such as the PV systems, which is the main target of this Chapter. An investigation into the solar radiation fluctuations and their spectra is shown to bring

improvements and innovations in the sizing of solar plants leading to more competitive solutions.

Prediction models for the estimation of the daily and hourly solar radiation profile have been presented and the results where compared with true measured values and values from available databases, revealing very promising methodologies. These are deemed very useful in the sizing of solar energy systems, such as PV generators, solar thermal systems for heating, cooling and other applications; since the amount of either heat or power produced by the solar radiation conversion through solar collectors and PV cell structures respectively, is significantly affected by the solar radiation fluctuations.

Methodological approaches for the effective sizing of PV systems to adequately cover the loads to a predetermined reliability level, may use either expected values resulting from a thorough analysis of past years data, or mean expected global solar radiation values through the use of stochastic prediction models, which showed to bring more cost-effective PV sizing figures, or, finally, benefit from hourly solar radiation on-line prediction models within the scope of a predictive management system for an intelligent energy building. The latter, is a very promising direction for highly cost-effective solutions for the installation and performance of solar energy plants, where the energy offer and the energy demand are both customized and highly optimized.

7. References

Aguiar, R.J.; Collares-Pereira, M. & Conde, J.P. (1988). Simple procedure for generating sequences of daily radiation values using a library of Markov transition matrices. *Solar Energy,* Vol.40, No.3, pp.269–279.

Aguiar, R. & Collares-Pereira, M.A., (1992). TAG: A time-dependent, autoregressive, Gaussian model for generating synthetic hourly radiation. *Solar Energy*, Vol.49, No.3, (September 1992), pp.167–174.

Balouktsis, A. et al., (2006). Sizing stand-alone photovoltaic systems. *International Journal of Photoenergy*, Vol.2006, Article ID 73650, pp.1-8.

Collares-Pereira, M. & Rabl, A. (1979). The average distribution of solar radiation-correlations between diffuse and hemispherical and between daily and hourly insolation values. *Solar Energy*, Vol.22, No.2, pp.155-164.

Duffie, J.A. & Beckman, W.A., (1991). *Solar Engineering of Thermal Processes*, John Wiley & Sons, 2nd ed., USA.

Festa, R.; Jain, S. & Ratto, C.F. (1992). Stochastic modelling of daily global irradiation. *Renewable Energy,* Vol.2, No.1, (February 1992), pp.23–34.

Gueymard, C. (2000). Prediction and performance assessment of mean hourly solar radiation. *Solar Energy,* Vol.68, No.3, (March 2000), pp.285–303.

Gueymard, C. (1993). Critical analysis and performance assessment of clear solar sky irradiance models using theoretical and measured data. *Solar Energy,* Vol.51, No.2, (August 1993), pp.121–138.

Hellenic National Meteorological Service, 2011, Databank of solar radiation data in Greece. Available from: http://www.hnms.gr/hnms/english/index_html

Hocaoglu, F.O. (2011), Stochastic approach for daily solar radiation modeling. *Solar Energy*, Vol.85, No.2, (February 2011), pp.278-287.

Iqdour, R. & Zeroual, A. (2007). Prediction of daily global solar radiation using fuzzy systems. *International Journal of Sustainable Energy*, Vol.26, pp.19–29.

Jain, P.C.; Jain, S. & Ratto, C.F. (1988). A new model for obtaining horizontal instantaneous global and diffuse radiation from the daily values. *Solar Energy*, Vol.41, No.5, pp.397-404.

Kalogirou, S.A. (2000). Applications of artificial neural-networks for energy systems. *Applied Energy*, Vol.67, pp.17-35.

Kalogirou, S.A. (2001). Artificial neural networks in renewable energy systems applications: a review. Renewable and Sustainable Energy Reviews, Vol.5, No.4, (December 2001), pp.373-401.

Kaplani, E. & Kaplanis, S. (2011). A stochastic simulation model for reliable PV system sizing providing for solar radiation fluctuations. *Proceedings of ICAE 2011, 3rd International Conference on Applied Energy,* Perugia, Italy, May 16-18, 2011, pp.3503-3516.

Kaplanis, S. et al., (2002). A comparative study of the clearness index for the region of Achaia using various techniques, *Proceedings of WREN Congress VII*, Cologne, Germany, June 29 –July 5, 2002.

Kaplanis, S. (2006). New methodologies to estimate the hourly global solar radiation; Comparison with existing models. *Renewable Energy*, Vol.31, No.6, (May 2006), pp.781-790.

Kaplanis, S. & Kaplani, E. (2006). A comparison of a new PV-sizing approach for stand alone systems with conventional methodologies. *Proceedings of IASTED International Conference EuroPES'2006*, Rhodes, Greece, June 26-28, 2006, pp.332-337.

Kaplanis, S. & Kaplani, E. (2007). A model to predict expected mean and stochastic hourly global solar radiation $I(h;n_j)$ values. *Renewable Energy*, Vol.32, No.8, (July 2007), pp.1414-1425.

Kaplanis, S. & Kaplani, E. (2010). Stochastic prediction of hourly global solar radiation for Patra, Greece. *Applied Energy*, Vol.87, No.12, (December 2010), pp.3748-3758.

Markvart, T.; Fragaki, A. & Ross, J.N. (2006). PV system sizing using observed time series of solar radiation. *Solar Energy*, Vol.80, No.1, (January 2006), pp.46-50.

Mellit, A. (2008). Methodology for predicting sequences of mean monthly clearness index and daily solar radiation data in remote areas: Application for sizing a stand-alone PV system. *Renewable Energy*, Vol.33, No.7, (July 2008), pp.1570-1590.

Messenger, R. & Ventre, J. (2000). *Photovoltaic Systems Engineering*, CRC Press, USA.

NASA, *Surface meteorology and Solar Energy*. A renewable energy resource web site (release 6.0), 2011, Available from: http://eosweb.larc.nasa.gov/sse/

PVGIS, *Photovoltaic Geographical Information System*, European Commission Joint Research Centre, 2008, Available from: http://re.jrc.ec.europa.eu/pvgis/

RETScreen International, Photovoltaic Project Analysis, 2011, Available from: www.retscreen.net

SoDa, *Solar Radiation Data*, 2011, Available from: http://www.soda-is.com/

Tan, C.W.; Green, T.C. & Hernandez-Aramburo, C.A. (2010). A stochastic method for battery sizing with uninterruptible-power and demand shift capabilities in PV (photovoltaic) systems. *Energy*, Vol.35, No.12, (December 2010), pp.5082-5092.

2

Solar Energy Resources Used in Building in Chongqing, China

Ding Yong[1], Li Bai-Zhan[1], Yao Run-Ming[2],
Lian Da-Qi[1] and Dai Hui-Zi[1]
[1]*The Faculty of Urban Construction and Environmental Engineering, Chongqing University, Chongqing*
[2]*Department of Construction Management and Engineering, University of Reading, Reading*
[1]*China*
[2]*UK*

1. Introduction

Our country is very rich in solar resource with annual total solar radiation about 3340-8360MJ/m^2, equivalent to 110-250kg standard coal/m^2 (Wei, 2006). Since energy crisis occurrence, an upsurge in application of new energy has been emerged in various countries of the world. In our country, "Solar Energy Roof Plan" and "Golden Sun" demonstration projects were also implemented in 2009 to accelerate the application of solar technology in our country. Now in areas of Tibet, Ningxia, and Gansu where solar resource is rich, solar resource has been widely used in the fields of power generation, lighting, refrigeration, heating, boiling and heating water, and cooking. In addition a large batch of solar building demonstration projects has been constructed, obtaining high social, economical, and environmental benefits (You, et al. 2002).

In Chongqing area, utilization of solar resource is still in groping stage due to its special geographic location and resource distribution characteristics. For a long time, traditional view considers that application of solar energy in Chongqing area is congenitally deficient, making its utilization very small in scale and most of the application modes are of general application type, which is not suitable to the local climate features (Wei, et al. 2002). In addition, building-shaped integrated application and research has not been conducted and efficient utilization of resources has not been realized in solar technologies. This article describes the research on proper utilization of solar technology and measures, search on the application potentials of solar resource in Chongqing area based on the geographic location and climate features in the area so as to strive to realize efficient utilization of solar resource at low cost and take the opportunity that Chongqing has been approved as "nation-wide demonstration city in the application of renewable energy resources in buildings" to effectively solve the expansion of the application of renewable energy and proper application of resources in Chongqing area to realize wider scope of building energy conservation.

2. Analysis of solar resource in Chongqing area

2.1 Briefing of solar resource in Chongqing area

Chongqing area is located in northern altitude 28°10′ - 32°13′, east longitude 105°11′-110°11′, with sea level elevation of 259.1m, and administrative area of 82,400km^2. Climate in the area belongs to typical climate extremely hot in summer and extremely cold in winter. In the hot summer, daily maximum temperature in July is above 35°C in average and the maximum air temperature can be as high as 43°C. In the cold and wet winter, annual mean temperature is about 18°C. Weather is cloudy and foggy (Annual mean foggy day is 104 days) (Ding, et al. 2007).

According to solar resource zoning in China, solar resource in Chongqing area belongs to Category 4 area – poor solar resource area. Annual total solar radiation in the area is equivalent to the cities of Tokyo, London, Paris, Hamburger, and Moscow (Wei, 2007). However, the utilization extent of solar resource is not as wide as these cities. Therefore, utilization quality of resource is not totally determined by its size. As long as proper technological measures are taken, limited size of resources can find abundant applications. Table 1 lists solar technologies used in areas having similar solar resource as Chongqing area. Comparatively speaking, application of solar resource in Chongqing area can only be found in solar water heater in some places. Application in other areas is rarely seen. How big the utilization potential of solar resource is and how the benefit brought up by its utilization is in Chongqing area will determine the promotion direction and technical guide of the application of solar resource in Chongqing area. This research work has analyzed the utilization potential of solar energy based on the distribution status of solar resource and made a comparative study and measurement analysis for multi-types of solar energy applications.

Area	Annual total solar radiation /MJ/m^2	Examples of solar energy application	Solar technology used
Tokyo	4220	Hotel Monterey Ginza	External sunshade technology of building
London	3640	London Tower	Natural lighting technology
		"Beddington Zero Energy Development" Eco-Village	Solar photoelectric technology , solar ventilation stack
Paris	4013	Signal Tower	Solar power and wind power generation
Hamburger	3430	Heating project in Hamburger area, Germany	Solar water heating system
Moscow	3520	Crystal Island	Solar photoelectric technology, solar ventilation, and cooling technology.

Table 1. Solar Technology Applications

By compilation of relevant meteorological data of "A Collection of Special Meteorological Data for Thermal Environmental Analysis on Chinese Buildings" and the websites of China Meteorological Administration, the authors analyzed the solar radiation distribution,

Sunshine duration, cloud cover, and solar altitude parameters in Chongqing area and made recommendations for the application of solar resource.

2.2 Distribution of solar radiation

Monthly total solar radiation in Chongqing area (see Figure 1) is not uniformly distributed and has significant difference. Monthly total solar radiation starts to increase from January with peak value appearing in July, about 500MJ/m^2. After that it starts to decrease with valley value appearing in December, about 100MJ/m^2. From Figure 1 it can be known that total solar radiation in January, February, October-December is in the range of 80-200MJ/m^2.

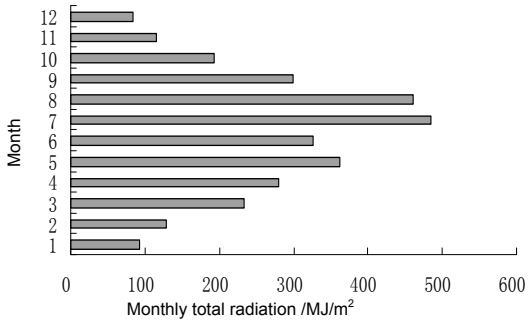

Fig. 1. Monthly total solar radiation

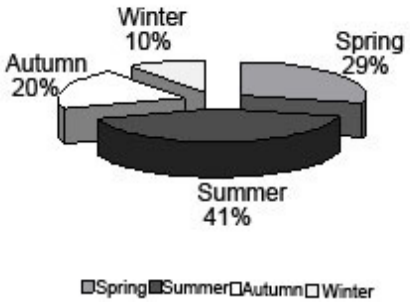

Fig. 2. Seasonal distribution of solar radiation

Solar resource is relatively poor in these months, which go against the application of solar technologies. Assume that the compact solar water heater installed has a collector area of 3m^2 (assuming annual mean heat collection efficiency of the collector is 0.5, installed angle of tilt is θ=33°-42°, heat loss of storage tank and pipeline is 0.25, and same below), when solar fraction is 40% (Zheng , 2006), if water with initial temperature of 15°C is heated to 60°C, then hot water produced each day is 12.9-32.2L/person (based on a 3-member family, same below), which is unable to meet the maximum daily hot water consumption quota "40-

80L/person" (Zheng , 2006; Wang, 2007; Shi 2008) as specified in the standard. However, in the period of May to September, solar radiation is over 300MJ/m², for water heater with collector area of 3m², 60°C hot water produced can be maintained at over 48L/person every day. Therefore, there will be at least 5 months in Chongqing area in which solar resource can be utilized to meet the requirement of domestic hot water. However, due to the significant periodicity of solar resource distribution, the application should be based on the time period and the object.

From figure 2 it can be seen that the fraction of solar radiation in summer is the highest in the four seasons of Chongqing area, about 1270MJ/m², about 41% of the total solar radiation of the year. This is the best period for solar thermal, solar photoelectric and solar ventilation and cooling applications. For a 3m² compact water heater, 60°C domestic hot water produced every day can be over 68.8L/person, well meeting the requirement of "40-80L/person" as specified in the standard. However, on the other hand, the high solar radiation will increase the heat receiving capacity of solar radiation for the buildings causing increase of air conditioning load. At this moment, if proper sun-shade technology and auxiliary solar assisted ventilation technology is used, not only the solar radiation heat receiving capacity of building envelope can be reduced, also energy consumption of building can decreased. In the transition season, average outdoor air temperature is in the range of 14~24°C. The climate is comfortable for people. If solar assisted ventilation is utilized in this period, not only the time for air conditioning operation can be reduced effectively, also fresh air can be supplied in the room improving indoor comfort.

2.3 Sunshine duration and monthly mean total cloud cover

From figure 3 it can be seen Sunshine duration in Chongqing area is longest on Summer Solstice (June 22), about 14h and is shortest on Winter Solstice (December 22), about 10h, with difference between the two of 4h, or theoretically speaking the daily Sunshine duration in Chongqing area is more than 10h. Especially in the late spring and early autumn and in the whole summer, there is sunshine for over half of the time of a day. Even in winter, Sunshine duration is also about 10h. However, the actual application of solar energy is affected by cloud cover. In cloudy days, solar radiation scattering only about 1/5 of the total solar radiation can reach to the ground. This part of scattered radiation can only be utilized by photoelectric transducer made of semiconductor material. Therefore, the quantity of cloud cover has direct influence on the selection and efficiency of solar energy utilization technologies. Figure 4 shows the monthly mean total cloud cover of several cities. It can be known from the figure that the annual mean total cloud over in Chongqing area is 78%, far more than the 54 % in Lanzhou, the 45% in Beijing, and the 48% in Urumqi, which is very disadvantageous to the yea-round utilization of solar resource. However, viewing from the seasons, cloud cover is the highest in winter, averaged at 85%, and is lowest in summer, averaged at 69%. Especially in July and August in summer, the cloud cover is significantly reduced, almost equivalent to that of Lanzhou City. Although cloud cover in Chongqing is high in Chongqing area, the long Sunshine duration of the whole year provides possibility for day lighting design of buildings. For solar thermal conversion and solar photoelectric conversion, the best season is summer, while spring and autumn take the second place.

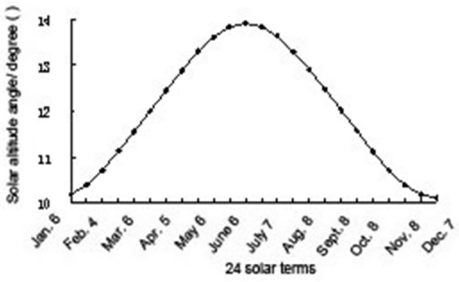

Fig. 3. Sunshine duration

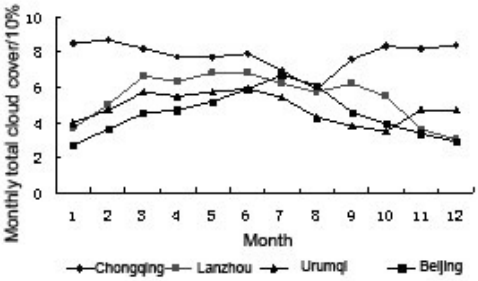

Fig. 4. Monthly mean total cloud cover of several cities

2.4 Solar elevation angle

Solar elevation angle reflects quantity of solar energy absorbed on the ground in unit time. The higher the elevation angle, more solar energy will be absorbed on the earth surface. Figure 5 shows the distribution law of Solar elevation angle in Chongqing area at noon for the 24 solar terms. It can be known from the figure, the maximum value of solar altitude appears in summer at about 65°~77°. At this moment solar energy absorbed by earth surface is the highest. Considering the analysis on the utilization period of time described previously, the angle of inclination of solar water heater or solar photovoltaic board ought to be set in the range of 13°~25° so that maximum conversion and utilization of solar energy can be realized. This is more advantageous to improve solar energy absorption and the efficiency of conversion device as compared with the normal practice of setting the angle of inclination as the local attitude of (28°~32°). For passive control and regulation, if the angle of exterior shading of building is properly designed, solar radiation entering the rooms in summer can be effectively reduced to reduce energy consumption of air conditioners. In winter in which Solar elevation angle is the lowest, at about 35°~50°, it is not advantageous for the efficient utilization of solar water heaters and solar photovoltaic board due to the high cloud cover in Chongqing area. Then passive application can be improved as possible, for example, day lighting, etc. For combined utilization in summer and winter, the "utilization" and "control" of solar energy should be improved. The exterior windows of buildings in Chongqing area is suitable for installation of movable and controllable exterior sunshade for the convenience of adjustment of out-extended length, angle of exterior sunshade to meet different sunshade and day lighting requirement.

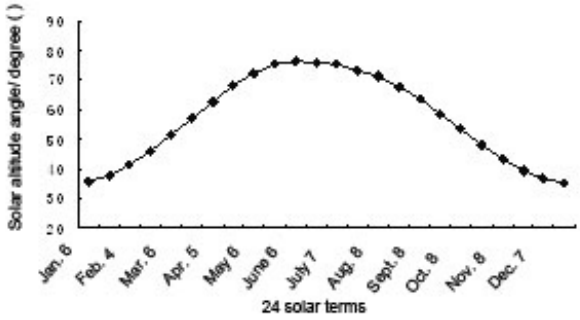

Fig. 5. Solar elevation angle at 12:00 sharp in Chongqing area

3. Potential for the application of solar resource in buildings in chongqing area

3.1 Sunshine duration and monthly mean total cloud cover

Comparatively speaking, solar water heater technology is mature. Photoelectric conversion has high efficiency and develops rapidly. They are mainly used to provide medium temperature warm water for shower bath and domestic hot water. Some applications can be found in Fengjie, Wulong, Changshou, and Wuxi areas. It can be known from analytical calculation, for the same compact panel type solar water heater system with collector area of 3.0m^2, 60℃ hot water that can be produced every day in the four seasons is 47.3L/person, 68.8L/person, 32.9L/person, and 16.5L/person respectively. The standard for Water Quality for Urban Residential Use requirement of 40-80L/person is well met in spring and summer. The standard can also be met in autumn and winter if auxiliary heating system is used. In the aspects of economy and environment, although initial investment is higher than electric or gas water heaters with cost per square meters (based on collector area) about 1500 RMB, the running costs is less, per square meter of collector can save electric power 700~800kWh, save standard coal 500kg, and what more is that it has no fume, SO_2, NO_x, and CO_2 exhaust emission and has little amount of maintenance, with service life as long as over 10 years (Wei, et al, 2007). With the improvement of peoples' living standard and the improvement of solar water heater technology, the application of solar water heater system in Chongqing area will further expanded.

For solar photoelectric system, since it is often cloudy in the whole year and the rainy season is long in Chongqing area, solar resource is characterized by typical non-uniform distribution. In addition, solar photovoltaic board has very low efficiency in overcast and rainy days, low light level, and high temperature conditions. This made the solar photoelectric system unable to be efficiently utilized in the whole year. Also initial investment of solar photoelectric system is relatively high. Therefore, the application of solar photoelectric system is tentatively not available with good economy.

3.2 Sunshine duration and monthly mean total cloud cover

It is cloudy in the whole year in Chongqing area. Rainy season is long. Sunshine duration is long. The time period in which solar radiation is high in fine day is mainly concentrated in

summer. Therefore, utilization of solar energy in summer must take protection and control into account. Typical practice is to arrange proper sunshade facility in the design of buildings. Especially in the low latitude Chongqing area and buildings having large area of glass panel wall, sun-shading technology can play the role of shading and heat insulation and reducing the load of air conditioners in summer. In the overcast ad rainy days or foggy days in other seasons, indoor day lighting will be utilized as much as possible to reduce artificial lighting, improve indoor light environment, and provide natural, gentle, and mild light comfortable sensation. The author demonstrated with experimental test that provision of interior sunshade can reduce about 17% of energy consumption for air conditioning. Other domestic and abroad study also indicated that window sunshade can save about 10%-24% energy while construction investment used in sunshade is less than 2% (Shi, 2008; Cao, et al,2006; Athienitis & zempelikos, 2002). Therefore, suitable sunshade and day lighting has good energy saving and economy for the operation of buildings. Currently, most of the buildings in Chongqing use fixed sunshades like awning, sunshade board, or out-extended balcony. The exterior sunshades in different orientations are basically the same in type and size, which are not provided based on the sunlight condition, causing poor climate adaptability. For this, the authors carried out research work on the effect of movable exterior sunshades of buildings.

3.2.1 Model experiment and test

The authors mimicked a physical model using wood boards according to similarity principle (Song, et al, 2003). The model is sized as 1.6 (L) x 1.5 (W) x 1.0m (H). Figure 6 is a schematic diagram of the test room model. In the experiment, rooms with three types of orientation of southeast, south, and southwest were provided. Test research has been made on the effectiveness of exterior sunshades with out-extending length of 0, 0.3, 0.6, and 1.2m for rooms having different orientation. The experimental tests were made in typical summer condition in Chongqing area. In the test period, weather was sunny with less cloud cover, damp, and hot. Maximum outdoor air temperature was 39.7°C with severe solar radiation. The test points for parameters were determined as shown in Figure 7 according to standard GBT 5699-2008 – Method of Day Lighting Measurement.

3.2.2 Analysis of test results

A. Horizontal exterior sunshade in southeast orientation

Figure 8 shows the variation curve of indoor average solar radiation intensity under horizontal exterior sunshades of different out-extended lengths in the southeast orientation and the variation curve of solar radiation intensity on vertical wall in the southeast orientation. It can be seen from analysis of the figure that indoor average solar radiation is the highest and has severe variation in the period of 8:00-10:00 in the morning. In the period of 10:00-16:00, indoor average solar radiation reduces gradually with the variation of outdoor solar radiation. However, the variation is very smooth, in the range of 8.1-23.2W/m^2. At 10:00, the indoor average solar radiation intensity is relatively high without sunshade provided, at about 139.5W/m^2 while at the moment, the indoor average solar radiation intensity having sunshade provided is significantly lower. When out-extending length of sunshade is at the level of 0.3m, indoor average solar radiation intensity is about 35.2W/m^2, reduced by about 104.3W/m^2 as compared with that having no sunshade provided. This indicates that the provision of horizontal exterior sunshade has effectively

kept out direct solar radiation entering into the room from exterior window, thus able to reduce indoor solar radiation heat.

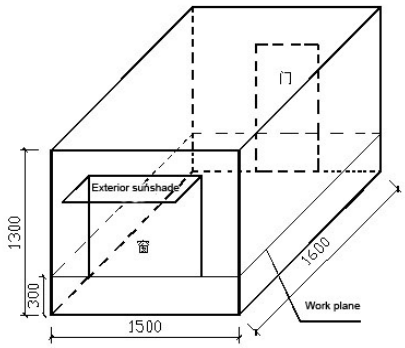

Fig. 6. Schematic diagram of test room model

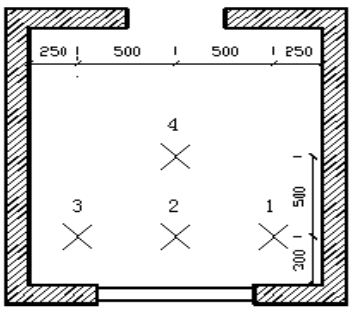

Fig. 7. Test points of indoor sola radiation intensity

Time period	Indoor average solar radiation intensity with horizontal exterior sunshade with different out-extended length/ (W/m²)					Reduction amplitude of indoor solar radiation as compared with no sunshade provided / %			
	0.0m	0.3m	0.6m	0.9m	1.2m	0.3m	0.6m	0.9m	1.2m
8:00-10:00	134.6	79.1	65.6	57.9	53.3	41.2	51.2	57	60.4
10:00-16:00	17.1	14.9	12.9	11.3	10.2	12.9	24.6	33.9	40.4

Table 2. Regulation and control effect of horizontal exterior sunshade in southeast orientation

Table 2 lists the regulation and control effect of horizontal exterior sunshades with different out-extended lengths in southeast orientation on the indoor solar radiation intensity. It can be found by comparison of the data in the table that in the time period of 8:00-10:00, the solar radiation intensity received by the vertical wall in the southeast orientation is the highest. At this moment, the regulation and control effect of horizontal exterior sunshade is relatively significant, maximum indoor solar radiation reduction is as high as 60.4% as compared with the situation without sunshades. While in the time period of 10:00-16:00,

indoor average solar radiation intensity has not much difference, indoor solar radiation reduction amplitude as compared without sunshade is 2.2W/m², 4.2W/m², 5.8W/m², and 6.9W/m² respectively, reduction amplitude is not as high as that in the time period of 8:00-10:00. This indicates that when horizontal exterior sunshade are provided in the southeast orientation, the best regulation and control time can be selected in the period of 8:00-10:00.

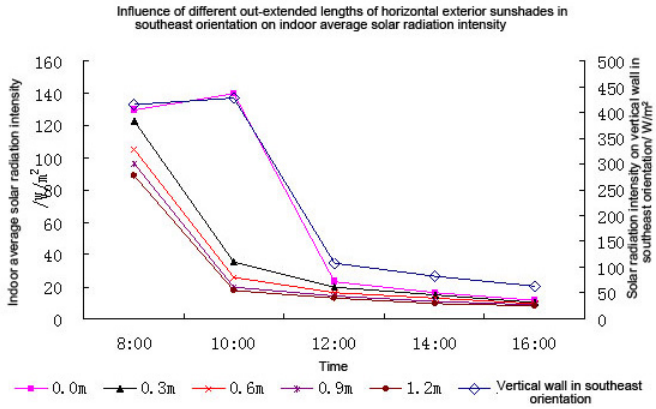

Fig. 8. Influence of horizontal exterior sunshade on indoor average solar radiation in southeast orientation

B. Horizontal exterior sunshade in south orientation

Figure 9 shows variation curve of indoor average solar radiation intensity with horizontal exterior sunshades having different out-extended lengths in the south orientation and the variation curve of solar radiation intensity on vertical wall in the south orientation. Form the figure it can be known indoor average solar radiation intensity reaches peak value 264.9W/m² at 12:00 noon and the variation curve is of single peak type. Indoor solar radiation intensity in the whole day with no sunshade provide is in the range of 12.5-26.2W/m², with maximum value appearing at 12:00, about 26.2W/m². While with sunshade provided, indoor average solar radiation intensity is significantly reduced. It can be known by the analysis of data, when horizontal exterior sunshade in the south orientation has an out-extended length of 1.2m, the whole day solar radiation reduction can be as high as 40.6% max. as compared with that of with other three out-extended lengths of sunshade, indicating that the longer the out-extended length of horizontal sunshade facility is, the better the sunshade effect will be.

C. Horizontal exterior sunshade in southwest orientation

Figure 10 shows variation curve of indoor average solar radiation intensity with different out-extended lengths of horizontal exterior sunshades and the variation curve of solar radiation intensity on the vertical wall in the southwest orientation. It can be known from the figure that in the time period of 14:00-16:00 in the afternoon, indoor average solar radiation reaches the maximum value in the whole day, in the range of 17.8-146.5W/m², and the indoor average solar radiation has severe variation. While in the time period of 8:00-14:00 in the morning and at noon, indoor average solar radiation rises gradually and the variation is very smooth in the range of 4.0-23.2W/m², regardless how the outdoor solar radiation varies.

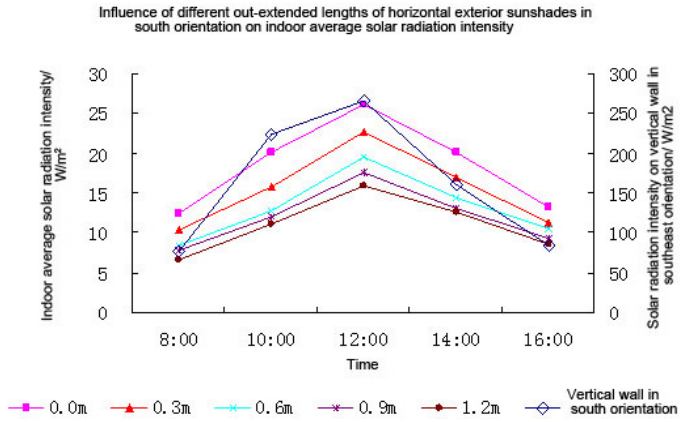

Fig. 9. Influence of horizontal exterior sunshade in south orientation on indoor average solar radiation

Time period	Indoor average solar radiation intensity at different out-extended lengths of horizontal exterior sunshades / W/m²					Reduction amplitude pf indoor solar radiation as compared with that without sunshade provided			
	0.0m	0.3m	0.6m	0.9m	1.2m	0.3m	0.6m	0.9m	1.2m
10:00-14:00	22.1	18.4	15.5	14.1	13.2	16.7	29.9	36.2	40.3
8:00-10:00 14:00-16:00	12.8	10.8	9.4	8.6	7.6	15.6	26.6	32.8	40.6

Table 3. Comparison of regulation and control effect of horizontal exterior sunshade in south orientation

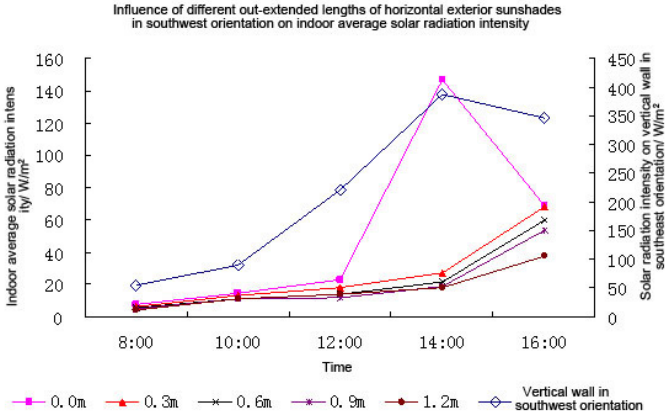

Fig. 10. Influence of horizontal exterior sunshade in southwest orientation on indoor average solar radiation

At 14:00, the measured indoor average solar radiation reaches the maximum value 146.5W/m² without sunshade provided. While at this moment, the indoor average solar radiation intensity is significantly reduced with sunshade provided. When out-extended length of horizontal exterior sunshade is at 0.3m, indoor average solar radiation is significantly reduced to 27.0W/m², reduced by about 119.5W/m² as compared without sunshade provided. In the time period of 14:00-16:00, solar radiation in the southwest is very high. Regulation and control effect of horizontal exterior sunshade on indoor solar radiation intensity is high. While in the time period of 8:00-14:00, solar radiation intensity in the southwest orientation is relatively low, the regulation and control effect of horizontal exterior sunshade on indoor solar radiation is relatively weak. Table 4 lists the regulation and control effect of horizontal exterior sunshades with different out-extended lengths in southwest orientation. It can be found from the comparison of data in the table that in the time period of 14:00-16:00, solar radiation intensity received by vertical wall in the southwest orientation is the highest. At this moment the regulation and control effect of horizontal exterior sunshade is very significant. Indoor solar radiation reduction amplitude is 55.8%, 62.2%, 66.5%, and 74.4% respectively as compared with that without sunshade provided. While in the time period of 8:00-14:00, indoor average solar radiation intensity has not much difference, indoor solar radiation reduction amplitude as compared without sunshade is 1.3 W/ m², 2.6 W/ m², 3.2 W/ m² and 3.5 W/ m² respectively, Reduction amplitude of indoor solar radiation is very small as compared with in the time period of 14:00-16:00, reduced by 11.8%, 23.6%, 27.3%, and 30.0% respectively.

Time period	Indoor average solar radiation intensity at different out-extended lengths of horizontal exterior sunshades / W/m²					Reduction amplitude of solar radiation as compared with no sunshade provided / %			
	0.0m	0.3m	0.6m	0.9m	1.2m	0.3m	0.6m	0.9m	1.2m
14:00-16:00	107.8	47.7	40.7	36.1	27.6	55.8	62.2	66.5	74.4
8:00-14:00	11.0	9.7	8.4	8.0	7.7	11.8	23.6	27.3	30.0

Table 4. Comparison of regulation and control effect of horizontal exterior sunshade in southwest orientation

This indicates that provision of horizontal exterior sunshade can effectively prevent direct solar radiation from entering the room from exterior window to reduce indoor solar radiation heat. When horizontal exterior sunshade is provided in the southwest orientation, the best time period for regulation and control is in the range of 14:00-16:00, at which time indoor solar radiation intensity can be effectively reduced, hence the indoor solar radiation heat. Therefore, sunshade effect is very significant when horizontal exterior sunshade is provided in southwest orientation and the best regulation and control time is in the range of 14:00-16:00.

3.3 Solar assisted ventilation technology

Chongqing area prevails over north-northern wind (NNW) in the whole year. It is in slight and gentle breeze area throughout the year and belongs to wind resource deficient zone. However, there is abundant of Summer Wind. Summer is extremely hot and full of sunny days. Solar radiation intensity is high and Sunshine duration is long. The scope of application

of solar assisted ventilation technology can be extended by utilizing this distribution feature of summer wind power resource and indoor ventilation can be organized and improved.

3.3.1 Examples of application and test

The research group designed and constructed a solar assisted ventilation system in a certain energy-saving demonstration building as shown in Figure 11. The main members of solar assisted ventilation system were tested and measured in a typical summer day in Chongqing area in July, 2009. The main member of the solar assisted ventilation system is the "sunlight well" on the exterior façade in the southwest orientation of the building. The "sunlight well" is sized as LxWxH=850x700x9000mm, consisting of two pieces of glass. Each corresponding floor in the "sunlight well" is provided with exterior windows opened to the "sunlight well".

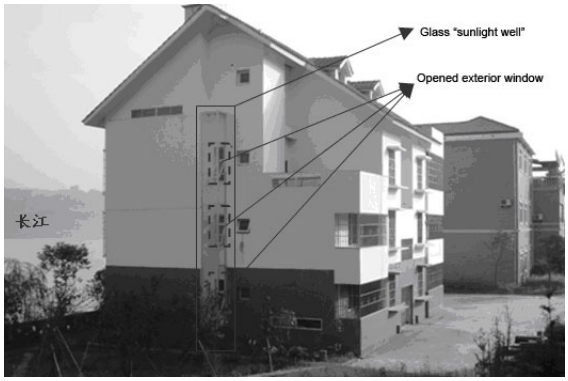

Fig. 11. Solar assisted ventilation system in an energy-saving demonstration building

In order to reflect the effect of thermal pressure ventilation, floor 2 and floor 3 were selected as the test floors. In the living rooms directly connected to the "sunlight well", test and measuring points were arranged according to the test point arrangement requirement of standard GBT 18204.13-2000 "Methods for Determination of Air Temperature in Public Places" and GBT 18204.15-2000 "Methods for Determination of Wind Speed in Public Places". The tri-section points on the diagonal lines in the living room were taken as the humidity and wind speed measuring points. These points are all 1.5m above the floor. During the test, the exterior windows of the ground floor facing the "sunlight well" were closed.

3.3.2 Analysis of test results

A. Temperature analysis

Since the "sunlight well" faces to southwest, it was subjected to most severe solar radiation in the afternoon. It can be seen from figure 15 that in the time period of 8:00-12:00, the temperature in the "sunlight well" on floor 2 is slightly lower than that on floor 3 with average temperature difference about 0.3°C and maximum temperature difference as high as 0.5°C. While in the time period of 12:00-18:00, temperature in the "sunlight well" on floor

2 is significantly lower than that on floor 3 with average temperature difference about 0.9°C and maximum temperature difference as high as 2.3°C. It can be seen from this that under the action of solar radiation heat, the air inside and outside the "sunlight well" has a density difference that causes the air flow to form a "chimney effect" producing extraction or suction action, thus guiding the indoor air to flow into the "sunlight well" from the open exterior windows and exhaust into the air from top of the "sunlight well." At the same time fresh air is led into the room forming natural ventilation in the room. Especially the average temperature difference in the "sunlight well" between floor 2 and floor 3 increases by 3 times in the afternoon compared with it in the morning.

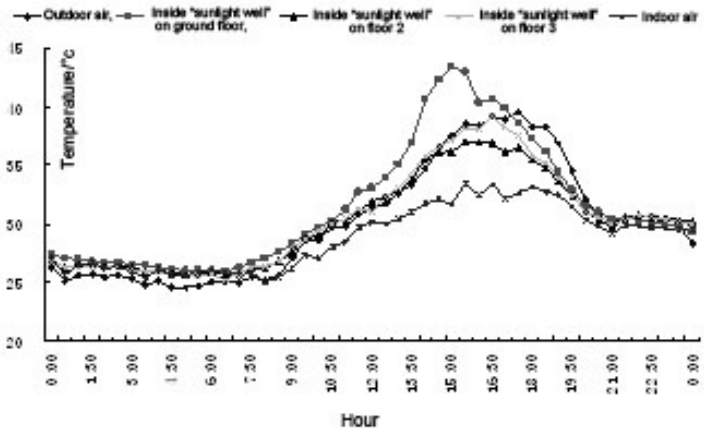

Fig. 12. Variation curves of wind speed in the "sunlight well" and at the exterior windows

It can be seen by analyzing the data in Figure 16 that both temperature in the "sunlight well" and the outdoor temperature is higher than the indoor temperature. During test, the average outdoor temperature was 33.5°C. The average temperature in the "sunlight well" on floor 2 and floor 3 were 32.7°C and 33.3°C respectively. While the average indoor temperature on floor 2 and floor 3 were 30.1°C and 29.9°C respectively. That is to say, the average outdoor temperature was about 3.4°C~3.6°C higher than average indoor temperature. The average temperature in the "sunlight well" was 2.6°C~3.4°C higher than the average indoor temperature. It can be obtained from thermal pressure ventilation calculation formula that the pressure difference that can be formed inside and outside the room is 0.46Pa-0.62Pa. It can be seen from this that the pressure difference formed by the "chimney effect" of "sunlight well", leading to indoor ventilation. Study shows that increase of indoor air speed increases the upper limit of acceptable indoor temperature to about 30°C, which is 2°C higher than the 28°C upper limit of the summer indoor design temperature in the design specification. To sum up, though the outdoor temperature was relatively high in the afternoon during the test and the maximum temperature was as high as 39.6C, the chimney effect of "sunlight well" enhanced the indoor ventilation effect keeping the average indoor temperature of floor 2 and floor 3 still within acceptable range. Thus the operation time of air conditioners can be significantly reduced to realize the goal of energy-saving and consumption reduction.

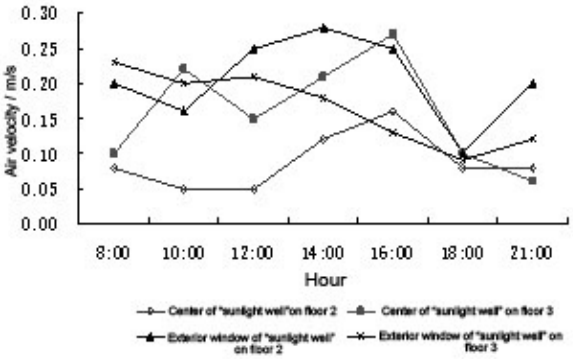

Fig. 13. Variation of temperature in the "sunlight well" and outdoor temperature

B. Air velocity analysis

Figure 16 and Figure 17 show the variation curves of air velocity in the center and at exterior windows of "sunlight well", in the living room and at double-acting doors. It can be seen from the figures that in the time period of 9:00-12:00, air velocity of the measuring points is very smooth and has little fluctuation. At 12:00 noon when solar radiation reaches it maximum, or about 790W/m², air velocity of the measuring points starts to rise up. In the afternoon when solar radiation received is the highest and the "chimney effect" formed is most powerful, air velocity of the measuring points reaches its maximum value especially at the double-acting doors, except the indoor air velocity on floor 3 and the air velocity at the inlet of "sunlight well" on floor 3. After sunset in the evening, air velocity of the measuring points decreases gradually and fluctuates smoothly. It can be seen from this that the "sunlight well" has made full use of solar radiation in the day playing the role of good indoor ventilation.

Under the condition that the interior cross section of "sunlight well" on floor 2 and floor 3 and the air intake area of the exterior windows opened are the same respectively, the average indoor air velocity on floor 2 is 0.15m/s in the morning and 0.22m/s in the afternoon with increase amplitude of 40%. The average air velocity at the double-acting doors on floor 2 is 0.46m/s in the morning and 0.60m/s in the afternoon, with increase amplitude of 30%. The average indoor air velocity on floor 3 is 0.14m/s in the morning and 0.16m/s in the afternoon with increase amplitude of 14%, the average air velocity at the double-acting doors on floor 3 is 0.39m/s in the morning and 0.56m/s in the afternoon, with increase amplitude about 44%. It can be seen from this that with solar assisted ventilation measures, air velocity of indoor ventilation is significantly increased with increase amplitude as high as 14%-40%, thus indoor thermal condition and air quality are improved significantly. Investment of this technology is low. Auxiliary equipment will no affect the appearance design of buildings. In addition, the prevailing wind direction in summer in Chongqing area can be considered to form good wind environment for the buildings for the benefit of applications of solar assisted ventilation and cooling technology to obtain enhanced indoor natural ventilation effect.

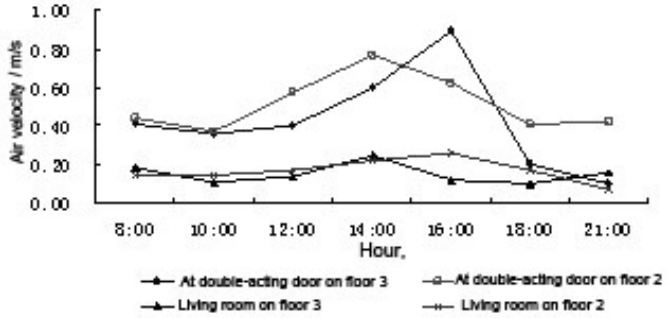

Fig. 14. Variation curves of air velocity in the house and at double-acting doors

4. Conclusion

It can be seen from the analysis of solar resource and by taking the climate features in Chongqing area into account that:

1. The use of solar resource in spring and summer in solar photo-thermal system in Chongqing can well meet the demand of domestic hot water by a three-member family. Although such demand cannot be sufficiently met in autumn and winter, remedy can be made by taking auxiliary heating measures. Solar photo-thermal system having good economic and environmental benefit, it will obtain further development with the increase of demand.
2. In the extremely hot summer, provision of horizontal exterior sunshades for the exterior windows of building in different orientations has significant effect of reducing the solar radiation intensity entering the houses from exterior windows. In addition, there exists the best regulation and control time period enabling the horizontal exterior sunshades to play the best role of control. however, in other seasons, much natural light should be let entering the house for the benefit of building lighting. Therefore provision of sunshade facility should take the use demand in summer and winter into account.
3. Solar assisted ventilation technology can effectively reduce indoor temperature in summer and increaseindoor air velocity so that acceptable indoor temperature can be increased to 30℃ to reduce Air conditioning operation time and the load of air conditioners and improve indoor thermal comfort.

In summary, although solar resource in Chongqing area is congenitally deficient, technical measures for the application of solar energy can be integrated with buildings so that solar resource in the deficient area can be utilized to its maximum in the proper time period and for proper objects through the above described technical measures.

5. References

Ling Wei. (2007). Technical and Economic Analysis of Solar Refrigeration and Solar Water Heating System in Chongqing [J]. China Science & Technology Information. No.11, (November 2007), pp 33-34. ISSN 1001-8972

http://paper.people.com.cn/zgnyb/html/2009-11/30/content_393907.htm, 2009-11-30.
http://bbs.tiexue.net/post_1683290_1.html, 2006-12-20.
Shijun You, Hejiang Sun, Degang Ma, Hongxing Yang. (2002). Solar Energy Resource and Application Potential in China [J]. Urban Environment & Urban Ecology, Vol.15, No.2, (April 2002), pp. 57-59, ISSN 1002-1264
Bingzhong Wang. (1983). Solar Energy Resource Division in China [J], Acta Energiae Solaris Sinica, Vol.4, No.3, (March 1983), pp. 221-228. ISSN 0254-0096
Xiuli Wei, Lihong Gao, Yanghua Gao, Ping Li, Jin Xu. (2008). Assessment on Solar Photo-Thermal Utilization in the Country Area of Chongqing [J], South China Agriculture. Vol.2, No.7, (April 2008), pp. 14-16. ISSN 1673-890X
Yong Ding, Baizhan Li, Qing Luo, Hong Liu. (2007). The Role of Natural Resources in the Improvement of Indoor Hot and Humid Conditions in Chongqing [J], Journal of Chongqing University(Natural Science Edition). Vol.30, No.9, (September 2007), pp. 127-133. ISSN 1000-582X
http://cdc.cma.gov.cn/shishi/climate.jsp?stprovid= Chongqing, China Meteorological Administration
Ministry of Construction of People's Republic of China, (2002), GB/T 50331-2002. The Standard for Water Quality for Urban Residential Use, China Architecture & Building Press, ISBN 1511211985, Beijing
Chongjie Wang, Yibing Xue. (2007). Design of Solar Buildings, China Architecture & Building Press, ISBN 9787112091249, Beijing.
Ruicheng Zheng. (2006). Technical Manual of Solar Water Heating System Engineering for Civil Buildings(First edition), Chemical Industry Press, ISBN 7-5025-7719-X, Beijing
Dan Shi, Study on Designing Optimized about Window External Shade Device of Resident Building [D], Chongqing, Master thesis of Chongqing University, 2008.
Guoqing Cao, Guangbei Tu, Bin Yang. (2006). Study of Optimum Horizontal Shading Device Dimensions for Energy Saving in Residential Buildings. Acta Energiae Solaris Sinica. Vol.27, No.1, (Jan 2006), pp.96-100, ISSN 0254-0096
A.K.Athienitis, and A.Tzempelikos. (2002). A methodology for simulation of daylight room illuminance distribution and light dimming for a room with a controlled shading device. solar energy. Vol.72, No.4, (April 2002), pp.271-281, ISSN 1003-0417
Huo Song, Guiwen Zhang, Xinghai Dang, et al. (2003). Specialties analysis of similar model and reduced-scale model. Journal of Architectural Education in Institutions of Higher Learning.Vol.12, No.4, (September 2003), pp.57-58, ISSN 1005-2909

3

Evaluation of Solar Spectra and Their Effects on Radiative Transfer and Climate Simulation

Zhian Sun[1], Jiangnan Li[2] and Jingmiao Liu[3]
[1]*Centre for Australian Weather and Climate Research, Australian Bureau of Meteorology*
[2]*Canadian Centre for Climate Modelling and Analysis, Science and Technology Branch, Environment Canada, University of Victoria*
[3]*Chinese Academy of Meteorological Sciences*
[1]*Australia*
[2]*Canada*
[3]*China*

1. Introduction

In this chapter we will discuss solar spectral distributions and their corresponding impact on the climate, especially on the Earth's atmospheric temperature and energy balance at the surface. Solar spectrum is defined as a spectral distribution of the solar radiation at the top of the atmosphere (TOA). It represents the incoming solar energy to the earth system containing the atmosphere and ocean. Solar radiation is the original driving force for the continuous circulations of atmosphere and ocean. It has been recognized that the variation of total solar irradiance (solar constant) at the TOA is one of the important factors impacting climate change, though the variation in total solar irradiance is very small, approximately only about 0.1% of the solar constant or about 1.3 W m^{-2} (Krivova *et al*, 2010). Besides the variation of the total solar irradiance the changes in the spectral distribution of the solar radiation can also affect the climate. However much less attention has been focused on this aspect.

The solar radiation at different wavelengths penetrates Earth's atmosphere to different depths. The high energy ultraviolet (UV) radiation is mostly absorbed by ozone in the mesosphere and stratosphere. The atmosphere is relatively transparent to the visible (VIS) radiation and allows most visible radiation to reach the earth's surface and heat the land and ocean surfaces. The atmosphere has strong absorption in the near infrared (NIR) radiation mainly due to the water vapor in the lower troposphere. Therefore, different solar spectral distributions at the TOA can affect the temperature structure in the atmosphere and the energy balance at the surface, and hence impact the weather and climate.

In this chapter, the most commonly used solar spectra will be summarized and their characteristics compared. These solar spectra will be applied to off-line radiation calculations and climate model simulations to quantify the impact on climate.

2. Measurement of the solar spectrum

Since the 1970s, the measurement of the solar spectral distribution at the TOA has become an important issue for climate modeling. Since then several solar spectra have been proposed and widely used. The solar spectrum can be measured at the earth's surface and on space platforms or estimated using proxy indicators such as sunspot and faculae. Before satellite measurements of the solar spectrum became available, the data were mainly from ground-based measurements and laboratory experiments. Since the historical time series of the solar spectrum is required for long-term climate simulations and the data from observations are not long enough for this purpose, reconstruction of the solar spectral time series using empirical regression is inevitable. The most commonly used solar spectrum in the early period was that provided by Neckel and Labs (1984) which was derived from long-term observations of the absolute solar intensity measured at Kitt Peak Observatory and from aircraft measurements. This solar spectrum became the reference and was used by many science communities such as radiation model groups and the remote sensing community. We refer to this solar spectrum as Neckel-Labs in the following discussions.

The second solar spectrum commonly used in the scientific community is that developed by Kurucz (1995) based on measurements at Kitt Peak Observatory and balloon-based measurements. This is a synthetic solar spectrum derived by a combination of measurements and a theoretical model. The development of this spectrum was motivated by research work performed by Gao and Green (1995) who found that the standard spectrum from Neckel-Labs contains many absorption features in the 2.0-2.5 μm region that cannot be seen in the observations from shuttle-borne instruments. These absorption features have been corrected in the refined Kurucz spectrum. We refer to this solar spectrum as Kurucz95. The advantage of the Kurucz95 spectrum is its high spectral resolution ($\sim$1 cm^{-1}) which is required by certain research applications, such as offline studies with line-by-line radiative transfer models. Since this spectrum was published it has been used by several organizations such as the UK Met Office, the US Atmospheric Environment Research and the Australian Bureau of Meteorology, etc,. The Kurucz95 spectrum was recently updated by Chance and Kurucz (2010) who corrected the absorption of solar irradiance by ozone and imported the cross-calibration with the solar spectrum measured from satellite. We refer to this updated version as Kurucz10 .

Lean (2000) provided the third solar spectrum which is a reconstruction of spectral irradiance using multi-component empirical models, based on activity indices such as sunspot and facular time series. This spectrum was updated with measurements from satellites from 1983 to 2004 covering the last two solar cycles and has been implemented into the UK Met Office atmospheric model (Zhong *et al.*, 2008). We refer to this spectrum as Lean00.

Satellites make it possible to directly measure the solar spectrum without the confounding influence of the Earth's atmosphere. In recent decades, a number of experiments have been performed on various space platforms which have resulted in the new and improved solar spectrum published by Thuillier *et al*. (2003). The spectrum provided by Thuillier were derived from two instruments flown on the European Retrieval Carrier missions. This spectrum covers the spectral range from 200 nm to 2400 nm and has been cross compared with observations from other missions (Thuillier *et al*., 2003). We combine this data with that

of the Kurucz10 for the wavelengths beyond 2400 nm to form a full spectrum. We use this solar spectrum as the standard reference spectrum.

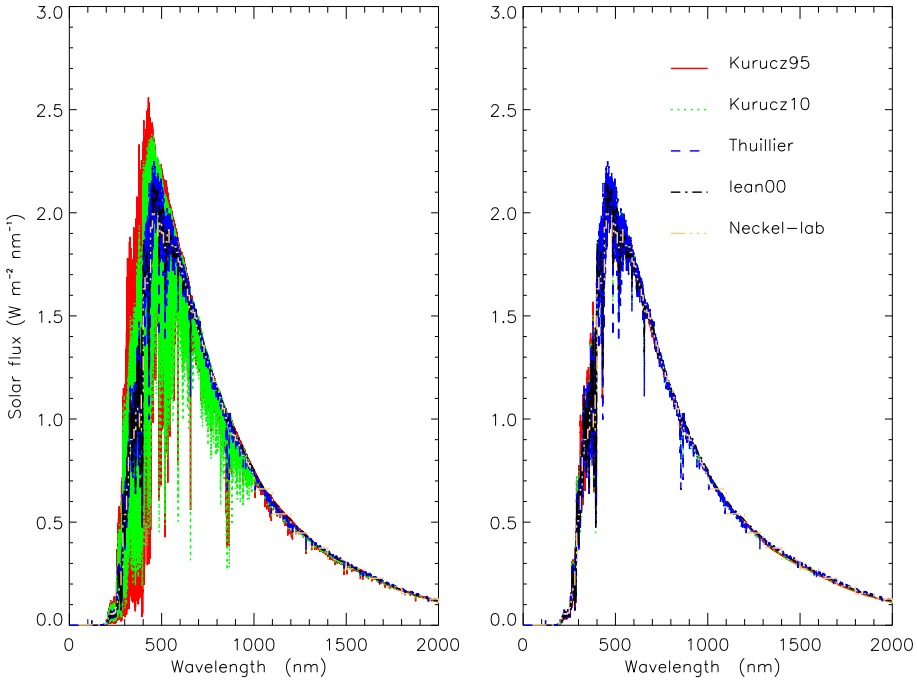

Fig. 1. Spectral distributions of solar irradiance at the top of the atmosphere. Left: plots on the original spectral grids; Right: two Kurucz spectra degraded by a moving average over 0.5 nm.

The five solar spectra mentioned above are shown in Fig.1. The major difference between these spectra is the spectral resolution. The spectral resolutions for the two Kurucz spectra are much higher than for the other three spectra and exhibit large oscillations in the spectral region 200-1000 nm. The right panel shows the two Kurucz spectra degraded by taking a moving average over the 0.5 nm spectral grids of the original spectrum. The degraded curves are relatively smooth and agree better with the other spectra. Chance and Kurucz (2010) also compared their modified spectrum with Thuillier's spectrum using a similar degradation.

It is seen that the spectral distributions of the five solar spectra are different. However, highly oscillatory spectral signatures make it hard to analyze these differences. In order to create a picture that can clearly show the spectral differences between the five solar spectra we calculate the fractional distribution of the incoming solar energy in the three solar spectral ranges of UV, VIS and NIR and the results are shown in Fig.2. The results presented in this figure have been normalized by the reference spectrum of Thuillier to explore the differences relative to the reference spectrum. It is seen that the fractions of the solar energy among the

five spectra are different in these spectral regions. These differences will result in significant differences in the radiative heating rates in the stratosphere and irradiances at the surface as will be shown in the following sections. The roles of the incoming solar energy in these three spectral regions are very different. In the UV region, the ozone absorption is dominant in the mesosphere and stratosphere and most of the solar energy is absorbed here. In the NIR range water vapor is a dominant absorber with the corresponding strong absorption occurring in the lower atmosphere. In the VIS range gaseous absorption is relatively weak allowing a large portion of the solar energy to penetrate through the atmosphere and reach the earth's surface. Therefore, different solar spectral distributions can produce different heating profiles inside the atmosphere and also influence the energy budget at the surface. These physical principles help us to understand the results of the model simulations shown in the following sections.

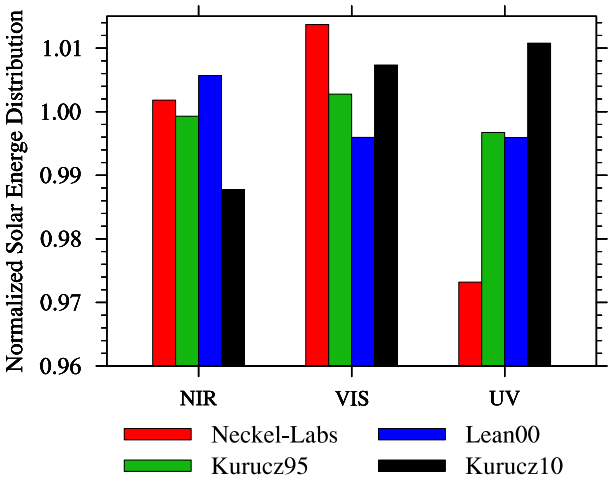

Fig. 2. The fractional distribution of solar energy over three spectral regions from 4 model spectral data. The results have been normalized by the fraction of the Thuillier reference data.

3. Radiation and climate models

In order to study the sensitivity of the different solar spectral distributions, three kinds of model will be used. The first is a high resolution line-by-line model, which is usually used as a benchmark to verify the accuracy of a radiation algorithm used in a climate model, but in this study, we use it to evaluate irradiance at the surface and the heating rate in the atmosphere determined using the different solar spectral data. With the line-by-line calculations, the detailed changes in the heating rates and irradiances corresponding to the variations of the solar spectral distributions can be revealed. The line-by-line radiative transfer model GENLN2 (Edwards, 1992) is used to perform these calculations at high spectral resolution. Version 3.0 of the GENLN2 model is used and this model has been modified to allow irradiance and heating rates calculations.

The broad-band model used in this study is the Sun-Edwards-Slingo version 2 (SES2) scheme (Sun, 2011). It has 9 spectral bands in the shortwave region, 4 bands in the UV-VIS and 5 bands

in the NIR. The 5 solar spectra have been implemented in the scheme so that their impact on radiative heating in the atmosphere can be assessed in both off-line calculations and in climate model simulations.

The Australian Community Climate Earth System Simulator (ACCESS) model is used to perform the climate sensitivity study. ACCESS is a fully coupled system developed at the Centre for Australian Weather and Climate Research. The atmospheric component is the UK Met Office Unified Model. The SES2 radiation has been implemented in ACCESS. We performed AMIP (Atmospheric Model Intercomparison Project) type simulations to assess the impact of the variation of solar spectrum on the earth's climate. The model used in this study has a horizontal resolution of 1.25° x 1.875° in latitude and longitude and 85 vertical levels. The model top height is about 85 km. The model dynamical core is a semi-implicit, semi-Lagrangian, predictor-corrector scheme solving the non-hydrostatic, deep-atmosphere equations (Davies *et al.*, 2005). In addition, the model includes a prognostic cloud fraction and condensate cloud scheme.

4. Impact of solar spectral distribution

There have been a number of studies investigating the possible impact on climate due to changes in the solar constant (e.g. Kopp and Lean, 2011), but there is a lack of systematic research on the intercomparison of those solar spectra mentioned above and the impact on climate model simulations due to the differences in these spectra. Mlawer *et al.* (2000) compared the solar spectral irradiance at the surface determined with their line-by-line model (LBLRTM) using the Neckel-Labs and Kurucz95 spectra with high spectral resolution observations obtained at the Southern Great Plains site of the US Atmospheric Radiation Measurement (ARM) program(Stokes and Schwartz, 1994). Their results suggested that Kurucz95 provides a better modelled irradiance at the surface. Zhong *et al*. (2008) compared the impact of shifting from the Neckel-Labs spectrum to the Kurucz95 and Lean00 spectra in a line-by-line radiation model and in a climate model. They found that the solar heating rate in the stratosphere generated by Kurucz95 is significantly larger than that generated by Neckel-Labs, because the larger incoming solar energy in the UV causes extra ozone absorption in the Kurucz95 spectrum. Since different climate models may use any of the solar spectra introduced above it will be useful to investigate the use of all of the spectra mentioned above and their influence on radiation and climate models, particularly in the context of AMIP style experiments. In addition, the recent satellite observation-based Thuillier spectrum was not accounted for in Zhong *et al*. (2008) and has not been evaluated in climate models. In this section, we present a comparison of the five solar spectral data, in which four of them (Neckel-Labs, Kurucz95, Kurucz10 and Lean00) have been used in AMIP style model simulations. The satellite observation-based Thuillier spectrum is used as the reference. It should be emphasized that although we use the Thuillier spectrum as a reference, it should not be regarded as the standard benchmark because the solar spectrum varies and a spectral data averaged from a longer period may be preferred. An appropriate comparison with observations may be desirable to assess the accuracy of these spectral data but this is beyond the scope of this study.

In Zhong *et al*. (2008), the related physical discussion focused on the temperature bias in the stratosphere due to changing the solar spectra. In our discussions, apart from the stratospheric

temperature issue, more attention is paid to the physics related to the changes in the lower tropospheric temperature and the surface energy balance.

4.1 Off-line radiation calculations

GENLN2 line-by-line calculations are performed using a middle latitude summer (MLS) atmosphere with 107 vertical levels to investigate the impact of the changes in solar spectrum on the solar heating rates in the atmosphere. The HITRAN2008 data base is used and 6 absorbing species (H2O, CO2, O3, CH4, N2O, O2) are included in the calculations. The water vapor continuum and oxygen collision-induced continuum are also included. The spectral resolution of 0.005 cm^{-1} and the Voigt line shape profile are used in the calculations. The solar constant is taken as 1368.8 W m^{-2}, the solar zenith angles is assumed to be 30° and the surface albedo is set to 0.2.

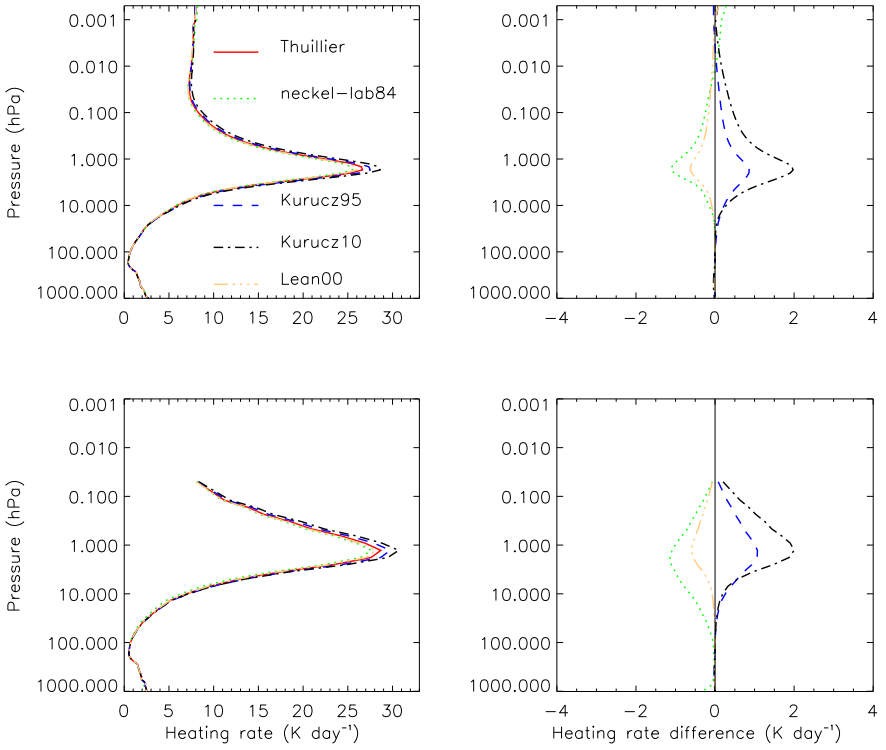

Fig. 3. Solar heating rates determined using GENLN2 line-by-line (upper panels) and SES2 broad-band (lower panels) schemes with five solar spectra. The calculations use the MLS atmosphere with a solar constant of 1368.8 W m^{-2} and a solar zenith angle of 30°. The Thuillier spectrum is treated as the reference and the left panels show the heating difference between the model spectra and this reference.

In Fig. 3, the upper left panel shows the solar heating rates calculated by GENLN2 for the five solar spectra. Taking Thuillier as the reference, the upper right panel shows the differences in heating rate between the model solar spectra and reference spectrum. It is seen that the maximum solar heating rate occurs at about 1 hPa. This is due to the absorption by ozone whose maximum concentration is close to this level. A large difference in heating rate also occurs around this region. Compared to the result from the reference spectrum, it is found that the Neckel-Labs and Lean00 spectra produce smaller heating rates, and the two Kurucz spectra produce larger heating rates. The difference in heating rate between Neckel-Labs and the reference is about -1.5 K day^{-1} and the difference in heating rate between Kurucz10 and the reference is about 2 K day^{-1} , which is about 10% of the heating rate close to 1 hPa. Since the total incoming solar energy is assumed to be the same for all five spectra, in the Neckel-Labs and Lean00 spectra, less solar energy is filtered out by ozone absorption before it reaches the lower atmosphere and ground.

The same calculations are also performed using the SES2 broad-band scheme. In the SES2 model Rayleigh scattering is included. The broad-band calculations use the MLS atmosphere with 60 vertical levels and the rest of the specifications are the same as those for the line-by-line calculations. It can be seen that the results from the broad-band calculations are very close to those of the line-by-line calculations. Since the SES2 radiation algorithm is used in the climate model calculations shown below, the results in 3 indicate that the radiation calculations in the climate model are reliable.

It is seen in Fig.2, the old solar spectrum of Neckel-Labs has the smallest solar energy input in the UV range. This is consistent with the result shown in Fig.3. The heating rate due to ozone absorption is the weakest for Neckel-Labs. It is found that the two Kurucz spectra have relatively large energy fraction in the UV spectral range. Therefore, the solar heating rates from these two spectra are larger than those from the other spectra in the ozone absorption region.

In order to verify the results of Fig.3, in Fig.4 we present the more detailed line-by-line spectral heating rates at the 1.5 hPa level, where the ozone absorption is at its peak value. Only the UV region is shown as the heating rate in other regions is essentially zero. In the upper panel the heating rates from the Kurucz10, Lean and Thuillier calculations are shown as a function of wavelength. It is seen that large heating rates occur in the Hartley band around 300 nm due to the ozone absorption there. Also large differences in heating rate are found in this region using the different solar spectra. The Lean spectrum produces the smallest heating rate and the Kurucz10 spectrum produces the largest heating rate.

Figure 2 shows that the Lean00 spectrum has the largest solar fractional input energy in the NIR region, so it is expected that the use of this spectrum would produce a larger heating rate in the lower troposphere where the water vapor absorption dominates. However, since the air density is high in the lower atmosphere, the heating rate becomes small, and the difference in heating rate is not obviously noticeable in Fig.3. Nevertheless the difference in heating rate in the lower troposphere can be more clearly found in climate simulations as shown later due to feedback effects involving water vapor.

It is also seen in Fig.2, that the two Kurucz spectra and Neckel-Labs spectrum have relatively larger solar input energy in the visible region. Since the atmosphere is relatively transparent

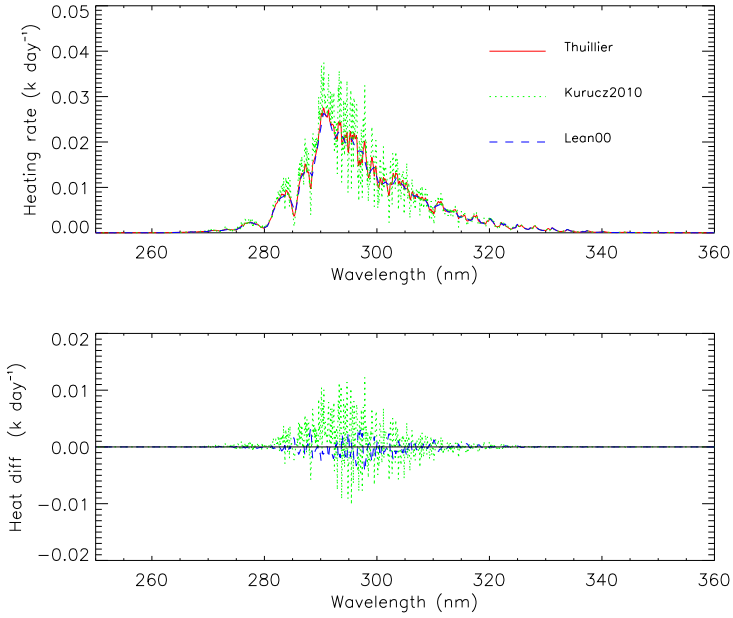

Fig. 4. Solar spectral heating rates at the 1.5 hPa level of a MLS atmosphere determined using the GENLN2 model for three solar spectra. The calculations assume a solar zenith angle of 30° and a surface albedo of 0.2. The lower panel shows the heating differences between Kurucz10, Lean00 and the reference.

in this region, the larger the input solar energy at the TOA will lead to a larger downward solar irradiance at the surface and this is demonstrated in Fig. 5.

In Fig.5, the downward solar irradiances versus solar zenith angle are plotted. The calculations are performed using the GENLN2 model. As in Fig.3, the results are determined taking the spectrum of Thuillier as the reference and the differences in the downward irradiance at the surface between the model spectra and reference are shown. The upper left panel of Fig.5 presents the differences in total downward solar irradiance at the surface. It is found that the downward solar irradiances at the surface obtained using the all four model solar spectra are higher than that using the reference spectrum. The irradiance difference between Kurucz95 and the reference is smallest and the difference between Kurucz10 and the reference is largest. At the solar zenith angle of zero, the Kurucz10 spectrum produces an extra 2 W m^{-2} solar downward irradiance at the surface compared with the result from the reference spectrum.

In order to understand the reason for the difference in the downward flux at the surface, we separate the broad band results into three spectral ranges and the corresponding results are shown in the other three panels. In the UV range (upper right panel), the downward irradiance at the surface from the Kurucz10 spectrum is higher than that from the reference spectrum, while the results from the other three spectra are less than that from the reference. It

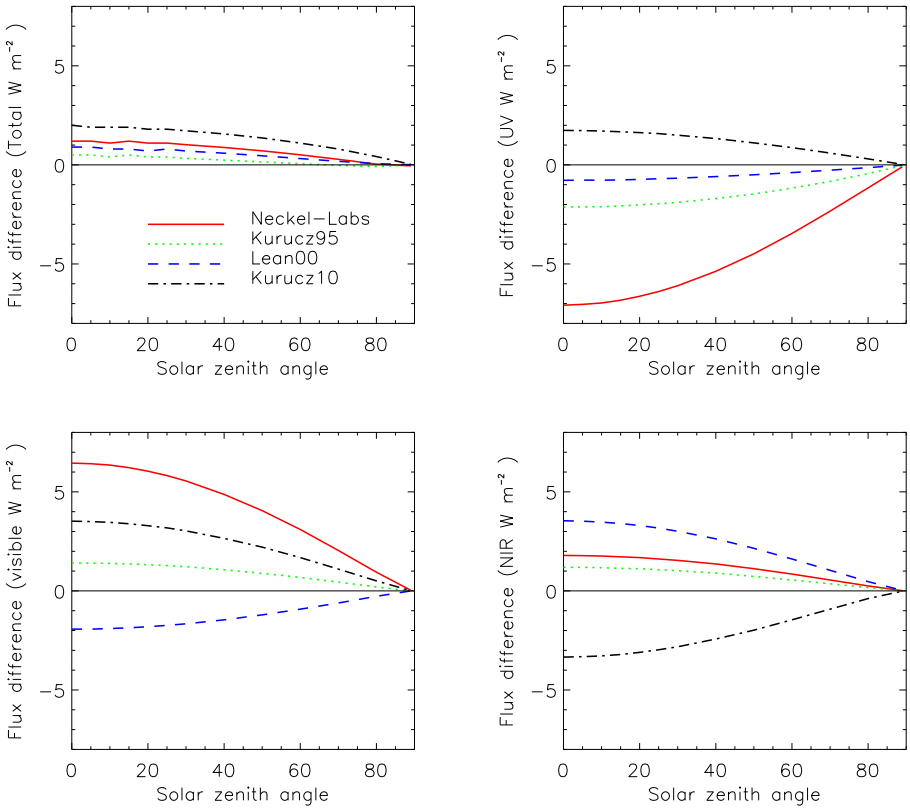

Fig. 5. Difference of downward solar irradiance between model spectra and the reference determined using the GENLN2 model. The upper left panel shows the difference in full spectrum, upper right for the UV spectrum, lower left for the VIS spectrum and lower right for the NIR spectrum.

is shown in Figs.2 and 3 that Kurucz10 has a larger portion of the solar energy in the UV region and produces the largest solar heating rate in the stratosphere. The downward irradiance at the surface is also high using this spectrum. The proportion of the solar energy for the Neckel-Labs spectrum is significantly smaller in this region and the surface irradiance from this spectrum is also small compared with the reference results. The difference in irradiance between Neckel-Labs and the reference can be as large as 7 W m^{-2} at zero solar zenith angle.

The differences in the downward solar irradiance in the VIS range are shown in the lower left panel of Fig.5. Since the atmosphere in the VIS region is relatively transparent to downward solar radiation, the results of the downward irradiance at the surface match well with those of the incoming solar energy at the TOA as shown in Fig.2. The spectrum of Neckel-Labs, Kurucz95 and Kurucz10 have a relatively larger proportion of the solar energy in this region compared with reference spectrum. The downward irradiances at the surface from these three

spectra are higher than that of reference, whereas the downward irradiance from Lean00 is less than the reference due to its relatively less incoming solar energy at the TOA. The difference between Neckel-Labs and Thuillier is close to 7 W m^{-2}, and difference between Neckel-Labs and Lean is up to 9 W m^{-2}.

The differences in downward solar irradiance in the NIR region are shown in the lower right panel of Fig.5. In contrast to the result of the UV, Kurucz10 is the smallest and Lean00 is the largest. According to Fig.2, Kurucz10 contains the smallest proportion of the solar energy compared to the other data, which leads to less downward flux at the surface. Also it is easy to understand why the Lean spectrum has the largest downward irradiance, since the solar incoming energy portion from this data is the largest one amongst the five spectra in the NIR range.

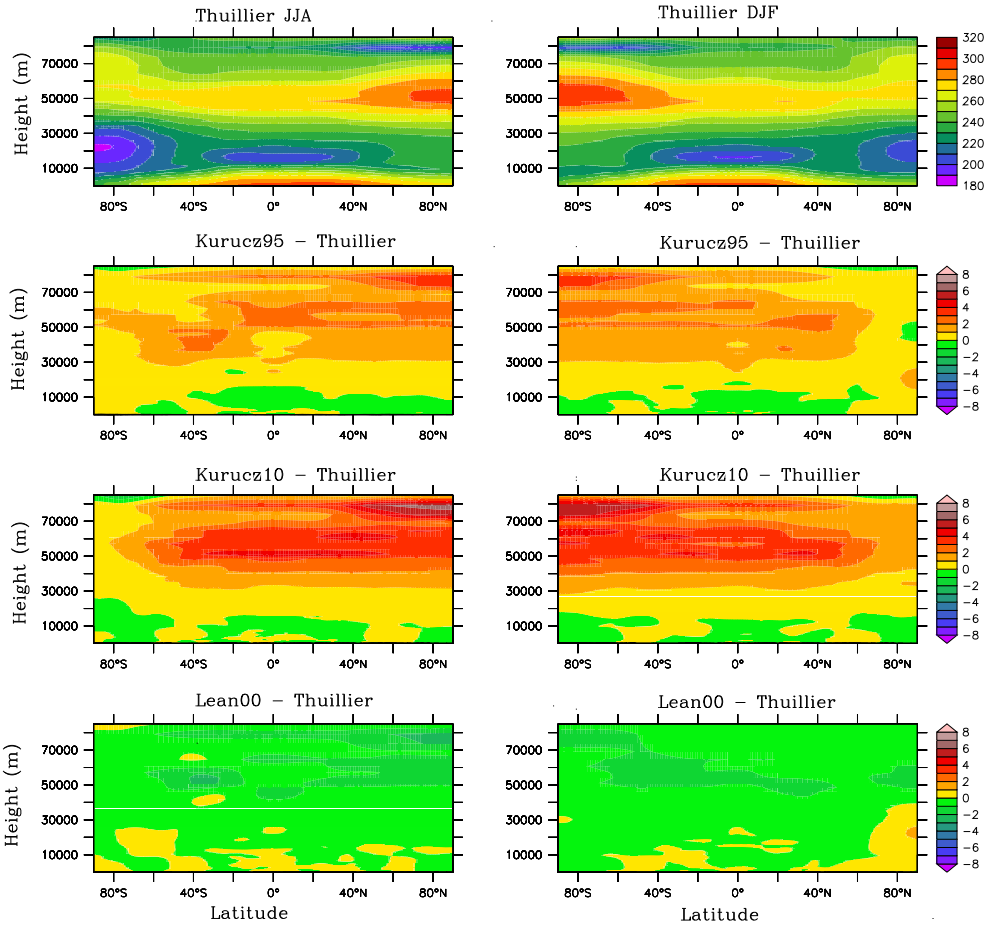

Fig. 6. Zonal mean temperature cross-sections determined by the ACCESS model for two seasons. The upper panels show the results corresponding to the reference solar spectrum and the following panels are the differences due to the model spectra relative to the reference.

Overall the spectral distributions of the downward irradiance at the surface are largely controlled by the distributions of the incoming solar radiation at the TOA, although gaseous absorption in the atmosphere can also have an effect. It is seen that although the changes in the downward total irradiance at the surface are within 2 W m^{-2} corresponding to the changes in spectral distribution at the TOA, the changes in spectral band irradiance are much larger, which will have large impacts on boundary layer and on land-surface processes. In the UV spectral region, for example, the changes in irradiance at the surface will affect the UVB forecasts that are important to the public. Radiation in the visible region (photosynthetically active radiation) is partially absorbed by plants and affects crop production and the carbon balance in the biosphere. In the NIR spectral region, water vapour absorption in the lower troposphere generates significant greenhouse warming. The radiation reaching the surface will be largely absorbed by the land surface because of the small albedo, which will lead to an increase in the surface temperature. The downward solar irradiance at the surface can strongly influence the surface energy budget and the surface sensible and latent fluxes. Therefore seeking an accurate solar spectrum is clearly an important issue for numerical modelling of weather and climate.

4.2 AGCM simulations

In this section, we focus on the impacts of the changes in solar spectral distribution on present-day model-simulated climate. The climate simulations are performed with the ACCESS atmospheric model, which has been discussed in the previous section. The AGCM simulations have been performed with an initial condition specified at September 1978. Prescribed sea surface temperature and sea ice data with seasonal variations are used as forcing from the ocean. A series of 30-year climate integrations were performed in order to find the influence of the different solar spectral distributions on climate simulations. A long time climate model simulation is required to reduce the noise due to natural variability. We present below the 30 year mean climatology.

The climate simulations based on four solar spectra (Thuillier, Kurucz95, Kurucz10 and Lean00) are performed. The Neckel-Labs spectrum is not considered in the climate simulations, since this old solar spectrum has became less popular in the last decade. As for the off-line radiative transfer comparisons, the climate simulation results are based on taking the Thuillier spectrum as the reference. Two seasonal mean results for summer June-July-August (JJA) and winter December-January-February (DJF) are presented.

We first investigate the temperature response inside the atmosphere. Figure 6 shows the zonal mean temperature cross-section for the two seasons and difference between the simulations using the different model spectra and reference spectrum. It is found that higher temperatures occur in the upper stratosphere due to the ozone absorption in the UV region. In the lower atmosphere below 2 km, the temperature is relatively large too due to water vapor absorption in the NIR range. In climate simulations feedback processes can play an important role. The absorption of solar energy in the NIR spectrum can cause a warming effect, and the temperature increase in the atmosphere can lead to more water vapor in return. This kind of feedback can make the temperature bias more sensitive to changes in the incoming solar spectral distribution.

The differences in temperature between the climate simulations using different solar spectra are shown in the lower panels. It is seen that the temperatures in the upper atmosphere from the simulations using the Kurucz95 and Kurucz10 spectra are systematically higher than that using the Thuillier spectrum. The difference can be as large as 5 K over large regions in the upper stratosphere. This is consistent with the results from the off-line line-by-line and broad-band calculations as shown in Figs.3 and 4. In contrast, the temperatures obtained by using the Lean spectrum are systematically lower than that using the Thuillier spectrum. Zhong et al. (2008) have performed GCM simulations to test the effect of the Kurucz95 and Lean solar spectra used in an early version of the UM model. They have shown that the use of the Kurucz95 spectrum results in a substantial warm bias above the stratosphere, and using the Lean spectrum can reduce the warm bias by about 4.3 K. The results obtained here are consistent with their finding. Furthermore, our results indicate that the use of Kurucz10 spectrum can cause an even larger warm bias in the stratosphere, which has not been studied by anyone before.

In the lower atmosphere, the Lean00 spectrum produces a noticeable warming bias compared to that of the Kurucz spectrum. As is shown in Fig.2 the Lean00 spectrum contains a larger portion of the incoming solar energy in the NIR region, and this energy can penetrate through the upper atmosphere and reach the lower troposphere where the water vapor absorption is relatively strong and leading to the larger solar heating rate which warms the lower troposphere and surface. The difference in temperature shown in the AGCM simulations is generally larger than the difference in heating rate shown in the off-line calculations. This is due to the positive feedback between the temperature and water vapor amount mentioned above.

In the top panels of Fig.7, the two seasonal (JJA and DJF) mean global distributions of the downward solar irradiances at the surface based on the simulations using the Thuillier spectrum are presented. It is seen that the downward solar irradiance is much larger in the northern hemisphere in the summer season and the opposite result happens in the southern hemisphere. In the lower panels (second to fourth rows), the differences in the downward solar irradiance are presented. It is seen that changes in solar spectra can cause changes in solar irradiance at the surface as large as 3 W m^{-2}, which is much lager than that due to the aerosol forcing (Nicolas et al., 2005). The difference is also larger in the summer hemisphere than in the winter hemisphere. Of the three model spectra, Kurucz10 has the largest difference in the downward irradiance and Kurucz95 has the smallest difference compared to that of the Thuillier spectrum. This is consistent with the off-line broad band results as shown in the upper left panel of Fig.5.

In Fig.8, the impacts on the surface temperature due to changing the solar spectra are presented. The upper two panels show the surface temperatures produced by the reference Thuillier spectrum, for the two seasons of JJA and DJF. The lower panels show the differences in surface temperature between the model spectra and the reference spectrum. The two Kurucz spectra produce lower surface temperatures compared to the Thuillier spectrum. It is seen that the temperature response to the changes in solar spectra is in a range of $\pm$2K. As seen in Fig.7, using the Kurucz10 spectrum leads to more solar irradiance (and hence, solar energy) reaching the surface. The surface temperature, however, does not respond in the same direction as this forcing. We therefore need to understand the related physical reasons behind this behavior. An obvious reason is that the surface albedo is very different in the different

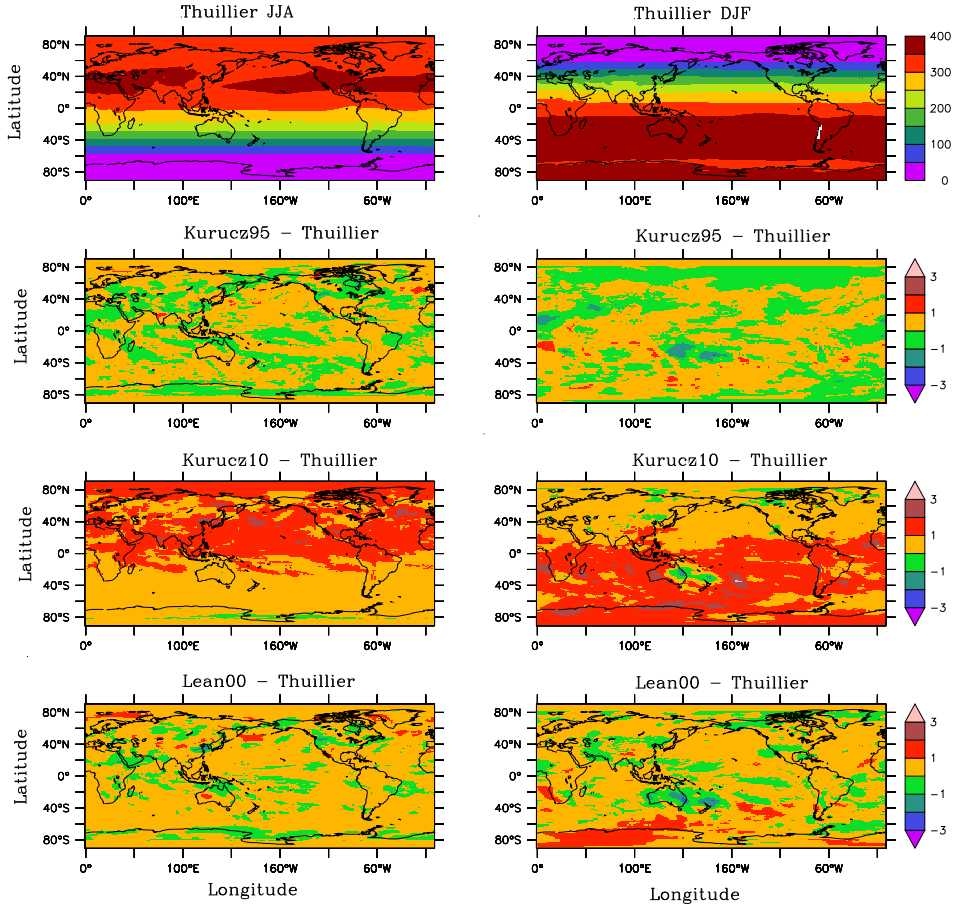

Fig. 7. Compared in the upper panel are the total downward solar irradiance (W m^{-2}) at the surface determined using the reference solar spectrum for winter (DJF) and summer (JJA) seasons with those determined by the model solar spectra, shown as separate differences (model minus reference) separately in the bottom three panels.

spectral regions. Generally, the surface albedo is relative lower in the NIR range and higher in the UV and VIS range. A higher surface albedo indicates a stronger surface reflection, which limits the energy absorption by the surface and produces a lower surface temperature. The surface albedo in the NIR is about 1/3 of that in the UV and VIS. Therefore, the surface solar energy absorption is largely determined by the downward solar radiation in the NIR range. In Fig.5, it has been shown that the Kurucz10 spectrum produces the lowest downward irradiance at the surface in the NIR range. This explains why the Kurucz10 spectrum produces the lowest surface temperature. Following the same argument, we can understand why the Lean00 spectrum produces the relatively highest surface temperature as shown in Fig.8, since the Lean spectrum corresponds to the largest downward solar irradiance in the NIR range.

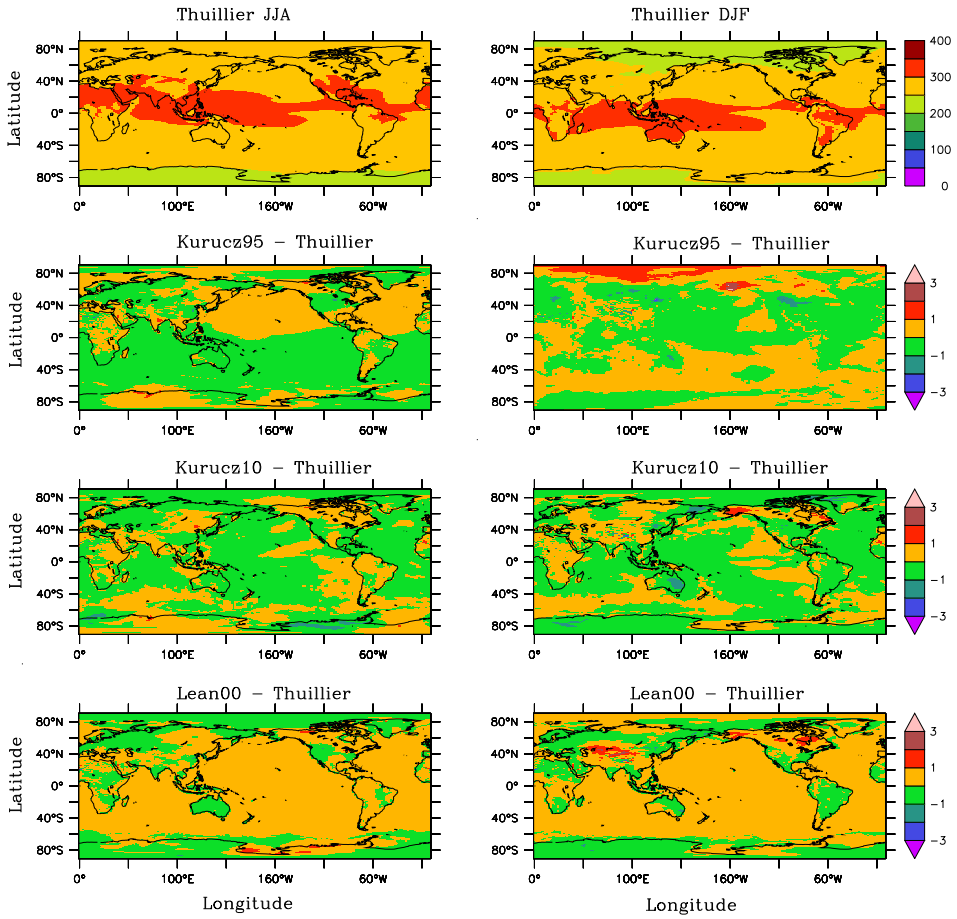

Fig. 8. Compared in the upper panels are the surface temperature distributions determined by the ACCESS model for two seasons using the reference solar spectrum with those determined using the model spectra displayed as separate differences in the bottom panels.

5. Summary and conclusions

In this chapter, we have analyzed the solar spectra currently used in climate models. The radiative impacts of the solar spectra are examined by using high spectral resolution line-by-line and broad-band radiative transfer models. It has been found that the solar heating rate in the stratosphere is very sensitive to the solar spectral distribution at the top of the atmosphere. The most sensitive spectral region is in the Hartley band near 300 nm where ozone has a strong absorption. The solar energy fraction from the Kurucz95 spectrum in this region is relative larger and the use of this spectrum leads to a large solar heating in the upper stratosphere. The modified spectrum of Kurucz10 contains an even larger proportion of energy in this region, which produces an even higher heating rate. The Lean00 spectrum which includes the latest observations from space platforms produces heating rates close to those using the reference Thuillier spectrum.

It is found that the radiative impact of the solar spectra is not limited to the ozone absorption in the UV range. The water vapor absorption in the lower atmosphere and the downward solar irradiance at the surface are also strongly influenced by the choice of the solar spectra. The effects of changes in the solar spectral distribution on the solar irradiance in three major spectral regions are much larger than on the total irradiance. The maximum difference in the total irradiance among the five solar spectra is about 2 W m^{-2} whereas those in the three spectral band irradiances are about 6 - 9 W m^{-2}. These spectral differences will in turn influence important processes, such as the forecast UVB, land-surface processes, and sensible and latent heat fluxes.

Four solar spectra have been evaluated using the ACCESS climate model. The climate model simulations show that the temperatures in the stratosphere and above from the Kurucz95 and Kurucz10 spectra are systematically higher than the result using the Thuillier spectrum. The difference is up to 5 K. On the other hand the stratospheric temperature due to use of the Lean00 spectrum is generally lower than the result using the Thuillier spectrum. In the lower atmosphere the Lean00 spectrum produces a noticeable warming bias compared to that of the Kurucz spectrum because this data contains a larger portion of incoming solar energy in the NIR range.

The climate model simulations also show that the changes in solar spectra can influence the downward solar irradiance at the surface. The difference can be as large as 3 W m^{-2} for different solar spectra. The changes in the downward solar irradiance is expected to have an influence on the surface temperature. However, it is interestingly found that the larger downward total solar irradiance at the surface does not necessarily correspond to higher surface temperature. The surface temperature strongly relies on the surface albedo and the surface albedo is generally much lower in the NIR range. Therefore the surface solar energy absorption is largely determined by the downward solar radiation in the NIR range.

From the results presented in this study, we cannot make a recommendation on which solar spectra should be used in a climate model because of the lack of the necessary comparison with observations. However, our results are of use for future work. For example, it may be better to examine the solar spectra against observations in the UV spectral region. This is because the differences in the solar irradiance amongst the five spectra are largest in this region where only the ozone absorption is important. The calculations in this region are not influenced by uncertainties from water vapour and other absorbing species. Although we cannot make a general recommendation our results suggest that the Lean00 spectrum should be used in the ACCESS (UM) model as it can reduce the model warm bias as identified by Zhong *et al.* and the current study.

6. Acknowledgment

Kurucz10 spectrum were downloaded from http://www.cfa.harvard.edu/atmosphere.

Prof. Gerard Thuillier is thanked for providing the solar spectrum used as a reference in this study.

Dr. Jingmiao Liu is supported by the Chinese National Natural Science Foundation of the project management under the grant No. 40775020

Dr. Lawrie Rikus is thanked for reviewing the manuscript.

7. References

Chance, K. & Kurucz, R. L. (2010). An improved high-resolution solar reference spectrum for earth's atmosphere measurements in the ultraviolet, visible, and near infrared, *J. Quant. Spec. Rad. Tran.*, Vol. 111, No. 9, (June 2010), pp.(1289-1295), 0022-4073.

Davies, T.; Cullen, M.J.P.; Malcolm, A.J.; Mawson, M.H. & Staniforth, A. (2005). A new dynamical core for the Met Office global and regional modelling of the atmosphere, *Q. J. R. Meteorol. Soc.*, Vol. 131, No. 608, (April 2005), pp. (1759-1782), 0035-9009.

Edwards, D.P. (1992). GENLN2: A general line-by-line atmospheric transmittance and radiance model, *Technical Note TN-367+STR*, NCAR: Boulder, Colorado, USA.

Gao, B.-C. & Green, R. (1995). Presence of terrestrial atmospheric gas absorption bands in standard extraterrestrial solar irradiance curves in the near-infrared spectral region, *App. Opt.*, Vol. 34, No. 27,(September 1995), pp. (6263-6268), 1559-128X.

Kopp, G & Lean, J. L. (2011). A new, lower value of total solar irradiance: Evidence and climate significant, *Geophys. Res. Lett.*, Vol. 38, No. L01706, (January 2011),pp. 7, 0094-8276.

Kurucz, R. L. (1995). The solar irradiance by computation, In: *Proceedings of the 17th Annual Conference on atmospheric transmission models*, Anderson, G. P.; Picard, R. H. & Chetwind, J. H. (ed.), 205-258, Phillips Laboratory Directorate of Geo-physics, PL-TR-95-2060, Hanscom Air Force Base, Mass.

Lean, J. (2000). Evolution of the Sun's spectral irradiance since the Maunder Minimum, *Geophys. Res. Lett.*, Vol. 27, No. 16, (August 2000), pp. (2425-2428), 0094-8276.

Mlawer, E.J.; Brown, P.D.; Clough, S.A.; Harrison, L.C.; Michalsky, J.J.; Kiedron, P.W. & Shippert, T. (2000). Comparison of spectral direct and diffuse solar irradiance measurements and calculations for cloud-free conditions, *Geophys. Res. Lett.*, Vol. 27, No. 17, (September 2000), pp. (2653-2656), 0094-8276.

Neckel, H. & Labs, D. (1984). The solar radiation between 3300 and 12500 Å, *Solar Physsics*, Vol. 90R, No. 2, (February 1984), pp. (205-258), 0038-0938.

Krivova, N. A.; Vieira, L. E. A. & Solanki, S. K. (2010). Reconstruction of solar spectral irradiance since the Maunder minimum, *J. Geophys. Res.*, Vol. 115, No. A12112, (December 2010), pp.(11), 0148-0227.

Nicolas, B.; Boucher, O.; Haywood, J. & Reddy, M.S. (2005). Global estimate of aerosol direct radiative forcing from satellite measurements, *Nature*, Vol. 438, No. 22, (December 2005), pp. 1138-1141, 0028-0836.

Stokes G. M & Schwartz S. E. (1994). The Atmospheric Radiation Measurement (ARM) Program: Programmatic background and design of the cloud and Radiation Testbed, *Bull. Amer. Meteor. Soc*. Vol. 75, No. 7, (July 1994), pp. 1201-1221, 0003-0007.

Sun, Z. (2011). Improving transmission calculations for Edwards-Slingo radiation scheme using a correlated k-distribution method, *Q. J. R. Meteorol. Soc.*, In press.

Thuillier, G.; Herse, M.; Labs, D.; Foujols, T.; Peetermans, W.; Gillotay, D.; Simon, P. C. & Mandel, H. (2003). The solar spectral irradiance from 200 to 2400 nm as measured by the SOLSPEC spectrometer from the ATLAS and EURECA missions. *Solar Physics*, Vol. 214, No. 1, (May 2003), pp. 1-22, 0038-0938.

Zhong, W.; Osprey, S.M. & Haigh, J.D. (2008). Influence of the prescribed solar spectrum on calculations of atmospheric temperature, *Geophys. Res. Lett.*, Vol. 35, No. L22813, (November 2008), pp. 5, 0094-8276.

4

Modified Degree-Hour Calculation Method

C. Coskun[1,*], D. Demiral[2], M. Ertürk[3] and Z. Oktay[3]
[1]*Turgut Kıran Maritime College, Department of Marine Engineering, Rize University, Rize,*
[2]*Mechanical Engineering Department, Faculty of Engineering, Aksaray University, Aksaray,*
[3]*Mechanical Engineering Department, Faculty of Engineering, Balikesir University, Balikesir, Turkey*

1. Introduction

A wide variety of building energy analysis methods are currently available to HVAC engineers and range from simple to sophisticated. The simplest methods involve the largest number of simplifying assumptions and therefore tend to be the least accurate. The most sophisticated methods involve the fewest assumptions and thus can provide the most accurate results. Generally, methods for building energy analysis can be given at three categories as follows:

- Single Measure Methods (example: Equivalent Full Load Hours)
- Simplified Multiple Measure Methods (example: Bin Method)
- Detailed Multiple Measure Methods (example: Hour by Hour)

Detailed Multiple Measure Method provides the most accurate results. In detailed Multiple Measure Method, energy calculations are on hour-by-hour basis. Within the detailed multiplemeasure categories are two major sub-categories worth discussing: The Reduced Hour-By-Hour Method and 8760 Hour-By-Hour Method. When consider the detailed methods, it is very difficult to find actual hourly weather data for each place. Also, detailed methods take much time for calculation [1]. The most detailed methods simulate the hourly dynamic heat transfer process inside the building envelope as well as the dynamic behavior of the heating system and the equipment. They are based on thermodynamic principles and solved numerically by using the initial and boundary conditions in addition to the geometry of the building. These procedures account for the influence of many factors such as weather, internal heat gains, building thermal inertia, solar gains, control system, etc., which may significantly vary with time. These methods are defined to be dynamic and they require hourly weather temperature data [2]. Dynamic methods are more detailed and usually require hourly calculations over the whole year for an accurate analysis of the annual load and the energy consumption [2-5].

* Corresponding Author

Forecasting the total or monthly energy requirement for cooling or heating purposes requires the determination of cooling or heating load profiles, for which identification of the two main external factors are necessary namely; the mean outdoor temperature probability distribution and the heat gain from sunlight. Monthly outdoor temperature probability distribution is very important input data for determining monthly heating and cooling degree-hour. It is known that degree-hour values are calculated simply by summing up the differences between the hourly dry-bulb temperatures and a standard reference temperature (base temperature). Outdoor temperature distribution and reference (base) temperature directly affect the heating or cooling load. Reference temperatures for heating in building applications vary from country to country. For instance, in the UK, heating degree-hour values are based on an outside dry bulb temperature of 15.5 °C, while Australia uses 18°C and the United States uses 18.3°C. After estimating the probable outdoor temperature distribution, the total cooling or heating degree-hours values are calculated.

Probability density functions are successfully applied in wind, solar, and hydrogen energy production as well as the outdoor temperature analyses and as such, they are commonly preferred by many researchers [6-13] for energy analyses in the literature. Coskun [13] applied this technique to outdoor temperature and proposed a new approach for degree-hours calculation. He used the sinusoidal function to specify the outdoor temperature probability distribution. Many scientists [14-20] focused on the total cooling/heating degree hours and degree-days values for different countries. In some studies, a constant base temperature method is employed to predict the cooling/heating degree-hours. In the literature, only a few studies are available that focus on both constant and variable base temperatures. More recently, hourly building energy simulations increasingly replaced the simplified load calculation methods such as the degree-days and degree-hours approaches. These simulations provide several advantages over such kinds of simplified methods during the design stage, including the ability to explore the equilibrium state of applying a large number of different combinations (or packages) of energy conservation measures and to account for any dynamic behavior such as the thermal energy storage in the structure itself. However, simplified models and methods are still preferred in practice over these sophisticated building energy simulation programs. In Turkey, people are generally in favor of using less complicated methods [21].

In this study, a modified degree-hours calculation method is developed to obtain more accurate results and then applied to four cities in Turkey.

2. Calculation method and new function

Coskun [13] proposed a sinusoidal function to estimate the probability density distribution of the outdoor temperatures. The proposed sinusoidal function is given by the equation below:

$$H_{T_{out}} = a + b \cdot Cos(c \cdot T_{out} + d) \tag{1}$$

where, a, b, c and d are the model parameters, T_{out} denotes the outdoor temperature in °C and $H_{T_{out}}$ gives the hours lapsed in a month at a temperature of T_{out} degrees. After estimation of the temperature probability density distribution, heating and cooling degree-hours were calculated using the equations below;

$$HDH_{Total} = \sum_{n=s}^{k} H_n \cdot (T_{Base} - T_n) \tag{2}$$

$$CDH_{Total} = \sum_{n=s}^{k} H_n \cdot (T_n - T_{Base}) \tag{3}$$

Temperature 'k' and 's' denotes the temperature limits of the function. HDH_{Total} and CDH_{Total} indicate the total heating and cooling degree-hour values for a chosen month, respectively. T_{Base} is a reference indoor temperature for both heating or cooling.

2.1 New modeling functions

In this study, two new functions are proposed. The proposed new functions are given by the equations below:

$$H_{T_{out}} = f \cdot e^{\left[\frac{-(T_{out}-g)^2}{2 \cdot h^2}\right]} \tag{4}$$

$$H_{T_{out}} = e^{\left[k + \frac{m}{T_{out}} + n \cdot \ln(T_{out})\right]} \tag{5}$$

where, f, h, g, k, m and n are the new model parameters, which are determined according to mean outdoor temperature probability density distribution, whose determination is explained detail in Section 3 below.

3. Determination of mean outdoor temperature probability density distribution

We calculated both temperature probability distribution and time elapsed in a month for any temperature interval of 1 °C. In the calculation, hourly dry-bulb outdoor temperature data, based on the last 32 years and recorded by the Turkish State Meteorological Station, were used. In this study, the general trend was tried to be obtained in one formulation. The outdoor temperature distribution frequency exhibits different characteristics in each year and month. Nevertheless, the mean outdoor temperature probability density distribution for each month can be determined by using the long term actual data for the past temperatures, which can be utilized as a reference distribution for degree-hours calculations. It was observed that outdoor temperature has a random fluctuation on general trend. In this study, the mean outdoor temperature probability density distribution was taken as a reference distribution for the modified degree-hours calculation method. Fig. 1 is given to illustrate the fluctuation of actual outdoor temperature frequency distributions for 32 years.

4. Results and discussion

The modified degree-hours calculation method was applied to four cities in Turkey. The model parameters are determined and given in Table 1. Analysis results show that the two new functions result in higher accuracy for the summer season. Therefore, the three functions are incorporated into a modified degree-hours calculation method in this study.

The two functions proposed in this study were also applied to a case study to demonstrate its accuracy. The province of Adana was chosen for this purpose. The actual outdoor temperature probability density distribution and the two functions are shown in Fig. 2 for the month of May. As it can be seen from Fig. 2, the new functions displayed better performance for cooling degree-hours calculations for the summer season. Also, actual and model outdoor temperature probability density distributions for six months were given in Fig. 3 for Adana.

Adana		Months											
		1.	2.	3.	4.	5.	6.	7.	8.	9.	10.	11.	12.
Model parameters	a	32.80	25.36	25.75	-	-	-	-	-	-	-	-	-
	b	36.37	28.30	29.35	-	-	-	-	-	-	-	-	-
	c	0.28	0.24	0.22	-	-	-	-	-	-	-	-	-
	d	-2.79	-2.61	-3.13	-	-	-	-	-	-	-	-	-
	f	-	-	-	64.87	-	-	-	-	-	-	59.48	73.53
	g	-	-	-	17.36	-	-	-	-	-	-	15.19	11.16
	h	-	-	-	4.44	-	-	-	-	-	-	4.84	4.04
	k	-	-	-	-	83.856	149.445	261.517	261.733	137.124	71.657	-	-
	m	-	-	-	-	-404.1	-858.3	-1652.7	-1668.4	-794.0	-340.7	-	-
	n	-	-	-	-	-19.87	-34.46	-59.45	-59.35	-31.45	-16.88	-	-
Temperature limits		0.5	0.5	2.5	5.5	11.5	15.5	17.5	17.5	13.5	9.5	1.5	-1.5
		19.5	21.5	25.5	33.5	39.5	40.5	43.5	43.5	41.5	38.5	30.5	24.5

Balıkesir		Months											
		1.	2.	3.	4.	5.	6.	7.	8.	9.	10.	11.	12.
Model parameters	a	-	-	-	-	-	24.11	-	-	-	-	-	24.00
	b	-	-	-	-	-	24.28	-	-	-	-	-	30.26
	c	-	-	-	-	-	0.21	-	-	-	-	-	0.21
	d	-	-	-	-	-	-4.66	-	-	-	-	-	-1.69
	f	67.07	53.76	60.37	51.70	-	-	-	-	53.81	62.06	60.80	-
	g	4.85	5.48	7.62	12.67	-	-	-	-	20.67	15.35	10.60	-
	h	4.43	4.99	4.92	5.57	-	-	-	-	5.36	4.79	4.73	-
	k	-	-	-	-	42.664	-	104.903	106.627	-	-	-	-
	m	-	-	-	-	-162.4	-	-566.7	-571.2	-	-	-	-
	n	-	-	-	-	-10.28	-	-24.29	-24.77	-	-	-	-
Temperature limits		-8.5	-10.5	-7.5	3.5	5.5	8.5	11.5	11.5	6.5	1.5	-3.5	-3.5
		20.5	22.5	26.5	32.5	37.5	35.5	40.5	40.5	36.5	32.5	27.5	19.5

Antalya		Months											
		1.	2.	3.	4.	5.	6.	7.	8.	9.	10.	11.	12.
Model parameters	f	71.70	61.35	66.30	66.10	63.15	58.40	-	-	-	-	61.79	71.50
	g	10.24	10.77	12.90	16.20	20.51	25.38	-	-	-	-	14.72	11.34
	h	4.16	4.39	4.49	4.36	4.72	4.94	-	-	-	-	4.68	4.17
	k	-	-	-	-	-	-	165.897	157.934	101.845	65.237	-	-
	m	-	-	-	-	-	-	-1034.5	-975.4	-557.6	-290.3	-	-
	n	-	-	-	-	-	-	-37.45	-35.7	-23.46	-15.58	-	-
Temperature limits		-1.5	-1.5	0.5	4.5	8.5	12.5	17.5	17.5	14.5	9.5	3.5	0.5
		21.5	22.5	26.5	30.5	36.5	40.5	44.5	44.5	39.5	37.5	29.5	23.5

Ankara		Months											
		1.	2.	3.	4.	5.	6.	7.	8.	9.	10.	11.	12.
Model parameters	f	60.96	51.50	51.90	54.17	52.80	49.98	50.18	50.45	48.08	55.00	53.65	64.80
	g	1.04	2.14	6.00	10.95	15.56	19.52	23.09	22.98	18.56	12.66	6.65	2.15
	h	4.89	5.23	5.75	5.33	5.65	5.83	5.99	6.00	6.09	5.44	5.40	4.60
Temperature limits		-12.5	-12.5	-9.5	-3.5	0.5	6.5	8.5	10.5	5.5	-0.5	-6.5	-10.5
		14.5	16.5	21.5	25.5	31.5	34.5	37.5	38.5	33.5	29.5	21.5	15.5

Table 1. Monthly model parameters for the four cities.

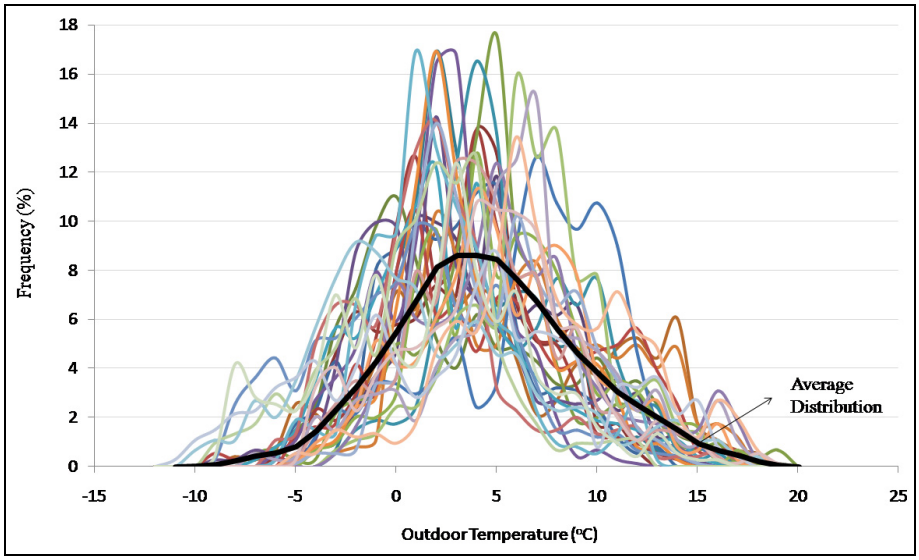

Fig. 1. Actual and mean outdoor temperature frequency distributions for Balikesir during the month of January

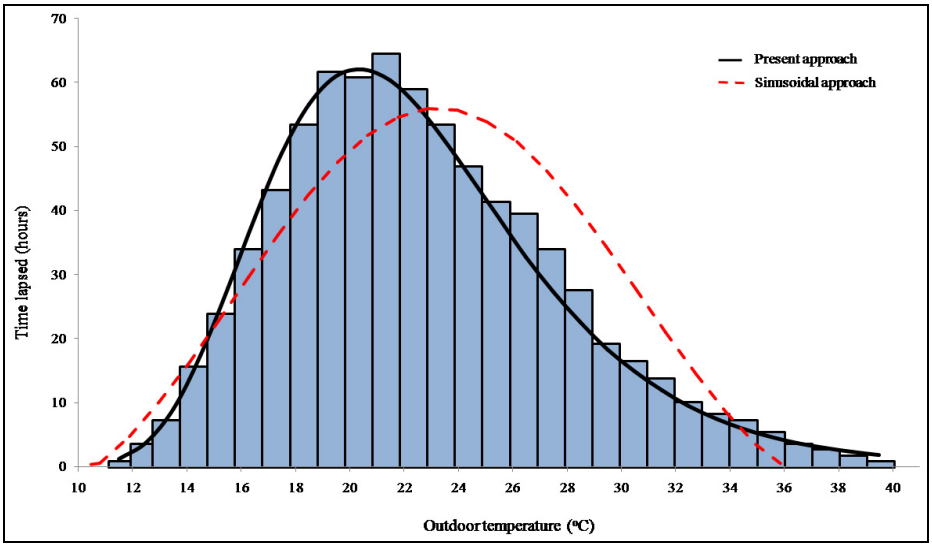

Fig. 2. Outdoor temperature probability density distribution for May

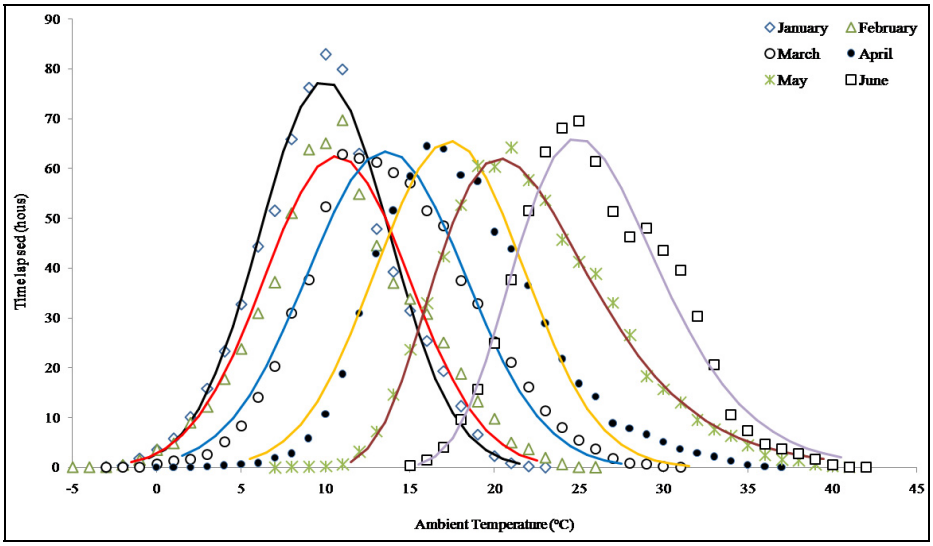

Fig. 3. Outdoor temperature probability density distribution for six months

5. Conclusions

Results of the analysis show that one function is not sufficient for determining the accurate outdoor temperature distribution during the year. In this regard, two new functions were proposed and added to the existing calculation procedure. As a result, the modified degree-

hours calculation method obtains more accurate results for each month by using all three outdoor temperature distribution functions. The main advantages of the approach can be listed as follows:

- Outdoor temperature distribution for each month can be determined precisely by using the modified degree-hours calculation method. Probable heating and cooling degree-hours value can be calculated by using probable outdoor temperature distribution for each month.
- Heating and cooling degree-hour values can be calculated for each month with respect to any chosen base temperature.
- The user can easily calculate the time elapsed in a month for temperatures below or above any chosen level of outdoor reference temperature.

6. References

[1] Pegues J. The benefits of 8760 hour-by-hour building energy analysis. Carrier Software Systems. New York, USA: HVAC Systems Engineer. 2002.

[2] Papakostas K, Kyriakis N. Heating and cooling degree-hours for Athens and Thessaloniki, Greece. Renewable Energy. 2005;30(12):1873–1880

[3] Hui SCM, Cheung KP. Application of building energy simulation to air conditioning design. In: Proceedings of the Mainland-Hong Kong HVAC seminar'98, Beijing. 1998. pp 12–20.

[4] ASHRAE Handbook – fundamentals (SI). Energy estimating methods. 1993. Chapter 28.

[5] Said SAM, Habib MA, Iqbal MO. Database for building energy prediction in Saudi Arabia. Energy Conversion and Management 2003;44(1):191–201

[6] Celik AN. On the distributional parameters used in assessment of the suitability of wind speed probability density functions. Energy Conversion and Management 2004; 45: 1735–1747

[7] Carta JA, Ramírez P., Velázquez S. Influence of the level of fit of a density probability function to wind-speed data on the WECS mean power output estimation. Energy Conversion and Management 2008; 49: 2647–2655

[8] Ibanez M, Rosell JI., Beckman WA. A bi-variable probability density function for the daily clearness index. Solar Energy 2003; 75: 73–80

[9] Ettoumi FY, Mefti A., Adane A., Bouroubi MY. Statistical analysis of solar measurements in Algeria using beta distributions. Renewable Energy 2002; 26: 47–67

[10] Tovar J, Olmo FJ., Batlles FJ., Alados-Arboledas L. Dependence of one-minute global irradiance probability density distributions on hourly irradiation. Energy 2001; 26: 659–668

[11] Coskun C, Oktay Z, Dincer I. Estimation of Monthly Solar Radiation Intensity Distribution for Solar Energy System Analysis. Energy 2011;36(2): 1319-1323

[12] Akyuz E, Coskun C, Oktay Z, Dincer I. Hydrogen Production Probability Distribution for a PV-Electrolyser System. International Journal of Hydrogen Energy 2011;36(17):11292-11299

[13] Coskun C. A novel approach to degree-hour calculation: Indoor and outdoor reference temperature based degree-hour calculation. Energy 2010;35: 2455-2460

[14] Sarak H, Satman A. The degree-day method to estimate the residential heating natural gas consumption in Turkey: a case study. Energy 2001; 28:929-39

[15] Dombaycı OA. Degree-days maps of Turkey for various base temperatures. Degree-days maps of Turkey for various base temperatures, Energy 2009;34:1807-12
[16] Sen Z, Kadıoglu M. Heating degree-days for arid regions. Energy 1997;23:1089-94
[17] El-Shaarawi MAI, Al-Masri N. Weather data and heating-degree days for Saudi Arabia. Energy 1996;21: 39-44
[18] Satman A, Yalcinkaya N. Heating and cooling degree-hours for Turkey. Energy 1999;24(10):833–40
[19] Duryamaz A, Kadıoglu M, Sen Z. An application of the degree-hours method to estimate the residential heating energy requirement and fuel consumption in Istanbul. Energy 2000;25:1245–56
[20] Büyükalaca O, Bulut H, Yılmaz T. Analysis of variable-base heating and cooling degree-days for Turkey. Applied Energy 2001;69(4):269-283
[21] Oktay Z, Coskun C, Dincer I. A new approach for predicting cooling degree-hours and energy requirements in buildings. Energy 2011; 36:4855-4863

5

Concentration of Solar Energy Using Optical Systems Designed from a Set of Conical Rings

Jorge González-García, Sergio Vázquez-Montiel,
Agustin Santiago-Alvarado and Graciela Castro-González
Technological University of the Mixteca (UTM) and the National Institute of Astrophysics, Optics and Electronics(INAOE)
México

1. Introduction

Different types of optic systems have been designed, manufactured, and used to concentrate energy, be it solar or otherwise. To mention just a few, we have for example, 1) the design and manufacture of a non-imaging Fresnel lens prototype for use in a solar collector of medium concentration (Leutz et al., 2000). This collector was evaluated in terms of the optical concentration ratio of its lens and the flux distribution on the absorber; 2) the design and manufacture of a low-frequency Fresnel mirror for a fluorescence detector (Diaz-Anzures et al., 2004), in which the Fresnel mirror was formed from a set of concentric spherical rings; 3) the design of mirrors from a set of spherical rings to generate an angular zone of energy concentration one order of magnitude smaller in comparison to the spot size generated with a spherical mirror (González-García et al., 2009), and 4) the optical design of a highly radiative solar flux furnace for Mexico (Riveros-Rosas et al., 2010) which consisted of an arrangement of 409 first surface spherical facets with a hexagonal shape. The configuration of this design was chosen because of its maximum peak concentration and also for economical reasons.

In the case of concentrator systems which involve polished elements such as lenses and/or mirrors, polishing techniques and optical tests are required for their manufacture. In order to reduce time and costs in the manufacture of solid mirrors designed by the concept of concentric spherical rings (a design method proposed more as an alternative in the design of energy concentrating lens and mirrors (González-García et al., 2009)), a classical polishing method was proposed using petal tools designed with Genetic Algorithms (González-García, et al., 2006) and with linear programming, (Santiago-Alvarado, et al., 2007). These lenses or mirrors can also be polished using different-shaped oscillating tools (Leal-Cabrera, et al., 2009). One alternative for testing the quality of polished surfaces is the application of the Ronchi Test (Cornejo-Rodríguez, 2007), which is an inexpensive test and easy to apply. Based on the ronchigram of the surface being tested, and applying Malacara's formula, cubic splines, and Genetic Algorithms, surface errors can be quantified (Cordero-Dávila & González-García, 2010; Cordero-Dávila, et al., 2011).

According to the analysis of the influence of the amount of circumsolar radiation in function of the acceptance angle of the absorber (Buie & Monger, 2004), the results showed that as the CSR of the sunshape increases, the size of the absorber must also increase to accommodate a similar amount of energy, that is, the size of the image increases. For this reason, a previous study proposed the design and manufacture of a mirror that would generate a desired angular size of the concentration of energy (González-García, et al., 2009). One hundred spherical rings, whose optimum curvature radius values were calculated with Genetic Algorithms (GA), were employed in the modeling process of the mirror (see Fig. 1). Using the Full With at Half Maximum criterion (FWHM), the size of the sun-image obtained with this mirror was 16.82 mm, as shown in Fig. 2.

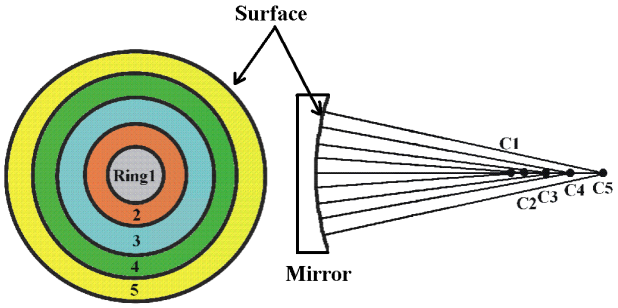

Fig. 1. Mirror modelled from a set of concentric spherical rings.

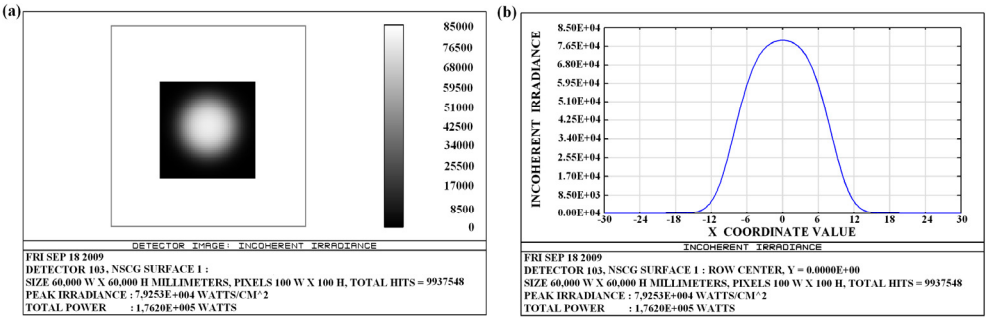

Fig. 2. Sun image generated with the mirror designed from a set of concentric spherical rings: (a) spot diagram and (b) graph of irradiance distribution.

The content of this chapter focuses on the description of a method for designing mirrors that would generate a desired angular size of a point source placed at infinity. Based on the simulation of the mirror by means of the ZEMAX optic design program (ZEMAX, Software For Optical System Design, 2008), the simulated mirror would later generate the corresponding image of the sun. The method for designing mirrors will be based on the above mentioned study of the design of mirrors from a set of concentric spherical rings. In order to be able to generalize the method not only spherical surface rings but also rings with any type of conic surface will be taken into account, that is, rings with any conic surface. One implication of this is that the angular size of the image (found during the optimization

stage using GA) will now be in function of the conic constant, be it through a predetermined value, or by considering it as a variable to be optimized together with the paraxial curvature radius of each ring. The sun images generated by four mirrors designed from rings whose surfaces have a determined value of the conic constant for each design will be simulated.

2. Design and optimization

In line with the procedure for designing a mirror from set of concentric spherical rings which reduce by one order of magnitude the size of an image of a point source placed at infinity, this section presents the design of four mirrors from concentric rings with conic profile whose conic constant for each case are: zero, (original design (González-García, et al., 2009) taken as a comparison), -1 (parabolic rings), -0.5 (rings with elliptical profile), and -1.6279, whose value was calculated with the GA together with the corresponding curvature radii.

2.1 Design of energy concentrating mirrors

Just like the original design (González-García, et al., 2009), these designs of the mirrors are also intended to reduce, by one order of magnitude the angular size of the image generated by a spherical mirror whose parameters are 1,500 mm in diameter, a curvature radius of 4,000 mm, and a focal distance of 2,000 mm. generating a disc of least confusion of 0.20966 degrees at a distance of -1,973.0 mm

The design procedure, considering the GA optimization method is expressed through the following steps:

1. 100 rings are used to model the shape of the mirror surface (from a reference sphere with a curvature radius of 3,900 mm, considered for the manufacture stage, by means of petal tool polishing (González-García, et al., 2006)). This involves calculating 100 curvature radii that are the variables to be considered in the optimization.
2. In order to reduce the number of variables to be optimized a recurrence formula was employed to reduce the number of variables from 100 to 20, expressed as

$$r_{i+1} = r_i + \Delta r_j \tag{1}$$

where r_i (i=1,…,100) are the curvature radii of each one of the rings and Δr_j (j=1,…,20) are the increments of the curvature radii, which would be the variables to be optimized by the GA. These increments are defined by the following equation

$$\Delta r_j = \begin{bmatrix} m_1 & if & 1 \le i \le 5 \\ m_2 & if & 6 \le i \le 10 \\ & \vdots & \\ m_{20} & if & 96 \le i \le 100 \end{bmatrix} \tag{2}$$

3. The fitness function is established as the error square of the differences between the simulated angular size (sas) and the desired angular size (das)

$$Fitness\ Fuction = S^2 = (sas - das)^2 \tag{3}$$

4. For the first three mirror designs the conic constant of the rings are considered constant whereas for the last design the conic constant is considered as just one more variable to be calculated by the GA, thereby establishing a more general method of design.

Once the design process of the energy concentrating mirrors has been established, the next process is the optimization of the twenty increments of the curvature radii defined by equations 1 and 2. The following is a description of the GA applied to optimize the design of the mirrors.

2.2 Genetic algorithm applied

The optimization method applied to calculate the optimum designs of the mirrors is a GA programmed in FORTRAN for LINUX. It has been used in classical surface polishing (González-García, et al., 2006), in the field of optical testing using Ronchi tests (Cordero-Dávila, et al., 2011), and in optical design (González-García, et al., 2009). The content of this chapter is one more example of this latter application. The stages of the GA applied are briefly described as follows:

A. Generation of the initial population

In this stage an initial random population of 240 individuals was created for each one of the twenty increments of the curvature radii. Hence, the total number of individuals or values randomly generated in this stage is the product 240X20. Within the area of programming 240 chromosomes were programmed, each one with a longitude of 320 genes. Each one of these chromosomes is divided into 20 chromosomes more (of 16 genes), and each one is used to calculate the value corresponding to each one of the increments of the curvature radii. Fig. 3 shows part of the programming corresponding to this stage.

```
INTEGER lcromosoma, tpoblacion,maxgeneraciones
PARAMETER (lcromosoma=320, tpoblacion=240 ,maxgeneraciones=160)

nvar = 20

do ii=1,tpoblacion
   do jj=1, lcromosoma

      CALL RA(srand)
      a =  rand(srand)
      CALL flips(0.5,a,gene)
      pob(ii,jj) = gene

   enddo
enddo
```

Fig. 3. Programming implemented for the generation of the initial population.

B. Evaluation stage

Once the initial population has been created, the evaluation stage is performed to determine, by means of the fitness function, Eq. (3), which chromosomes (of 16 genes) are the best values assigned to the increments of the curvature radii, with which Eq. (3) generates a minimum value. This stage was programmed as a subroutine within which the subroutine of ray tracing is found, and with which the simulated angular size is calculated.

C. The selection stage

The next stage in the GA is the selection stage in which the best values of the curvature radii increments are selected by means of the corresponding chromosomes graded as such in the evaluation stage. The selection process employed the tournament technique (González-García, et al., 2009), which consists of randomly taking a certain number of individuals from the population, called tournament size; from this, one of the individuals of the set is chosen for the next generation. The process is repeated as many times as there are individuals in the population, in the present case 240 times. Fig. 4(a) shows the subroutine corresponding to this stage.

```
SUBROUTINE SelecTorneo(tpoblacion,FSE,croele)
integer nnn,st,stf,srand,tpoblacion,ab(10)
integer ab1,ab2,croele(tpoblacion),stcroele
REAL a,FSE(tpoblacion),ps_st
nnn = 0
ps_st = 0.95
do st=1,tpoblacio
   nnn = nnn+1
   do stf=1,2
      CALL RAV2(stf,nnn,srand)
       a = rand(srand)
       ab(stf) = int( float(tpoblacion)*a )
   enddo
   ab1 = ab(1)
   ab2 = ab(2)
   CALL RAV1(nnn,srand)
   a = rand(srand)
   if ( FSE(ab1).gt.FSE(ab2) ) then
      stcroele1 = ab1
      stcroele2 = ab2
   else
      stcroele1 = ab2
      stcroele2 = ab1
   endif
   if ( a.le.ps_st) then
      croele (st) = stcroele1
   else
      croele (st) = stcroele2
   endif
enddo
END
```

(a)

```
CALL aleatoriocruza(lcromosoma,nvar,ii,acru2)
jcruza = acru2
ii = nnn+1
CALL aleatoriocruza(lcromosoma,nvar,ii,acru2)
jcruza1 = acru2
if ( jcruza1.lt.jcruza ) then
   band = jcruza
   jcruza = jcruza1
   jcruza1 = band
else
endif
do jcru=1,jcruza
   hijo1(icru,jcru) = pobp1(conyugue2,jcru)
   hijo2(icru,jcru) = pobp1(conyugue1,jcru)
enddo
do jcru=jcruza+1,jcruza1
   hijo1(icru,jcru) = pobp1(conyugue1,jcru)
   hijo2(icru,jcru) = pobp1(conyugue2,jcru)
enddo
if ( jcruza1.ne.lcromosoma ) then
   do jcru=jcruza1+1,lcromosoma
      hijo1(icru,jcru) = pobp1(conyugue2,jcru)
      hijo2(icru,jcru) = pobp1(conyugue1,jcru)
   enddo
else
endif
do jei=1,lcromosoma
   pobpn(conc,jei) = hijo1(icru,jei)
   pobpn(conc+1,jei) = hijo2(icru,jei)
enddo
```

(b)

```
pm = 1.0 / tpoblacion
do imuta=1,tpoblacion
   do jmuta=1,lcromosoma
      muta = muta + 1
      nnn = muta
      CALL RAV1(nnn,srand)
      a = rand(srand)
      if ( a.lt.pm ) then
         if ( pobp1(imuta,jmuta).eq.1 ) then
            pobp1(imuta,jmuta) = 0
         else
            if ( pobp1(imuta,jmuta).eq.0 ) then
               pobp1(imuta,jmuta) = 1
            else
            endif
         endif
      else
      endif
      enddo
   enddo
```

(c)

Fig. 4. Parts of the program implemented for Genetic Algorithm in FORTRAN corresponding to the stages of (a) selection, b) crossing, and c) mutation.

D. Crossing stage

The next stage to be applied is the crossing stage which involves combining two values of each increment of the curvature radius selected from the previous stage with a view to creating better values of these increments, in other words, values which would make the fitness function generate values close to zero. The crossing technique defined was implemented at two points. Fig. 4(b) shows part of the programming of this implementation.

E. Mutation stage

The mutation technique implemented was one in which all the genes of each chromosome of the population have the same probability of being mutated. The mutation probability value

was the inverse of the size of the population. Fig. 4(c) shows the programming corresponding to this stage.

Once the mutation stage has been completed, the evaluation stage is applied once more to determine which members are the best solutions. The whole process is repeated all over again (application of the selection, crossover and mutation stages) to generate populations with better solutions. Each repetition of the process is known as a generation, and as generations come and go, the solutions generated get closer and closer to the optimum solution to the problem. In our application, a population of 240 members was used from a search throughout 160 generations, see Fig. 3.

2.3 Results obtained from optimization

The results obtained from GA correspond to the design of 4 mirrors to reduce by one order of magnitude the angular size of the spherical mirror considering as object a point source located at infinity. As previously mentioned, in each design the concentric rings which model the surface of the mirror now have a conic surface profile.

Fig. 5 shows the evaluation graphs of the GA by means of the fitness function against the number of generations corresponding to each one of mirrors designed with different conic constants. Table 1 shows the energy distribution data generated by each mirror.

Parameter	Type of conical ring used: Spherical	Type of conical ring used: Parabolic	Type of conical ring used: Elliptical	Type of conical ring used: Optimized conic constant
Conic constant	0	-1	-0.5	-1.6279
Image position (mm)	-1973	-1973	-1973	-1973
Total spot size (mm)	0.8405	0.7399	0.7456	0.8449
Geometrical spot size (mm)	0.2370	0.1996	0.1907	0.2105
Geometrical rms X/Y spot size (mm)	0.1676	0.1411	0.1349	0.1488
Angular spot size (^{o})	0.0244	0.0215	0.0217	0.0240

Table 1. Data of energy distribution of the four designed mirrors.

Fig. 6 shows the energy distribution generated by each mirror, while Fig. 7 shows the corresponding values of the optimal curvature radii found with GA by means of increments of the curvature radii.

Based on the results obtained from the optimization of the designed mirrors, one can conclude that it is possible to design mirrors which concentrate energy in a smaller area reducing the angular size of the concentration, based on the concept of concentric rings which have a conic type surface, establishing in the design process a conic constant with a specific value or considering it as one more variable to be calculated with the GA.

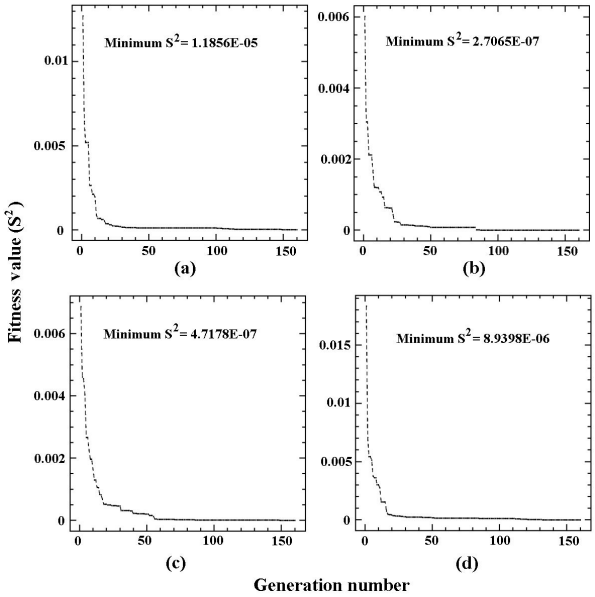

Fig. 5. Graphs of the fitness function as a function of the number of generations produced by the GA for the design of mirrors by means of concentric rings with conic constants of a) 0, b) -1, c) -0.5, and d) -1.6279

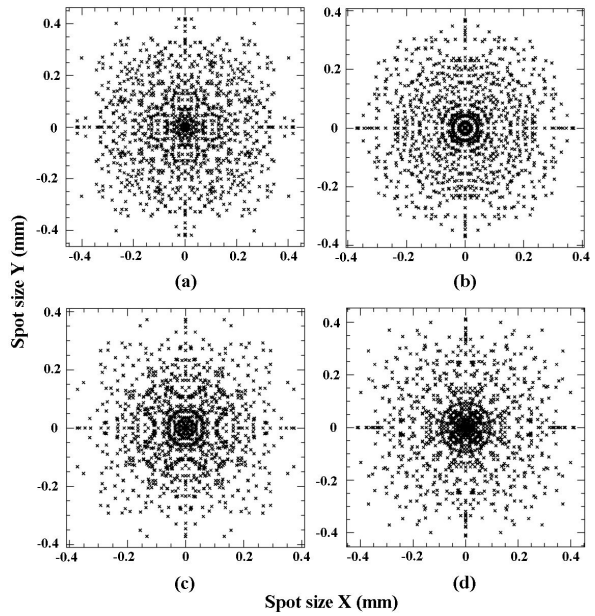

Fig. 6. Distribution of energy generated by the mirrors designed with conic constants of a) 0, b) -1, c) -0.5 and d) -1.6279.

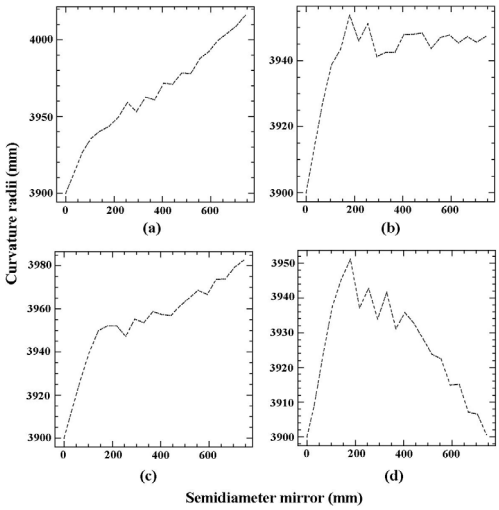

Fig. 7. Graphs of the optimized curvature radii of the concentric rings which model the 4 mirrors designed with conic constants of a) 0, b) -1, c) -0.5 and d) -1.6279.

3. Simulations done with ZEMAX. Images generated from the sun source

To consider the sun as an object in the mirrors designed in the previous section, these designs were simulated using the commercial optical design program in version EE of ZEMAX. In order to verify the results obtained of the angular size from each mirror in the optimization stage, see Table 1, the simulations were first done considering as object a point source placed at infinity. Afterwards, the point source was replaced by the sun source in order to generate the corresponding images.

3.1 Simulations done using a point source

To do the simulations of the designed mirrors from the concentric rings, the Non-Sequential Mode option was selected in the ZEMAX program. This mode is primarily used for non-imaging applications and its main analysis feature is the ray-trace detector which gives spatial and angular data on incoherent or coherent rays. Fig. 8 shows the statement of the point source, while Fig. 9 shows the statement of some of the curvature radii of the concentric rings through their corresponding aperture and conic constant data. Fig. 10 shows the diagram of rays in the mirror, while Fig. 11 shows the mirror as seen from the front.

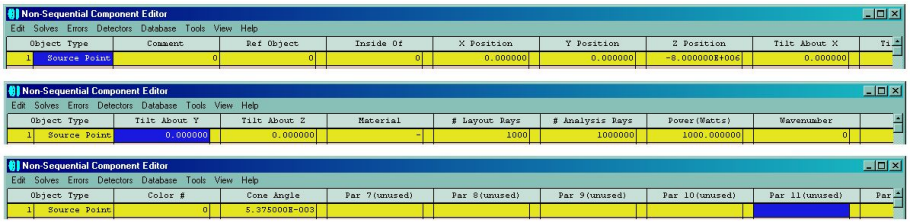

Fig. 8. Statement of the point source in ZEMAX used in the simulation of the designed mirrors.

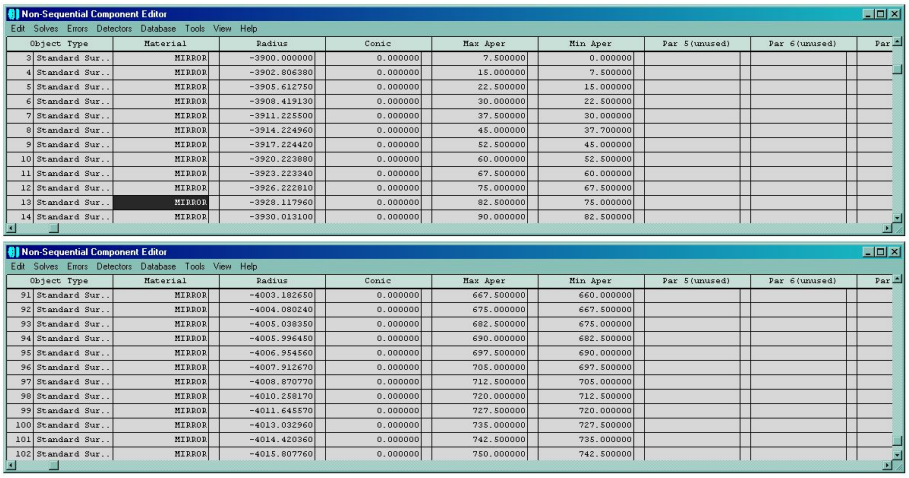

Fig. 9. Statement of the concentric rings in ZEMAX.

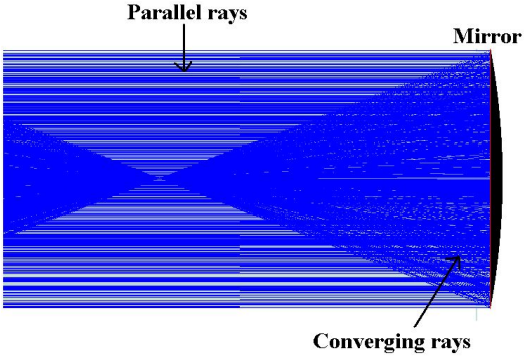

Fig. 10. Diagram of rays which arrive and are reflected by the designed mirrors.

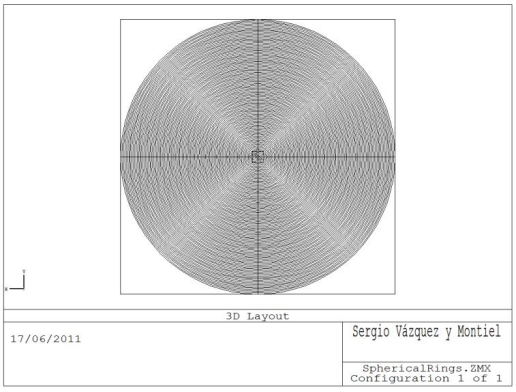

Fig. 11. Front view of the designed mirror, simulated with ZEMAX.

The results obtained of the images generated of the point source at infinity by each mirror, and their corresponding irradiance distributions, are shown in Figs. 12 to 15. These figures show the respective results of the design using spherical, parabolic, and elliptical rings, and with conic constant calculated with GA. The image sizes shown in each one of these figures agree with those reported in Table 1 from the optimization stage.

Once the results obtained from the optimization stage have been validated with ZEMAX, the final stage in the simulation process, in which the sun is considered as object, is to replace the point source with the sun source in ZEMAX.

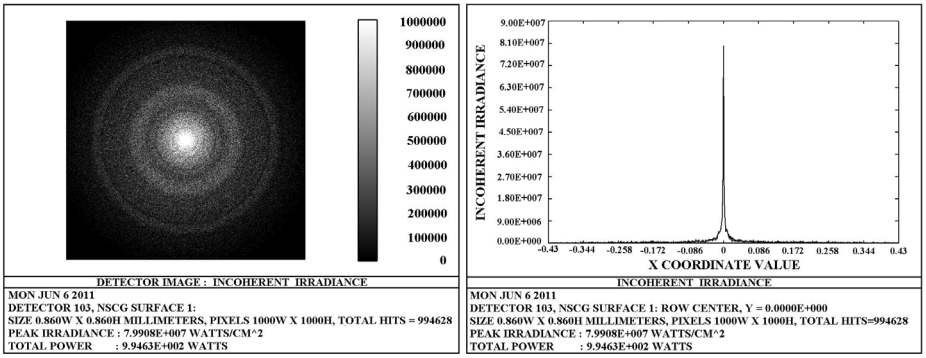

(a) (b)

Fig. 12. a) Image of the point source, placed at infinity, generated by the mirror designed with spherical surface rings, and b) its corresponding irradiance distribution graph.

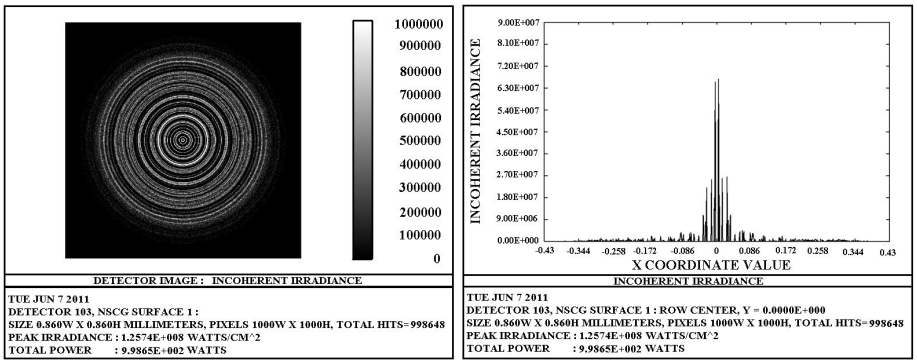

(a) (b)

Fig. 13. a) Image of point source, placed at infinity, generated by the mirror designed with parabolic surface rings, and b) its corresponding irradiance distribution graph.

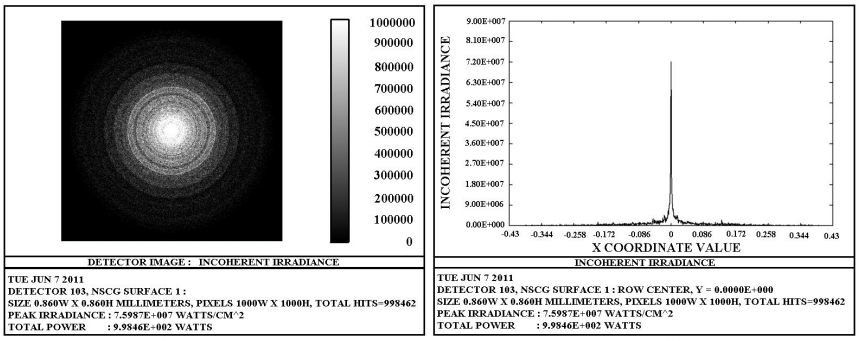

Fig. 14. a) Image of the point source placed at infinity, generated by the mirror designed from elliptical surface rings (conic constant equal to -0.5), and b) its corresponding irradiance graph.

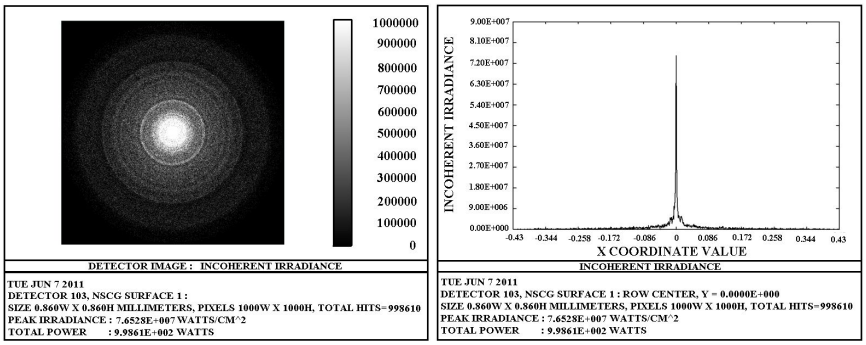

Fig. 15. a) Image of the point source, placed at infinity, generated by the mirror designed with rings having a conic constant calculated with GA equal to a -1.6279, and b) its corresponding irradiance distribution graph.

3.2 Simulations done using the sun source as object

To simulate sun images generated by the designed mirrors, the sun source was generated in a DLL file by means of the following equation

$$B(\theta) = B_d\left[1-(0.5051\theta/\alpha)^2-(0.9499\theta/\alpha)^8\right], \tag{4}$$

where B_d =13.639×10^6 W/m^2 stereorad and α=4.653 rad.

While the aureola region was adjusted by the following equation

$$B(\theta) = B_\alpha(\theta/\alpha)^{-2}, \tag{5}$$

where B_α=72,200 W/m^2 stereorad.

Fig. 16 shows the statement of the sun source in the ZEMAX program, while Fig. 17 shows the image of the sun before arriving at the mirror, at a distance of 150 mm from the vertex.

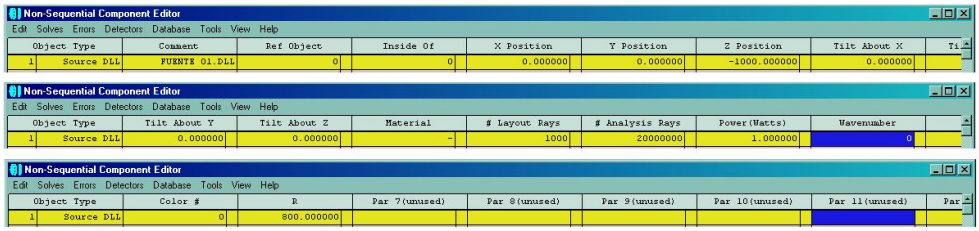

Fig. 16. Statement of the sun source in the ZEMAX program.

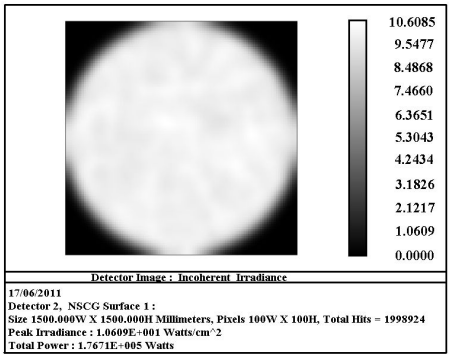

(a)

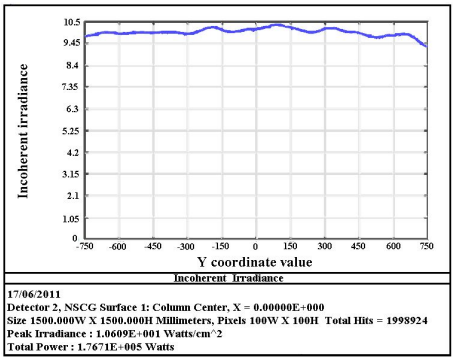

(b)

Fig. 17. a) Simulation of the sun source before arriving at the mirror, and together with b) its respective irradiance distribution.

Figs. 18 to 21 show the simulations of sun images with their respective distributions of irradiance generated with the mirrors designed with spherical, parabolic, elliptical rings, and rings with conic constant calculated with GA, respectively. Each one of these images was simulated with the ZEMAX program at a distance of -1973 mm. According to the FWHM criterion, the sizes of sun images generated by each mirror are shown in Table 2.

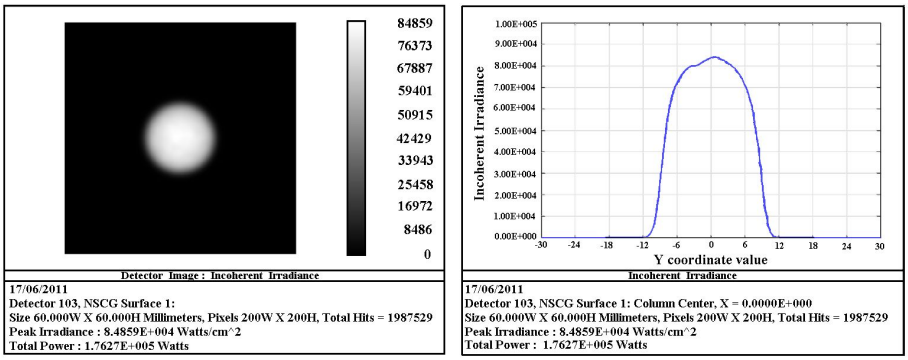

(a) (b)

Fig. 18. a) Image of the sun source generated by the mirror designed with spherical surface rings, and b) their corresponding graph of irradiance distribution.

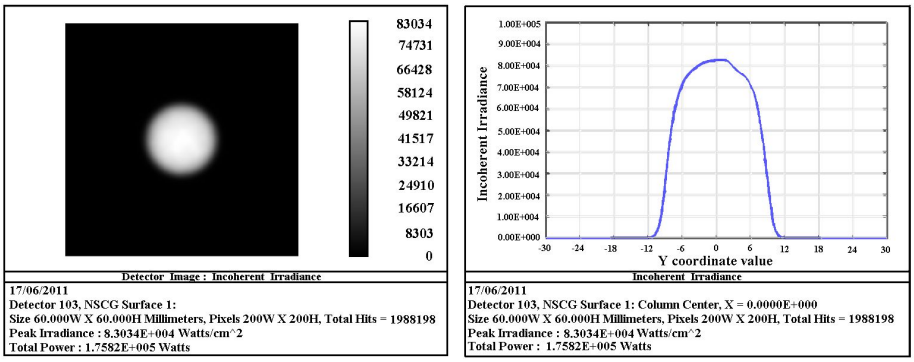

(a) (b)

Fig. 19. a) Image of the sun source generated by the mirror designed with parabolic surface rings, and b) their corresponding graph of irradiance distribution.

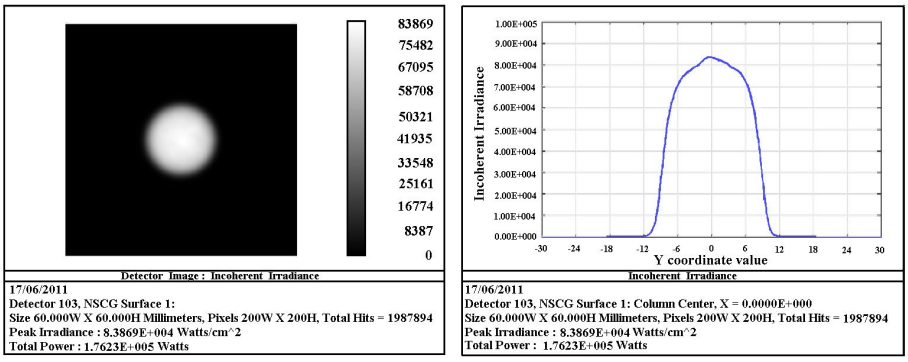

(a) (b)

Fig. 20. a) Image of the sun source generated by the mirror designed with elliptical surface rings, with a conic constant of -0.5 and b), its corresponding graph of irradiance distribution.

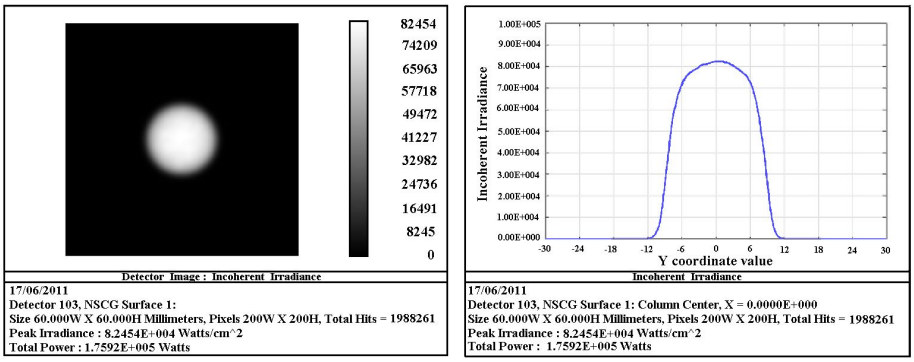

(a) (b)

Fig. 21. a) Image of the sun source generated by the mirror designed from rings with a conic constant equal to -1.6279 calculated with GA, and b) its corresponding graph of irradiance distribution.

Mirror designed with	Conic constant	Size of sun image (mm)
Spherical rings	0	16.97
Parabolic rings	-1	16.75
Elliptical rings	-0.5	16.89
Rings with a conic constant calculated with the GA	-1.6279	16.97

Table 2. Results of sun image sizes generated by the designed mirrors using the FWHM criterion.

As can be seen in Table 2, the sun image sizes obtained correspond to the angular sizes obtained from the images of the point source (see Table 1), that is, the biggest angular sizes correspond to the mirrors with rings whose conic constant was 0 and -1.6279. These very same mirrors are the ones that generate the biggest sun images, whereas the smallest images are generated with the mirror designed with elliptical surface rings with a conic constant of -0.5. Furthermore, the sun image sizes agree with the image size reported from using a mirror designed from concentric spherical rings (González-García, et al., 2009).

4. Conclusions

From the design of four mirrors which reduce by one order of magnitude the angular size of the image of a point source placed at infinity compared to an image generated by a spherical mirror, we could generalise the optical design method that uses the concept of concentric spherical rings for designing energy concentrators. The generalization of the method consisted in using concentric rings with conic surfaces in the optimization stage, considering two cases: 1) a constant value of the conic constant, and 2) the conic constant as one more variable to be optimized. The mirror designs could thereby remain in function of the value of the conic constant, as well as the paraxial curvature radii of the rings. The four mirrors

designed were simulated with the commercial optic design program ZEMAX, considering the sun as object. The images of the sun were compared to the images of the point source placed at infinity, and this revealed that the sizes of the images of the sun are related to the angular sizes of the images of the point source: the mirror design which generates the smallest angular size is the mirror which generates the smallest sun image, while the mirror which generates the biggest angular size is the mirror which generates the biggest sun image.

Finally, the results obtained show that it is possible to design mirrors, solar energy concentrators, from the concept of concentric rings with conic surfaces, thereby generating an alternative method of optical design for this type of mirrors. This type of method can also be applied in the design of lens concentrators.

5. Acknowledgment

We wish to thank Patrick Rafferty (KFUPM University, Saudi Arabia. rpatrick@kfupm.edu.sa) for translating the original document from Spanish to English.

6. References

Buie, D. & Monger, A. G. (2004). The effect of circumsolar radiation on a solar concentrating system. *Sol. Energy*, Vol.76, No. 3, (March 2004), pp. 181-185, ISSN 0038-092X

Cornejo-Rodríguez, A. (2007). Ronchi Test, In: *Optical Shop Testing*, Daniel Malacara (Ed.), 317-360, John Wiley & Sons, Inc., ISBN 978-0-471-48404-2, New Jersey USA

Cordero-Dávila, A. & González-García, J. (2010). Surface evaluation with Ronchi test by using Malacara formula, genetic algorithms and cubic splines. *Proceedings of International Optical Design Conference (IODC),* ISBN 9780819480828, Jackson Hole, WY, June 2010

Cordero-Dávila, A.; González-García, J.; Robledo-Sánchez, C. I. & Leal-Cabrera I. (2011). Local and global surface errors evaluation using Ronchi test, without both approximation and integration. *Appl. Opt.,* Vol.50, No.24 (August 2011), pp. 4817-4823, ISSN 0003-6935

Diaz-Anzures, J.; Cordero-Dávila, A.; González-García, J.; Martinez-Bravo, O.; Robledo-Sanchez, C.; Khrenov, B. A. & G. K. Garipov, G. K. (2004). Low frequency Fresnel mirrors for flourescence detector telescopes. *Astroparticle Phys.,* Vol.21, No.4, (July 2004), pp. 407-413, ISSN 0927-6505

González-García, J., Cordero-Dávila, A., Leal-Cabrera, I., Robledo-Sánchez, C.I. & Santiago-Alvarado, A. (2006). Calculating petal tools using genetic algorithms. *Appl. Opt.* Vol.45, No. 24, (August 2006), pp. 6126-6136, ISNN 0003-6935

González-García, J.; Vazquez-Montiel, S.; Santiago-Alvarado, S.; Cordero-Dávila, A. & Castro-González, G. (2009). A proposed design and fabrication of lenses and mirrors from a set of spherical rings that produce desired energy distributions for solar energy applications. *Sol. Energy*, Vol.83, No.12, (December 2009), pp. 2205-2216, ISSN 0038-092X

Leutz, R.; Suzuki A.; Akisawa, A. & Kashiwagi T. (2000). Nonimaging Fresnel Lens concentrator-the prototype. *J. Opt. A: Pure Appl. Opt.*, Vol.2, No.2, (March 2000), pp. 112-116, ISSN 1741- 3567

Leal-Cabrera, I.; Cordero Dávila, A. & Gonzalez-Garcia, J. (2009). Analytical and numerical classification of wear profiles produced with different shape oscillating tools. *Opt. Eng.* Vol.48, No.10, (October 2009), pp. 1-9, ISSN 0091-3286

Riveros-Rosas, D.; Herrera-Vázquez, J.; Pérez-Rábago, C. A.; Arancibia-Bulnes, C. A.; Vázquez-Montiel S.; Sánchez-González M.; Granados-Agustín F.; Jaramillo, O. A. & Estrada, C. A. (2010). Optical design of a high radiative flux solar furnace for Mexico. *Sol. Energy*, Vol.84, No.5, (May 2010), pp. 792-800, ISSN 0038-092X

Santiago-Alvarado, A., González-García, J., Castañeda-Roldan, C., Cordero-Dávila, A., Vera-Díaz, E. & Robledo-Sánchez C. I. (2007). Use of linear programming to calculate dwell-times for the design of petal tools. *Appl. Opt.* Vol.46, No.21, (July 2007), pp. 4642-4649, ISNN 0003-6935

6

Solar Mirrors

Rafael Almanza and Iván Martínez
Universidad Nacional Autónoma de México,
Universidad Autónoma del Estado de México
México

1. Introduction

Solar concentration utilises devices that range from simple designs, such as flat solar collectors surrounded by mirrors, to solar concentrators that employ a parabolic trough, a parabolic dish or a central tower surrounded by heliostats to achieve temperatures of a few hundred to several thousand degrees Celsius. All of these designs use flat or curved mirrors and several decades' worth of development have resulted in improved specular reflectance, half-life and cost.

First surface mirrors use reflective material deposited on a substrate (glass or plastic) and coated with a protective, transparent film to eliminate abrasion and corrosion. In second surface mirrors, silver or aluminium is deposited on the back of the transparent substrate.

The development of these mirrors, in particular second surface mirrors, have been reviewed by numerous authors, including Dennis (1979), Ashley et al. (1988), Jorgensen et al. (1994), Schissel et al. (1994), Kennedy and Jorgensen (1994), Martin et al. (1994), Fend et al. (2000, 2003), Kennedy et al. (2005), and Kearney and Price (2005).

The 3M® thin mirror (ECP-305), which employs silver deposited on acrylic (PMMA), has been used for several years at the Solar Power Plant Engineering Institute (National University of Mexico), where numerous problems have been identified. In particular, cracks developed rapidly over the acrylic (after 1 year) in Mexico City, which is a very polluted city, and the acrylic adhered poorly to the silver, resulting in corrosion and the formation of a tunnel in the mirror during the wet season. Thin silver mirrors (1 mm or less) exhibit additional limitations, such as weakness, manoeuvrability and high cost, as discussed by Kennedy et al. (1996). Kearney and Price (2005) discussed the behaviour of the seven commercial silver mirrors, including a silver-coated first surface mirror. The performance, based solely on accelerated time, produced a specular reflection coefficient above 95% after the equivalent of 5 years of exposure and a reflection above 90% after 6 years.

Compared to silver, aluminium is the most abundant metal, is relatively inexpensive and is the most widely used non-ferrous metal. Aluminium reflectors generally provide an initial reflection (of solar radiation) of 85-91%, exhibit good mechanical properties and are easy to recycle. However, exposure to air causes serious degradation of the optical properties of unprotected aluminium surfaces in just a couple of years. Compared to untreated aluminium, anodised aluminium exhibits improved behaviour because of the Al_2O_3 layer,

which protects the metal from further reaction. For this reason, anodising is often used to prolong the life of aluminium reflectors. Nonetheless, high purity aluminium must be used in order for the mirror to obtain good reflectance. The Alanod MIRO® brand manufactures this type of aluminium mirror utilising highly reflective aluminium foil. However, SiO_2 protects against abrasion and improves corrosion resistance, making it an attractive candidate for the development of aluminium mirrors; however, its economic feasibility must be demonstrated.

One of the advantages of aluminium first surface mirrors is that they do not require glass with low iron content. However, first surface mirrors made of aluminium and silver have not been thoroughly investigated as alternatives to solar concentrators.

Mirror Type	Reflectance $\rho_s(\pm 0.01)$		Time [years]	Comments
	Initial	Final		
FEK-244	0.86	0.72	16	Tunnel effect and corrosion
Kingston	0.86	0.49	16	Very poor reflectance
PMMA (3mm) Mexican Mirror	0.85	0.72	16	Poor adhesion and corrosion
ECP-305	0.95	0.92	2	Corrosion, tunnel effect and crack on PMMA
Al-first surface	0.85	0.85	2	Without important problems
ReflecTech®	0.94	0.94	2	Silver Mirror Film

Table 1. Specular reflectance of commercial mirrors after 16 years of weather exposure at the Solar Power Plant of Engineering Institute

Kennedy et al. (1996) have shown progress in aluminium mirrors (Al_2O_3) protected with polyethylene terephthalate (PET); the use of glass substrates and stainless steel were also reported. Morales and Ajona (1996, 1999) have developed sol-gel technology for silver mirrors and explored protection using SiO_2 and different substrates. Fend et al. (2000) have explored anodised or coated aluminium sheets and report accelerated aging, Brogren et al. (2004) developed aluminium-polymer-laminated steel reflectors using stainless steel as the substrate. Almanza et al. (1992, 1995) and Martinez et al. (2000) have developed the first aluminium mirror surface using quartz (SiO_2) as a protective layer and soda lime float glass. Table 1 shows the specular reflectance (200 to 2200 nm) of some commercial mirrors after 16 years (1979-1995) of exposure to the aggressive weather of Mexico City at the Solar Plant Engineering Institute (National University of Mexico). In the international literature, long-term outdoor tests are hard to find because most studies are performed in simulated weather conditions. Table 1 also shows results for the ECP-305 and the aluminium mirror first surface after two years of exposure. The tabulated results show a considerable decrease in the specular reflectance, in addition to numerous other problems, of mirrors with 16 years of exposure. An alternative product is the silver-based ReflecTech® Mirror Film, which exhibits an initial specular reflectance of 94%.

Primary aluminium mirror surfaces have also been applied to semiconductor lithography where a high reflectance (90%) is required (Hernandez et al., 2003) and high-quality mirrors are needed for different management systems to measure the distance in thermonuclear reactors (Yang et al., 2006).

2. Manufacture of mirrors for solar applications

This section reviews the utilisation of tungsten filament evaporation, electron guns, sputtering and coatings made from fluids via the sol-gel technique or chemical baths.

Filaments, electron guns (e-guns), linear magnetrons, sol-gel techniques and chemical baths have all shown promise in the deposition of thin film metals and dielectrics. In reviewing the use of these devices in Mexico, this paper presents the fabrication of aluminium first surface mirrors, in which reactive evaporation, such as the change of SiO into Si_2O_3 under specific oxygen conditions in a low pressure evaporator, is an important deposition method. The resulting film forms a conveniently thin and transparent layer, protecting the aluminium first surface mirror. Alternatively, quartz (SiO_2) can be substituted for SiO in the protective layer.

Coatings employing substances with high melting points (metals and dielectrics) are made possible via the use of e-guns, while linear magnetrons enable the deposition of metals or dielectrics at lower temperatures by using a plasma to sputter the material (Rossnagel et al., 1990; Wasa, 1992) into larger areas. In this last case, the mirror area depends on the number and size of the available magnetrons, as well as the size of the chamber.

These devices have been used to obtain first surface solar aluminium mirrors (Almanza et al., 1992, 1995) as well as in other applications related to film deposition. Figure 1 shows some of the devices that are used to make thin films, including the vacuum chamber, which has a volume of nearly 1.5 m^3.

In addition to their size, one of the problems with first surface solar mirrors is the likelihood of contamination during the evaporation process. After certain period of time of exposure to the environment, corrosion and tunnelling can degrade the mirror, especially in high humidity conditions. Nonetheless, these mirrors have been successfully used in numerous applications, including high UV reflectance measurements involved in water detoxification (Blake, 1992), as solar mirrors under natural and extreme conditions (Almanza et al., 1992, 1995) using the visible spectrum and in laser and IR applications (Haas et al., 1982).

Fig. 1. Photograph of vacuum chamber, high voltage source, and vacuum gauges

2.1 Filaments

A single, 1 to 2 mm-diameter tungsten filament is usually used to thermally evaporate aluminium using a low voltage transformer. Because aluminium exhibits good wetting (Glang, 1970), it is possible to evaporate it directly onto the sample. It took approximately 10 minutes to evaporate a film of approximately 4000 Å using a 60 A power supply in a vacuum of $4x10^{-5}$ Torr. The cylindrical chamber employed had a diameter of 1.35 m and a length of 1 m. The filament-substrate distance was fixed at approximately 250 mm. A 99.999% purity aluminium wire was rolled around the filament and used as the evaporable substance. After the aluminium evaporation, SiO was thermally evaporated. Commercial SiO was obtained in either powder or grain form. Evaporation of the SiO was achieved using a 40 mm long, 3 mm (external diameter) tantalum tube into which three small holes of approximately 0.5 mm were bored. Heating the tube forced SiO vapours through the holes toward the glass substrate located approximately 250 mm away. The tube was heated with a current on the order of 100 A, reaching a temperature between 1150 and 1250 °C (Glang, 1970).

When the vacuum chamber was opened immediately after evaporation, observation of the mirror surface by optical microscopy revealed a SiO film with the texture of small worms. This was interpreted as a strong contraction because 1) the SiO evaporation occurred at very high temperatures even upon reaching the substrate and 2) when the chamber was opened, the cool air produced a thermal shock. This phenomenon disappeared when the mirrors were kept for several hours inside the chamber under poor vacuum conditions. The total specular reflectance of these mirrors, measured with a solar spectrum reflectometer that simulates the visible spectrum ($270< \lambda <2940$ nm), was approximately 0.80. When the SiO was changed into Si_2O_3 by reactive evaporation (during which oxygen was injected into the chamber) at a pressure of ~10^{-4} Torr and at an evaporation rate of ~3 Å/s (Haas et al., 1982; Drummeter & Haas, 1967), the reflectance increased to 0.86.

During the aluminium evaporation, some filament contamination occurred (Almanza et al., 1995). This was because Al reacted with W to form an alloy (Glang, 1970); W reacted with oxygen to form WO_3 (Haas et al., 1982). As a result, pinholes (Glang & Gregor, 1970) appeared on the mirrors. These pinholes served as the initiation sites for environmental corrosion (Almanza et al., 1992). Thus, the main reason for building two e-guns was to avoid air particle contact during the opening of the chamber.

2.2 Electron guns

Our laboratory designed two electron guns, adopting existing technology to evaporate high purity aluminium and SiO or SiO_2 (quartz) films. The electron guns were of the bent-beam type (Glang, 1970). Figure 2 shows the main components of such a device.

Each e-gun used a permanent Alnico magnet, one with a capacity of 450 gauss and the other with a capacity of 161 gauss. This range of magnetic fields allowed the deflection of the beam to the targets. On each e-gun, two iron vertical plates were placed in contact with the magnet in order to create an extension of the magnetic field, which deflected the electron beam to the target.

The power supply that provided the kinetic energies to the electrons operated in the range of 3.5 to 4.5 kV. Based on this energy, the magnetic rigidity ($B\rho$) was estimated for the

electrons using tables from the published literature (Siegbahn, 1966). For example, for 3.5 keV, Bρ = 202 gauss-cm and ρ = 1.25 cm (radius of curvature); for 4.5 keV, Bρ = 228 gauss-cm and ρ = 1.42 cm. For the other magnet and with an average kinetic energy of 4 keV, Bρ = 228 gauss-cm and ρ = 1.3 cm.

Both magnets could focus the electron beam onto crucibles by orienting them via the deflection radius (Figure 2).

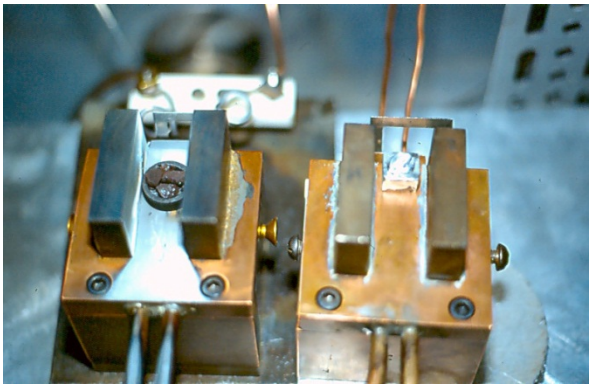

Fig. 2. Close-up photography of the two electron guns

The size of the beam is approximately 1 cm^2. Generally, commercial e-guns produce a point beam; however, in order to achieve this, it is necessary to design and develop a complete optical study. Such a study is not necessary in the present case because it is useful to spread the beam as much as possible. The irregular beams of these e-guns are practical because they enable the evaporation of a larger target area than is generally obtained by a point beam e-gun.

Another important parameter is the tungsten filament in which the electrons are produced. This filament was adapted from a halogen car lamp. Its mean life is determined by the evaporated substances that react with it and the sputtering of the incident high-energy positive ions.

Two types of mirrors were fabricated: Al-Si_2O_3 and Al-Si_2O_3. For the evaporation of Al, a boron nitride (NB) crucible was used, thereby utilising the good wetting that occurred on the melted aluminium (Glang, 1970). A graphite crucible was used for the higher melting SiO or SiO_2.

The evaporation procedure was as follows: a 1000 Å Al film was evaporated onto a clean floated glass substrate by applying 50 mA for 5 min at a pressure of $4x10^{-5}$ Torr. Then, in order to produce reactive evaporation of SiO, oxygen was introduced until a pressure of 10^{-4} Torr was reached, and a current of 30 mA was applied to the e-gun for one hour, so that a 3200 Å Si_2O_3 film was integrated. The low oxygen pressure conditions and low evaporation rate(s) required long time evaporation to assure high composition quality of the dielectric film(s).

Both e-guns are depicted in Figure 2. The pinholes were minimised due to the contaminant-free conditions inside the chamber and on the glass surface. The total specular reflectance of the mirrors was 0.89. Similar mirrors were previously reported to behave well under severe environmental conditions (Almanza et al., 1995).

2.3 Magnetron sputtering

The goals of magnetron sputtering, depending on the magnetron size, are film purity and the capable of coating large areas. There are two kinds of magnetrons widely used for film deposition: the cylindrical type and the planar type. As with e-guns, the use of two magnetrons reduces deposition time and produces higher quality films.

In this study, a planar magnetron with a target area of 125x250 mm was used. An Al target with a thickness of 12.5 mm and a quartz target of 6.4 mm were also used. The latter was thermally bonded to the backing plate, improving thermal conductivity and allowing simple water cooling of the target. Behind the target, permanent magnets produced a magnetic field, acting as a magnetron sputter source, of several hundred gauss parallel to the cathode surface (Rossnagel et al., 1990). As a result, the electrons were forced to move in a spiral, forming a long ring over the cathode surface.

This electron confinement, in conjunction with the gas confined in the evaporator chamber, produced an argon-plasma. When DC power was used, generation of the sputtering plasma required high currents (approximately 1.5 A) due to the effect of electron accumulation in a relatively low voltage field (450V). Increasing the current density increased the sputtering rate. The electrons' spiral movement increased the collision probability (with the existing gas molecules inside the chamber). Thus, the plasma was kept at lower working pressures (from $1x10^{-4}$ to $1x10^{-2}$ Torr).

Because of the lower density of gas molecules in this study compared to diode sputtering, the majority of sputtered atoms were less thermalised and, therefore, reached the substrate at higher energies. In both cases, the atom directions were randomised due to multiple collisions with sputtering gas particles, which improved the step coverage over all directions before arriving at the substrate (Pulker, 1999).

Two magnetrons were used to produce aluminium mirrors with areas of 300x600 mm. These were made via continuous movement of the glass substrate facing each magnetron (Figure 3). Depending on the target, a DC or RF source power supply was used.

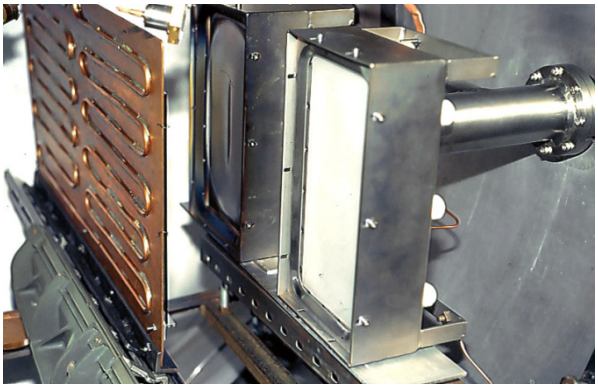

Fig. 3. Photograph of two magnetrons: aluminium and quartz targets; and mirror bracket

To protect it from particle attack, the magnetron body was covered with a stainless steel shield (non-magnetic material). The distance between this cover and the target was critical and had to be maintained at approximately 5 mm. Because of this close proximity, the radiofrequency impedance between the electrode (source material) and the shield was small, and the applied energy was dissipated (and lost) across the ground connection.

Because of their sensitivity to heat, water and air, the magnets were covered by a stainless steel, water-cooled shield and embedded in a protective epoxy coating.

The DC power supply produced an output of 3 A and 600 V while feeding the magnetron with the aluminium-target (99.99% purity and 125x250 mm area). The radiofrequency power supply operated at 13.6 MHz and was capable of producing an output of 1250 W, which fed the quartz-target magnetron. Because a matching network was required between the RF power supply and the plasma chamber in the radiofrequency system, it was necessary to convert the electrical load impedance of the plasma chamber to a value of 50-70 Ω. The matching network consisted of a tuner and a control panel. The tuner was composed of two variable, motor-driven (via an outer control circuit) air capacitors and a coil.

The radiofrequency generator (RFX-II model, from Advanced Energy) was capable of producing an output of 1250 W and maintaining a steady-state for the time period required. Their wide variety of functions were controlled by two microprocessors, providing excellent signal precision and stability. The entire device was automated and controlled using a computer. The reflected power, the forward power, the set point and the running time were all tracked.

The RF generator was connected to the tuner using a 50 Q coaxial wire. The tuner was connected to the magnetron with a Teflon®-covered copper-plated tube that was shielded with an iron pipe so that its operator was protected (note that this describes only the segment outside the evaporator chamber). The plated tube dissipated the heat easily. The length, shape and composition material of this connection had a major influence over the system performance, requiring the optimal configuration to be determined empirically. In addition, it was necessary to mount the tuner as close as possible to the magnetron and in a particular position because any changes produced different impedance values, implying a mismatch between plasma and RF generator. A bad connection produced overheating due to large amounts of dissipated energy.

The experiments were performed inside the same 1.35 m diameter cylindrical tank (Figure 4). The vacuum was produced using two different kinds of pumps: diffusion and mechanical. It was necessary to keep the working pressure in the range of $5x10^{-4}$ to $1x10^{-3}$ Torr in order to obtain adequate impedance and deposition rates. All the aluminium deposition processes were carried out in approximately 30 minutes. The real deposition time was 15 minutes for a 1000 Å aluminium film at 400 W and a DC Bias of -35 to -47 V. The film quality was higher than that obtained by thermal evaporation and e-gun evaporation due to pinhole minimisation, film uniformity and nucleation.

For the deposition of SiO_2, the working pressure was in the range of $2x10^{-3}$ to $3x10^{-3}$ Torr. The real deposition time for a 3200 Å film was 40 minutes at 850 W and a DC Bias ranging from -55 to -60 volts.

Fig. 4. Photograph of the vacuum chamber and diffusion pump for high vacuum

2.4 Sol-gel

Although this study did not involve the sol-gel technique, we find it pertinent to provide a comprehensive overview of this technique. The sol-gel process, also known as chemical solution deposition, is a wet-chemical technique widely used in the fields of materials science and ceramic engineering. Such methods are used primarily for the fabrication of materials originating from a chemical solution (or sol) that acts as the precursor for an integrated network (or gel) of either discrete particles or network polymers. The sol-gel technique offers a low-temperature method for synthesising materials that are either totally inorganic in nature or both inorganic and organic. The process, which is based on the hydrolysis and condensation reactions of organometallic compounds in alcoholic solutions, offers many advantages for the fabrication of coatings, including excellent control of the stoichiometries of precursor solutions, ease of compositional modifications, customisable microstructures, ease of introducing various functional groups or encapsulating sensing elements, relatively low annealing temperatures, the possibility of depositing coatings on large area substrates, and simple and inexpensive equipment (Morales & Duran, 1997). Within the past several years, a number of developments in precursor solutions, coating processes and equipment have made the sol-gel technique even more widespread.

Several methods can be used to make sol-gel coatings. Spin coating and dip coating are two basic techniques used to deposit sol-gel coatings. Spin coating produces a one-sided coating, while dip coating yields a double-sided coating. Both techniques are used in manufacturing to make different coatings and thin films.

2.5 Conclusions and suggestions

As demonstrated, the two most feasible methods for the deposition of films are e-guns and magnetron sputtering. Both methods allow metallic and dielectric evaporation with a minimum of contamination on any type of substrate, as demonstrated by the aluminium first surface solar mirrors used in this study. The method used depends on the substrate area needed. E-guns have been used for substrates with small areas (100x40 mm). Large area substrates can be deposited using several guns, resulting in uniformity of nucleation on the deposited film, an important concern in electronic and other applications. However, such devices are more costly.

In magnetrons, the metallic targets are deposited using a DC power supply employing considerable current, which is the principal limitation with regard to the area and the rate of evaporation. For dielectrics, a RF power supply is needed to perform the process, and the main problems are grounding and match-coupling; thus, it is important to avoid unnecessary equipment and ground all necessary electronic components as well as shield the RF reflectance by the substrate or any other undesirable metallic material around it.

3. Manufacturing technique

This third section discusses in detail the results obtained during the development of first surface solar mirrors, describing the main parameters involved in the implementation of each type of manufacturing technique as well as associated problems and suggestions to solve them.

3.1 Cleaning glass substrate

A clean substrate is important for the successful deposition of any film or coating. The cleaning process is required to break the links between pollutant molecules and between contaminants and the substrate (Almanza et al., 1992, 1995, 2009; Correa et al., 1998; Martinez et al., 2000). Thus, the technique chosen depends on the materials that compose the substrate, the type of pollutants and the degree of cleanliness required.

Substrate cleaning is essential, both to increase the adhesion between the film and the glass and to minimise corrosion of the mirrors. Any dust, grease, gel (i.e., the natural gel layer of glass deposited on the surface of the glass during its manufacture), oxide layers, etc., should be removed from the sheets of glass before they are placed inside the evaporation chamber.

Any contamination on the surface of the glass can cause defects in the deposited film and reduce the lifetime of the mirror. The glass can be cleaned chemically or it can be exposed to enough energy to remove the impurity, either by heating or by particle bombardment (Almanza et al., 1992, 1995, 2009; Correa et al., 1998; Martinez et al., 2000). A simple mechanical process, such as grinding, can be carefully and efficiently performed to avoid damaging the surface. The most common chemical methods are based on acid cleaning, which involves the conversion of oxides and fat-soluble compounds.

One of the most practical chemical cleaning methods employs a chromic mixture. Its use as a cleaning agent is based on its extremely strong oxidising power. For instance, the addition of chromic salts to concentrated sulphuric acid does not result in a simple solution. Instead, it produces the reaction 1.

$$K_2Cr_2O_7 + 3H_2SO_4 \Longrightarrow 2K^+ + H_3O^+ + 3HSO_4^- + 2CrO_3 \quad (1)$$

In the technique used for the substrate, there is always as a final treatment the so-called glow discharge that is applied within the evaporation chamber. It is a physical process that involves the exposure of glass to a glow discharge using argon or oxygen. This discharge is established between an anode (the evaporator chamber walls) and a circular aluminium cathode and close to the substrate to make cleaning more efficient. The required voltages range from 500 to 5000 V. Either AC or DC voltage can be used, although the latter is more common.

In glow discharge cleaning, impurities are removed as a result of the following mechanisms (Brawn, 1970):

1. Direct heating by the collision of charged particles.
2. Desorption of impurities by the continuous bombardment of electrons.
3. Desorption of impurities as a result of the bombardment of low energy ions and neutral particles.
4. Surface modification of glass by the continuous addition of the particles that make up the plasma.

Mechanism 4 is very important, particularly for substrates containing a substantial amount of SiO_2. It facilitates bridging between glass oxidisers and reactive metals, such as aluminium or chrome. It has also been observed to aid nucleation during the subsequent deposition of reflective films.

This study employed bathing in an acid solution (chromic mixture) and ion bombardment. The cleaning procedure was as follows:

- A 600x300x3 mm glass sheet was washed with commercial detergent and a soft sponge, then rinsed with water until the surface no longer felt soapy.
- The washed glass sheet was dipped in a chromic solution at 80 °C for half an hour. The composition was as follows: 24 g $K_2Cr_2O_7$, 408 mL H_2SO_4 and 144 mL H_2O.
- The glass was removed carefully from the chromic mixture and was allowed to cool for a few minutes. Next it was rinsed with water and wiped with a cloth to remove residues of the solution. Then it was dried in the atmosphere or using a hot air gun.
- The substrate was then rinsed with distilled water and placed in a container with isopropyl alcohol. Finally, the glass sheet was air dried at a temperature of 90-110 °C for 10 minutes.

The wetting of the surfaces must be examined to determine if the substrate is clean. This is known as the "water-break test" (Maissel, 1970): "If a clean substrate is removed from a container of pure water, a continuous film of water remains on the surface." This correlates with a good wetting between the substrate and water.

3.2 Sputtering of aluminium and silicon dioxide

Sputtering is one of several techniques used for the deposition of metals on glass substrates. The others are chemical deposition and evaporation.

With regard to producing and evaluating mirrors, we specifically describe the deposition process with flat magnetrons developed in this part.

After installing the glass in front of the magnetron and performing glow discharge cleaning, the aluminium film is deposited. Argon is introduced into the tank at a pressure of $6x10^{-4}$ Torr, and direct current is applied to the system at 810 V with low power (200 W). This generates an electrical current that ionises the gas, causing the surface of the magnetron with the aluminium target to become bright, at which point it is said that one has "lit the magnetron".

There are situations in which no plasma is formed at a pressure of $6x10^{-4}$ Torr. This usually occurs when the magnetrons, their targets, and/or the interior of the tank are exposed to the

atmosphere for extended periods of time, causing the formation of oxides and the adsorption of other contaminants in the air. In this case, the pressure must be raised an order of magnitude. Consequently, there are numerous molecules exposed to the stream that feeds the ionisation, increasing the collision probability and causing the cascade effect (where the first ionisation of argon atoms produces electrons that ionise more atoms) and ionisation to rapidly occur.

Once plasma is formed, the voltage drops to 200-300 V, and the current increases from nearly zero to ~0.5A, indicate that a flow of electrons has been established between the electrodes. The system is left under these conditions for a few minutes to ensure that undesirable substances in/on the target surface (mainly aluminium oxide) are removed. As the minutes elapse, the voltage gradually increases as the current decreases (because the power output remains constant), indicating that the undesirable substances have burned off.

At this point, the power can be increased to almost 400 W or left at 300 W, depending on the aluminium deposition rate desired. Sputtering begins when the potential between the electrodes reaches between 400 and 500 V. The aluminium target is negatively biased (also called the cathode) so that the bombarding Ar ions arrive with energies of approximately 100-500 eV. Atoms on the aluminium surface are joined by energies of 2-10 eV (sublimation energy), while the average energy of detached atoms lies between 10 and 40 eV. The difference, the remaining energy, is dissipated in the magnetron as heat, making it very important to cool this device in order to improve its durability and to prevent melting of the target and damage to the magnets that make up the magnetron.

The rate of erosion was determined experimentally with the data obtained regarding the film thickness and deposition time. The deposition rate also depends on the angle of incidence of ions from the normal of the target surface. At angles above 80°, the ion is most likely reflected, while angles of 60°-80° produce the maximum shedding of particles from the cathode (Rossnagel, 1990, see Figure 5). Detached particles reach the substrate after suffering multiple collisions. The net result is the arrival of atoms at a maximum solid angle (covering an entire hemisphere) (Gambino, 1978).

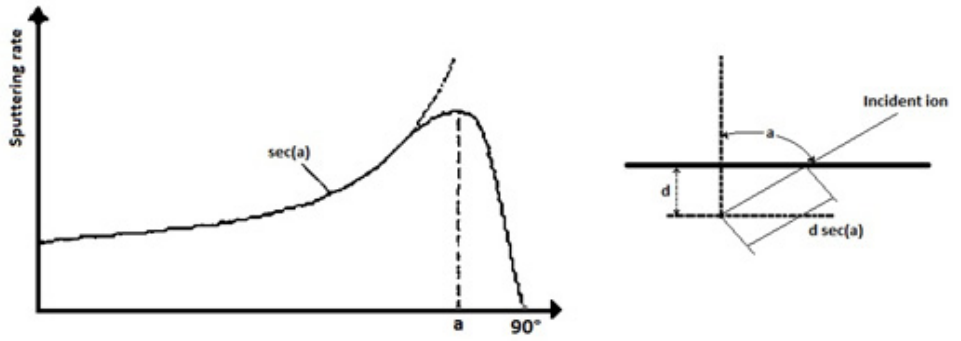

Fig. 5. Dependence on the amount of target particles detached from the angle of incidence of the ions. Note that the distribution is the secant at angles less than ~60° from the normal to the surface

Tables 2 and 3 show typical parameters for the operation conditions employed during the deposition of aluminium and quartz. When the aluminium foil has reached the desired thickness, quartz deposition is initiated. As previously explained, when dielectric quartz sputtering is required, it is obtained via a radiofrequency power supply rather than direct current.

System Pressure [Torr]	Power supply [W]	Current [A]	Voltage [V]	Run time [h:m]	Effective time [min]
$7.4x10^{-4}$	160	0.6 – 0.7	269 – 280	11:17	0
$7.8x10^{-4}$	200	0.72	274-	11:22	0
$7.5x10^{-4}$	250	0.86	287	11:27	0
$7.3x10^{-4}$	250	0.46	528	11:30	0*
$7.2x10^{-4}$	300	0.55	539	11:32	2
$7.2x10^{-4}$	350	0.64	545	11:34	4
$7.4x10^{-4}$	350	0.65	535	11:48	18

(P_{min}= $4.4x10^{-5}$ Torr; Film thickness ≈1000 Å)
*Note: at this time the mirror is placed in front of the magnetron.

Table 2. Typical run for the deposition of aluminium using direct current for sputtering

System Pressure [Torr]	Power [W]			Polarisation of electrodes [V]	Run time [h:m]	Effective time [m:s]
	Selected	Reflected	Supplied			
$7.8x10^{-3}$	3	2	5	0	12:21	0
$2.2x10^{-3}$	100	2	102	-12	12:23	2:20
$2.1x10^{-3}$	200	2	202	-23	12:25	4:40
$2.0x10^{-3}$	300	2	302	-31	12:27	6:40
$2.1x10^{-3}$	400	2	402	-39	12:29	8:40
$2.3x10^{-3}$	500	3	503	-47	12:31	10:40
$2.5x10^{-3}$	600	3	603	-54	12:33	12:40
$2.2x10^{-3}$	700	3	703	-59	12:35	14:40
$2.5x10^{-3}$	800	3	803	-59	12:37	16:40
$2.4x10^{-3}$	800	3	803	-59	12:39	18:00*
$2.1x10^{-3}$	790	2	792	-64	12:49	28:00
$2.6x10^{-3}$	790	2	792	-65	12:59	38:00
$2.7x10^{-3}$	790	2	792	-64	13:19	58:00
$2.1x10^{-3}$	790	3	793	-63	13:29	68:00
$3.2x10^{-3}$	790	3	793	-63	13:39	78:00

(P_{min}= $1.9x10^{-5}$ Torr; atmosphere with 25% O_2; Film thickness ≈5000 Å)
*Note: at this time the mirror is placed in front of the magnetron.

Table 3. Typical run for the deposition of quartz with radiofrequency ion erosion

The argon plasma does not guarantee quartz deposition; therefore, deposition depends on the power required to ensure an acceptable evaporation rate, which can also cause Si-O bonds to break. This decomposition of some molecules of quartz (SiO_2) was evident by the yellowing appearance of the substrate; this yellowing is typical of films of silicon monoxide used in mirrors. Because this undesirable colour lowers the reflectance of the mirrors, we introduced a percentage of oxygen as a working gas to ensure that the SiO molecules reacted and this yellow colour was eliminated (by oxygen's action via reactive evaporation over the quartz film (Hass, 1982).

However, the presence of oxygen decreases the ion erosion rate. This is because, in order for this gas (oxygen) to be reactive and to adsorb and coat the quartz target surface to cause the formation of SiO_2 molecules, one must spend an ion to remove the oxygen out of the way that stands. The associated kinetics was studied by Jones et al. (1968). High concentrations of oxygen (at 50% -35%) slowed the process and caused plasma instability manifested by small oscillations in pressure. This caused the impedance of the system to vary continuously, causing the reflected power to increase.

The optimum oxygen levels were determined to be from 15% to 30%. The magnetron was lit at pressures of 6 to $8x10^{-3}$ Torr. The working pressure was 2 to $2.5x10^{-3}$ Torr and the deposition time was 1 hour at a power from 800 to 850 W.

During sputtering of both substances, the glass substrate is kept in constant motion with the help of an engine adapted for this purpose (in order to provide coverage for a larger area). This allows the uniform deposition of 60x30 cm mirrors. Mirror size was determined by the space limitations imposed by the evaporation chamber.

It is important to note that the erosion rate depends on the RF-biased electrodes with respect to the plasma (Figure 6). The larger the polarisation, the more ions it will attract and, along the way, the more kinetic energy it will acquire. Thus, during the experimental polarisation of -65 V, the quartz deposition rate was almost double that obtained at -40 V.

The origin of this polarisation arises from the high mobility of electrons compared to ions. The high flow of electrons to the electrodes causes the plasma to acquire a positive potential because of the excess positive ions.

In our case, the cathode was connected to the RF source through a capacitor in series with the coupling impedance, and the area of the substrate was greater than the cathode.

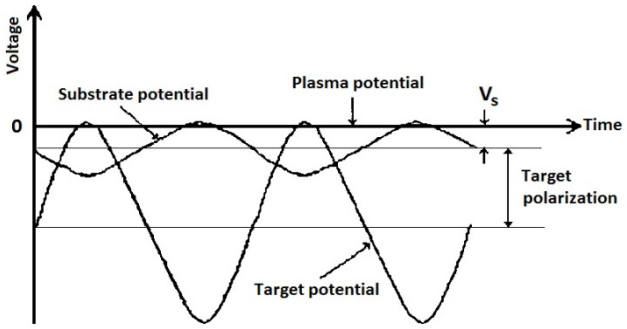

Fig. 6. An approximation of voltage versus time based on the potential of the plasma during radiofrequency sputtering, V is the potential of the substrate

Thus, the average current of ions and electrons reaching the electrodes is the same condition that is met if the electrodes were to acquire a negative bias, thereby slowing down the electrons and speeding up the ions. The extent of polarisation depends on the system pressure. If the pressure increases to maintain constant power, the polarisation decreases. This is partly due to the drop in voltage caused by the increase of neutral particles that reduce the impedance of the plasma.

3.3 Formation mechanism of the films

In magnetron sputtering, the substrate is far away from the bulk of the plasma, which is confined near the target surface by the magnetic field of the magnetron. It, therefore, suffers little bombardment by high energy electrons or plasma ions. In addition, the presence of the magnetic field enables the use of lower pressures because the particles are confined to a small region due to the collisions between them. To maintain low pressure, the mean free path of the atoms sputtered over the substrate increases with very little loss of kinetic energy (15 to 25 eV for light metals and up to 50 eV for heavy metals).

Several atomic processes determine the growth of a film in its initial phase, including condensation, adsorption, surface diffusion, diffusion into the film and nucleation (Lüth, 1993) (Figure 7).

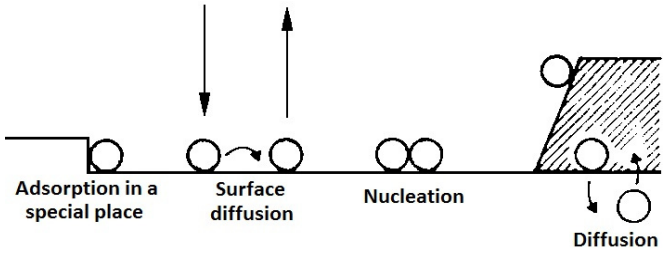

Fig. 7. Representation of the processes involved in film growth on a solid surface. Substrate atoms are open circles

Film depositions occur via the condensation of atoms incident to the glass substrate. The condensation of a new material is given by the amount of particles arriving/cm^2 per second. It can be divided into three stages. In the first stage, the bombarding atoms transfer kinetic energy to the atoms of the substrate network and are incorporated with weak bonds (adsorption). In the second phase, they spread over the surface, exchanging energy with the structural network of the substrate and some other species that are adsorbed, until they obtain favourable locations or low energy and effectively become defects on the surface of the substrate. At these sites, more atoms begin to accumulate, forming small islands. This phenomenon is called nucleation. The nuclei grow and coalesce to become a continuous layer of the substance on the substrate. The density and size of the islands have great influence on the interface with the substrate and, thus, the film adhesion. The ion bombardment and the high kinetic energy of the atoms arriving favours the creation of zones of nucleation, resulting in more areas of growth and less crowding in one place. This effect also decreases the amount of micro holes (Mattox, 1978), such that the interface of the film is described as more continuous or fine-grain. However, if nucleation areas are few, the

interface will have a "coarse type" structure. Once the film is continuous, growth happens on the surface as the result of the diffusion of newly arriving atoms. Finally, in the third stage, the incorporated atoms are rearranged by diffusion processes. Substrate and film atoms are exchanged, and the interface between the two substances becomes gradual. This enhances the film adhesion and reduces tension in the solid network caused by the creation of the interface between the two substances. In other words, the atoms of both materials are rearranged and settle at energetically favourable sites.

This is true for aluminium, but not for quartz (SiO_2), where the surface diffusion of atoms is almost zero. The phenomenon is manifested in the variation of film thicknesses along the mirror as a function of the target position (direction of arrival). Another consequence is the appearance of holes or trenches in the film (up to the microscopic level), which are caused by shading phenomena due to oblique incidence angles. This leads to the production of less dense and porous films with low refractive indexes.

Films with grain structures occur in systems with low substrate temperatures and relatively high pressures and where the mean free paths are short. This results in oblique incidence angles that favour growth atop the defects on the substrate surface, which in turn induces a shadow effect that accentuates the lack of uniformity throughout the film.

These defects are reduced when the polarization of the electrodes is increased, resulting in an increase in particle bombardment on the target surface and deposit on the substrate, so that there is a re-sputtering making it possible most particles are deposited on the substrate and fill the gaps that still remain (Müller, 1987).

The films have different structures depending on which of the three processes were more important during the film formation. This importance is given by the ratio T/Tm, where T is the substrate temperature and Tm is the melting point of the sputtered material in degrees absolute (Thornton, 1974).

4. Accelerated ageing tests

This chapter describes accelerated environment ageing tests for Al-Si_yO_x first surface solar mirrors, including humidity, thermal cycling, temperature, salt water immersion, sulphur dioxide, and abrasion. Experimental procedures are described in detail. Specular reflectance measurements of tested mirror samples are used as the basis for an inspection technique for assessing performance degradation. The main goals of these tests were to determine the protection provided by a Si_yO_x layer over an Al reflecting film and to assess the environmental stability of such mirrors. The experimental results show that Si_yO_x layers play an important role in protecting the mirrors, enabling them to be quite stable under the test conditions employed.

Two approaches can be applied to evaluate environment ageing tests and to study the degradation of solar mirrors: 1) outdoor natural weathering exposure and 2) accelerated environment ageing tests. Accelerated environment ageing tests are very often employed to evaluate and examine the performance of solar mirrors by means of simulated artificial environment conditions. In general, commercially available reflector materials are exposed to accelerated ageing in a climatic test chamber. In some cases, the experimental tests will substitute devices when the chamber is not available.

4.1 Preparation and selection of mirrors for tests

All Al-Si_yO_x first surface mirrors were manufactured using a high Al deposition rate and a low Si_yO_x deposition rate (Jiefeng et al., 1992). Their dimensions were 100 x 40 x 3 mm. The main difference among these samples was the thickness of the Si_yO_x layer over the Al reflecting film, which varied from 1500 Å to 2800 Å. In each test, samples with different SiyOx layer thicknesses were included. In order to determine the influence of tin from the glass surface on mirror properties, some sample films were deposited over the tin-poor surface of float glass substrates, while others were deposited over the tin-rich surface.

Humidity tests were used to examine three other kinds of mirror samples (in addition to Al-Si_yO_x first surface mirrors) obtained from different manufacturers, as follows: silver second surface mirrors with low iron glass and with plastic film (3M® Company) as substrates, and polished Al-sheet first surface mirrors. These three kinds of mirrors provided a comparison with the Al-Si_yO_x first surface mirrors.

4.2 Experimental program

a) Humidity Tests: The exposure box used in these tests is illustrated in Figure 8. The box was made of stainless steel and heat-insulating materials. Its inner dimensions were as follows: 100 cm long, 100 cm wide and 100 cm high. The test chamber was connected to a steam generator, a Samsung HU-820A Ultrasonic Humidifier, by a tube. The relative humidity (RH) in the chamber was measured with a Vaisala Humidity and Temperature Indicator HMI31 and was controlled and adjusted by changing the vapour flow produced by the steam generator. To prevent water vapour loss, the box was sealed with a rubber gasket. The electric heater and cryogenic refrigerator provided higher or lower temperature conditions inside the box. Thermocouples were used to monitor the inner temperature of the chamber during the experiment. A fan was used to maintain a constant uniform temperature and humidity inside the chamber.

The humidity tests were performed using two exposure conditions:

1. Room Temperature, 100% RH
2. 50°C, ~ 60% RH.

Clean mirror samples were deployed on a sample-frame, which was then placed at the centre of the bottom of the chamber. When the steam humidifier began to work, the cover of the chamber was closed. At this point, water vapour began to flow. The desired rate was obtained by adjustments. When temperatures that were higher or lower than room temperature were needed, the heater or the cryogenic refrigerator was used. Thus, various combinations of humidity and temperature were obtained. During the tests, reflectance of the samples was measured periodically.

b) Thermal Cycling: Under outdoor applications, solar mirrors were subjected to high and low temperature conditions. Tests were conducted to examine the bonding between films and their glass substrates under the above environmental thermal cycling (Figure 8).

Firstly, mirror samples were placed into an oven at 50°C with an ambient humidity for 1 h, then removed from the oven, cooled down to room temperature and maintained at that temperature for another 1 h. Then, the samples were dipped into a tank filled with liquid nitrogen for 20 min. Then they were removed from the liquid nitrogen, were allowed to reach

room temperature again and were maintained at that temperature for 1 h. The above process was repeated several times. The appearance of the mirrors was recorded after every cycle.

Fig. 8. Box for Humidity Test and Temperature Control Unit

c) Temperature Test: In general, temperature is very important with regard to mirror degradation because of its obvious effects on degradation rates. High temperature can cause mirror performance to degrade rapidly. According to the recommendation contained in Masterson et al. (1983), high temperature exposures must not exceed 80°C. The objective of temperature tests was to examine the thermal stability and performance degradation of first surface mirrors under high temperature conditions.

The specimens were heated by inserting them into a laboratory furnace kept at 70°C under ambient laboratory humidity. All samples were maintained at the same uniform temperature. After every successive 24 h, the appearance and reflectance of the mirrors were evaluated.

d) Salt Water Immersion: For this test, a solution with 5% (w/w) concentration of NaCl (instead of salt mist) was used. The immersion of the mirrors was conducted at temperatures ranging from 13 to 16°C in our study. In order to monitor the corrosion, appearance and reflectance of the tested mirrors, they were examined at intervals of 24 h after immersion.

e) Exposure to Moist Sulphur Dioxide: In order to simulate industrial atmospheric corrosion, sulphur dioxide (SO_2) was chosen as a pollutant. Samples were placed in a glass desiccator having a volume of ~10 dm^3 and containing 50 mL of water. SO_2 was produced by the chemical reaction 2.

$$Na_2SO_3 + H_2SO_4 \rightarrow Na_2SO_4 + H_2O + SO_2 \quad (2)$$

By introducing 5 g of Na_2SO_3 into the glass chamber, then adding sulphuric acid slowly and intermittently, SO_2 was produced (Dennis & McGee, 1980). It was introduced into the chamber through a rubber hose. In order to detect SO_2 in the chamber, a piece of wetted pH value paper was placed in the same position of the exposed samples. When the pH paper showed a null (0) pH value, introduction of SO_2 was stopped and the chamber sealed. The appearance and optical properties of the mirrors were examined periodically. The chamber was refilled with SO_2 after each inspection.

f) Abrasion Test: Under outdoor environments, solar mirrors will accumulate dust and wind-borne particles; therefore, repeated cleaning of their surfaces is needed during the service period. These likely damage the specularity and lower the efficiency of a concentrating

mirror. Thus, abrasion-resistance for first surface mirrors is clearly an important avenue for advancement.

A simple abrasion test using a clean, soft cloth was performed under dry and wet conditions separately. The procedure for the abrasion test was as follows: 1) the surfaces of the test mirrors were wiped using a dry, clean and soft cloth; 2) wet abrasion tests were performed using a clean, soft cloth soaked with an aqueous solution of a common detergent. Every 10 wipes, the surfaces of the tested mirrors were observed in order to determine whether any film damage occurred. After such tests, mirror surfaces were cleaned and reflectance measurements were conducted.

4.3 Results and analyses

a) Humidity Tests: were performed in triplicate. Two tests were performed at room temperature and 100% RH, and the third was conducted at 50°C and ~ 60% RH. The experimental results are listed in Tables 4, 5 and 6.

Spots appeared early in the humidity tests and remained unchanged in size thereafter. It is assumed that these consisted of alumina formed as a result of pinhole defects in the Si_yO_x film, where the Al film would have been exposed to water vapour and, therefore, oxidized during the test.

As a result, formation of Al_2O_3-H_2O would block and seal the original defect, preventing oxidation of the Al film around the holes and thereby limiting the size of the spots. Sample 4-8-2 showed a severe drop in reflectance. The reason was that the Si_yO_x layer was too thin to protect the Al reflecting film.

Additional mirrors with thicker films were manufactured. These were subjected to two humidity tests. Firstly, the samples listed in Table 3 were tested at room temperature and 100% RH for three and four weeks. After that, they were exposed to 50 °C and ~ 60% RH for two weeks. The experimental parameters and results are summarised in Tables 4, 5 and 6.

Sample	Thickness		Reflectance (ρ)*					Comments
	Al film [Å]	SiO_x film [Å]	Unexposed	Exposed [weeks]				
				1	2	3	4	
4-8-2	1517	748	0.786	0.776	0.767	0.763	0.767	Small holes
4-27-2	2000	2000	0.804	0.817	0.814	0.815	0.809	
4-20-1	2000	2200	0.776	0.790	0.785	0.785	0.785	Very small holes
3-11-2	1340	2230	0.813	0.825	0.822	0.822	0.818	Very small holes
5-4-3	2000	2500	0.829	0.839	0.839	0.841	0.835	
4-29-3	4000	2500	0.827	0.837	0.833	0.833	0.831	
4-1-1	1500	2520	0.807	0.811	0.809	0.808	0.808	Very small holes
4-27-9	2000	2000	0.786	0.776	0.767	0.763	0.767	Small holes

*Reflectance measurements of samples were performed using SSR.
Slide glass sheet. Corning 7059 Sheet glass.

Table 4. Reflectance of mirrors exposed at room temperature and 100% RH environment for up to four weeks

Tables 5 and 6 show superior experimental results compared to Table 4. No obvious degradation of performance occurred except in the case of the 3M silvered-tape sample, which showed severe edge corrosion after exposure to room temperature and 100% RH for 3 days. Water vapour permeated between the silver reflecting layer and covering (plastic film) causing degradation of the silver layer reflectance.

Sample	Thickness		Reflectance (ρ)*				Comments
	Al film [Å]	SiO_x film [Å]	Unexposed	Exposed [weeks]			
				1	2	3	
10-7-1	1257	2850	0.888	0.887	0.887	0.887	
10-1-1	980	1557	0.852	0.853	0.852	0.853	
9-29-2	1413	1552	0.850	0.850	0.851	0.851	
9-24-1	1454	2600	0.879	0.880	0.879	0.879	
9-18-1	1225	2534	0.886	0.887	0.886	0.887	
9-14-2	1247	2361	0.884	0.884	0.882	0.884	
9-8-2*	1012	2053	0.868	0.868	0.866	0.868	
7-16-2	1000	2200	0.875	0.876	0.873	0.875	
7-8-1	1092	2000	0.871	0.873	0.870	0.873	
Al sheet			0.896	0.896	0.893	0.894	
Ag mirror			0.920	0.919	0.920	0.920	
3M® silvered-tape			0.963	0.962	--	--	Heavy edge corrosion

*Films were deposited on the tin-rich surface of float glass substrate

Table 5. Reflectance of mirrors exposed to room temperature and 100% RH environment for up to three weeks

Sample	Thickness		Reflectance (ρ)		
	Al film [Å]	SiO_x film [Å]	Unexposed	Exposed [weeks]	
				1	2
10-7-1	1257	2850	0.887	0.888	0.887
10-1-1	980	1557	0.853	0.853	0.853
9-29-2	1413	1552	0.851	0.851	0.850
9-24-1	1454	2600	0.879	0.879	0.879
9-18-1	1225	2534	0.887	0.887	0.886
9-14-2	1247	2361	0.884	0.884	0.884
9-8-2	1012	2053	0.868	0.867	0.867
7-16-2	1000	2200	0.875	0.874	0.867
7-8-1	1092	2000	0.973	0.871	0.872
Al sheet			0.894	0.893	0.893
Ag mirror			0.920	0.918	0.918

Table 6. Reflectance of mirrors exposed to 50 °C and ~60% RH environment for up to two weeks

b) Thermal cycling: After every thermal cycle, the surfaces of tested mirrors were carefully checked to determine if any damage, crack or exfoliation of the films took place. When the tests were finished, the surfaces of the samples were cleaned and reflectance measurements were carried out. Five cycling times were performed and the results are summarised in Table 7.

During thermal cycling, the experimental conditions were very harsh. Two samples cracked, but the properties of the films in all five samples remained intact. When liquid nitrogen is used as the low temperature environment, the ageing test can be accelerated further and the test period reduced. However, if experimental conditions permit, a low temperature environment of dry ice plus alcohol is preferable.

Sample	Thickness		Reflectance (ρ)		Comments
	Al film [Å]	SiO_x film [Å]	Previous	After 5 cycles	
10-7-3	1257	2850	0.884	0.88	
9-24-2	1454	2600	0.877	0.874	
9-18-2	1225	2534	0.885	--	Glass was cracked
8-26-3	1000	2300	0.886	0.883	
7-16-1	1000	2200	0.878	0.878	Glass was cracked

Table 7. Results of thermal cycling test

c) Temperature test: Four pieces of mirror samples were heated in the oven at 70°C for 72 h. At 24 h intervals, the samples were removed from the oven, and the appearance and reflectance were checked and measured. The samples were then returned to the oven for further treatment. No detectable change in the samples was observed after thermal treatment for 72 h. Table 8 shows the results of the temperature test.

Sample	Thickness		Reflectance (ρ)			
	Al film [Å]	SiO_x film [Å]	Initial	Heated		
				24 h	48 h	72 h
9-24-3*	1413	1552	0.846	0.847	0.848	0.847
9-22-3*	1208	2500	0.868	0.869	0.867	0.866
9-14-1	1247	2361	0.885	0.886	0.885	0.885
7-1-2	1000	2000	0.865	0.864	0.863	0.863

Table 8. Results of temperature test of mirrors in air at 70 °C

d) Exposure to moist sulphur dioxide: was conducted for 48 h. At regular intervals, the samples were removed from the test chamber, and their appearance and reflectance were measured. The samples were then returned to the chamber for further exposure. The experimental results are given in Table 9. After 24 h exposure, sample 9-24-3 first showed very obvious corrosion (transparent small holes were present). Its reflectance decreased as well, even though a thicker Si_yO_x layer (2600 Å) was deposited on its surface. This may be exceptional and related to the preparation processes of the batch containing sample 9-24-3.

Sample	Thickness Film		Reflectance (ρ)						
	Al [Å]	SiO_x [Å]	Initial	Exposed					
				1 h	3 h	6 h	12 h	24 h	48 h
9-29-1	1413	1552	0.852	0.853	0.853	0.852	0.852	0.840	0.830
9-24-3	1453	2600	0.874	0.873	0.873	0.874	0.874	0.872	0.864
9-18-3	1225	2534	0.881	0.881	0.880	0.881	0.880	0.881	0.881
8-20-1	1167	2105	0.881	0.880	0.880	0.880	0.879	0.880	0.879
7-8-2	1092	2000	0.872	0.873	0.873	0.872	0.872	0.873	0.872

Table 9. Results of exposure to moist sulphur dioxide

e) Salt water immersion: At every 24 h interval, the samples were withdrawn from the salt solution, rinsed with distilled water and dried. Then the appearance was checked and the reflectance measured. Table 10 summarises the results of the salt water immersion test. After 72 h immersion, there was no drop in the reflectance nor change in the appearance of three of the samples. However, noticeable corrosion occurred at a local area of sample 10-1-3 after 24 h immersion (Figure 9).

Sample	Thickness		Reflectance (ρ)*				Comments
	Al film [Å]	SiO_x film [Å]	Initial	Immersed			
				24 h	48 h	72 h	
10-7-3	1257	2850	0.884	0.884	0.884	0.884	
10-1-3	980	1557	0.845	0.845	0.847	--	
9-14-3	1247	2361	0.879	0.878	0.881	0.880	Local corrosion
7-16-3	1000	2200	0.868	0.868	0.869	0.868	

Table 10. Results of salt water immersion

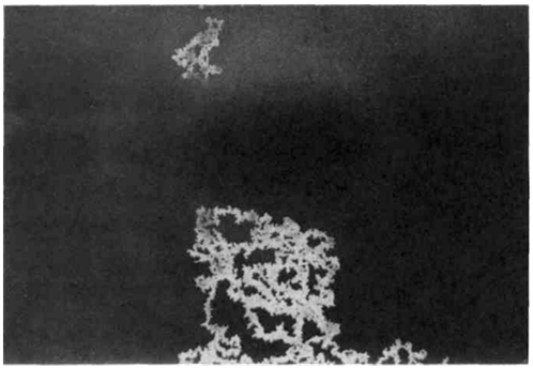

Fig. 9. Photograph of Sample 10-1-3 after 24 h immersion showing corrosion

On the corroded area, the Al reflecting film disappeared. However, no corrosion was observed in the rest of this sample, including its edges. Therefore, it was determined that the local corrosion of sample 10-1-3 resulted from defects in the Si_yO_x layer.

f) Abrasion test: On each sample surface, 200 wiping strokes of dry or wet abrasion were conducted. No obvious changes in the appearance or the reflectance of tested samples were observed.

5. Conclusions

The manufacture and performance of solar mirrors are already considered to be successful. The main limitation has been their durability in real environments such as Mexico City. The reflectance remained at 82% after 16 years of exposure in the Solar Plant of Engineering Institute (see table 11), supporting the use of this technology in solar concentrators that use aluminium as mirrors. The biggest application is currently for reflectance of ultraviolet solar radiation that reaches us from the Sun. This is applied in photocatalytic processes for the detoxification of substances that cannot be degraded by other methods. These substances are oxidised to carbon dioxide (a process called mineralisation).

Mirror Type	Reflectance $\rho_s(\pm 0.01)$		Test applied	Comments
Manufacture Date (dd/mm/yyyy)	Initial	Final		
First surface				
22-04-1995	0.85	0.82	Mexico City's weather (16 years)	A few, very thin scratches on the SiO_2 layer

Table 11. Specular reflectance of aluminium first surface mirror

Increasing the SiO_2 protective layer beyond 300 nm is suggested in order to eliminate or minimise the 'few very thin scratches' effects on specular reflectance. Additionally, during the accelerated environmental tests for the integrated and compound mirrors, the main degradation parameters were high humidity and atmospheric salinity.

The development of mirrors for solar applications continues to be a process of improvement. A lot of considerations are involved in the development of high specular reflectivity mirrors that demonstrate long lives, low cost and adaptability to any solar concentrator technology. The compilation of data presented in this chapter is a small part of a larger team effort that aims to provide additional knowledge to further us along the difficult path toward practical, renewable energy, particularly solar energy.

6. References

Almanza, R., Chen, J., Correa, G. & Mazari M., (1995). Further Option for Solar Concentrators: Aluminium First Surface Mirrors. *Solar Energy*, Vol. 54, No. 5, pp. (333-343), ISSN 0038-092X

Almanza, R., Hernandez, P., Martinez, I. & Mazari, M. (2009). Research and mean life of aluminium first surface mirrors for solar energy applications. *Solar Energy Materials and Solar Cells*. Vol. 93, No. 9, pp (1647-1651), ISSN 0927-0248

Almanza, R., Muñoz, F. & Mazari, M. (1992). Development of aluminium first surface mirrors for solar energy applications. *Solar Energy*. Vol. 48, No. 5, pp. (339-343), ISSN 0038-092X

Ashley, C., Reed, S. & Mahoney, A. (1988). Planarization of metal substrates for solar mirrors. *Proceedings 121 of the Material Research Society Symposium*, USA, ISSN: 0272-9172

Blake, D., Link, H. & Eber, K. (1992). Solar photocatalytic detoxification of water, In: *Advances in solar energy*, ed. K.W.Boer, American Solar Energy Society, ISSN 0731-8618

Brawn, R. (1970). Thin Film Substrates, In: *Handbook of Thin Film Technology*. McGraw Hill, USA, ISBN 978-0070397422

Brogren, M., Helgesson, A., Karlsson, B., Nilsson, J. & Roos, A. (2004). Optical properties, durability, and system aspects of a new aluminium-polymer-laminated steel reflector for solar concentrators. *Solar Energy Materials & Solar Cells*. Vol. 82, No. 3, pp. (387-412), ISSN 0927-0248

Correa, G., Almanza, R., Martínez, I. & Mazari, M. (1998). Use of linear Magnetrons for the fabrication of Aluminium first Surface Solar Mirrors. *Solar Energy Materials and Solar Cells*, Vol. 52, No. 3-4, pp. (231-238), ISSN 0927-0248

Dennis, W. & McGee, J. (1980). Silicone resins for protection of first surface reflectors. *Solar Energy Materials*, Vol. 3, No. 1-2, pp. (285-300), ISSN 0165-1633

Dennis, W. (1979). *Protective coatings for front surface reflectors*. Phase I. Report DOE/ET/21070-TI, USA

Drummeter, L. & Haas, G. (1967) Solar absorptance and thermal emittance of evaporated coatings, In: *Physics of thin films, Volume 4*, Haas, G. & Thun, R. p. (4), Academic press, New York, ASIN B004YWF47Y

Fend, T., Hoffschmidt, B., Jorgensen, G., Küster, H., Küster, H., Krüger, D., Pitz-Paal, R., Rietbruck, P. & Riffelmann, K. (2003). Comparative assessment of solar concentrator materials. *Solar Energy*, Vol. 74, pp. (149-155), ISSN 0038-092X

Fend, T., Jorgensen, G. & Küster, H. (2000). Applicability of highly reflective aluminium coil for solar concentrators. *Solar Energy*, Vol. 68, No. 4, pp. (361-370), ISSN 0038-092X

Gambino, R. & Cuomo, J. (1978). Selective resputtering-induced anisotropy in amorphous films. *Journal of Vacuum Science and Technology*, Vol. 15, No. 2, p. (6), ISSN 0734-2101

Glang, R. & Gregor, L. (1970). Generation of patterns in thin films, In: *Handbook of thin film technology*, Maissel, L. & Glang, R., McGraw Hill, ISBN 978-0070397422

Glang, R. (1970). Vacuum evaporation, In: *Handbook of thin film technology*, Maissel, L. & Glang, R., McGraw Hill, ISBN 978-0070397422

Haas, G., Heaney, J. & Hunter, W. (1982). Reflectance and preparation of front surface mirrors for use at various angles of incidence from the ultraviolet to the far infrarred, In: *Physics of thin films, Volume 12*, Haas, G., Francombe, M. & Vossen, J., p. (12), Academic Press, ISBN 9780125330121

Hass, G. (1982). Reflectance and preparation of front-surface mirrors for use at various angles of incidence from the ultraviolet to the far infrared. *Journal of the Optical Society of America*, Vol. 72, No. 1, pp. (27-39), ISSN 0030-3941

Hernandez, T., Moroño, A. & Hodgson, E. (2003). Radiation enhanced degradation of aluminium mirrors for remote handling and diagnostics applications. Effect of humidity. *Fusion Engineering and Design*. Vol. 69, pp. (177-182), ISSN 0920-3796

Jiefeng, C., Almanza, R., Mazari, M. & Correa, G. (1993). Accelerated Ageing Test For Al-Si_yO_x First Surface Solar Mirrors. *Series del Instituto de Ingeniería en Lenguas Extranjeras E-61*, pp. (1-39). Instituto de Ingeniería, UNAM, México.

Jones, R., Winters, H. & Maissel, U. (1968). Effect of oxygen on the rf-sputtering rate of SiO_2. *Journal of Vacuum Science and Technology*, Vol. 5, No. 3, p. (4), ISSN 0734-2101

Jorgensen, G., Williams, T. & Wendelin, T. (1994). Advanced reflector materials for solar concentrators. Proceedings of the 7th International Symposium on Solar Thermal Concentrating Technologies, Russia

Kearney, D. & Price, H. (2005). Recent advances in parabolic trough solar power plant technology, In: *Advances in Solar Energy. An annual review of research and development. American Solar Energy Society*, Earthscan, pp. (175-179), ISSN 0731-8618

Kennedy, C. & Jorgensen, G. (1994). State of the art low-cost solar reflector materials. NREL/TP-471-7022, DE95000260, USA, pp. (1-15)

Kennedy, C., Smilgys, R., Kirkpatrick, D. & Ross J. (1996). *Optical performance and durability of solar reflectors protected by an alumina coating*. National Renewable Energy Laboratory. NREL/TP-471-21413, No. SE612033, USA

Kennedy, C., Terwill, K., & Jorgensen, G. (2005). Analysis of accelerated exposure testing of thin glass mirror matrix. *Proceedings of the ISES World Congress*, USA, pp. (1-7)

Lüth, H. (2001). *Solid Surfaces, Interfaces and Thin Films*. (4th edition), Springer, Berlin, ISBN 978-3540423317

Maissel, L. & Glang, R. (1970). *Handbook of Thin Film Technology*. McGraw-Hill, New York, USA, ISBN 978-0070397422

Martin, P., Affinito, J., Gross, M., & Bennet, W. (1994). Coatings for large area low-cost solar concentrator and reflectors. *Proceedings of SPIE*, USA

Martinez, I., Almanza, R., Mazari, M. & Correa, G. (2000). Parabolic trough reflector manufactured with aluminium first surface mirror thermally sagged. *Solar Energy Materials and Solar Cells*, Vol.64, No. 1, pp. (85-96), ISSN 0927-0248

Masterson, K., Czanderna, A., Blea, J., Goggin, R., Gutierrez, M., Jorgensen, G., McFadden & J. (1983). Matrix Approach to Testing Mirrors, Part 2. SERI/TR-255-1627 DE 83 011996

Mattox, D. (1978). Thin film adhesion and adhesive failure - a perspective, In: *Adhesion Measurement of Thin Films, Thick Films, and Bulk Coatings,* Mittal, K.L., ASTM STP640-EB, American Society for Testing Materials, p. (9), USA, ISBN 978-0803155466

Morales, A. & Ajona, J. (1996). Durability and performance test of sol-gel front surface silver mirrors. *Proceeding of the 8th International Symposium on Solar Thermal Concentrating Technologies*, Germany, pp. (463-476)

Morales, A. & Ajona, J. (1999). Durability, performance and scalability of sol-gel front surface mirrors and selective absorbers. *Journal of Physics IV*, France, pp. (513-518)

Morales, A. & Durán, A. (1997). Sol-Gel Protection of Front Surface Silver and Aluminium Mirrors. *Journal of Sol-Gel Science & Technology,* Vol. 8, No. 1-3, pp. (451-457), ISSN 0928-0707

Pulker, H. (1999). *Coatings on Glass*. (2nd edition), Elsevier Science, The Netherlands, ISBN 978-0444501035,

Rossnagel, S., Cuomo, J. & Westwood, W. (1991). *Handbook of plasma processing technology, fundamentals, etching, deposition and surface interactions*. Noyes publications, New Jersey, USA, ISBN 978-0815512202

Schissel, P., Jorgensen, G., Kennedy, C. & Goggin, R. (1994). Silvered-PMMA reflectors. *Solar Energy Materials & Solar Cells*, Vol. 33, No. 2, pp. (183-197), ISSN 0927-0248

Wasa, K. & Hayakawa, S. (1993). *Handbook of sputter deposition technology, principles, technology and applications*. Noyes publications, New Jersey, USA, ISBN 978-0815512806

Yang, M., Gatto, A. & Kaiser, N. (2006). Highly reflecting aluminium-protected optical coatings for the vacuum-ultraviolet spectral range. *Applied Optics*. Vol. 45, No. 1, pp. (178-183), ISSN 1559-128X

Part 2

Environment

7

Application of Solar Energy in the Processes of Gas, Water and Soil Treatment

Joanna Pawłat and Henryka D. Stryczewska
Lublin University of Technology
Poland

1. Introduction

Shortening of natural resources will impose greater limitations on electric energy consumption in various fields including treatment technologies. Moreover, with increasing of environmental awareness in the society there comes the need of shifting industry and farmers towards clean and eco-friendly techniques, which allow to avoid formation of secondary pollutants during the treatment process.

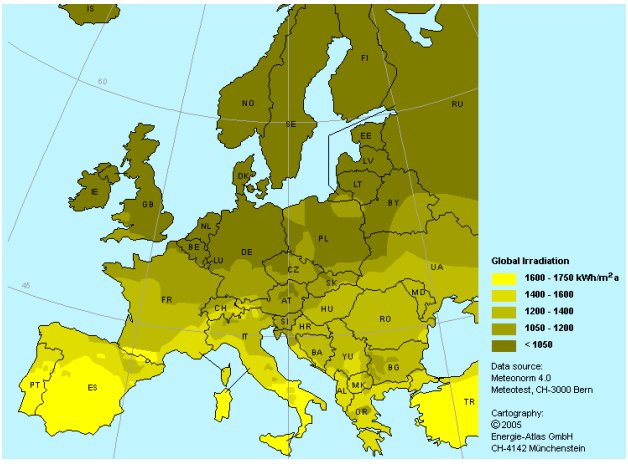

Fig. 1. Global irradiation in Europe (Energie-Atlas GmbH, 2005).

Small water, wastewater, gas and soil treatment installations supplied with electric energy from renewable energy sources are perfect example of zero-emission technology achieved with reasonable cost (Pawłat et al., 2011). Possibility of solar energy application, as one of the alternative energy resources for decontamination processes is strongly dependent on geographical location. Near-equatorial places called "sunny belt" are much more favorable and cost-effective for solar installations. However, constant growth of fuel prices in the last decade caused rapid development of solar technology across Europe, including its northern parts. The average insolation of Europe territory is presented in Fig. 1. (Energie-Atlas GmbH, 2005).

Poland is situated in the moderate climatic zone between 49° and 54.5° of the northern latitude. Daily interval (time from the sunrise to the sunset) covers over 51% of 8767 hours in the average year, and this period is 24 hours longer in the northern parts compared with the southern ones. In winter, day is almost 1 hour longer in southern regions of Poland comparing with the northern regions whereas it is opposite in summer (Nalewaj et al., 2003).

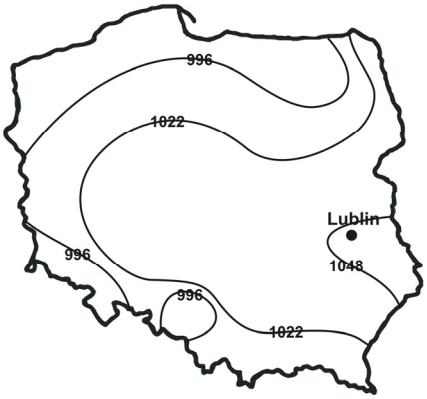

Fig. 2. Total radiation (KWh/m²).

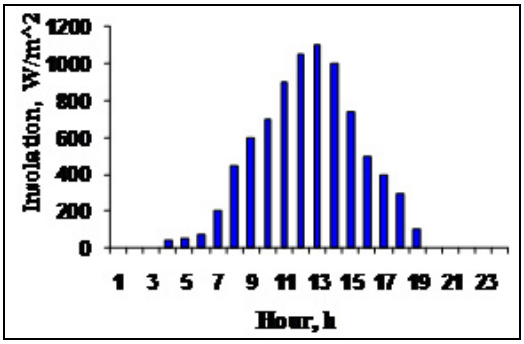

Fig. 3. Insolation in Lublin between 1-3 June 2002, (Nalewaj et al., 2003).

The average annual insolation on Poland's territory amounts to about 1100 kWh/m² (3500MJ/m²) per year on a horizontal area, which corresponds to the calorific value of 120 kG of theoretical standard fuel (29300 kJ/kg of hard coal, 41860 kJ/kg of petroleum). Fig. 2 depicts insolation map of Polish territory. The insolation of this area is characterized by a big annual diversification. For example, the annual amount for the Lublin city is about 1107 kWh, and while over 15% of annual energy reaches Lublin in August, in December it is only 1,6%. The typical daily insolation in Lublin area in Summer is depicted in Fig. 3.

In Europe solar thermal collectors are primarily used for hot water production and space heating (use of solar energy for cooling is rather limited). According to (EUROBSERV'ER, 2010), the solar thermal panel area installed in the EU during 2009 was 4166056 m² giving 22786,1MW_{th} of the accumulated installed solar thermal capacity. Prevailing technology is flat glazed collectors integrated into an insulated casing (heat transport fluid circulates in an

absorber sheet placed behind a panel of glass- 3608711 m² and 106494 m² installed in 2009 in Europe and Poland, respectively) over the vacuum tube collector (fluid circulates inside a double vacuum tube and insulation is provided by the vacuum- 408998 m² and 37814 m² installed in 2009 in Europe and Poland, respectively) and unglazed collectors (matrix of black plastic tubes, stacked against each other left out in the fresh air- 148347 m² installed in 2009 in Europe).

The largest national collector bases were in Germany (12899800 m² and 9029,9 MW_{th}) and in Austria (4330000 m² and 3031 MW_{th}). The 10th place on the EU2009 list belonged to Poland with 509836 m² of collectors installed, giving 356,9 MW_{th}). Poland had 13,4 m² of solar thermal collectors installed per 1000 inhabitants and produced 9,4 kW_{th} per 1000 inhab. in 2009. Leaders per capita were Cyprus (873,9 m²/1000inhab.and 611,7 kW_{th}/1000 inhab) and Austria (517,1 m²/1000 inhab. and 362 kW_{th}/1000 inhab.). In UE on average 64,9 m² and 45,5kW_{th} were installed and produced per 1000 inhabitants, respectively (EUROBSERV'ER, 2010).

In 2010 Europe also continued photovoltaic plants' installation reaching over 80% of global installed photovoltaic's capacity and generating 22,5 TWh of photovoltaic power. The additional installed capacity in the EU over twelve months to the end of 2010 ranged 13023,2MW_p (growth of 120,1%).The cumulated predicted photovoltaic capacity of EU in 2010 is presented in Fig.4 (EUROBSERV'ER, 2011).

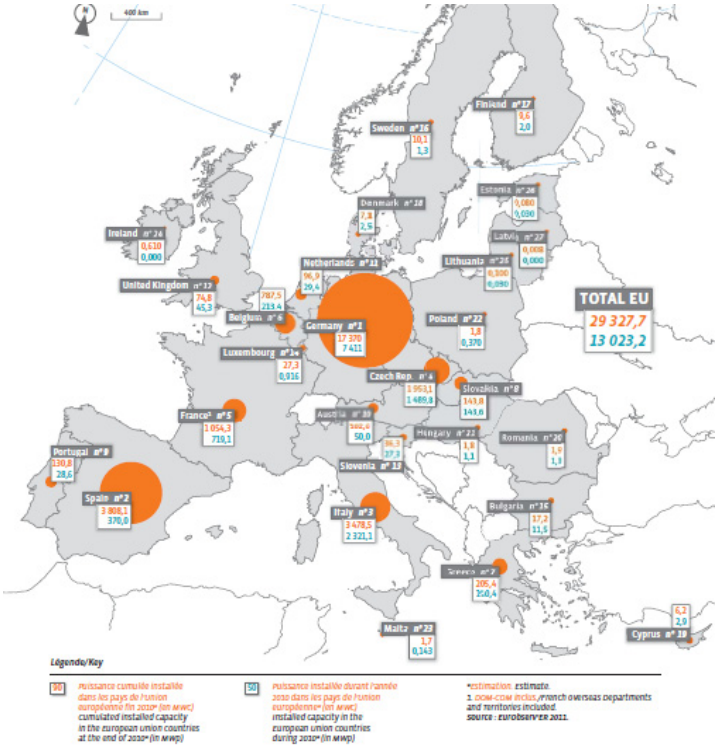

Fig. 4. Cumulated photovoltaic capacity in the European Union countries in 2010 (in MW_p) (EUROBSERV'ER, 2011).

Average photovoltaic power per inhabitant in European Union in 2010 was 58,5 W_p/inhab, with leading Germany and Czech Republic with 212,3 and 185,9 W_p/inhab., recpectively. The most of 2009-2010 electricity production from this source took place in Germany (12000 GWh) and Spain (6302 GWh). In Poland it was only 1,8 GWh (EUROBSERV'ER, 2011).

2. Solar energy in water treatment

Inadequate access to clean water and lack of its sanitation are persistent world-wide problems affecting humans on each continent (according to UN number of people who lack access to safe drinking water will increase from over 1 bilion to over 1.8 billion in in 2025). Moreover, industry and agriculture also require huge amounts of water causing further deterioration of water quality and its scarcity in the region.

There are many conventional technologies of water decontamination but with growing environmental pollution they are sometimes insufficient besides being energy-consuming. These technologies often require addition of suplemental chemical compounds, which lead to secondary pollution. Ozone based technologies combined with advanced oxidation processes (AOP), already investigated and tested for three decades proved to be a good alternative to traditional methodes. However, AOP methodes are also considered expensive and power-consuming. Thus combining treatment technologies with alternative energy sources can be a perfect solution allowing optimum purification due to combination of variety of decontamination techniques. In this part applicationof solar power for water desalination, drinking water and wastewater treatment is described.

2.1 Solar desalination

Desalination aims to remove any salts and mineral from water to make it suitable for drinking or for industrial application. The most common process is thermal desalination, which uses boiling water and is based on evaporation and vacuum distillation. Energy required to evaporate water is 2.3 MJ per kilogram. The installations, which belong to this category are simple stills, MEH (Multi Effect Humidification), MED (Multi Effect Distillation), MES (Multi Effect Solar Desalination) and MSF (Multi Stage Flash). Novel desalination plants use reverse osmosis (RO), electrodesalinization (EDI) and membrane distillation (MD). Despite of used method, desalination of water requires tremendous amount of energy. The main criteria for desalination system in developing countries are affordability, reliability, simplicity and good quality of output medium. Areas, where shortage of drinking water limits the socioeconomic development are often highly insolated. Thus, using solar power for desalinization purposes seems to be economically justified. Moreover, water can be obtained in environmentally-friendly process.

Two examples of small thermal desalinization installations for use in remote arid areas are depicted in Fig. 5 (Chaibi, 2000; Al-Kharabsheh and Goswami, 2003).

Solar powered humidification– dehumidification principle is evaporation of seawater and condensation of water vapor from the humid air in the unit at ambient pressure and at temperatures between 40°C and 85°C (Al-Hallaj et al., 2006). Simplicity of the set up made it popular in different parts of the world. Typical MEH desalination unit is presented in Fig. 6a.

Multi-effect distillation unit was developed in Germany (Muller-Hoist et al., 1999) and then applied on the island of Fuerteventura, where it is working for several years without almost any maintenance or repair. The optimized module produced 40 L/h of fresh water, but it was shown that production of 1000 L/d is possible when the unit was operated continuously for 24 h. Based on a collector area of 38 m², the daily productivity of the optimized module is about 26 L/m² of collector area for a 24-h run and with thermal storage under optimized laboratory conditions (Parekh et al., 2004).

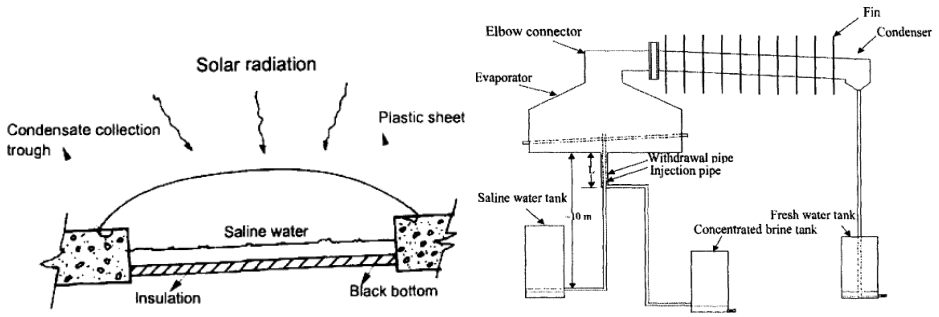

a b

Fig. 5. Simple solar still (Chaibi, 2000) (a), desalination system using low-grade solar heat (Al-Kharabsheh and Goswami, 2003) (b).

Application of solar chimney to generation of energy and sea water desalination, which is shown in Fig. 6 is also an interesting approach. Through theoretical analysis, it has been demonstrated that the integrated system can significantly improve the solar energy utilization efficiency as well as the land resources utilization efficiency (Zuo, 2011).

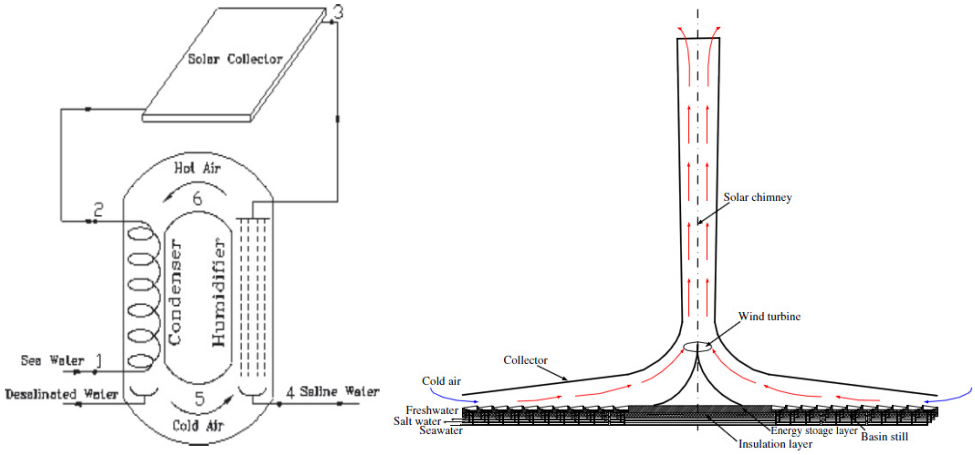

a b

Fig. 6. Sketch of a natural draft air circulation MEH desalination unit (Parekh et al., 2004) (a), Schematic diagram of the integrated desalination system with solar chimney (Zuo, 2011) (b).

The Solarflow water treatment system for remote indigenous communities was invented at The Environmental Technology Centre, Murdoch University (the Murdoch ETC) in Perth, in the early 1990s and it is constantly modified since then (Dallas et al., 2009). The Solarflow is a self-contained solar-powered unit capable of producing 400 L/d of high quality drinking water from brackish water via reverse osmosis and requires only 120W of photovoltaic power.

Other project combining solar thermal and seawater or brackish water reverse osmosis is SOFRETES system, which was already in operation in the early 1980s (Delgado et al., 2007).

As an output of the project SMADES, employing membrane distillation and aiming in design of large solar powered desalination system, the pilot plant was built in Aqaba, Jordan in 2006. Feed water was seawater directly from the Red Sea (55,000 μS/cm) (Banat et al., 2007).

MEDSOL is an EU project on seawater desalination by innovative solar-powered membrane distillation system (Galvez et al., 2009). Commercial sea water purification system is offered by Blue Spring Company, (Fig. 7). Models EC-1MS, through EC-30MS with output capacity ranging from 1.2 m^3/d to 30 m^3/d can serve the fresh water needs of communities from 6 to 160 households.

Fig. 7. Blue Spring Solar desalination system.

2.2 Solar energy for water conditioning

Availability of drinking water is an ultimate condition for the inhabitation. Extraction of water from air (EWA) (Scrivani et al., 2007) is the solution in the case of lack of primary source of water. The total quantity of water contained in 1 km^2 of atmospheric air, that is, in most regions around the globe, ranges from 10,000 to 30,000 m^3 of pure water.

In proposed solution, the refrigerator was operated by an electricity driven compressor and the cold fluid going into the heat exchanger was produced by a reverse compression-expansion thermodynamic cycle (Fig. 8). It was claimed by the manufacturers that approximately one liter of diesel fuel operating the electrical generator could provide four liters of water from air. In fact, system integration with PV panels could make it more reasonable from economy point of view.

In the developing countries, where sophisticated water purification methods are not available, solar water disinfection (SODIS) revealed a great potential to reduce the global diarrhoeal diseases burden, which affects over 1.8 million people (Meierhofer and Landolt, 2009; Acra et al., 1980).

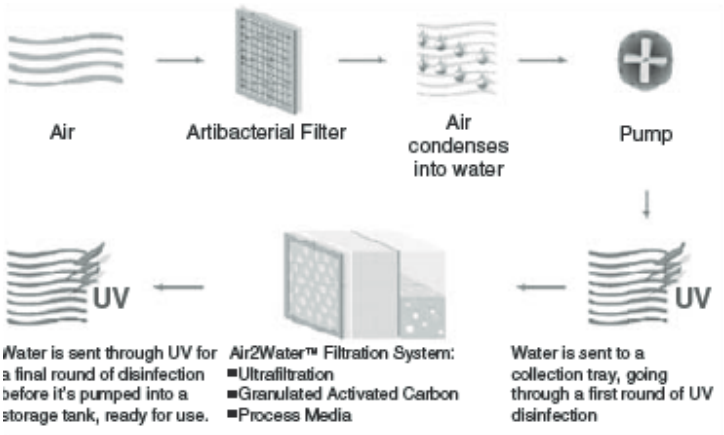

Fig. 8. Typical EWA plant for potable water production (condensation occurs by passage of the air on the cold coils of a heat pump) (Scrivani et al., 2007).

According to extensive microbiological investigation, 30°C water temperature, a threshold solar radiation intensity of at least 500 W/m^2 (all spectral light) is required for 3-5h for SODIS to be efficient for destruction of diarrhoea-causing pathogens in contaminated drinking water. Water can be stored in any transparent container. Since the year 2000, SODIS is being promoted in developing countries through information and awareness campaigns and currently used in 33 countries (Fig. 9) by more than 2 million people and decreasing diarrhoea outbreaks by 16–57%.

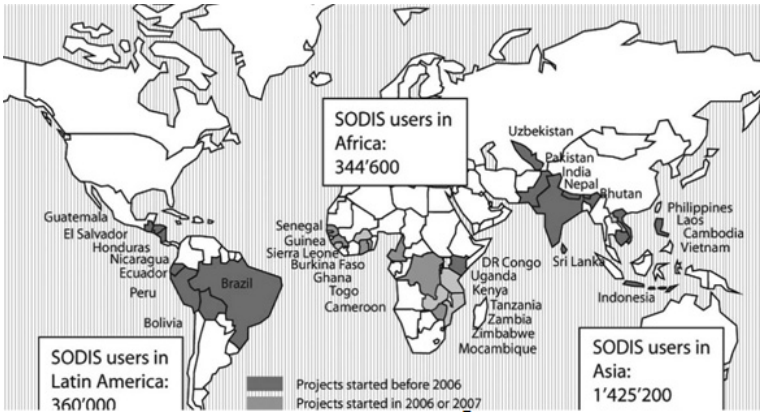

Fig. 9. More than 2 million users currently practise SODIS in 33 countries (Meierhofer and Landolt, 2009).

Single-basin solar stills, presented in Fig. 10 for the removal of a selected group of inorganic, bacteriological, and organic contaminates were investigated (Hanson et al., 2004) and turned to be efficient in removing non-volatile contaminants from the water. Removal efficiencies of more than 99% were noted on salinity, total hardness, nitrate, and fluoride.

The group of Sixto Malato has been investigating the solar photocatalysis and proposing various innovations in the process for more than decade. Mechanism of solar driven photocatalysis is depicted in Fig. 11, (Robert and Malato, 2002).

Malato group was often using compound parabolic collectors (CPC), however variety of shapes and solutions including trough reactor (PTR), thin-film-fixed-bed reactor (TFFBR), double skin sheet reactor (DSSR, pilot plant in Wolfsburg factory of the Volkswagen AG), etc. can be employed (Bahnemann, 2004).

In areas where water is heavily contaminated standalone systems, which were used for desalination and simple light disinfection might be not sufficient. AOP methods and catalytic processes can bring rapid improvement of the effluent water quality. Many research groups were investigating the catalytic systems based on titanium compounds and Fenton process.

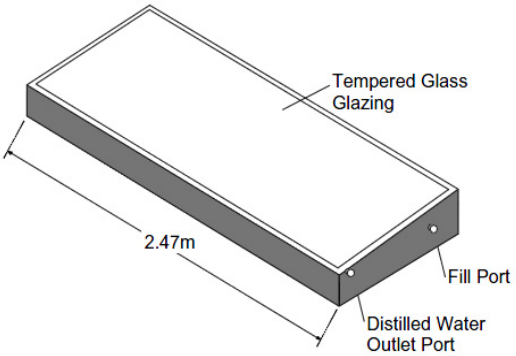

Fig. 10. Isometric view of El Paso Solar Energy Association still (Hanson et al., 2004).

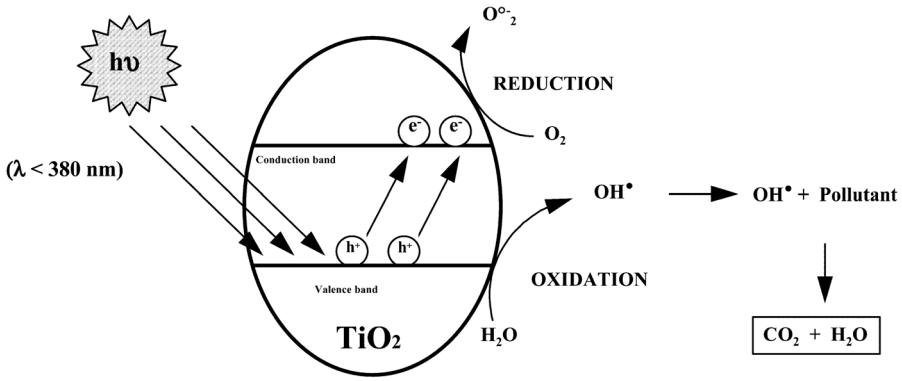

Fig. 11. General mechanism of the photocatalysis, (Robert and Malato, 2002).

Solar driven photocatalytic oxidation processes are presented in Tab. 1. (Blanco et al., 2009). Tab 2. (Malato et al., 2009) compares various factors, which must be taken into the consideration when TiO_2 and photo-Fenton process are used.

TiO_2-persulfate photocatalytic system ($\lambda < 390$ nm)	Photo-Fenton method (H_2O_2 and Fe^{2+}) irradiated in the UV–vis range ($\lambda < 580$ nm)
$TiO_2 + h\nu \rightarrow e^-_{CB} + h^+_{VB}$	
$h^+_{VB} + H_2O \rightarrow {}^\bullet OH + H^+$	$Fe^{2+} + H_2O_2 \rightarrow Fe^{3+} + OH^- + {}^\bullet OH$
$S_2O_8{}^{2-} + e^-_{CB} \rightarrow SO_4{}^{\bullet-} + SO_4{}^{2-}$	$Fe^{3+} + H_2O + h\nu \rightarrow Fe^{2+} + H^+ + {}^\bullet OH$
$SO_4{}^{\bullet-} + H_2O \rightarrow {}^\bullet OH + SO_4{}^{2-} + H^+$	

Table 1. Photocatalytic oxidation processes that can be driven by solar energy (Blanco et al., 2009).

	TiO_2	**Photo-Fenton**
Stress on reactor materials	Corrosive liquids: oxidative process, pH and salt concentration depend on application.	Corrosive liquids: oxidative process, H_2O_2, iron ions, usually acidic pH (2–3.5), salt concentration and temperature depend on application.
Cleaning procedures	TiO_2 may adsorb on the reactor walls preventing illumination, effective chemical cleaning agents are HCl, and mostly, H_2F_2.	Iron oxides may deposit on the reactor walls preventing illumination, effective chemical cleaning agents are chelating agents, such as oxalic acid and acidic pH.
Residence time in collector	Long residence time in the collector may cause dissolved O_2 depletion.	Long residence time in the collector may cause H_2O_2 depletion.
Temperature	Not relevant to process performance between 20 and 80 °C.	Strongly influential on process performance, beneficial if higher.
Reactor diameter/ depth— optical pathlength	Light distribution in the collector is largely governed by absorbance and scattering by the catalyst particle. A direct correlation between ideal catalyst concentration and diameter exists.	Light distribution is governed by absorbance of the solution, which is a function of catalyst concentration and wastewater. Absorbance varies strongly along the treatment due to the appearance and destruction of compounds.
Effective wavelength range	<390 nm for TiO_2, being approx. 4% of sunlight's irradiance power (sunny days).	Depends strongly on the presence of complexes, may be up to 550–600 nm being 28–35% of sunlight's irradiance power (sunny days).
Light intensity	Rate law changing from first through half order to zero-order dependency as the light intensity increases.	Little research performed, first order rate law suggested over a broad range of light intensity, applicable as long as ferric iron predominates over ferrous iron.
Dark zones	No reactions taking place in dark zones.	Fenton process takes place in dark zones, elevated temperature influences the reaction rate positively. Alternating dark and illumination intervals have shown to reduce the necessary illumination time.
Process control	Process control mainly includes the determination of treatment end.	Process control includes the determination of the treatment end. pH must be controlled to avoid iron precipitation.

Table 2. Comparison of TiO_2 and photo-Fenton process aspects relevant to the photoreactor's design requirements, (Malato et al., 2009).

EU supported several different projects with the aim of developing a cost effective technology based on solar photocatalysis for water decontamination and disinfection in rural areas of developing countries, for instance: SOLWATER and AQUACAT (Malato et al., 2009) (Fig. 12).

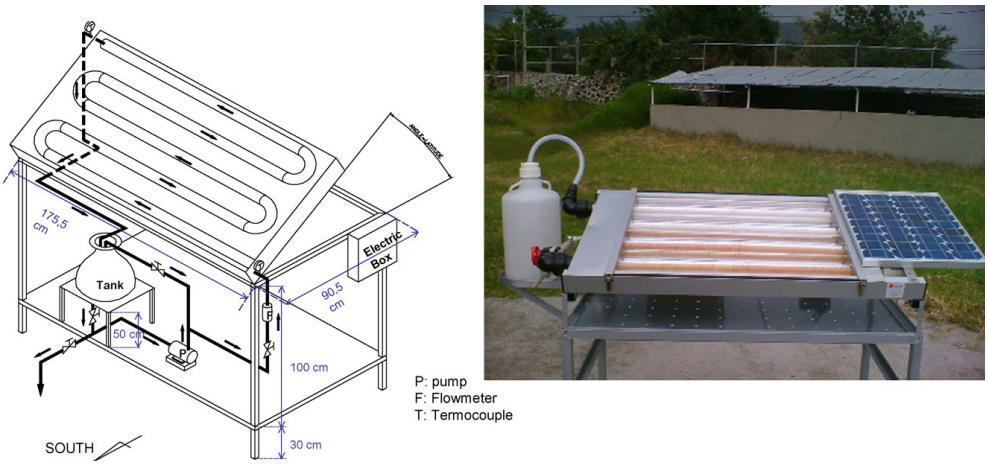

Fig. 12. Schematic diagram and photograph of the photoreactor developed in AQUACAT and SOLWATER projects for photocatalytic disinfection in developing countries (Malato et al., 2009).

Fig. 13. View of the solar detoxification demonstration plant erected by ALBAIDA at La Mojonera (Almerı´a, Spain), (Malato et al., 2007).

Huge solar driven photocatalytic plant, presented in Fig. 14, was built in Almeria, Spain under the ''SOLARDETOX'' EU project on solar detoxification technology for the treatment of industrial non-biodegradable persistent chlorinated water contaminants, (Malato et al., 2007). Nowadays, facility allows to investigate following technologies (Bahnemann, 2004):

a. Solar Desalination, from two different approaches, combined solar power and desalination plants (MW range), and medium to small solar thermal desalination systems (kW range).
b. Solar Detoxification, by making use of the near-ultraviolet and visible bands of the solar spectrum (wavelengths shorter than 390 nm for TiO_2 and 580 nm for photo-Fenton) to

promote a strong oxidation reaction by generating oxidizers, either surface-bound hydroxyl radicals (OH^-) or free holes, which attack oxidizable contaminants, producing a progressive break-up of molecules yielding CO_2, H_2O and dilute mineral acids.

c. Solar Disinfection, which applies the detoxification techniques mentioned above, using a supported photocatalyst, to generate powerful oxidizers to control and destroy pathogenic water organisms.

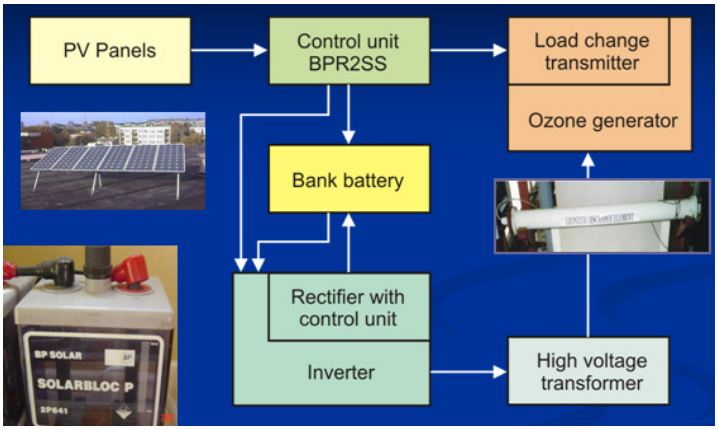

Fig. 14. Integrated PV water/gas/soil conditioning system based on ozone.

Integrated PV system based on AOP and application of ozone (Fig. 14) for water and gas conditioning was developed by Stryczewska group (Stryczewska, 2011; Komarzyniec et al., 2010; Pawłat et al, 2011a; Pawłat et al, 2011b). System was applied for conditioning of the pool waters, soil and gas. It will be further described in part 5.

2.3 Solar wastewater treatment

Wastewater treatment processes can be basically divided into 3 groups: mechanical, chemical and biological. They are used in various combinations depending on the type and concentration of pollutants. Some of discharged industrial impurities are not decomposable by conventional technologies, require tremendous amount of energy, thus, must be treated with alternative methods such as AOP. Those needs can be at least partly assured by using solar supported technologies. Examples of solar power employing in the processing of hardly-treatable compounds from various industrial branches such as pharmaceutics, chemical, semiconductor, dye, paper, food and for farms' and landfills' leachates are known.

Fig. 15 presents solar photocatalytic treatment plant developed to treat wastewater from recycling pesticide bottles (Albaida plant, Almeria, Spain) (Blanco et al., 2009). Water from washing the pesticide bottles was treated in batches until 80% of the TOC has been mineralized. At this point, the water was transferred to the post-treatment (iron precipitation, sedimentation and recuperation), and either reused for bottle washing or discharged for irrigation through an activated carbon filter to ensure discharge quality. About 75% of the total volume of the treatment circuit was continuously exposed to sunlight in 150 m^2 of CPC solar reactors.

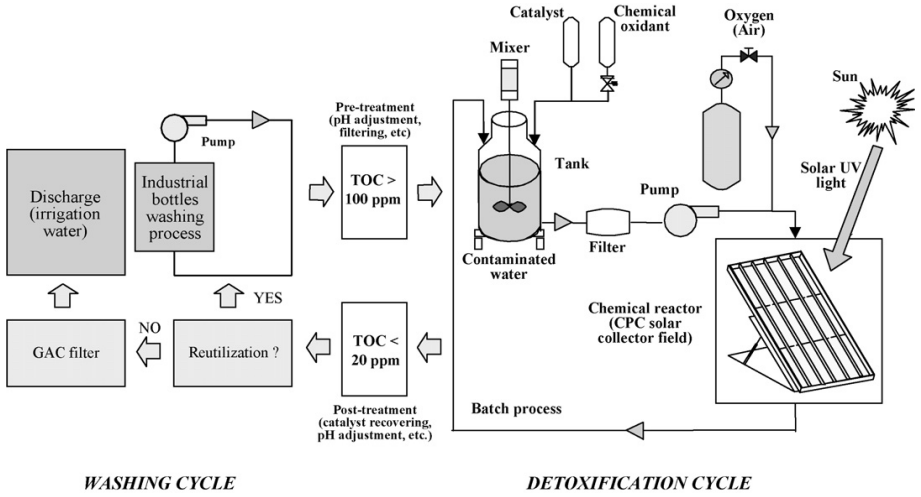

Fig. 15. Conceptual design of the ALBAIDA solar photocatalytic plant for the treatment of wastewater from washing shredded plastic pesticide bottles for recycling, (Blanco et al., 2009).

Another coupled solar-biological system at field pilot scale based on CPC and fixed bed reactor (Fig. 16) for the treatment of biorecalcitrant pollutants was developed in EPFL (Sarria et al., 2003). The photo-Fenton system was the most appropriate AOP for the degradation of a model biorecalcitrant compound, 5-amino-6-methyl-2-benzimidazolone (AMBI). The coupled reactor, operating in semicontinuous mode achieved 80-90% mineralization performance depending on the range of initial dissolved organic carbon.

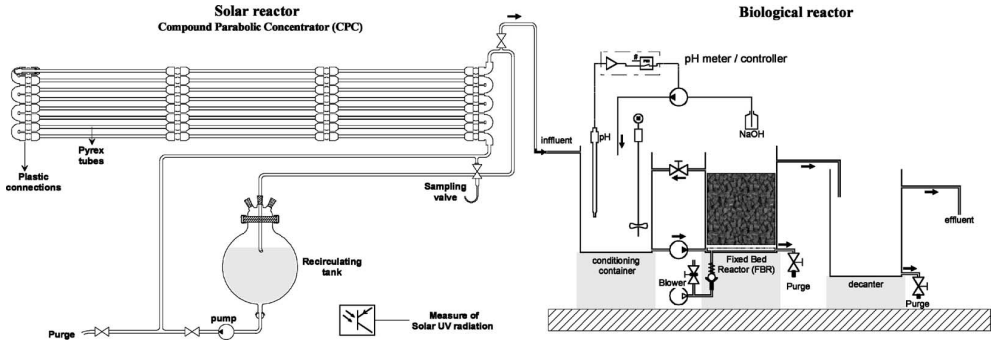

Fig. 16. Schematic representation of the coupled solar-biological flow reactor (Sarria et al., 2003).

100% of the cyanides and up to 92% of TOC in wastewater effluent from an Integrated Gasification Combined-Cycle was degraded in the cycle utilizing concentrated solar UV energy (UV/Fe(II)/H_2O_2) in a Solar CPC pilot plant (Duran et al., 2010) under the optimum conditions ([H_2O_2] = 2000 ppm, [Fe(II)] = 8 ppm, pH = 3.3 after cyanide oxidation, and [$(COOH)_2$] = 60 ppm).

Different solution was design of solar heated reactor for anaerobic wastewater or biological sludge treatment at temperatures higher than the ambient air temperature (Yiannopoulos et al., 2008). For the proposed reactor system, the solar energy absorbed by flat plate collectors was transferred to a heat storage tank, which continuously supplied an anaerobic-filter reactor with water at a maximum temperature of 35°C. At this temperature the COD removal efficiency was approximately 80%.

3. Solar energy in conditioning of air and drying the crops

3.1 Cooling and air conditioning

There are two main ways to convert solar radiation into cooling or conditioning of air, based on PV panels and solar collectors combined with variety of thermodynamic processes (Fig. 17), (Henning, 2007). Solar buildings and using of gravitational ventilation is gaining more and more popularity in Europe but this topic will not be a subject of the present chapter.

Techniques allowing use of solar thermal collectors, which are currently prevailing over PV panels for air-conditioning of buildings can be basically divided into thermally driven chillers (to produce chilled water which can be used for any type of air-conditioning) and open cycles, also referred to as desiccant cooling systems, (for direct treatment of air in a ventilation system). Typical system based on thermal process is presented in Fig. 18.

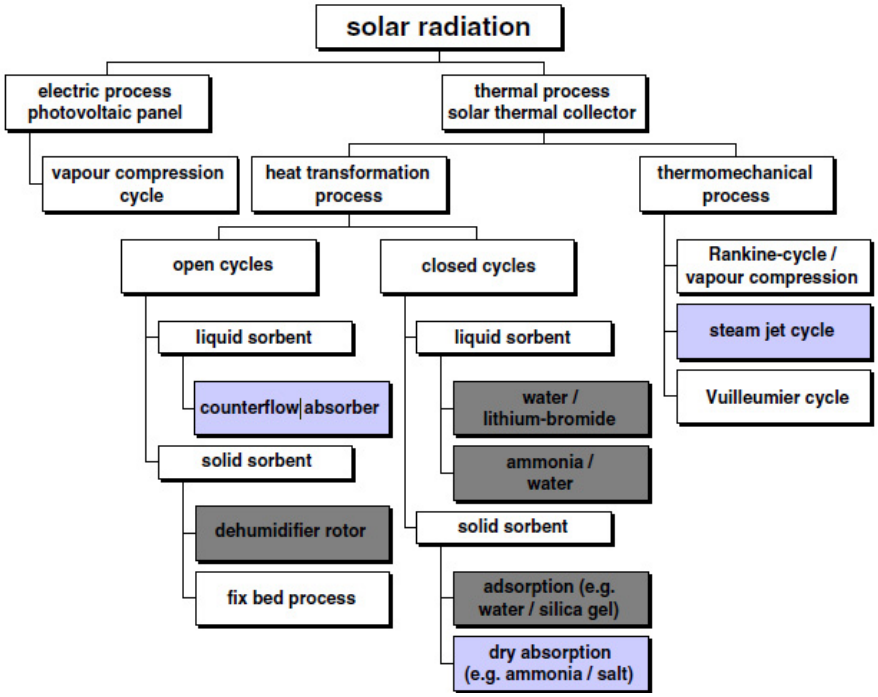

Fig. 17. Solar radiation for air-conditioning. Processes marked in dark grey: market available technologies which are used for solar assisted air-conditioning. Processes marked in light grey: technologies in status of pilot projects or system testing (Henning, 2007).

Following processes, depicted in Fig. 18 are taking place: 1- intake, 2-sorptive dehumidification of supply air; 3-pre-cooling of the supply air in counter-flow to the return air from the building; 4-evaporative cooling of the supply air to the desired supply air humidity by means of a humidifier; 5-the heating coil is used only in the heating season for pre-heating of air; 6-a small temperature increase is caused by the fan; 7-supply air temperature and humidity are increased by means of internal loads; 8-return air from the building is cooled using evaporative cooling close to the saturation line; 9-the return air is pre-heated in counter-flow to the supply air by means of a high efficient air-to-air heat exchanger, e.g., a heat recovery wheel; 10-regeneration heat is provided for instance by means of a solar thermal collector system; 11-the water bound in the pores of the desiccant material of the dehumidifer wheel is desorbed by means of the hot air;) 12-exhaust air is blown to the environment by means of the return air fan.

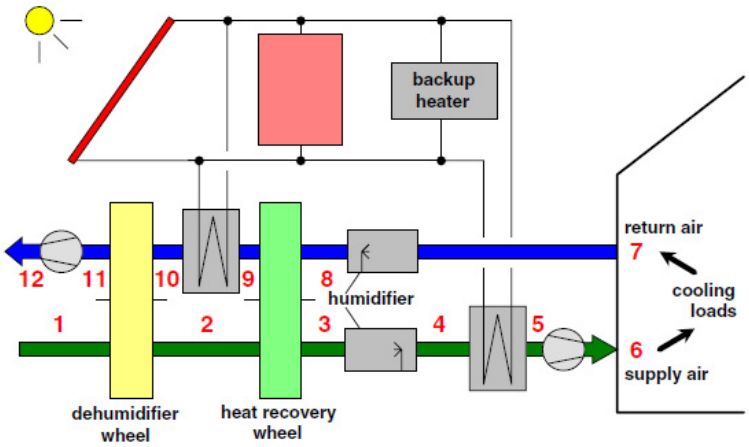

Fig. 18. Standard desiccant cooling cycle using a dehumidifier wheel with solar thermal energy as driving heat input, (Henning, 2007).

In Europe thermal systems are mostly installed in Germany and Spain. Large ones are installed at the Sarantis cosmetics factory in Greece and the federal office for environmental issues of Bavaria in Augsburg. In Freiburg/Germany a solar cooling system is operated by the University hospital for air-conditioning of a laboratory.

The system, presented in Fig. 19 consists of an adsorption chiller with a capacity of 70 kW and a field using evacuated tube collectors with an aperture area of 170 m^2 (Henning, 2007).

Integration of air conditioning especially for cooling purposes with PV panels is another eco-friendly approach as cooling is usually used in the period of high insolation. Thus, use of PV supplied energy could stabilize the grid. PV panels integrated with air conditioning system are already commercially offered on the market by LG (Fig. 20a). LG's solar-assisted air conditioner requires only 727 watts per hour of energy for cooling.

Another solution is a hybrid system (photovoltaic + solar thermal) proposed by SolarWall® PV/T , which provides up to 4 times the total energy from the same surface area. ICL Co Ltd, Mitsubishi Chemical Corp and Nippon Fruehauf Co Ltd co-developed the air conditioning system "i-Cool Solar" (Fig. 20b), which stores electricity via the photovoltaic

panels in special on-board batteries and uses the stored energy to power the cabin air conditioner when the truck is idle.

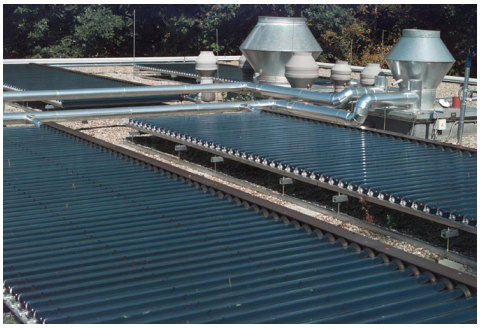

Fig. 19. Solar collector field (evacuated tubes) installed in system at University hospital in Freiburg (Henning, 2007).

a

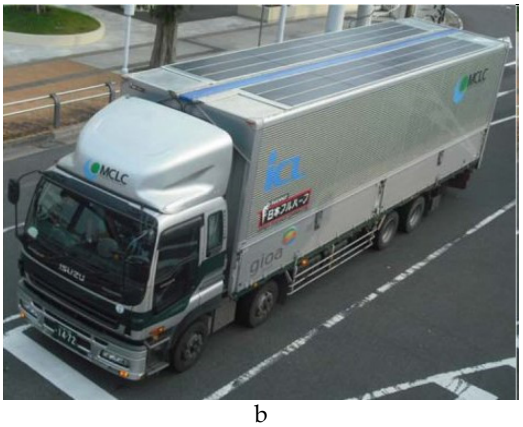

b

Fig. 20. LG solar hybrid air conditioner (a), ICL Co Ltd, Mitsubishi Chemical Corp and Nippon Fruehauf Co Ltd solar cooled truck (b)

3.2 Drying of crops

Application of solar energy for drying crops, clothes, building materials is one of the oldest one. The first installation for drying by solar energy was found in South France and is dated at about 8000 BC. Two basic moisture transfer mechanisms are involved in drying: migration of moisture from the mass inside to the surface and transfer of the moisture from the surface to the surrounding air, in the form of water vapor. Drying by solar radiation can be divided into direct, or open-air sun drying, the direct exposure to the sun and indirect solar drying or convective solar drying, (Belessiotis and Delyannis, 2011; Leon et al. 2002). Selecting the perfect conditions for drying is not easy as the food materials are very sensitive and their color, flavor, texture or nutritional value should not be seriously affected. According to (Belessiotis and Delyannis, 2011) outdoor sun-air heating suits to fruits because of high sugar and acid content but vegetables have low sugar and acid content

increasing the risk of spoilage during sun- and open-air drying. The basic classification of solar drying modes is summarized in Tab. 3. Basically, direct solar dryers, indirect solar dryers, mixed-mode dryers and hybrid solar dryers can be distinguished (Fudholi, 2010). Fig. 21 gives examples of basic design of solar dryiers.

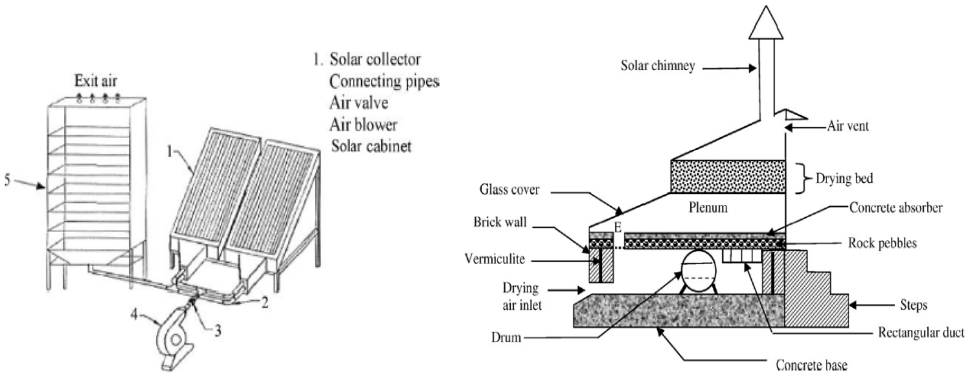

a b

Fig. 21. Examples of solar crops dryers: indirect-mode forced dryer, (Al-Juamily et al., 2007) (a), indirect type natural convection solar dryer with an integrated thermal mass and a biomass-backup heat, (Madhlopa and Ngwalo, 2007) (b).

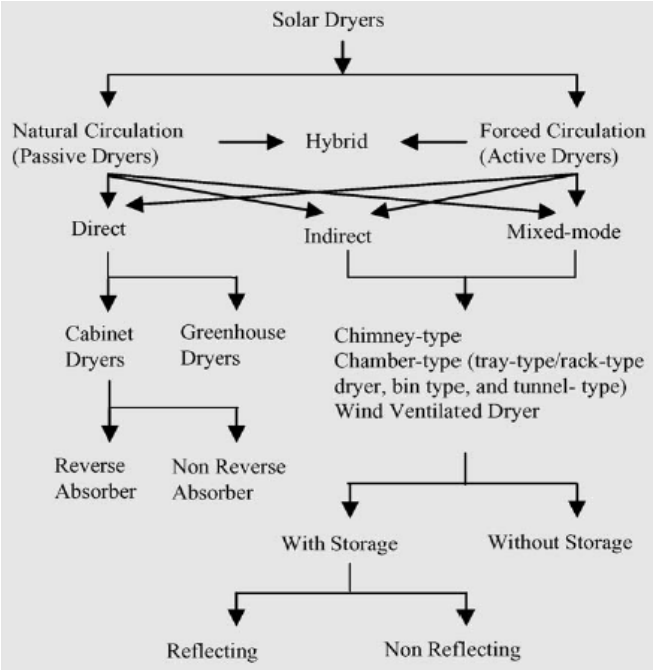

Table 3. Classification of solar dryers and drying modes (Fudholi, 2010).

4. Solar energy for wastes and solids treatment

Solar energy might be used in processing of solid and liquid wastes on several stages of their treatment. PV panels might be used for generating of electrical power for each devices but commonly rather thermal solar power is used to maintain or increase the temperature required for the treatment process.

Solar power can be used in the process of gasification of carboniferous materials including wastes of high carbon content. Solar steam-gasification of biomass makes use of concentrated solar energy to convert solid biomass feedstocks into high-quality synthesis gas (syngas) – mainly H_2 and CO – applicable for power generation in efficient combined cycles and fuel cells, or for Fischer-Tropsch processing of liquid biofuels (Lede, 1999; Perkins and Weimer, 2009; Melchior, 2009). Conventional auto-thermal gasification requires a significant portion of the introduced feedstock to be combusted with pure O_2 to supply high temperature process heat for the highly endothermic gasification reaction. For example, the energy required to gasify bituminous coal of LHV 34 MJ/kg is supplied by burning 35% of the injected coal mass (Piatkowski and Steinfeld, 2008). In contrast, the solar-driven gasification eliminates the need for a pure stream of oxygen (Melchior, 2009).

Solar-driven steam-gasification is free of nearly all combustion by-products and produced syngas has a lower amount of CO_2 (calorific value is over that of the original feedstock by an amount equal to the enthalpy change of the reaction).

The solar hydrogen technology can be divided into water thermolysis (needs a high temperature heat source at above 2500 K), thermochemical cycles for water-splitting, and hybrid solar/fossil fuels processes.

Thermochemical gasification of tires and plastic bottles into synthesis gas using ZnO as a donor of oxygen in the infra-red furnace and concentrated solar energy was studied (Matsunami et al., 1999). Another solution for concentrated-solar supported gasification was two phase biomass char (biochar) steam gasification in a bubbling fluidized bed (Fig. 22). Hydrogen was the principal expected product followed by carbon monoxide (Gordillo and Belghit, 2011).

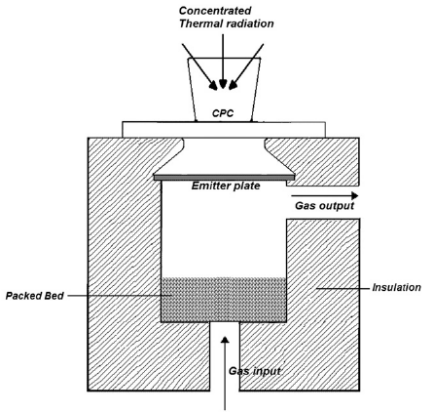

Fig. 22. A bubbling fluidized bed gasifier with concentrated thermal radiation as source of energy (Gordillo and Belghit, 2011).

3kW solar reactor prototype was invented for continuous steam-gasification of biochar (ultimately for the biomass feedstock) (Melchior et al., 2009). High-temperature thermochemical reactor, depicted in Fig. 23, used cavity-type configuration to capture effectively the incident concentrated solar radiation entering through a small opening (aperture) and multiple internal reflections.

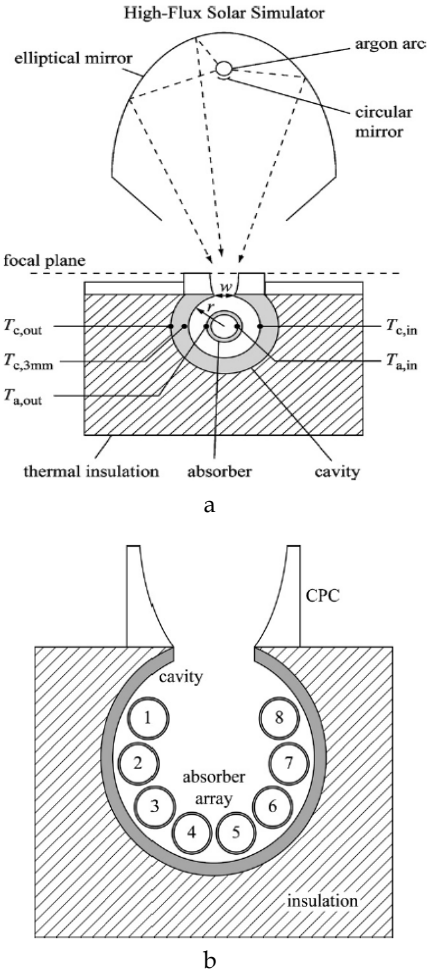

Fig. 23. Schemata of the solar chemical reactor configuration (cross-sectional view) at ETH's High-Flux Solar Simulator (a), and of scaled-up reactor consisting of a cavity-receiver containing an array of 8 tubular absorbers (b), (Melchior et al., 2009).

A novel system of hydrogen production by biomass gasification in supercritical water (SCWG) using concentrated solar energy has been constructed, installed and tested with biomass model compounds (glucose) and real biomass (corn meal, wheat stalk) (Chen et al., 2010). The system's schema is shown in Fig. 24.

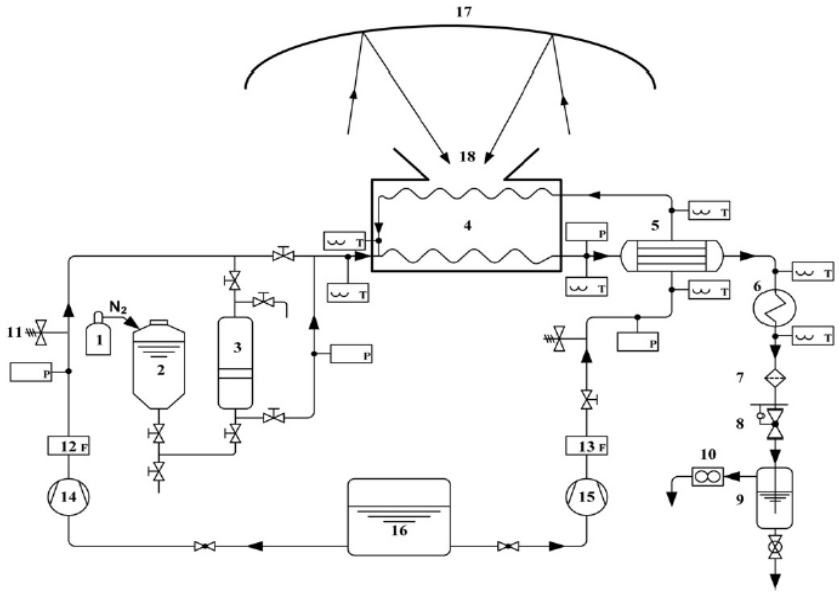

Fig. 24. Schematic diagram of SCWG using concentrated solar energy system [Chen et al., 2010]. (1: nitrogen bottle; 2: feedstock tank; 3: feeder; 4: solar receiver/reactor; 5: heat exchanger; 6: cooler; 7: filter; 8: back-pressure regulator; 9: liquid-gas separator; 10: wet test meter; 11: relief valve; 12, 13: mass flow meter; 14, 15: high pressure metering pump; 16: water tank; 17: toroidal surface heliostat with the two axis spinning-elevation sun tracking; 18: secondary cone surface concentrator).

The maximal gasification efficiency (the mass of product gas/the mass of feedstock) in excess of 110% was reached, hydrogen fraction in the gas product approached 50%.

Big Belly System (Fig. 25) is an interesting initiative for small scale application of PV power for compression of city wastes. It reduces collection frequency by up to 80%, freeing up resources, slashing fuel costs and increasing recycling opportunities. Innovative container allows accommodating 8 times more trashes than traditional one and will bring about 12 mln USD savings in 10 years period in Philadelphia city.

Fig. 25. Big Belly System.

5. Prototype installation of air, water and soil treatment suppliedd from PV panels

Autonomous water treatment installation supplied from PV panels and installation for air, water and soil treatment were developed in Lublin University of Technology in cooperation with Japanese partners. Set-ups were extensively described (Pawlat et al., 2011; Stryczewska, 2011; Komarzyniec et al., 2010; Pawłat et al, 2011a; Pawłat et al, 2011b; Ebihara et al., 2011; Takayama et al., 2006; Komarzyniec et al., 2010).

Small water treatment installations with ozone generation using electric energy from renewable energy sources could be the good solutions to variety of environmental problems. Fig.26 depicts a small household water ozonation installation. Proposed system was made of three basic sub-systems: electric energy power system, ozone production system and water treatment system. It was totally autonomous, designed for a constant work in difficult climatic conditions. The devised technological solution is excellent to be utilized in remote terrains, which are distant from electroenergetic network or in the places where the electroenergetic main is unstable and fallible.

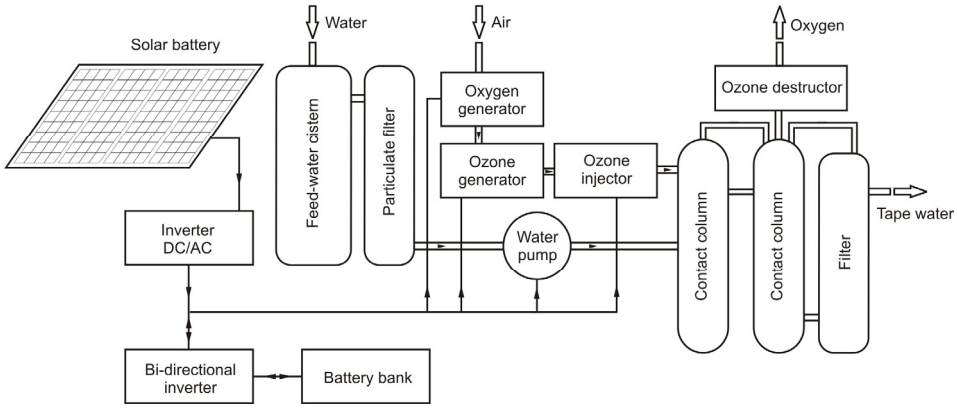

Fig. 26. Water ozonation system

Ozone based techniques in the case of soil contamination are good alternative to the traditional techniques like heating, flushing with chemical additives, landfilling, incineration, etc. Benefits of ozone applications in agriculture might be summarized as follows:

- use of ozone in soil treatment will not result in the build-up of any environmentally persistent or toxic compounds as O_3 is immediately consumed in the soil treatment process.
- ozone is manufactured on site so it cannot be stored and its sudden release to the atmosphere is not possible like it could occur with compressed methyl bromide or other persistent toxic gases or chemicals used for soil sterilization.
- minimum human toxicity.

Integrated system for ozonation of soil was presented in Fig. 27.

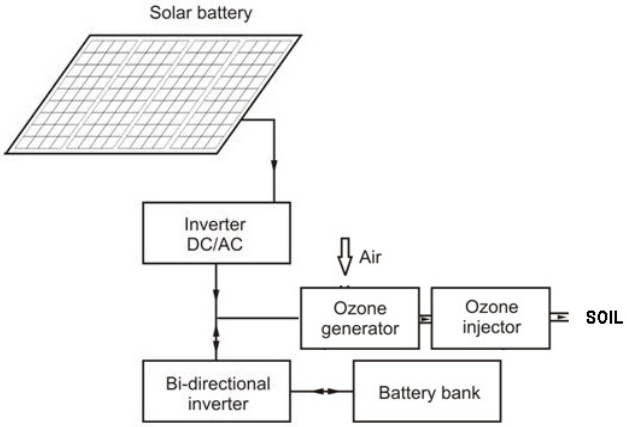

Fig. 27. Soil ozonation system

Currently, the total cost of generating electrical energy from solar batteries is one order of magnitude higher than in case of nuclear energy. However, the application of solar batteries becomes profitable, as far as the demand for electrical energy is small. The correctly selected system should cover about 95÷100% of electrical energy demand during summer. Tab. 4 collects photovoltaic cell parameters, used to supply water ozonation system with electrical energy.

Maximum Power	Maximum System Voltage	Maximum Power Voltage	Maximum Power Current	Open Circuit Voltage	Short Circuit Current
210 W	600 V	26.6 V	7.9 A	33.2 V	8.58 A

Table 4. Photovoltaic cell parameters

5.1 Production of ozone

The ozone generation took place with the usage of corona discharge. The ozonizer was powered with high frequency supplier with pulse control and amplitude modulation. It was possible to control ozone concentration. The basic parts of ozone generator were titanium electrodes (one covered with ceramic dielectric material). In order to lower the ozonier's consumption of electric energy, the complex system of radiators was used, so electrodes were efficiently cooled with atmospheric air (Fig. 28).

The utilized ozone generator operated with both: pure oxygen and atmospheric air as substrate gases, 1.5 g/h and 6 g/h of O_3 were generated, respectively. Gas flow ranged 3,3-4,7 l/min with 180 W of power consumption.

Ozone production chart and voltage characteristics are depicted in Fig. 29 and 30, respectively.

Through an increase of frequency not only the increase of efficiency, but also reduction of electric energy consumption was achieved.

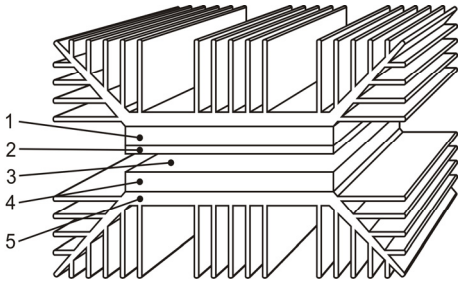

Fig. 28. Ozone generator: 1, 4 – titanium electrode, 2 – ceramic layer, 3 – discharge gap, 4 – radiator

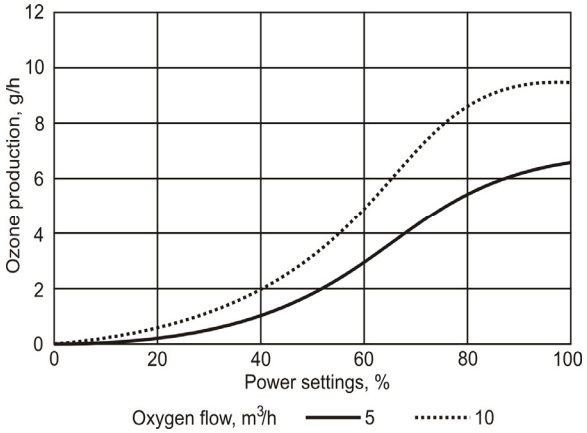

Fig. 29. Ozone generation chart.

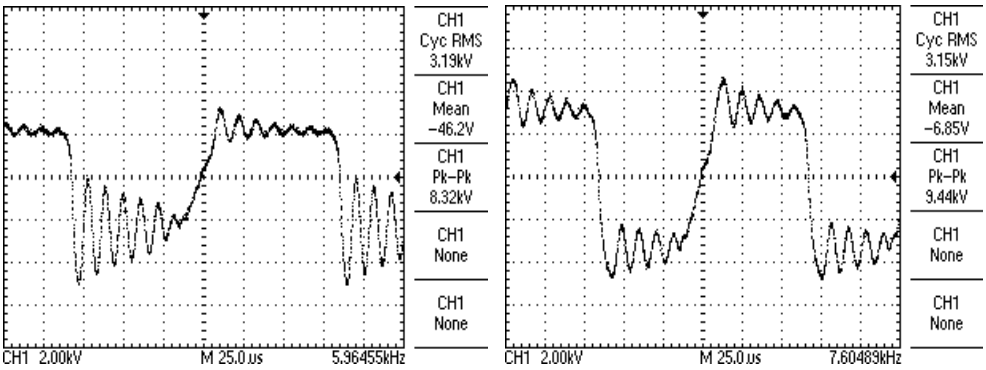

Fig. 30. The voltage characteristics for various frequencies.

5.2 Water ozonation system

The appropriately made contact container has a fundamental influence on stability and final quality of water ozonation process. In the majority of ozonation systems ozone is added to

water in the form of bubbles through diffuser. The effectiveness of such a process is low because ozone is not evenly mixed with water, and when in large quantities, ozone evaporates from water into ozone destructors, from where the unused oxygen is blown out to the atmosphere. To reduce influence of factors mentioned above innovative WOFIL system was used. In this solution, raw water was initially aerated and oxidized with the oxygen mixed with ozone, which evaporated from the contact container. This solution enabled the increase of ozonation process' efficiency by almost 30% (in comparison with the competitive ideas) without the increase of electrical energy consumption. It also resulted in reduction of amount of gas which was blown out to ozone destructors and in lower values of residual ozone after the contact container.

In order to remove the excess of the produced and the residual ozone the catalytic destructors were used. System is presented in Fig. 31.

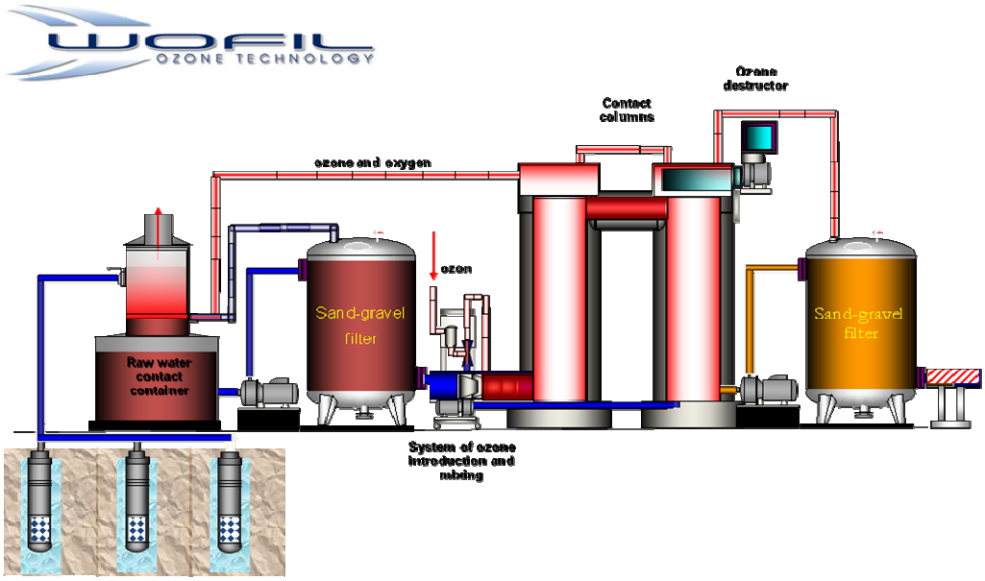

Fig. 31. WOFIL water ozonation system

5.3 Power supply

The main element of the circuit was bi-directional inverter, administering loads, the flow of energy and the work of accumulators. Inverter provided 24 V grid of DC voltage and a typical grid of AC voltage 110 V/60 Hz or 230 V/50 Hz. Thus, it enabled integration ranging from electric generators to energy receivers.

Photovoltaic systems, air turbine, generators with diesel motors, water-power plants are connected together with load on the side of alternating voltage. The batteries of accumulators, fuel cells and DC receivers, however, are integrated on the side of DC voltage. Fig. 32 depicts a flow chart of electric grid which cooperates with water ozonation system.

The connection of solar batteries on the side of alternating voltage required application additional DC/AC inverter, what allowed to avoid using an expansive DC wiring and additional adjustment.

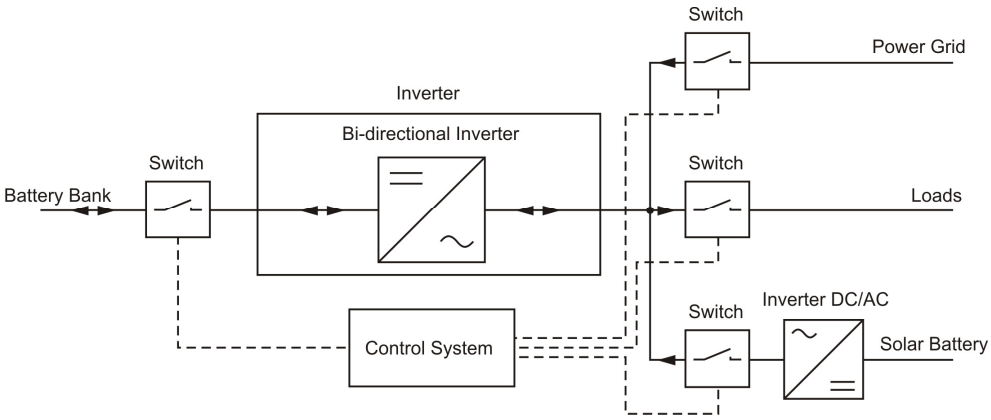

Fig. 32. Grid supplying water ozonation system with electric energy.

5.4 Energy distribution

Limited power value received from photovoltaic cells poses the main problem in designing an efficient treatment system. Power consumption of individual electric elements in integrated ozonation system is shown in Fig.33.

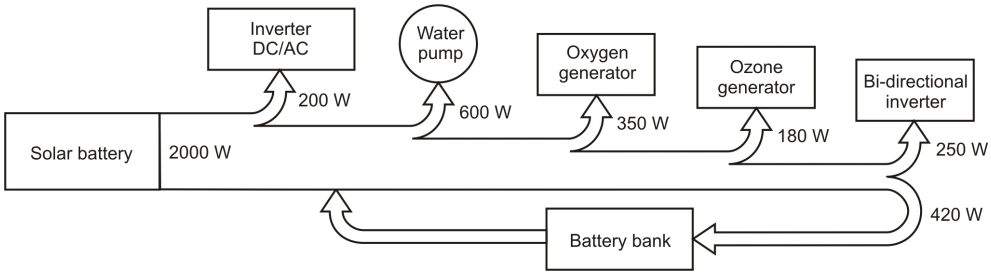

Fig. 33. Electric energy consumption in the system.

When the whole system is accurately aligned, usage of some of electronic elements, utilized in pilot installation, which are responsible for controlling functioning of the system might be omitted. Thus, power consumption could be lowered to several hundred Watts.

6. Conclusions

Usage of solar power via thermal collectors or photovoltaic panels to the water, air, waste and soil treatment is an environmental-friendly and cost-effective solution, especially on areas with yearly uniform and high insolation.

The presented water and air/water/soil ozonation set-ups are currently being prepared for implementation procedures. Since being fully autonomic systems of modular construction, they could be easily adjusted to individual needs. Power from PV panels could cover up to 95-100% energy needs in summer period in optimized integrated system.

Efficiency of ozone application and AOP methods for water is already well known. Ozone usage in the case of soil allowed to achieve 99.9% sterilization efficiency in the case of Fusarium oxysporum at the ozone dosage over 20 gO_3/m^3.

7. References

Acra, A., Karahagopian, Y., Raffoul, Z., Dajani, Z. (1980), Disinfection of oral rehydration solutions by sunlight, Lancet, Vol. 316, (No. 8206), pp. 1257–1258

Al-Hallaj, S., Parekh, S., Farid, m.,Selman, J. (2006) Solar desalination with humidification–dehumidification cycle: Review of economics, *Desalination*, Vol.195, pp. 169–186

Al-Juamily, K., Khalifa, A.,Yassen, T. (2007), Testing of performance of fruit and vegetable solar drying system in Iraq, *Desalination, Vol. 209, pp. 163–70.*

Al-Kharabsheh, S., Goswami D. (2003), Analysis of an innovative water desalination system using low-grade solar heat, *Desalination,* Vol. 156, pp. 323-332

Bahnemann, D. (2004), Photocatalysis: Photocatalytic water treatment: solar energy applications, *Solar Energy*, Vol. 77, (No. 5), pp. 445-459

Banata, F., Jwaied, N., Rommel, M., Koschikowski, J., Wieghaus, M. (2007), Performance evaluation of the "large SMADES" autonomous desalination solar-driven membrane distillation plant in Aqaba, Jordan, *Desalination*, Vol. 217, pp. 17–28

Belessiotis, V., Delyannis, E. (2011), Solar drying, *Solar Energy*, Vol. 85, pp. 1665–1691

Big Belly System, http://bigbellysolar.com/

Blanco, J.Malato, S.,Fernandez-Ibanez, P., Alarcon, D., Gernjak, W., Maldonado, M. (2009), Review of feasible solar energy applications to water processes, *Renewable and Sustainable Energy Reviews*, Vol. 13, pp.1437–1445

Blue Spring Company, http://www.bluspr.com/solar_desalinators.html

Chaibi, M. (2000), An overview of solar desalination for domestic and agriculture water needs in remote arid areas, *Desalination,* Vol. 127, pp. 119-133

Chen, J., Lu, Y., Guo, L., Zhang, X., Xiao, P. (2010), Hydrogen production by biomass gasification in supercritical water using concentrated solar energy: System development and proof of concept, Int. Journal of Hydrogen Energy, Vol. 35, pp. 7134-7141

Dallas, S., Sumiyoshi, N., Kirk, J., Mathew, K., Wilmot, N. (2009), Efficiency analysis of the Solarflow – An innovative solar-powered desalination unit for treating brackish water, *Renewable Energy*, Vol. 34, pp.397–400

Delgado-Torres, A., García-Rodríguez, L. (2007), Status of solar thermal-driven reverse osmosis desalination, *Desalination, Vol.* 216, pp. 242–251

Duran, A., Monteagudo, J.,San Martın, I., Aguirre, M. (2010), Decontamination of industrial cyanide-containing water in a solar CPC pilot plant*, Solar Energy*, Vol. 84, pp. 1193–1200

Ebihara, K., Stryczewska, H., Ikegami, T., Mitsugi, F., Pawlat, J. (2011), On-site ozone treatment for agricultural soil and related applications, *Przeglad Elektrotechniczny*, Vol. 7, pp. 148-152

Energie-Atlas GmbH, CH-4142, Munchenstein, 2005, http://www.helpsavetheclimate.com/insoleurope.html

Eurobserv'er, 2010, Solarthermal barometer, May 2010

Eurobserv'er, 2011, Photovoltaics barometer, May 2011

Fudholi, A., Sopian, K., Ruslan, M., Alghoul, M., Sulaiman, M. (2010), Review of solar dryers for agricultural and marine products, *Renewable and Sustainable Energy Reviews*, Vol. 14, pp. 1–30

Gálvez, J., ,García-Rodríguez, l., Martín-Mateosc, I., (2009), Seawater desalination by an innovative solar-powered membrane distillation system: the MEDESOL project, *Desalination*, Vol. 246, pp. 567–576

Gordillo, E., Belghit, A. (2011), A bubbling fluidized bed solar reactor model of biomass char high temperature steam-only gasification, Fuel Processing Technology, Vol. 92, pp. 314–321

Hanson, A., Zachritz, W., Stevens, K., Mimbela, l., Polka, R., Cisneros, L. (2004), Distillate water quality of a single-basin solar still: laboratory and field studies, *Solar Energy, Vol.* 76, pp. 635–645

Henning, H., (2007), Solar assisted air conditioning of buildings – an overview, *Applied Thermal Engineering*, Vol. 27, pp. 1734–1749

Komarzyniec, G., Stryczewska, H. Muszanski, R. (2010), Autonomous Water Treatment Installation Energized from PV Panels, *Journal of Advanced Oxidation Technologies*, Vol. 13, (No. 2), pp. 146-152(7)

Komarzyniec, G., Stryczewska, H., Muszanski, R. (2009), Autonomous water treatment installation energized from PV panels, Proc. *15th International Conference on Advanced Oxidation Technologies for Treatment of Water, Air and Soil (AOTs-15), New York, USA*

Lede, J., (1999), Solar thermochemical conversion of biomass, *Solar Energy*, Vol. 65, pp. 3–13

Leon, M., Kumar, S., Bhattachaya, S., (2002), A comprehensive procedure for performance evaluation of solar dryers, *Renewable and Sustainable Energy Reviews,* Vol. 6, pp. 367–393.

LG- http://www.lg-solar.com/

Madhlopa, A., Ngwalo, G. (2007), Solar dryer with thermal storage and biomass-backup heater, *Solar Energy*, Vol. 81, pp. 449–462

Malato, S., Blanco, J., Alarcon, D., Maldonado, M., Fernandez-Ibanez, P., Gernjak, W., (2007), Photocatalytic decontamination and disinfection of water with solar collectors, *Catalysis Today,* Vol. 122, pp. 137–149

Malato, S., Fernández-Ibáñez, P., Maldonado, M., Blanco, J., Gernjak, W. (2009), Decontamination and disinfection of water by solar photocatalysis: Recent overview and trends, *Catalysis Today*, Vol. 147 (No. 1), pp. 1-59

Matsunami, J., Yoshida, S., Yokota, O., Nezuka, M., Tsuji, M., Tamaura, Y. (1999), Gasification of waste tyre and plastic (PET) by solar termochemical process for solar energy utilization, *Solar Energy*, Vol. 65,(No. 1), pp. 21–23

Meierhofer, R., Landolt, G. (2009), Factors supporting the sustained use of solar water disinfection - Experiences from a global promotion and dissemination programme, *Desalination*, Vol. 248, pp. 144–151

Melchior, T., Perkins, C., Lichty, P., Weimer, A., Steinfeld, A. (2009), Solar-driven biochar gasification in a particle-flow reactor, *Chemical Engineering and Processing, Vol. 48, pp. 1279–1287*

Müller-Holst, H.,Engelhardt, M., Schölkopf, W. (1999), The International Workshop on Desalination Technologies for Small and Medium Size Plants With Limited Environmental Impact, *Desalination*,Vol. 122, (No. 2-3), pp. 255-262

Nalewaj, K., Janowski, T., Złonkiewicz, Z. (2003) *Solar Energy for a Sustainable Future, ISES Solar World Congress*, Göteborg, Sweden 2003

Parekh, S., Farid, M., Selmana J., Al-Hallaj, S. (2004), Solar desalination with a humidification-dehumidification technique - a comprehensive technical review, *Desalination,* Vol. 160, pp.167-186

Pawłat, J., Diatczyk, J., Komarzyniec, G., Giżewski, T., Stryczewska, H., Ebihara, K., Mitsugi, F., Aoqui, S., Nakamiya T. (2011) Solar Energy for Soil Conditioning, Proc. International *Conference on Computer as a Tool (EUROCON),* Lisboa, Portugal, 2011, pp. 1-4

Pawłat, J., Stryczewska, H., Ebihara, K. (2010), Sterilization Techniques for Soil Remediation and Agriculture Based on Ozone and AOP, *Journal of Advanced Oxidation Technologies*, Vol. 13 (No. 2), pp. 138-145(8)

Pawłat, J., Stryczewska, H., Ebihara, K., Mitsugi, F., Aoqui, S., Nakamiya, T. (2010), Plasma sterilization for bactericidal soil conditioning, Proc. *HAKONE XII conference*, Trenčianske Teplice, Slovakia, 2010, pp.407-411

Perkins, C., Weimer, A., Solar-thermal production of renewable hydrogen, *AIChE Journal*, Vol. 55, pp. 286–293

Piatkowski, N., Steinfeld, A., (2008), Solar-driven coal gasification in a thermally irradiated packed-bed reactor, *Energy Fuels*, Vol. 22, pp. 2043–2052.

Robert, D., Malato, S. (2002), Solar photocatalysis: a clean process for water detoxification, *The Science of the Total Environment*, Vol.291, pp. 85–97

Sarria, V., Kenfack, S., Guillod, O., Pulgarin, C. (2003), An innovative coupled solar-biological system at field pilot scale for the treatment of biorecalcitrant pollutants, *Journal of Photochemistry and Photobiology A: Chemistry*, Vol. 159, pp. 89–99

Scrivani, A., Asmar, T., Bardi, U. (2007), Solar trough concentration for fresh water production and waste water treatment, *Desalination,* Vol. 206, (No. 1-3), pp. 485-493

Solar truck- http://energygreen.tk/tag/mitsubishi-chemical-corporation/

SOLARWALL http://solarwall.com/

Stryczewska, H. (2011), Wykorzystanie energii słonecznej w procesach obróbki wody, powietrza i gleby, Presentation for Lublin University of Technology, 04.2011

Takayama, M., Ebihara, K., Stryczewska, H., Ikegami, T., Gyoutoku, Y., Kubo, K., Tachibana, M. (2006), Ozone generation by dielectric barrier discharge for soil sterilization, *Thin Solid Films*, Vol. 506-507, pp. 396-399

Yiannopoulos, A., Manariotis, I., Chrysikopoulos, C. (2008), Design and analysis of a solar reactor for anaerobic wastewater treatment, *Bioresource Technology*, Vol. 99, pp. 7742–7749

Zuo, L., Zheng, Y., Li, Z., Sha, Y. (2011), Solar chimneys integrated with sea water desalination, *Desalination*, Vol. 276, pp.207–213

8

The Behaviour of Low-Cost Passive Solar Energy Efficient House, South Africa

Golden Makaka*, Edson L. Meyer,
Sampson Mamphweli and Michael Simon
University of Fort Hare, Institute of Technology, Alice, South Africa

1. Introduction

A comfortable indoor environment is one of the main requirements of a well-designed house yet most of the low-cost houses are characterised by poor thermal performance. Mainly poor design, sub-standard building materials and poor craftsmanship contribute to the poor performance. The inclusion of energy-efficient passive solar design features in the construction of affordable housing offers many benefits which include; reduced operating costs, reduced energy related greenhouse emissions, and reduced need for expensive heating and cooling of the house and above all, improved comfort. The basic natural processes used in passive solar energy are the thermal energy flows associated with radiation, conduction, and natural convection. When solar radiation strikes a building, the building materials can reflect, transmit, or absorb the solar radiation [Makaka, Meyer; 2008]. Additionally, solar energy causes air movement that can be predictable in designed spaces. These basic responses to solar heat lead to design elements, material choices and placements that can provide heating and cooling effects in buildings. The thermal state is determined by the difference of the sums of the heat gains and heat losses. Bricks form the about 80% of the building materials and their physical properties play a role in determining the indoor thermal behaviour. These properties include thermal conductivity, water absorption, sound dumping and compressive strength. The addition of fly ash to clay in a defined ratio can really improves these properties and at same time reducing the manufacturing process. South Africa produces about 90 tones of fly ash annually posing a huge problem on the disposal management of fly ash. The use of fly ash in the manufacturing of bricks is one of the ways of the management of this waste.

The aim of this chapter is to establish the impact of passive solar design and building materials properties on the indoor temperature and to establish a statistical correlation of the indoor temperature with outdoor weather parameters [Makaka, Meyer; 2008]. It seeks to develop an understanding of the criteria used for the selection of an appropriate passive solar architecture that is sensitive to both energy use and climatic conditions, i.e., it gives the details of the design and the selection of building materials used, energy efficient design optimization using ECOTECT building design software and ventilation efficiency. Most of

* Corresponding Author

computer based prediction models are complicated for an average trained builder this results in the construction of poor thermal performing buildings. In this chapter a statistical method is used to develop a simple indoor temperature predicting model.

2. Principles of passive solar design

The building design phase integrates the site, floor plan, building orientation, landscaping, materials, mechanical systems and architectural characteristics. The design of an energy-efficient house requires a careful analysis and evaluation of all proposed design alternatives throughout the different design stages. The central issue in passive solar design is to minimize the energy required for heating, cooling and artificial day lighting. This can be achieved through the use of a range of different features that improve the building's thermal and lighting performance. The properties of the building materials vary and selection must be in accordance with the climate of specific regions [Makaka, Meyer; 2008]. The decisions of the architect and builders in the early stages of the design process are fundamental to a holistic approach in constructing a passive solar house (PSH). In the schematic design phase of the PSH, prior to making any sizing of windows, wall thickness, etc., decisions on broader issues such as building orientation and the appropriate spatial organization of the building must be made. As the design is developed, more accurate investigations are needed to obtain the appropriate size of building components based on design criteria and objectives that are determined at the outset. Passive solar design integrates several issues that can be rather contradictory; larger glazing to achieve solar gains can result in overheating, and an airtight building can produce bad indoor air quality [Wray *et al*., 1979]. These issues must be dealt with carefully by seeking the best balance between the passive solar design requirements and the budget. Consequently, in the Southern Hemisphere, the house must be oriented north to maximize the heat gain of the low north winter sun but eliminating the possible indoor solar radiation penetration in summer. The direction of the prevailing winds determined the layout of major outdoor features and the placement of windows to enhance optimal natural ventilation. The basic components of passive solar design are discussed in the following sections.

3. Advantages of energy efficient design features

A whole-house "system" approach to design and construction is the appropriate method of developing energy-efficient and sustainable houses. A system approach considers the interaction between the site, building envelope, mechanical systems, occupants, and other factors. This system recognizes that the features of one component of the house can greatly affect others. Energy efficient houses are more comfortable because of stable indoor temperature. The indoor humidity is better controlled and drafts are reduced. Energy-efficient houses protect the planet and offers greater fire safety. Energy efficient houses experience less condensation, which protects framing, windows and finish materials [Kunzel *et al*, 2003].

4. Fly ash bricks

Bricks of different proportions of clay and fly ash were molded and compressive strength, water absorption and thermal conductivity were measured. The amount of fly ash was

increased in steps of 10% (in volume). The clay-fly ash ratio which produced a brick with high compressive strength, low water absorption and low thermal conductivity was then used to mold bricks for the construction of a passive solar house. The ratio of 1:1 (clay : fly ash) was found to produce a brick with the ideal properties, i.e., low water absorption capacity, low thermal conductivity, high heat capacity, high compressive strength and high sound damping. Table 1 shows the chemical composition of fly ash collected from two different sites. The properties of fly ash bricks depend mainly on two factors: (i) the energy content of the fly ash used and (ii) the chemical composition of the fly ash [Makaka, Meyer, 2008]

Site	Sulphate (as SO_4^{2-})	Phosphate (as PO_4^{3-})	Silicate (SiO_2^{2-})	Calcium (Ca^{2+})	Magnesium (Mg^{2+})	Potassium (K^{+})	Aluminum (Al^{3+})
A	0.3	<0.1	20.3	0.36	0.05	1.63	14.1
B	0.2	0.1	20.9	2.15	0.12	2.68	19.6

Table 1. Percentage chemical composition of fly ash [Makaka, Meyer, 2008]

The other constituents include FeO, Na_2O, K_2O and unburnt carbon that form the bulk part of the fly ash. The South African fly ash has high-energy content, making it excellent for manufacturing bricks. Chemical composition of the fly ash and the temperature attained during burning determine the brick colour.

Figure 1 shows the variation of thermal conductivity with the increase percentage of fly ash in the brick composition, i.e., the insulating property of the fly ash brick increases with the increase of the amount of fly ash. The fly ash bricks are observed to have high heat making them ideal for use as thermal mass. From figure 1, it can be seen that thermal conductivity decreases with increase in the proportion of fly ash with a minimum value of about 0.0564 W/mK, which correspond to a mixing proportion of 50% fly ash to 50% clay by volume. The mixing proportion of 50% fly ash to 50% clay result in 93% reduction in thermal conductivity as compared to a pure clay bricks. The fly ash bricks are very light in weight (density 400-1190 kgm^{-3}) making it much easier to transport the bricks [Makaka, Meyer; 2008]. As the carbon in the brick burns the trace elements melts thus sintering the brick and at the same time small-unconnected cavities are created, giving the brick effective heat insulating properties (low conductivity). Above 50% of fly ash, the cavities start to decrease in size and number as the metallic elements starts to dominant, thus increasing the thermal conductivity of the brick. The fly ash bricks have an added advantage of being very smooth with an attractive colour thereby doing away with the need for external plastering and painting.

Water is associated with deterioration processes affecting masonry materials. Its presence within the interior pore structure of masonry can result in physical destruction if the material undergoes wet/dry or freeze/thaw cycles [Raman *et al.*, 2001]. The freeze/thaw process is particularly damaging if the masonry material has high water absorption. The high water absorption results in high expansion and contraction thus weakening the brick. Because of these factors, the water permeability of a masonry material is related to its durability.

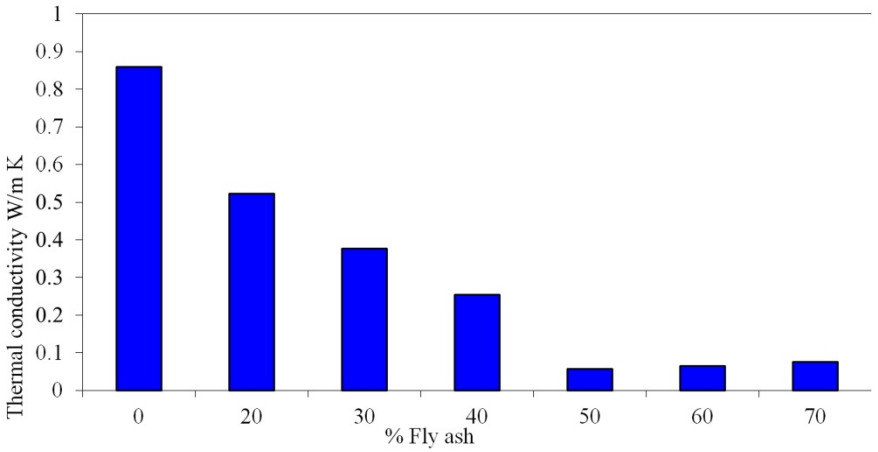

Fig. 1. The variation of thermal conductivity.[Makaka, Meyer; 2008]

Figure 2 shows the variation in water absorption as the amount of fly ash in the brick increases. Water absorption of fly ash bricks decreases with increase in fly ash. A mixing proportion of 50% fly ash to 50% clay produces a brick with minimum water absorption. According to the South African Building Standard Code (SABSC), the brick water absorption must be less than 20% by weight [Agrement South Africa, 2002].

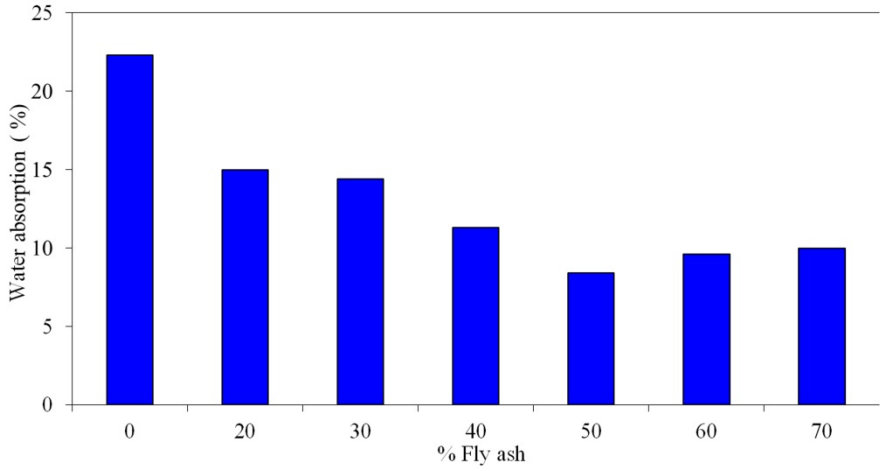

Fig. 2. Water absorption of fly ash bricks [Makaka, Meyer; 2008].

From figure 2 it is clear that the addition of 20% fly ash by volume reduces the water absorption by 32%, while the addition of 50% fly ash lowers the water absorption by 62%. Since the created cavities are unconnected, permeability and porosity are reduced. The reduction in permeability and porosity implies the reduction in freezing/thawing damage of the brick since there will be minimal amounts of water in the brick. As the content of fly ash increases beyond 50%, the amount of unburnt carbon increases and upon burning a

significant proportion of the brick will be burnt [Makaka, Meyer; 2008]. In this case the trace metallic elements are insufficient to bind the remaining proportion thereby creating connected cavities, which results in high water absorption bricks with low compressive strength. During brick firing the unburnt carbon enhance the burning process raising the temperature higher thus initiating the vitrification process to take place.

Figure 3 shows the variation in compressive strength of fly ash bricks for different proportions of fly ash. The compressive strength generally increases in comparison to bricks manufactured without fly ash. The SABSC specify the minimum brick compressive strength of 5 Mpa [Agrement South Africa, 2002]. The addition of fly ash significantly improves the compressive strength. The mixing proportion of 50% fly ash to 50% clay produced a brick with the desired properties, i.e., high compressive strength (12 MPa), low water absorption (8.84%) and low thermal conductivity (0.0564 W/mK). Fly ash bricks with this mixing proportion (50% fly ash) were recommended for wall construction. These bricks were bought from a local brick maker approximately 600 m from the site of construction.

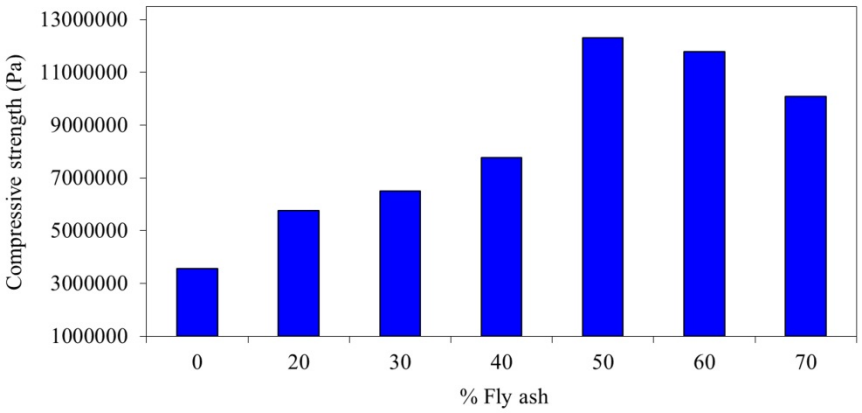

Fig. 3. Compressive strength of fly ash bricks [Makaka, Meyer; 2008].

Somerset East experiences high humidity, and there was need to use wooden doorframes and window frames which are resistant to rust. Being a poor heat conductor the wood minimizes the unwanted heat gain/loss. The wooden doorframes and window frames were found to have the added advantage of being cheaper than the metal frames. Corrugated iron sheets were selected for roofing as they were found to be much cheaper than other roofing materials such as roofing tiles. Asbestos was disregarded for health reasons since it causes asbestosis. Metallic purlins were selected based on strength; however they were not to protrude to the external. This was done to minimize heat/loss and fast corrosion.

5. Experimental passive solar house

5.1 Design of the passive solar house

A passive solar house was designed, simulated using Ecotect building design software and constructed on a land that slopes facing north with an average gradient of about 0.134, having good solar access, making it ideal for passive solar design. Figure 4 shows the transverse

section of the building. The design tried to harmonize the benefits of compactness and the requirements of natural day lighting, passive heating/cooling and natural ventilation. The sun's path determined the orientation of the house. The house was constructed to face north with more window area on the north wall to allow solar radiation penetration in winter to serve as solar heating thereby reducing the need of winter artificial heating. This orientation was to optimize the solar radiation that penetrates indoor in winter. The roof was split into two, the lower and upper roof. The lower roof faces north while the higher roof faces south.

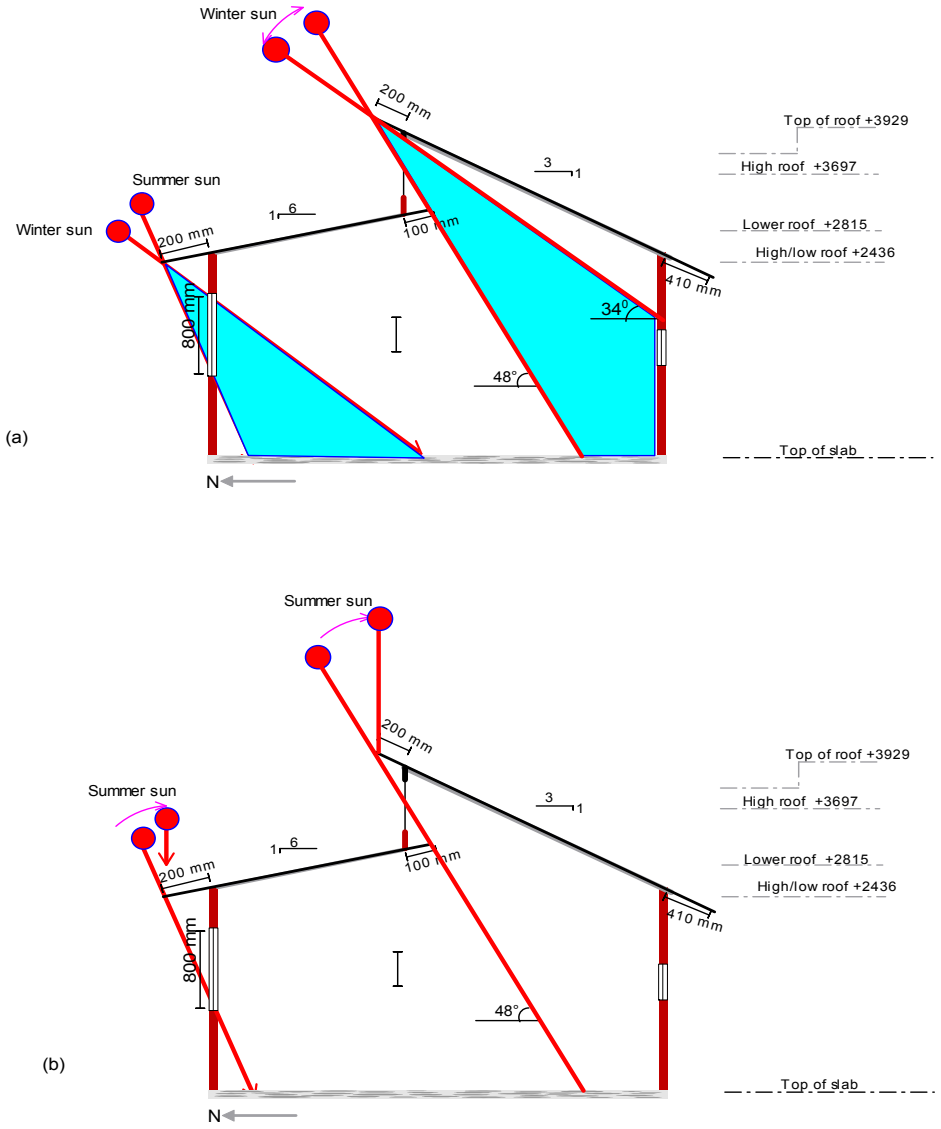

Fig. 4. Transverse building section: Solar radiation in (a) winter and (b) summer.

This was done in order to enable the insertion of clerestory windows making it possible to direct solar radiation to the desired rear zone (floor and southern wall) and to maximize day lighting, thus minimizing the use of electricity during the day. The northern roof is ideal for mounting photovoltaic modules as active solar energy converters.

5.2 Operation of the passive solar house

In summer, the sun almost rises from the east and sets in the west. In this case, the roof overhangs were made long enough (simulation was done ECOTECT) to eliminate the possibility of sunrays penetrating indoor. With reference to the clerestory windows, the upper roof was extended out by 200 mm while the lower roof was extended in by 100 mm. This eliminates the possible direct penetration of the solar radiation in summer while allowing maximum penetration in winter.

In winter (May to August) the sun rises almost northeast, but following a low northern path in the sky and then set in the northwest. From May to August the daily maximum angle of the sun ranges from 34° to 48° and this maximum angle occurs at around 12h15 with June 21st having the smallest angle. Thus, the north facing windows allows solar radiation to penetrate indoor, while the clerestory windows allow the south wall and the far south floor (thermal mass) to receive solar radiation. The thermal masses of high heat capacity (i.e. concrete floor of 100 mm thickness and the wall made from fly ash bricks) absorb solar radiation during the day.

The thermal masses used are of high heat capacity thus absorbing large amounts of solar energy with minimal temperature variation. This prevents overheating of the indoor environment, thus keeping the indoor temperature within the comfort levels. At night, as the outdoor temperature decreases; the thermal mass slowly radiates long-wave radiation heating the indoor air therefore keeping the indoor air temperature within the thermal comfort levels. Since the window glazes are opaque to the long wave thermal radiation, the thermal radiation emitted by the thermal mass is trapped indoor, and heat loses are minimized.

Somerset East experiences westerly prevailing winds in summer, so the small windows on the west and east make it possible to control the ventilation rate. The clerestory windows and the south windows enhance controllable natural ventilation rate and helps to maintain temperature within the comfort levels (16°C to 28°C).

6. Predicted performance of the passive solar house

The mathematical description of thermal behaviour of building systems is complex. It involves the modelling of several interconnected subsystems, each containing long-time constants, non-linearities and uncertainties such as convection coefficients, material properties, etc. Moreover, external unpredicted perturbations, i.e., external weather (e.g. temperature and humidity), soil temperature, radiation effects and other sources of energy, such as people, illumination and equipments, should also be taken into account.

The analysis of the different design alternatives was carried out by averages of an hourly dynamic simulation using Ecotect™ Building Design Software [Marsh, 2004]. Many building energy simulation software packages use the thermal zones concept to define thermal

properties for the simulation. The effects of building parameters on the façade thermal performance were studied through the simulations. Building models were built in the simulation program. The South African Building Standard Code specifies the lower and upper comfort levels to be 16°C and 28°C respectively and relative humidity levels of 30% to 60%.

Figure 5 shows the simulation results of the PSH. The simulation results indicate that the indoor temperature of the passive solar house was within the limits of the comfort levels for about 98% of the total period (380 hours) tested. However, the outdoor was outside the comfort levels for 44% of the period with 30% being above the upper comfort level (28°C) and 14% below the lower comfort level (16°C). With reference to figure 5, the PSH was observed to have an average thermal time lag of 3 hours and a decrement factor of 0.67.

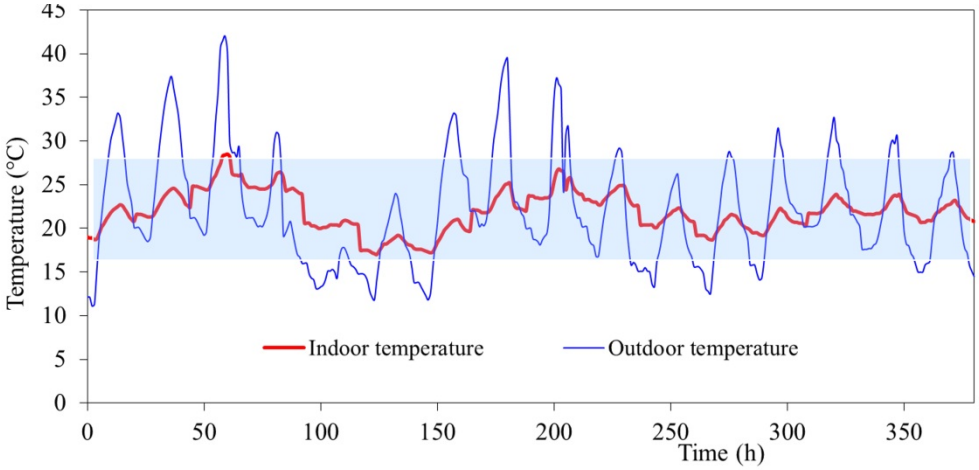

Fig. 5. Indoor and outdoor air temperature of the PSH simulated over a 380 h period (Summer).

The maximum indoor temperature attained was about 28°C and a minimum of 17°C giving a temperature swing of 10°C, while the outdoor temperature swing was about 31°C. However, it must be noted that the actual performance of the house is not only restricted to design and materials used, but also to the operation of the house on the part of the occupants.

7. Ventilation

7.1 Ventilation efficiency

Natural ventilation provides a cheaper and simpler way of cooling buildings. Low cost energy efficient passive solar buildings rely on natural ventilation and the building ventilation components must be positioned to capture the prevailing winds. Pollutants can build up to levels that may negatively impact human health unless they are removed or diluted with fresh outside air. The natural ventilation efficiency and air quality of the passive solar house was measured using the carbon dioxide tracer gas method. Reducing air leakage from the house envelope is one of the ways to reduce energy use, as well as improve

the comfort, health and building durability. Traditionally, residential construction greatly relied on air infiltration through the building envelope, i.e. through the unintended gaps in walls, roofs, windows, doors, and other construction elements to provide ventilation. Low cost energy efficient passive solar buildings rely on natural ventilation and the building ventilation components must be positioned to capture the prevailing winds [Myers, 2004].

House operation plays a key role in controlling a comfortable indoor environment. Somerset East experiences westerly prevailing winds (W (60 ± 15) N) and the passive solar house was designed to make use of these winds to control the indoor environment, i.e., indoor temperature and humidity, which are the key factors that determine thermal comfort. The South African Residential Ventilation Building Code [Agrement South Africa] recommends an average natural specific air exchange rate of 0.35 h^{-1} and an indoor carbon dioxide concentration less than 0.500%.

Equivalent outdoor airflow rate corresponds to the outdoor airflow rate that would result in the same CO_2 concentration in the measured room without inter-zone air flows.

An adult person produces on average (i.e. quiet or doing light work, about 100 W metabolic rate) carbon dioxide at about 20 *l/h*. At steady state, assuming that occupants are the only CO_2 sources, the equivalent airflow rate per person, Q_e, is related to CO_2 concentration (C_{in} indoors and C_{out} outdoors) by [Roulet, 1991]:

$$Q_e = \frac{S}{C_{in} - C_{out}} \ [m^3/h] \tag{1}$$

where S is the CO_2 source rate, i.e. about 20 l/h. Assuming a steady state (constant carbon dioxide concentration), equation 6.1 can be used to assess the equivalent outdoor airflow rate per person.

Another way is to use the CO_2 concentration records when there is no CO_2 source in the building. During these periods, the concentration decays down to the background concentration, by dilution with the outdoor air flow. If there is good mixing and if the outdoor air flow rate is constant, the decay is exponential and the factor corresponds to the air change rate and the concentration at any time t, is given as [Penman, 1982]:

$$C = C_0 e^{-\mu t} \tag{2}$$

where μ is the specific air exchange rate [h^{-1}] C_0 is the initial concentration above the background concentration. Taking logarithms both sides of equation 2 and differentiating with respect to time the specific air exchange rate can be approximated by the following expression:

$$\mu = -\frac{\Delta(In(C))}{\Delta t} \tag{3}$$

If the outdoor airflow rate is not constant, the decrement calculated from two measurements of concentration taken at time t_1 and t_2 provides an unbiased estimate of the average equivalent outdoor specific airflow μ.

7.2 Ventilation rate

Tracer gas tests were conducted over a period of time to measure actual air change rates. Figure 6 shows the indoor air currents due to the westerly prevailing winds. Carbon dioxide was injected into the house and its concentration monitored over time to determine how quickly the gas dissipates through the house's envelope. The west side ventilation components were used to control the indoor environment by regulating the amount of air flowing into the house. A carbon dioxide sensor was placed in the centre of the house at a height of about 0.45 m above the floor.

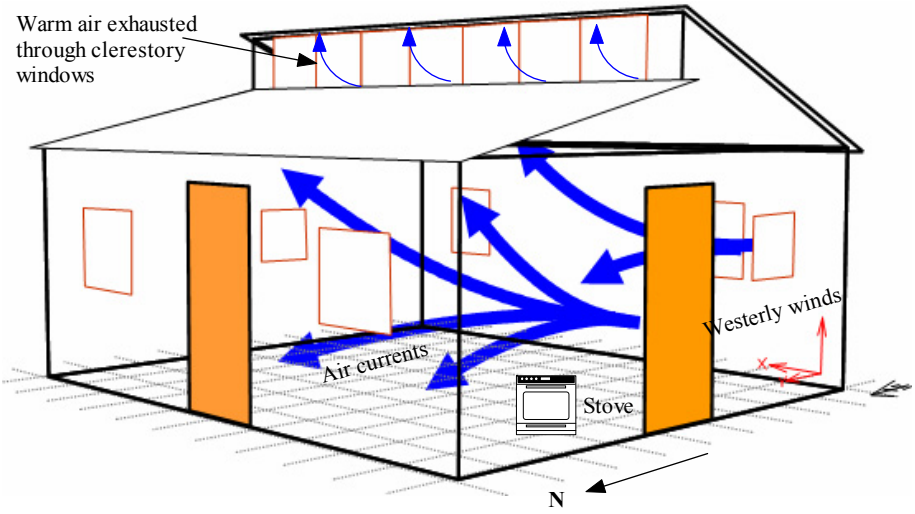

Fig. 6. Air current movements.

A fan was used to pump the indoor air into the sensor at a rate of about 300 *ml*/min. To investigate the effects of each of the ventilation component configurations, i.e., windows and doors, the ventilation rate tests were done in four configurations. A carbon dioxide sensor connected to a CR1000 datalogger and a computer was used to monitor carbon dioxide concentration in the house.

Configuration I

The carbon dioxide gas was injected into the house when all doors and windows were closed and a fan was used to mix the air in the house for about 5 minutes. The operation of the fan was intended as a contingency plan to evenly distribute the initial tracer dose throughout the space for the calculation of exchange rates. The *windows and doors were then opened* and carbon dioxide concentration was recorded at 1-minute time intervals until a constant concentration was achieved.

Configuration II

Carbon dioxide was injected into the house with doors and windows closed; a fan was switched on for 5 minutes to mix the air. *Windows were then opened but keeping the doors closed* and carbon dioxide concentration readings taken at 1-minute intervals.

Configuration III

The procedure of configuration II was repeated but *doors were opened and windows closed* and the carbon dioxide concentration recorded at a 1-minute intervals.

Configuration IV

The procedure cited in phase 2 was repeated but all *windows and doors were closed* and carbon dioxide concentration recorded at 1-minute interval.

In all the above cases it was not possible to inject equal amounts of the tracer gas as the equipment used could not allow the measurement of the amount of gas injected.

7.3 Ventilation rate

The tracer gas technique was used to measure the air exchange rate. Figures 7 and 8 illustrate the tracer gas concentration profiles measured for different ventilation component configurations, i.e., opening and closing of doors and windows. The average indoor and outdoor temperatures during these tests were, T_{in} = 20 °C and T_{out} =17 °C, and an average wind speed of 0.5 m/s blowing from W($60^0 \pm 15^0$)N. Figure 7 show the tracer gas concentration variation for configuration I, i.e., when both windows and doors were open. Results indicate that the concentration decays exponentially to the background concentration within a period of 16 minutes. Assuming that the west window and door are the only paths through which the westerly winds enter the house, then the mass air flow rate through the door and window is approximated by equation $\dot{m} = C_d A\sqrt{2\rho\Delta P}$. Taking the average air density to be 1.2 kg/m^3 and an average indoor and outdoor pressure difference of 4 Pa. For wide-open windows and doors, the opening area is the sum of the windows and doors areas, which gives 2.06 m^2, and taking the discharge coefficient C_d = 0.6, the average mass airflow was found to be approximately 3.83 kg/s.

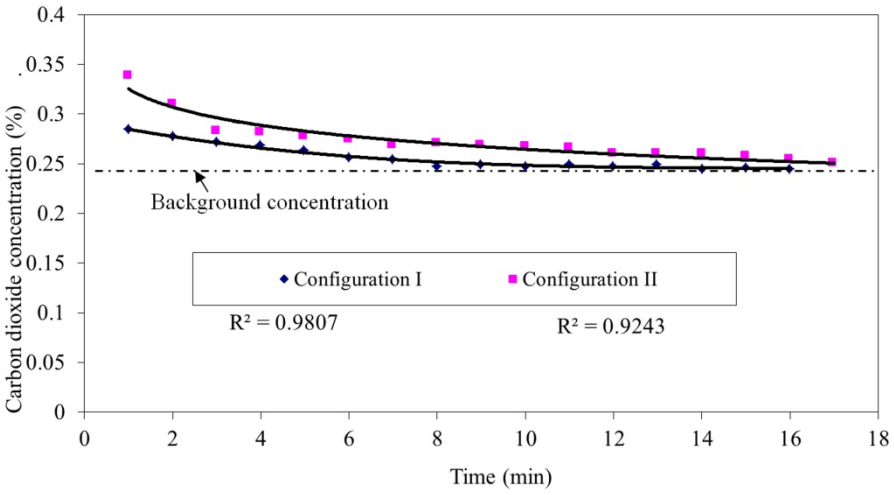

Fig. 7. Tracer gas concentration decay for configuration I and II [Makaka, Meyer; 2008].

From figure 7 it was observed that the closing of doors significantly reduced the carbon dioxide concentration decay rate implying a reduction in the ventilation rates achieved when both doors and windows were open. Opening windows and closing doors reduced the mass flow rate to 3.16 kg/s (i.e. a reduction of 17%). This means doors play a significant role in the ventilation of the PSH.

Figure 8 illustrates the decay of the tracer gas concentration for configurations III and IV, i.e., for open doors and closed windows, and for when both windows and doors were closed. Comparing configurations I and III it was found that the opening of doors and closing windows reduced the mass flow rate from 3.83 kg/s to 0.67 kg/s (i.e. a reduction of 82%). Configuration IV produced the minimum tracer gas concentration decay rate. It took approximately 69 minutes for the tracer gas to decay to the background concentration. When both doors and windows were closed, the infiltration and exfiltration airflow was through the unintended gaps, such as, gaps between floor and door, roof and wall, etc.

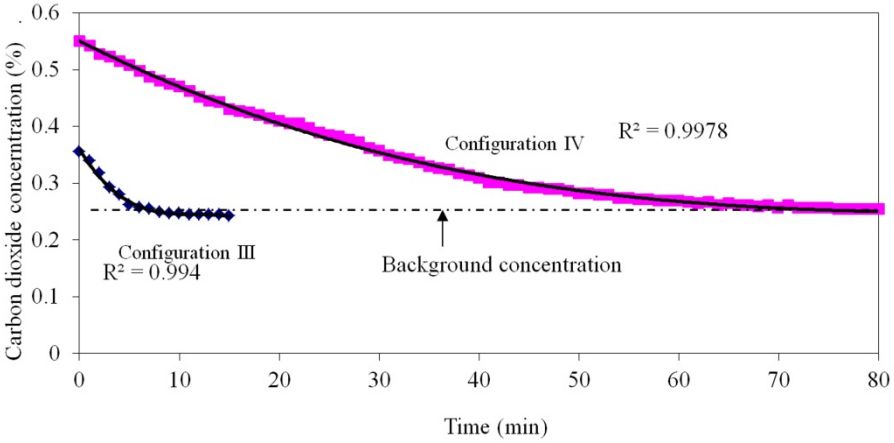

Fig. 8. Tracer gas concentration decay for configuration III and IV [Makaka, Meyer; 2008].

With reference to figures 7 and 8 and taking a reference initial tracer gas concentration of 0.28% the time taken for the tracer gas concentration to decay to the background concentration varied depending on the type of the ventilation components in use. Table 2 summarizes the time taken for the carbon dioxide concentration to decay from 0.28% to the background concentration. From Table 2 it can be seen that windows have a higher ventilation effect (shorter decay time) than doors. However this depends on the wind speed and direction and the orientation of the ventilation component with respect to the wind direction.

Somerset East experience W($60^0 \pm 15^0$)N prevailing winds, and when windows are open and doors closed, the west side windows capture the prevailing winds which then escape through the east and south windows, and to a lesser extent through the north side windows. This gives an effective controllable air inflow and outflow by adjusting the opening area of windows.

In the case where windows are closed and doors open, the west side door captures the prevailing winds. Since the prevailing winds are not purely westerly, components of the inflow air currents also penetrate through the north side door. These currents are then opposed by the inflow air current through the west side door which will try to escape though the north side door as it is the only designed escape path under this configuration. This results in reduced concentration decay time, implying a reduced air exchange rate as compared to when windows are open and doors closed.

Ventilation components state	**Decay period** (minutes)
Configuration I: All windows closed and doors open	16
Configuration II: All doors closed and windows open	17
Configuration III: All doors and windows open	13
Configuration IV: All windows and doors closed	69

Table 2. Decay periods for different ventilation components status.

7.4 Air quality

Several decay periods can be observed from figures 12 through 13. For each period, the initial and final times were determined and a normalized concentration, C_n, was calculated for each measurement time:

$$C_n = \frac{C(t) - C(0)}{C(0) - C_0} \tag{4}$$

where C(0) is the initial concentration at the beginning of the decay period and C_0 is the background concentration and was found to be 0.234%. This background concentration was first deducted from the carbon dioxide concentration to get the increase resulting from the instant of injection. Figures 9 and 10 show the graphs of $Ln(C_n)$ versus time for different ventilation component configurations. The air change rate, which is the slope of the line that represents $Ln(C_n)$ versus time was calculated for each graph.

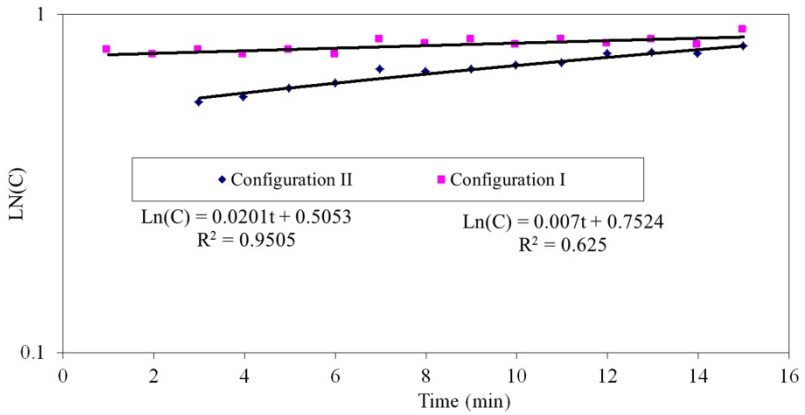

Fig. 9. Logarithmic graph of concentration: configuration I and II [Makaka, Meyer; 2008].

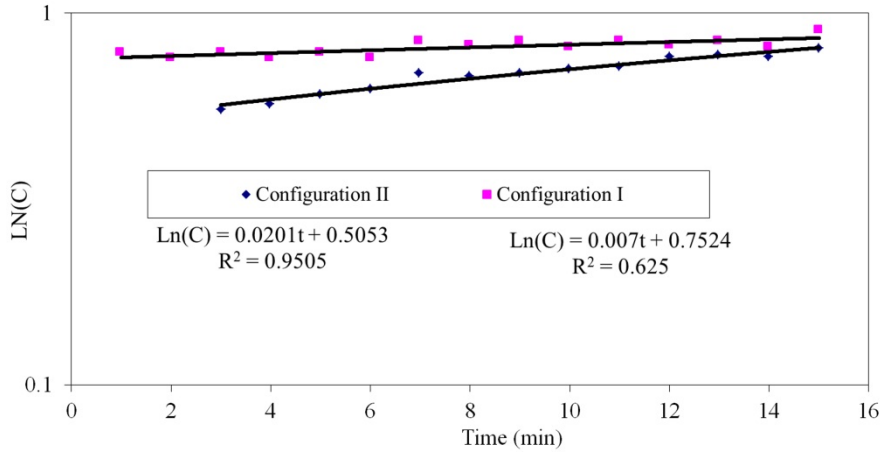

Fig. 10. Logarithmic graph of concentration: configuration III and IV [Makaka, Meyer; 2008].

Table 3 shows the calculated specific airflow exchange rates (μ) for different ventilation component configurations. In this table, the confidence intervals were calculated from the dispersion of the concentration measurements around the regression line, using 0.1% probability (99.9% confidence). When all the designed ventilation components were closed (configuration IV) the least specific air exchange rate (μ) of (0.29 ± 0.03) h^{-1} was observed as compared to other ventilation component configurations. The equivalent outdoor airflow rates (M_{eq}) for each ventilation component configurations were calculated using the expression: $M_{eq} = \mu V$, where V is the volume of the house. The house has a volume of 34.56 m^3 and an envelope area of 61.1 m^2. Assuming that the flows are due to the envelope leakage the specific leakage rate (S_L) was obtained using the expression: $S_L = \frac{M_{eq}}{A}$ where A is the area of the envelope and results are summarized in table 3

Configuration	Ventilation component status	Specific air exchange rate μ (h^{-1})	Equivalent outdoor air flow rate M_{eq} (m^3/h)	Specific leakage rate S_L ($m^3/h.m^2$)	Rate of ventilation heat flow Q_v (J/s)
I	Doors and windows open	9.58 ± 0.04	331.08 ± 1.38	5.42	772
II	Doors closed and windows open	1.74 ± 0.02	60.13 ± 0.69	0.98	140
III	Doors open and windows closed	0.84 ± 0.04	29.03 ± 1.38	0.48	68
IV	Doors and windows closed	0.29 ± 0.03	10.02 ± 1.04	0.16	24

Table 3. Specific airflow rates calculated from the various CO_2 concentration decays [Makaka, Meyer,; 2008]

The ventilation rate determines the indoor environment as the incoming air carries with it thermal energy. If the outdoor temperature is higher than the indoor, and as the outdoor air flows indoors, the tendency is to raise the indoor temperature. The rate of ventilation heat flow is approximated by equation. $Q_v = 1200 M_{eq} \Delta T$. Taking the average indoor-outdoor temperature difference ΔT to be 7°C and the ventilation rates from Table 3, the ventilation heat flow rates were calculated. Table 3 also shows the summary of results for the rate of ventilation heat flows for different ventilation component configurations. Depending on the indoor and outdoor temperature difference, configuration I, which has the highest rate of ventilation heat flow, can result in excess heat gains or losses. However, adjusting the effective open areas of the ventilation components can regulate the heat gain/loss, thus keeping the indoor environment within the comfort levels.

It must be noted that the rate of ventilation heat flow for configuration IV is through the unintended ventilation path ways, i.e. through gaps between doors and floors, etc, since all designed ventilation components were closed.

8. Indoor temperature variation

8.1 Prediction of indoor temperature

The mathematical description of thermal behaviour of building systems is a complex process. It involves the modelling of several interconnected subsystems, each containing long-time constants, non-linearities and uncertainties such as convection coefficients, material properties, etc. The indoor temperature is affected by a number of stochastic parameters, which include, wind speed and direction, relative humidity, solar radiation and outdoor temperature. The random infiltration rate and thermophysical properties (such as thermal conductivity of the walls and heat capacity of the room) have an impact on the indoor temperature.

The statistical approach allows estimating the probabilistic future thermal behaviour of buildings based on monitored statistical information, such as outdoor temperature, relative humidity, etc. The stochastic behaviour of the occupants in operating the ventilation components and other indoor human activities greatly affects the thermal performance of buildings. Some can even choose to close doors to avoid pets to get indoor thus compromising the thermal performance of the house. These parameters sometimes are uncertain and in some cases are difficult to find the exact information.

8.2 Correlating T_{in} and T_{out}

Figure 11 shows the best-fit linear regression correlations of the indoor and outdoor temperatures for summer. It was seen that the indoor and outdoor temperatures had different correlations for low temperatures (less than 28°C), and for high temperatures (greater than 28°C). At low temperatures the correlation factor was found to be $R^2 = 0.8064$ while for high temperatures the correlation factor was $R^2 = 0.6028$. At low temperatures the correlation was found to be stronger implying that at low temperatures there is less dependence on other parameters such as relative humidity as compared to high temperatures. At high temperatures relative humidity was found to be very low (minimum),

while the solar radiation was maximum. This suggests that relative humidity and solar radiation have significant influence on the indoor temperature at high outdoor temperatures. The peak indoor temperatures were found to occur during cooking periods and thus creating a departure from the low temperature variation trend. A departure of about 57% was observed from the low temperature variation trend to high temperature variation trend and this departure is indicated in figure 11 by a double arrow. This departure can be due to indoor heat sources, such as heat from stove. At low temperatures the correlation between the indoor and outdoor temperature was found to be:

$$T_{in} = 0.691T_{out} + 11.67 \tag{5}$$

while at high temperatures it was found to be:

$$T_{in} = 1.088T_{out} + 0.308 \tag{6}$$

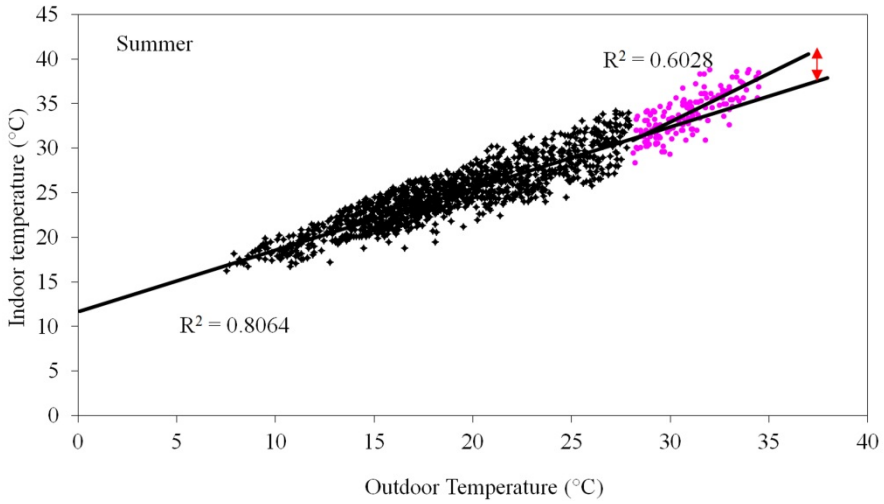

Fig. 11. Summer: Correlation of indoor and outdoor temperature [Makaka, Meyer; 2011].

Figure 12 shows the best-fit correlation of the indoor to the outdoor temperature for winter period. At high outdoor temperatures (above 28°C) the correlation factor was found to be $R^2 = 0.4568$ while at low temperatures (less than 28°C) it was $R^2 = 0.7391$. At low temperatures the correlation is relatively stronger than at high temperatures implying that the outdoor temperature has a greater influence on the indoor temperature at low temperatures. The departure from the low temperature variations trend was found to be about 62% and is indicated in figure 19 by a double arrow. This departure may be attributed to indoor heating and activities which are independent to the outdoor temperature.

At low temperatures the correlation function between the indoor and the outdoor temperature was found to be:

$$T_{in} = 0.657T_{out} + 8.671 \tag{7}$$

while at high temperatures it was found to be:

$$T_{in} = 1.052T_{out} + 1.449 \tag{8}$$

From the correlation functions for summer and winter it was observed that the outdoor temperatures have significant influence on the indoor temperature. It must also be noted that, if a change occurs in the comfort parameters (e.g., temperature) that might result in discomfort, occupants react in a way that tend to restore their comfort, and there is no precise temperature at which one opens a window, but as the temperature rises there is an increase in probability that windows need to be opened. In figure 12, a significant number of data points appear as outliers. Although the occupants never used a proper heater, it is highly likely that at times they used a two-plate electrical stove to heat the indoor environment, thus giving rise to outliers. It must be noted that the outliers are above the trend line, confirming that at times a heating system was used. However the occupants never reported the use of a heater or fan.

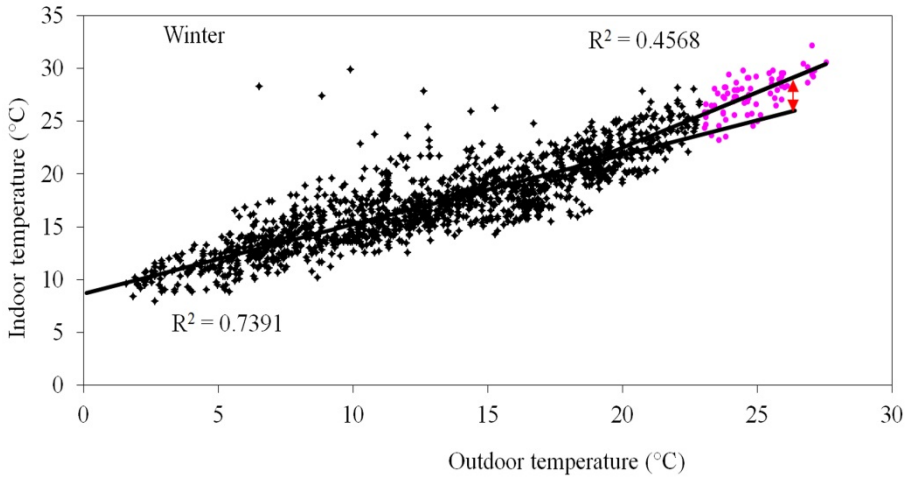

Fig. 12. Winter: Correlation of indoor and outdoor temperature [Makaka, Meyer; 2011].

The wide dispersion of the points about the trend line also indicates that the indoor temperature is not affected by the outdoor temperature only but by other factors such as ventilation rate, relative humidity, wind speed and solar radiation. The correlations also suggest that the passive solar house is freeze resistance since when the outdoor temperature is 0ºC, the indoor temperature would be about 8°C in winter and much higher (about 12°C) in summer. From the measured data it was observed that on the 29/5/29 at around 06h30 the outdoor temperature dropped to about 1.6°C and the indoor temperature only dropped to 9.4°C. This indicates the high heat retention capacity of the thermal mass (fly ash bricks), such that when the outdoor temperature drops to zero, the stored thermal energy in the wall continue to heat the indoor air keeping it at a temperature above 8°C.

8.3 Correlating T_{in} and outdoor relative humidity

Figure 13 shows the correlation of indoor temperature to outdoor relative humidity for summer. The data points were found to follow two distinct distribution trends, i.e., at low (less than 34%) and high (greater than 34%) relative humidity. The correlations factors were found to be very weak, for low relative humidity the correlation factor was found to be, $R^2 = 0.2774$ while for high relative humidity it was found to be $R^2 = 0.3099$. The differences in correlation strength at low and high relative humidity suggest that there are other variables which dominate at low relative humidity and not at high relative humidity. At low relative humidity solar radiation was found to have a greater influence on the indoor relative humidity variation. The low correlation factors indicate that there are other parameters which have a higher impact on the indoor temperature than the outdoor relative humidity. At low outdoor relative humidity (less than 34%) the correlation was found to be:

$$T_{in} = -0.3395(RH)_{out} + 40.464 \tag{9}$$

while at high relative humidity the correlation was:

$$T_{in} = -0.1184(RH)_{out} + 33.389 \tag{10}$$

Figure 14 shows the correlation of the indoor temperature and outdoor relative humidity for the winter period. The data points were found to be more scattered than for the summer. The high scatter is due to the variability of the Somerset East weather, which can change two to three times a day and a change of indoor activities due to the change of season. The dependence of the indoor temperature with the outdoor relative humidity was found to be different for low and high outdoor relative humidity. For low relative humidity the correlation factor was found to be $R^2 = 0.2657$ while for high relative humidity the correlation factor was $R^2 = 0.4027$. Low relative humidity was found to correspond to high temperatures, which is directly related to the solar radiation. High solar radiation was found to correspond to low relative humidity. At low relative humidity the correlation function was found to be:

$$T_{in} = -0.6862(RH)_{out} + 36.65 \tag{11}$$

while at high relative humidity the correlation function was found to be:

$$T_{in} = -0.1004(RH)_{out} + 22.70 \tag{12}$$

8.4 Effect of solar radiation on indoor temperature

Figure 15 shows the correlation of the indoor temperature and solar radiation. The correlation factor was found to be $R^2 = 0.5873$. It must be noted that the indoor temperature is affected by a number of factors, which include heat generated by the occupants and from equipments such as stove and refrigerator.

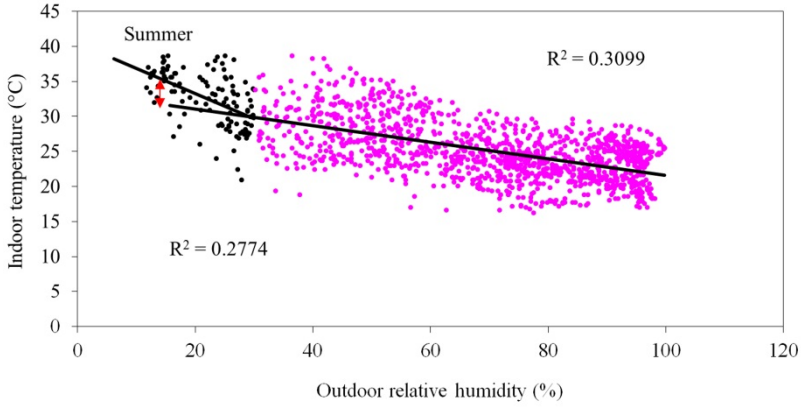

Fig. 13. Summer: Correlation of indoor temperature and outdoor relative humidity

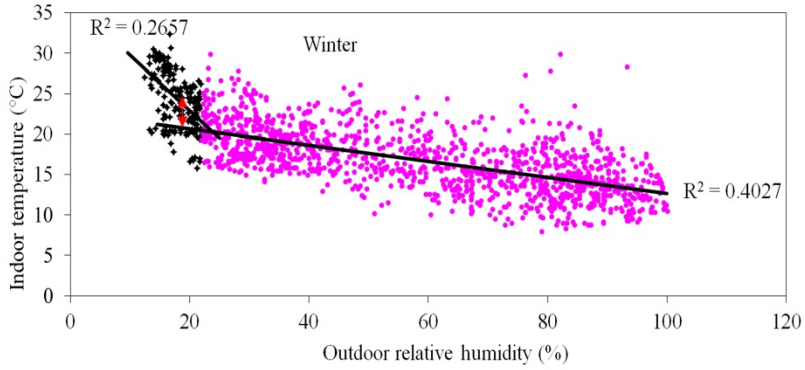

Fig. 14. Winter: Correlation of indoor temperature and outdoor relative humidity.

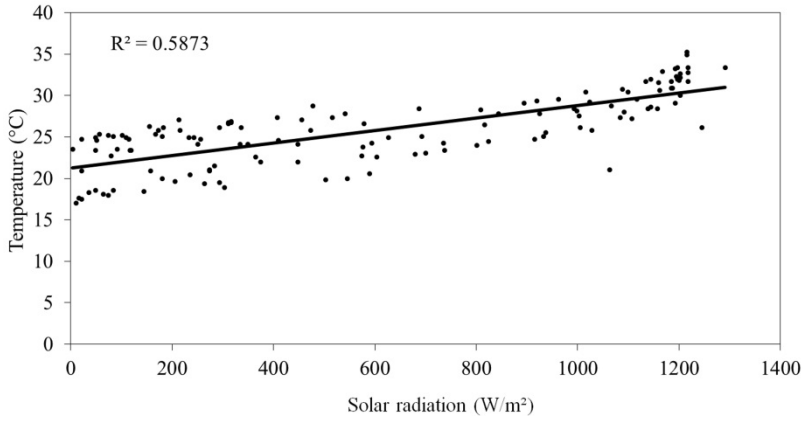

Fig. 15. Evolution of indoor temperature with solar radiation [Makaka, Meyer; 2011].

The indoor and outdoor temperature difference gives the direction of heat flow. High solar radiation was found to be associated with low indoor and outdoor temperature differences. Maximum indoor temperatures were found to occur at around 14h00. In summer the roof was found to attain high temperatures and the roof being of iron sheets (good thermal conductor) contributed significantly to the indoor temperature distribution. The high roof temperature diminishes the indoor and outdoor temperature difference. The correlation function between indoor temperature and solar radiation, I, was found to be:

$$T_{in} = 0.0075I + 21.27 \tag{13}$$

Equation (13) shows that when the solar radiation is zero (at night), the indoor temperature would be within the thermal comfort levels (about 21°C). During the day the thermal mass would have absorbed solar radiation and releases it at night thus keeping the indoor environment within the comfort levels.

8.5 Temperature modeling

The generalized mathematical model for predicting indoor temperature of any building has to take into account two types of data: on one hand the climatic conditions to which the building is exposed and, on the other hand, the thermal properties of the building. In an unoccupied house one can have a complete control over the conditions of the house, whether to open or close; shade or unshade the windows, etc. During the experimental period, the ventilation components can be maintained at the same configuration without indoor heat generation or cooling.

In occupied buildings the situation is very different, as the occupants have complete freedom to change the conditions according to their changing needs or desires. The activities of the occupants have a significant influence on the indoor temperature distribution. Predicting the indoor temperature is a very difficult and complex process, as random variables come into play, such as the closing and opening of the ventilation components. Outdoor weather variables such as wind speed, temperature, solar radiation and relative humidity are key determinant factors of the indoor temperature. However it must be noted that the indoor temperature is also linked to the heat fluxes generated in the house by appliances.

The performance of the house was observed to depend on how the occupants operate the house, and the thermal behaviour of the house in winter was seen to be different from that in summer. Based on the monitored results, the first stage in the development of the experimental predictive model was to analyze the patterns between (i) T_{in} and T_{out} (ii) T_{in} and I (iii) T_{in} and RH_{out} (iv) T_{in} and V_w. Taking into account these possible dependences predictive models for the indoor temperature for summer and winter were developed. A linear dependence was proposed as the above relation patterns were observed to be linear.

$$T_{in} = a_1 * T_{out} + a_2 * RH_{out} + a_3 * I + a_4 * V_w + a_5 \tag{14}$$

Where:

T_{in} = Indoor temperature
T_{out} = Outdoor temperature
V_w = Wind speed
I = Solar radiation
RH_{out} = Outdoor relative humidity
a_i = Regression coefficient

The constant a_5 takes into account heat generated indoors either by appliances or occupants. The above-proposed model is a simplification of a complex dependence. It must be noted that all the parameters involved are not independent. For example, the outdoor temperature greatly depends on irradiance and wind speed. Using regression analysis, the coefficients in equation (14) were determined.

For summer the following model was obtained:

$$T_{in} = 0.818207T_{out} + 0.013562(RH)_{out} - 0.12907V_w + 0.00038I + 8.18 \quad (15)$$

For winter the following model was obtained:

$$T_{in} = 0.898116T_{out} + 0.03914(RH)_{out} - 0.2545V_w + 0.00575I + 4.20 \quad (16)$$

Figures 16 and 17 show the comparison of the measured and predicted indoor temperatures for summer and winter, respectively.

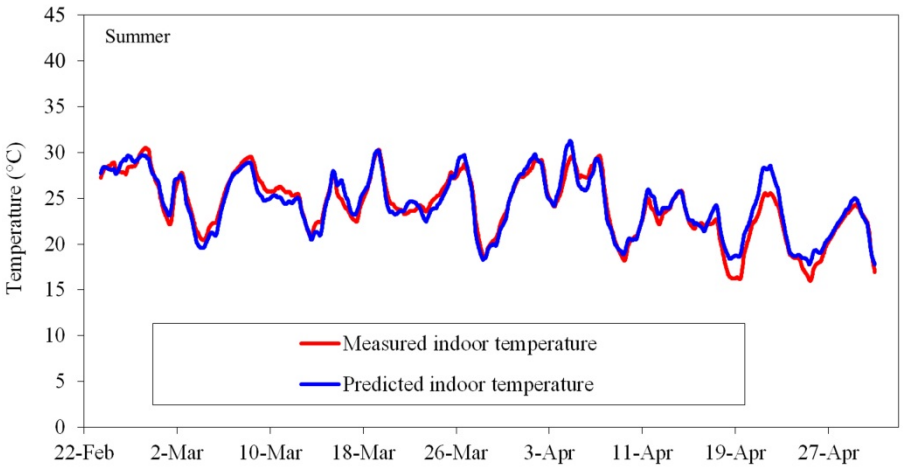

Fig. 16. Summer: measured and predicted indoor temperature [Makaka, Meyer; 2011]..

From equations (15) and (16) it can be noted that the outdoor temperature, solar radiation and outdoor relative humidity have a positive contribution to the indoor temperature, i.e.

when the outdoor temperature, solar radiation and relative humidity increase, the indoor temperature increases. But when the wind speed increases the tendency is to lower the indoor temperature. From the models it was seen that the outdoor weather parameters do have varying impact on the indoor temperature but with high sensitivity to the outdoor temperature. The determination of the sensitivity of the models revealed that the indoor temperature could be predicted to 85% accuracy in summer and to 87% accuracy in winter, considering the outdoor temperature only.

From figures 16 and 17, it can be seen that the predicted temperatures agree well with the measured data, however in summer there were some significant differences at some peak temperatures, with the measured temperature being higher than the predicted. These peak temperature differences were due to the indoor heat generating activities such as cooking and ironing. It must be noted that in the model thermal properties of the building were not taken into consideration.

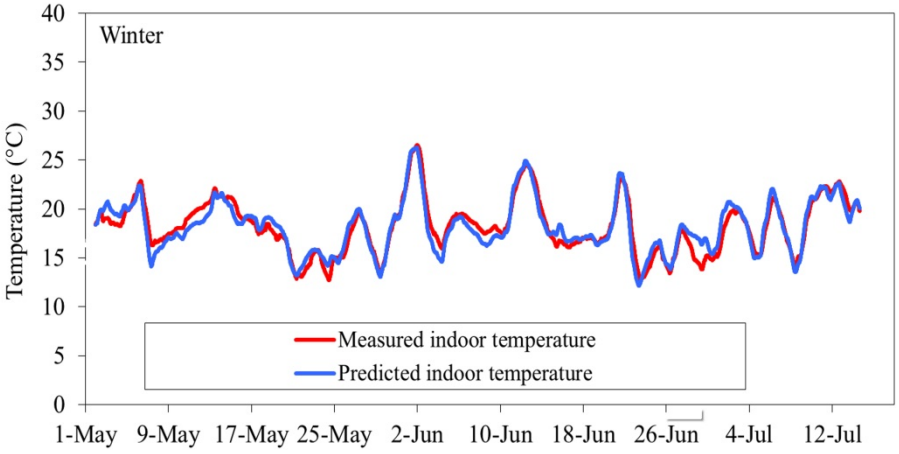

Fig. 17. Winter: Measured and predicted indoor temperature [Makaka, Meyer; 2011].

9. Conclusions

Fly ash bricks with the ratio 1:1 clay to fly ash mixing ratio were found to have the low water absorption, low thermal conductivity, high compressive strength and attractive decorative colour that eliminates the need for external plastering.

The monitoring results suggest that the building behaviour cannot be restricted to construction issues only. The thermal behaviour was the result of construction and non-construction factors, and their interaction as well.

Passive solar gain, ventilation mechanisms, orientation, and socio-environmental factors such as the life style and behaviour of the occupants, associated with the use of

complementary heating, operative heating (cooking, metabolic heat production), were found to have a significant impact on the indoor temperature distribution. The house performed differently in summer and winter. The indoor temperature followed the outdoor temperature implying that the solar radiation has a great impact on the indoor temperature variation.

The ventilation rate was found to depend on the ventilation component in use, windows were found to have a higher ventilation effect than doors. Correct opening and closing of windows can regulate the air infiltration thus controlling the indoor air quality.

When the day-to-day indoor temperature variations and the outdoor weather parameters are known, it is possible to reconstruct an approximate indoor temperature patterns during a given period. An indoor temperature prediction formula was modelled; it was shown that knowing the outdoor weather data parameters, the indoor temperature could be predicted. Outdoor temperature was found to have the largest impact on the indoor thermal environment. Significant differences were noted during cooking periods when a lot of heat was generated indoors, resulting in much higher measured indoor temperature than the model can predict. It is worth mentioning that the activities of the occupants play an important role in indoor temperature distribution.

10. References

[1] Agrement South Africa, (2002), Assessment criteria: Building and walling systems: Acoustics performance of buildings, http://www.agrement.co.za/.

[2] Kunzel, H. M, Zirkelbach, D. and Sedlbaur, (2003), Predicting indoor temperature and humidity conditions including hygrothermal interactions with the building envelope. Published in proceedings of the 1st International Conference on sustainable Energy and Green Architecture., Building Scientific Research Centre (BSRC), King Monkut's University Thornburi, Bangkoki 8-10 Oct. 2003.

[3] Makaka, G and Meyer, E. (2008), Thermal behaviour and ventilation efficiency of low-cost passive solar energy efficient house, Renewable energy 33 (2008), page 1959-1973

[4] Marsh, A., (2004), www.squ1.com

[5] Myers, E and George, F., (2004), Effect of ventilation rate and board loading on formaldehyde concentration: a critical review of literature. Forest products journal 2004, Vol. 34, number 10.

[6] Penman, R., (1982), Experimental determination of airflow in a naturally ventilated room using metabolic CO_2: Building and Environment, 17, 4.

[7] Raman, P., Mande, S. and Kishore, V. V. N., (2001), A passive solar system for thermal comfort conditioning of buildings in composite climates. Tata Energy Research Institute, Darbari Seth Block, Habitate place, Lodhi Road, New Delhi, India.

[8] Roulet, C. A., (1991), Simple and cheap air change rate measurement using CO_2 concentration decays. Air infiltration and ventilation centre Technical Note: 34.

[9] Wray, W., Balcomb, J.D., and Macfarland, R.D., (1979), A Semi Empirical method for estimating the performance of direct gain passive solar heated buildings. Proc. 3rd National Passive solar conference, San Jose California.

9

Nanogold Loaded, Nitrogen Doped TiO_2 Photocatalysts for the Degradation of Aquatic Pollutants Under Sun Light

Zahira Yaakob[1], Anila Gopalakrishnan[2], Silija Padikkaparambil[1], Binitha N. Narayanan[2,*] and Resmi M. Ramakrishnan[2]

[1]*Department of Chemical and Process Engineering, Faculty of Engineering and Built Environment, Universiti Kebangsaan Malaysia, Bangi, Selangor,*

[2]*Department of Chemistry, Sree Neelakanta Government Sanskrit College Pattambi, Palakkad, Kerala,*

[1]*Malaysia*

[2]*India*

1. Introduction

Along with the rapid development of industry, various issues related to energy and environment got generated which are now grown into a significant level. The hazardous waste materials with high concentrations are being discharged directly or indirectly into water bodies without adequate treatment to remove harmful compounds. The World Bank estimates that 17 to 20 percent of industrial water pollution comes from textile dyeing and treatment causing a major global problem. A facile and cheap method for removing inorganic and organic pollutants from wastewater has much relevance in modern world. Dyes are an important class of aquatic pollutants. Its complexity and variety makes it difficult to find a unique treatment procedure that entirely covers the effective elimination of all types of dyes. Particularly, biochemical oxidation suffers from significant limitations since most dyestuffs commercially available have been intentionally designed to resist aerobic microbial degradation and also they may get converted into toxic or carcinogenic compounds. The physical methods such as flocculation, reverse osmosis and adsorption on activated charcoal are nondestructive and merely transfer the pollutant to other media, thus causing secondary pollution (Binitha, 2009, as cited in Belver, 2006) Heterogeneous photocatalysis with various oxide semiconductor photocatalysts is an efficient and rapidly expanding purification technique for water and air. Semiconductor-oxides are a popular class of materials because of their functionalities and applications in the field of photocatalysis and generation of photoelectricity.

There has been greater attention on the photocatalytic activity of nanocrystalline TiO_2 after the discovery of photodecomposition of water on Titania [Ali, 2009; Hao, 2008; Parida, 2007;

* Corresponding Author

Xiang, 2008; Dambar, 2007; Wang, 2004; Colmenares, 2006; Kolenko, 2005; Shengli, 2006; Baiju, 2007]. Titania (titanium oxide) is considered as one of the most promising heterogeneous photocatalyst owing to the facts such as high photocatalytic activity, strong oxidizing power, low cost, chemical and thermal stability, resistance to photo corrosion and non-toxicity. In addition, TiO_2 possess favorable optoelectronic properties which makes it a well accepted photocatalyst for the degradation of various environmental pollutants (Meenal, 2009; Pirkanniemi; 2002).

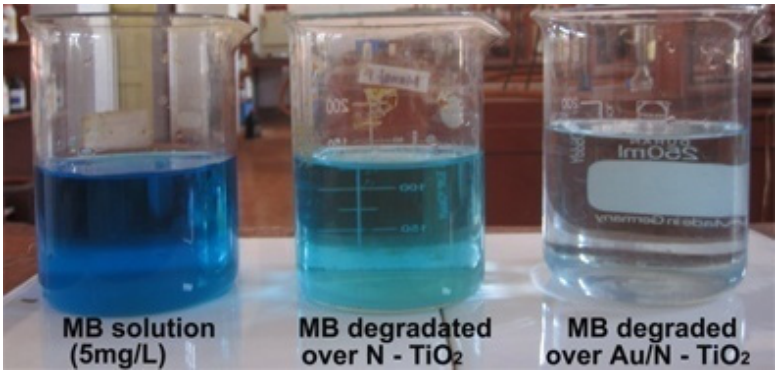

Fig. 1. Degraded methylene blue solution under 1 h exposure to sun light over N doped TiO_2 and Au loaded N doped TiO_2

However, the high intrinsic band gap energies of major crystalline forms of TiO_2 (3.2 eV for anatase phase and 3.0 eV for rutile) makes them effective photocatalysts only when the wavelengths of light is shorter than 387 nm. Thus only a small part of solar light is harvested if we use bare TiO_2 photocatalysts (Haijian, 2008, as cited in Fujishima & Honda, 1972; Li, 2000). It is known that the UV part of the solar spectrum accounts only for about 4% of the incoming solar energy while the major part of the rest is visible light (Binitha, 2010). It is therefore of great significance to adjust the band structure of TiO_2 to improve the photoreaction rate for the efficient use of solar energy for photocatalysis. There are several studies in recent years attempting the incorporation of the visible range of solar spectrum also in the photocatalytic process, which include dye sensitization, metal ion doping, nonmetal doping, etc. (Meenal, 2009, as cited in Choi, 1994; Shockley & Read, 1952; Asahi, 2001). The incorporation of specific dopants in TiO_2 should improve the efficiency of the photocatalytic behavior by creating new band structures or by suppressing the recombination of photogenerated electron–hole pairs resulting in improved quantum efficiency (Zhiqiao, 2009).

The most feasible method for improving the photocatalytic performance of titania are considered as doping with metals as well as non metals. Recent researches concerning TiO_2-doped with nonmetal elements such as nitrogen (Yohei, 2004, as cited in Sato, 1986; Asahi, 2001; Morikawa, 2001), fluorine (Yohei, 2004, as cited in Hatori, 1998), sulfur (Yohei, 2004 as cited in Umebayashi, 2002) and carbon (Yohei, 2004, as cited in Khan, 2002) have been reported. Among the different anion dopants, nitrogen is observed to be the most effective one and is widely studied.

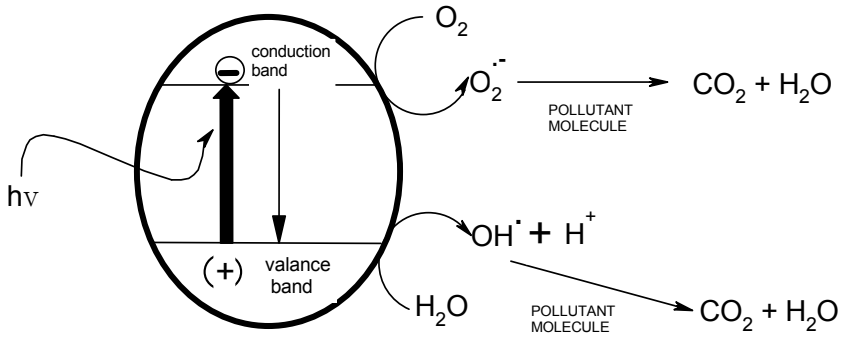

Fig. 2. Band structure of semiconductor titania: Making it suitable for pollutant degradation

Sato (Sato, 1986) was the first person who reported N-doped titania by annealing the mixtures of a commercial titanium hydroxide and NH4Clor NH4OH, which showed higher photocatalytic activity in the visible-light region. Asahi et al. (Asahi, 2001) reported that nitrogen-doped titania could induce the visible-light activity in which nitrogen atoms substitute a few oxygen atoms (0.75%), and the doped nitrogen was responsible for the visible-light sensitivity. These two studies had kicked off a new area of research to extend the absorbance of TiO_2 into visible-light region by means of nitrogen-doping. There has been several methods reported thereafter for the preparation of N doped TiO_2, such as high temperature treatment of TiO_2 under NH_3 flow (Hao, 2008, as cited in Asahi, 2001; Irie, 2003; Diwald, 2004), hydrolytic process (Hao, 2008 as cited in Ihara, 2003; Noda, 1986; Salthivel, 2003), mechanochemical (Hao, 2008 as cited in Yin, 2003; Wang, 2004), reactive DC magnetron sputtering (Hao, 2008, as cited in Lindgren, 2003; Chen, 2004), sol–gel (Hao, 2008, as cited in Burda, 2003), solvothermal process [(Hao, 2008, as cited in Aita, 2004), calcination of a complex of Ti ion with a nitrogen containing ligand (Hao, 2008, as cited in Sano, 2004), calcination in nitrogen atmosphere etc.

Among the different preparation procedures, sol gel route is the preferred one because of its endowed nature. The temperatures required for all stages of the process involved in the conversion of sol to gel apart from densification are low, avoiding material degradation and resulting in high purity and stoichiometry of the products. The fact that the precursor metal alkoxides are volatile in general and thus are easily purifiable, substantiates the formation of high purity products. Also, since the organometallic precursors involving different metals are normally miscible with each other, a homogeneous controlled doping can be achieved easily. In addition, during sol gel synthesis the chemical conditions are mild and thus even biological species including enzymes and whole cells may be entrapped retaining their functions after doping on sol gel prepared metal oxides. Besides, the formation of highly porous and nanocrystalline materials can be achieved by sol gel method, by means of appropriate chemical modification of the precursors, adequate control over the rates of hydrolysis and condensation, resulting in the formation of colloid particles of suitable size, porosity and the pore size, and thus achieving a fine control over the pore wall chemistry of the final material. However, there are only a few reports on the anion-doped photocatalysts prepared using wet-methods such as sol–gel and co-precipitation owing to the difficulties involved in the procedure (Hao,2008). Still there are some reports on the N doped sol gel titania which shows good visible light activity for the degradation of pollutants (Dewi, 2010; Hu, 2010; Jian, 2006; Liu, 2005; Min, 2008)).

In the previous studies, the shifting of the absorbance of TiO_2 to visible light upon nitrogen doping is explained in two ways. One proposed mechanism is the narrowing of the band gap by mixing the N2p and O2p states. Another explanation is the existence of two absorption edges in the UV visible spectra, the one around 400 nm, the resultant of the band structure of original TiO_2 and second one around 530 nm which is attributed to the newly formed N2p band located above the O2p valence band. The incorporation of nonmetal dopant atoms into the lattice structure of titania is believed to decrease the band gap, and shift its response to the visible part of the solar spectrum (Xin & Quingquan, 2008, as cited in Asahi, 2001; Khan, 2002; Ohno, 2004; Lin, 2007).

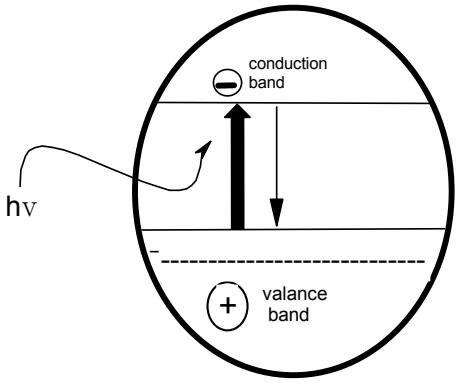

Fig. 3. Schematic picture of reduced band gap of titania as a result of mixing of N 2p and O 2p stages

As clear from the pictorial representation, the hole and electron pair separation is small when the electron is excited by the visible light after N doping and thus they can recombine easily, which will reduce the efficiency of photons. Thus suppression of the recombination of hole–electron pairs is a necessity for visible light active photocatalysts.

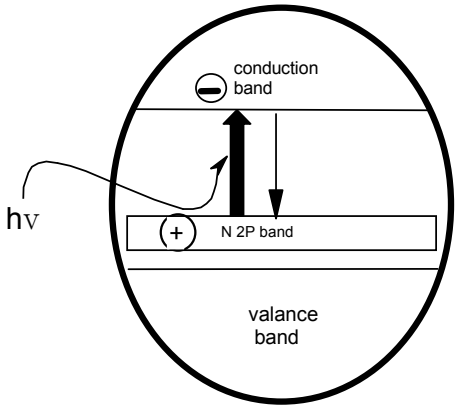

Fig. 4. The schematic diagram representing the shifting of TiO_2 absorption to visible region as a result of the newly formed N2P band above the TiO_2 valance band

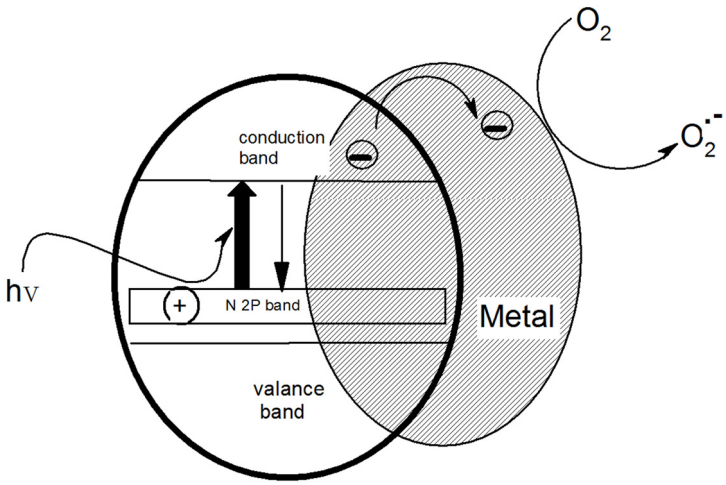

Fig. 5. The schematic diagram showing the role of doped metal nanoparticles in the photocatalytic activity. Metal nanoparticles act as an electron sink, supporting interfacial charge transfer and reduce the chances for charge recombinations.

Doped metal nanoparticles are believed to suppress the recombination of photo-induced electron-hole pairs, when they migrate from the interior of the photocatalyst to the metal surface resulting in increased photo quantum efficiency (Xin & Quingquan, 2008, as cited in Choi, 1994; Lin & Yu, 1998). Thus, metal nanoparticles can be considered as an electron sink, which can promote interfacial charge transfer and consequently less charge recombinations occur.

Thus in the present work, we are looking for a synergestic effect from both dopings. That is the anion doping can provide the narrowing of the band gap and the noble metal nanoparticles are suppose to suppress recombinations. Our objective is the preparation of unsurpassed photocatalysts which are sun light active. Nano gold loaded nitrogen doped TiO_2 photocatalyst was prepared through the sol–gel route using titanium isopropoxide as titanium source, ammonium nitrate as nitrogen precursor and chloroauric acid was used as the precursor for gold nanoparticles. The combined doping of nano gold and nitrogen leads to the high activity of the prepared system for the photodegradation of MB under visible light irradiation. Here, nanogold is observed to provide substantial progress in the photocatalytic activity compared to that of simple nitrogen doped titania for the MB degradation under sunlight.

2. Experimental

2.1 Preparation of photocatalysts

Au-loaded N doped TiO2 nano powders were prepared by sol–gel process. The sol was prepared following a reported procedure (Sunajadevi & Sugunan, 2004). Titanium isopropoxide (98%, Aldrich) was used as the precursor of TiO2. 50 ml of Titanium (IV) isopropoxide was hydrolyzed in 600 ml water containing 5 ml nitric acid. Precipitation occurred immediately and the mixture was stirred continuously at room temperature to

form a highly dispersed sol. To this, 4.39g ammonium nitrate was added to get the N-doped titania and stirring was continued for another 4h. The sol was then aged for two days and dried at 70°C. The powdered sample was then calcined at 400 °C for 5h to get the yellow coloured nitrogen doped titania.

Nano gold loading: Different percentage of nanogold are loaded on loaded on N- doped TiO2 photocatalysts by deposition– precipitation method, which can provide nano-sized gold particles with strong contact of Au particles with the support. Chloro auric acid was used as the gold precursor. The aqueous Chloroauric acid solution($2.1x10^{-3}$M) is heated to 70 ^{0}C. Then the pH of the solution was adjusted to 8 by dropwise addition of 0.5M NaOH solution. The required amount of the support was added in to it with vigourous stirring. The stirring was continued at 70°C for 2h. The pH was maintained as 8 throughout the preparation. It was then cooled to room temperature, filtered and washed with distilled water to make it free from chloride ions. Subsequently it was dried at 80°C for overnight followed by calcination at 200 °C for 5 h. The catalytic systems thus produced are designated as $NTiO_2$, $1AuNTiO_2$ and $2AuNTiO_2$ for nitrogen doped TiO_2 with no gold loading, 1% and 2% Au loading respectively.

2.2 Catalyst characterization

XRD patterns of the samples were recorded for 2θ between 10 and 80° on a Bruker AXS D8 Advance diffractometer employing a scanning rate of 0.02°/S with Cu Kα radiation (λ=1.5418). The FTIR spectra were recorded in Thermo Nicolet, Avatar 370 spectrometer in the region 400–4,000 cm^{-1}. TEM photographs of the prepared systems were taken in JEOL JEM 2100 Electromicroscope. SEM pictures are collected using a JEOL Model JSM - 6390LV.

2.3 Photocatalytic degradation studies

Photocatalytic degradation of Methyleneblue (MB) was done by the use of solar energy. All outdoor experiments were carried out in closed Pyrex flasks at room temperature with stirring. The irradiation was performed on sunny days, from 11.00 to 14.00 h when solar intensity fluctuations were minimum. The samples were immediately centrifuged and the quantitative determination of dye was determined using colorimeter (CL 157 - ELICO) before and after the irradiation. Experiments were repeated to get better results. The MB concentraction of 5 mg/L mmol at 2h of exposure to sunlight are used for all measurements except for time study.

3. Results and discussion

With an objective to develop a visible light or solar energy responsive photocatalyst, nitrogen doping is done on titania where ammonium nitrate is used as the N precursor. N dopant is added to the stable sol and with gelation the development of a yellow colour is observed whereas introduction of gold changes the colour to violetish ash. With the increase in gold loading, the colour was found to deepen. The different catalytic systems prepared are characterized using various techniques.

3.1 Photocatalyst characterization

It is well established that the electron and hole recombination can be suppressed by increasing the crystallinity of the Semiconductor, minimizing the crystal defects which act as

recombination centers (Tsugio, 2006, as cited in Sclafani, 1990). Our objective here is the preparation of fine particles of small band gap semiconductor with high degree of Crystallinity, which can make photocatalysts that are capable of showing visible light activity. The crystalline nature of the present samples were analyzed using XRD analysis. Both anatase as well rutile phase were visible in the samples where anatase phase was the predominant one. The foremost peak corresponding to (1 0 1) reflections of the anatase phase of TiO_2 was well evident at the angle of 25.28◦, as well as the minor peaks were appeared around 37.8◦, 48.0◦, 53.8◦ and 55.1◦. The major peak of the (1 1 0) diffraction of rutile was observed at the angle of 27.50◦, whereas the minor peaks appeared at 36.15◦, 41.33◦, 54.44◦, 56.76◦, 62.89◦ and 69.17◦. Weight ratios of each phase were calculated using the following equation:

$$W_r = \frac{A_R}{0.884A_A + A_R}$$

Here A_A represents the integrated intensity of the anatase (1 0 1) peak and A_R the integrated intensity of the rutile (1 1 0) peak (jirapat, 2009, as cited in Gribb, 1997). Increase in gold loading increases the anatase to rutile ratio. This observation is apparently is surprising since we are adding gold precursor to the calcined gel. Thus it is expected that the $2AuTiO_2$ can show maximum photoactivity, since anatase is considered as the most photocatalytically active form of TiO_2. TiO_2 obtained by following the same procedure without any N doping is also showing the existence of both anatase and rutile as the crystalline phases (XRD is not shown) (Sunajadevi & Sugunan, 2004). The crystallite size of different systems were calculated using Scherrer equation and the results are provided in table 1.

Catalyst	Weight fractions of phase (%)		Crystal size (nm)	
	Anatase	Rutile	Anatase	Rutile
1% $AuNTiO_2$	65.74	34.26	6.17	11.62
2% $AuNTiO_2$	86.78	13.22	6.98	7.71

Table 1. Anatase to rutile ratio and crystallite size of gold loaded catalysts

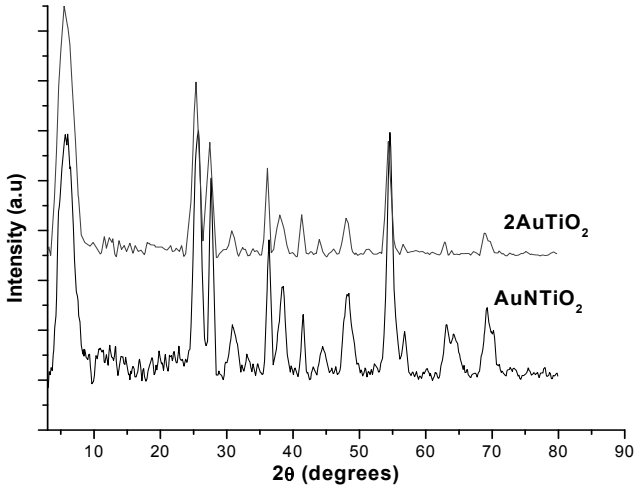

Fig. 6. XRD patterns of different systems

The surface morphology of different systems was analyzed using SEM. In Fig. 7, SEM micrographs of $1AuNTiO_2$ and $2AuNTiO_2$ are given. All samples appeared as agglomerations of smaller particles with a high tendency for crystallization.

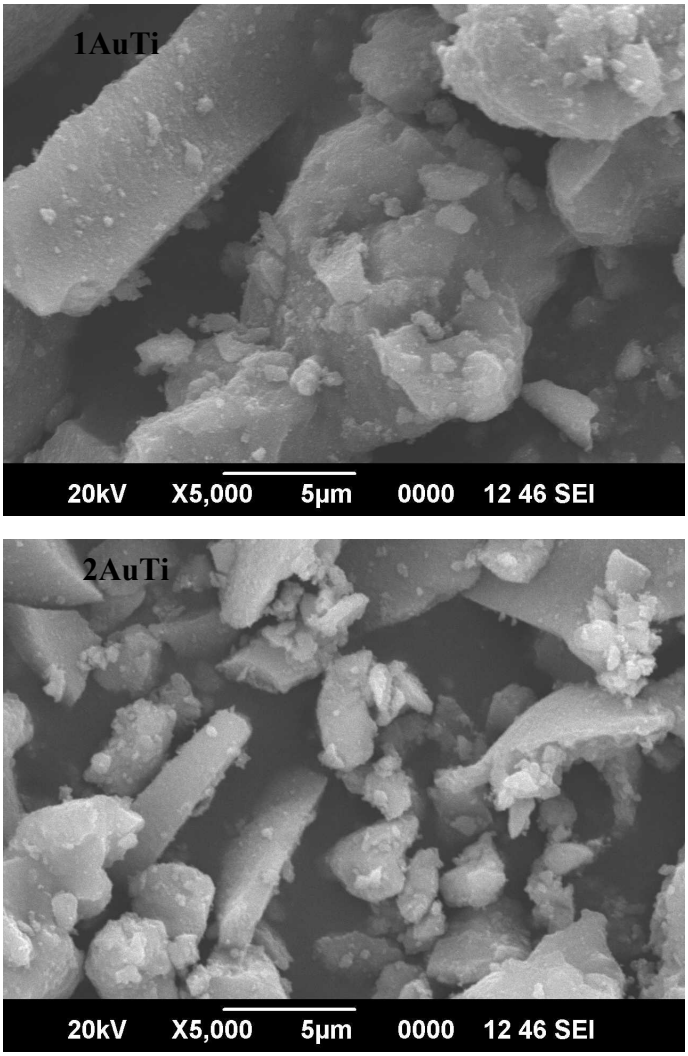

Fig. 7. SEM images of the prepared systems

The TEM micrographs of the photocatalysts show that the gold particles are highly dispersed on the surface of N doped TiO_2 and the mean diameter of gold particles estimated from the TEM images are less than 5nm. In the case of $1AuNTiO_2$, only few gold particles are visible and its size is also found to be smaller when compared to that in $2AuNTiO_2$. At higher gold loading of 2%, there is competent dispersion for the nanoparticles and the gold particles are visible as sharp dark spots over the gray coloured support. Furthermore, the

lattice fringes of the crystallographic planes of anatase and rutlies are found to be visible, consistent with the XRD patterns. The visible TiO2 particles are more or less spherical in shape and are found to be of lower size of around 10 – 20 nm diameter

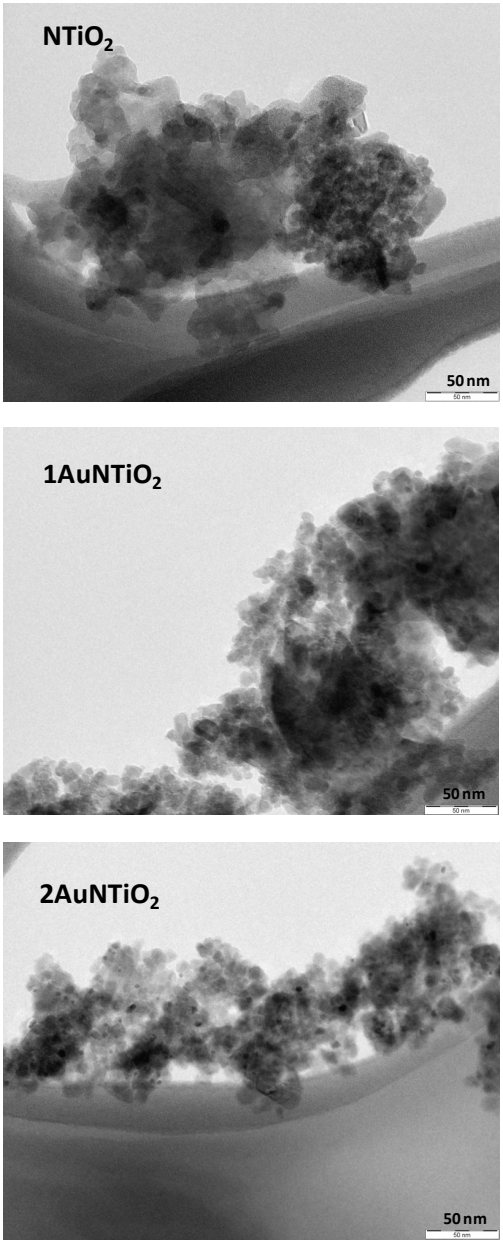

Fig. 8. TEM images of the prepared systems

In the FTIR spectra of the systems shown in Fig. 9, a broad peak seen around 3400 cm^{-1} can be assigned to stretching vibration mode of the OH groups within the TiO_2 sol–gel. The corresponding bending vibration band was observed at 1637 cm^{-1}. The TiO_2–OH bonds arise from the hydrolysis reactions occurring during the gelling of the titanium alkoxide. In the low energy region of the spectrum, the bands around 500 cm^{-1} can be assigned to bending vibrations of Ti–O bonds.

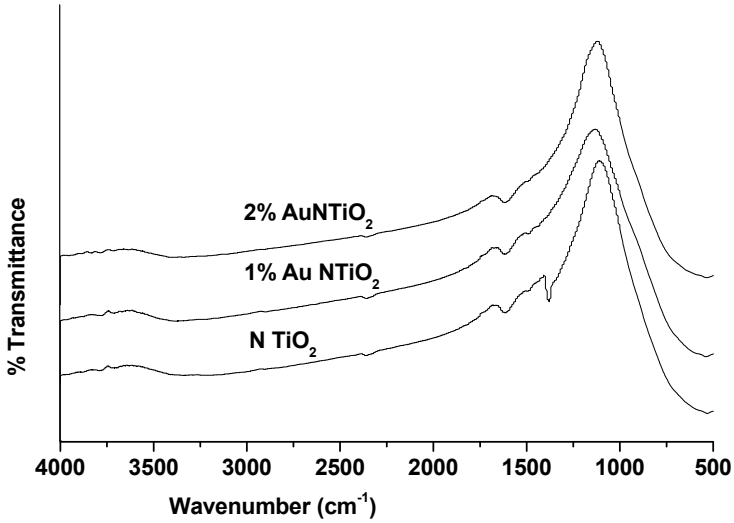

Fig. 9. FTIR spectra of the prepared systems

3.2 Photoactivity results

Photodegradation of MB was done to get the information on the pollutant degrading capability of the present systems. The reaction variables were optimized using $2AuNTiO_2$ to achieve the conditions for maximum degradation.

3.2.1 Effect of catalyst dosage

A series of experiments were carried out to optimize the catalyst loading by varying the amount catalyst from 0.05g – 0.20g/50ml MB solution of concentration 5 mg/l. The degradation results for 2 h irradiation are shown in Fig. 10. The rate of degradation increased linearly with increase in catalyst weight from 0.05g to 0. 10g which then decreases with further increase in the amount of catalyst used. The initial enhancement in photoactivity with catalyst weight may be due to the increase in number of photons absorbed and the number of dye molecules adsorbed on the catalyst molecules. Also the density of the catalyst particles in the area of illumination increases with the catalyst dosage. When the amount of catalyst is exceeding certain limit, the dye molecules available are not sufficient for adsorption and hence the additional catalyst powder is not taking part in the photocatalytic activity and consequently the rate becomes independent of the amount of catalyst beyond certain limit. It is reported that the increase in opacity of the solution at high catalyst dosage decreases the penetration of light inside the solution with a consequent decrease in the photoreduction of the

dye (Binitha, 2011, as cited in Maruthamuthu, 1989). Thus, the optimum amount of catalyst needed to get maximum degradation of pollutant in the present case is 0.1 g.

3.2.2 Effect of volume of MB

The influence of volume of MB on degradation rate was studied by varying the volume of the dye from 25 to 100 ml at a constant TiO_2 loading of 2 g/L for 2 h exposure to sunlight. It was observed from Fig. 11, that the degradation rate increased from 25 ml to 50 ml and then decreased with further increase in the amount of dye. The absorption of light by the pollutant may be dominated at higher volumes which in turn decrease the absorbance of light by the catalyst causing a reduction in the photocatalytic activity.

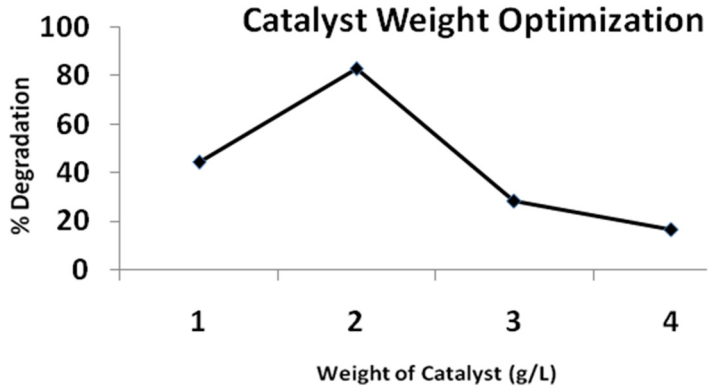

Fig. 10. Effect of catalyst dosage on the degradation of 50 ml of 5 mg/L MB for 2h irradiation

3.2.3 Effect of time

The degradation of 50 ml of 5mg/L MB was investigated by changing the irradiation time from 1 h to 3 h and the activity over the three catalytic systems is plotted in Fig. 12. It is

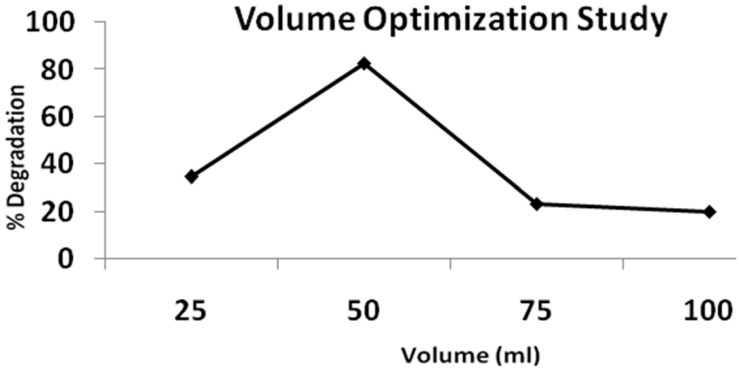

Fig. 11. Effect of volume of MB solution on the degradation of 5 mg/L MB for 2h irradiation using 2g/L catalyst

observed that the degradation reaches 100 % within 3 h of exposure to sunlight in the case of 2AuNTiO$_2$. This system is thus found to be capable for complete degradation of dye pollutants within this short duration of 3 h solar irradiation. Lower loading of gold (1%) also showed improvement in the photocatalytic activity when compared to N doped TiO$_2$ without metal nanoparticles. All the three catalytic systems studied showed far better activity than undoped titania which showed very low photodegradation of MB (not included in the figure) , less that 10% even after keeping for 3 h under sunlight.

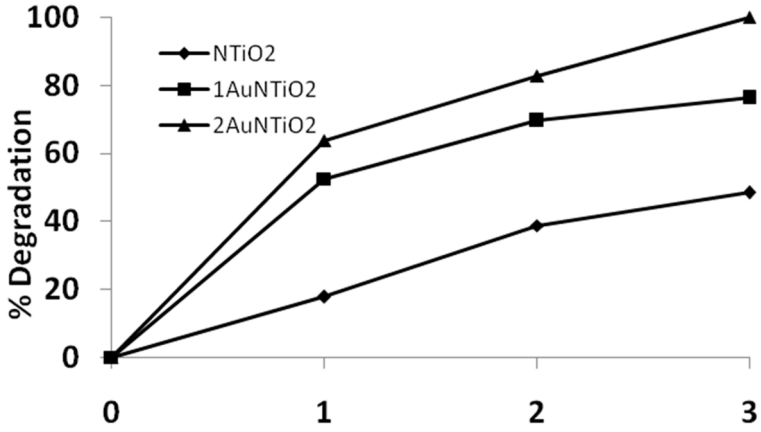

Fig. 12. Effect of Time on the degradation of 50 ml of 5 mg/L MB over a catalyst dosage of 2g/L

4. Conclusion

In conclusion, we are reporting the successful preparation of highly efficient photocatalytic systems, N-doped TiO$_2$ and Au nanoparticle incorportated N doped TiO$_2$. The photodegradation of aquatic pollutant methylene blue over N-doped TiO$_2$ and Au nanoparticle incorportated N doped TiO$_2$ catalysts were investigated and the catalytic performances were compared. Visible light activity was achieved for TiO$_2$ upon anion doping. It was found that Au nanoparticle loading over TiO$_2$ is capable of improving the photocatalytic activity of N doped TiO$_2$ to a greater extent and the inserted metal nanoparticles are believed to act as electron sinks to prevent the recombination of electron-hole pairs. In addition, X-ray diffraction patterns reveal the suppression of rutile phase with increase in the percentage of gold loading which also can be considered as a favorable factor to obtain superior photoactivity. The inserted gold particles were found to have spherical morphology of less than 5 nm dimension as evident from TEM micrographs. The 2AuNTiO$_2$ catalytic system was found to be the best among the three showing complete removal of the pollutant within 3 h exposure to sunlight.

5. Acknowledgment

The authors acknowledge the UKM, the grant number UKM-OUP-NBT-27-118/2009 for the financial support. STIC, CUSAT, Kochi, India is acknowledged for XRD, FTIR and SEM analyses.

6. References

Ali, A., Hossein, S., & Mehrdad, K. (2009). Sol–gel preparation of titania multilayer membrane for photocatalytic applications. *Ceramics International* , Vol. 35, No. 5, (January 2009), pp. 1837–1843

Asahi, R., Morikawa, T., Ohwaki, T., Aoki, K., Taga, Y.(2001). Visible-Light Photocatalysis in Nitrogen-Doped Titanium Oxides. *Science*, Vol. 293, No.5528, (July 2001) pp. 269-271

Baiju, KV., Periyat, P., Krishna Pillai, P., Mukundan, P., Warrier, K.G.K., & Wunderlich, W. (2007). Enhanced photoactivity and anatase thermal stability of silica–alumina mixed oxide additives on sol–gel nanocrystalline titania. *Materials Letters*, Vol. 61, (August 2007), pp. 1751–1755

Binitha, NN., Zahira, Y., Ranjana, K., Soumini, C., Sankaran, S., Femina, KS., & Vineetha, M. (2009). Photodegradation of Methylorange over Zirconia Doped TiO_2 Using Solar Energy. *European Journal of Scientific Research,* Vol. 28, No. 4, (2009), pp. 567-572, ISSN 1450-216X

Binitha, NN., Yaakob, Z., Y., & Resmi, R. (2010). Influence of synthesis methods on zirconium doped titania photocatalysts. *Central European Journal of Chemistry*. Vol. 8, No. 1, (2010), pp. 182–187

Binitha, NN., Yaakob, Z., Silija, PP., Suraja, PV., Tasirin, SM. (2011). Effect of Co-Doping of Nano Silver, Carbon and Nitrogen on Titania on the Visible Light Activity for Methylorange Degradation. *Defect and Diffusion Forum*, Vols. 312-315, (April 2011), pp. 776-781

Colmenares, JC., Aramendı´a, MA, Marinas, A., Marinas, J.M., & Urbano, FJ., (2006). Synthesis, characterization and photocatalytic activity of different metal-doped titania systems. *Applied Catalysis A: General* , Vol. 306, (March 2006), pp. 120–127

Dambar, BH., Kenneth, JK. (2007). Synthesis, characterization, and visible light activity of new nanoparticle photocatalysts based on silver, carbon, and sulfur-doped TiO2. *Journal of Colloid and Interface Science*, Vol.311, (March 2007), pp. 514–522

Dewi, P S., Madhavi , S., Melvin, L., & Teik-Thye, L. (2010). Photocatalytic degradation of bisphenol-A by nitrogen-doped TiO2 hollow sphere in a vis-LED photoreactor. *Applied Catalysis B: Environmental*, Vol. 95, No. 3-4, (April 2010), pp. 414-422

Haijian, S., Huiling, L., Jun, M., Xiangyu, W., Bin, W., & Lei, H. (2008). Preparation and characterization of sulfur-doped TiO_2/Ti photoelectrodes and their photoelectrocatalytic performance. *Journal of Hazardous Materials,* Vol. 156, (January 2008), pp. 552–559

Hao, LQ., Guo, BG., & Song, L. (2008). Preparation of nitrogen-doped titania using sol–gel technique and its photocatalytic activity. *Materials Chemistry and Physics*, Vol. 112, (May 2008), pp. 346–352

Hu, Y., Liu, H., Chen, W., Chen, D., Yin, J., & Guo, X. (2010) Preparation and visible light photocatalytic activity of N-doped titania. *Journal of Nanoscience and Nanotechnology*, Vol.10, No. 3, (March 2010), pp. 2232-7

Jirapat, A., Puangrat, K., & Supapan, S., (2009). Visible light absorption ability and photocatalytic oxidation activity of various interstitial N-doped TiO2 prepared from different nitrogen dopants. *Journal of Hazardous Materials,* Vol. 168, pp.253–261

Kolen'ko, YV., Garshev, AV.,. Churagulov, BR., Boujday, S., Portes, P., & Colbeau-Justin, C. (2005). Photocatalytic activity of sol–gel derived titania converted into

nanocrystalline powders by supercritical drying. *Journal of Photochemistry and Photobiology A: Chemistry*, Vol. 172 , (January 2005), pp. 19–26

Liu, Y., Chen, X., Li, J., & Burda C. (2005). Photocatalytic degradation of azo dyes by nitrogen-doped TiO2 nanocatalysts, *Chemosphere*, Vol. 61, pp.11–18

Meenal, MJ., Nitin, KL., Priti, AM., Saumitra, NT., Sanjay, PK., & Sadhana, SR. (2009). Visible light induced photoreduction of methyl orange by N-doped mesoporous titania. *Applied Catalysis A: General,* Vol. 357, (January 2009), pp. 26–33

Min, Li., Qun, ZH., Dong, FQ., Zhu, JJ., Zhao, HM., & Heng, ZS. (2008). Study on anti-fungal activity of nitrogen-doped TiO2 nanophotocatalyst under visible light irradiation. *Chinese Chemical Letters*, Vol. 21, pp.117–121

Parida, KM., Sahu, N., Biswal, NR., Naik, B., & Pradhan, AC., (2008). Preparation, characterization, and photocatalytic activity of sulfate-modified titania for degradation of methyl orange under visible light. *Journal of Colloid and Interface Science* , Vol. 318, (Novenmber 2007), pp. 231–237

Pirkanniemi, K., & Sillanpaa, M. (2002).Heterogeneous water phase catalysis as an environmental application: a review. *Chemosphere,* Vol. 48, No.10, (2002), pp.1047-1060

Sato, S.,(1986). Photocatalytic activity of NO_x-doped TiO_2 in the visible light region. *Chemical Physics Letters*, Vol. 123, No. 1,2, pp.126-128

Shengli, C., King, LY., & Po-Lock, Y. (2006). Preparation of freestanding and crack-free titania–silica aerogels and their performance for gas phase, photocatalytic oxidation of VOCs. *Applied Catalysis B: Environmental* , Vol. 68 (September 2006), pp. 99–108

Sunajadevi, KR., & Sugunan, S. (2004). Preparation and characterization of nanocrystalline transition metal-loaded sulfated titania through sol–gel method. *Materials Letters,* Vol. 58, No.26, (July 2004), pp. 3290– 3296

Tsugio, S., Yohei, A., Masakazu, K., & YIN, S. (2006). Synthesis of Nitrogen-doped Titania by Solvothermal Reactions in Alcohols. *The Chinese Journal of Process Engineering,* Vol. 6, No.3, (June 2006), pp. 472-476

Wang , J.A., Cuan, A., Salmones, J., Nava, N., & Castillo, S., Mora´n-Pined, M., & Rojas, F. (2004). Studies of sol–gel TiO2 and Pt/TiO2 catalysts for NO reduction by CO in an oxygen-rich condition. *Applied Surface Science* , Vol. 230, (April 2004), pp. 94–105

Xiang, ZS., Jun, G., Zhi-Cheng, L., & Shan-Mei, X. (2008). Visible-light-driven titania photocatalyst co-doped with nitrogen and ferrum. *Applied Surface Science,* Vol. 254, (January 2008, pp. 4726–4731

Xin, Z., & Qingquan, L. (2008). Visible-light-induced degradation of formaldehyde over titania photocatalyst co-doped with nitrogen and nickel. *Applied Surface Science,* Vol. 254, (February 2008), pp. 4780–4785

Yohei, A., Masakazu, K., Shu, Y., & Tsugio, S. (2004). Phase-compositional control and visible light photocatalytic activity of nitrogen-doped titania via solvothermal process. *Journal of Solid State Chemistry,* Vol.177, No. 9, (July 2004), pp. 3235–3238

Zhiqiao, H., Lei, X., Shuang, S., Cheng, W., Jinjun, T., Fangyue, H., Qi, L., Jianmeng, C., Xinhua, X. (2010). The impact of silver modification on the catalytic activity of iodine-doped titania for p-chlorophenol degradation under visible-light irradiation. *Journal of Molecular Catalysis A: Chemical*, Vol. 319, (December 2009), pp. 78–84

10

Estimation of Solar Energy Influx to the Sea in the Light of Fast Satellite Technique Development

Adam Krężel and Katarzyna Bradtke
University of Gdańsk, Institute of Oceanography
Poland

1. Introduction

"Solar radiation plays a fundamental role in the marine environment. It supplies the energy that drives thermodynamic and photochemical processes in the sea, including the heating of waters, their stratification and movement, and their evaporation, also the warming of the atmosphere, the photosynthesis of the organic matter essential for the maintenance of life and the functioning of marine ecosystems, and the photo-oxidation of marine pollutants" (Dera & Woźniak, 2010). The amount of solar energy reaching the sea surface can be determined by means of direct measurements or calculations with the use of various models of different precision and complexity. Due to obvious reasons, systematic, direct measurements in the area of oceans and seas with the spatial resolution satisfactory for monitoring and analysis of several processes like the ones mentioned above, are impossible in practice. On the other hand, credibility of modelling strongly depends on model's input data – their quality and time resolution. The most difficult task in calculating the solar energy stream at the sea surface using a model is to obtain its momentary value. It is caused by the lack of precise information on the components of the Earth's atmosphere influencing the solar radiation along its way from the upper boundary to the sea surface. The most important of these components is the cloudiness but other parameters like aerosol optical thickness, the content of water vapour or ozone should also be taken into account.

Fast development of satellite technique in the field of Earth observation and monitoring makes it possible to get more or less precise information about the atmosphere properties which play an important role in solar energy transfer to the Earth's surface in every place and further into the sea.

The idea of our consideration is to provide a broad overview of contemporary space-borne sources of data necessary to increase the accuracy of simple models of solar energy transfer through the Earth's atmosphere, especially over the oceans and seas.

2. Solar radiation

The Sun, a medium-sized star, produces energy as a result of thermo-nuclear processes in its interior. Recently it has been estimated to be about 3.9×10^{26} W. This power is radiated into

space uniformly in all directions. Fundamental physical laws tell us that the intensity of this radiation decreases as the inverse square of the distance from the source. At the mean distance from the Sun to the Earth this energy, in total, is known as solar "constant". Its spectral distribution is close to the radiation of a blackbody at the temperature about 6000 K but, due to different processes inside and on the surface of the Sun, this dependence is not as smooth as it results from Planck's law. It is the reason that the first step to obtain the spectrum of solar energy at the Earth's surface is to determine, by means of measurements, its value in the upper frontier of the atmosphere (TOA[1]). Along the path to the Earth's surface, the incoming solar radiation undergoes the wave dependent processes of absorption and scattering. As a result, a part of it is reflected back to space, another part is absorbed by the elements of the air and the rest reaches the surface. It consists of two components: the direct radiation from the Sun and the diffuse radiation from the atmosphere. Under cloudless conditions the relationship between them depends on the position of the Sun in the sky - the higher the Sun elevation angle the higher the difference between them. In Fig. 1 one can see an exemplary spectral distribution of the solar irradiance at the sea level calculated for real cloudless atmosphere over the Baltic Sea near the solar noon on 2011-06-21 at 11:00 UTC (the Sun elevation angle was about 59^{o}). The evident differences between the shapes of the extraterrestrial and other curves are due to the light absorption and scattering processes which depend on some components of the air. The most important of these processes are: molecular scattering, absorption by water vapour, ozone, and other atmospheric gases as well as attenuation (absorption and scattering) by atmospheric aerosols. The strength of these processes depends to a different degree on concentration and distribution in the atmosphere of the accounted components. The most spectacular consequences of strong deviations of some components' concentrations from their common state are known as the global warming (due to the increase in the greenhouse gases concentration - the water vapour is one of them) or the "ozone hole" - the effect of decreased ozone concentration in the so-called ozone layer. The importance of such phenomena for life on our planet causes the need of their continuous monitoring. It is done by the networks of ground-based measuring stations like for instance WMO-Global Atmospheric Watch observing system, Network for the Detection Atmospheric Composition Change, NOAA Earth System Research Laboratory/Global Monitoring Division etc. It is obvious, that such networks do not cover the whole Earth's surface and the shortage of information concerns in particular the atmosphere over the oceans and seas (Fig. 2). It is also true for the solar radiation monitoring . New opportunities in the area of global monitoring of the Earth's atmosphere and surface arose due to fast development of the space-based measurements. The satellite-based instruments provide regular views of any place of the Earth. Despite the fact that such measurements must still be supplemented by the ground-based measurements, it enables fast progress in broadening our knowledge in this area.

The traditional way of getting the information on the solar energy reaching the Earth's surface in the case of lack of direct measurements was to use more or less complicated models of light transmission in the atmosphere. To run the model it is necessary to gather the input data which characterize actual state of the atmospheric components important from this point of view, namely: the atmospheric pressure and humidity, aerosol optical

[1] Top of the atmosphere

thickness (*AOT*), content of ozone, and cloudiness. One can do it using routine measurements or values obtained by interpolation between them, results of calculations with the use of other (meteorological) models, climatological values, models of the Earth's atmosphere etc. The space-based measurements of *AOT*, content of ozone, and water vapour in the column of the atmosphere, and cloudiness used as the input data can rise the precision of such models to a significant degree. To check this thesis we shall compare the results of calculations of solar energy input at the Baltic Sea surface performed with a simple model for irradiance on the horizontal plane at the Earth's surface presented in part 3.

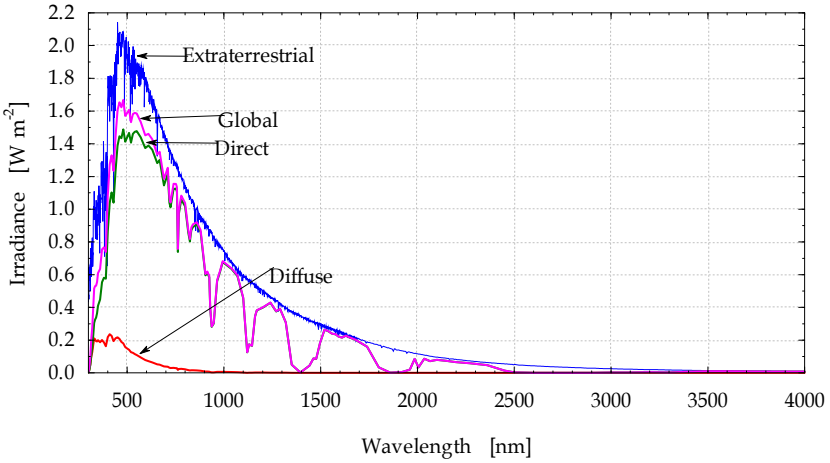

Fig. 1. Direct, diffuse, and total solar irradiance for a real cloudless atmosphere over the Baltic Sea (long. 18.82°E, lat. 54.60°N) on 2011-06-21 near solar noon (11:00 UTC)

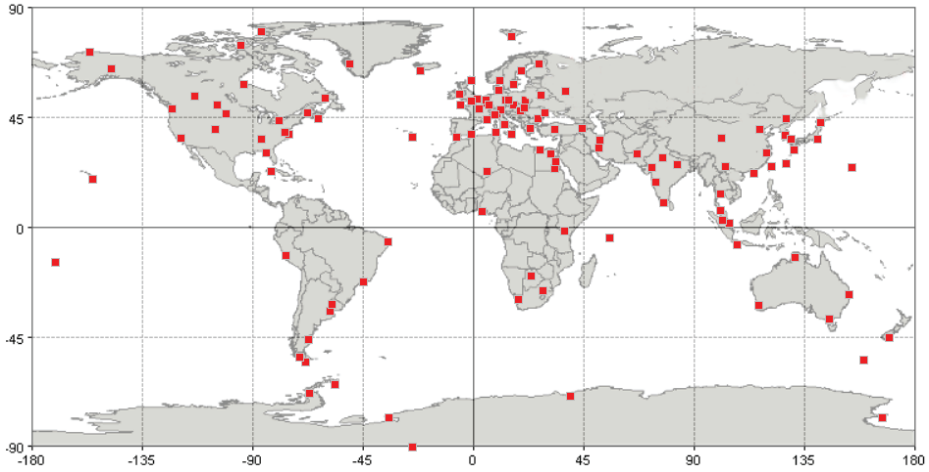

Fig. 2. The 132 WMO-GAW stations measuring total ozone with Dobson and/or Brewer spectrophotometers (GCOS-GAW ..., 2007)

3. Model

There are many ways of calculation of light transmission through the Earth's atmosphere from complicated models like developed in the 1970's LOWTRAN[2] or MODTRAN[3] to the simplest ones that take into account the dependence of the incoming radiation only on one variable (e.g. mean cloudiness). To compare the influence of different sources of the input data on the results of solar irradiance calculations at the sea level we have chosen a simple model proposed by Bird and Riordan (1986) with several later modifications (Krężel & Kozłowski, 2001; Krężel et al., 2008). The model enables one to calculate easily the contribution of the main constituents to the total attenuation of the solar radiation on its way from the upper frontier of the Earth's atmosphere to the sea surface.

3.1 Calculation algorithms of direct solar radiation

Considering the most important processes of interaction of the solar radiation passing to the sea surface with the atmosphere constituents, the direct irradiance of the horizontal area by the solar beam incidence (at the sea surface) could be expressed as:

$$E_s(\lambda) = \cos\vartheta \frac{F_s(\lambda)}{\beta^2} T_R(\lambda) \cdot T_a(\lambda) \cdot T_{wv}(\lambda) \cdot T_{O_3}(\lambda) \cdot T_G(\lambda) \tag{1}$$

where: λ – the wavelength; ϑ - the solar zenith angle, $F_s(\lambda)$ – the spectral density of the solar constant; $\beta = R_s/R$ - the factor defining the annual variability of the distance between the Earth and the Sun (R and R_s – actual and mean distance between the Earth and the Sun, respectively); $T_R(\lambda)...T_G(\lambda)$ – the functions of the atmosphere transmission describing irradiance attenuation in the processes of molecular scattering, scattering and absorption by aerosols and absorption by water vapour, ozone and the most important constant gaseous components of the atmosphere, respectively.

In the algorithms the presented $F_s(\lambda)$ values and the coefficients of absorption of water vapour $a_{wv}(\lambda)$, ozone $a_{O3}(\lambda)$ and constant gaseous components of the atmosphere $a_G(\lambda)$ for 122 wavelengths were accepted after Neckel and Labs (1981). The algorithms allowing to determine β value and the solar zenith angle at a given place and any time were taken from Michalsky (1988).

To calculate the succeeding transmission functions one should know the so-called relative optical atmospheric mass M. At the sea level the expression of Kasten & Young (1989) considering curvature of the atmosphere was applied:

$$M = [\sin\gamma_s + 0.50572 \cdot (\frac{180\gamma_s}{\pi} - 6.07995)^{-1.6364}]^{-1} \tag{2}$$

where: the solar altitude $\gamma_s = \frac{\pi}{2} - \vartheta$ is expressed in radians

[2] Low-resolution propagation model and computer code for predicting atmospheric transmittance and background radiance from 350 to 40,000 cm^{-1} at a resolution of 20 cm^{-1}

[3] MODerate resolution atmospheric TRANsmission – computer program designed to model atmospheric propagation of electromagnetic radiation from 100 to 50,000 cm^{-1} spectral range at a resolution of 0.2 cm^{-1}.

In the calculations of the atmospheric transmission functions (1) the following algorithms were used:

a. molecular scattering (Kneizys et al., 1980):

$$T_r(\lambda) = \exp\left[\frac{-M'}{\lambda^4 \cdot (115.6406 - \frac{1.335}{\lambda^2})}\right] \tag{3}$$

where: $M'=M\cdot(P/P_0)$, P - the atmospheric pressure [hPa], P_0=1013 hPa; the wavelength λ is expressed in [μm].

b. aerosol attenuation:

The influence of aerosols on the light transmission is taken into consideration by determination of so-called aerosol optical thickness of the atmosphere (AOT):

$$AOT(\lambda) \equiv \tau_a(\lambda) = -M \ln T_a(\lambda) \tag{4}$$

where T_a – the light transmission through the cloudless atmosphere resulting from the presence of aerosols. For determination of AOT the classical formula of Angström (1963) was used:

$$AOT(\lambda) = \beta_n \lambda^{-b_n} \tag{5}$$

For the Baltic Sea area the values of b_n and β_n coefficients, typical for the regions of relatively low atmosphere dustiness, were applied, i.e. β_n=0.12 and b_n=1.0274 for λ<0.5 μm and 1.2060 for λ>0.5 μm.

c. absorption by ozone is calculated from the formula:

$$T_0(\lambda) = \exp[-a_0(\lambda) \cdot O_3 \cdot M_0] \tag{6}$$

where the relative optical mass of the atmospheric ozone M_0 was defined after Iqbal (1983):

$$M_0 = \frac{(1 + \frac{h_0}{6370})}{(\cos^2\vartheta + \frac{2 \cdot h_0}{6370})^{0.5}} \tag{7}$$

and h_0 = 22 km was accepted as the mean height of the maximum ozone concentration. The mean nine-year (1997-2005) O_3 values, defining the ozone concentration in an atmospheric air column of a unit base area, for latitudes 50°- 60°N in individual months are shown in Table 1.

Month	Jan	Feb	Mar	Apr	May	Jun	Jul	Aug	Sep	Oct	Nov	Dec
O_3 [cm]	0.37	0.39	0.40	0.39	0.38	0.36	0.33	0.32	0.31	0.30	0.32	0.35

Table 1. Mean ozone concentration in the atmosphere in latitudes 50°- 60°N (TOMS, 2007)

d. absorption by water vapour; the expression presented by Leckner (1978) was used:

$$T_w(\lambda) = \exp\left[\frac{-0.2385 \cdot a_w(\lambda) \cdot W \cdot M}{[1+20.07 \cdot a_w(\lambda) \cdot W \cdot M]^{0.45}}\right] \tag{8}$$

where W is the water vapour mass in an atmospheric air column of unit base area and is calculated from the data on the water vapour pressure e_0 at the sea level, according to the relation (Reitan, 1960):

$$W = (0.123+0.152 \cdot e_0)\frac{P}{1000} \tag{9}$$

where: e_0 and P are expressed in [hPa].

e. absorption by the other significant components of the atmosphere; the expression from the paper by Leckner (1978) was applied:

$$T_u(\lambda) = \exp\left[\frac{-1.41 \cdot a_u(\lambda) \cdot M'}{[1+118.3 \cdot a_u(\lambda) \cdot M']^{0.45}}\right] \tag{10}$$

In the model for determination of illumination at the sea level by direct solar radiation, the algorithms (1) to (10) were used. The source of the highest errors is undoubtedly the way of determination of solar radiation attenuation by aerosols. This error is the greatest when the instantaneous illumination values are calculated and it decreases with the extension of averaging period.

3.2 Calculation algorithms of scattered radiation

Algorithms presented in the paper of Bird and Riordan (1986) were used in the model construction.

It should be assumed that scattered radiation incident on the horizontal area is the total of three components:

$$E_d(\lambda) = E_{dR}(\lambda) + E_{da}(\lambda) + E_{dg}(\lambda) \tag{11}$$

- resulting from molecular scattering $E_{dR}(\lambda)$,
- resulting from aerosol attenuation $E_{da}(\lambda)$ and
- resulting from multiple reflection between the sea (land) surface and the atmosphere $E_{dg}(\lambda)$.

These components have the following forms:

$$E_{dR}(\lambda) = F_s(\lambda) \cdot \beta^{-2} \cdot \cos\vartheta \cdot T_{O_3}(\lambda) \cdot T_G(\lambda) \cdot T_{wv}(\lambda) \cdot T_{aa}(\lambda)[1 - T_R(\lambda)^{0.95}] \cdot 0.5 \tag{12}$$

$$E_{da}(\lambda) = F_s(\lambda) \cdot \beta^{-2} \cdot \cos\vartheta \cdot T_{O_3}(\lambda) \cdot T_G(\lambda) \cdot T_{wv}(\lambda) \cdot T_{aa}(\lambda) T_R(\lambda)^{1.5} \cdot [1 - T_{as}(\lambda)] \cdot F \tag{13}$$

$$E_{dg}(\lambda) = \frac{[F_s(\lambda)\cos\vartheta + E_{dR} + E_{da}(\lambda)] r_s(\lambda) r_g(\lambda)}{1 - r_s(\lambda) r_g(\lambda)} \tag{14}$$

$T_{aa}(\lambda)$ and $T_{as}(\lambda)$ are transmission functions determined by aerosol absorption and scattering, respectively:

$$T_{as}(\lambda) = \exp[-\omega_0(\lambda) \cdot \tau_a(\lambda) \cdot M] \tag{15}$$

$$T_{aa}(\lambda) = \exp\{-[1-\omega_0(\lambda)] \cdot \tau_a(\lambda) \cdot M\} \tag{16}$$

where: $\omega_0(\lambda)$ is the so-called single scattering albedo (from definition $\omega_0 = \frac{b}{a+b}$; b and a are the volume coefficients of scattering and absorption, respectively), $\tau_a(\lambda)$ - the optical thickness of the atmosphere resulting from aerosol occurrence. For its determination formulas (4) and (5) were used.

It is assumed here that molecular scattering and scattering by aerosols are independent and also, that half of the irradiance is directed towards the lower hemisphere in the process of Rayleigh`s scattering, regardless of actual direction of incident solar radiation.

The dependence of single scattering albedo on the wavelength is defined by the relation:

$$\omega_0(\lambda) = \omega_0(0.4\,\mu m) \cdot \exp[-\omega'(\ln\frac{\lambda}{0.4})^2] \tag{17}$$

where: $\omega_0(0.4\ \mu m)$ - the single scattering albedo for the wavelength of 0.4 μm, ω' - the wavelength variation factor.

In the regions of relatively low atmospheric turbidity $\omega_0(0.4)=0.945$ and $\omega'=0.095$, $r_g(\lambda)$ represents surface albedo and is one of the input data necessary for calculations whereas atmosphere albedo could be expressed as:

$$r_s(\lambda) = T'_{O3}(\lambda)T'_{wv}(\lambda)T'_{aa}(\lambda)\left\{ 0.5\ \left[1 - T'_r(\lambda)\right] + \left(1 - F'\right)T'_r(\lambda)\left[1 - T'_{as}(\lambda)\right] \right\} \tag{18}$$

In the relation (13) F denotes the contribution of radiation scattered towards the lower hemisphere, which in the case of molecular scattering could be accepted as 0.5 and for aerosol attenuation depends on the solar zenith angle:

$$F = 1\text{-}0.5 \cdot \exp[(AFS + BFS \cdot \cos\vartheta) \cdot \cos\vartheta] \tag{19}$$

$$AFS = ALG \cdot [1.459 + ALG \cdot (0.1595 + ALG \cdot 0.4129)] \tag{20}$$

$$BFS = ALG \cdot [0.0783 + ALG \cdot (-0.3824 - ALG \cdot 0.5874)] \tag{21}$$

$$ALG = \ln(1 - \langle \cos\theta \rangle) \tag{22}$$

Asymmetry factor $\langle\cos\theta\rangle$ was accepted for so called rural atmosphere model (0.65). In relation (18) the parameters with apostrophe were calculated applying M=1.8, and in the formula defining F - $\cos\vartheta = \frac{1}{1.8}$. Finally, the obtained expression for $E_d(\lambda)$ is multiplied by C coefficient:

$$C = \begin{cases} (\lambda + 0.55)^{0.8} & \text{for } \lambda \le 0.45\ \mu\text{m} \\ 1.0 & \text{for } \lambda > 0.45\ \mu\text{m} \end{cases} \tag{23}$$

Reassuming, the determination of the illumination or radiation dose at the sea level by means of the presented algorithms requires the knowledge only on two parameters of atmospheric conditions, the atmospheric pressure and the water vapour pressure, routinely registered at the sea level at meteorological stations. Albedo of the sea area was accepted as constant and equal to 0.06.

3.3 Cloudiness

Traditionally, clouds have been observed visually by trained technicians at weather stations and onboard ships around the world (often in units of eighths, or oktas), following the general rules outlined by the World Meteorological Organization (WMO, 1975). Before "the satellite epoch" the influence of cloudiness on the solar irradiation at the Earth's surface has been taken into account by using these visual observations of the cloud cover as input data in the simple models. The longer the averaging time was the better coherence of measured and calculated results was obtained. Apart from the subjectivity of such observations, their number as well as time and spatial resolution over the seas and oceans, make these results unreliable. Accounting for high temporal variability of cloudiness, meteorological models as a source of the input data are also a source of serious errors (Krężel & Kozłowski, 2001). Nevertheless, if the cloudiness over the area of interest is known the average energy flux at the horizontal plane can be expressed as:

$$E = E_0 T_{Cl} \tag{24}$$

where: E_0 - irradiance reaching the sea surface in the case of cloudless atmosphere; T_{Cl} - a function describing the influence of an average cloudiness on the light transmission, given by Krężel (1985):

$$T_{Cl} = 1 - a_{Cl} c - b_{Cl} c^2 \tag{25}$$

where: c - cloudiness in tenth, a_{Cl} i b_{Cl} – best-fit coefficients.

Assuming the independence of T_{Cl} on the wavelength the formulas (24) and (25) complement the model with this very important component and make it applicable for the atmosphere.

4. Satellite sources of input data

4.1 Aerosol optical thickness

In the next approximation, it is assumed to utilise the Advanced Very High Resolution Radiometer (AVHRR) data. The upward radiance over the dark sea surface within red and infrared bands depends primarily on the type and concentration of aerosols in the atmosphere. The amount of solar radiation backscattered by aerosols is proportional to the aerosol optical thickness τ_a and the phase function $P^A(\gamma)$. Light attenuation by marine aerosols arises mainly from the scattering processes (i.e. the single scattering albedo $\omega' = 1$). Therefore, the

dependence between the radiance measured by the space-borne radiometer and τ_a should also allow for the light source-observation direction geometric configuration. This means that $P^A(\gamma)$ has to be known in order to determine the value of τ_a (Stowe et al., 1997).

Results of hitherto investigations indicated that the variability of $P^A(\gamma)$ in the case of backscattering is considerably lower than the τ_a variability, and even, to a certain extent, does not depend on the type of aerosols (Stowe et al., 1997). Koepke & Quenzel (1979) showed that the variability of $P^A(\gamma)$ is contained within the range of about ±25% (and can be lowered down to ±4% in the case of optimal geometric configuration), whereas τ_a can range even over an order of magnitude. The feasibility of τ_a determination based on a single spectral channel data on reflectance was proved by Kaufman (1993) who stated the universality in the dependence between τ_a and the path radiance.

Standard algorithms used to determine the aerosol optical thickness on the basis of data from a single spectral channel (1 or 2) of the AVHRR, which were developed for NOAA/NESDIS[4] (first-generation algorithm), allow for the geometric configuration of the system. Moreover, the correction referring to the actual distance between the Earth and the Sun is considered, and the values are rescaled according to the wavelength of 0.5 μm (rescale coefficient is 1.348). Additional parameters used as the input data are i) the ocean albedo (Lambert's reflection coefficient), ii) volumetric absorption and scattering coefficients and iii) the phase function $P^A(\gamma)$ which is determined on the basis of the Mie theory and redefined for the model of aerosol particles.

The values of AOT(500 nm) calculated by means of the above-mentioned algorithm are rendered accessible in a quasi-operational mode by NOAA/NESDIS. Utilisation of AVHRR data in AOT determination enables gaining information on the values of this parameter within a spectral interval of 100 nm with the central value at 630 nm. The algorithm enabling one to determine the AOT variability within the whole visible spectrum was developed basing on the analysis of measurement data recorded mainly on Gotland, within the framework of AERONET[5] program. Functional dependencies enabling determination of AOT for optional wavelength within PAR band were obtained (Krężel et al., 2008):

$$AOT(\lambda) = AOT(500)a\exp b(\lambda) \tag{26}$$

where: AOT(500) – the aerosol optical thickness at 500 nm determined on the basis of AVHRR data by means of the first-generation algorithm, a – empirical coefficient equal to 1.63, λ – the wavelength [nm], $b(\lambda)$ – coefficient related to the wavelength λ, which can be described by the following formula:

$$b(\lambda) = 4.588\exp(-2.981\lambda/1000) \tag{27}$$

Dependencies (26) - (27) make it possible to obtain digital images of $\tau_a(\lambda)$, which are presented in Fig. 3.

[4] National Oceanic and Atmospheric Administration /National Environmental Satellite, Data, and Information Service

[5] Aerosol Robotic Network - http://aeronet.gsfc.nasa.gov/

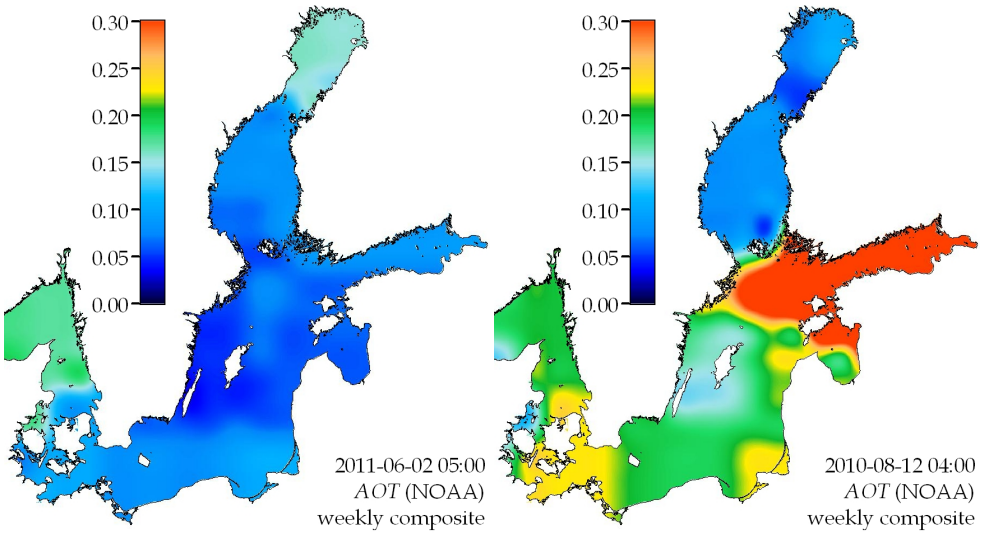

Fig. 3. Exemplary maps of aerosol optical thickness over the Baltic Sea calculated on the basis of interpolated AVHRR channel 1 data

4.2 Water vapour

The water vapour is present in the troposphere – the lower part of the atmosphere. Its content varies significantly with space and time, being dependent on the air temperature. At the sea level, concentration of water vapour can change from 10^{-2} gm^{-3} at high latitudes up to 30 gm^{-3} in the equatorial regions. It is one of the most important atmosphere constituents that attenuates radiation. The strongest absorption occurs far out in the infrared part of the solar spectrum, making atmosphere almost opaque for the wavelengths in the range of about 30-900 μm. Weaker water vapour absorption bands affect transmittance windows that are useful for remote sensing in the near infrared (NIR), thermal-infrared (IR) and microwave (MW). It provides a way to retrieve water vapour content on the basis of satellite measurements of reflected solar NIR radiation or emitted by the Earth's surface IR and MW radiation.

The humidity of the atmosphere can be expressed in different ways, e.g. absolute humidity, specific humidity, dew point temperature or integrated precipitable water vapour (IPWV). In the satellite techniques the latter one, also called the integrated column water vapour or total atmospheric water vapour (denoted W), is used. It expresses the height of the layer of liquid water, obtained by condensing all the water vapour in the zenith direction at the surface of a unit area. A layer of 1 cm thickness corresponds to 1 g of precipitable water per 1 cm^2 of the area.

In the NIR part of the spectrum, the absorption peaks of the water vapour are located mainly around 720, 820 and 940 nm. The differential absorption technique utilizing this region of spectrum assumes, in general, that the integrated water vapour content is related to the transmission in a spectral channel affected by the water vapour absorption and that the transmission can be estimated using the radiance ratio of two bands - absorption and

non-absorption ones. It comes from the simplification of the Lambert's law (Gao & Goetz, 1990; Bouffiès et al., 1997; Tahl & von Schoenermark, 1998). As the assumptions undergoing the theory cannot be true in reality, nonlinear relationships are used in practice. The disadvantage of this method is limitation to daytime measurements and its high sensitivity to aerosols and thin clouds – their occurrence can lead both to overestimation (photon path enlarged due to multiple scattering) or underestimation (photon path reduced due to backscattering) of the atmospheric humidity content.

In the recent years, studies in retrieving total atmospheric water vapour content based on the absorption technique has been carried out using sensors such as the Medium Resolution Imaging Spectrometer (MERIS) working onboard the European Envisat satellite (Fischer & Bennartz, 1997) and Moderate Resolution Imaging Spectrometer (MODIS) onboard two U.S. American platforms, Terra and Aqua (Gao & Kaufman, 2003; Albert et al., 2005; Moradizadeh et al., 2008). The general form of the water vapour retrieval algorithm for MERIS level 2 products is (ESA, 2006):

$$W = k_0 + k_1 \log\left(\frac{L_{Ch15}}{L_{Ch14}}\right) + k_2 \log^2\left(\frac{L_{Ch15}}{L_{Ch14}}\right)^2 \tag{28}$$

where L_{Ch14} and L_{Ch15} are the radiances measured in MERIS channels 14 and 15 respectively, and k_0, k_1 and k_2 are the regression coefficients, dependent on few factors, with the geometry of observation among them. The absorption band 15 is centred at 900 nm and the reference non-absorption band 14 at 885 nm. Above land surfaces, top of the atmosphere (TOA) radiances are corrected for the spectral slope of the surface albedo prior to applying the algorithm. Above water surfaces, the algorithm additionally takes into account the aerosol optical thickness, except for regions where the Sun glint is significant. Correction is made using *AOT* at 900 nm estimation based on the radiances measured at MERIS bands 12 (775 nm) and 13 (865 nm). The advantage of the second instrument, MODIS, is that it has two more channels in the infrared spectral region, where the water vapour absorption occurs. Thus, the water vapour content is calculated as the weighted mean of three independent estimations (NASA MOD05 algorithm) performed according to (Gao & Kaufman, 1998, 2003):

$$W_i = a_0 + a_1\left(\frac{L_{Chi}}{L_{Ch2}}\right) + a_2\left(\frac{L_{Chi}}{L_{Ch2}}\right)^2 \tag{29}$$

where L_{Chi} are the radiances measured in MODIS water vapour absorption channels 17, 18 or 19, centred around 905, 936 and 940 nm respectively. Non-absorption reference band 2 has its centre at 865 nm. It have to be mentioned that these three bands have different water vapour sensitivity (Sobrino & El Kharraz, 2003), so weighting factors for averaging are calculated based on the range of possible water vapour content and the transmissivities in band *i*.

Global data of both sensors are available with the nadir resolution of 1 km. MERIS full resolution of 300 m can be used locally for more detailed water vapour estimation (Fig. 4). Near polar orbits and wide swath of these systems enable to observe each point at the Earth's surface at least once every two days. Higher temporal resolution can be provided

using sensors measuring emitted infrared radiation, such as AVHRR or the Spinning Enhanced Visible and Infrared Imager (SEVIRI). The AVHRR, which is carried by the American TIROS-N/NOAA series of satellites since 1979, provides long time series of data with about 1 km spatial resolution. NOAA satellites, working in pairs, can give information on the same point of the surface at least 4 times per day. SEVIRI, operating on board of meteorological geostationary satellites provides data with coarser spatial resolution depending on distance from the sub satellite point (about 3.3 km at the central Baltic Sea) but with very high temporal resolution – up to 15 min from the recently working Meteosat Second Generation satellite (MSG).

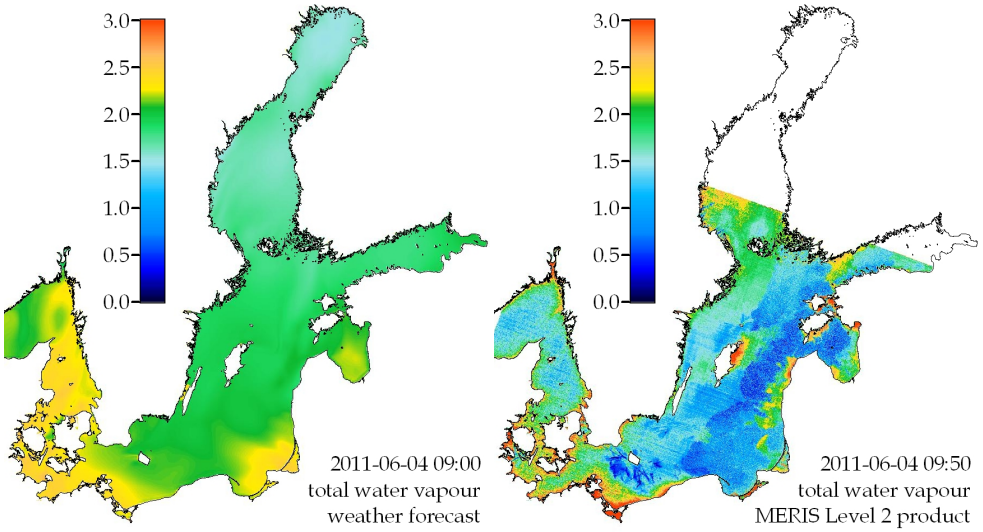

Fig. 4. Exemplary maps of total atmospheric water vapour over the Baltic Sea region calculated on the basis of a weather prediction model (left) and a standard MERIS Level 2 product under clear sky conditions (right) for the same day

Both instruments have two spectral bands in the range of 8.5-12.5 μm atmospheric window, which is affected by the water vapour absorption. These are AVHRR's band 4 (10.3-11.3 μm) and 5 (11.5-12.5 μm) or SEVIRI's band 9 (9.8-11.8 μm) and 10 (11.0-13.0 μm). Using measurements of radiation at two wavelengths in retrieving the surface brightness temperature makes it possible to limit the influence of the atmosphere brightness temperature on the calculated values of the water vapour content. This is a so-called split-window technique, that can be used directly to obtain the surface brightness temperature and, if an independent estimate of the mean brightness temperature of the atmosphere is available, also the column-integrated water vapour.

In practice the split-window technique is rarely used directly to obtain water vapour from sensors measuring emitted infrared radiation. Several simplified methods utilising regression have been proposed instead of it. To retrieve humidity content from the AVHRR and SEVIRI thermal channels a method based on the linear atmosphere–surface temperature relationship (LASTR) can be used (Sobrino et al., 2002; Sobrino & Romaguera, 2008). It

considers a simple linear relationship between W and the atmospheric transmittance (τ) in channel 4 of AVHRR or 9 of SEVIRI. Best fit regression coefficients for each instrument was derived based on simulations of atmospheric models. In the case of SEVIRI they are a function of the viewing geometry by means of the cosine of satellite zenith angle. The transmittance through the atmosphere from the surface to the satellite in channel i, for a cloud-free situation, and considering the emissivity as being equal to one for a blackbody, can be obtained from the radiative transfer equation as:

$$\tau_i = \frac{T_i - T_{ai}}{SST - T_{ai}} \tag{30}$$

where T_i is the brightness temperature retrieved from the radiance measured in channel i, T_{ai} is the effective atmospheric temperature (resulting from the whole column of the atmosphere) and SST is the sea surface temperature. SST can be derived from the same data using the split-window algorithm. Its nonlinear form NLSST is recommended (Walton et al., 1998). The effective atmospheric temperature is strongly correlated with SST values thus can be obtained with sufficient accuracy using linear regression.

The new SEVIRI instrument has two more water vapour channels at 6.2 and 7.3 μm, that improves possibilities of water vapour retrieval. However, IR radiometry has the same limitation as mentioned before – it allows to estimate the humidity content only under clear sky conditions. In the presence of clouds, only the microwave techniques can be used. Similar methods, accounting for measurements at two frequencies (22.235 and 31 GHz) has been developed. They can be used to retrieve precipitable water over the ocean (but not over the land) based on observations provided for example by the Special Sensor Microwave/Imager (SSM/I) and its successor (SSMIS) onboard a series of platforms in the US Defence Meteorological Satellite Programme (DMSP) or the Advanced Microwave Scanning Radiometer (AMSR-E) onboard NASA's Aqua satellite. The advantage of 'seeing through clouds', however, is reduced by coarse ground resolution, that cannot be finer than 25 km.

4.3 Ozone

The amount of the total stratospheric ozone has been regularly measured since the mid 1950s. It is usually expressed in Dobson units (DU). 100 DU correspond to the amount of ozone that would produce a layer of 1 mm of thickness at pressure of 1 atm. The highest concentrations of ozone in the stratosphere occur at about 25 km at the equator and 20 km in the northern polar regions. The average values are about 300 DU but they vary significantly in space and over the year.

Ozone has absorption lines in all major portions of the electromagnetic spectrum so it can be measured with a variety of techniques. The most important for the satellite measurements of integrated ozone are the ultraviolet Huggins bands (310-350 nm) and Chappuis bands in the visible part of the spectrum (380-750 nm), where absorption occurs due to dissociation of ozone. There is also an infrared ozone absorption band at 9.6 μm connected with changes in the vibrational state of the molecules.

Satellite remote sensing of the total ozone in both the stratosphere and troposphere is based mainly on measurements of the ultraviolet albedo of the Earth. Instruments which currently

measure these albedos are the Solar Backscatter Ultraviolet Spectrometer (SBUV/2) and the Global Ozone Monitoring Experiment (GOME-2) onboard NOAA and METOP 2 satellites. Previous GOME instrument operated from the ESA platforms as well. Both instruments are nadir-looking sensors, thus ozone maps are generated using interpolation and smoothing procedures.

Algorithms to retrieve the total ozone utilize the split-window technique using measurements of radiation in two closely spaced channels in the Hartley-Huggins bands. Channels 2 and 3 of GOME fulfil these requirements. They are characterised by limited interference from other trace gas absorbers and a smaller interference of Ring effect (partially filled Fraunhofer lines in the backscattered spectrum). SBUV/2 measures backscattered radiance at 12 discrete wavelengths in the range of spectrum between 252 and 340 nm, giving possibility to retrieve vertical profiles of the ozone concentration (Bhartia et al., 1996).

The infrared ozone absorption band is utilized by TIROS-N Operational Vertical Sounder (TOVS) processing the data recorded by High Resolution InfraRed Sounder (HIRS/2). The ozone retrieval regression algorithm uses channels 9 (9.71 μm), 8 (11.11 μm), and 3 (14.49 μm) (Engelen & Stephens, 1997). Channels 3 and 8 are incorporated in order to correct the ozone-sensitive channel 9 for the temperature dependence. Climatological data are used to incorporate the unobserved upper layer of the atmosphere (Neuendorffer, 1996). The 9.7 μm IR channel is also present in the SEVIRI. This channel measures ozone concentration at high temporal and spatial resolution, in near-real-time mode. The algorithm uses an optimal estimation approach to fit the calculated 9.7 channel radiances to the observed values by adjusting the ozone quantity in the 1000-30 hPa layer with constraining boundary conditions from the European Centre for Medium-Range Weather Forecasts (ECMWF) and the 10.8 μm channel observations (EUMETSAT, 2010).

Reanalised SBUV/2 and TOVS ozone products are provided in form of global ozone grids with spatial resolution of 1° and temporal resolution of 1 day by TOAST System[6]. GOME-2 products can be obtained from NESDIS with the same temporal resolution but at 1°×1.25° spatial grids. Our solar irradiance model does not utilize the satellite ozone data yet.

4.4 Cloudiness

It is out of discussion that pretty-nearly any space born information on cloudiness, especially over the seas and oceans, is better than that calculated even by advanced meteorological models (Fig. 5). Nevertheless, because of the complicated structure of clouds in the terrestrial atmosphere, variability in their consistency, diversification of water drops size and ice particles' shape etc. there is no easy way to presume the optical thickness of clouds basing on the analysis of the solar radiance reflected from their surface and recorded by a satellite-borne radiometer. For instance the problem of the cloudiness influence on the solar energy flux reaching the sea surface can be divided into two stages:

- it has to be determined whether the Sun was obstructed by clouds at a given point and time or not – wrong answer to this question leads to over- or underestimation of considered parameter value almost by an order of magnitude,

[6] Total Ozone Analysis using SBUV/2 and TOVS

- if the Sun is obstructed by clouds, it has to be determined which and to what degree the properties of clouds influence the value of considered parameter – correct solution to this problem improves the accuracy of estimation by several percent.

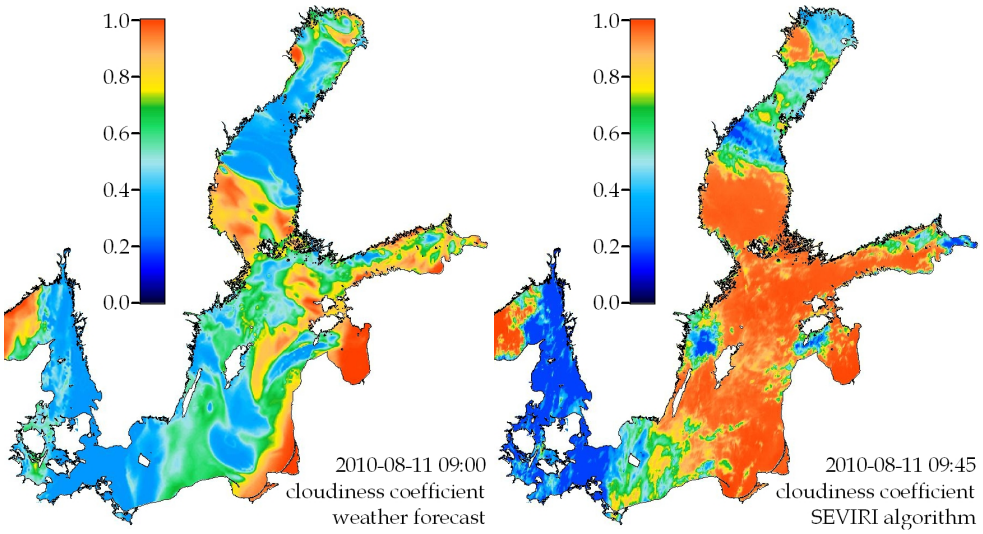

Fig. 5. Exemplary maps of the cloudiness coefficient over the Baltic Sea region calculated on the basis of a weather prediction model and SEVIRI observation for the same day

Previous studies (see e.g. Krężel, 1985) showed that if i) the differences arising from astronomical reasons are filtered, ii) the areas with direct reflection of the solar radiation are omitted and iii) the period of time or places where the sea is covered with ice are not taken into consideration, then the most important factors significantly affecting the radiance reaching a satellite-born sensor are the degree of the sky cloud cover over the area from which the signal recorded by a satellite is generated and the optical thickness of clouds obstructing the sun rays. The basic problem to solve in this case is to determine the threshold values, i.e. to determine the values of albedo under cloudless sky and total cloud cover conditions and to decide how to analyse the in-between cases. The difficulty arises from the fact that the threshold value is a function of many variables, i.e. the surface type (land, sea and their variability), its physical properties (e.g. temperature, humidity, concentration of some substances in the water etc.), current weather conditions (e.g. wind, fog) and the Sun–pixel–satellite geometric configuration. It means that in the case of the water surface the problem is a little bit lighter. Maybe the simplest method to solve it is to adopt formulas (24) and (25) by introducing another variable in the place of c. It has been suggested (Krężel et al., 2008) to introduce a cloudiness coefficient c_T, a function of albedo determined on the basis of the analysis of Meteosat visible channel data, into formula (25). Within the area of the sea, the albedo is the lowest where the sky is cloudless and the highest where a thick layer of clouds covers a whole pixel. In-between values depend mainly on the degree of cloud and/or fog cover of each pixel and, on a smaller scale, on the transmittance of clouds and fog. Theoretically, the value of albedo determined from a satellite contains resultant information, i.e. the value of albedo is almost the same in the case

of a pixel covered in 50% with a thick layer of opaque clouds and a pixel totally covered with clouds characterized by transmittance of 50%. In the former situation the cloudiness c = 0.5 and the cloudiness coefficient c_T = 0.5, whereas in the later case c = 1 and c_T = 0.5.

Replacing c in formulas (24) and (25) with c_T should result in significant improvement of obtained results. Nevertheless, the differences between calculated and measured instantaneous irradiance (especially in the case of extreme values) can be still expected, because the coefficient c_T does not contain information on such phenomena as light reflection from side edges of the clouds of cumulus type, or the thickness of the cloud layer, because when the thickness exceeds a certain value its further increase does not affect the satellite-measured albedo. The decrease in averaging period will result in higher differences between modelled and measured values. Of course, on account of introduction of a new variable, new values of regression coefficients in equation (25) should be determined.

5. Conclusion

We calculated the downwelling PAR irradiance over the Baltic Sea applying the model with the use of two sources of input data: no-satellite and satellite in order to evaluate the influence of application of the information on the atmosphere constituents obtained by means of remote sensing technique on the accuracy of the light transmission model retrievals. The sources of the non-satellite data on cloudiness and total atmospheric water vapour (retrieved from modelled dew point temperature) were numerical weather predictions provided by ICM[7] UM model (spatial resolution 4 km, four 48-h forecasts per day with temporal resolution of 1 h). In the case of the *AOT* the average climatological values were applied (Krężel, 1985). As the satellite sources, SEVIRI and AVHRR observations were used together with calculations described in previous sections to provide the cloudiness coefficient and *AOT*. Water vapour content was taken from the standard Level 2 products of MERIS (only for clear sky conditions). Ozone concentration was assumed as constant, averaged over the whole region (Table 1). The results of calculations were validated on the basis of the values of the downward irradiance recorded at the Institute of Oceanography's automatic measurement station in Hel in the period since August 2010 to May 2011. The comparison was made using a reference pixel whose central point was located about 7 km north-east of the station (Fig. 6).

The values of PAR irradiance modelled on the basis of non-satellite data appear to be in good agreement with measurements, which is confirmed by high correlation coefficient (Fig. 7). It proves the correctness of used formulae and the quality of model calibration. However, the cloud of points on the scatterplot, pointing both overestimation and underestimation of irradiance by modelled data, indicate that for individual cases the differences may be even more than 100%. The irradiance time series show it more clearly (Fig. 8). Deviations of modelled values from measured ones lay within the range of - 265 ÷ 210 Wm^{-2}. Using satellite data improves results of the modelling even in case of applying only the satellite evaluation of cloudiness (Fig. 7, Table 2). It reduces the statistical error by over 10 Wm^{-2}. It proves that the most important factor affecting the irradiance, the cloudiness coefficient,

[7] ICM - Interdisciplinary Centre for Mathematical and Computational Modelling, University of Warsaw, Poland (http://www.icm.edu.pl)

should be determined with better accuracy than that of a weather prediction model. High temporal resolution of SEVIRI observations enabled to reproduce diurnal fluctuations in the illumination under variable clouds condition with better accuracy (Fig. 8).

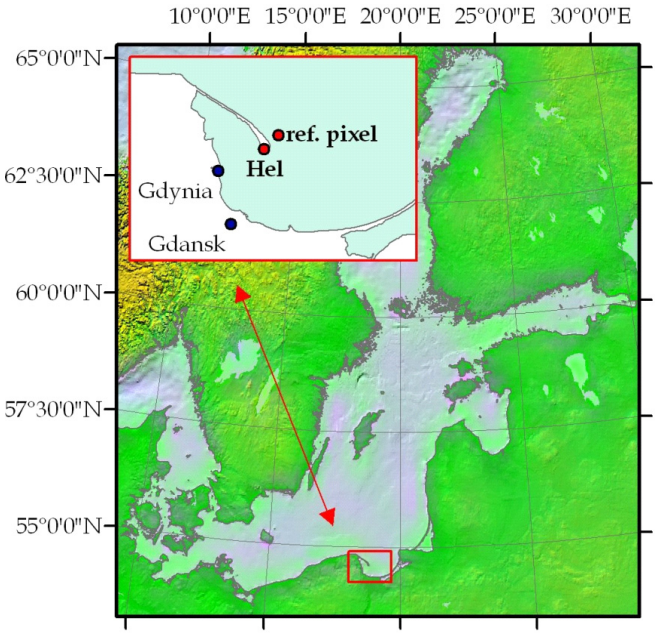

Fig. 6. Area of investigation

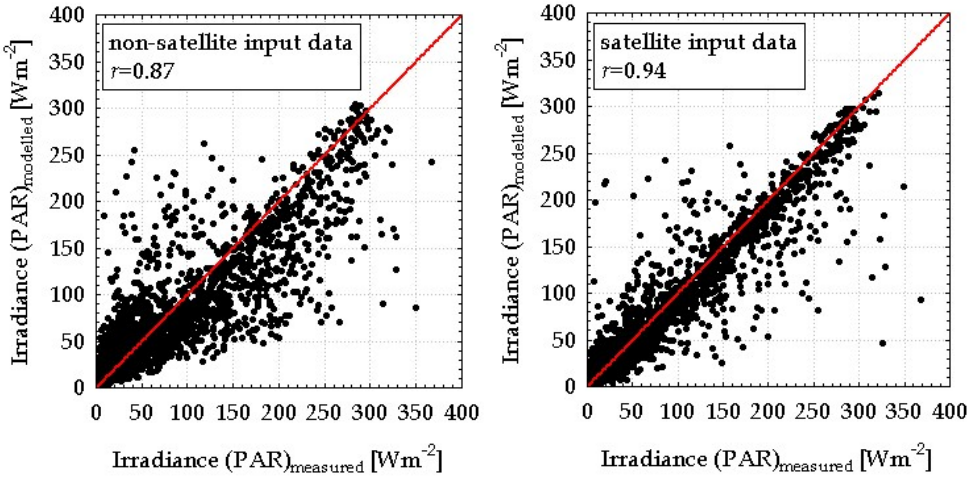

Fig. 7. Values of PAR irradiance at Hel - observed and modeled with two sets of input data for the period of 2010-08-26 to 2011-05-24 (r – linear correlation coefficient between modelled and measured data)

input data source			statistics				
c	*AOT*	*W*	*n*	*min*	*max*	*mean*	*st.dev.*
ns	ns	ns	2535	-264.8	211.0	-8.07	38.68
s	ns	ns	2535	-282.1	185.1	-10.00	26.94
s	s	ns	2535	-281.2	196.5	-4.79	26.89
s	s	s	2535	-281.2	196.9	-4.75	26.90

Table 2. Statistical characteristics of modeled PAR irradiance values deviation from measured ones [Wm^{-2}] (*n* – number of data, *st.dev.* – standard deviation) for different input data sets (satellite – s; non-satellite – ns) of cloudiness coefficient (*c*), aerosol optical thickness (*AOT*) and total atmospheric water vapour (*W*)

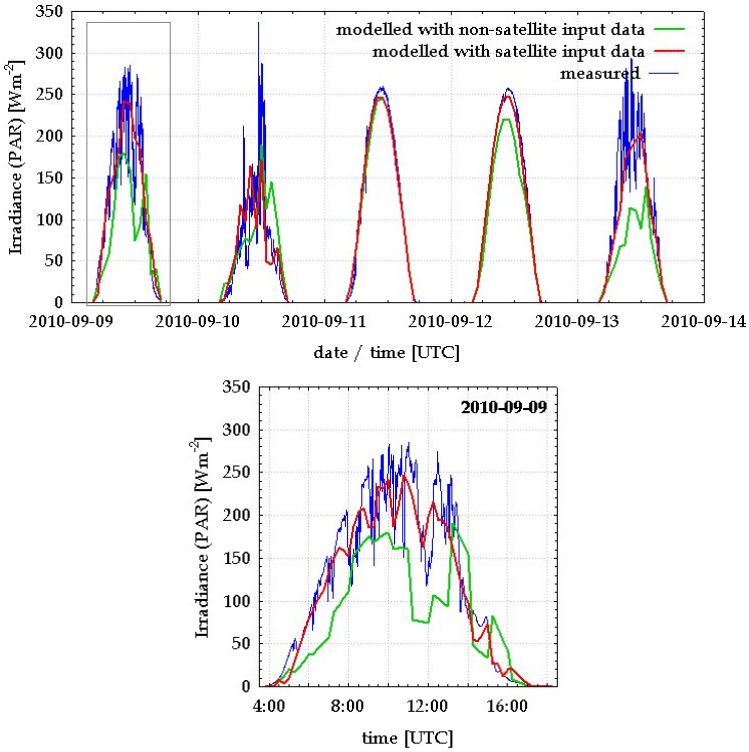

Fig. 8. Values of PAR irradiance at Hel - observed and modelled with two sets of input data for 5 day time series (temporal resolution of calculations 1h) and 1 day time series (temporal resolution of calculations 15 min.)

Accounting for the satellite *AOT* data instead of climatological values makes further decrease in errors reducing the systematic underestimation of modelled data (Table 2). The water vapour influences the whole PAR irradiance in a less degree. More realistic spatial distribution of evaluated PAR irradiance seems to be the most valuable improvement of

modelling provided by the satellite input data set. As it results from the presented examples (Fig. 9), applying the satellite data in the solar radiation transmission models significantly reduces the calculation errors. Consequently, it can influence the evaluation of other processes and phenomena occurring in the sea or estimations of the energy budget etc. Considering the fact that most of the satellite data are now available for operational use, their utilisation should become common.

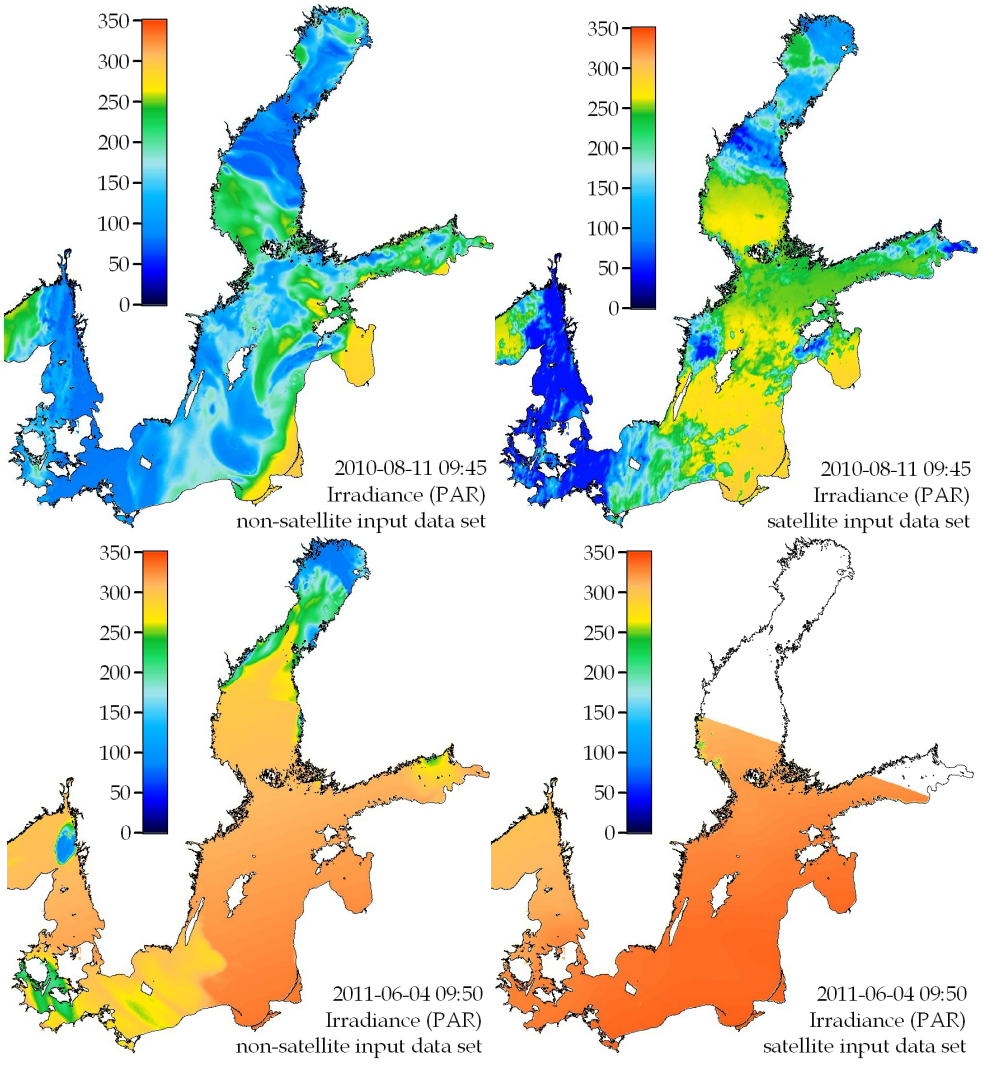

Fig. 9. Exemplary maps of PAR irradiance at the Baltic Sea surface modelled on the basis of two input data sets (non-satellite or satellite) under cloudy (2010-08-11) and clear–sky (2011-06-04) conditions

It is worth noticing that clouds are the most important atmosphere constituent which influences the accuracy of calculations of the solar energy flux at the sea surface. On the other hand, due to radiometers working onboard geostationary satellites, nowadays the cloudiness can be determined, in operational mode, with temporal resolution of 15 minutes. The scale of the temporal and spatial variability is shown in Fig. 10. Consequently, there is an opportunity to monitor the short-term variability in the sea surface layer resulting from the changes in the intensity of the solar radiation, e.g. water mixing, phytoplankton blooms, primary production rate.

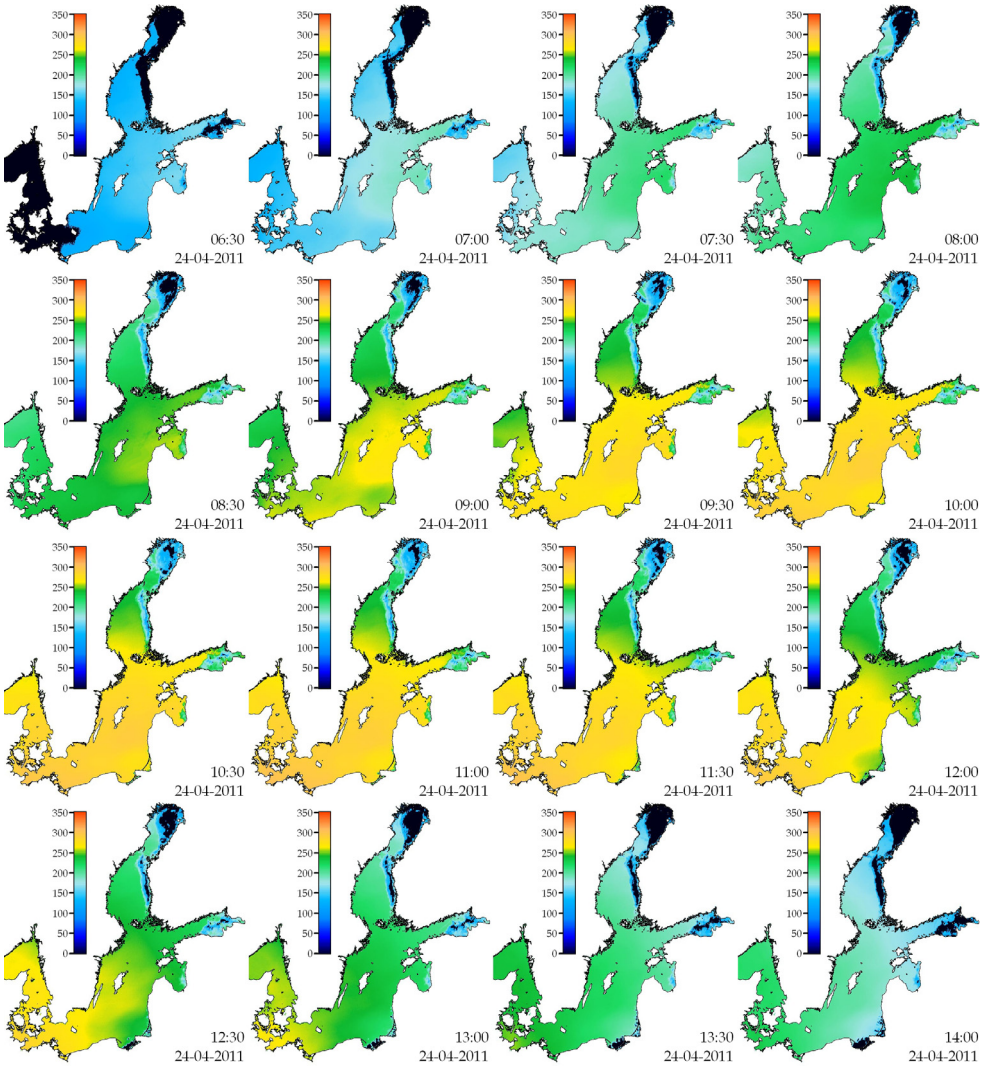

Fig. 10. Exemplary time series of PAR irradiance at the Baltic Sea surface modelled using the satellite (SEVIRI) data

6. References

Albert P., Bennartz R., Preusker R., Leinweber R., Fischer J. (2005). Remote Sensing of Atmospheric Water Vapor Using the Moderate Resolution Imaging Spectroradiometer, *Journal of Atmospheric and Oceanic Technology*, 22, 309-314.

Angström A. (1963). The parameters of atmospheric turbidity, *Tellus*, 16, 64-75.

Bhartia P.K., McPeters R.D., Mateer C.L., Flynn L.E., Wellemeyer C.G. 1996. Algorithm for the estimation of vertical profiles from the backscattered ultraviolet technique, *J. Geophys. Res.*, 101, 18793-18806.

Bird R.E., Riordan C. (1986). Simple solar spectral model for direct and diffuse irradiance on horizontal and tilted planes at the Earth's surface for cloudless atmospheres, *J. Clim. Appl. Meteor.*, 25, 1, 87-97.

Bouffiès S., Bréon F. M., Taneé D., Dubuisson P. (1997). Atmospheric water vapor estimate by a differential absorption technique with the Polarization and Directionality of the Earth Reflectances (POLDER) instrument, *J. Geophys. Res.*, 102 (D3), 3831–3841.

Dera J., Woźniak B. (2010). Solar radiation in the Baltic Sea, *Oceanologia*, 52(4), 533-582.

Engelen R.J., Stephens G.L. 1997. Infrared radiative transfer in the 9.6 μm band: Application to TIROS operational vertical sounder ozone retrieval, *J. Geophys. Res.*, 102, D6, 6929-6939.

EUMETSAT. (2010). Total Ozone - Factsheet, *EUM.OPS.DOC.09.5179*, http://www.eumetsat.int/idcplg?IdcService=GET_FILE&dDocName=PDF_TOZ_FACTSHEET&RevisionSelectionMethod=LatestReleased.

ESA. (2006). MERIS Product Handbook, 130 pp. http://envisat.esa.int/pub/ESA_DOC/ENVISAT/MERIS/meris.ProductHandbook.2_1.pdf.

Fischer J., Bennartz R. (1997). Retrieval of total water vapour content from MERIS measurements, *Algorithm Theoretical Basis Document ATBD 2.4, Doc. PO-TN-MEL-GS-0005*, 19 pp.

Gao B.-C., Goetz A. F. H. (1990). Column atmospheric water vapor and vegetation liquid water retrievals from airborne imaging spectrometer data, *J. Geophys. Res.*, 95, 3549–3564.

Gao B.-C., Kaufman J. (1998). The MODIS near-IR water vapour algorithm, *Algorithm Technical Background, Doc. ATBDMOD-03*, 25 pp.

Gao B.-C., Kaufman J. (2003). Water vapor retrievals using Moderate Resolution Imaging Spectroradiometer (MODIS) near infrared channels, *J. Geophys. Res.*, 108, 4389, doi:10.1029/2002JD003023.

GCOS-GAW Agreement Establishing the WMO/GAW Global Atmospheric Ozone Monitoring Networks as Global Baseline Networks of GCOS. (2007), *GCOS AOPC-XIII, Doc. no. 25, 18 April 2007, Revised version 29 August 2007*, 24 pp.

Iqbal M. (1983). An introduction to solar radiation, *Acad. Press*, 101.

Kaufman Y. (1993), Aerosol optical thickness and atmospheric path radiance, *J. Geophys. Res.*, 98, 2677-2692.

Kasten F., Young A. T. (1989). Revised optical air mass tables and approximation formula *Applied Optics* 28 (22), 4735-4738.

Kneizys F.X., Shettle E.P., Gallery W.O., Chetwynd J.H., Abreu L.W., Selby J.E.A., Fenn R.W., McClatchey R.A. (1980). Atmospheric transmittance/radiance: Computer Code LOWTRAN 5, *Tech. Rep. AFGL-TR-80-0067 USAF Geophysics Laboratory*, Hanscom AFB, MA.

Koepke P., Quenzel H. (1979). Turbidity of the atmosphere determined from satellite: Calculation of optimum viewing geometry, *J. Geophys. Res.*, 84, 7847-7856.

Krężel A. (1985). Solar radiation at the Baltic Sea surface, *Oceanologia*, 21, 5-32.

Krężel A, Kozłowski Ł. (2001). Verification of the model of a solar energy radiation input to the sea surface against actinometric data, *Oceanol.Stud.*, 30, 3-4, 17-38.

Krężel A., Kozłowski Ł., Paszkuta M. (2008). A simple model of light transmission through the atmosphere over the Baltic Sea utilising satellite data, *Oceanologia*, 50 (2), 125-146.

Leckner B. (1978). The spectral distribution of solar radiation at the earth's surface-elements of a model, *Sol. Energy*, 20, 143-150.

Michalsky J.J. (1988). The astronomical Almanac's algorithm for approximate solar position (1950–2050). *Solar Energy*, 40 (3), 227–235.

Moradizadeh M., Momeni M., Saradjian M.R. (2008). Estimation of atmospheric column and near surface water vapor content using the radiance values of MODIS, *The International Archives of the Photogrammetry, Remote Sensing and Spatial Information Sciences. Vol. XXXVII. Part B8. Beijing 2008*, 523-528.

Neckel H., Labs D. (1981). Improved data of solar spectral irradiance from 0.33 to 1.25 mm, *Solar Phys.*, 74, 231-249.

Neuendorffer A.C. (1996). Ozone monitoring with TIROS-N operational vertical sounders, *J. Geophys. Res.*, 101, D13, 18807-18828.

Reitan G.H. (1960). Mean monthly values of precipitable water over the United States, *Month. Weath. Rev.*, 88, 25-35.

Sobrino J.A., Jiménez J.C., Raissouni N., Sòria G. (2002). A simplified method for estimating the total water vapor content over sea surfaces using NOAA-AVHRR channels 4 and 5, *IEEE Transactions on Geoscience and Remote Sensing*, 40, 357–361.

Sobrino J.A., Kharraz J.El. (2003). Surface temperature and vapor retrieval from MODIS data, *Int. J. Remote Sensing*, 24, 24, 5161-5182.

Sobrino J. A., Romaguera M. (2008). Water-vapour retrieval from Meteosat 8/SEVIRI observations, *Int. J. Remote Sensing*, 29, 3, 741-754.

Stowe L.L., Ignatov A.M., Singh R.R. (1997). Development, validation, and potential enhancements to the second-generation operational aerosol product at the National Environmental Satellite, Data, and Information Service of the National Oceanic and Atmospheric Administration, *J. Geophys. Res.*, 102, D14, 16923-16934.

Tahl S., von Schoenermark M. (1998). Determination of the column water vapour of the atmosphere using backscattered solar radiation measured by the Modular Optoelectronical Scanner (MOS). *Int. J. Remote Sensing*, 19, 3223–3236.

TOMS. (2007). http://toms.gsfc.nasa.gov/ozone/ozoneother.html.

Walton C.C., Pichel W.G., Sapper J.F., May D.A. (1998). The development and operational application of nonlinear algorithms for the measurement of sea surface temperatures with the NOAA polar-orbiting environmental satellites, *J. Geophys. Res.*, 103, C12, 27999-28012, doi:10.1029/98JC02370.

WMO. (1975). Manual on the observation of clouds and other meteors. *WMO Publication* 407, 155 pp.

Part 3

Power Generation

11

Mems-Concept Using Micro Turbines for Satellite Power Supply

Daniel Schubert
DLR German Aerospace Center, Bremen, Germany

1. Introduction

Since the mid-nineties the power demand of GEO satellites has increased immensely (Nobbe, Tappert, 2004). This increased power demand is needed for applications like telecommunication, navigation and Earth observation. Conventional solar cells are producing the necessary electrical power through photovoltaic, whereas often large solar arrays are needed because of the relatively low cell efficiency and the temperature dependency of the Maximum Power Point (MPP). But solar cells are not the only possible concept to convert solar energy into electrical energy. The key concept of present paper is the use of a thermo-dynamic conversion principle, using the Organic Rankine Cycle (ORC).

Extensive research work has been conducted in the last fifty years related to ORC spacecraft applications. The new approach, which will be highlighted in this work, is the use of so called Power-MEMS (Power Micro Electro-Mechanical Systems) in order to convert solar into electrical energy. Here, a Micro-Turbine-Generator-Module (MTG-Module), consisting of a Cassegrain collector system, a vapor generator, a turbine-generator system and a condenser/ radiator, works by the use of the organic fluid Toluene. Final goal is the use of many MTG-Modules integrated on a spacecraft panel in order to supply a satellite with electrical power.

2. Background Power MEMS

Within the last five years many laboratories have put a lot of effort in research of different system concepts for Power-MEMS. Main focal point within this effort was set on the open Joule process, where a work gas (e.g. Butan, Methan or Hydrogen gas) is fired together with Oxygen in a micro combustion chamber. The hot combustion gases impel a micro turbine feeding a micro generator.

These Power-MEMS will be used as an alternative to batteries for laptops, camcorders or other power consuming mobile applications. The research group of Reynaerts (Department of Mechanical Engineering, University of Leuven, Belgium) (Peirs et al., 2003) has developed a Power-MEMS using a single-stage axial micro turbine with a rotor diameter of 10 mm (compare Figure 1). This turbine is a first step in the development of a micro generator. The expansion of the gas takes place in the stationary nozzles. The turbine is made of stainless steel using die-sinking electro-discharge machining (EDM).

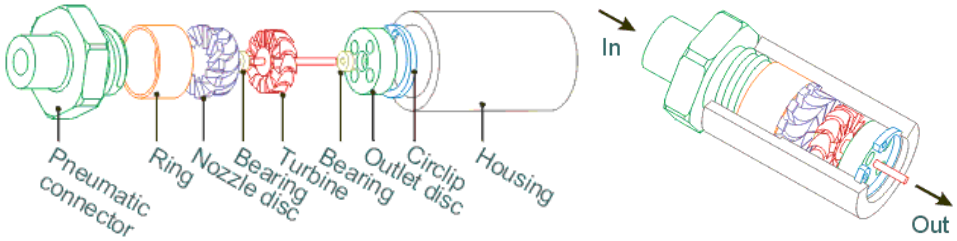

Fig. 1. Micro turbine design from Reynarts, University of Leuven, Belgium; (Peirs et al., 2003)

The Power-MEMS weighs 66 g, which is hold by a micro bearing system (compare Table 1). The turbine has been tested to speeds up to 160,000 rpm and generates a maximum mechanical power of 28 W with an efficiency of 18.4 %. When coupled to a small generator, it generates 16 W of electrical power, which has an efficiency for the total system of η=10.5 % (Peirs & Reynaerts, 2004).

Part	Mass (g)
Turbine	36
Pneumatic connector	15.8
Ring	0.77
Nozzle disc	1.78
Small bearing	0.03
Large bearing	0.07
Rotor	1.63
Outlet disc	0.35
Circlip	0.27
Housing	15
Generator	30
Total*	**66**

* including Turbine & Generator

Table 1. Masses of different parts of the Prof. Reynarts Power-MEMS turbine; (Peirs et al., 2003)

Another Power-MEMS is designed by the research group of Epstein at the MIT, USA (Jacobson et al., 2006). Here, the Power-MEMS is a 5-level wafer-bonded micro-machined turbine/bearing rig. The production process involves the use of 5 wafers, 16 masks, and 9 deep silicon etching steps, double-sided deep reactive ion etching (DRIE), and Laser-Assisted-Etching (LAE) (Lin et. al., 2006). Materials like ceramics such as silicon carbide (SiC) and silicon nitride (Si3N4) are used for this chip turbine engine. Figure 2 shows a cutaway of the engine as well as a Si-wafer of radial inflow turbine stages.

The micro engine also uses the open Joule process, where Hydrogen was chosen as a first fuel. Figure 3 shows a cross section of the H2 demo engine. The centrifugal compressor and radial turbine rotor diameters are 8 mm and 6 mm respectively (Epstein, 2004). The compressor discharge air wraps around the outside of the combustor to cool the combustor walls, capturing the waste heat and is so increasing the combustor efficiency while reducing the external package temperature.

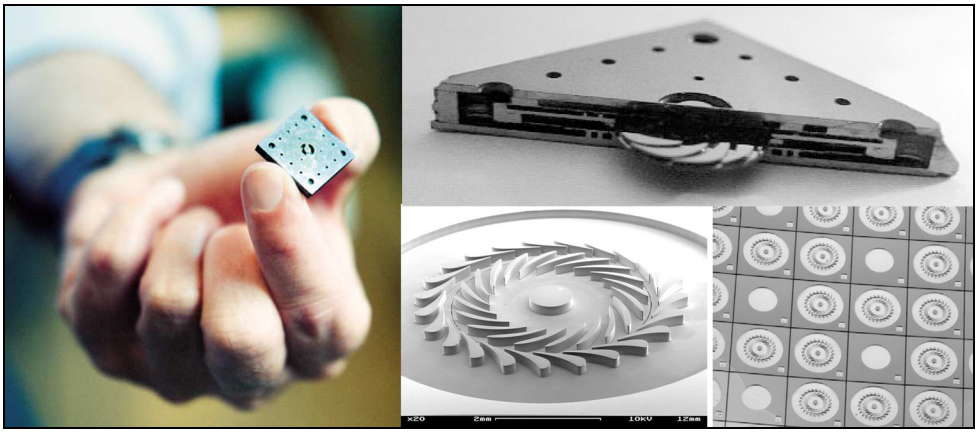

Fig. 2. Upper side: Cutaway H2 demo gas turbine chip; Lower left & right: A 4:1 pressure ratio, 4 mm rotor dia radial inflow turbine stage a swell as a Si wafer of radial inflow turbine stages; (Epstein, 2004)

Thrust bearings on the centreline and a thrust balance piston behind the compressor disk support the axial loads. The peripheral speed of the compressor is 500 m/s so that the rotation rate is 1.2 Mrpm. With 400 µm span airfoils, the unit is sized to pump about 0.36 g/sec of air, producing 0.1 Newton of thrust or 17 W of shaft power (Epstein, 2004).

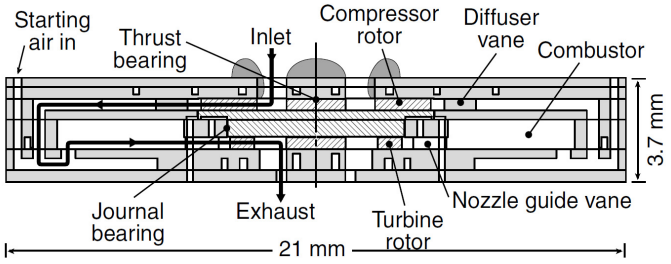

Fig. 3. H2 demo engine with conduction-cooled turbine constructed from six silicon wafers developed by the MIT research group of Prof. Epstein; (Epstein, 2004)

A Power-MEMS that is working with the closed Rankine cycle is under development at the Department of Mechanical Engineering - Columbia University, USA (Frechette, 2003a). Here, a system-level and component design study of a micro steam turbine power plant-on-a-chip was conducted. The Power-MEMS is similar build up as the H2 demo engine from Epstein, MIT (compare Figure 4). Possible application for this type of Power-MEMS is power generation from waste energy (e.g. PCU-cooling, illumination heat or car radiator heat). The work fluid for this Power-MEMS is water.

The micro fabricated device consists of a steam turbine that drives an integrated micro feed pump (3 mm thick by 1 cm², planar form). Two-phase flow heat exchangers are also integrated on-chip with the rotating components to form a complete micro heat engine unit,

which is converting heat to electricity. Expected power levels range from 1-12 W per chip with energy conversion efficiency in the range of 1-11% (compare Figure 5) (Frechette, 2003b). The figure presents the predicted performance for three different configurations:

- Top bars are for a high superheated temperature (800°C) and high pressure (8 MPa) by 50°C ambient temperature,
- mid bars represent lower temperature (400°C) and lower pressure (0.6 MPa), and
- lower bars are the same device, but with 25°C ambient temperature. This last configuration requires active cooling with a fan that is driven by a fraction of the micro Rankine device output.

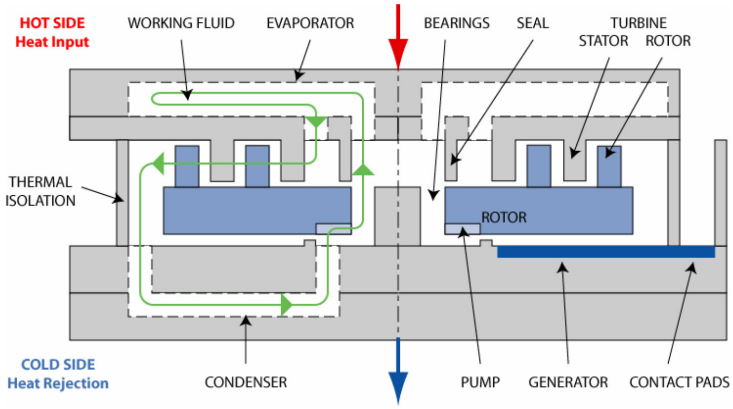

Fig. 4. Cross-section schematic of micro steam-turbine power plant-on-a-chip; (Frechette, 2003a)

Summarized, all shown Power-MEMS have an increasing Technology Readiness Level (TRL), although some concepts are still in its preliminary design phases. Nevertheless, an implementation for a spacecraft application seems conceivable.

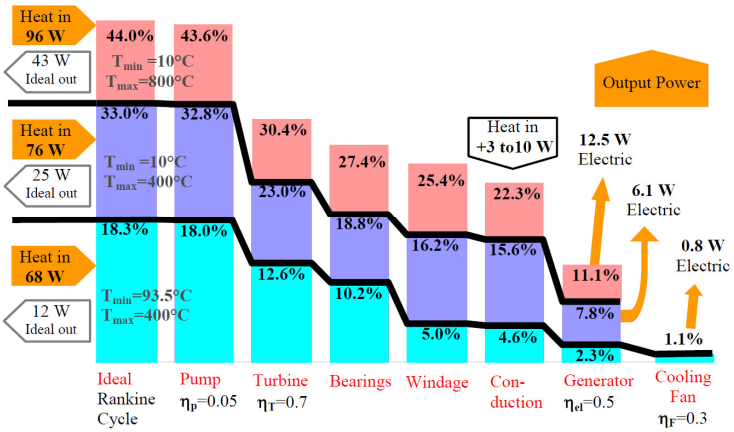

Fig. 5. Predicted performance of the micro steam turbine power Plant-on-a-chip for three configurations. (water 24 mg/s, Pmax=0.6 MPa); (Frechette, 2003b)

3. Requirements & assumptions

First step is the determination of the MTG's electrical power output. From here, the thermodynamic Rankine cycle can be calculated. The resulting thermodynamic values directly affect the geometric construction of the module. During this preliminary study several requirements and assumptions were made.

The key system requirements are:

- Electrical power output P > 10 Watt per MTG-Module
- Solar radiation concentrated by the use of a Cassegrain collector system
  Modular design shall be used for the MTG many modules on one solar panel
- Closed Rankine cycle principle used as conversion principle
- MTG concept shall offer high average temperature of condenser in order to keep radiator surface small
- System shall be robust
- Lifetime of system > 10 a

The key assumptions are:

- Only energy conversion system within the power subsystem is subject of evaluation here (no batteries or PCUs)
- Negligence of microgravity effects for Rankine cycle process
- Calculation of stationary mode only (no considerations concerning start or end working phases)
- Negligence of Albedo and IR-radiation due to GEO orbits
- Specific solar flux S=1350 W/m²
- Vertical incidence of sun's radiation towards collector system

4. Description of concept

As major work principle the Organic Rankine Cycle (ORC) was selected. The ORC works at lower temperatures than the normal Rankine cycle. Here, the working fluid is not water but an organic fluid with a lower evaporation temperature. To match the system requirements a fluid with a long stable life time and a low degradation factor had to be chosen. The decision was made for Toluene (C7H8), which has excellent characteristics for the MTG process (Prabhu, 2006). Toluene has the following characteristics:

- Molar mass: 92.14 g/mol
- Melting point -93°C (189 K)
- Boiling temperatue: 110.6 °C
- Boiling pressure: 1.01325 bar
- Critical temperature: 320.95
- Critical pressure: 42.365 bar
- Thermal conductivity: 0.134 W/mK
- Density: 0.87 g/cm³

Key principle for the Rankine cycle (organic or not organic) is the isobar evaporation of a liquid work fluid within a vapor generator. The hot vapor impels a turbine, which again

drives a generator for the electrical power generation. After the steam passes through the turbine, the condenser detracts the thermal heat so that the steam condensates and returns again into its liquid form. A feed pump transports the fluid towards the vapor generator and compresses the fluid to boiler temperature (compare Figure 6).

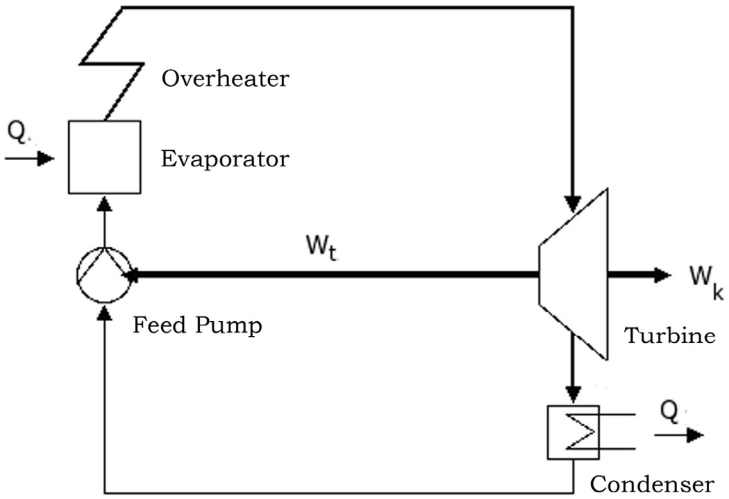

Fig. 6. Thermal dynamic flowchart of the closed Rankine cycle process.

The MTG Module concept is build up of five subsystems:

- Cassegrain mirror collector system
- Micro receiver system/ vapor generator
- Turbine-Generator system
- Condenser/ radiator system
- Micro feed pump

Figure 7 (left) depicts the schematic cross-section of a MTG-Module, where the collector system, the thermal engine section and the radiator system are assembled to a single module.

The Cassegrain mirror collector system has a parabolic primary mirror and a hyperbolic secondary mirror that reflects the light back down through a hole in the primary mirror (compare Figure 7, right). An advantage of this collector concept is the possibility to place the Power-MEMS behind the primary mirror. This way the radiator is always in the shadow of the primary mirror, which is important for a sufficient radiation.

The receiver system is an evaporator or heat exchanger that consists of single metal foils, which are connected by a diffusion bonding process to form a nearly monolithic body. The number of integrated micro channels is in the order of several hundreds to several thousands (comp. Figure 8).

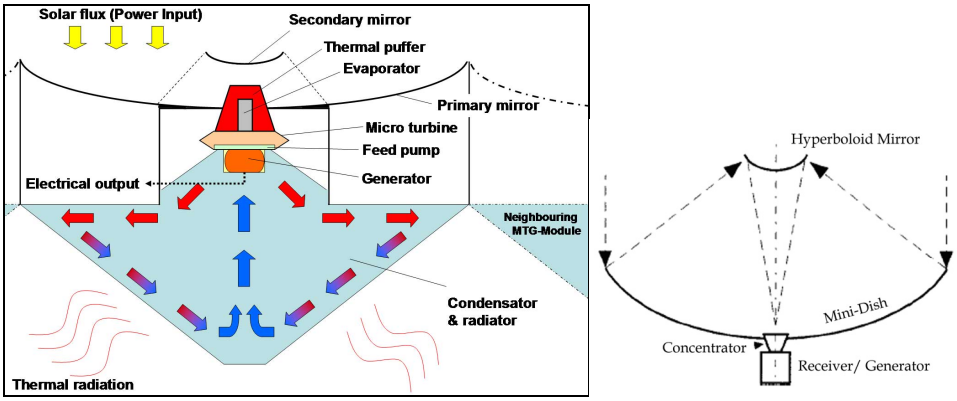

Fig. 7. Left: Schematic cross-section of a Micro-Turbine-Generator (MTG-Module); Right: Schematic drawing of a Cassegrain collector & concentration system

The devices have an extremely high heat transfer to volume ratio of about 30,000 m^2 per m^3, which makes it possible to transfer thermal power in the range of several kilowatts within a volume of some cubic centimeters only (Brandner & Schubert, 2005).

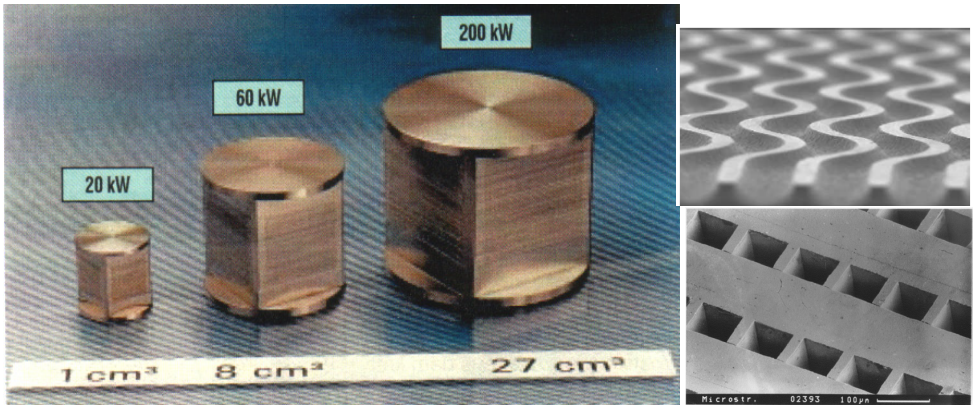

Fig. 8. Different microstructure heat exchanger made of stainless steel, each channel at 100µm edge length; (Brandner & Schubert, 2005)

The turbine-generator system consists of a micro turbine, as to some extent discussed in the previous chapter, and a micro generator. The study revealed that concerning the micro generator a great demand for research exists due to the fact that until now no applicable micro generator is available (concerning long-life expectance). Although, some research is performed on the field of micro generators, like the generator from the research group of Schmidt at Technical University of Berlin, Germany (compare Figure 9) (Walter, 2004).

The condenser/ radiator system, where the hot Toluene vapor has to condensate after leaving the turbine, consists of the same micro channel heat exchange system as the evaporator system. In addition to the condenser a radiator must radiate the heat.

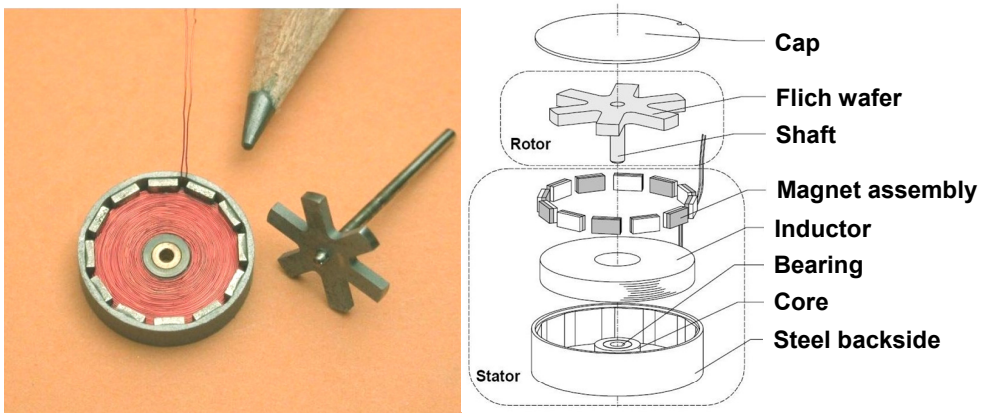

Fig. 9. Prototype for a micro fabricated generator, developed at the Technical University Berlin, Germany (Walter, 2004)

For the optimal geometric design several preliminary concepts were discussed during the study. A promising solution is a radiation dome at the back side of the MTG Module (compare Figure 10). The dome inhabits a secondary passive fluid cycle system (hot tube principle) transporting the heat from the condenser to the outer side of the MTG-Module (shadow side). The domes avoid mutual radiation effects between the different radiation systems, when many MTG modules are implemented on one solar panel.

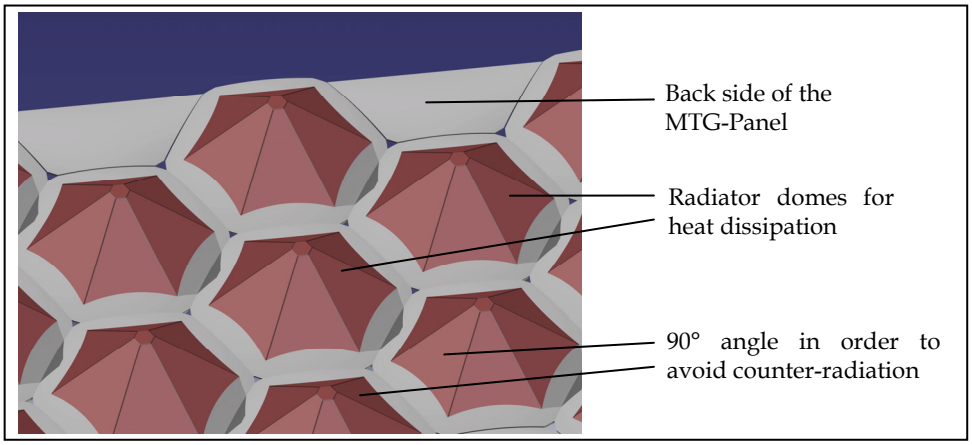

Fig. 10. Key principle for the condenser/ radiator, where radiation domes shall optimize the radiation area, the opposite radiator plates always stand with an angle of 90° to each other in order to avoid counter-radiation

After the Toluene vapor has condensated and returned into its liquid form, a micro feed pump transports the work fluid back to the evaporator system. An additional task of the feed pump is the compression of the fluid to the required boiler pressure. Many feed pumps within Rankine cycle machines are coupled directly (over the shaft) with the turbine. The

Rankine Power-MEMS designed by the Columbia State University already has an integrated micro feed pump (compare Figure 4). For the MTG-Module a similar micro pump system would be conceivable.

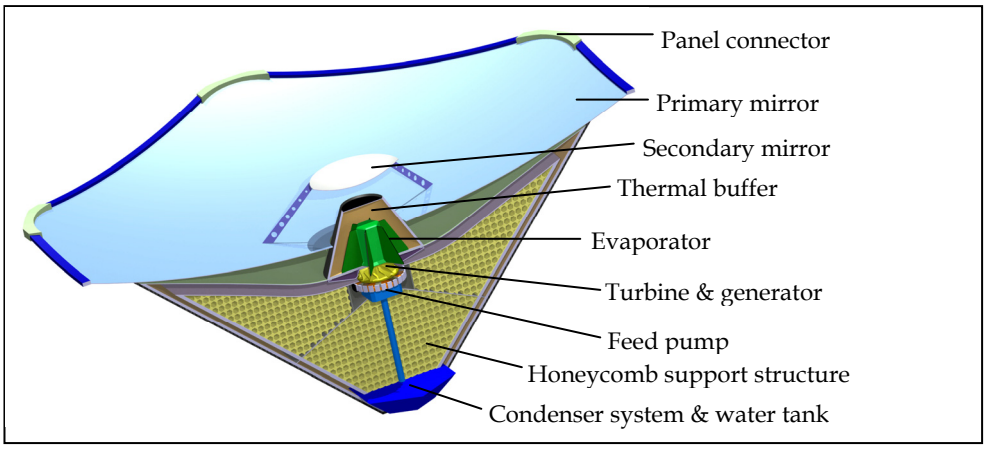

Fig. 11. Cross section of a Cassegrain collector mirror system with a MTG-Module attached

Figure 11 shows a first drawing on the actual design of a MTG-Module. The cross section shows all necessary subsystems and elements for one Module. A honey comb support structure fills the not needed volume between mirror system and radiator and adds additional stiffness to the module.

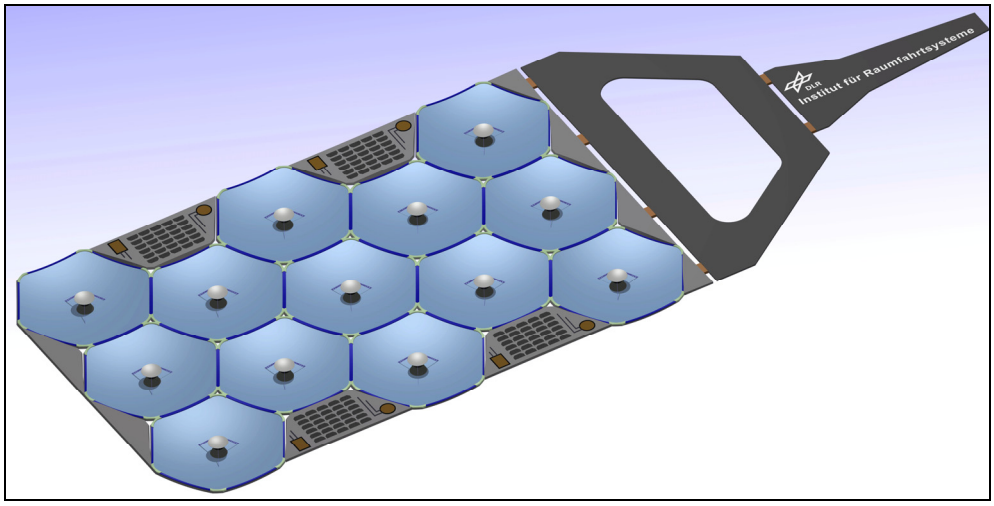

Fig. 12. Example of a perspective depiction of an assembled solar panel with many Cassegrain MTG-Modules

Figure 11 also depicts the micro thermal buffer system that is placed within the receiver system. This heat buffer system, which usually consists of a thermal salt compound, stores the thermal load during on daylight phase. During shadow phase the Rankine process is empowered by the heat dissipation of the thermal buffer. With such a buffer system several positive implications on the overall system could be established like for example the possible reduction of battery mass due to the fact of ongoing cycle power during shadow phases.

The final goal is to integrate many MTG-Modules on a solar panel. As seen in Figure 12 the primary mirrors have a hexagon-type form in order to optimize usable panel area. This way a maximum of solar flux can be captured and concentrated. Every single MTG-Module will convert the solar energy into electrical energy. The partial electrical power outputs from each of the small steam power plants will be interconnected and serve the power subsystem as primary energy conversion source.

5. Thermodynamic calculation

The ORC process can be divided into seven sub processes (compare Figure 13):

1-2 Isobar heat supply
2-3 Isobar heat supply (saturated vapor)
3-4 Isobar overheating
4-5 Isentropic relaxation
5-6 Isobar heat dissipation
5-7 Isobar heat dissipation (saturated vapor)
7-1 Isentropic pressure boosting

The Toluene cycle process was calculated for boiler pressure of 5 bar within the isobar heat supply. The starting fluid temperature (point 1) starts at 290 K and has an end temperature of 508 K before it enters the turbine.

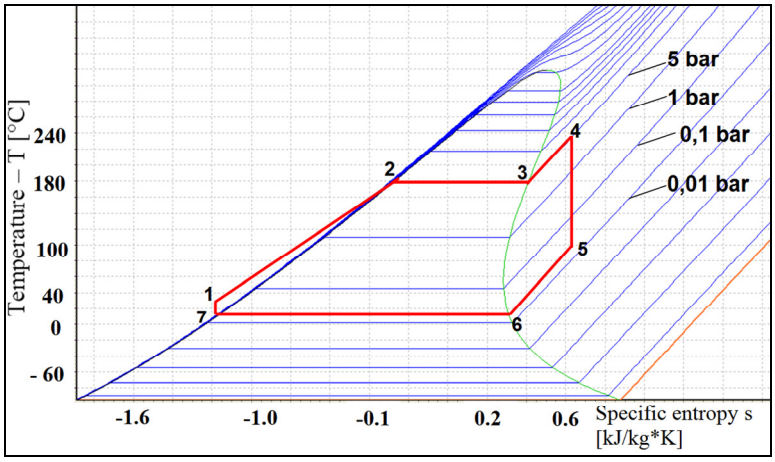

Fig. 13. Temperature-Entropy Diagram for the Toluene Rankine cycle within the MTG-Module.

Within the turbine the vapor relaxes from 5 bar to 0.03 bar and leaves the turbine at a temperature of 373 K (point 5). During the vapor/ fluid mixture flows through the condenser, heat dissipation decreases the temperature to 290 K. Table 2 shows the key thermodynamic working parameters of the chosen and calculated Toluene Rankine cycle (Goodwin, 1989).

Working point	Temp-erature [K]	Pressure [bar]	Specific Enthalpy [kJ/kg]	Entropy [kJ/kg*K]	Average specific heat capacity cp [kJ/kg*K]
1	290	5	-420	-1.15	1.8183
2	453	5	-163	-0.3	1.8183
3	453	5	163	0.4	1.4469
4	508	5	313	0.648	1.4469
5	373	0.03	100	0.648	0.9780
6	290	0.03	-13	0.312	0.9780
7	290	0.03	-430	-1.15	1.029 (cv)

Table 2. Different working points for Toluene Rankine cycle

Having determined the key parameters for the cycle process the specific enthalpies can be calculated for the heat supply and for the heat dissipation. Using the standard thermo dynamical calculation methods one receives the following specific enthalpies:

$$\left.\begin{aligned} dh_{1-2} &= 295\frac{kJ}{kg} \\ dh_{2-3} &= 326\frac{kJ}{kg} \\ dh_{3-4} &= 79\frac{kJ}{kg} \end{aligned}\right\} \dot{q}_{in} = dh_{1-2} + dh_{2-3} + dh_{3-4} = dh_{1-4} = 700\frac{kJ}{kg}$$

$$\left.\begin{aligned} dh_{5-6} &= -81\frac{kJ}{kg} \\ dh_{6-7} &= -417\frac{kJ}{kg} \end{aligned}\right\} \dot{q}_{out} = dh_{5-6} + dh_{6-7} = dh_{5-7} = -498\frac{kJ}{kg}$$

For the turbine an enthalpy gradient of 213 kJ/kg results and the pump needs an enthalpy effort of 571 J/kg or 0.571 kJ/kg. Within the requirements electrical power output for the MTG-Module was set to 10 Watt. To fulfil this goal the necessary mass flow of the work fluid Toluene needs to be calculated. Equation (1) represents the method to calculate the different power consumptions:

$$P = \Delta h \cdot \dot{m}$$

$$P = Power; \quad \Delta h = spec.\ Enthalpy\ difference; \quad \dot{m} = mass\ flow \tag{1}$$

The turbine and the generator efficiency factor was chosen each to η=0.7 so that a needed thermal gross power output of at least 20 Watt is required. Because the feed pump is going to be impelled by the turbine shaft the efficiency factor of the feed pump (η=0.2) has to be considered as well:

$$P_{T(net)} = P_{th(gross)} - \frac{P_{pump}}{\eta_p}$$

$$\Rightarrow P_{th(gross)} = P_{T(net)} + \frac{P_{pump}}{P_{pump}} \tag{2}$$

$$P_{T(net)} = Net\ power\ turbine; \quad P_{th(gross)} = Gross\ power\ thermal;$$
$$P_{pump} = Power\ feed\ pump; \quad \eta_p = efficiency\ factor\ pump$$

Table 3 shows the different possible mass flows with the according calculated thermal input and output powers for the MTG-Module. The blue highlighted mass flow of 0.1 g/sec was chosen for the ongoing calculation process. This way for a net turbine power output of 21 Watt a thermal input power of 70 Watt is required. An average temperature of ØTrec=548 K on the surface of the receiver was calculated (by use of general heat transition equations) under the special consideration of Toluene mass flow and the resulting thermal transfer and absorption from the fluid.

Mass flow [kg/sec]	Total input power [Watt]	Total output power [Watt]	Power feed pump** [Watt]	Gross power turbine [Watt]	Net power turbine* [Watt]
0.00001	7.008	-4.983	0.029	2.130	2.101
0.00005	35.042	-24.914	0.143	10.650	10.507
0.0001	**70.084**	**-49.827**	**0.286**	**21.300**	**21.014**
0.0005	350.418	-249.136	1.428	106.500	105.072
0.001	700.836	-498.271	2.855	213.000	210.145

* Net turbine power under consideration of feed pump power

** Feed pump power under consideration of efficiency factor: η=0.2

Table 3. Different calculated net turbine power values as a function of the impelled mass flow

Having calculated the mass flow and the required thermal power input of the overall system, the geometric size of the primary mirror can be determined. Here, it has to be considered that the secondary mirror shadows the centre part of the primary mirror. Not the full primary mirror system can be used for the solar concentration process (compare Figure 14).

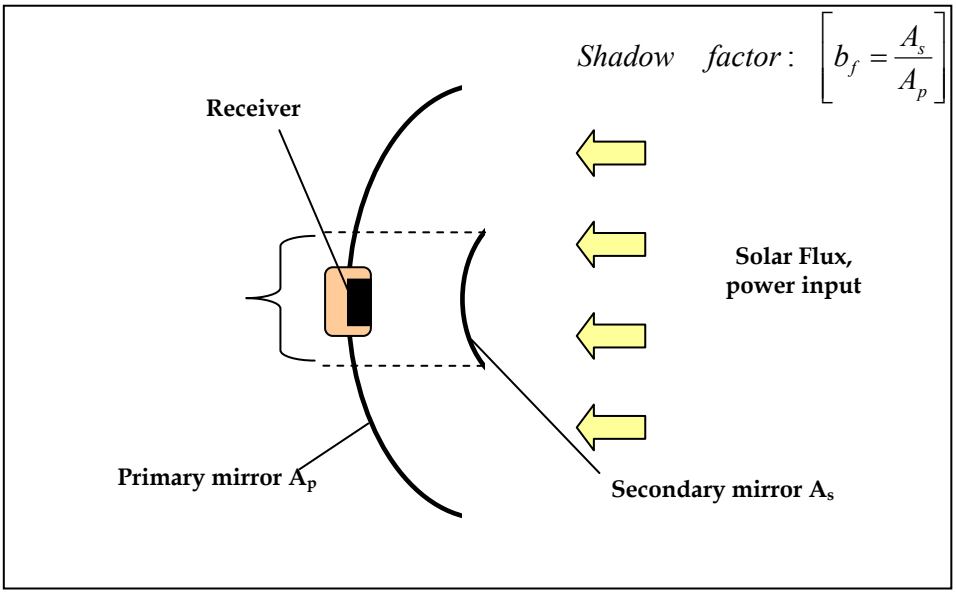

Fig. 14. Depiction of shadowing area of the secondary mirror towards the primary mirror

Since the solar flux is concentrated onto the receiver, the receiver surface itself emits radiation to some extent, which has to be considered as loss energy. The required thermal power for the Cassegrain collector system was calculated with a thermal power balance approach (equation 3):

$$\dot{Q}_{in} + \dot{Q}_{emi} = \dot{Q}_{coll} \tag{3}$$

$\dot{Q}_{in}$ = required input power ; $\dot{Q}_{emi}$ = emitted loss power;
$\dot{Q}_{coll}$ = Power collector system

Considering the shadowing effects of the secondary mirror and the emitted loss energy of the hot receiver, the needed mirror area can be calculated as follows (Zörner, 1991):

$$\dot{Q}_{in} + \dot{Q}_{emi} = A_p \cdot S \cdot (1 - b_f) \cdot \alpha_s$$
$$\Rightarrow A_p = \frac{\dot{Q}_{in} + \dot{Q}_{emi}}{S \cdot (1 - b_f) \cdot \alpha_s} \tag{4}$$

$\dot{Q}_{in}$ = required input power ; A_p = Area of primary mirror;
$\dot{Q}_{emi}$ = emitted loss power; S = Spec. solar const.;
b_f = shadow factor; α_s = Absorption factor

Outgoing from equation (4) and by considering a specific solar flux constant of S=1350 W/m² and a high absorption factor (α= 0.8), the needed primary mirror area results to 703 cm² with a theoretical radius of rp=15 cm.

The closed-loop configuration also introduces the need to remove high heat fluxes from the condenser side. To determine the geometric deviations of the condenser/ radiator system, 49.8 Watt has to be emitted by the radiator (compare Table 4). According to a hint estimate using the heat transition equation and the Boltzmann equation a total radiator area of 1508 cm² (theoretical radius of 21 cm) is needed. Table 4 summarizes all required and calculated values for the MTG Module.

Category	Calculated Value		Category	Calculated Value
Electrical Power (System output)	10.3 Watt		Area of primary mirro	703 cm²
Generator power (η=0.7)	14.7 Watt		Absorptions factor rec	0.8
Turbine power (η=0.7)	21 Watt		Radius of primary mir	15 cm
Feed pump power (η=0.7)	0.286 Watt		Shadow factor	0.02
Thermal gross power (turbine)	21.3 Watt		Average temperature r	548 K
Primary mirror power	95 Watt		Area of receiver	10.4 cm²
Power receiver (from cycle proces	70 Watt		Radius of receiver	1.8 cm
Power loss receiver (from radiatic	4.3 Watt		Area of heat dissipatio	15 cm²
Power radiator (from cycle proces	-50 Watt		Average temperature r	306 K
Mass flow Toluene	100 mg/sec		Area of radiator	1508 cm²
Specific solar flux (concentraded)	67500 W/m²		Radius of radiator	21 cm
Concentration factor C	50			

Table 4. Summarized values of calculated values and technical facts of the Micro-Turbine-Generator (MTG-Module)

Efficiency factor for the MTG-Module, considering the previous assumptions and the geometrical design (703 cm² of primary mirror) and a power output of 10.3 Watt results to η=10.85 % (solar-to-electrical efficiency). The comparing solar cell alternative (same area of 703 cm², triple junction, EOL conditions, working temperature T=100°C) has a solar-to-electrical efficiency of η=18.7 % (Schubert, 2006).

6. Conclusions

The principle of MTG-Modules reveals a huge development potential not only for space application but also for terrestrial regenerative energy conversion. Nevertheless, several arguments have to be examined carefully in order to evaluate the potential of the MTG-Module. Until now, the module cannot compete with the solar-static principle (solar cell). The efficiency factor as calculated in the previous chapter is by a factor of 1.72 lower than the efficiency factor of the competing system (solar cell, triple junction, EOL conditions, T=100°C) (Schubert, 2006). But while the needed cell area for the solar cells increases linear with the required power output most of the MTG area is non-imaging-mirror. These mirrors are relatively easy to produce and therefore low-priced.

Management of two-phase flow in a closed micro system comes with its own set of challenges. Achieving complete evaporation (droplet-free) and superheating before the vapor enters the turbine are critical. The condenser has a similar technical challenge, with

the requirement of preventing vapour from entering the pump. Also the heat transition between the condenser and the passive hot tube system of the radiation dome has to be evaluated in more detail. Especially, the difficulties to establish a constant heat sink only by radiation might be a source for future problems. In addition to it, the radiator has a bigger area than the primary mirror so that a modular design requirement is difficult to fulfil although the use of radiation domes was considered.

A successful development of highly integrated systems, such as the Micro-Turbine-Generator (MTG-Module), requires acceptable operation of all involved components. Manufacturing tolerances, simplified components models, and two-phase flow physics in micro gravity environment are examples of potential sources of variability that can affect a future development program.

For a dynamical system with rotating parts requires high translational speeds and therefore high frequencies. This in turn implies that such parts will be highly stressed. Therefore, the components have to be a high degree of robustness in mechanical design and manufacture. It also limits material choices to those capable of carrying the loads. Nevertheless, from a system level point of view the MTG-Module has several pros & cons that are summarized as follows:

Pros:

- No power loss due to temperature dependency and shifting Maximum Power Point (MPP) like for solar cells
- Thermal buffer system also provides necessary thermal energy during eclipse phases => battery mass reduction
- Most of MTG area is a "non-imaging-mirror", which can be produced at little cost
- No danger of hot-spots, as they typically occur at solar cells
- Theoretical efficiency factor is the Carnot efficiency factor
- Advantageous overall energy balance during production process compared to solar cells
- In general: MTG-Modules can also be used for terrestrial applications within the regenerative energy industry

Cons:

- By now the theoretical efficiency factor is lower than for solar cells
- Difficulties of two-phase flow systems in micro gravity environment
- Moving parts
- The potential mass will be higher than for solar cells
- Fluid consistency cannot be determined by now
- Radiator is bigger than the collector system => mutual radiation effects for panel use

7. Acknowledgement

Presently (by end of 2010) the subject is under review of the System Analysis Group (SARA) at the German Aerospace Centre (DLR) Bremen, Germany. Future research work will create general concept and design work

8. References

Brandner, J., Schubert, K. (2005). „Fabrication and testing of microstructure heat exchanger for thermal applications“, Proceedings of ICMM 2005, 3rd International Conference on Microchannels and Minichannels, Canada, 2005

Epstein, (2004). “Milimeter-Scale, MEMS Gas Turbine Engines”. *Journal of Engineering for Gas Turbines and Power*, Vol. 126, Issue 2 pp 205-226, GT-2003-38866

Frechette, L., (2003). “Design of a Microfabricated Rankine Cycle Steam Turbine for Power Generation”, Proceedings of IMECE’03, ASME International Mechanical Engineering Congress & Exposition, Washington, D.C., November 16-21, 2003

Frechette, L., (2003) “Preliminary Design of a MEMS Steam Turbine Power Plant-on-a-chip”, Proceedings of 3rd Int’l Workshop on Micro & Nano Tech. for Power Generation & Energy Conv. (PowerMEMS’03), Makuhari, Japan, 4-5 Dec. 2003

Goodwin, R., (1989) “Thermophysical Properties of Toluene”, *J. Phys. Chem. Ref. Data*, Vol. 18, No. 4,

Jacobson, Epstein, et.al: „Progress toward a microfabricated gas Turbine generator for soldier portable power applications“, Proceedings of 6th Int. Workshop Micro Nanotechnology For Power Generation and Energy Conversion Apps., Berkeley, CA, November 2006.

Lin, C., Ghodssi, R., Ayon, A., Chen, D., Jacobson, S.,Breuer, K., Epstein, A. & Schmidt, M., (2006) „Fabrication and Characterization of a Micro Turbine/Bearing Rig”, Microsystems Technology Laboratories and Gas Turbine Lab, MIT, USA

Nobbe, D., Tappert, C., (2004). “Space-based GPS lowers satellite costs”, In: *EETimes – The newspaper for engineers and technical management*, 20.09. 2004

Prabhu, E., (2006). “Solar Trough Organic Rankine Electricity System”, Subtracted Report, NREL – National Re-newable Energy Laboratory, 2006

Peirs, J., Reynaerts, F. & Verplaesten, F., (2003). „Development of an Axial Micro Turbine for a Portable GasTurbine Generator”, *Journal of Micromechanics and Microengineering*, Vol. 13, 2003, pp 190-195

Peirs, J., Reynaerts,, F., (2004) “A Micro Gas Turbine Unit for Electric Power Generation: Design and Testing of Turbine and Compressor”, *Proceedings of 9th International Conference on New Actuators*, Actuator 2004, Bremen

Schubert, D., (2006) „New Power System for Satellites based on Power-MEMS-Modules using Micro Turbines and the Rankine-Cycle-Process”, Institute of Space Systems, Technical University Berlin, Germany

Walter, S:, (2004) “Entwicklung miniaturisierter elektrodynamischer Energiewandler mit Reluktanzläufer“, Dissertation at Technical University Berlin

Zörner, W., (1991)„Konzept und Optimierung einer solardynamischen Energieversorgungsanlage im Weltraum“, (1991) – XVIII

12

Performance Analysis of Low Concentrating PV-CPC Systems with Structured Reflectors

Sylvester Hatwaambo
University of Zambia
Zambia

1. Introduction

The conventional sources of energy such as coal, oil, natural gas, etc are undoubtedly dwindling on a world scale at the current rate of consumption. Other sources of energy like nuclear power have a nuclear waste disposal problems and the creation of large water reservoirs for hydro-electricity generation brings about migration and a disturbance in the general ecosystem. It is for this reason that alternative sources of energy are being sought. One of the promising sources of energy is the solar energy. Solar thermal collectors can easily harness the heat from the sun while photovoltaic systems can convert solar energy directly into electricity. The major problem with solar energy is that it is not evenly distributed over the globe and that its conversion efficiency is generally low.

In concentrator photovoltaic systems, highly specular (high reflecting) materials are used to concentrate radiation on the module solar cells. Ultimately, this increases the temperature of the module solar cells. Module solar cells made from silicon show a drop of 0.5% in power for each degree rise in temperature [1]. High grade silicon solar cells have been used in space applications but these are too expensive for conventional use. These specular materials are not only expensive but also cause un-even illumination in certain geometries of solar collectors. One way of going round this problem of un-even illumination is to use diffuse reflectors that have a potential to scatter the radiation flux onto module solar cells.

Non-imaging static concentrators have been tested using converging (Fresnel) lenses as refractive elements [2, 3, 4]. On the other hand, non-imaging static concentrators with reflective elements for low concentration have been tested for high latitudes [5, 6, 7]. Specular reflectors have shown to have a long life but the problem of non-uniformity of illumination has been prominent [6]. Low cost and partly diffuse reflectors have a great potential for overall cost reduction in photovoltaic-thermal hybrids provided the problem of non uniform irradiance could be solved [8, 9].

2. Specific objectives

In this chapter, we analyze the performance of a photovoltaic concentrator system with structured reflectors. These material reflectors are anodized aluminium (oxide layer of Al_2O_3

forms on aluminium during anodization), rolled aluminium foil (lacquered rolled aluminium foil, laminated on plastic PET or mylar, and miro (commercial aluminium sheet coated with $TiO_2/SiO_2/Al$). The overall objective was to test whether a reflector with low-angle anisotropic scattering in one direction and specular in the other could be characterized for use in low concentrators.

In the second case, we investigate one alternative of improving the performance of a low concentrating photovoltaic system using semi-diffuse rolled reflective elements. Our results indicate that rolling marks on the reflector aligned parallel to the plane of the solar module cell improve the performance of the photovoltaic system.

3. Methodology

3.1 The compound parabolic concentrator (CPC) geometry

The studied symmetrical compound parabolic concentrator is shown in figure 1. The acceptance half angle θ_c and the geometrical concentration ratio C_g were 15° and 3.6 respectively. The optical properties of the reflector materials in terms of their integrated specular reflectance were analyzed using the Perkin Elmer Lambda 900 spectrophotometer. In the second analysis, two identical CPCs were constructed as shown in the figures 2(a) and 2(b). In figure 2(a), the diffuse rolled aluminium sheet had its rolling grooves aligned parallel (HG) to the plane of the solar module cell and in figure 2(b), we show the same rolled aluminium sheet with the rolling marks aligned perpendicular (VG) to the plane of the solar module cell.

In both CPCs, the half acceptance angle was 15°, the exit and the entrance apertures were 12.5cm and 42cm respectively, making a geometrical concentration ratio of 3.36. The CPCs were truncated to a height of 49cm and a total length of about 61cm. The solar cell used was a standard, high grade mono-crystalline silicon solar cell with dimensions of 12.5cm x 12.5cm inserted at the base of CPC.

Fig. 1. Truncated CPC with 10 cell module string

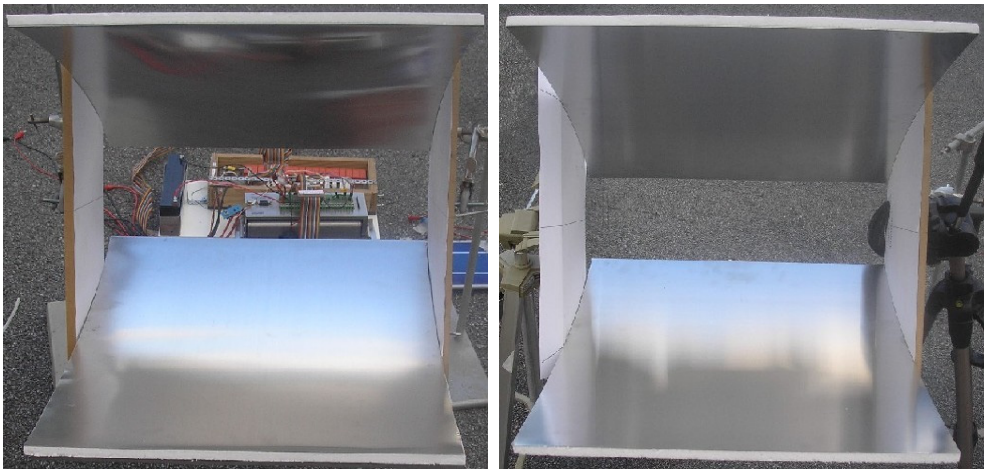

2(a) 2(b)

Fig. 2. Photograph of CPCs with horizontal grooves(HG) in 2(a) and vertical grooves(VG) in 2(b). module string

4. Current-voltage curve measurements

The current-voltage (I-V) curves were measured using an electronic load instrument [10] by adjusting the voltage through a logging system of potentiometers, operational amplifiers and power transistors as shown in the background of figure 2(a). The CPC was tilted manually below and above normal incidence *(0º)* in one degree intervals to ± 20º. At every angle of incidence, an I-V curve was plotted for each reflector material. The current values were compensated for irradiance at 950 W/m² and the voltage values were compensated for temperature increase on the module at 25ºC. From each plotted I-V curve, the short-circuit current I_{sc}, the open circuit voltage V_{oc}, the maximum current I_{max} and the maximum voltage V_{max} were extracted. Subsequently, the maximum power P_{max} and the fill-factor FF were calculated at each angle of incidence.

The effective specular reflectances (R_{eff}) for each material was also estimated from the short-circuit current equation (1) at normal incidence.

$$I_{sc}^{conc} = \left[1 + (C_g - 1)R^{eff}\right]\frac{I_b}{I_t} I_{sc}^{ref} + \left[\frac{1 + (C_g - 1)R^{eff}}{C_g}\right]\frac{I_d}{I_t} I_{sc}^{ref} . \quad (1)$$

The first expression on the right gives the current contribution from beam radiation with reflectance losses and the second expression accounts for the current contribution from diffuse radiation. The parameter I_{sc}^{conc} is the short-circuit current measured under concentration, I_{sc}^{ref} is the short-circuit current measured on a reference module placed at the entrance aperture of the CPC, I_b is the beam radiation, I_d is the diffuse radiation and I_t is the total radiation. The parameter C_g = 3.6, is the geometrical concentration ratio of the used CPC. The ratio of the beam radiation to the total and the ratio of the diffuse radiation to the total on a typical blue sky day are 0.9 and 0.1 respectively.

In the second scenario, a standard current-voltage (I-V) plotter [10] was used to generate a series of I-V curves at each angle of incidence (tilt). From each I-V curve and at a particular angle of incidence, short-circuit current I_{sc}, open-circuit voltage V_{oc}, maximum power P_m, maximum current I_m, and maximum voltage V_m were extracted and the fill-factor (*FF*) was evaluated from equation (2).

$$FF = \frac{P_m}{I_{sc}.V_{oc}} \cong \frac{I_m}{I_{sc}}\left(1 - \frac{I_m R_s}{V_{oc}}\right) \tag{2}$$

Where R_s is the series resistance of the module. The corresponding cell efficiency may be calculated from equation (3).

$$\eta = \frac{FF.I_{sc}V_{oc}}{I_N A_m} \cong \frac{I_m V_{oc}}{I_N A_m}\left(1 - \frac{I_m R_s}{V_{oc}}\right) \tag{3}$$

Where I_N is the incident solar radiation and A_m is the active solar module area.

5. Un-even illumination profile measurements (Flux distribution)

The non-uniform illumination profile apparatus used in the measurements is shown in figure 3. The rotation of the motor also rotates the potentiometer which in turn moves the wiper and the attached photo-diode in the clockwise direction.

A small hole of 1 mm diameter was used to increase the resolution of the Photo-diode measurements. The flux distribution profile measurements were averaged at four regular intervals along the length of the CPC to minimize errors due to non-linearity of the CPC geometry. The non-uniform illumination was compared for the three reflectors in terms of their local concentration ratios *(C_L)* from the flux distribution measurements.

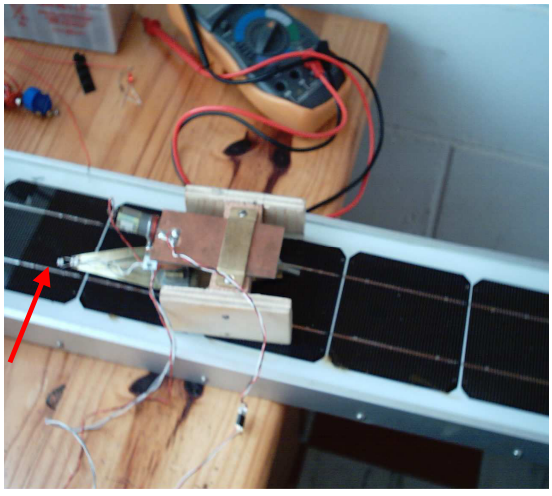

Fig. 3. Flux distribution profile apparatus resting on module string.

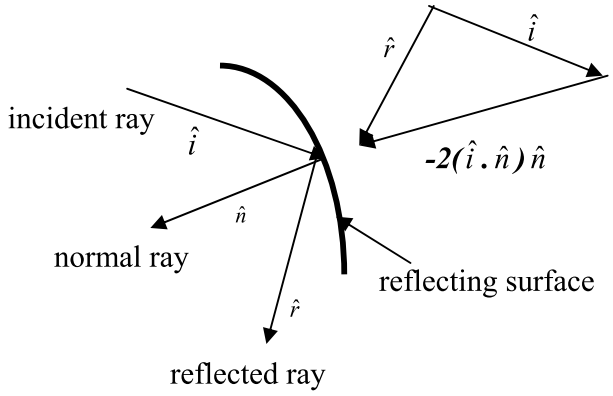

Fig. 4. Vector representation of light reflection for a specular surface.

6. Ray-tracing techniques

The ray-tracing was performed using commercial Zemax software [11] and the Matlab programmes. If we denote the incident unit vector $\hat{i}$, the normal unit vector $\hat{n}$ and the reflected unit vector $\hat{r}$, we may make a representation of ray-tracing profile for a specular surface as shown in figure 4. If the incident ray is known, the reflected ray may be calculated from the standard reflection equation (4).

$$\hat{r} = \hat{i} - 2(\hat{i}\,.\,\hat{n})\,\hat{n} \tag{4}$$

A known number of rays were sent through the aperture of the CPC and monitored statistically the fraction of rays that hit the absorber directly f_0, the fraction of those that hit the absorber after the first reflection f_1 and the fraction of those that hit the absorber after the second reflection f_2 etc. From these statistics, the effective specular reflectance (R_{eff}) for each reflector material was estimated from equation (5). Note that equation (5) was evaluated for normal incidence only as was the case for equation (1) as a comparison.

$$\frac{C_L}{C_g} = f_0 + f_1 R_{eff} + f_2 . R_{eff}^{\,2} + \ldots\ldots . \tag{5}$$

6.1 Goniometric measurements

A photograph of the reflected light distribution from the reflector surface on to the screen is shown in figure 5. The incident beam was entering through a small hole on the screen and was reflected by the sample with the rolling grooves aligned vertically (y-direction). A goniometer instrument was then used to obtain the angular distribution of the reflected radiation along the x- and y-directions as defined in the figure. We observed the relative intensity of the detector signal as the alignment of the rolling grooves were either perpendicular to the scattering direction (scattering plane) or parallel to the scattering plane.

A photo-detector was used to record the relative signal intensity at each scattering angle.

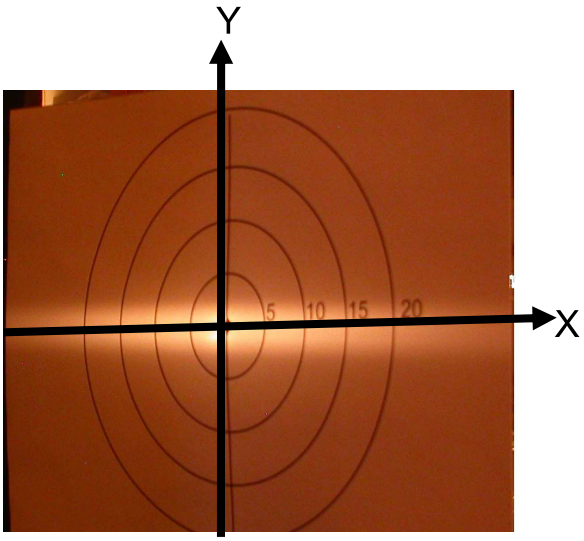

Fig. 5. Screen showing the reflected intensity. White band indicates direction of more scattering, hence anisotropic.

7. Experimental results

7.1 I-V characteristic curves

The dependence of the short-circuit current as a function of angle of incidence were analyzed as shown in figure 6 for the three materials.

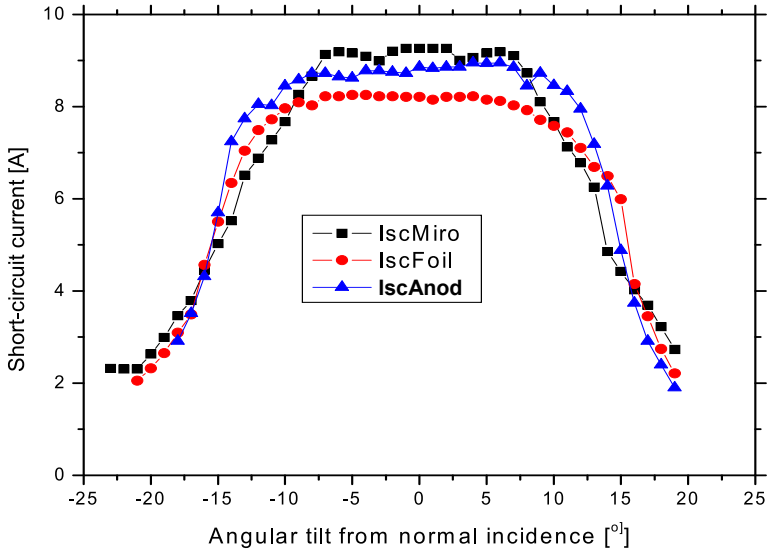

Fig. 6. Angular dependence of short-circuit current for three reflector materials.

The increase in the short-circuit current was proportional to the increase in irradiance on the cells. The short circuit current curve for anodized material followed the ideal optical behaviour because it was used as the base reflector. The miro and the rolled foil short circuit current curves show narrower angles of acceptance due to loose binding to the reflector geometry.

The reduction in short-circuit current at angles of incidence less than the acceptance half angle were due to optical imperfections of the reflector.

The fill factor for each material seemed to be fairly constant within ±10° of angular tilt as shown in figure 7. The fill factor for the anodized reflector dropped sharply at ±14° because all the rays fell on the edge of the cells and hence increased resistive losses. The increase in fill factor outside these angles of incidence were due to the decrease in generated current. Figure 8 shows typical current-voltage curves for the different groove orientations on the diffuse aluminium reflector sheet. The calculated fill-factor values at normal incidence are shown in the inset. It is observed that the percentage drop in the fill-factor for horizontal orientation of the rolling marks was about 1.6% and that for the vertical rolling grooves was about 2.4%. The smaller drop in the fill-factor for horizontal grooves was due to uniform illumination of the solar flux causing an even distribution of currents within the solar cell. The larger the fill-factor, the larger the power output and hence the efficiency from a solar cell as seen in equations (2) and (3).

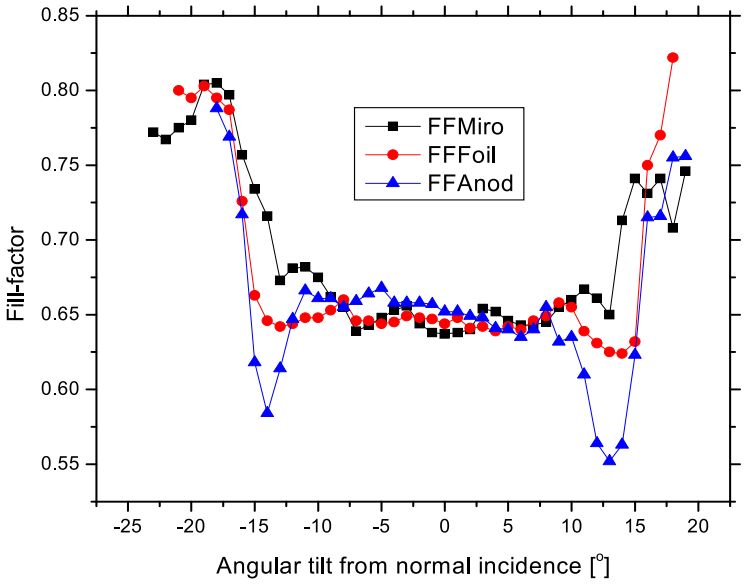

Fig. 7. Angular dependence of fill-factor for three reflector materials.

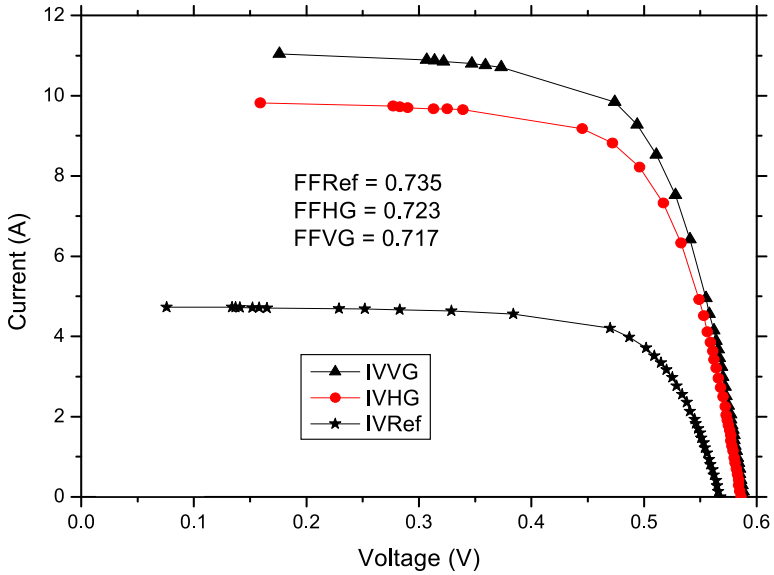

Fig. 8. I-V curves for different groove orientations at normal incidence.

Figure 9 shows the variation of short-circuit current *(I_{sc})* for the two groove orientations as a function of the angular tilt of the CPC. It is observed that short-circuit current for the rolling marks vertical was higher than the short-circuit current for the horizontal grooves within the acceptance angle. The vertical grooves behaved similar to a specular material.

High short-circuit currents generated with vertical grooves are not desirable in low concentrating systems as they induce high intensity peaks caused by local heating.

Figure 10 shows the variation of the fill-factor *(FF)* as a function of the angular tilt of the CPC within the acceptance angle (15^o). We observe that the fill-factor for the horizontal rolling marks was better than the corresponding fill-factor for the vertical grooves. The moderate short-circuit currents generated from the horizontal grooves tended to lower the heating effect by spreading the illumination flux.

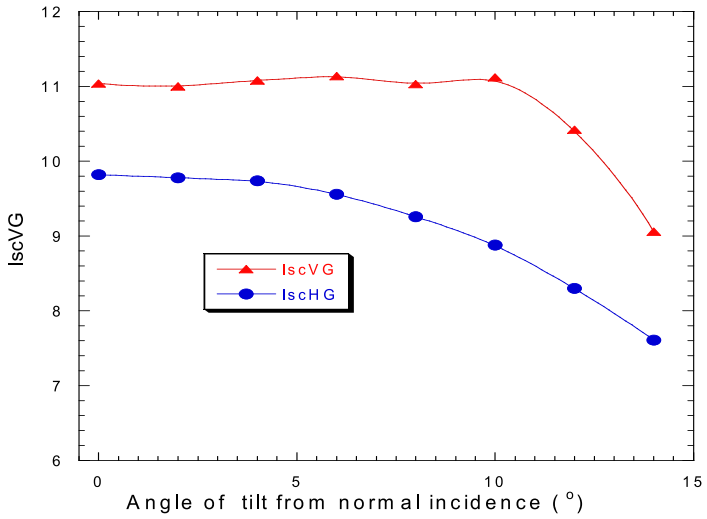

Fig. 9. Comparison of short-circuit currents for horizontal and vertical grooves.

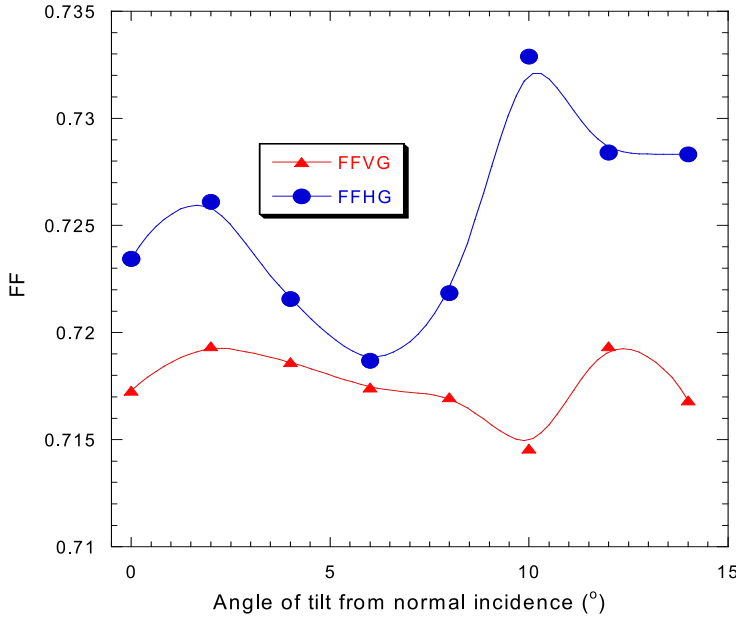

Fig. 10. Comparison of fill-factor for horizontal and vertical grooves.

8. Flux distribution and ray-tracing results

The local concentration ratios (C_L) and the ray-tracing results are shown in table 1. The effective specular reflectance (R^{eff}) is also compared as shown in table 1.

Reflector material	C_L ratio (From flux measurements)	R^{eff} (From flux and Ray-tracing Eqn. 4)	R^{eff} (From I-V measurements Eqn. 1)	Integrated specular reflectance
Miro	2.72	0.73	0.74	0.86
Rolled Foil	2.59	0.68	0.61	0.55
Anodized Aluminium	2.70	0.72	0.69	0.85

Table 1. Comparison of the local concentration ratios for the different reflector materials and the ray-tracing results.

Figure 11 shows the comparison of the local concentration ratio *(C_L)* of the solar cell illumination for the different groove orientations on the reflector as a function of the position along the solar cell width at normal incidence. It is observed that vertical orientation of the rolling marks give high concentration peaks along the surface of the solar cell, which is an indication of high heating. The horizontal rolling marks on the other hand give reduced peaks across the solar cell width an indication of an even illumination of the solar flux *(C_LHG curve on the figure)*. There is no concentration at the centre of the solar cell because all the rays reach the solar cell directly without any reflection *(C_LVG curve on the figure)*.

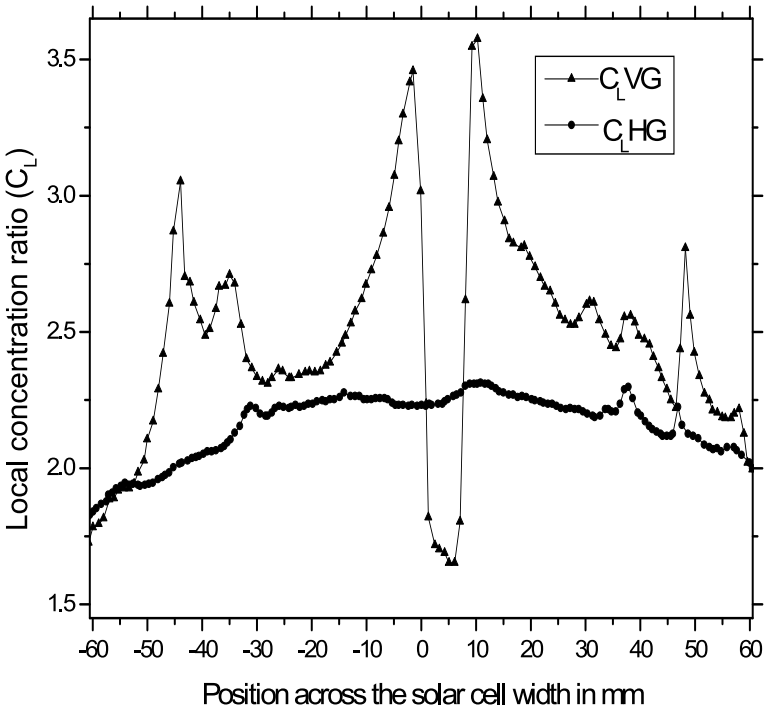

Fig. 11. Comparison of the local concentration ratio for the different groove orientations measured by the flux distribution apparatus. currents for horizontal and vertical grooves.

9. Conclusions

The CPC element with a geometrical concentration ratio of 3.6 has been analysed with different reflector materials. The short circuit current increased within a factor of 2.4 and 2.7. The fill factors decreased from 0.72 for the reference module to 0.65 under concentration, giving a percentage decrease of about 10%. The decreased fill factor during concentration was a result of high and non-homogenous irradiance that increased the resistive losses during concentration. The rolled aluminium reflector did not perform as expected in the fill factor improvements although behaved relatively well with the flux distribution measurements. From the flux distribution measurements, the rolled aluminium could performance better with an improved CPC geometry. Concentrator geometry with a uniform intensity distribution would be desirable since the cell with the lowest irradiance limits the power output from a module.

The effective specular reflectance values from the short-circuit current and those from the ray-tracing techniques were comparable to within 10% at normal incidence.

However, the rolled aluminium reflector has a potential for use as PV-CPC reflector for cost reduction. The cost of rolled aluminium is 2 to 3 times less than the cost of anodized aluminium and 6 times less than the cost of the Miro reflector per square metre. It is recommended that further work be done on different groove sizes and different groove orientations in improved geometries. It is expected that reflectors with grooves parallel to the trough would give stronger scattering across the module and better performance in terms of fill factor.

We have further demonstrated that a semi-diffuse aluminium sheet reflector with rolling grooves oriented parallel (HG) to the plane of the solar cell module can improve the fill-factor as it scatters the solar flux evenly across the solar cell module. It is the even scattering that causes uniform distribution of currents within the solar cell and therefore reduces the heat spot formation. Although the differences in the fill-factor were minimal between horizontal grooves and vertical grooves, the Goniometric measurement results show remarkable differences in the angular scattering of the light flux across the solar cell. From the Goniometric results, larger scattering angles are observed from the rolling grooves aligned perpendicular to the direction of scattering or the plane of scattering.

10. Acknowledgements

This work was sponsored by Uppsala University through the financial support of the International Science Programme (ISP). The hospitality at Lund University is highly acknowledged. The University of Zambia through the Dean, School of Natural Sciences and the Head, Department of Physics are acknowledged for their logistical support.

11. References

[1] Wenham S. R., Green M. A, and Watt M. E (1994): Applied Photovoltaics. Centre for Photovoltaic Devices and Systems, University of New South Wales

[2] Saitoh T. and Yoshioka K,; Preparation and properties of photovoltaic static concentrators: Renewable Energy 15 (1998) 566 – 571

[3] Goma S., Yoshioka K and Saitoh T.; Effect of concentration distribution on cell performance for low-concentrators with a three dimensional lens.: Solar Energy Materials and solar cells 47 (1997) 339 – 344.

[4] Luque A., Sala G. and Arboiro J. C.: Electric and thermal model for non-uniformly illuminated concentration cells: Solar Energy Materials and Solar Cells 51 (1998) 269 – 290.

[5] Perers B., and Karlsson B., External reflectors for large solar collector arrays, simulation model and experimental results. Solar Energy 51(5) (1993) 327 - 337

[6] Ronnelid M., Perers B., and Karlsson B: Construction and testing of a large-area CPC collector and comparison with a flat-plate collector; Solar Energy 57 (1996) 177 – 184.

[7] Karlsson B., A large bifacial photovoltaic-thermal low concentrating module. 17th PVSEC, Munich, Germany, 2001.

[8] Brogren M., Nostell P., and Karlsson B., Optical Efficiency of a PV-thermal hybrid CPC module for high latitudes: Solar Energy, 69(6): (2001) 173 – 185

[9] Brogren M., Karlsson B., and Hakansson H.: Design and modeling of low- concentrating Solar Energy Systems and investigation of irradiation distribution on modules in such systems, in 17th EUPVSEC 2001. Munich, Germany.

[10] Hatwaambo S., H. Hakansson, J. Nilsson and B. Karlsson: Angular characterization of low concentrating PV-CPC using low cost reflectors, Solar Energy Materials and Solar Cells 92 82008) 1347-1351

[11] Nilsson J., Optical design and characterization of solar concentrators for photovoltaics, Lund University, Licentiate Thesis, 2005.

13

Contribution of Spectrally Selective Reflector Surface to Heat Reduction in Silicon Concentrator Solar Cells

Christopher M. Maghanga and Mghendi M. Mwamburi
Kabarak University, Kabarak,
Moi University, Department of Physics, Eldoret,
Kenya

1. Introduction

Energy has been playing an important role for civilization. In the early ages, wood was the main source of energy. Industrialization and modernization which started around two hundred years ago were mainly based on fossil fuels and even now they are being used on a large scale. Huge demand of such energies has caused environmental problems and rises in coal and oil prices as well. With ever expanding cities consuming more and more energy, the fuel reserves for example oil, gas, coal, etc., throughout the world may not be able to match the demand. There is a drive towards biofuels but unless the world's food energy needs are addressed, the viability of such fuels will remain a mirage for many decades. This therefore calls for alternative sources of energy such as those employing wind, photovoltaic, biomass, geothermal and wave power technology. The sun alone is continually releasing an enormous amount of radiant energy into the solar system. The Earth receives a tiny fraction of this energy; yet, an average of 1367 watts reaches each square meter of the outer edge of the Earth's atmosphere. The atmosphere absorbs and reflects some of this radiation, including most X-rays and ultraviolet rays but still, the amount of solar energy received by the surface of the earth per minute is greater than the energy utilization by the entire population in one year (Sen, 2004).

1.1 Solar radiation

Electromagnetic radiation occurs over widely different wavelength ranges: from cosmic, gamma, X-rays to long radio waves. Sunlight is electromagnetic radiation in the spectral range of 0.3 μm to 4 μm with its maximum intensity around 0.5 μm. This spectrum corresponds to an effective blackbody temperature of about 5800 K (McVeigh, 1977, Sze, 1991). The wavelengths for many solar energy applications are found in the range from the ultra violet at 0.3 μm to the infrared at 50 μm covering the solar spectral range and the spectral range of the thermal radiation emitted from a surface having a temperature of about ambient up to 100^{o}C (2 to 50 μm).

Terrestrial solar radiation is a low-intensity, variable energy source reaching a maximum of about 1000 W/m^{2}. The intensity of the terrestrial spectrum depends on the distance

travelled through the atmosphere. Outside the atmosphere the spectrum is denoted air mass zero, AM 0, while the radiation that travels through the atmosphere is AM X where

$$X = \frac{1}{\cos\theta_z} \tag{1.1}$$

θ_z is the angle of incidence with respect to zenith (Blatt, 1991). Equation 1.1 is valid only for zenith angles less than 70° (Kreith and Kreider, 1978). At greater zenith angles, the accuracy degrades rapidly, with X becoming infinite at the horizon. Figure 1.1 shows a normalized solar spectrum for air mass 1.5 (AM 1.5). It represents a satisfactory energy-weighted average for terrestrial applications. It has several local minima, which are caused by absorption in the atmosphere mainly by water vapour, carbon dioxide and ozone (Duffie and Beckman, 1991). AM 1.5 has been used later in this chapter to calculate average solar values of reflectance given that it is advisable to compare different optical properties in devices within certain spectral regions. These regions can be defined for certain environments, eye adaptation abilities, material temperatures etc. An expression that gives the average, H_ξ, for the measured reflectance, transmittance, absorptance or emittance of a device H(λ), has been defined as (Mwamburi & Wäckelgård,, 2000):

$$H_\xi = \frac{\int_a^b H(\lambda)\cdot\phi_\xi(\lambda)d\lambda}{\int_a^b \phi_\xi(\lambda)d\lambda} \tag{1.2}$$

where $\phi_\xi(\lambda)$ is the source function of a specified property, ξ, which can be the solar irradiance on earth at a certain level and angle, the range of the human eye sensitivity or the thermal spectrum of a black body. In this work, $\phi_\xi(\lambda)$ is the solar irradiance (AM 1.5) and $H(\lambda)$ is the reflectance in some specified wavelength range.

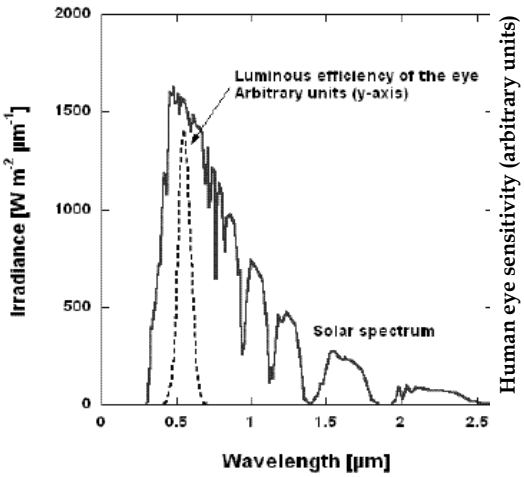

Fig. 1.1. Solar irradiation spectrum at air mass 1.5 and the relative spectral sensitivity of the human eye (ISO 9845-1, 1992)

1.2 Overview of photovoltaic technologies and materials

Research on solar cells can be divided into three areas: technologies that can make current solar cells cheaper and/or more efficient to effectively compete with other energy sources, developing new technologies based on new solar cell architectural designs and developing new materials to serve as light absorbers and charge carriers. The technologies can be classified into three generations.

The first generation photovoltaic cell consists of a large-area, single-crystal, single layer p-n junction diode, capable of generating usable electrical energy from light sources with the wavelengths of sunlight. These cells are typically made using a diffusion process with silicon wafers. First-generation photovoltaic cells are the dominant technology in the commercial production of solar cells, accounting for more than 86% of the terrestrial solar cels (Goetzberger and Hebling, 2000).

The second generation of photovoltaic materials is based on the use of thin epitaxial deposits of semiconductors on lattice-matched wafers. There are two classes of epitaxial photovoltaics - space and terrestrial. Space cells typically have higher air mass zero efficiencies in production, but have a higher cost per watt (Yamaguchi et. al, 2006, Takamoto et. al, 2006). There are a number of technologies/ semiconductor materials under investigation or in mass production. Examples include amorphous silicon, polycrystalline silicon, micro-crystalline silicon, cadmium telluride, copper indium diselenide/sulfide. An advantage of thin-film technology theoretically results in reduced mass so it allows fitting panels on light or flexible materials (Shah , et al. 2004). Thin GaAs-based films for space applications with very high potential air mass zero efficiencies are being produced (Merrill and Senft, 2007).

Third-generation photovoltaics are very different from the previous semiconductor devices as they do not rely on a traditional p-n junction to separate photogenerated charge carriers. For space applications, quantum well devices and devices incorporating carbon nanotubes are being studied with a potential for very high efficiency (Hoffmann, 2006). For terrestrial applications, these new devices include photoelectrochemical (Fahrenbruch and Bube, 1983) cells and polymer solar cells (Brabec et. al., 2001), among others.

1.3 The pn junction solar cell

The conventional p-n junction solar cell has a single energy band gap, E_g, so when the cell is exposed to solar radiation; a photon energy of less than E_g makes no contribution to the cell output if phonon assisted absorption is neglected. A photon with energy greater than Eg contributes to energy E_g to the cell output and the excess over E_g is wasted as heat.

The equivalent circuit in Figure 1.2 shows a constant current source in parallel with the junction.

The source I_L results from the excitation of excess carriers by the solar radiation. I_s is the diode saturation current as derived by the Shockley equation (Sze, 1991) and R_L the load resistance. The shunt resistance R_{sh} is caused by surface leakage along the edges of the cell, and by metal shorts in defects and grain boundaries. The series resistance is as a result of the front and back contact resistance, the base resistance and the thin top layer resistance. Ideally $R_s = 0$ and $R_{sh} = \infty$, but even for a high value of R_{sh} (say about 100 Ω) its effect on the *I-V* characteristics of the cell is negligible. So it is R_s that should be kept as low as possible.

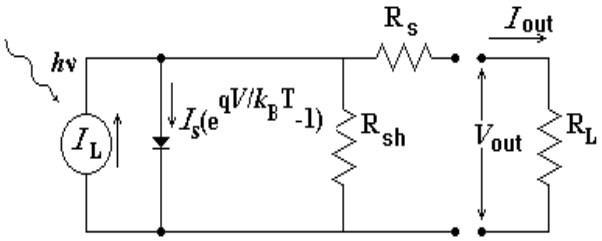

Fig. 1.2. Equivalent circuit of a solar cell

The *I-V* characteristics of such a device are given by

$$I = I_s(e^{qV/k_BT} - 1) - I_L \,, \tag{1.3}$$

One important parameter of the cell, open circuit voltage V_{oc} is related to the I_L and I_s as

$$V_{oc} = \frac{k_B T}{q} \ln\left(\frac{I_L}{I_s} + 1\right) \approx \frac{k_B T}{q} \ln\left(\frac{I_L}{I_s}\right) \tag{1.4}$$

and since $I = 0$, hence for a given I_L, the open circuit voltage increases logarithmically with decreasing saturation current I_s.

1.3.1 Loss mechanisms in pn junction solar cell

1.3.1.1 Surface reflection losses

On the top of the solar cell, reflection of incident solar energy do occur and affect short circuit current of the cell. This is because refection reduces the absorbed carriers and hence the I_{sc}. For a bare silicon, these losses account for more than 30% due to high reflectivity of silicon in the UV and visible regions which is about 0.3 (Green, 1992), However use of antireflective coatings and texturing of the surface are some of the methods used to minimize efficiency loss by top surface reflection.

1.3.1.2 Recombination losses

Basically, photovoltaic conversion occurs through three separate processes: (1) the absorption of light to create electron-hole pairs in an appropriate semiconductor; (2) collection and separation of these carriers by an internal electric field; (3) distribution to an external load. Photon incident on the solar cell generates electron hole pairs; Generated carriers need to be separated before they recombine, with emission of energy. Recombination causes loss of carrier and reduces the open circuit voltage V_{oc} of the cell.

Recombination can occur by having an electron from the conduction band combining with the hole in the valence band with emission of energy, the so called band-to-band recombination. Another recombination method which is the dominant form in solar cells is trap assisted type. This is attributed to impurities present in the semiconductor which introduce an additional energy level within the forbidden energy gap. This added energy level acts as a trap and captures electrons and holes leading to recombination.

Also, the surface of the solar cells have large number of dangling bonds due to abrupt termination of crystal structure. These dangling bonds act as recombination centers. Carriers generated at the surface fall in to the dangling bond and recombine with the hole.

Another type of recombination referred to as Auger recombination occurs when a solar cell is exposed to high intensity of photons. It may involve two electrons and a hole or two holes and an electron. When hole from the valence band recombine with the electron in the conduction band the excess energy released during recombination is absorbed by the neighboring electron in the conduction band which then goes to some higher energy level and then again falls back to the conduction band with release of energy.

1.3.1.3 Series resistance losses

As already explained in the previous section, series resistance losses arises from power loss due to R_s. and contribute to around less than 20% of the total input power (Markvart, 1994). The losses increase tremendously when solar cell is operated at high intensities and they are the subject of this chapter.

1.4 Concentrating photovoltaics

Concentrating Photovoltaic systems use a large area of lenses or mirrors to focus sunlight on a small area of photovoltaic cells. Concentration of sunlight onto photovoltaic cells, and the consequent replacement of expensive photovoltaic area with less expensive concentrating mirrors or lenses, is seen as one method to lower the cost of solar electricity. Because of the reduction in solar absorber area, more costly, but higher efficiency PV cells may be used (Dalal and Moore, 1997; Kurtz and Lewandowski, 2004).

1.4.1 Concentrator geometries

1.4.1.1 Single cells

In small point-focus concentrators, sunlight is usually focused onto each cell individually. This means that each cell has an area roughly equal to that of the concentrator available for heat sinking, as shown in Fig. 1.3. Single cell systems commonly use various types of lenses for concentration (Royne et. al., 2005).

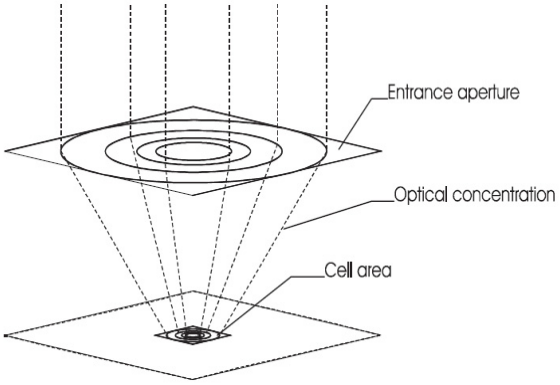

Fig. 1.3. Single-cell concentrator (Royne et. al., 2005)

1.4.1.2 Linear geometry

Line focus systems typically use parabolic troughs or linear Fresnel lenses to focus the light onto a row of cells as shown in Figure 1.4. The areas available for heat sinking extend from two of the sides and the back of the cell. Compound parabolic concentrators (CPC) shown in Figure 1.5 fall under this category and have been used for PV and thermal applications and have been well discussed in literature (Winston, 1974; Tabor, 1984; Brogren et. al., 2000) .

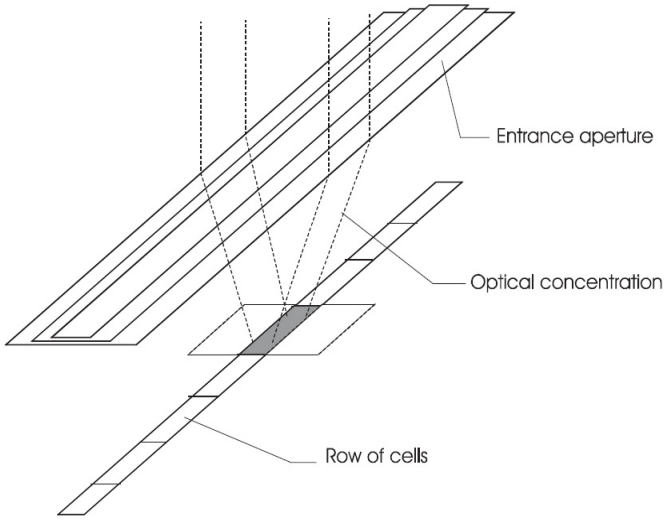

Fig. 1.4. Linear concentrator (Royne et. al., 2005)

Fig. 1.5. Photograph showing an array of compound parabolic concentrators for PV and Thermal application

1.4.1.3 Densely packed modules

In larger point-focus systems, such as dishes or heliostat fields, the receiver generally consists of a multitude of densely packed cells as shown in Figure 1.6. The receiver is usually placed slightly away from the focal plane to increase the uniformity of illumination. Secondary concentrators may be used to further improve flux homogeneity (Kreske, 2002).

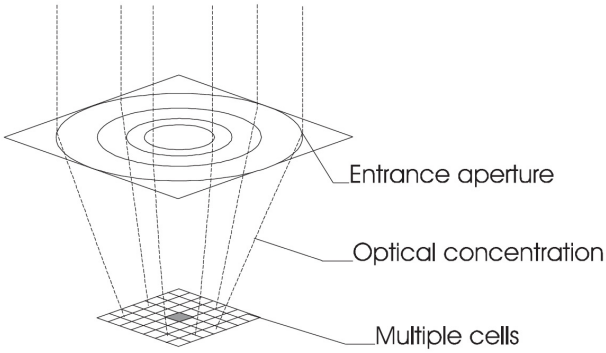

Fig. 1.6. Densely packed cells (Kreske , 2002)

1.5 Design considerations

Only a fraction of the incoming sunlight striking a solar cell is converted into electrical energy. A typical efficiency value for concentrator cells is about 25% (Royne et. al, 2005). The remainder of the absorbed energy is converted into thermal energy in the cell and may cause the junction temperature to rise unless the heat is efficiently dissipated to the environment. The major design considerations for cooling of photovoltaic cells are given below:

1.5.1 Cell temperature

The four main parameters used to characterize solar cell outputs are the short circuit current, I_{sc}, the open circuit voltage, V_{oc}, the fill factor, FF, and the conversion efficiency, η_x. In order to evaluate the conversion efficiency of systems where the radiation is concentrated it is important to calculate the influence of the value of the solar flux on the efficiency. The ratio of the illumination level incident on a cell to the level corresponding to AM1.5 illumination is the concentration factor. At constant temperature the short circuit current is proportional to the concentration factor (Green, 1992). An influence on the efficiency results from the relation between V_{oc} or FF and illumination level. The fill factor is strongly dependent on the series resistance, R_s, of the solar cell. This has profound consequences on the efficiency of a cell working under concentrated sunlight because the power loss, caused by R_s, increases with the square of the current. For a silicon solar cell with conversion efficiency of about 24% at 293 K, its efficiency reduces to less than 10% if the temperature goes beyond 400 K (Figure 1.7).

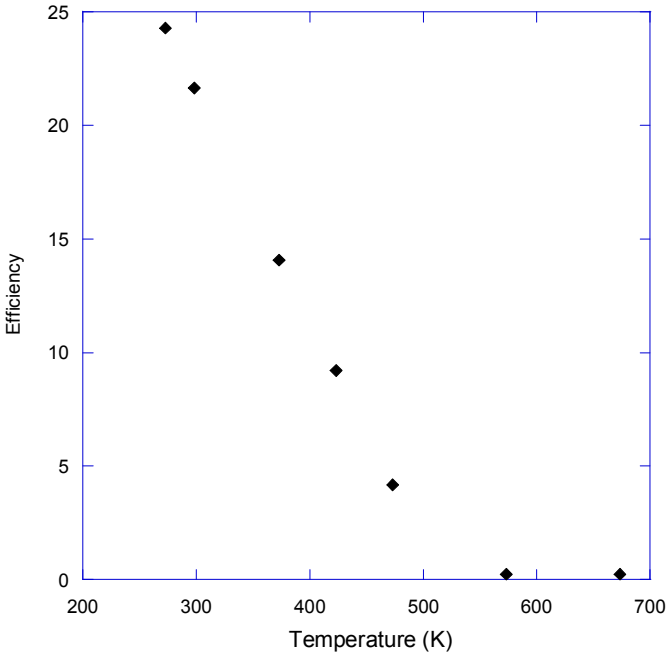

Fig. 1.7. Theoretical silicon solar cell efficiency as a function of temperature. The data was extracted from Fig. 7 in Wysocki and Rappaport, 1960 using digitization software.

1.5.2 Uniformity of temperature

The cell efficiency is known to decrease due to non-uniform temperatures across the cell (Luque et. al, 1998; Mathur et. al, 1984; Chenlo, 1987). In a photovoltaic module, a number of cells are electrically connected in series, and several of these series connections can be connected in parallel. Series connections increase the output voltage and decrease the current at a given power output, thereby reducing the ohmic losses. However, when cells are connected in series, the cell that gives the smallest output will limit the current. This is known as the 'current matching problem'. Because the cell efficiency decreases with increasing temperature, the cell at the highest temperature will limit the efficiency of the whole string. This problem can be avoided through the use of bypass diodes (Edenburn and Burns, 1981) which bypass cells when they reach a certain temperature or by keeping a uniform temperature across each series connection. Also, the cells exhibit long-term degradation if the temperature exceeds a certain limit (SunPower, 2002; Horne, 1993). The cell manufacturer will generally specify a given temperature degradation coefficient and a maximum operating temperature for the cell.

1.6 Cooling options for solar cells

As already indicated in the previous sections, the energy conversion efficiency of solar cells decreases as the temperature of the solar cells increases. Furthermore, increasing temperature may also have detrimental effects on other components of the photovoltaic

system, including thermal stress which may result in failures in the photovoltaic system. Whether the cells are singular, linear or densely packed, passive or active cooling can be employed to maintain low operating temperatures depending on the complexity and the scale of the concentrating PV system.

To keep operational costs to a minimum, a simple and low maintenance solution should be sought. This also includes minimizing the use of toxic materials due to health and environmental concerns. Reliability is another important aspect because a failure of the cooling system could lead to the destruction of the PV cells.

A passive convection cooling system for photovoltaic panels utilizes principles of aerodynamics to channel natural air flow across photovoltaic panels to increase the rate of heat transfer and increase the convection rate and decrease the temperature of the photovoltaic panels thereby increasing the efficiency of the solar cells and increasing the durability of the photovoltaic system. There is a wide variety of passive cooling options available. The simplest ones involve solids of high thermal conductivity, like aluminium or copper, and an array of fins or other extruded surfaces to suit the application. More complex systems involve phase changes and various methods for natural circulation.

Active cooling systems are a little bit more complicated. They require additional hardware and costs such as a heat pump device having a refrigerating cycle comprising a compressor, a heat radiator, a decompression device, a heat exchanger etc. The advantage of such a system is the possibility of cogeneration – electrical and thermal energy.

1.7 Spectrally selective solar reflectors SSR

In principle, any transparent conductor film deposited on a reflecting surface exhibits to some degree of spectral selectivity. Aluminium is commonly used as a reflecting material basically due to its very high specula reflectance and its relatively low cost. Parabolic or planar aluminium reflectors are common in concentrating troughs for photovoltaics, but they are not spectrally selective. This leads to the concentration of light that is not useful in the production of electricity in the PV cells and is dissipated in the system as heat

A possible way of reducing the heat buildup on a solar cell is to have only the photons with energy greater than the band gap of the absorber to illuminate the cell. Thus, if the reflecting concentrator is replaced with a spectrally selective reflector (SSR), the SSR should separate the radiation necessary for electricity production from the solar radiation and be directed to the cell (Figure 1.8).

In some materials like transparent conductors, the spectral position of the plasma absorption band can be tailored with doping and can reflect selectively when coated on a reflecting surface by absorbing radiation in the near infra red region with the relationship between plasma frequency ϖ_P and carrier concentration n_e being

$$\omega_{\mathrm{P}}^2 = \frac{n_e q^2}{\varepsilon_0 m_e}. \tag{1.5}$$

where, m_e and q are the electron mass and electron charge respectively while ε_0 is the permittivity of free space.

Some good examples are doped tin oxide, zinc oxide and indium tin oxide. Due to the hardness and inertness of some oxides, they also serve as an excellent protective layer to the aluminum surface.

The ideal properties of an SSR for use with crystalline silicon solar cells are shown in Fig. 1.9. The wavelength λ_c for switching from high to low reflectance lies at 1100 nm and corresponds to the silicon band gap. R_{cell} and R_{therm} are the integrated reflectance values which for a Si solar cell are given by

$$R_{cell} = \frac{\int_{300}^{1100} G(\lambda)R(\lambda)d\lambda}{\int_{300}^{1100} G(\lambda)d\lambda} \quad , \tag{1.6}$$

$$R_{therm} = \frac{\int_{1100}^{2500} G(\lambda)R(\lambda)d\lambda}{\int_{1100}^{2500} G(\lambda)d\lambda} \quad , \tag{1.7}$$

where $G(\lambda)$ is the AM 1.5 solar spectrum [19]. For an SSR with ideal properties, $R_{cell} = 1$ and $R_{therm} = 0$ will ensure that solar radiation in the range $300 < \lambda < 1100$ nm is reflected towards the solar cell while the rest is absorbed by the SSR and hence does not contribute to the heating of the solar cell.

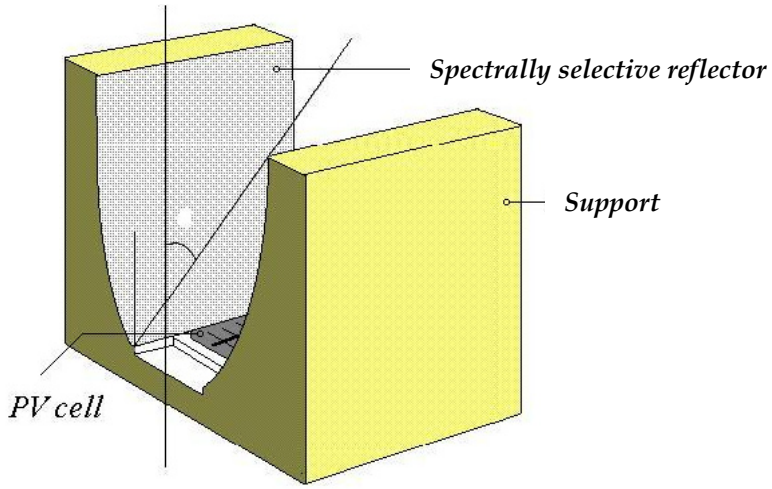

Fig. 1.8. Integration of a spectrally selective reflector surface on a PV concentrator

1.7.1 The SSR model

The basic optical properties of a transparent conductor (TC) coated aluminum reflector are hypothesized. Here energy absorption from plasma oscillations in degenerate transparent-conducting-oxide semiconductor films in combination with a highly reflecting metal substrate can be used in the fabrication of solar selective reflector surfaces (Figure 1.10).

The classical Drude theory for metals is often used to calculate the optical constants n and k for the TCs and Fresnel's formulae is employed for the reflectance simulations.

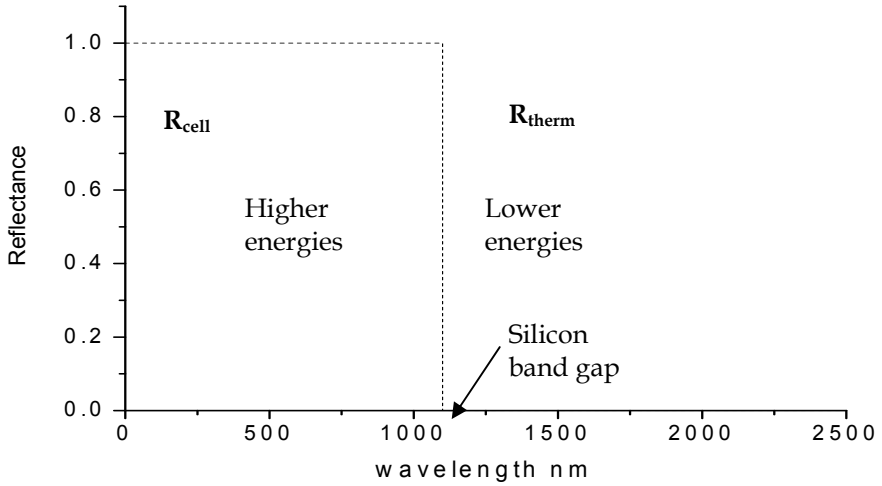

Fig. 1.9. Ideal Reflectance properties of an SSR

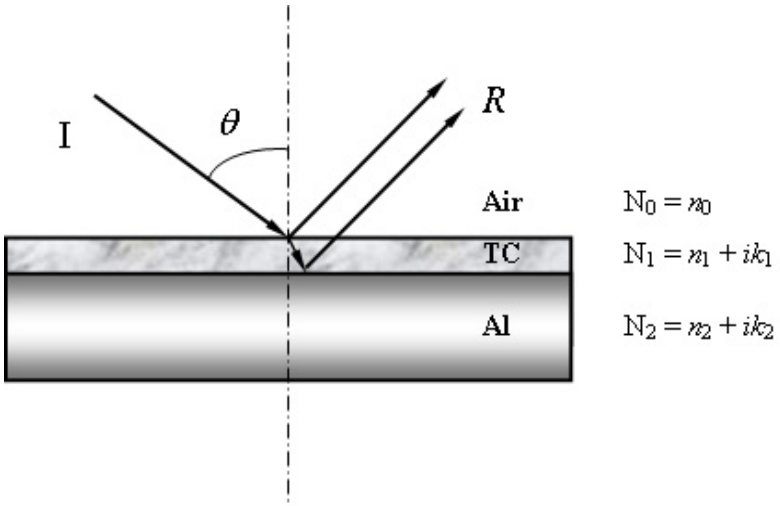

Fig. 1.10. Theoretical model used for the reflectance simulations.

The Drude model gives a phenomenological approach to the problem, based on some of the fundamental material properties of TCs as the DC mobility, the effective mass and the concentration of the free charge carriers. As the plasma absorption shifts to shorter wavelengths for higher doping concentration, an optimum doping can be found theoretically for a specific choice of SSR.

So far two types of SSR surfaces have been studied - one based on fluorine doped tin oxide and the other on niobium doped titanium oxide. For both cases a thin layer of aluminium oxide was sandwiched between the oxide conducting oxide and aluminium. Figure 1.11 shows the optical properties of TiO_2:Nb/Al_2O_3/Al SSR surfaces deposited by DC Magnetron sputtering tailored for Si solar cell application with minimum reflectance centred around 1500 nm.

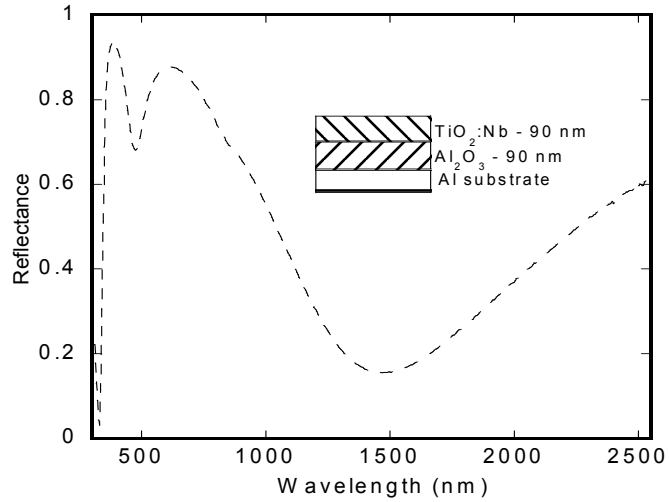

Fig. 1.11. Experimental spectral reflectance for a TiO_2:Nb/Al_2O_3/Al structures. The layer thicknesses are indicated.

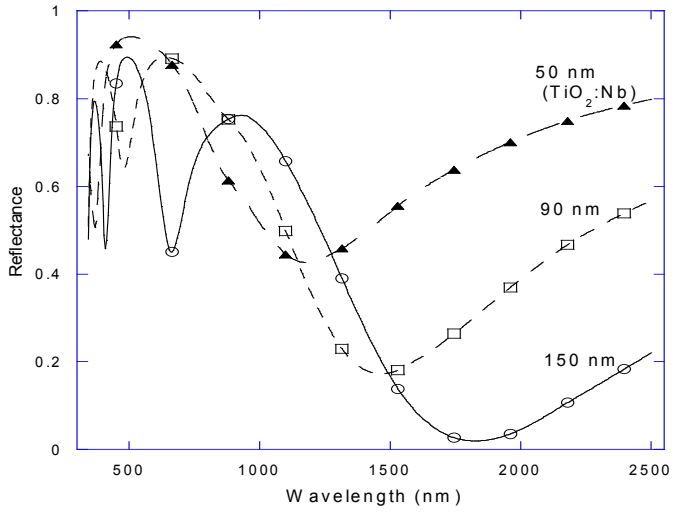

Fig. 1.12. Influence of the thickness of TiO_2:Nb film on the reflectance of the SSR. Al_2O_3 thickness is 90 nm (Maghanga et al, 2011).

Expectedly, the properties of SSR such as those plotted in Figure 1.11 vary with thickness of the layers as shown in Figure 1.12 and 1.13. An optimum must therefore be established which can be achieved by mathematical modelling of the multilayer structure. This requires the knowledge of optical data of the substrate, TCO and the intermediate layer (Maghanga et. al, 2009).

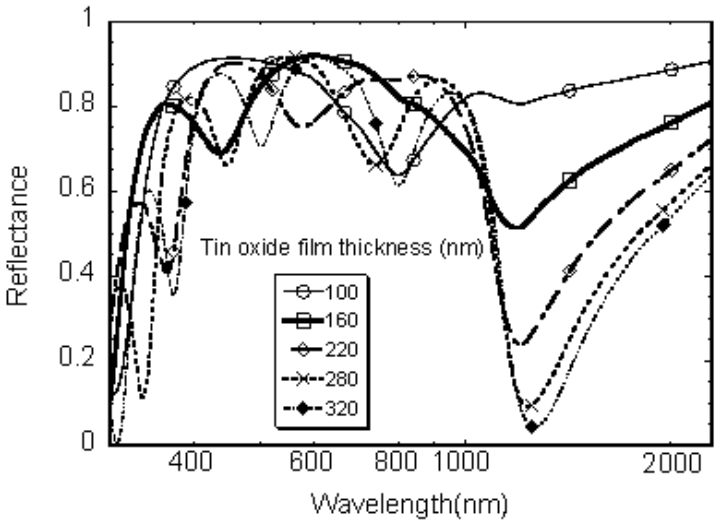

Fig. 1.13. Computed reflectance spectrum for 100, 160, 220, 280 and 320 nm thick fluorine doped tin oxide on aluminum (Mwamburi et al., 2000)

1.7.2 Heat balance on solar cell

The energy conservation equation for concentrator solar cells is crucial is estimating the temperature of the solar cell when concentration varies which for concentrator cells employing parabolic concentrators and can be expressed as

$$\xi\alpha A_o C q_o - \eta\xi\alpha A_o C q_o - A_r \varepsilon\sigma_B (T^4 - T_o^4) - A_c h(T - T_o) = 0\,, \tag{1.8}$$

where the first term denotes the luminous power reflected to the cell with reflectance ξ, the cell surface absorptivity α, the cell area A_o, the geometric concentration ratio C and the energy density q_o. The second term in the equation is the electric power delivered to the external load with the conversion efficiency η. The third term represents the power dissipated through radiation with the surface area A_r, the surface emissivity ε, the Stefan-Boltzmann constant σ_B, the surface temperature T and the ambient temperature T_o. The last term characterizes the power dissipated through convection, which depends on the surface area A_c and the convective transfer coefficient h.

If a cell relies only on the cell surface area for cooling through radiation and convention, equation 1.8 reduces to

$$\xi\alpha C q_o - \eta\xi\alpha C q_o - \varepsilon\sigma_B(T^4 - T_o^4) - h(T - T_o) = 0 \quad (1.9)$$

For case of a concentrator cell employing a reflector material with SSR properties, the cell absorbs only the useful radiation i.e., energy corresponding to the wavelengths $\leq \lambda_C$ while without the SSR property the wavelength range of absorption spans the whole solar spectrum, say $300 \leq \lambda_C \leq 2550nm$. Using the parameters in Table 1, the variation of temperature with concentration for a solar cell with and without an SSR was estimated using equation 1.8 and plotted in Figure 1.14. At low concentration ratios, the cell temperature is low and the difference in temperature between the two cases is small. The effect of the SSR is evident at higher concentration ratios where the temperature of the cell without the SSR is higher than that with the SSR. The model assumes minimum cooling from convection and radiation such that $A_r = 4A_0$ and $A_c = 10A_0$.

Parameter	Description	Value
α	Surface absorptivity of the cell	0.85
η	Efficiency of the cell	0.2
τ_0	Ambient temperature	300 K
H	Convective heat transfer	5 W/m²K
C	Concentration factor	Variable
ε	Emissivity of the cell	0.85

Table 1. Parameters used in calculations of solar cell temperature (Maghanga et. al, 2011)

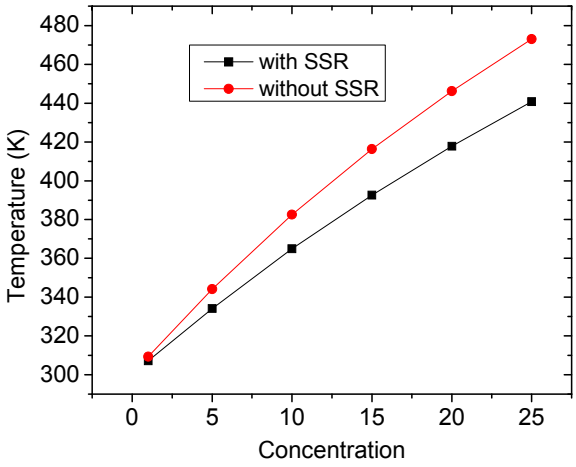

Fig. 1.14. Solar cell temperature *versus* concentration calculated for constructions with and without a SSR. The following values were assumed: $A_r = 4A_0$ and $A_c = 10A_0$ (Maghanga et. al, 2011).

1.7.3 Evaluation of SSR

The extent at which the SSR reflects solar in the region below and above the solar cell band gap E_g can be calculated for silicon solar using equation 1.6 and 1.7. For instance, for the SSR properties shown in Figure 1.11, the R_{cell} and R_{thermal} values are 0.756 and 0.28 respectively. Based on this data, a Figure of Merit (*FOM*) of an SSR can be estimated using the formula (Maghanga et. al, 2011):

$$FOM \approx 0.8 + 0.2\frac{R_{therm}}{R_{cell}}. \tag{1.10}$$

The value attains a minimum value of 0.8 for an ideal SSR and should approach this value as closely as possible for real SSR coatings. For a non-selective reflecting surface, the *FOM* is equal to 1.0.

2. Conclusion

This chapter has explained various loss mechanisms in a pn junction solar cell with emphasis on losses due to heat build-up on concentrator cells. Using the heat balance equation, the chapter has illustrated the possible contribution of the SSR to heat reduction on a solar cell. Specific experimental cases have been cited including a formula that can be used to evaluate the quality of a spectrally selective reflector surface.

3. Acknowledgements

Research based on this work was supported by the International Science Programme of Uppsala University, Sweden through Photovoltaic Group of Moi University, Kenya.

4. References

Blatt F. J. (1991) *Roots of the Quantum Theory in Modern Physics*,.: New York: McGraw Hill Inc.

Brabec C. J. et. al., (2001) "Plastic Solar Cells." In: *Advanced Functional Materials* vol. 11 (1): 15-26.

Brogren M., et. al., (2000) "Optical efficiency of a PV-Thermal hybrid. CPC module for high latitudes." In: *Solar Energy* vol. 69 (1–6):173-185.

Chenlo F., and Cid M. (1987) A linear concentrator photovoltaic module: analysis of non-uniform illumination and temperature effects on efficiency." In: *Solar Cells* vol. 20: 27-39.

Dalal V. L. and Moore A. R. (1977) "Design considerations for high-intensity solar cells." In: *Journal of Applied Physics* vol. 48 (3): 1244-1251.

Duffie J. A. and Beckman W. A. (1991) *Solar radiation, Atmosphere attenuation of solar radiation in Solar Energy of Thermal Process*, New York: John Wiley & Sons.

Edenburn M. W., and Burns J. R. (1981) "Shading analysis of a photovoltaic cell string illuminated by a parabolic trough concentrator." *Conference record* 15th IEEE PVSC: 63 –68.

Fahrenbruch, A. and Bube, R.H. (1983) *Fundamentals of solar cells*. Orlando: Academic Press..

Goetzberger A. and Hebling C. (2000) "Photovoltaic materials, past, present, future." In: *Solar Energy Materials and Solar Cells*, vol. 62 (1-2): 1-19.

Green M. A. (1992) *Solar Cells: Operating Principles, Technology and System Applications*. Kensington: University of New South Wales.

Hoffmann W. (2006) "PV solar electricity industry: market growth and perspective." *Solar Energy Materials & Solar Cells* vol. 90: 3285-3311.

Horne W. E. (1993) Solar energy system, patent US5269851, USA.

ISO 9845-1 (1992) Solar energy – Reference solar spectral irradiance at the ground at different receiving conditions. Part 1: Direct normal and hemispherical solar irradiance for air mass 1.5.

Kreith, F., and Kreider, J. F. (1978) *Principles of Solar Engineering*. New York: McGraw-Hill.

Kreske K. (2002) "Optical design of a solar flux homogenizer for concentrator photovoltaics." , In: *Applied optics* vol. 41: 2053-2058.

Kurtz S. and Lewandowski A. (2004) *Recent Progress and Future Potential for Concentrating Photovoltaic Power Systems,* World Renewable Energy Congress VIII and Expo Denver, Colorado.

Luque A., et. al., (1998) Sala G., and Arboiro J.C. "Electric and thermal model for non-uniformly illuminated concentration cells." In: *Solar Energy Materials and Solar Cells* vol. 51: 269-290.

Maghanga C. M,. Niklasson. G. A and. Granqvist C. G, (2009) Optical Properties of Sputter Deposited Transparent and Conducting TiO_2:Nb Films Thin Solid Films, 518 1254-1258

Maghanga C.M., Niklasson G.A., Granqvist C.G., Mwamburi M. M., (2011), Spectrally selective reflector surfaces for heat reduction in concentrator solar cells: Modeling and applications of TiO2:Nb-based thin films, *Applied Optics 50 (16) 1-8.*

Markvart. T, (1994) Solar Electricity. John Wiley and Sons.

Mathur R.K., et. al., (1984) "Thermal non-uniformities in concentrator solar cells." In: *Solar Cells*, vol. 11: 175-178.

McVeigh J. C. (1977) *Solar Radiation in Sun Power.* Oxford: Pergamon Press.

Merrill J. and Senft D. C., (2007) "Directions and Materials Challenges in High-Performance Photovoltaics." In: *Journal of the Minerals, Metals and Materials Society*, *Springer* vol. 59: 26-30.

Mwamburi M., and Wäckelgård E. (2000) "Doped tin oxide coated aluminium solar selective reflector surfaces," In: *Solar Energy* vol. 68: 371-378.

Mwamburi M., et. al., (2000) "Preparation and characterisation of solar selective SnOx:F coated aluminium reflector surfaces," In: *Thin Solid Films* 374: 1-9.

Royne A, Dey J. C., and Mills R. D. (2005) "Cooling of photo- voltaic cells under concentrated illumination: A critical review." In: *Solar Energy Materials & Solar Cells* vol. 86: 451-483.

Sen Z. (2004) "Solar Energy in Progress and Future Research trends." In: *Progress in Energy and Combustion Science* vol. 30 (4): 367- 416.

Shah A. V., et. al., (2004) "Thin-film silicon solar cell technology." In: *Progress in Photovoltaics: Research and Applications*, vol. 12 (2-3): 113-142.

SunPower, (2002) Application notes for HED312 Silicon Concentrator Solar Cell.

Sze, S. M. (1991) *Physics of Semiconductor devices.* New Delhi: Wiley Eastern Limited.

Takamoto T., et. al., (2006) "InGaP/GaAs-based multijunction solar cells." In: *Progress in Photovoltaics: Research and Applications* vol. 13: 495-511,

Winston R. (1974) "Principles of solar concentrators of a novel design." In: *Solar Energy* vol. 16: 89-95.

Wysocki J.J and Rappaport P. (1960) "Effect of temperature on photovoltaic solar energy conversion." In: *Journal of Applied Physics* vol. 31 (1960): 571-578.

Yamaguchi M., et. al., (2006) "Super high-efficiency multi-junction and concentrator solar cells." In: *Solar Energy Materials and Solar Cells* vol. 90: (18-19), 3068-3077

14

Issues on Interfacing Problematics in PV Generator and MPP-Tracking Converters

Teuvo Suntio
Tampere University of Technology,
Department of Electrical Energy Engineering
Finland

1. Introduction

The need for large-scale harvesting of renewable and clean energy such as solar or photovoltaic (PV) energy has been recently fully recognized for reducing greenhouse gas emissions and securing the availability of energy in the future (Bull, 2001; Bose, 2010; Rahman, 2008). PV energy can be utilized by converting it into thermal energy or directly to electrical energy by means of solar cells (Rahman, 2008).

The simplified electrical equivalent model of a solar cell composes of a photocurrent source and a diode connected across the current source as depicted in Fig. 1a (Lyi & Dougal, 2002; Villalva, et al., 2009). The solar cell is a highly non-linear and non-ideal current source yielding limited output voltage and power as depicted in Fig. 1b. In addition with the non-linear static terminal behaviour, its dynamic behaviour in terms of dynamic resistance and capacitance is equally non-linear and dependent on the operating point (Anantha Krishna, et al., 2011; Kumar, et al., 2006; Mäki, et al., 2010; Thongpron, et al., 2006). Typical maximum voltage of a single-junction silicon cell is in the order of 0.5 V (Kumar, et al., 2006). As a consequence, a large number of cells usually have to be connected in series to form a PV generator for fulfilling the practical solar energy harvesting.

In order to maximally utilize the energy provided by the PV generator, its operating point has to be kept at the maximum power point (MPP) (Fig. 1b, the point (1,1)), where the static and dynamic resistances coincide (Thongpron, et al., 2006; Xiao, et al., 2007a) according to the maximum power theorem (MacLaughlin & Kaiser, 2007). Innumerable methods and algorithms have been developed for tracing the location of the MPP as discussed e.g. in (Esram & Chapman, 2007; Jain & Agarwal, 2007; Salas, et al., 2006).

The output of a PV generator is very seldom suited as such for powering the load because of its highly varying terminal characteristics due to the changes in the environmental conditions such as ambient temperature, level of irradiation, cloud passing, etc. The terminal characteristics in Fig. 1b imply that the PV generator exhibits both constant-current-source behaviour and constant-voltage-source behaviour as well. The dynamic characteristics (i.e., the dynamic resistance (r_{sc})) in Fig. 1b confirm also the dual source nature. In practice, this means that the interfacing can be accomplished either by using voltage-fed (VF) or current-fed (CF) converters (Capel, et al., 1983) but the different

interfacing constraints such as the validity of Kirchhoff's current law and stability under output-side feedback control have to be carefully considered (Suntio, et al., 2010a&b).

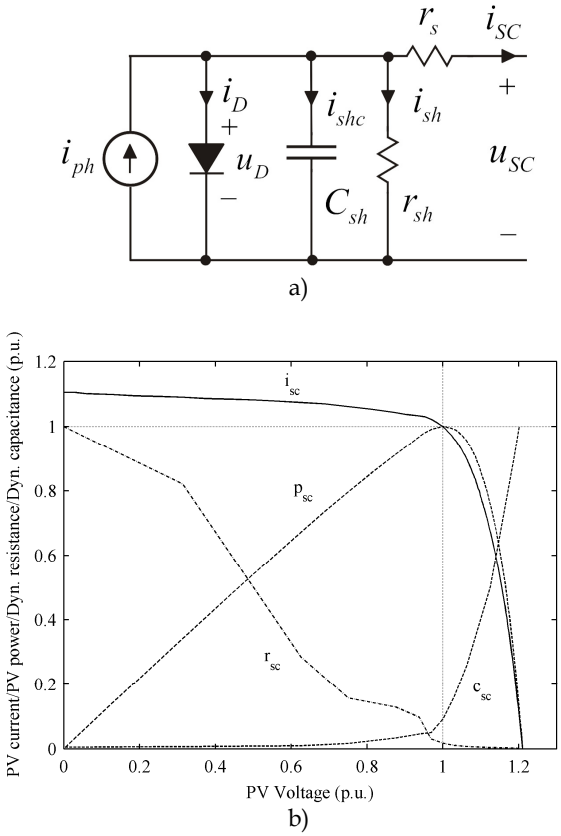

Fig. 1. Solar cell characteristics: a) Simplified electrical model, and b) static and dynamic terminal characteristics as normalized I/U, P/U, r/U, and c/U curves

In order to supply maximum power from the energy source, the feedback-control arrangement shall be such that the input-side feedback loop is the outmost loop within every converter in the process as depicted in Fig. 2. The dual source nature of the PV generator makes it possible to use either conventional VF converters or CF converters as the interfacing media. According to control engineering principles (Suntio, 2009), the input current of a VF converter and the input voltage of a CF converter have to be used as the feedback variables. This means, in practice, that the feedback arrangements determine also the nature and dynamic behaviour of the converter. Despite this fact, it is usual that the distinction between the VF and CF interfacing converters is not made but all the converters are considered to be conventional VF converters as in (Dehbonei, et al., 2009a&b; Femia, et al., 2008) even if special control arrangements (i.e., inversing the polarity of the feedback and reference signals in the controller) have to be made for proper operation as explicitly shown e.g. in (Siri, 2001). The same applies also to the grid-connected inverters in the renewable

energy applications as depicted in Fig. 2. The lack of real recognition of the static and dynamic differences in the converters compared to the conventional converters has led to a situation, where the proposed PV converters have not been tested by using a proper input source as discussed e.g. in (Menti, et al., 2011; Sanchis, et al., 2007). Therefore, the suitability of the converter for the intended application has to be carefully tested by using a real PV generator or a solar array simulator, which is known to have the same static and dynamic properties as the real PV generator.

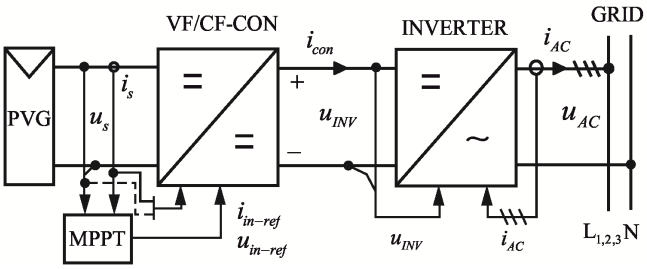

Fig. 2. Principle of grid-connected PV energy system in grid-parallel operation mode

According to (Petrone, et al., 2008), there are a number of issues related to the MPP-tracking converters and grid-connected inverters, which reduce the reliability of the PV energy systems. One of those issues is the stability of the interconnected system, which can be assessed at an arbitrary interface within the system by means of the small-signal impedances determined for the upstream (source) and downstream (load) subsystems at the selected interface (Middlebrook, 1976; Suntio, et al., 2010a&b; Zenger, et al., 2006).

The rest of the chapter will treat the topics discussed above more in detail and is organized as follows: The basic static and dynamic properties of a real PV panel are introduced in Section 2 including the effect of partial shading (Wang&Hsu, 2011) as well as the characterization of a certain commercial solar array simulator as a substitute for the real PV generator. General dynamic representations of interfacing converters are given in Section 3 including the parameters affecting mostly the quality of the interfacing as well as stability of the system. A short introduction to the implementation CF converters is given in Section 4. Experimental evidence is provided in Section 5 to validate the theoretical findings presented in Section 3. Section 6 summarizes the topics of the chapter and recommends further actions to be taken.

2. Basic properties of a PV generator

The current-voltage characteristics of a PV cell can be represented with sufficient accuracy by using the single-diode equation given in (1) (Lyi & Dougal, 2002), where i_{sc} and u_{sc} are the current and voltage of the cell, i_{ph} is the light-generated current, i_0 the diode saturation current, r_s the series resistance, r_{sh} the shunt resistance, A the diode ideality factor, k the Boltzmann constant, T the cell temperature, and q the elementary charge. The PV generator consists of series-connected cells. As a consequence, its current-voltage characteristics can be given by adding the effect of the number of series-connected cells N_s in the single-diode equation as shown in (1). Naturally, $N_s = 1$ for a single cell.

$$i = i_{ph} - i_0 \left[\exp\left(\frac{u_{sc} + r_s i_{sc}}{N_s AkT / q} \right) - 1 \right] - \frac{u_{sc} + r_s i_{sc}}{r_{sh}} \quad (1)$$

The electrical equivalent circuit corresponding to (1) is given in Fig. 1a. The behaviour of the dynamic resistance (r) and capacitance (c) of the PV module (See Fig. 1) can be easily understood based on the behaviour of a silicon diode and constant-current source: If the diode current is low, the resistance of the circuit is high and capacitance low. The increase in the diode current reduces the resistance and increases the capacitance. The circuit exhibits lowest resistance and highest capacitance at the open-circuit condition, because all the photocurrent is flowing through the diode.

The silicon diode has a negative temperature coefficient approximately of -2.5 mV/^{o}C (Anantha Krishna, et al., 2011). This means that the voltage and maximum output power of the PV generator decreases along the increase in the cell temperature and vice versa but the photocurrent remains effectively constant. The effect of the temperature on the resistance and capacitance is such that the resistance decreases and capacitance increases along the increase in the temperature and naturally vice versa.

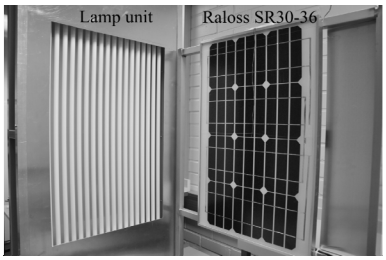

Fig. 3. Fluorescent lamp unit and Raloss SR30-36 PV module

The above described behaviour of the dynamic parameters without the temperature effect is clearly visible in Fig. 1b, where all the curves represent normalized measured data from an actual PV module of Raloss SR30-36, which is illuminated by using a lamp unit shown in Fig. 3 producing illumination of 500 W/m^2. The corresponding short-circuit current and open-circuit voltage are 1.0 A and 19.2 V as well as the MPP current and voltage 0.91 A and 16.0 V at the module temperature of 44 ^{o}C, respectively.

The experimental frequency responses shown below are extracted from the PV module by means of Venable Industries' frequency response analyzer Model 3120 with an impedance measurement kit. The dynamic resistance is extracted from the measurements at the frequency of 100 Hz. The dynamic capacitance is extracted based on the cut-off frequency of the first-order filter behaviour or the resonant frequency caused by the cabling inductance of 2 μH and the capacitance of the generator.

2.1 Dynamic resistance and capacitance

The measured output impedances of Raloss SR30-36 panel from the short-circuit (SC) to open-circuit (OC) conditions are shown in Fig. 4. The low-frequency dynamic resistance is explicitly normal positive resistance not negative resistance as assumed e.g. by (Xiao, et al.,

2007a). It is extremely important that the behaviour of the low-frequency dynamic resistance is correctly considered when analyzing its effect on the dynamic behaviour of the interfacing converters, otherwise the result of the dynamic analyses are incorrect as e.g. in (Xiao, et al., 2007a&b; Femia, et al., 2008). The measured dynamic resistance at the dark current conditions as in (Xiao, et al., 2007a) does not correctly match with the real dynamic resistance experienced at the illuminated or normal conditions as clearly shown in (Mäki, et. al., 2010).

The extracted operating-point-dependent dynamic resistance and capacitance values are shown in Fig. 5, where the normalizing factors are 1 kΩ and 22 µF, respectively. Fig. 6 shows the behaviour of the static ($r_{con} = U_{pv}/I_{pv}$) and dynamic resistance (r_{sg}) of the PV panel in the vicinity of the MPP: The resistances coincide at the MPP.

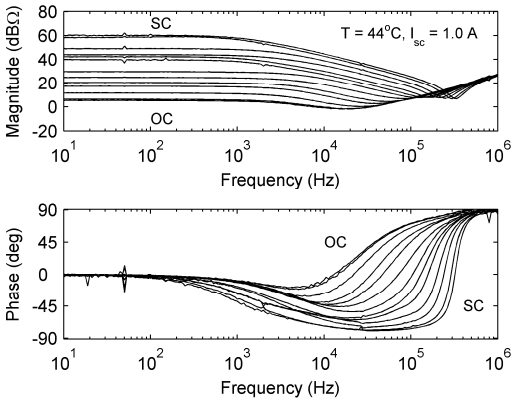

Fig. 4. The measured output impedances of Raloss SR30-36 panel from the short-circuit (SC) to open-circuit (OC) conditions

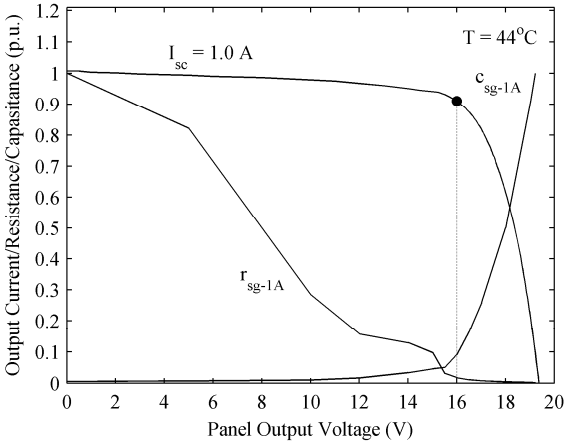

Fig. 5. The measured dynamic resistance and capacitance, where the scaling factors are 1 kΩ and 22 µF

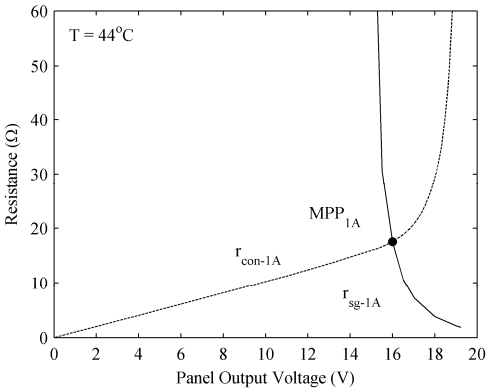

Fig. 6. The behaviour of the static (r_{con-1A}) and dynamic (r_{sg-1A}) resistances in the vicinity of MPP

2.2 Shading effect

Two Raloss SR30-36 panels were connected in series and Schotky-type shunt diodes were connected across each panel. One of the panels was illuminated as defined above and the other with reduced illumination yielding short-circuit current of 0.3 A, respectively. Fig. 7 shows the measured IU curves for the individual panels (I_{sg-1}, I_{sg-2}) and the series connection (I_{sg-tot})) of them. The behaviour of the dynamic resistance is shown in Fig. 8, respectively.

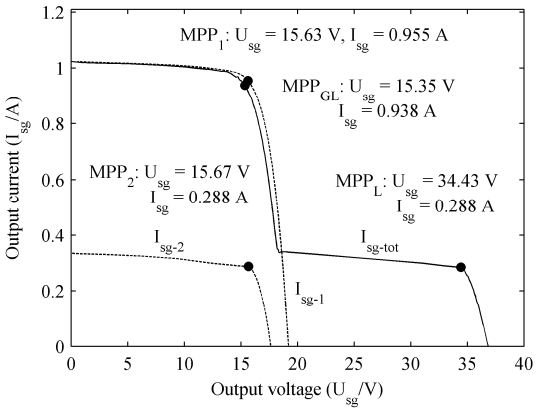

Fig. 7. The static IU curves of the individual panels and their series connection

The static and dynamic resistances will coincide at each of the MPPs. Fig. 8 implies also clearly that each of the MPPs divides the operation of the PV generator into constant-current and constant-voltage sub-regions, which will limit the operation of the VF converters in the constant-voltage region at the voltages higher than the highest-voltage MPP. The behaviour of the dynamic resistance implies also problems for the performance of the incremental-conductance-based methods to locate the real global MPP.

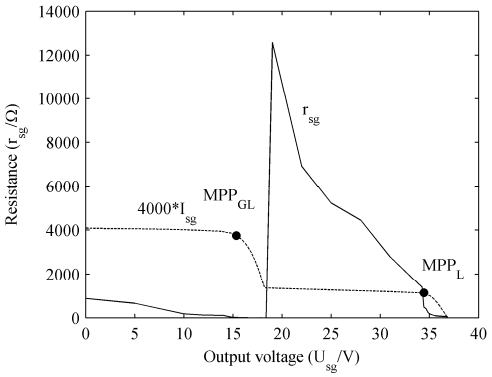

Fig. 8. The behaviour of the dynamic resistance r_{sg} of the series connected panels

2.3 Solar array simulator

It is not very well understood that the PV generator has unique properties resembling both constant-current and constant-voltage sources. As a consequence of this, the PV generator is most often considered to be just a voltage source with rather high output impedance especially when a capacitor is always connected between the PV generator and the interfacing converter. Therefore, the proposed converters may not be tested at all by using a real PV generator or a source simulator having the dynamic properties similar to the real PV generator (Menti, et al., 2011; Sanchis, et al., 2007). Usually a pure constant-voltage source with a small resistance in series is only used as in (Park, et al., 2006). As discussed above, it is, however, extremely important that the input source has the characteristics of a PV generator especially in respect to the dynamic-impedance behaviour.

A certain commercial solar array simulator (SAS) was programmed to emulate the behaviour of the Raloss SR30-36 panel by using the voltage and current of the three remarkable points (OC, SC, and MPP) (Villalva, et al., 2009). The resulting static IU curves are presented in Fig. 9 showing a perfect match in the constant-current region but a slight deviation in the constant voltage region.

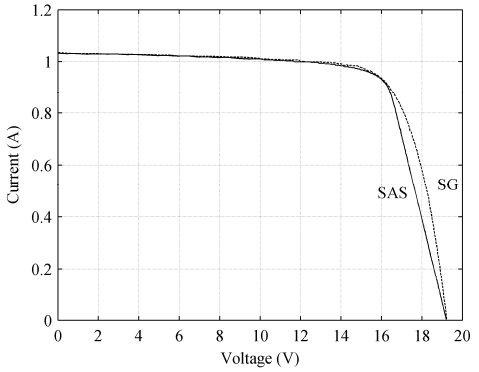

Fig. 9. The measured static IU curves of the Raloss panel (SG) and the solar array simulator (SAS)

The frequency responses of the solar array simulator were measured and the dynamic resistance was extracted similarly to the Raloss panel. The comparison of the dynamic resistances is shown in Fig. 10, where Fig. 10a shows the overall behaviour of resistances, and Fig. 10b, the behaviour of resistances in the vicinity of the MPP. The overall dynamic resistance of the SAS emulates quite well the dynamic resistance of the Raloss panel. It can be expected that the testing with such an input source would very well ensure the working of the tested converters also in the practical applications. The reason for the inaccuracy of the static curve in the constant-voltage region is the method to establish the output resistance as a constant value of approximately three ohms as shown in Fig. 10b.

A multitude of proposed techniques to design solar array simulators can be found in the open literature but they are very seldom characterized in such way that their dynamic properties are shown. The correct dynamic behaviour of the electronic solar array simulator may be possible only when the base of the simulator is a real current source.

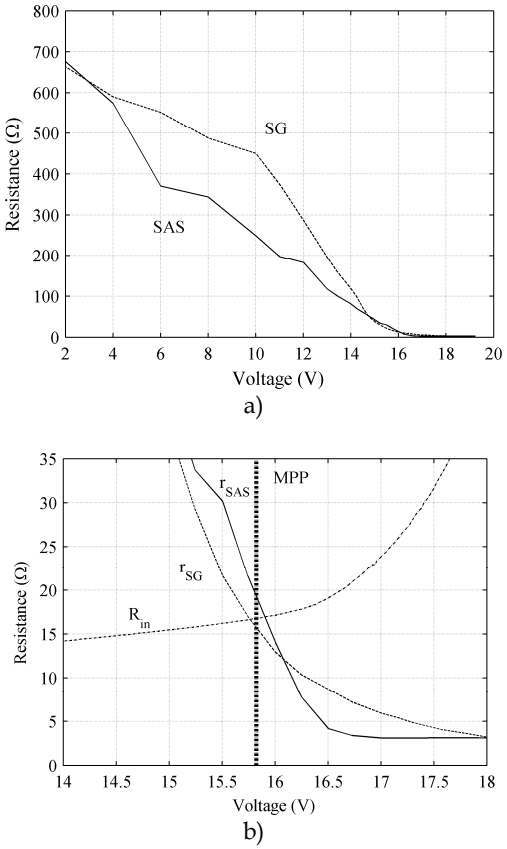

Fig. 10. The comparison of dynamic resistances of the Raloss panel (r_{SG}) and a commercial solar array simulator (r_{SAS}): a) Overall impedance behaviour, and b) behaviour in the vicinity of the MPP, where R_{in} is the static resistance of the PV generator and the simulator

3. General dynamic representations

The dynamics of a switched-mode converter can be represented by using certain two-port-network parameters, which are uniquely determined by the input and output sources as well as the output variable kept constant (Suntio, 2009). It shall be noted that a resistor as a load does not change the output mode of a converter but the load has to be either a constant-current or constant-voltage-type source. In general, the converters can be classified as voltage and current-fed converters based on their actual input source. Their output mode can be further classified into voltage and current. As a consequence, there exist four different types of converters- namely voltage-to-voltage, voltage-to-current, current-to-current, and current-to-voltage converters, which can be represented by means of G, Y, H, and Z network parameters, respectively (Tse, 1998). The corresponding two-port models are shown in Fig. 11. The output mode in Fig. 11 is visible as the dual of the ideal load. It shall be also noted that the direction of the output current is opposite what is used in the theoretical two-port-network models (Tse, 1998).

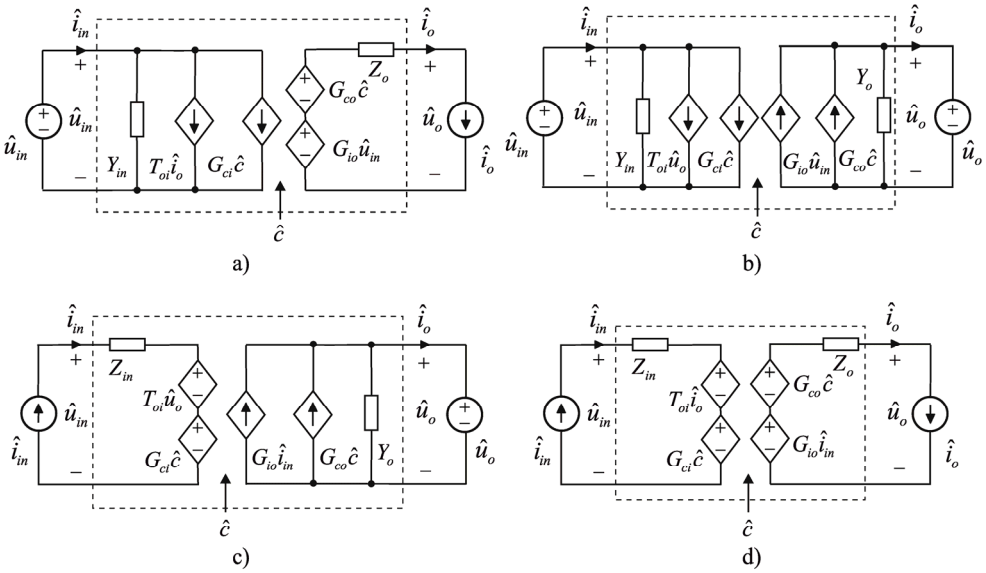

Fig. 11. Linear two-port models representing converters defined by a) G, b) Y, c) H, and d) Z parameters

According to Fig. 11, it may be obvious that only the current-fed converters (Figs. 11c&d) can offer an ideal interfacing condition for the PV generator due to its current-source nature at the input terminal, because the ideal interfacing requires the existence of duality in the connection interface (Suntio, et al., 2010b). The voltage-fed converters (Fig. 11a&b) are prone to the violation of Kirchhoff's current law when the operating point moves into the voltages below the MPP (Suntio, et al., 2010a). The nature of the input port shown in Fig. 11 is valid also at steady state justifying the above presented conclusions.

3.1 General treatment of the converter dynamics

The two-port models shown in Fig. 11 can be equally represented by using matrix representations having typically three input variables $\left[\hat{x}_{\text{in}} \quad \hat{x}_{\text{out}} \quad \hat{x}_{\text{c}}\right]^T$ and two output variables $\left[\hat{y}_{\text{in}} \quad \hat{y}_{\text{out}}\right]^T$, where the subscript 'in' denotes the variables at the input terminal, 'out' the variables at the output terminal, and 'c' the general control variable. The variables can be either voltage or current. This yields six transfer functions G_{ij} shown in (2). The sign of the transfer function G_{22} is minus, because the direction of current at the output terminal is opposite (See Fig. 11) what is generally defined for the two-port networks as shown in (Tse, 1998).

$$\begin{bmatrix} \hat{y}_{\text{in}} \\ \hat{y}_{\text{out}} \end{bmatrix} = \begin{bmatrix} G_{11} & G_{12} & G_{13} \\ G_{21} & -G_{22} & G_{23} \end{bmatrix} \begin{bmatrix} \hat{x}_{\text{in}} \\ \hat{x}_{\text{out}} \\ \hat{x}_{\text{c}} \end{bmatrix} \tag{2}$$

3.1.1 Converter under feedback control

According to the control engineering principles (Suntio, 2009), the feedback can be based only on the output variables of the system (i.e., $\hat{y}_{\text{in}}$ and $\hat{y}_{\text{out}}$) yielding two different sets of closed-loop transfer functions. Under the input-side feedback control, the closed-loop transfer functions can be presented as shown in (3) based on Fig. 12, where the subscript 'o' denotes the open-loop transfer functions, $L_{\text{in}} = G_{\text{se-in}} G_{\text{a}} G_{\text{c-in}} G_{13}$ the input-side loop gain, $G_{\text{se-in}}$ the input-side sensor gain, G_{a} the modulator gain, and $G_{\text{c-in}}$ input-side-controller transfer function, respectively. Input variable $\hat{x}_{\text{r-in}}$ is the reference for the controlled variable. The special transfer functions $G_{21-\infty}$ and $G_{22-\infty}$ are known as certain ideal output-side transfer functions and defined in (4).

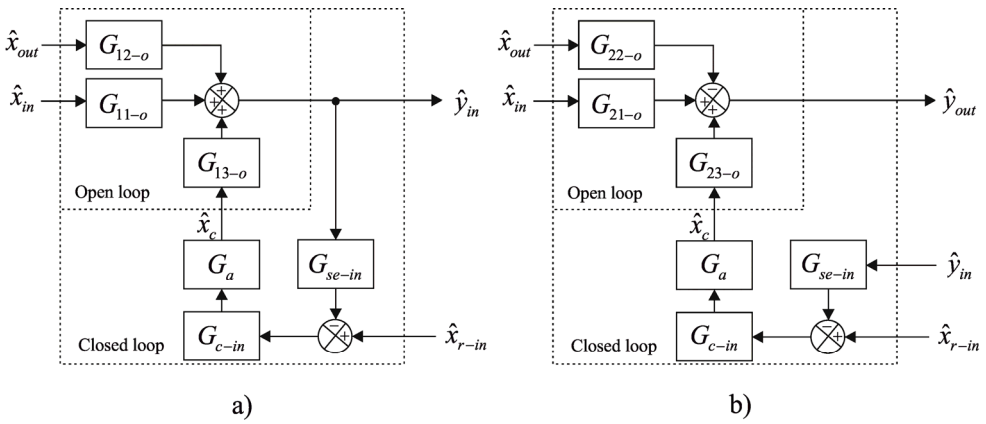

Fig. 12. General closed-loop a) input and b) output control block diagrams under input-side control

$$\begin{bmatrix} \hat{y}_{\text{in}} \\ \hat{y}_{\text{out}} \end{bmatrix} = \begin{bmatrix} \dfrac{G_{11\text{-o}}}{1+L_{\text{in}}} & \dfrac{G_{12\text{-o}}}{1+L_{\text{in}}} & \dfrac{1}{G_{\text{se-in}}}\dfrac{L_{\text{in}}}{1+L_{\text{in}}} \\ \left(\dfrac{G_{21\text{-o}}}{1+L_{\text{in}}}+\dfrac{L_{\text{in}}G_{21\text{-}\infty}}{1+L_{\text{in}}}\right) & -\left(\dfrac{G_{22\text{-o}}}{1+L_{\text{in}}}+\dfrac{L_{\text{in}}G_{22\text{-}\infty}}{1+L_{\text{in}}}\right) & \dfrac{G_{23\text{-o}}}{G_{\text{se-in}}E_{13\text{-o}}}\dfrac{L_{\text{in}}}{1+L_{\text{in}}} \end{bmatrix} \begin{bmatrix} \hat{x}_{\text{in}} \\ \hat{x}_{\text{out}} \\ \hat{x}_{\text{r-in}} \end{bmatrix} \tag{3}$$

$$G_{21\text{-}\infty} = G_{21\text{-o}} - \frac{G_{11\text{-o}}G_{23\text{-o}}}{G_{13\text{-o}}} \qquad G_{22\text{-}\infty} = G_{22\text{-o}} + \frac{G_{12\text{-o}}G_{23\text{-o}}}{G_{13\text{-o}}} \tag{4}$$

Under the output-side control, the closed-loop transfer functions can be presented as shown in (5) based on Fig. 13, where the subscript 'o' denotes open-loop transfer functions, $L_{\text{out}} = G_{\text{se-out}}G_{\text{a}}G_{\text{c-out}}G_{23}$ the output-side loop gain, $G_{\text{se-out}}$ the output-side sensor gain, G_{a} the modulator gain, and $G_{\text{c-out}}$ output-side-controller transfer function, respectively. Input variable $\hat{x}_{\text{r-out}}$ is the reference for the controlled variable. The special transfer functions $G_{11-\infty}$ and $G_{12-\infty}$ are known as certain ideal input-side transfer functions and defined in (6).

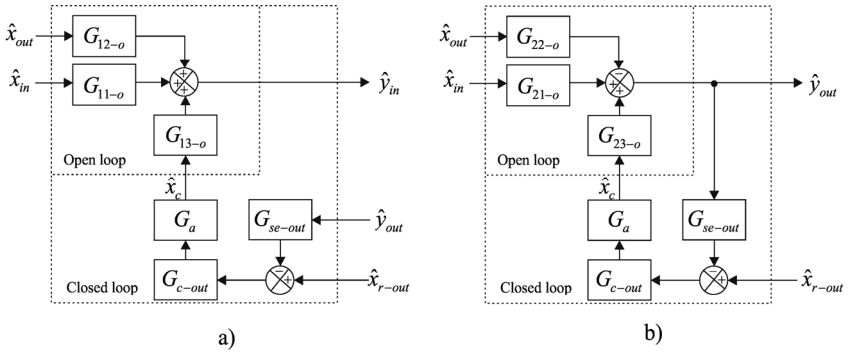

Fig. 13. General closed-loop a) input and b) output control block diagrams under output-side control

$$\begin{bmatrix} \hat{y}_{\text{in}} \\ \hat{y}_{\text{out}} \end{bmatrix} = \begin{bmatrix} \left(\dfrac{G_{11\text{-o}}}{1+L_{\text{out}}}+\dfrac{L_{\text{out}}G_{11\text{-}\infty}}{1+L_{\text{out}}}\right) & \left(\dfrac{G_{12\text{-o}}}{1+L_{\text{out}}}+\dfrac{L_{\text{out}}G_{12\text{-}\infty}}{1+L_{\text{out}}}\right) & \dfrac{G_{13\text{-o}}}{G_{\text{se-out}}G_{23\text{-o}}}\dfrac{L_{\text{out}}}{1+L_{\text{out}}} \\ \dfrac{G_{21\text{-o}}}{1+L_{\text{out}}} & -\dfrac{G_{22\text{-o}}}{1+L_{\text{out}}} & \dfrac{1}{G_{\text{se-out}}}\dfrac{L_{\text{out}}}{1+L_{\text{out}}} \end{bmatrix} \begin{bmatrix} \hat{x}_{\text{in}} \\ \hat{x}_{\text{out}} \\ \hat{x}_{\text{r-out}} \end{bmatrix} \tag{5}$$

$$G_{11\text{-}\infty} = G_{11\text{-o}} - \frac{G_{21\text{-o}}G_{13\text{-o}}}{G_{23\text{-o}}} \qquad G_{12\text{-}\infty} = G_{12\text{-o}} + \frac{G_{21\text{-o}}G_{13\text{-o}}}{G_{23\text{-o}}} \tag{6}$$

The ideal transfer functions defined in (4) and (6) reserves their values despite the state of any feedback and they are usually also specific for a given topology (Suntio, 2009). It may be also obvious that they usually define, especially, the low-frequency behaviour of the corresponding closed-loop transfer functions. The low-frequency value of the ideal transfer function $G_{11-\infty} \approx -Y_{\text{in}} / X_{\text{in}}$ (Suntio, 2009), which is usually the origin of the instability problems in the interfacing of a PV generator.

3.1.2 Source and load interactions

The input and output sources are, in practice, non-ideal containing some source impedance, which may significantly affect the dynamic performance of the converter in terms of transient behaviour and stability. The source effect can be computed, in general, based on Fig. 14, where the converter subsystem **C** is connected in cascade with the source subsystem **S** containing either voltage or current source with an internal ohmic non-ideality denoted by S_{22}. The input variables of the system are denoted by ($\hat{x}_{\text{in1}}, \hat{x}_{\text{out2}}, \hat{x}_c$), the output variables by ($\hat{y}_{\text{in1}}, \hat{y}_{\text{out2}}$), and the intermediate variables by ($\hat{x}_{\text{s}}, \hat{y}_{\text{s}}$), respectively. The dynamic representations of the subsystems are given in (7), and the source-affected representation of the converter in (8), respectively, where $G_{11\text{-xo}}$ (9) denote the ohmic characteristics of the input port when the output port is either short circuited (sc) or open circuit (oc) depending on the nature of the ideal load (i.e., the output port is terminated with the inverse of the ideal load impedance). According to (8), the ideal transfer function $G_{11\text{-}\infty}$ (6) determines partly the source effect on the control-to-output transfer function G_{23}, i.e., the output control dynamics.

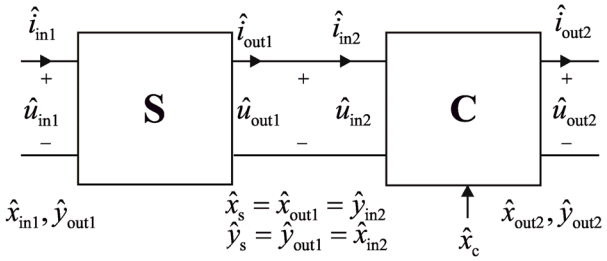

Fig. 14. The cascaded connection of the non-ideal source and the converter

$$\begin{bmatrix} \hat{y}_{\text{in1}} \\ \hat{y}_{\text{s}} \end{bmatrix} = \begin{bmatrix} 0 & 1 \\ 1 & -S_{22} \end{bmatrix} \begin{bmatrix} \hat{x}_{\text{in1}} \\ \hat{x}_{\text{s}} \end{bmatrix} \quad \begin{bmatrix} \hat{x}_{\text{s}} \\ \hat{y}_{\text{out2}} \end{bmatrix} = \begin{bmatrix} G_{11} & G_{12} & G_{13} \\ G_{21} & -G_{22} & G_{23} \end{bmatrix} \begin{bmatrix} \hat{y}_{\text{s}} \\ \hat{x}_{\text{out2}} \\ \hat{x}_{\text{c}} \end{bmatrix} \tag{7}$$

$$\begin{bmatrix} \hat{y}_{\text{in2}} \\ \hat{y}_{\text{out2}} \end{bmatrix} = \begin{bmatrix} \dfrac{G_{11}}{1+S_{22}G_{11}} & \dfrac{G_{12}}{1+S_{22}G_{11}} & \dfrac{G_{13}}{1+S_{22}G_{11}} \\ \dfrac{G_{21}}{1+S_{22}G_{11}} & -\dfrac{1+S_{22}G_{11\text{-xo}}}{1+S_{22}G_{11}}G_{22} & \dfrac{1+S_{22}G_{11\text{-}\infty}}{1+S_{22}G_{11}}G_{23} \end{bmatrix} \begin{bmatrix} \hat{x}_{\text{in1}} \\ \hat{x}_{\text{out2}} \\ \hat{x}_{\text{c}} \end{bmatrix} \tag{8}$$

$$G_{11\text{-xo}} = G_{11\text{-sco}} = G_{11\text{-oco}} = G_{11} + \frac{G_{12}G_{21}}{G_{22}} \tag{9}$$

The load effect can be computed based on Fig. 15, where the converter subsystem **C** is connected in cascade with the load subsystem **L** containing either a current or voltage sink with the internal ohmic non-ideality denoted by L_{11}. The input, output, and intermediate variables are the same as defined above. The dynamic representations of the subsystems are

given in (10), and the load-affected representation of the converter in (11), respectively, where $G_{22\text{-xi}}$ (12) denote the ohmic characteristics of the output port when the input port is either open circuit (oc) or short circuited (sc) depending on the nature of the ideal source (i.e., the input port is terminated with the inverse of the impedance of the ideal load). According to (11), the ideal transfer function $G_{22\text{-}\infty}$ (4) determines partly the source effect on the control-to-input transfer function G_{13}, i.e., the input control dynamics.

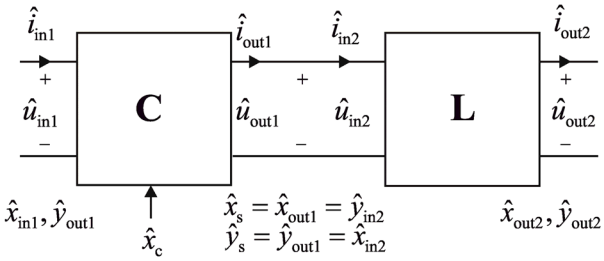

Fig. 15. The cascaded connection of the converter and the non-ideal load

$$\begin{bmatrix} \hat{y}_{\text{in1}} \\ \hat{y}_{\text{s}} \end{bmatrix} = \begin{bmatrix} G_{11} & G_{12} & G_{13} \\ G_{21} & -G_{22} & G_{23} \end{bmatrix} \begin{bmatrix} \hat{x}_{\text{in1}} \\ \hat{x}_{\text{s}} \\ \hat{x}_{\text{c}} \end{bmatrix} \qquad \begin{bmatrix} \hat{x}_{\text{s}} \\ \hat{y}_{\text{out2}} \end{bmatrix} = \begin{bmatrix} L_{11} & 1 \\ 1 & 0 \end{bmatrix} \begin{bmatrix} \hat{y}_{\text{s}} \\ \hat{x}_{\text{out2}} \end{bmatrix} \tag{10}$$

$$\begin{bmatrix} \hat{y}_{\text{in1}} \\ \hat{y}_{\text{out1}} \end{bmatrix} = \begin{bmatrix} \dfrac{1+L_{22}G_{22\text{-xi}}}{1+L_{22}G_{22}} G_{11} & \dfrac{G_{12}}{1+L_{22}G_{22}} & \dfrac{1+L_{22}G_{22\text{-}\infty}}{1+L_{22}G_{22}} G_{13} \\ \dfrac{G_{21}}{1+L_{22}G_{22}} & -\dfrac{G_{22}}{1+L_{22}G_{22}} & \dfrac{G_{23}}{1+L_{22}G_{22}} \end{bmatrix} \begin{bmatrix} \hat{x}_{\text{in1}} \\ \hat{x}_{\text{out2}} \\ \hat{x}_{\text{c}} \end{bmatrix} \tag{11}$$

$$G_{22\text{-xi}} = G_{22\text{-sci}} = G_{22\text{-oci}} = G_{22} + \frac{G_{12}G_{21}}{G_{11}} \tag{12}$$

3.1.3 General stability assessment

It is well known that the stability of a VF interconnected system consisting of a source and load subsystem can be determined by means of a certain impedance ratio known as minor-loop gain by applying Nyquist stability criterion (Middlebrook, 1976; Zenger, et al., 2006). The impedance-ratio-based method can be generalized to cover all type of interconnected systems with an assumption that the output mode of the source subsystem has to be a dual of the input mode of the load subsystem at the interface under consideration (See Fig. 11).

Fig. 16 shows an arbitrary interconnected system, where the source (**S**) and load (**L**) subsystems are assumed to contain the merged dynamical effects from the downstream and upstream parts of the overall system, respectively. The input, output, and intermediate variables are the same as defined in Section 3.1.2 but the control variable $\hat{x}_{\text{c}}$ is assumed to be zero without loss of generality.

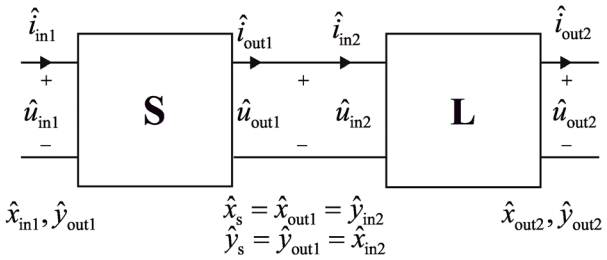

Fig. 16. An interconnected system

The subsystems can be represented by their transfer functions as defined in (13) by utilizing the intermediate variables (See Fig. 16). The stability of the interconnected system can be studied by developing the mappings from the system input variables to the intermediate variables and to the system output variables. These mappings are given in (14) and (15), respectively. If the original subsystems are stable as stand-alone systems then the stability of the interconnected system is dependent on $1/(1+S_{22}L_{11})$ (Zenger, et al., 2006). Stable operation requires that the roots of $(1+S_{22}L_{11})$ have to locate on the left half plane (LHP) of the complex plane (Zenger, et al., 2006), which is ensured when the term $S_{22}L_{11}$ is stable in Nyquist sense. The boundary for the instability is $S_{22}L_{11} = -1$, which means that the impedances forming the term have equal magnitudes and phase shift of 180 degrees. In case of VF interconnected system, $S_{22}L_{11} = Z_{\text{out-S}} / Z_{\text{in-L}}$ (i.e., the minor-loop gain defined by (Middlebrook, 2006)). In case of CF interconnected system, $S_{22}L_{11} = Z_{\text{in-L}} / Z_{\text{out-S}}$ (i.e., the inverse minor-loop gain defined by (Suntio, et al., 2010b)).

$$\begin{bmatrix} \hat{y}_{out1} \\ \hat{y}_s \end{bmatrix} = \begin{bmatrix} S_{11} & S_{12} \\ S_{21} & -S_{22} \end{bmatrix} \begin{bmatrix} \hat{x}_{in1} \\ \hat{x}_s \end{bmatrix} \qquad \begin{bmatrix} \hat{x}_s \\ \hat{y}_{out2} \end{bmatrix} = \begin{bmatrix} L_{11} & L_{12} \\ L_{21} & -L_{22} \end{bmatrix} \begin{bmatrix} \hat{y}_s \\ \hat{x}_{in2} \end{bmatrix} \tag{13}$$

$$\begin{bmatrix} \hat{x}_s \\ \hat{y}_s \end{bmatrix} = \begin{bmatrix} \dfrac{S_{21}L_{11}}{1+S_{22}L_{11}} & \dfrac{L_{12}}{1+S_{22}L_{11}} \\ \dfrac{S_{21}}{1+S_{22}L_{11}} & -\dfrac{S_{22}L_{12}}{1+S_{22}L_{11}} \end{bmatrix} \begin{bmatrix} \hat{x}_{in1} \\ \hat{x}_{out2} \end{bmatrix} \tag{14}$$

$$\begin{bmatrix} \hat{y}_{in1} \\ \hat{y}_{out2} \end{bmatrix} = \begin{bmatrix} S_{11} + \dfrac{S_{12}S_{21}L_{11}}{1+S_{22}L_{11}} & \dfrac{S_{12}L_{12}}{1+S_{22}L_{11}} \\ \dfrac{S_{21}L_{21}}{1+S_{22}L_{11}} & -\left(L_{12} + \dfrac{S_{12}S_{22}L_{12}}{1+S_{22}L_{11}}\right) \end{bmatrix} \begin{bmatrix} \hat{x}_{in1} \\ \hat{x}_{out2} \end{bmatrix} \tag{15}$$

3.1.4 Theoretical interfacing constraints

As discussed earlier, the constant-current property of the input port of VF converters (See Fig. 11) implies that their operation is limited to the constant-voltage region of the PV generator, because the input current controller would easily saturate due to the violation of Kirchhoff's current law if the operation point is moved to the constant-current region

(Suntio, et al., 2010a). This means also that the real global MPP cannot be traced in the case of shaded PV generator, because the only possible operation region is the constant-voltage region locating at the highest voltages. Similar violation of the Kirchhoff's laws would not take place in the CF converter under input-voltage control (Suntio, et al., 2010b).

According to (5), the low-frequency value of the closed-loop ohmic transfer function G_{11-c} under output-side feedback control (Fig. 13) equals the ideal transfer function $G_{11-\infty}$, which is known to posses the properties of negative resistance (Middlebrook, 1976; Suntio, 2009; Suntio, et al., 2010a&b). According to (Mäki, et al. 2010) the dynamic output impedance of the PV generator is pure resistance at the low frequencies and equals the corresponding static resistance at any of the MPPs (Thongpron, et al., 2006). As a consequence, VF and CF converters become unstable if the operating point is moved to the MPP under output-side feedback control, because both of the minor-loop gains equal -1 at the MPP. According to this, the operation region of the VF converter is limited to the voltages higher than the MPP and the operation region of the CF converter to the voltages lower than the MPP, respectively (Suntio, et al., 2010a&b).

Under input-side feedback control, the closed-loop ohmic transfer function G_{11-c} (See (3)) does not possess properties, which resembles negative resistance. Therefore, the converter stays stable in the minor-loop sense (Suntio, et al., 2010a&b).

The source-affected control-to-output transfer function G_{23}^{S} in (8) has a numerator term $(1+S_{22}G_{11\text{-}\infty})$, which is dependent on the internal impedance of the source and the ideal ohmic behaviour of the input terminal of the converter. According to the discussions above, the numerator term will be zero at the vicinity of the MPP and will also change the phase of the transfer function by 180 deg. This implies instability to take place under output feedback control, when the operating point crosses the MPP. It may be obvious that in case of the cascaded control, where the output-side feedback loop is the inner loop as in the grid-connected PV inverters (See (Blaabjerg, et al., 2006)), the output feedback loop will be unstable and will experience high gain reduction in the vicinity of the MPP. The consequences are not treated here.

4. Current-fed converter implementation

A CF converter can be implemented in three distinct ways such as i) constructing intuitively the converter based on the application of capacitive switched cells (Shmilovitz, 2006), ii) from a VF converter applying duality-transformation methods (Ćuk, 1979), and iii) adding a capacitor at the input terminal of a VF conventional (Leppäaho, et al., 2010). The first method produces a converter with the desired feature defined by the designer. The second method produces a converter having similar static and dynamic properties as the original VF converter has but the input and output variables are interchanged. The third method produces a converter, which has the properties of the dual of the original VF converter, i.e., a VF buck converter transforms into a CF boost converter and vice versa. The converter produced by the third method is not usually recognized to be a CF converter but treated as if it has the properties of the original converter. This is explicitly shown in (Villalva, et al., 2010) and justified by means of the voltage-type characteristics of the PV generator when a capacitor is placed at its output.

4.1.1 Duality transformation

The most convenient method to perform the duality transformation is to place a dot inside every mesh of the electrical circuit, one outside the circuit, and connecting the nodes with the dual of the branch circuit between the nodes (Ćuk, 1979). The duality-transformation process is described by means of an example in Fig. 17: Fig. 17a shows the original VF converter known as superbuck converter (Suntio, 2009). Fig. 17b shows the placement of the nodes inside the meshes and the duals of the branches between the nodes. Fig. 17c shows the resulting CF superbuck converter, which is described more in detail in (Leppäaho & Suntio, 2011). The described method is straightforward and quite easy to apply. The superbuck converter provides continuous input and output voltages and currents, which makes it a desired converter in many applications. The detailed properties of the VF superbuck converter can be found from (Suntio, 2009).

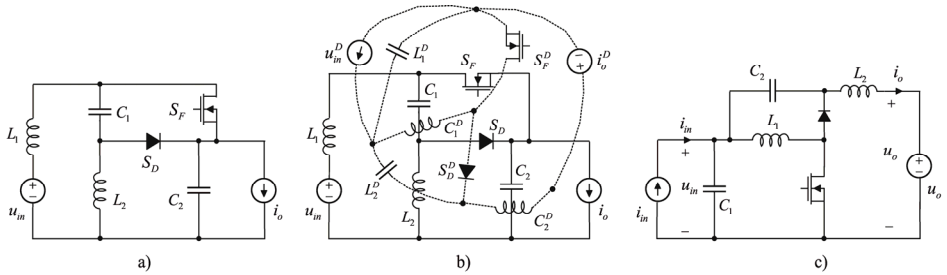

Fig. 17. Performing the duality transformation: a) VF superbuck converter, b) duality process, and c) CF superbuck converter

4.1.2 Input-capacitor-based transformation

The conventional buck converter in the PV applications is shown in Fig. 18 equipped with an input capacitor. The ideal voltage source at the output terminal short circuits the output capacitor and therefore, it is usually omitted as in (Villalva, et al., 2010). The normal switch control scheme in the conventional buck converter is such that the high-side switch conducts during the on time and the low-side switch during the off time, respectively. The intention is usually to control the input voltage to the MPP of the PV generator. It has been observed that the normal negative feedback control does not work but the polarity of the feedback signal and its reference has to be inverted. This can be easily deduced from Fig. 18: If the input voltage (i.e., the PV voltage) is too low and the conduction time of the high-side switch is increased, the PV voltage would further decrease. If the conduction time of the high-side switch is, however, decreased, the desired effect will be obtained. Similar effect can be obtained by inversing the switch control signals (Leppäaho, et al., 2010) or using a descending PWM ramp signal.

The described controlling scheme of the converter implies that the ideal input-output relation *M(D)=1/(1-D)*, which is a characteristic property of a boost converter. The buck power stage with an input capacitor is, actually, the power stage of a CF boost converter. This fact is not usually recognized but the input capacitor is assumed not to contribute to the dynamic processes inside the converter. Leppäaho, et al., 2010, have definitively shown that the converter contains a right-half-plane (RHP) zero and duty-ratio-dependent resonant behaviour (i.e., second-order dynamics) in its output control dynamics, which are not

present in the original buck converter when its output is terminated with a constant-voltage type load. The PV generator removes the RHP zero and the resonant behaviour when the operating point moves to the constant-voltage region. This is understandable, because the low resistance value of the output impedance of the PV generator effectively removes the effect of the input capacitor.

Similarly, the conventional boost power stage with an input capacitor will constitute a converter having properties of a CF buck converter with an input LC filter (See e.g. (Xiao, et al., 2007a&b)).

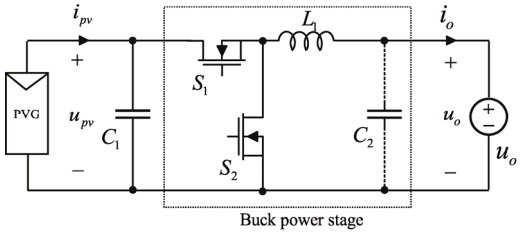

Fig. 18. Buck-power-stage-based converter

5. Experimental evidence

The experimental converters are shown in Fig. 19 and supplied by Raloss SR30-36 panel discussed earlier in Section 2. The more detailed information on the converters can be found from (Huusari, et al., 2010; Leppäaho, et al., 2010). The same frequency response analyzer as in Section 2 is used to extract the frequency responses shown below.

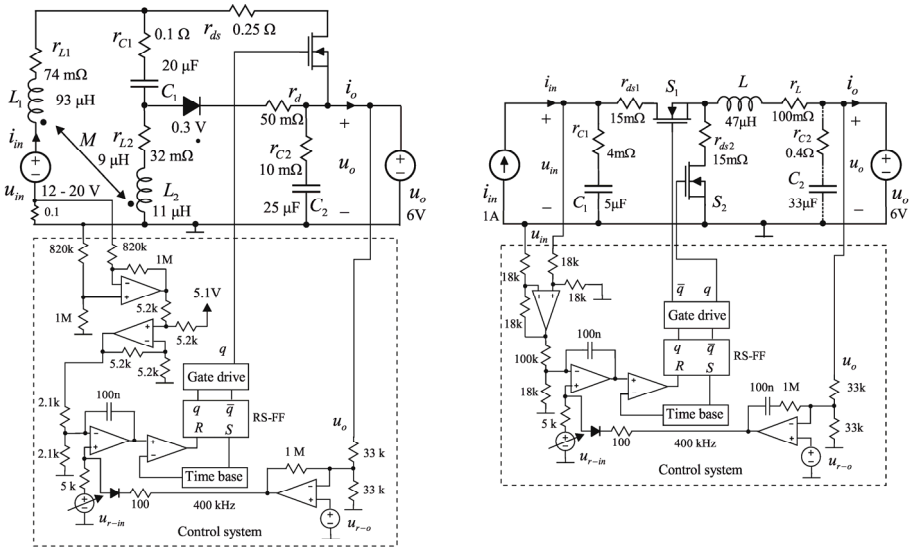

Fig. 19. The experimental converters: a) VF superbuck converter, and b) CF boost converter

Fig. 20a shows the measured input impedances and the output impedances of the PV generator covering the same operating points as Fig. 20b, where the time-domain behaviour of the VF superbuck converter (Fig. 19a) is shown when its input-current reference is swept from 0.25 A to 0.92 A and back, and where the highest-current operating point is slightly in the constant-current region beyond the MPP.

According to Fig.20a, it is clear that the converter is stable in the minor-loop-gain sense (Middlebrook, 1979). Fig. 20b shows that the input voltage (u_{sg}) collapses and the converter ceases to operate when the Kirchhoff's current law (KCL) is violated but recovers when the reference is sufficiently changed back to the constant-voltage region. The behaviour of the VF converter is as discussed in Subsection 3.1.4 when the violation of the KCL takes place.

Fig. 21a shows the measured input impedances of the CF converter (Fig. 19b) and the output impedances of the PV generator when the output-voltage-limiting control is active and the operating point approaches the MPP from the constant-current region. The corresponding minor-loop gain indicates instability to take place at the MPP (Suntio, et al., 2010b). Fig. 21b shows the time-domain behaviour of the converter when the operating point is placed in the constant-voltage region (17 V) and the output-voltage-limiting control is activated. The instability moves the operating point quickly to the constant-current region, where the operation is stable. This phenomenon is one of the beneficial features of the CF converters but it shall be noticed that the MPP-tracking device shall not try to move the operating point anymore back to the MPP because of the instability to take place. Fig. 21a shows also that the low-frequency input impedance of the CF converter under output-side control is a negative resistance as discussed in Subsection 3.1.4. Under input-voltage control, the CF converters are capable to operate within the whole range of the PV operating points valid for the certain converter topology.

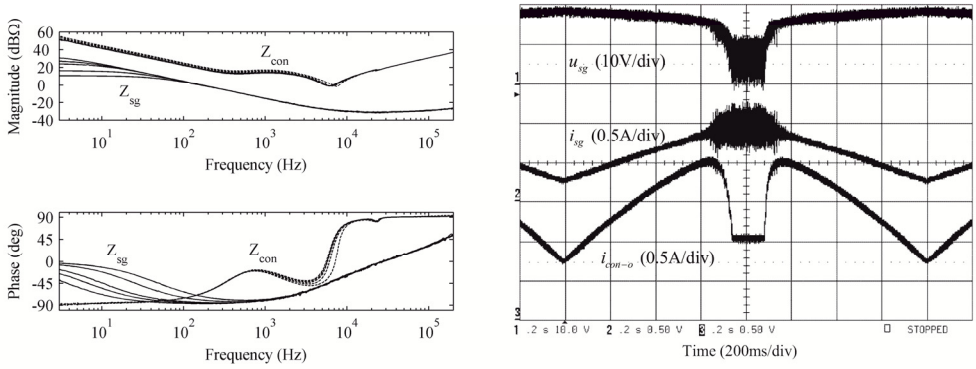

a) b)

Fig. 20. a) The input impedances of the VF converter and the output impedances of the PV generator, and b) The time-domain behaviour of the VF converter when its input-current reference is swept from 0.25 A to 0.92 A and back starting from the constant-voltage region and entering slightly into the constant-current region beyond the MPP

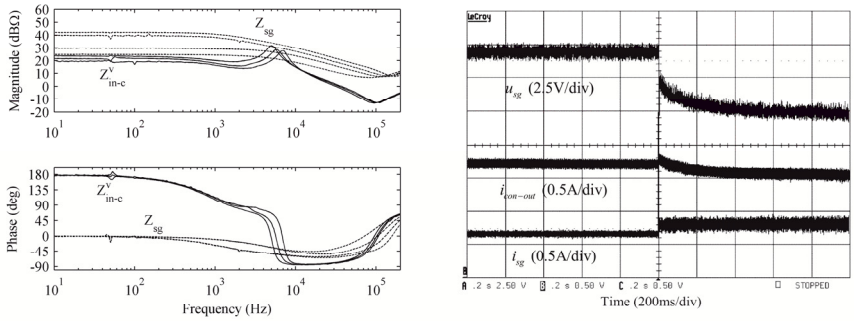

a) b)

Fig. 21. a) The input impedances of the CF converter under output-voltage-limiting control and the output impedances of the PV generator when the operating point moves toward the MPP, and b) The time-domain behaviour of the CF converter when its operating point is placed in the constant-voltage region at 17 V and the output-voltage-limiting controller is activated

Fig. 22 shows the behaviour of the measured control-to-output-current transfer function of the CF boost converter (Fig. 19b) when the operating point crosses the MPP. It shows that the phase of the transfer function changes by 180 degrees implying instability to take place under output-side feedback control as discussed in Subsection 3.1.4 and shown to take place in Fig. 22b. The transfer function (14 V) shows also the existence of RHP zero and second-order nature of the converter, which are removed in the constant-voltage region (16 V).

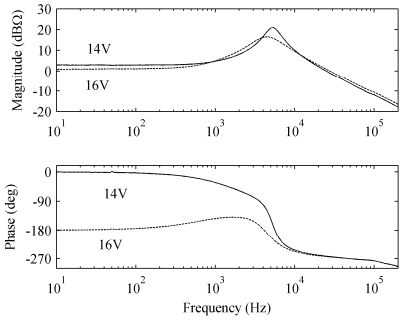

Fig. 22. The behaviour of the control-to-output-current transfer function of the CF boost converter when the operating point is moved from the constant-current region (14 V) to the constant-voltage region (16 V)

6. Summary

The interfacing constraints of PV generator as well as the real nature of the interfacing converters were introduced. It was defined and experimentally proved that the VF converter can operate only in the constant-voltage region of the PV generator. This means also that the MPP, up to which it can operate, is the highest-voltage MPP. Therefore, its MPP-tracking efficiency is rather poor especially in case of the shaded conditions in the PV generator. The

CF converters do not suffer from similar constraints when the input voltage is controlled but become unstable at the MPP or the voltages higher than the MPP under output voltage or current feedback control.

It was also explicitly stated that the power stage of the converter does not necessarily determine the true nature of the converter but the input and output sources and the feedback signals used. These facts are not well understood and therefore, the analyses of the converter in PV applications are most often deficient or even erroneous.

The resistive nature of the output impedance of the PV generator has tremendous effect on the dynamics of the converter connected directly to it. The most significant changes are taken place in the output control dynamics such as the change of phase by 180 degrees when crossing the MPP, the reduction of the gain of the control-to-output transfer function significantly at the MPP, the appearing/disappearing of right-half-plane zeros, etc. All these changes may have fundamental and catastrophic effect on the operation of the PV converters and inverters.

7. Acknowledgment

The contributions of Professor *Seppo Valkealahti*, and the PhD students *Juha Huusari*, *Jari Leppäaho*, *Tuomas Messo*, *Anssi Mäki*, *Lari Nousiainen*, *Joonas Puukko,* and *Diego Torres Lobera* are greatly appreciated and vital to the content of this chapter.

8. References

Anantha Krishna, H.; Misra, N. K. & Suresh, M. S. Solar Cell as a Capacitive Temperature Sensor. *IEEE Transactions on Aerospace and Electronic Systems*, Vol.47, No.2, (April 2011), pp. 782-789, ISSN 0018-9251.

Blaabjerg, F.; Teodorescu, R; Liserre, M., & Timbus, A. Overview of Control and Grid Synchronization for Distributed Generation Systems. *IEEE Transactions on Industrial Electronics*, Vol.53, No.5, (October 2006), pp. 1398-1409, ISSN 0278-0046.

Bose, B. K. Global Warming: Energy, Environmental Pollution, and the Impact of Power Electronics. *IEEE Industrial Electronics Magazine*, Vol.4, No.1, (March 2010), pp. 6-17, ISSN 1932-4529.

Bull, S. R. Renewable Energy Today and Tomorrow. *Proceedings of The IEEE*, Vol.89, No.8, (August 2001), pp. 1216-1226, ISSN 0018-9219.

Capel, A.; Marpinard, J. C.; Jalade, J. & Valentin, M. Current Fed and Voltage Fed Switching DC/DC Converters – Steady State and Dynamic Models, Their Applications in Space Technology. *International Telecommunications Energy Conference*, pp. 421-430, ISBN 83CH1855-6, Tokyo, Japan, 18-21 October, 1983.

Dehbonei, H.; Lee, S. R. & Nehrir, H. Direct Energy Transfer for High Efficiency Photovoltaic Energy Systems. Part I: Concepts and Hypothesis. *IEEE Transactions on Aerospace and Electronic Systems*, Vol.45, No. 1, (January 2009a), pp. 31-45, ISSN 0018-9251.

Dehbonei, H.; Lee, S. R. & Nehrir, H. Direct Energy Transfer for High Efficiency Photovoltaic Energy Systems. Part II: Experimental Evaluation. *IEEE Transactions on Aerospace and Electronic Systems*, Vol.45, No. 1, (January 2009b), pp. 46-57, ISSN 0018-9251.

Ćuk, S. General Topological Properties of Switching Structures. *IEEE Power Electronic Specialists Conference*, pp. 109-130, ISBN 79CH1461-3, San Diego, CA, USA, 18-22 June, 1979.

Esram, T. & Chapman, P. L. Comparison of Photovoltaic Array Maximum Power Point Tracking Techniques. *IEEE Transactions on Energy Conversion*, Vol. 22, No.2, (June 2007), pp. 439-449, ISSN 0885-8969 .

Femia, N.; Lisi, G.; Petrone, G. & Vitelli, M. Distributed Maximum Power Point Tracking of Photovoltaic Arrays: Novel Approach and System Analysis. *IEEE Transactions on Industrial Electronics*, Vol.55, No.7, (July 2008), pp. 2610-2621, ISSN 0278-0046.

Huusari, J.; Leppäaho, J. & Suntio T. Dynamic Properties of PCM-Controlled Superbuck Converter – Discrete vs. Coupled Inductor Implementation. *European Power Electronics and Drives Journal*, Vol.20, No.2, (June 2010), pp. 31-40, ISSN 0939-8368.

Jain, S. & Agarwal, V. Comparison of Performance of Maximum Power Point Tracking Schemes Applied to Single-Stage Grid Connected Photovoltaic Systems. *IET Electrical Power Applications*, Vol. 1, No.5, (September 2007), pp. 753-762, ISSN 1751-8660.

Kumar, R. A.; Suresh, M. S. & Nagaraju, J. Effect of Solar Array Capacitance on the Performance of Switching Shunt Regulator. *IEEE Transactions on Power Electronics*, Vol.21, No.2, (March 2006), pp. 543-548, ISSN 0885-8993.

Leppäaho, J.; Nousiainen, L.; Puukko, J.; Huusari, J. & Suntio, T. Implementing Current-Fed Converters by Adding an Input Capacitor at the Input of Voltage-Fed Converter for Interfacing Solar Generator. *International Power Electronics and Motion Control Conference*, pp. 81-88, ISBN 978-1-4244-7855-2, Ohrid, Republic of Macedonia, 6-8 September, 2010.

Leppäaho, J. & Suntio, T. Dynamic Characterization of Current-Fed Superbuck Converter. *IEEE Transactions on Power Electronics*, Vol.26, No.1, (January 2011), pp. 200-209, ISSN 0885-8993.

Lyi, S. & Dougal, R. A. Dynamic Multiphysics Model for Solar Array. *IEEE Transactions on Energy Conversion*, Vol. 17, No.2, (June 2002), pp. 285-294, ISSN 0885-8969.

McLaughlin, J. C. & Kaiser, K. L. Deglorifying the Maximum Power Transfer Theorem and Factors in Impedance Selection. *IEEE Transactions on Education*, Vol.50, No.3, (August 2007), pp. 251-255.

Menti, A.; Zacharias, T. & Milias-Argitis, J. Harmonic Distortion Assessment for Single-Phase Grid-Connected Photovoltaic Systems. *Renewable Energy*, Vol.36, No.1, (January 2011), pp. 360-368, ISSN 0038-092X

Middlebrook, R. D. Input Filter Considerations in Design and Applications of Switching Regulators. *IEEE Industry Application Society Annual Conference*, pp. 366-382, ISBN 76CH1122-1-IA, Chigago, IL, USA, 1976.

Mäki, A.; Valkealahti, S. & Suntio, T. Dynamic Terminal Characteristics of a Solar Generator. *International Power Electronics and Motion Control Conference*, pp. 76-80, ISBN 978-1-4244-7855-2, Ohrid, Republic of Macedonia, 6-8 September, 2010.

Park, J.-H.; Ahn, J.-Y.; Cho, B.-H., & Yu, G.-J. Dual-Module-Based Maximum Power Point Tracking Control of Photovoltaic Systems. *IEEE Transactions on Industrial Electronics*, Vol.53, No.4, (August 2006), pp. 1036-1047, ISSN 0278-0046.

Petrone, G.; Spagnuolo, G.; Teodorescu, R.; Veerachary, M. & Vitelli, M. Reliability Issues in Photovoltaic Power Processing Systems. *IEEE Transactions on Industrial Electronics*, Vol.55, No.7, (July 2008), pp. 2569-2580, ISSN 0278-0046.

Rahman, S. Green Power: What Is It and Where Can We Find It? *IEEE Power & Energy Magazine*, Vol.1, No.1, (January-February 2003), pp. 30-37, ISSN 1540-7977.

Salas, V., Olias, E.; Barrado, A. & Lazaro A. Review of the Maximum Power Point Tracking Algorithms for Stand-Alone Photovoltaic Systems. *Solar Energy Materials & Solar Cells*, Vol.90, No.12, (July 2006), pp. 1555-1578, ISSN 0927-0248.

Sanchis, P.; Lopez, J., Ursua, A.; Gubia, E. & Maroyo, L. On Testing, Characterization, and Evaluation of PV Inverters and Dynamic MPPT Performance under Real Varying Operating Conditions. *Progress in Photovoltaics: Research and Applications*, Vol.15, No.6, (September 2007), pp. 541-556, ISSN 1099-159X.

Shmilovitz, D. & Singer, S. A Switched Mode Converter Suitable for Superconductive Magnetic Energy Storage (SMES) Systems. *IEEE Applied Power Electronics Conference*, pp. 630-634, ISBN 7803-7404, Dallas, TX, USA, 10-14 March, 2002.

Shmilovitz, D. Gyrator Realization Based on a Capacitive Switched Cell. *IEEE Transactions on Circuits and Systems I: Regular Papers*, Vol.53, No.12, (December 2006), pp. 1418-1422, ISSN 1549-8328.

Siri, K. Study of System Instability in Solar-Array-Based Power Systems. *IEEE Transactions on Aerospace and Electronic Systems*, Vol.36, No.3, (July 2000), pp. 957-964, ISSN 0018-9251.

Suntio, T. (2009). Dynamic *Profile of Switched-Mode Converter: Modeling, Analysis and Control*. Wiley-VCH, ISBN 978-3-527-40708-8, Weinheim, Germany

Suntio, T.; Huusari, J. & Leppäaho, J. Issues on Solar-Generator Interfacing with Voltage-Fed MPP-Tracking Converters. *European Power Electronics and Drives Journal*, Vol.20, No.3, (September 2010a), pp. 40-47, ISSN 0939-8368.

Suntio, T.; Leppäaho, J.; Huusari, J. & Nousiainen, L. Issues on Solar-Generator Interfacing with Current-Fed MPP-Tracking Converters. *IEEE Transactions on Power Electronics*, Vol.25, No.9, (September 2010b), pp. 2409-2418, ISSN 0885-8993.

Thongpron, J.; Kirtikara, K. & Jivicate, C. A Method for Determination of Dynamic Resistance of Photovoltaic Modules under Illumination. *Solar Energy Materials & Solar Cells*, Vol.90, No.18/19, (November 2006), pp. 3078-3084, ISSN 0927-0248.

Tse, C. K. (1998). Linear Circuit Analysis. Addison-Wesley, ISBN 0-201-34296-0, Harlow, England.

Villalva, M. G.; Gazoli, J. R. & Filho, E. R. Comprehensive Approach to Modeling and Simulating Photovoltaic Arrays. *IEEE Transaction on Power Electronics*, Vol. 24, No.5, (May 2009), pp. 1198-1208, ISSN 0885-8993.

Villalva, M.; de Siqueira, T. G., and Ruppert, E. Voltage Regulation of Photovoltaic Arrays: Small-Signal Analysis and Control Design. *IET Power Electronics*, Vol.3, No.6, (November 2010), pp. 869-880, ISSN 1755-4535.

Wang, Y.-J. & Hsu, P.-C. Modelling of Solar Cells and Modules Using Piecewise Linear Parallel Branches. *IET Renewable Power Generation*, Vol.5, No.3, (May 2011), pp. 215-222, ISSN 1752-1416.

Xiao, W.; Dunford, W. G.; Palmer, P. R. & Capel, A. Regulation of Photovoltaic Voltage. *IEEE Transaction on Industrial Electronics*, Vol.54, No.3, (June 2007a), pp. 1365-1374, ISSN 0278-0046.

Xiao, W.; Ozog, N. & Dunford, W. G. Topology Study of Photovoltaic Interface for Maximum Power Tracking. *IEEE Transactions on Industrial Electronics*, Vol.54, No.3, (June 2007b), pp. 1696-1704, ISSN 0278-0046.

Zenger, K.; Altowati, A. & Suntio, T. Dynamic Properties of Interconnected Power Systems – A System Theoretic Approach. *IEEE International Conference on Industrial Electronics and Applications*, pp. 835-840, ISBN 7803-9514, Singapore, 24-26 May, 2006.

15

Research and Application of Solar Energy Photovoltaic-Thermal Technology

Jiang Wu and Jianxing Ren
School of Energy and Environmental Engineering
Shanghai University of Electric Power
P.R. China

1. Introduction

It is believed that in the past 100 years, new technology created by mankind not only provides unprecedented power of economic development, but also provides mankind with a great ability to be harmony with the environment. Modern society should be conservation-minded society, and social life should also be energy-saving. As an inexhaustible source of new environment-friendly energy source, solar energy has become an important issue of energy research in this world.

Solar energy is a kind of renewable energy. It is rich in resources, free, non- transportation, and no pollution to the environment. Solar energy creates a new lifestyle for mankind, and takes society and human into an era of energy conservation to reduce pollution. Solar thermal conversion device industry makes solar energy technology fulfill its potential in the construction area, including hot water, heating, and air conditioning. Solar thermal conversion industry is studying solar water heating systems and building integration with the construction industry, and there have been some demonstrations. Solar air conditioning has been included in the science and technology research, and there is a large-scale demonstration plant whose economy has yet to be assessed.

As an inexhaustible security, energy-saving, environmental protection, new energy source, solar energy has attracted more and more concern in this world, and governments or companies have put their eyes on the sustainable development of the emerging solar energy field. Now, with solar technology improving continuously and the supporting of the state government, solar energy applications are increasingly widespread. Solar energy reaching the surface per second can be up to 80MW (million kilowatts), if 1% of which is transferred to electrical power, with 5% of conversion rate, then the annual generating capacity may be up to $5.6 \times l0^{12}$ kWh, equivalent to 40 times of the current world energy consumption.

Light - heat transfer adopts sunlight to heat the water tank for potential application, which is the most common and basic form of solar thermal, and the essence of solar thermal is to collect solar radiation and convert it into heat energy by working substance. Currently, the mature technology and widely adopted solar thermal applications include solar thermal, solar water heaters, solar cookers and solar house, of which solar water heaters are the most widely used. China's solar water heater production and application began in the late 1970s, and after decades of development, China has become the largest water heater production and

consumption country in this world. Due to the factors, such as the dispersion of solar energy resources, its needing high-performance materials to get high energy transfer efficiency, and other aspects, the application of advanced solar thermal technology is not widely put into the social practice, and its research and development has a long way to go.

The main contents of this chapter include experimental research on a solar flat-plate collector, the systematic research on staged solar photovoltaic/solar thermal collectors, solar air conditioning systems and solar drying systems.

2. Research on solar flat-plate collector

The direct usage of solar radiation energy is to collect solar radiation using greenhouse effect to heat an object to obtain thermal energy. Currently the flat plate collector and concentrating solar collector are the two main solar energy collection devices [1, 2]. Solar collector is a key component of solar thermal system, whose manufacturing cost accounts for about half of solar water heater and its level of development processes and quality standards represent the level of development of solar thermal and solar collector technology [3].

2.1 Principles of solar collectors

Solar collector is a device to receive solar radiation and transfer heat to working fluid in a solar thermal system. If it adopts water as heat transfer medium, it constitutes a variety of solar water heaters, and if when using air, it yields a variety of solar dryers. Heat-absorbing board is the core of solar collector to absorb the sun's radiation to heat the heat transfer medium. Non-concentrating solar collectors apply hot-box principle, also known as the greenhouse effect, to make solar energy become inner energy [4]. Concentrating collectors use focusing principle to change directions of the sun to concentrate sunlight on a heat-absorbing body of a small area, increasing radiation intensity on unit area, so that collectors arrive at a higher temperature [5, 6]. In this chapter, a solar flat-plate collector is designed and studied.

2.2 Data analysis of solar flat-plate collector

The schematic diagram and picture of solar flat plate collector system are shown as Fig. 1(a) and (b). As the main parameter, temperature is measured with K-type thermocouple and TES -1310-type temperature display made in Taiwan.

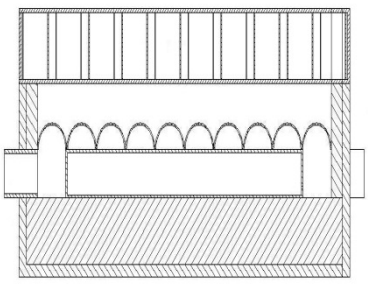

(a) Schematic diagram

(b) Picture

Fig. 1. Schematic diagram and picture of flat-plate solar collector

2.2.1 The effect of different insulation materials on the collector performance

Two systems, system A and system B, are studied, and they are with 5cm thickness of glass wool and 5cm thickness of polyurethane foam board as insulation material respectively. The cover plates are both double-layer with honeycomb structure. The shell of the collector is three-ply wood, which is agglunated by three pieces of thin wood boards. The heat-absorbing bodies are corrugated copper board, and heat transfer working medium is air. The pumping equipment is a 12V blower. When the ratio of height to width is 1.43, the effective transmittance of the cellular structure is 0.61. The comparison between different insulations is shown as Table 1.

Time	Atmospheric temperature (°C)	Atmospheric wind speed (m/s)	irradiation intensity	A_1	A_2	A_3	A_4	B_1	B_2	B_3	B_4
9:30	28.8	0.86	630.53	44.2	49.6	33.4	34.7	49.3	57.4	34.7	40.8
10:00	29.5	0.72	707.18	48.0	64.2	32.2	42.0	56.6	67.0	35.0	48.0
10:30	30.3	1.09	727.26	47.4	75.8	32.5	47.2	67.1	78.8	33.6	55.8
11:00	28.3	1.61	766.49	44.5	83.9	33.0	51.5	75.8	90.3	34.4	62.9
11:30	28.0	1.41	861.39	58.7	89.0	32.0	54.2	81.7	94.8	35.5	64.0
12:00	29.0	0.66	785.66	83.4	92.0	37.4	58.9	84.9	97.2	32.2	65.5
12:30	25.2	0.50	716.31	79.1	86.7	30.2	56.2	81.6	91.2	37.3	63.0
13:00	29.1	1.12	685.28	79.2	86.4	36.0	56.8	83.3	92.2	39.2	62.7
13:30	28.2	1.74	714.48	73.7	86.7	33.0	57.0	81.3	90.4	36.6	61.6
14:00	26.3	0.40	684.37	76.7	84.3	36.0	56.0	79.5	87.2	37.5	63.0
14:30	28.3	0.35	563.92	75.5	81.4	39.4	55.5	77.8	85.2	41.4	60.3
15:00	27.3	0.68	500.96	68.1	74.3	33.7	50.4	70.2	78.0	35.5	56.8
15:30	27.6	0.35	412.45	65.4	70.6	31.6	48.3	66.6	73.0	34.6	53.8

Note: The inlet velocity is 0.2 m / s; A_1, A_2, A_3, A_4 are respectively the internal temperature of the cover, the surface, inlet and outlet temperature of the heat-absorbing of the system A. B_1, B_2, B_3, B_4 are respectively the corresponding parameters of the system B. Different insulation material systems are used for systems A and B: A-glass wool; B-polyurethane foam board

Table 1. Comparison of experimental data between different insulation systems

The history of the atmospheric temperature, wind speed and radiation intensity changing with time is shown as Fig. 2. Fig. 2 (a) shows that the atmospheric temperature at the daytime is relatively stable, so it has no obvious effect on the systems. From Fig. 2 (b), it can be seen that dynamic performance testing does not depend on wind speed, so the wind speed is only as the reference conditions of the atmospheric factor. Fig. 2 (c) shows that the fluctuation trend of the irradiation intensity is not unusual, so the data attained at different time are reliable.

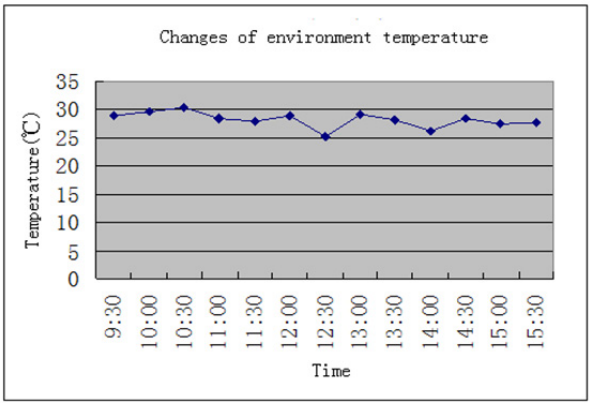

(a) Atmospheric temperature

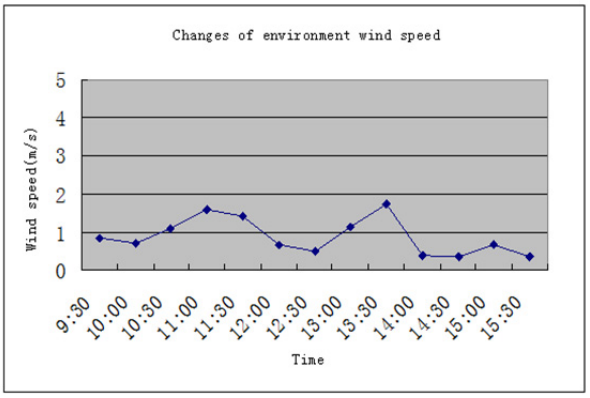

(b) Atmospheric wind speed

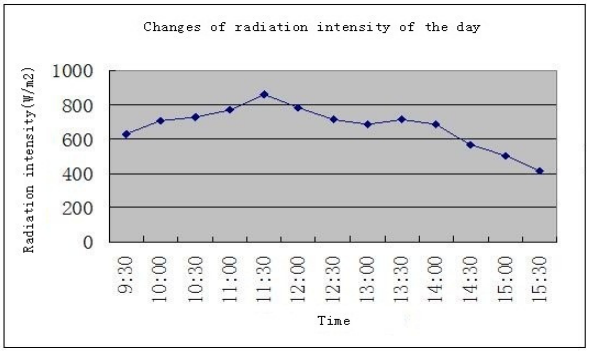

(c) Radiation intensity

Fig. 2. The history of atmospheric temperature, wind speed and radiation intensity changing with time

The history of internal temperature of the cover plate changing with time is shown in Fig. 3. It demonstrates that during the temperature-increasing process the temperature rising trend of system B is more obvious than that of system A, and system B is more stable than system A. It shows that the insulation system has effects on the plate performance during temperature rising process. The flat covers of the two systems are stable and the temperature changing trend are almost unanimously, so the effect of heat preservation system on the cover plate performance during a stable and cooling process is unobvious.

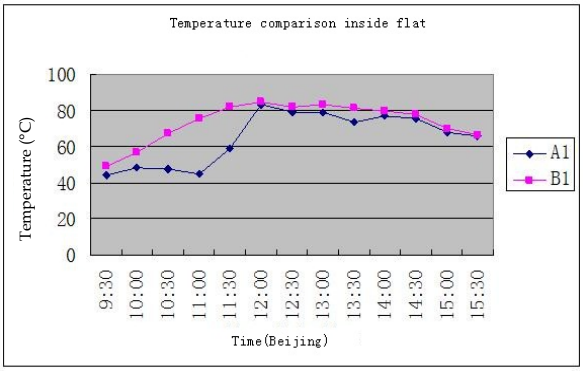

Fig. 3. The history of internal temperature of the cover plate changing with time

The history of heat absorber temperature changing with time is shown as Fig.4. The two heat-absorbing lines are almost overlapped, and the effect of heat insulation layer on heat-absorbing body is less when air, heat transfer medium, is of good flow characteristics. The effect of insulation layer on the flat cover is so small that it can be regarded because of the same cover plate structures, the working temperature of heat absorbers in the two systems may keep almost the same and not affected by the insulation structure.

The temperature at the inlet and outlet changing with irradiance is shown as Fig.5. It demonstrates that the temperature-rising speed in system B is faster than that in system A, but the irradiance is not maximum at the highest temperature. The reason is that insulation layer can delay the effect of irradiation and keep temperature-rising process in the collector continue for some time. After reaching the maximum temperature difference, system B can maintain the temperature higher than that of system A, which shows that the insulation system adopting polyurethane foam board as insulation layer is better than that of glass wool insulation during the heating process till the highest temperature. But it should be noted that the temperature transition in system A with the glass wool insulation layer is more stable at a relatively low temperature and irradiance condition, while system B is with a sudden drop point, which illustrates that glass wool insulation has better insulation performance when heat released by the working substance is in the end. As the economic advantage of glass wool is far greater than that of polyurethane foam, to achieve the best insulation, polyurethane foam may be considered as insulation material used at the zone closer to the working fluid, and glass wool is used as insulation at the external wall where temperature is relatively low, so as to reduce the cost of the system.

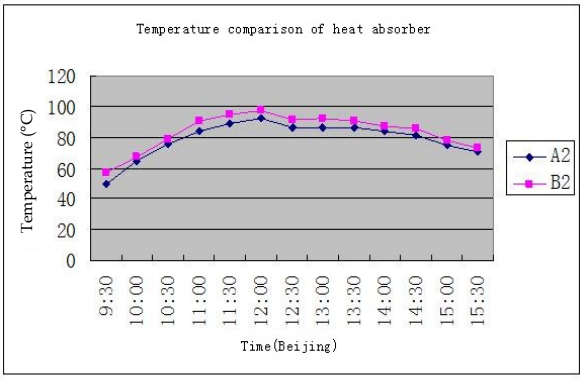

Fig. 4. The history of the heat absorber temperature changing with time

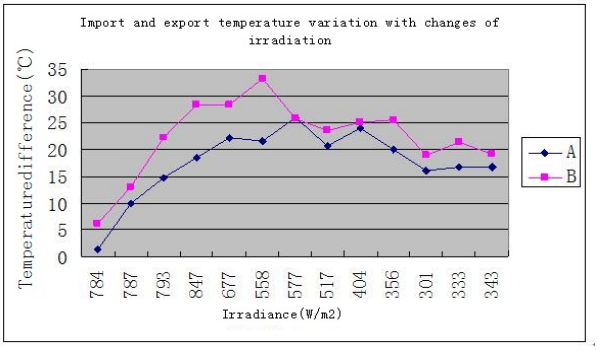

Fig. 5. The inlet and outlet temperature changing with the irradiance

2.2.2 The comparative experiments and data analysis on the cover performance

In this set of experiments, single-layer PC board and double-layer honeycomb structure are applied as the covers for system A and B, respectively. In the two systems, the shells are both wooden three plywood, the insulation are both polyurethane foam, and heat-absorbing bodies are both waveform copper plates. Temperature measurement points are on the surfaces of the cover (two points) and heat-absorbing surface (two points) respectively.

The history of heat-absorbing body temperature of system A, B changing with time is shown as Fig. 7. It demonstrates that ignoring other factors, although due to the difference placement or angle, the initial temperature of system A is higher than that of system B, the heating rate of system B is significantly higher than that of system A. It shows that there are heat losses in the two systems during the endothermic process, but the heat loss of system B is significantly less than that of system A when other conditions are the same. It tells that honeycomb structure plate plays a great role on inhibition of the heat loss due to air convection inside the cover.

Time	Atmospheric temperature (°C)	Atmospheric wind speed (m/s)	Irradiance (w/m^2)	A_1	A_2	A_3	A_4	B_1	B_2	B_3	B_4
9:30	27.2	0.55	783.83	41.6	38.5	69.1	69.7	37.5	35.7	54.4	55.7
10:00	29.2	1.57	787.48	48.2	46.1	82.0	81.1	43.1	42.0	70.7	68.9
10:30	29.9	0.99	792.96	49.5	48.5	82.6	80.7	43.0	42.3	72.8	70.3
11:00	27.3	1.33	846.79	49.6	42.0	85.0	86.5	41.3	42.8	78.2	76.1
11:30	25.6	0.57	677.07	49.4	45.0	86.1	88.3	45.3	47.0	85.2	83.9
12:00	27.6	0.73	558.46	47.2	43.4	83.2	86.6	46.1	46.5	86.0	85.1
12:30	26.3	0.41	576.70	44.7	43.3	77.9	77.5	46.3	48.3	85.4	84.2
13:00	28.3	1.72	517.38	45.9	41.2	82.2	80.7	44.7	45.7	83.4	82.3
13:30	29.3	0.33	404.23	41.8	38.0	71.9	71.4	40.2	39.9	78.3	78.5
14:00	27.5	2.42	355.87	38.3	35.2	61.3	60.9	36.5	37.5	67.7	66.6
14:30	25.9	0.48	301.12	38.6	36.1	58.9	59.6	38.6	38.5	65.4	64.0
15:00	25.2	2.58	333.06	43.6	39.5	70.5	68.2	40.2	40.3	68.1	67.3
15:30	26.5	1.63	343.10	39.0	35.9	61.6	60.4	37.2	36.5	64.3	63.7

Note: A_1 and A_2 are the temperature on the cover surface of system A at the different sites, A_3 and A_4 are the temperature on the heat-absorbing surface of system A at different sites, taking the average as the calculation value. B_1, B_2, B_3 and B_4 are the corresponding parameters of system B.

Table 2. Comparison between experimental data of the cover performance

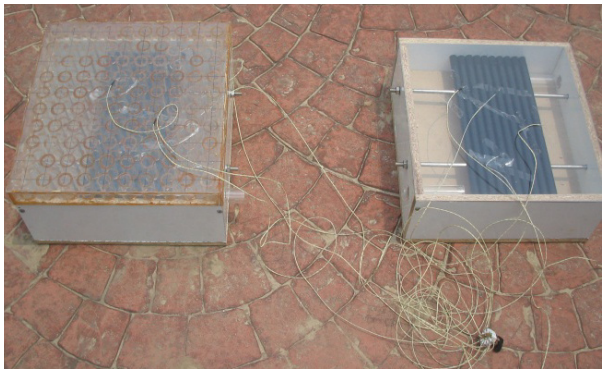

Fig. 6. Comparative testing on cover performance

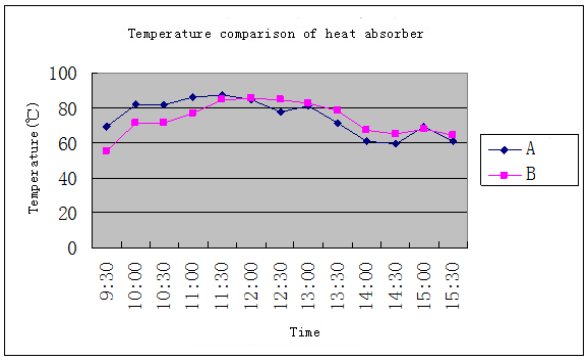

Fig. 7. Heat-absorbing body temperature changing history

In the comparative experiments on the cover performance, the changing of atmospheric temperature, wind speed, radiation intensity, and cover surface temperature with time is shown as Fig. 8 (a) to (d). From Fig. 8 (a) and (b), it can be seen that the changing of atmospheric temperature is stable, and its fluctuation is less than 5 °C. Fluctuation of wind speed is also small, less than 2m/s. From Fig. 8 (c), it can be seen that radiant intensity reaches the maximum at 11 a.m., and then as the time goes on, the radiation intensity declines gradually. According to table 2, the experimental conditions meet the requirements of dynamic performance testing. From Fig. 8 (d), it can be seen that the atmospheric temperatures are the same, and the covers are both PC board material, so that the surface temperature difference is very little, and the changing trends are the same. Therefore, the cover structure will not affect solar energy absorption of the cover surface.

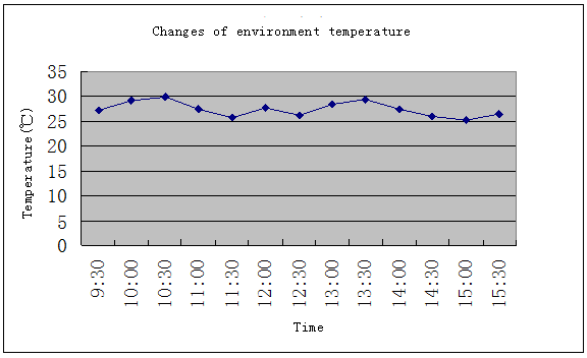

(a) Atmospheric temperature

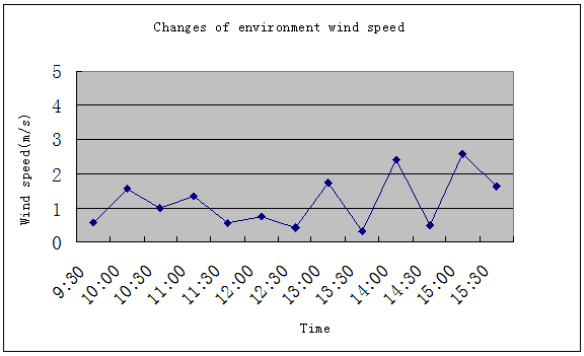

(b) Atmospheric wind speed

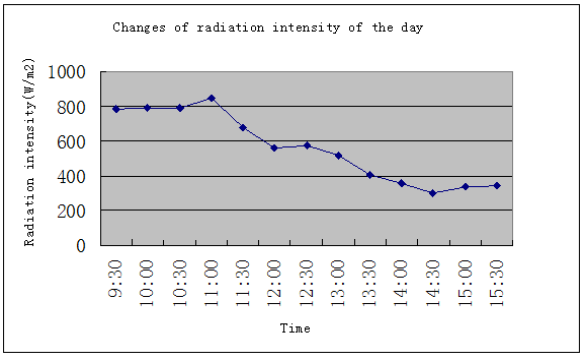

(c) Radiation intensity

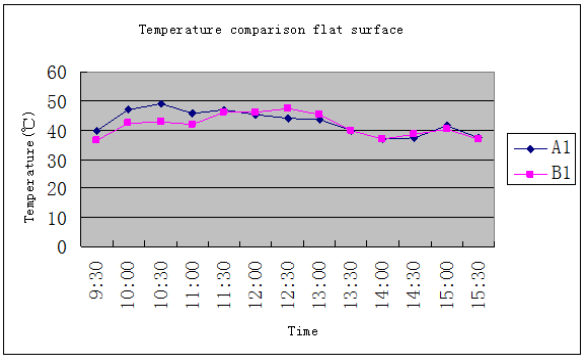

(d) Cover surface temperature

Fig. 8. The history of some parameters changing with time

3. Staged solar photovoltaic / thermal collector

Solar cell is the core unit of solar photovoltaic power generation. Currently the commercial solar cells are mainly silicon solar cells, including mono-crystalline, polycrystalline and amorphous silicon solar cells. The effects of temperature on silicon solar cells mainly include open circuit voltage, short circuit current, peak power and other parameters of the solar cells [7-10]. In the photovoltaic solar thermal flat-plate collector PV/T, there is a conflict between the photovoltaic power generation efficiency and solar thermal heat production efficiency, which means that one of them decreases while the other increases. How to further lower temperature of the solar cell plate and optimize the whole PV/T system to improve photovoltaic power generation efficiency of the PV/T collectors is the main study content of our research, which has important significance to improve the integrated utilization of PV/T solar collectors.

3.1 Structure and working principle of PV / thermal collector

The main structure of the PV/thermal collector consists of cover, solar modules, heat-absorbing plate, gas or liquid flow path, the edge, back insulation, metal frame and so on, which is without big difference from the traditional photovoltaic solar thermal (PV/T) collector system, and it is shown as Fig. 9. However the system adopts a staged PV/T system, which is different from the traditional photovoltaic solar thermal (PV/T) collector system. The absorber plate of this solar panel collector is no longer composite as a whole, which applies staged form, i.e., it is divided into two parts: the primary stage is solar photovoltaic system and the secondary stage is solar thermal system. There is no direct heat exchange in the space between the two parts, and heat transfer is through the cooling pipes connected between them.

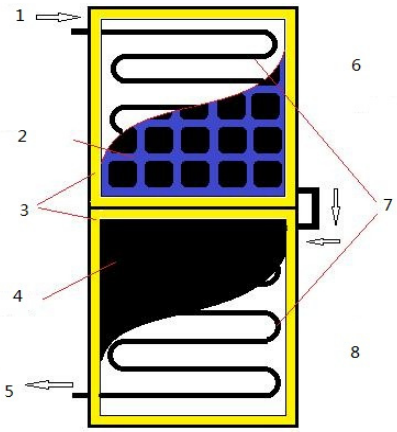

1. Water inlet 2. Solar panels 3. Insulation layer 4. Absorber plate 5. Water outlet
6. The primary stage system 7. Cooling water channels 8. The secondary stage system

Fig. 9. System diagram of staged type PV/T

For the primary stage of the solar cell system, usually the photoelectric conversion efficiency is 15% to 17% by using single crystal silicon solar panels, and the rest of the solar radiation

will transform into heat, while the efficiency of solar panels will decrease with the temperature rising on the board surface, which will make solar panels enter a vicious cycle. For the secondary stage of solar thermal system, the solar radiation heat is mainly absorbed by the heat-absorbing panels, and then the heat is delivered to the cooling substance so as to heat the working fluid. The heat production efficiency and the quality of output water of the system will be improved when the temperature at the inlet of the working fluid increases.

The heat on the solar plate board surface is taken away by cooling water flowing through the primary stage, which can increase the power generation efficiency of the solar photovoltaic. The heat of solar collectors is absorbed through the secondary stage by the cooling water, whose temperature is increased by first stage. The flat-plate solar collector efficiency increases because of the temperature rising of inlet working fluid, which in turn makes the overall utilization efficiency of solar energy increase.

3.2 Overall structural design and layout of solar photovoltaic / thermal collector

3.2.1 The size of solar photovoltaic / thermal collector

The design concept of staged photovoltaic solar thermal collector is proposed in this chapter, and the collector consists of two parts. The primary part is the ordinary solar photovoltaic thermal collector mainly for power generation, however in this design, water is adopted as the working fluid for the thermal collector to cool the panels so as to improve its efficiency and the water is preliminarily heated. The secondary part is a flat-plate collector, playing the role of thermal collector, which is used to heat water flowing out of the primary part.

The structure of the staged collector is shown as Fig. 9. The upper is the primary part covered with solar panels, and the lower side is the secondary part, whose bottom is covered with blackened copper to enhance heat absorption.

The equipment specifications are as followings:

1. Cabinet: Its material adopts galvanized iron sheet with dimension 1000 × 500 × 150mm.
2. Endothermic board: Endothermic board adopts 1mm thickness of copper with the surface sprayed black in order to reduce glare and enhance the endothermic effect.
3. The circulation line: The circulation line applies copper pipe, whose diameter is 10mm, to enhance the heat-absorbing and heat transfer, and the copper surface is blackened with black paint and fixed on the back of absorber plate closely.
4. Transparent cover: It uses ordinary glass, and its size is 505 × 490 × 4mm.
5. Insulation: Insulation adopts fiberglass, whose thickness is about 50mm.
6. Solar panels: Its power is 20W, and its voltage is 17.6V, current is 1.14A, open circuit voltage is 21.6V, short circuit current is 1.33A, and its size is 426 × 406 × 30mm, weight 2.6kg.

3.2.2 The distribution of PV/T heat collector

In this issue, the distribution of PV/T heat collector is two-stage, i.e., the primary stage is photovoltaic subsystem and the secondary stage is photo-thermal subsystem. The principle of this system has been discussed above. Now we focus on its dimensions.

The primary-stage system (PV system) is shown as Fig. 10(a). The dimensions of the system is 500x500x150 mm, and its bottom and all-around are covered with the heat insulating material with 50mm of thickness. Its inner space is with the dimensions of 400×400mm, where a single crystal silicon solar panel of 400×300mm is arranged in it. S-shaped cooling line made of copper, whose outer diameter is 10mm, is installed on the back of solar panel. The copper tube is closely fixed on the back of solar panel to fully absorb the heat and to decrease the temperature of the latter, and heat cooling water inside the tube at the same time. There is an inlet and an outlet of water in the primary stage system.

The secondary stage system (PT system) is shown as Fig. 10(b). The overall size is equal to the primary stage system. The size of heat-absorbing aluminum plate is 400×400mm, which is mounted inside the system. It is covered with black heat-absorbing paint. Compared with previous arrangement, the S-shaped copper tube is arranged on heat-absorbing aluminum plate. It closely contacts the heat-absorbing plate through fiche to enhance its heat transfer efficiency. Furthermore, the copper tube is covered with black heat-absorbing paint to absorb radiation directly. In the secondary stage system, there exists an inlet and an outlet of water as well.

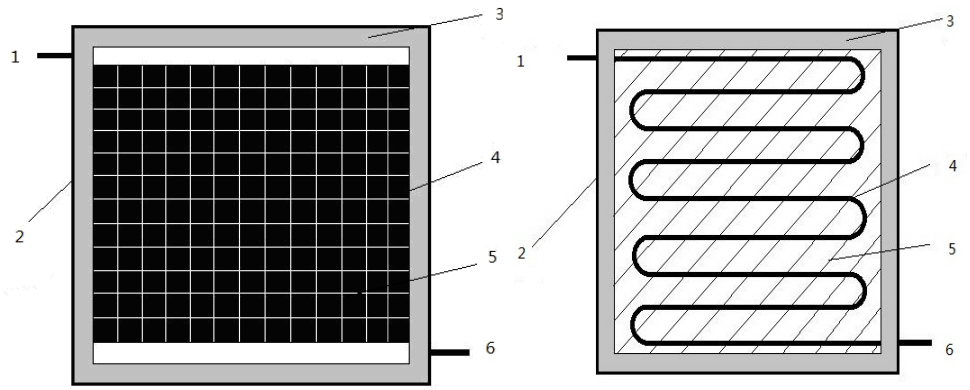

(a) The primary stage system (PV) (b) The secondary stage system (PT)

1. Inlet 2. External wall 3. Heat insulating material 4. S-shaped tube 5. Heat-absorbing plane 6. Outlet

Fig. 10. The primary and secondary stages of the PV/T system

3.3 The experimental system of PV/T heat collector

3.3.1 The system transform valve

A valve, which is called transform valve, is used to link the primary and the secondary stage systems to control the connection or disconnection of the two stage systems to conduct a single PV, single PT and PV/T experiment studied in this chapter. The overall system scheme is shown as Fig. 13. When transform valve is closed and the auxiliary valve is open, the primary stage system is dependent from the secondary stage, and the experiment can be conducted on the primary and secondary stage respectively. When the transform valve is open and the auxiliary valve is closed, the primary is linked to the secondary stage system, and the cooling water or air enters into the primary stage system through the inlet and take

the heat of solar panel away. Then, it continues to absorb heat when it enters into the secondary stage system, which produces hot water and hot air.

3.3.2 The distribution of data collection points

In order to measure the data better, high accuracy thermocouple is mounted on each monitor node shown as Fig.11. Thermocouples A, B, C and D are to measure the inlet and outlet temperature of the primary and secondary stage system, respectively. Thermocouple E and F are to measure internal cavity temperature of the primary and secondary stage system respectively. At the same time, there are testing points to measure the atmospheric temperature, wind speed, voltage and current of the solar panel.

3.3.3 The principle of measurement

The electric performance testing of the solar panel may be attributed to test its voltage current characteristics. Since the voltage current characteristics is relative to the testing conditions, the performance of solar panel needs to be tested under standard condition or the measured results need to be transformed into standard condition. The standard testing condition consists of standard sunshine, which includes standard spectrum and radiation, and standard testing temperature, which can be controlled manually. The standard sunshine can be simulated or attained in nature. When simulated sunshine is applied, the spectrum depends on the sort of electric light source and filtering and reflecting systems. Radiation can be adjusted through the calibrated value of the short-circuit current of the solar battery. In order to reduce unmatched error of the spectrum, the spectrum of simulated sunshine should be close to the standard sunshine spectrum or the standard solar battery, whose response is almost the same as that of the tested battery, should be chosen[11,12].

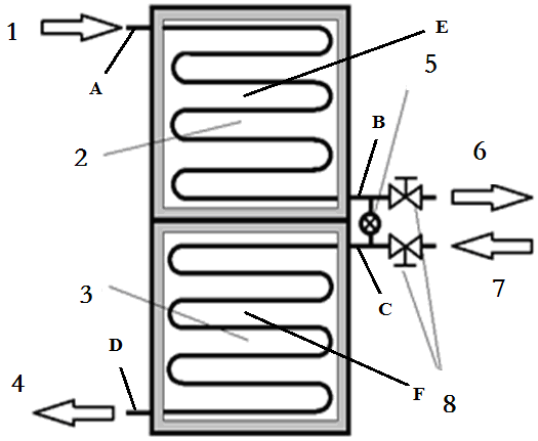

1. The primary stage outlet system 2.The primary stage system 3.The secondary stage system 4. The secondary stage outlet system 5.Transform valve 6.The primary stage outlet 7. The secondary stage inlet system 8. Auxiliary valve A. Thermocouple A B. Thermocouple B C. Thermocouple C D. Thermocouple D E. Thermocouple E F. Thermocouple F

Fig. 11. The valve control and distribution of data acquisition diagram

3.3.4 Electric performance testing conditions

a) The standard testing conditions

Overall radiation is measured by AM 1.5 standard action spectrum. The radiation is 1000W/m², and the testing temperature is 25°C.

As for the standard testing, the tolerance error of standard temperature measurement is ±1°C, while the tolerance error is ±2°C for the nonstandard testing. If the testing can only be conducted under nonstandard condition due to the restriction of the objective condition, the tested results should be transformed into the standard testing condition.

b) Testing devices and apparatus

The testing devices and apparatus include standard solar battery, voltmeter, ammeter, sample resistance, load resistance, thermometer, and indoor tested light source. The standard solar battery is used to adjust the radiation of tested light source. When AM 1.5 standard solar battery is tested, the radiation is adjusted by secondary-rank AM 1.5 standard. In nonstandard measurement, the radiation is only adjusted by AM 1.5 standard. The accuracy of voltmeter is no less than class 0.5 and its internal resistance is no less than 20kΩ/V, generally using digital voltmeter. The accuracy of ammeter is no less than class 0.5 and its internal resistance should guarantee the tested voltage is no more than 3% of open circuit voltage when short circuit current is tested. When better accuracy is necessary, it can take advantage of voltage's linear relationship with current to deduce short circuit current when full short circuit is below 3% of open circuit voltage. The current can be measured by measuring the voltage drop of sample resistance through digital millivolt meter.

The product of short circuit current and sample resistance is no more than 3% of open circuit voltage. Load resistance can be adjusted from 0 to more than 10kW smoothly. Subsequent power volume should be guaranteed to the accuracy, which is influenced by heating power produced by electricity. When the variable resistance can't meet condition above, an equal electron variable load should be adopted. The error of thermometer or thermometric coefficient is no more than ±0.5°C. Response time of the testing system is no more than 1s. The radiation, uneven extent of radiation, stability, accuracy, and spectral distribution must meet some demand.

c) Testing items

The testing items include open circuit current (V_{oc}), short circuit current (I_{sc}), optimum operating voltage (V_m), optimum operating current (I_m), maximum output (P_m), photoelectric conversion efficiency(η), filling factor (FF), I—V characteristic curve, short circuit current temperature coefficient (α), open circuit voltage temperature coefficient (β), internal series connection resistance (R), internal parallel connection resistance (R_{sh}).

d) Basic testing method

Of the above testing items, open circuit voltage and short circuit current are tested by ammeter directly, and the other parameters are calculated through voltage current characteristics. The voltage current characteristics of solar battery is tested under standard sunshine, solar simulator or other equal solar simulators.

e) Convert nonstandard testing condition into standard testing condition

When the testing temperature and radiation differs from the standard condition, it can be corrected according to the following equations:

$$I_2 = I_1 + I_{sc}\left(\frac{I_{SR}}{I_{MR}} - 1\right) + \alpha\left(T_2 - T_1\right) \tag{1}$$

$$V_2 = V_1 - R_s\left(I_2 - I_1\right) - kI_2\left(T_2 - T_1\right) + \beta\left(T_2 - T_1\right) \tag{2}$$

Where I_1, V_1: Tested voltage, tested current or the parameter to be corrected; I_2, V_2: Corrected result; I_{sc}: Short circuit current; I_{MR}: Short circuit current of standard battery under practical condition; T_1: Testing temperature; T_2: Standard testing temperature; R_s: The internal series electric resistance of tested battery; k: Curve correction factor, which can be set as $1.25\times10^{-3}\Omega/°C$; α: Short circuit current temperature coefficient under standard radiation condition and certain temperature window; β: Open circuit voltage temperature coefficient under standard radiation condition and certain temperature window.

3.4 Experimental data analysis

3.4.1 Experimental apparatus

The apparatus needed in the experiment for solar panel PV/T heat collector consists of distributed solar panel PV collector, TRM-PD artificial solar panel simulator, 10mm outer diameter of rubber tube, 18W pump, 12VDC electrical source, K thermocouple, data acquisition card, Agilent 34970A data acquisition and a computer.

3.4.2 Data analysis

The experimental data are collected and recorded by data acquisition system, and exported to CSV format or excel charts. Different variation curve corresponding temperature, current, and the voltage are as follows.

The relationship between current and voltage, and the history of voltage and current changing with the surface temperature are shown as Fig. 12 and Fig. 13 (a) and (b) respectively. It can be seen from Fig. 12 that the current curve and voltage curve merged gradually with the changing of time, and they combined at last. The current and voltage affected each other, and the current has the same trend as the voltage, i.e., when voltage goes up or down, the current also goes up and down. As shown in Fig. 12, the current curve is steady, so that no matter how the flux of cooling water varies, the voltage curve is almost without any effect. The current drops down immediately at the data point of 333, and after this point, the current is around 0.12A. There are some abnormal points in Fig. 12, which are assumed due to the random error [11, 13].

As shown in Fig. 13 (a) and (b), the higher the surface temperature, the lower the output voltage. However, the curve is relatively gentle. It is obvious that the higher the surface temperature the lower the output current. There are some abnormal points due to error. And then, it can be seen that the generating efficiency of solar panel is greatly influenced by surface temperature of solar panel. Furthermore, the higher the surface temperature it has,

the lower the generating efficiency. It agrees well with the initial hypothesis of the experiment. Through data analysis, the stable data can be chosen from each flux part. The average data at each flux are shown as table 3.

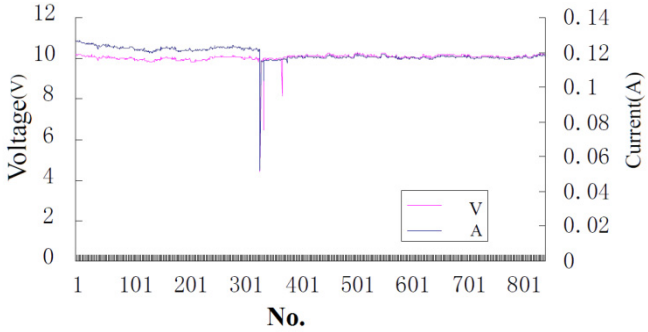

Fig. 12. Relationship between current and voltage

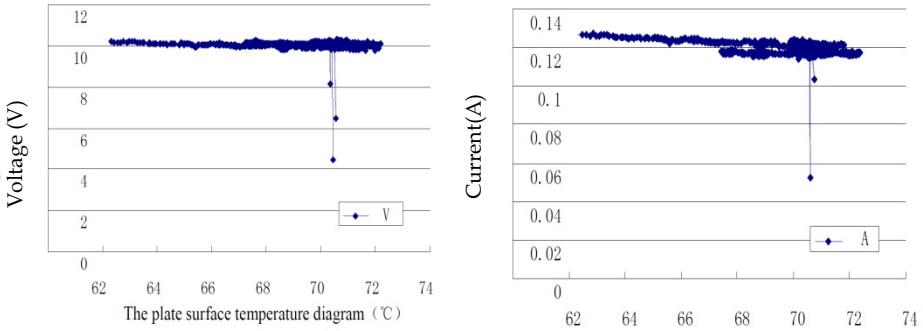

(a) The voltage (b) The current

Fig. 13. The history of voltage and current changing with surface temperature

Due to the limited range of the data acquisition instrument, the streaming triage method is used to collect the data. An electric resistance with the same resistance value as that of the data acquisition instrument is paralleled into the data collection section to share the electric current. The diagram is shown as Fig. 14.

It can be attained from Fig. 14:

$$U_i = U_r = U_{total} \tag{3}$$

$$I_{total} = I_i + I_r = I_i + U_{total} / R \tag{4}$$

Where U_{total} is the voltage of the cell plate, U_i and U_r are the voltage of collector and the voltage between the two ends of the parallel resistance respectively; I_{total} is the current of the panels; I_i and I_r are the current flowing through the collector and the parallel resistance; R is the parallel resistance, 10Ω.

Therefore, generating power of the solar panels is calculated as follows:

$$P_{total} = P_i + P_r = U_i \bullet I_i + \frac{U^2}{R} \tag{5}$$

Based on the data in table 3, according to eq. (5), it can get P_{total} and $P_{average}$ shown in table 4.

Flux (L/h)	2.647	3.103	7.895	15.000	27.692	36.000
Inlet temperature (°C)	28.809	29.155	27.808	28.012	28.088	28.049
Outlet temperature of the primary stage (°C)	39.206	42.445	34.967	32.021	31.905	30.026
Outlet temperature (°C)	45.718	50.780	38.633	34.551	34.271	31.356
Heat-absorbing plate Temperature (°C)	52.507	64.114	51.873	50.649	52.356	50.082
Glass Cover-Plate Temperature (°C)	63.945	66.650	68.197	55.286	68.084	66.934
Back surface Temperatureof solar Panel (°C)	67.014	69.870	70.851	72.231	72.604	71.927
Front surface Temperature of solar Panel (°C)	67.262	69.591	71.242	72.582	73.084	72.128
Atmospheric temperature (°C)	29.581	30.258	29.770	30.506	30.169	30.409
Voltage (V)	10.083	10.088	9.940	9.962	10.152	10.176
Current (A)	0.1246	0.1170	0.1216	0.1201	0.1176	0.1167

Table 3. Average Tested Data

Q_v (L/h)	2.647	3.103	7.895	15.000	27.692	36.000
P_{total} (W)	11.423	11.357	11.089	11.117	11.500	11.543
$P_{average}$ (W)	11.34					

Table 4. The P_{total} and $P_{average}$ at different Q_v

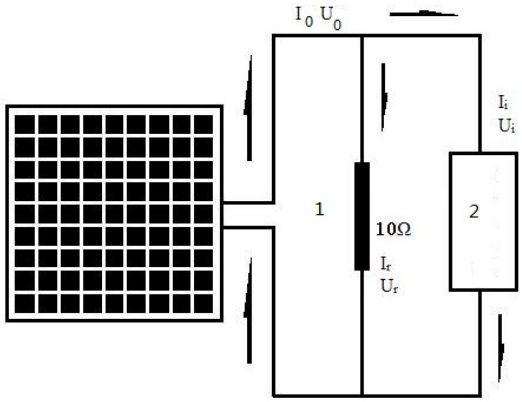

Fig. 14. The diagram of data acquisition circuit

The light intensity of solar simulator that the system adopts is 800W and the effective area used in the system is 400 × 300 mm². Therefore, the input power of the solar panels can be calculated as following.

$$P_{inlet} = 800W / m^2 \times 0.12m^2 = 96W \tag{6}$$

The utilization efficiency of solar system can be calculated as following:

$$\eta = \frac{P_{average}}{P_{inlet}} \times 100\% = 11.8\% \tag{7}$$

The generation powers corresponding to the above flux are shown as Fig. 15.

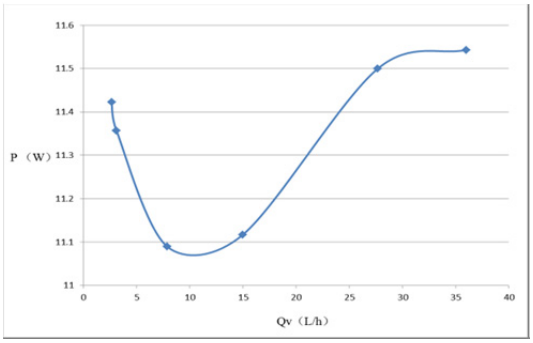

Fig. 15. The generation power changing with the flux

It can be seen from Fig. 15 that generating power of the solar panels decreased and then increased with the increasing of the cooling water flow. This may be because the board surface temperature is not high when the panels start to work, and the battery plate board surface is of higher photoelectric conversion efficiency. But with the increasing of the working hours, accumulation of heat on the plate is increasing more and more, and at the same time the cooling water flowing on the back surface of the solar panels is so small that it can't transfer heat of the battery plate board's surface out well, which makes solar panels generating power present a downward trend at this stage. When the cooling water flow rate on the back surface of the panels increased to 10L/h or so, the generation power of panels began to increase with the increasing flow rate of cooling water and when the flow rate reached up to 30L/h or so, the curve of the generation power of the panels becomes stable. This shows that when flow rate of the cooling water is between 10L/h and 30L/h, the effect of cooling panels is better, which makes the temperature of battery plate board surface be controlled, so that the generating power of the solar panels gradually increased. When flow rate of the cooling water is higher than 30L/h, the generation power of the solar panel hardly changes with the flow rate, and it can be inferred that 30L/h is the best flow rate for the cooling water.

In the experiment, power output of the solar panel is 20W, radiation intensity of the solar simulator is 800W, and the rated power output of the solar panel is calibrated with the solar radiation output at 1000W. The output power of the solar panel is basically linear with photovoltaic intensity, so the power output under 800W of radiation intensity is

$$P_{800} = 20W \times 800W / 1000W = 16W \quad (8)$$

$P_{average}$, the calculated average power output of the generation system, equals to 11.34 W, which is 4.66W less than the output power when radiation intensity is at 800W, that is to say, the actual power output of the generation system is 70.88% of the rated power output.

4. Solar air-conditioning/heating system

At present, the solar energy air-conditioning becomes the key research and development of the energy projects in some countries [14, 15]. In the late 1970s, with the development of solar energy technology, solar air conditioning technology emerged. The research on using solar energy to provide heating and cooling for the buildings has been developed rapidly in many ways. New industrial district of solar energy has been born in many countries and many solar energy devices have been commercialized. International and regional academic, exhibition and cooperation have become frequently and many countries allocated money to subsidize solar energy utilization every year. However solar air-conditioning industry is still in the developing stage [16, 17], and the market still needs time to be mature.

The solar energy air conditioning is developed well mainly in Italy, Spain, Germany, the United States, Japan, Korea, Singapore, and Hong Kong [18]. China mainland has conducted a lot of research on the usage of solar heating and cooling. The first small-scale solar energy building was built in Gansu, China in 1977, mainly for heating. And a practical large-scale solar water heating and air conditioning system was built in Jiangmen, by Guangzhou Institute of Energy in 1998, but the use of solar energy cooling in summer and heating in winter and providing hot water for living in the transition seasons is still in its initial stage. Furthermore, with improvement of living standard and formation of high income class, the demand on the indoor and outdoor environment of constructions is gradually increasing, so that the combination of solar and villa construction have a bright prospect of development because of its non-pollution characteristics [19].

In summer, the hot water heated by heat collector goes to the storage tank. When the water temperature reaches a certain value, the storage tank provides water, the heat medium, to the refrigeration machine. When hot water comes out of the refrigeration machine, its temperature drops and as the heat medium, it goes back to the storage tank to be heated by the solar collector. Refrigerating machine produces chilled water for air conditioning box to achieve the purpose of air conditioning. When solar radiation is insufficient to provide enough heat for high temperature hot medium water, the auxiliary heat source is turned on. In winter, hot water heated by solar collector goes to storage tank, and when its temperature reaches a certain value, the heat storage water tank directly provides hot water to air conditioner box. When heat provided by solar radiation is not sufficient, the auxiliary heat source will switch on. During the transition season, the hot water heated by the collector flows through the heat exchanger into the hot water tank, to heat water in it.

4.1 The purpose of the research on solar air conditioning / heating system

With the improvement of living standard, human demand for energy is increasing day by day. But along with the price of the coal and demand of air pollution emission controls gradually increase, the cost of electricity has arisen. So the development of efficient, environmentally friendly and safe energy has great prospects.

At present, there are two main ways to use solar energy, i.e., photovoltaic and solar thermal. PV is no good chance to develop due to its high costs. Photo-thermal is fairly popular in people's living by using solar water heater [13]. However solar water heater only plays a small part for living energy supply. Furthermore, currently the solar cells of single crystal and polycrystalline silicon on the market have an average efficiency of around 15%.

The design of the solar air conditioning /heating system in this chapter occupies little electricity, using clean energy to cool in the summer and heat in the winter. It makes full use of light energy, through photovoltaic and photo thermal effects to produce heat and power generation at the same time. The gravity heat pipe is installed on the back surface of a solar panel, so that heat from the solar panel can be transferred to the house. Thus, the photovoltaic efficiency of the solar cell is obviously improved without changing its solar board structure.

Traditional heating and heat preservation facilities are adopted for the solar panels and solar collector individually. But solar energy density is so low that considerable area of the collection and conversion equipment are often required to get some conversion power, whose cost is very high. In fact, how to make good use of solar energy for building energy saving, and some passive solar application facilities, which combine heating in winter with heat insulation in summer, are even now continuing to be studied [20].

Currently, many organizations have developed the system similar to solar air-conditioning system, but the actual mature technology of solar air conditioning is still very rare [21].

A solar air conditioning/heating system has been developed in this chapter, and the efficiency of photovoltaic solar panel system increases 6% and output power of the simulated system in the experiment is 558.66w. In heat supply conditions in winter, the heat exchanger can output 467w heat to the house. It can accomplish the combination of heating in winter and cooling in summer, and it can save energy and improve the efficiency of photovoltaic solar panels on the market. Based on the photovoltaic and photoelectric effects, the system applies solar radiation as the energy source so that it can reduce energy consumption and become a heating-cooling two-way solar air conditioning / heating system.

4.2 Experimental study on solar air conditioning / heating system

4.2.1 Description of the solar air conditioning / heating system

The solar air conditioning / heating system in this chapter is as the following:

1. The solar air conditioning / heating system in this chapter has the function of cooling in the summer and heating in the winter using clean energy, with a little or without electricity.
2. The system makes full use of light energy. It applies photovoltaic effect to generate electricity as well as photo thermal effect to produce heat. The gravity heat pipe is installed in the back surface of the solar panel, so that heat from the solar panel can be guided into the house.
3. The system can obviously improve the efficiency of the solar photovoltaic on the market without changing the structure of solar panel.

4.2.2 The structure of the system

The solar air conditioning / heating system is shown as Fig. 16, and it consists of the solar panels, heating pump, gravity heat pipe, indoor and outdoor heat exchanger. The working principle of the system is that under normal working conditions of the solar cell, the heat of battery panel is taken away by the flow of the working fluid, water and water vapor, in the gravity heat pipe made of copper materials. In the wind tunnel, the heat is exchanged between pipe and fin by convection. Through the density difference between hot and cold air, the hot air is brought into indoor to heat the room. In summer, solar radiation are so abundant that electricity generated by the solar panels can drive heat pumps to accomplish endothermic cooling.

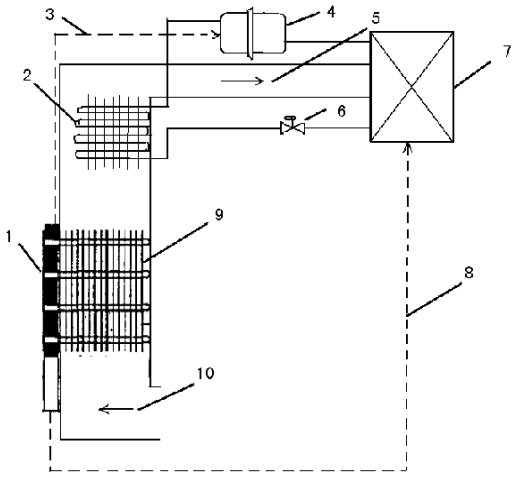

1. Solar panels 2. Outdoor air heat exchanger 3. Power supply 4. Compressor 5. A warm air outlet 6. Expansion valve 7. Air heat exchanger 8. Power supply 9. Heat pipe and fin 10. Cold wind inlet

Fig. 16. The structure of solar air conditioning / heating system

4.2.3 The system processing

a. The heat exchanger composed of heat pipe and fin

Heat pipe is a high efficient heat transfer element, which can transfer large amount of heat with a small area. The heat of the solar battery plate can be concentrated by the heat pipe through its one-way heat conduction. Gravity heat pipe without a capillary structure has the advantages of simple structure and convenient manufacturing process, and liquid returns naturally to the evaporator by gravity, so the working fluid flow is stable and reliable. At the same time, it's flexible for piping arrangements. Compared with the capillary structure of heat pipe, it is easier to design and its cost is much lower. So it can adapt to most situations, however the position of the condenser must be higher than the evaporation end. The schematic diagram of heat exchanger composed of heat pipes and fins is shown as Fig. 17.

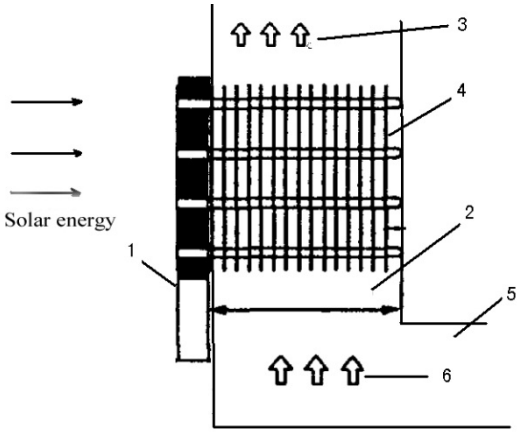

1. Solar panel 2. Cooling section 3. Warm air 4. Fins 5. Hot air channel 6. The cold wind

Fig. 17. Schematic diagram of heat exchanger composed of heat pipes and fins

b. The connection between solar panels and heat pipes

The gravity heat pipe cooling mode is adopted in the system and water is the working substance. For the heat pipe, the design of evaporation end is an important part, which directly affects its ability to deal with the heat produced in solar concentrator photovoltaic cells and the ability to control its temperature. A good design of the evaporation end should ensure evaporation end transfer enough heat to make the operating temperature of the solar concentrator photovoltaic cell as low as possible, not exceeding the critical temperature, enabling it to continue working properly. The evaporation end of the heat pipe contacts the concentrator solar cells, and its temperature field has an obvious effect on performance of the battery and efficiency of the heat pipe. In this chapter, the evaporation end is designed as a cuboid with the dimensions of length 100mm, width 100mm and height 30mm. The diagram of the heat pipe on solar evaporation end is shown as Fig. 18.

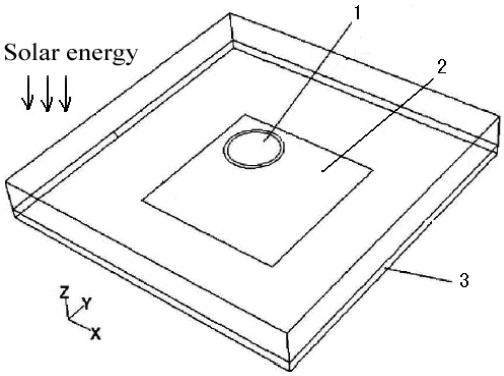

1. Gravity heat pipe 2 Layer of metal thermal conductivity 3 the back surface of solar panels

Fig. 18. The connection diagram of solar panels and heat pipes

c. Throttle switch

In summer, the air damper is put downward, which separates the vertical air channel from the horizontal air channel, letting the hot air directly emit into the atmosphere. While in the winter, the air damper is put upward, so the vertical and horizontal air channels are connected, letting the system heat the indoor room.

4.3 The theoretical analysis of experimental data on the solar energy air conditioning / heating system

4.3.1 Cases in the summer

The photoelectric conversion efficiency of solar panels on the market is 16%, and it drops about 0.5% with each 1°C rising of the temperature. In this chapter, TRM-PD artificial sun simulation emitter, whose light intensity ranges from 0 to 800 W/m^2, is adopted, from which the solar panels receive the simulated illumination.

The parameters of the equipment are as follows:

a. The heat-absorbing plate: 1 mm thickness of copper plate painted black to reduce the reflection to enhance absorption effect
b. The transparent cover: ordinary glass with dimension of 505 × 490 × 4 mm
c. The thermal insulation layer: glass silk, with around 5 cm of thickness
d. The solar panels: its power is 20 W, working voltage 17.6 V, working current 1.14 A , open circuit voltage 21.6 V, short-circuit current 1.33 A, with dimension of 426 ×406 ×30 mm

The average values of the measured data of the solar panels are shown as Table 5.

$$P_{average} = \frac{\sum_{i=1}^{n} P_{Total\ i}}{n} = 17.18W \tag{9}$$

The light intensity output of solar energy simulator in the experimental system is 800W, and the effective area of the solar energy panels is 400 mm × 300 mm, so the input power of panels is:

$$P_{inlet} = 96W \tag{10}$$

Without a cooling device, the solar energy utilization η_1 is:

$$\eta_1 = \frac{P_{average}}{P_{inlet}} \times 100\% = 11.8\% \tag{11}$$

Adding the cooling device, the solar energy utilization η_2 is：

$$\eta_2 = \frac{P_{average}}{P_{inlet}} \times 100\% = 17.8\% \tag{12}$$

It can be inferred that after adding the cooling device, the solar energy utilization rate is increased $\Delta\eta = \eta_2 - \eta_1 = 6\%$. Under this condition, with solar panels area of 8m², the electric power output is

$$P = 558.66W \tag{13}$$

Flux (L/min)	Inlet Temperature (°C)	Outlet temperature (°C)	Surface temperature of battery board (°C)	Atmospheric temperature (°C)	Voltage(V)	Current(A)
2.647	28.809	45.718	57.262	29.581	10.083	0.1246
3.103	29.155	50.780	59.591	30.258	10.088	0.1170
7.895	27.808	38.633	61.242	29.770	9.940	0.1216
15.000	28.012	34.551	62.582	30.506	9.962	0.1201
27.692	28.088	34.271	63.084	30.169	10.152	0.1176
36.000	28.049	31.356	62.128	30.409	10.076	0.1167

Table 5. The average of the measured data during each flow period

4.3.2 Cases in the winter

The winter condition is also designed according to performance parameters of the solar battery and the heat pipe installation model as mentioned above. It is assumed that the solar radiation intensity is 400 W/m², the average temperature of solar panels is 55 °C, the average temperature of the heat pipe and fins $t_f^{'} = 40^oC$, inlet temperature $t_f^{'} = 10^oC$, heat length is 2.5m, and air flow velocity $u_m = 2m/s$.

Heat exchanging unit of this system is shown as Fig. 19.

Assuming air temperature at the outlet $t_f^{''} = 25^oC$, then the qualitative temperature $t_f = (10+25)^oC/2 = 17.5^oC$, and the corresponding physical parameters of air are $\lambda = 0.0276W/(m\cdot K)$, $\nu = 16.96\times10^{-6}m^2/s$, $\mathrm{Pr}_f = 0.699$, and $\eta_f = 19.1\times10^{-6}Pa\cdot s$.

It can be inferred that

$$\mathrm{Re}_f = \frac{ud}{v} = 11793 > 10^4 \tag{14}$$

The air flow in the turbulent field,

$$Nu_f = 0.023\mathrm{Re}_f^{0.8}\mathrm{Pr}_f^{0.4} = 30.752 \tag{15}$$

$$h_f = Nu_f\frac{\lambda}{d} = 8.7W/(m^2\cdot K) \tag{16}$$

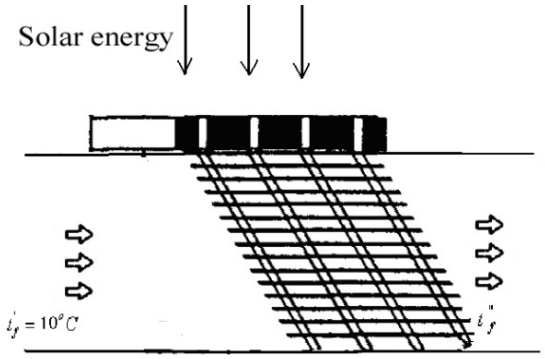

Fig. 19. Heat exchanging unit of this system

According to the assumed exit temperature, the logarithmic mean temperature difference of air flow along the total tube length is equal to

$$\Delta t_m = \frac{t_f'' - t_f'}{\ln[(t_f' - t_w)/(t_f'' - t_w)]} = 22.46^oC \tag{17}$$

According to the surface heat transfer coefficient, the quantity of convective heat transfer can be calculated as

$$\Phi_1 = h_f 4lL\Delta t_m = 522W \tag{18}$$

According to the flow rate and the temperature rising from inlet to outlet, the total heat exchanging can be calculated as

$$\Phi_2 = q_m c_p (t_f'' - t_f') = 445.3W \tag{19}$$

The results of two total heat exchanging don't match each other because the assumed outlet temperature is not correct. Through the iterative computation to eliminate deviation, the result is:

$$h_f = 8.32W/(m^2 \cdot K), \quad t_f'' = 22.4^oC, \quad \Phi = 467W \tag{20}$$

Under winter heating condition, the reachable heat output of exchanger is 467 W.

5. Research on the solar drying system

In some countries, such as in China, sometime clothes are suspended outside the window to dry, which are uneven in length, affecting the scene of the city, and the water drop may either wet passers-by or commodities. At the same time, domestic appliances are getting more various to meet the modern living, making it possible to design a novel device to combine the existed domestic appliances to dry the clothes besides their existing functions.

In this chapter, a novel device is designed to connect with solar energy collector, and it can also be connected to domestic solar water heater to effectively use excess energy of the solar water heater. The device mainly consists of insulation shell, heat transfer system, ventilation system, drainage system, temperature humidity control system, ultraviolet radiation sterilization disinfection system and some auxiliary systems. Compared with the published patents, this device just needs a small area, and it can work under a complete indoor situation of natural environment. It is installed with ultraviolet disinfection lights and hollowed aromatherapy box, so it may sterilize clothes and fresh the air during drying clothes so as to achieve better results than clothes are dried outside the window. This device may be effectively applied to lots of occasions, such as families, hotels, schools and so on. It shows high practical value and economic and social benefits.

5.1 Backgrounds of the solar drying system

The high price of the house and apartment is an outstanding issue in modern society, so that small living space becomes very popular in some regions. To save space, the clothes are suspended outside the window to dry. If a sudden rain happens, clothes will be wet and dirty again. In order to solve this problem to help people living more convenient, some devices using solar energy to dry clothes have been on the market, while they can only be used outdoor. The authors have designed a kind of solar drying system, which occupies a small area so that it may be installed in the house, and has the same drying effect as the clothes are put outside the window,.

At present, there is no similar device on the market yet, and sometime warm air blower or electrical heater is used to dry clothes for emergencies, which consumes a lot of energy and seriously damages the clothes, so it is not a good choice for a long time.

Solar energy water heater are widely used in lots of region, so if we can link solar energy water heater with a drying oven, using its original power cycle system to make hot water circulate in the designed oven and the heat flow through the pipe to distribute inside the box, the clothes will be dried quickly with the convection of hot air. The device can accomplish this function in small indoor space. It can not only make full use of the solar energy water heater during idle time, but also can shorten the drying time, so it may increase the solar energy utilization efficiency and improve the quality of people's daily life.

5.2 Technical requirements on the solar drying system

For the solar energy dryer, due to its small working area, long working hours, and strong dependence on the weather, the following specifications are required:

1. Materials with good heat conduction performance are used to manufacture the pipe in the oven, so that they can absorb the maximum quantity of heat from hot water to ensure a high constant temperature of the oven.
2. Ultraviolet disinfection lamp is installed in the oven to sterilize the clothes, which can make the dryer arrive at the unique advantage of drying out of the window as far as possible.
3. A small fan is installed in the oven. It not only accelerates the wet loss of moisture, making humid air quickly spread to the external to increase dryness of the internal air, but also strengthens the flow of hot air to improve drying efficiency.

4. A hollowed aromatherapy box is specially installed inside the oven, so that the clothes will have a light faint scent, making our body more comfort.
5. The probes of thermometer and humid meter are installed inside the oven, which can readily record the temperature and humidity. The flow valves at the bottom of the box may be adjusted to control the heat transfer according to the feedback of temperature and humidity together with the materials of the clothes.
6. Thermal insulation material is installed up and down and back and forth of the dryer to prevent heat loss. The left and right sides are made of movable glass, so it is easy to put the clothes into the oven, and adjust ventilation rate according to temperature and humidity.
7. The drying oven and solar energy collector share one set of power cycle system.

5.3 Design scheme of solar drying system

5.3.1 The main body structure of solar drying system

The solar drying system not only needs to solve the city image problem due to clothes being hanged to dry outdoor, but also needs to simulate the situation of drying outdoor as far as possible. For example, the sterilization of outdoor sunlight and other characteristics need to be reflected in the design, making it come from the nature and be better than the natural

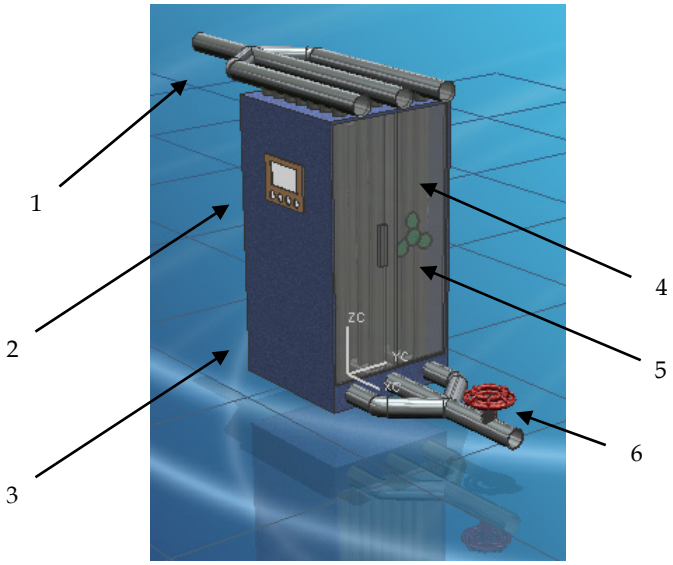

1. Heat transfer conduit 2. Thermo-humidometer 3. Heat preservation box shell 4. Movable glass door 5. Fan 6. The regulator

Fig. 20. Main body structure design of solar drying oven

The main body structure of the solar drying device is shown as Fig. 20. It demonstrates that the main body of the solar drying device includes ultraviolet disinfection system, ventilation system, temperature and humidity control system, drainage system, heat transfer system and additional system.

5.3.2 Heat transfer and ventilation system

Heat transfer system is the main system of the drying device. In order to increase the relative area of the heat transfer, three rows of pipe with staggered pattern are added within limited space conditions, dividing the oven into two parts so as to let clothes be hanged between the pipe rows. The heat transfer system is shown as Fig. 21(a). Hot water flows in the pipe and convection heat transfer happens between pipelines, heat transfer between pipeline walls is conduction, and heat is transferred to the clothes in the oven through thermal radiation and convection. Because the hot water in the unceasing cycle ensures the heat supply, and the pipe made of good thermal conductivity material has good heat transfer characteristics, the heat loss is strongly reduced to the minimum to increase the heat transfer efficiency.

The ventilation system is necessary in the drying device. It is confirmed through a large number of experiments that during clothes drying, because the air is too wet, movable glass of drying device are full of water mist so that drying effect is greatly reduced. To solve this problem, a small speed-adjustable fan is installed, which can not only appropriately speed up the wet loss of air according to the practical situation, but also accelerate the hot air convection. Ventilation system is shown as Fig. 21(b). In addition, both sides of movable glass walls can regulate ventilation rate according to the specific situation.

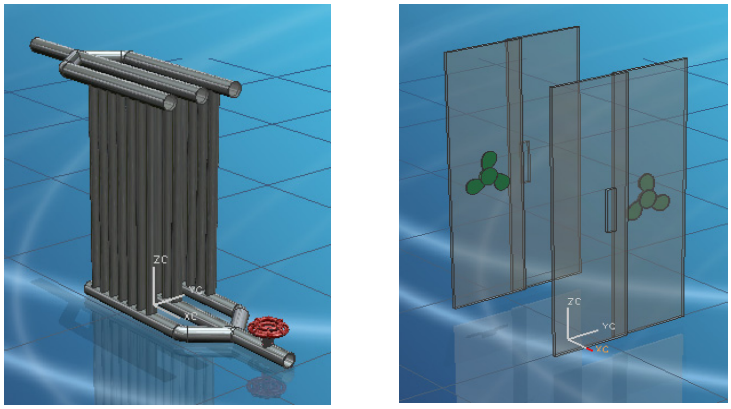

(a) The heat transfer system (b) The ventilation system

Fig. 21. The diagram of the heat transfer and ventilation system

5.3.3 Temperature and humidity control system

In order to achieve better drying effect and reflect people-oriented design concept, a temperature and humidity control system is installed with the probes of the thermometer and humidity meter being inserted into the oven. The probes can sensitively detect the internal temperature and air humidity and digitally display on the external side of the box. The flow control valves at the bottom of the oven is adjusted by evaluating data on the meters, the material of the clothes and its drying difficulty level to change the hot water velocity, in turn, change the heat flux. Temperature and humidity control system is shown as Fig. 22.

5.3.4 Drainage system

The clothes are now usually washed by washing machine, and then most water is eliminated by a spin-drier, so that the water remaining in the clothes is relatively low, and the clothes would be much easier to dry. However, not all the clothes are washed with a washing machine, especially those small ones in the summer are usually washed by hand. Based on this consideration, the bottom of this drying machine is designed as four corners so that dripping water can deviate from the drain outside the oven by their own gravity. Drainage system is shown as Fig. 23.

5.3.5 Ultraviolet sterilization system

Except for the limited indoor space, the main reason people hang clothes out in the sun is to get the sterilization effect of the ultraviolet rays in sunlight to make clothes more clean and fresh. In order to simulate outdoor conditions completely, two ultraviolet disinfection tubes are installed on the top side inside the dryer so as to reach natural ultraviolet ray sterilization effect.

5.3.6 Auxiliary system

In order to let solar drying machine more considerate to provide more practical assistance to people's life, a hollow aromatherapy box is installed inside the oven, which makes the clothes more pure and fresh during drying. And the hollow box is removable, and people can replace box spices according to their favorite tastes.

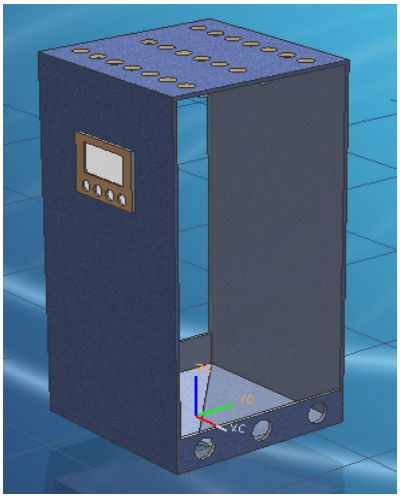

Fig. 22. Thermo-humido-control system

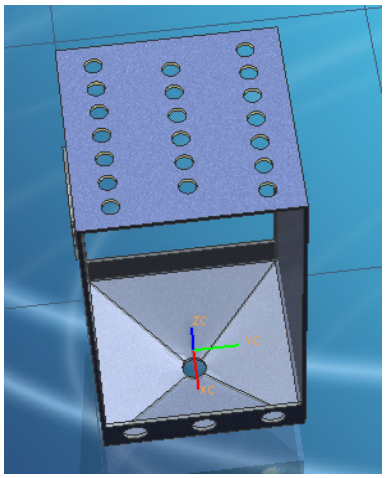

Fig. 23. Drainage system

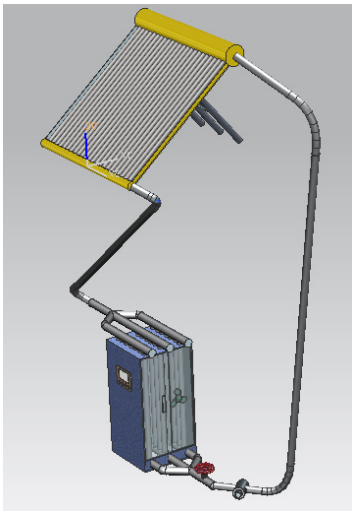

Fig. 24. Solar drying machine system

5.4 Device characteristics

The invented solar drying machine can illustriously combine with solar water heater, adjust the heat flux and ventilation rate, accommodate all kinds of clothes, and dry quickly. It has a good performance to work for a long time in good sunlight, and it has a high stability, reliability, and strong practicability. The whole system is shown as Fig. 24.

6. Summary

As one kind of inexhaustible, safe, energy saving, environmental protective new energy, solar energy is getting more and more attention in this world and it has a huge development potential. Through the research of solar flat-plate collector, staged solar photovoltaic and thermal collector, solar air-conditioning system and solar drying system, the authors explore a research and developing approach of solar energy.

7. References

[1] Grasse W. Solar PACES Annual Report. DLR Germany, 1998.
[2] Rabl A., Optical and thermal properties of compound parabolic concentrator, Solar Energy, 1976(18): 497–511.
[3] Kostic LT, Pavlovic TM, Pavlovic ZT. Influence of reflectance from flat aluminum concentrators on energy efficiency of PV/Thermal collector, Applied Energy, 2010(87): 410–416.
[4] Chiasson A.D., C. Yavuzturk, Assessment of the viability of hybrid geothermal heat pump systems with solar thermal collectors, ASHRAE Transactions, 2003, 109 (2): 487–500.
[5] Ozgener O., Hepbasli A., A review on the energy and energy analysis of solar assisted heat pump systems, Renewable and Sustainable energy reviews, 2007(11): 482-496.
[6] Dossier Géothermie, Revue bimestrielle Systeèmes solaires – L'observateurdes énergies renouvelables, 2002(148): 20–60.
[7] Hellstrom B, Adsten M, Nostell P, Karlsson B, Wackelgard E., The impact of optical and thermal properties on the performance of flat plate solar collectors, Renew Energy, 2003(28): 331–344.
[8] Tanaka H, Nakatake Y., Improvement of the tilted wick solar still by using a flat plate reflector. Desalination 2007(216): 139–146.
[9] Tanaka H, Nakatake Y., Increase in distillate productivity by inclining the flat plate external reflector of a tilted-wick solar still in winter, Solar Energy, 2009(83): 785–789.
[10] Tanaka H., Tilted wick solar still with external flat plate reflector: optimum inclination of still and reflector, Desalination, 2009(249): 411–415.
[11] S.X. Yi, H.X. Sheng, F.F. Wang, Test of ventilation and lowering moisture on late indicia rice of high moisture content in large warehouse, Grain Storage, 2005(35): 32-34.
[12] Jain D., Modeling the performance of the reversed absorber with packed bed thermal storage natural convection solar crop dryer, J Food Eng, 2007(78): 637–647.
[13] Alvarez A,, Cabeza O,, Muñiz MC,, Varela LM., Experimental and numerical investigation of a flat-plate solar collector, Energy, 2010(35):3707-3716.
[14] Henning H-M., editor. Solar assisted air-conditioning in buildings—a handbook for planners. ISBN3-211-00647-8, Wien: Springer, 2004.
[15] Syed A., Maidment G., Missenden J., Tozer R., Optimal solar cooling systems. HPC 2004, the third international conference on heat powered cycles, Larnaca, 10–13 October, Cyprus, 2004.
[16] Carrier product data, active and passive chilled beams, model 36CBPB14, Carrier Corporation, 2008.

[17] Matsui H., Okada K., Kitamura T., Tanabe N., Thermal stability of dye-sensitized solar cells with current collecting grid, Energy Mater Sol Cells, 2009(93): 1110–1115.
[18] H. Liu, L.L. Zhang, L.M. Ren, The in-store drying experiment of high moisture content by mechanical ventilation, Journal of Henan University of Technology, 2007 (28): 22-25.
[19] K. Daou, R.Z. Wang, Z.Z. Xia, Desiccant cooling air conditioning: a review, Renewable Sustain Energy Rev., 2006(10): 55–77.
[20] Akhtar N., Mullick SC., Computation of glass-cover temperatures and top heat loss coefficient of flat-plate solar collectors with double glazing, Energy, 2007(32): 1067-1074.
[21] Madhlopa A., Ngwalo G., Solar dryer with thermal storage and biomass-backup heater, Solar Energy, 2007(81): 449–462.

16

High Temperature Annealing of Dislocations in Multicrystalline Silicon for Solar Cells

Gaute Stokkan, Christoffer Rosario, Marianne Berg and Otto Lohne
Norwegian University of Science and Technology (NTNU)
Department of Materials Science and Engineering
Norway

1. Introduction

Dislocation clusters have been shown to constitute the main efficiency reducing factor for multicrystalline silicon solar cells (Sopori et al. 2005). Multicrystalline silicon is made under less ideal conditions compared to monocrystalline silicon, in the sense that thermal fields and the lack of seeding create material with increased density of crystal defects, but also since the direct contact between crystal/melt and crucible/coating provides a rapid channel for impurity contamination. These two factors make multicrystalline silicon inferior compared to monocrystalline silicon in terms of solar cell efficiency (Green et al. 2009). It has been shown by Kveder et al. (Kveder et al. 2001) that the interaction between dislocation levels and impurity levels in the band gap may provide very efficient recombination channels, thus enhancing the efficiency reduction both of the dislocations and the impurities. Furthermore it has been shown that gettering of impurities is far less efficient in regions of high dislocation density (Bentzen et al. 2006).

Measures to reduce dislocation density in multicrystalline silicon is therefore of high interest. Interesting methods have been proposed to create more ideal conditions during solidification, such as seeding (Stoddard et al. 2008) and control of the nucleation conditions (Fujiwara et al. 2006); these conditions have also been shown to influence dislocation density (Stokkan 2010; Usami et al. 2010).

It appears however very difficult to avoid or restrict the generation of dislocation clusters during solidification. Models have been proposed to explain the observed dislocation patterns from grain boundary sources (Ryningen et al. 2008; Takahashi et al. 2010; Usami et al. 2010). Therefore the possibility of improving dislocated structures by the process of recovery (Cahn et al. 1996) which has been shown to be very efficient for other materials such as aluminium and iron, may be investigated. Investigations by Patel on recovery in bent monocrystalline silicon rods indicated that a prolonged annealing times of 48 hours was necessary to achieve noticeable recovery at a temperature of 1300°C(Patel 1958). In contrast to this observation, more recent experiments performed on String Ribbon multicrystalline silicon indicated that it was possible to significantly reduce the dislocation density by a high temperature annealing step of the wafer (Hartman et al. 2008; Bertoni et al. 2010). These results were compared to models proposed by Kuhlmann (Kuhlmann 1951) and Nes (Nes 1995) and suggested to be explained by pairwise annihilation of dislocations.

Further work by the same group indicated that residual or applied stress was a key factor for achieving the reported reduction in dislocation density (Bertoni et al. 2011).

Multicrystalline silicon wafers grown by the directional solidification technique (Bridgman or HEM-type furnace) are however principally different from the String Ribbon samples investigated in (Hartman et al. 2008; Bertoni et al. 2010; Bertoni et al. 2011), as well as the bent silicon rods of (Patel 1958). In this material dislocations exist in clusters that extend parallel to the growth direction, possibly starting at the bottom of the ingot and remaining all the way to the top, as shown e.g. by (Ryningen et al. 2011). The dislocation clusters, as observed by etch pits on wafer surfaces typically attain geometric shapes where etch pits align in particular crystallographic directions (Ryningen et al. 2011), examples of which are shown in Figure 1. Such configurations may be indicative of multiplication, in which case residual stress may remain, or of recovery as observed by (Patel 1958), in which case low energy configurations have already been achieved. The dislocation lines in the clusters also preferentially align in the growth direction, and when wafers are cut perpendicular to this, it is very possible that dislocations extend from one face of the wafer to the other. The forces imposed by the surfaces will significantly affect the mobility of dislocations in this configuration. An investigation of high temperature annealing of dislocations in directionally solidified multicrystalline silicon in a different configuration is therefore justified. This is a report of such an experiment.

2. Background theory

The term *recovery* refers to all changes to a deformed structure that reduces the stored energy in the system, which does not involve sweeping of high angle grain boundaries (Cahn et al. 1996). This can involve the activation of point defects, line defects and planar defects, characterised by increasing activation energy. Since multicrystalline silicon is cooled very slowly after crystallisation, it is not likely that much of the stored energy is due to point defects. In this case we are interested in the mechanisms involving dislocations, and the interesting effect in question is reducing the impact of dislocations on carrier recombination (Rinio et al. 2002; Stokkan et al. 2007), therefore also processes that do not directly influence the actual dislocation density, but only their configuration are of interest.

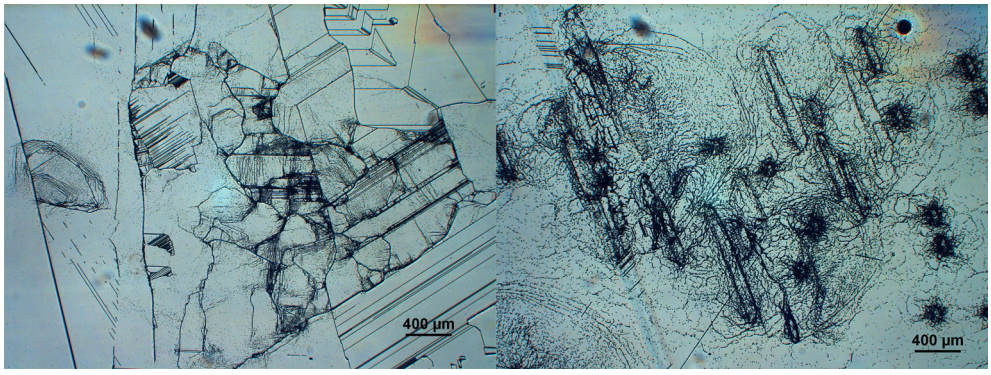

Fig. 1. Typical etch pit geometries as observed on wafers. Note that such geometries cannot be observed on vertically cut samples, as are shown e.g. in Figure 4 and Figure 5.

The recovery mechanisms which may be in effect to reduce dislocation density or influence the recombination properties are: Elimination of stable dislocation dipoles (parallel, opposite dislocations with a small spatial separation), pairwise annihilation of dislocations of opposite sign, also called *network growth*, rearrangement of dislocations into stable configurations and increase in subgrain size.

Dislocation dipoles are created by interaction of gliding dislocations with either other dislocations or other obstacles (Nabarro 1987). They are therefore likely to be present in areas of high dislocation density and little symmetry in the dislocation arrangements, i.e. dislocation tangles. They are stable at the temperature they are created, but activation of other mechanisms such as climb and cross slip at higher temperature will allow the reduction of stored energy by their annihilation. Since the separation of dipoles is small, this is the process which is expected to be affecting the dislocation density first. Dipoles are observed in strained silicon (Jacques et al. 2000), but it is not clear to which extent such dipoles constitute a significant part of the total dislocation density, i.e. if their recovery will produce a noticeable reduction in dislocation density.

A general model for recovery by network growth in combination with growing subgrains has been formulated by Nes (Nes 1995) where recovery is analysed in terms of rate controlling mechanism: glide, cross slip, climb or solute drag. For dislocations to annihilate, the opposite sign dislocations need to glide on parallel slip planes into a favourable position and then migrate into the same slip plane, either by climb or cross slip. Silicon has a very low stacking fault energy of ~50 mJ/mm^2 which leads to the well known dissociation of dislocations into Shockley partial dislocations. It has been a subject of debate whether this dissociation appears during the glide process, or when the dislocations come to rest. Investigations by Sato and Sumino (Sumino 1994) indicate that dislocations are dissociated during glide. The resulting stacking fault makes both climb and cross slip difficult (Cahn et al. 1996; Jacques et al. 2000) so we may well expect these mechanisms to be rate controlling in a possible recovery process by network growth (pairwise annihilation). Cross slip is a thermally activated process with activation energy 5.5 eV (Möller et al. 1979), and if there is no supersaturation of vacancies or interstitials, climb is also a thermally activated process with activation energy equal to that of self diffusion, i.e. 3.6 eV for temperature below 1250 K and 5 eV above 1300 K (Siethoff 1984). The different values are explained by different diffusing species in the temperature ranges: Vacancies at lower and interstitials at higher temperature. For the climb process it is the diffusion of these point defects from sources to sinks that are rate limiting.

Arranging the dislocations into more energetically favourable positions may to some degree happen only by gliding of a dislocation in one glide plane. To reduce stored energy further, dislocations also need to move out of the primary slip plane by climb or cross slip.

It must also be mentioned that the degree to which recovery may happen by the processes described above depends very much on the thermal history and the type of sources active in the generation of dislocations. For instance a Frank-Read source will create dislocation loops where the opposite sides of the loop have opposite sense but same Burgers' vector; a configuration well suited for pairwise annihilation and network growth. Other sources may primarily generate dislocations of one sign only, like in the model of Kuhlmann (Kuhlmann 1951). An example of this may be a grain boundary source.

In this context it should also be mentioned that directionally solidified multicrystalline silicon is routinely subjected to an annealing phase following the crystallisation and before cooling down to room temperature. This anneal is performed at a temperature higher than the brittle to ductile transition temperature, commonly between 1000 and 1200°C. It was historically introduced to reduce long range residual stresses which would result in the material cracking upon being subjected to mechanical impact (sawing) after cooling to room temperature (Hukin) and is appropriately termed *stress relief*. The equipment used today offers more ideal thermal conditions than the early equipment, and the need for stress relief may not be as high as it was.

Recent TEM investigations (Kivambe et al. 2011) on dislocation clusters which show the above mentioned alignment of etch pits along crystallographic directions have shown that the dislocations have an edge component, and that the alignment is perpendicular to the direction of the Burgers' vector, i.e. the slip plane. This result indicates that the dislocations have aligned in order to reduce their total energy, i.e. some degree of recovery has already occurred during growth, and the dislocations have already attained low energy configurations, which may make further recovery difficult. This indicates that the residual stresses believed to be responsible for the dislocation density reduction reported in (Bertoni et al. 2011) may already have been relieved in directionally solidified multicrystalline silicon.

The above discussion indicates that recovery by the process of dipole annihilation and arranging into more stable configurations are likely to occur when silicon is annealed, depending on to which degree the already existing dislocation structures are already a result of recovery. The process of pairwise annihilation involves processes of higher activation energy and it is therefore more questionable if this recovery process will occur and at which rate it will be effective.

Another process that may change the configuration of dislocations is when they move under the influence of image forces (Hirth and Lothe 1992). Image forces are used to describe the forces between dislocations and crystal surfaces and interfaces. The simplest case is the interaction between a dislocation and a free surface. In this case the force can be modelled by extending the crystal lattice on the other side of the surface and placing a dislocation of opposite sign at the same distance from the surface. These dislocations attract each other, and the dislocation will be attracted by the surface. If the surface is not free, but rather an interface to a different medium, the properties will be changed accordingly. The governing parameter is the elastic modulus E; the smaller the difference in stiffness between the silicon and the other medium, the smaller is the attraction. If the other medium is stiffer than the silicon, the dislocation will be repulsed from the surface.

Image forces from the surface may influence the dislocation density near the sample surface during annealing if dislocations are attracted towards the surface, as shown in Figure 2. Depending on the dislocation distance from the surface, it may annihilate at the surface or change its direction to lower the total length and reduce its energy. Further into the sample the effect may not be so efficient, primarily since the attractive force is inversely proportional to the distance, but also because of screening by other dislocations. Since the dislocations annihilate at any point they meet the surface, they can in principle move towards the surface only by glide if the slip plane is favourably oriented. The high activation energy processes of climb and cross slip should therefore be of less importance than for pairwise annihilation discussed above.

A native oxide on the sample surface is only 1-2 nm thick (Zhang 2001) and will not influence the image forces very much. If a layer is deliberately added to the surface, like a diffusion barrier, or if a thermal oxide builds up on the surface during the process, the situation may be different.

Lastly the work of Siethoff et al. should be mentioned, who in a series of reports (Siethoff and Schroter 1978; Siethoff and Schroter 1983; Siethoff 1984; Siethoff et al. 1984; Siethoff et al. 1986) investigated the mechanisms of dynamic recovery. Dynamic recovery differs from the process studied here in that it describes reduction of stored energy *during* hot working (Cahn et al. 1996), i.e. under an applied stress. Nevertheless much information about the mechanisms for dislocation movement is gained from this work, as will be discussed later.

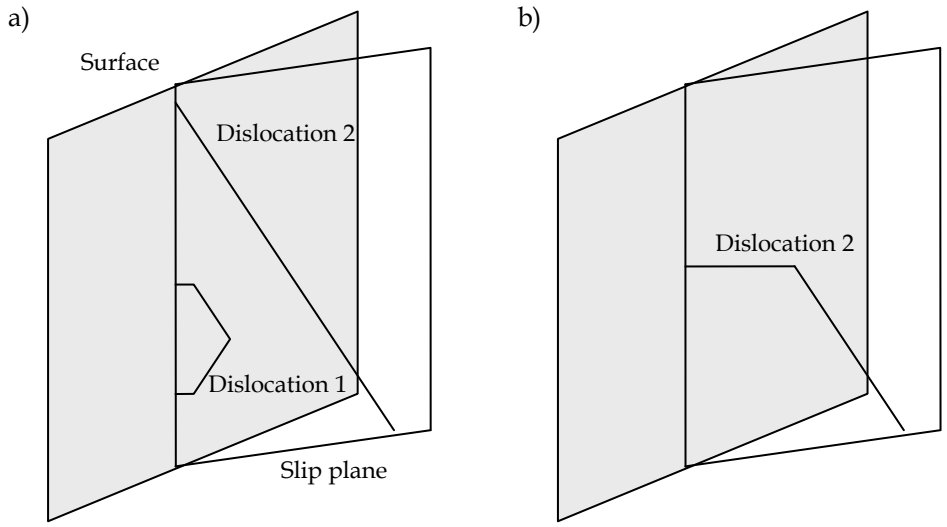

Fig. 2. Illustration of the effect of image forces on dislocations moving in a slip plane crossing the sample surface. a) Before annealing. b) After annealing. Dislocation 1 close to the surface has disappeared while dislocation 2 further away from the surface has changed direction to reduce its total energy.

3. Experimental work

Slices of approximately 2 mm thickness were cut from two different multicrystalline silicon ingots (A and B) produced in a pilot scale directional solidification furnace. In this type of furnace, crystal growth proceeds by heterogeneous nucleation at several points on the interface between the crucible lining and the melt, followed by dendritic growth in a supercooled part of the melt close to the crucible bottom. This growth is largely parallel to the crucible bottom, and directional solidification proceeds on top of this solidified layer. The size of the ingots produced in this particular furnace is 100-120 mm high and 250 mm in diameter. The slices were cut parallel to the growth direction to avoid the direct interaction between dislocations extending in the growth direction, and the surfaces. They were

subjected to a series of surface preparation techniques, measurements, high temperature treatment, followed by surface preparation and measurements again, all detailed in Table 1.

The sample was ground and polished as a prerequisite for the defect delineation by etching, but also as preparation for measurements of Carrier lifetime and substitutional carbon and interstitial oxygen. The lifetime was measured with Carrier Density Imaging (CDI) (Isenberg et al. 2003; Schubert et al. 2003). The surfaces were not passivated, so only relative differences in lifetime could be observed. However since the surfaces were polished, optical measurement problems (Schubert et al. 2007) could be avoided and high quality images were obtained. The interstitial oxygen and substitutional carbon level was measured with Fourier Transform Infrared Spectroscopy (FTIR).

Step	Purpose	Procedure
1	Sample surface preparation	Plane grinding, grinding, mechanical polishing, chemical mechanical polishing
2	Characterisation	CDI, FTIR
3	Defect delineation	Sopori etch 30 s
4	Characterisation	PVScan, dislocation counting
5	Removal of defect delineation	Polishing, chemical mechanical polishing
6	Thermal ramp up	20°C/min (A) and 7°C/min (B)
7	Anneal	4 h at 1350 °C
8	Thermal cool down	7°C/min
9	Removal of surface deposit	Grinding and/or polishing, chemical mechanical polishing
10	Characterisation	CDI, FTIR
11	Defect delineation	Sopori etch 30 s
12	Characterisation	PVScan, dislocation counting

Table 1. Sequence of the experiments

Dislocations are delineated by the use of the Sopori etch, which creates large etch pits (~5 μm, round or elliptical depending on whether the dislocation line penetrates the surface perpendicular or at an angle (Sopori 1984). This property can be used to substantiate the hypothesis that dislocations lines primarily run in the direction parallel to the growth direction, i.e. parallel to the sample surface here, since this should cause a higher occurrence of elliptical etch pits compared to an etched wafer surface. PVScan is a tool designed to provide a quantitative measurement of etch pit density on samples etched with this solution (Sopori et al. 2000). The quantitative measurement of etch pit density is interpreted as dislocation density. Dislocation density is however defined as total length of dislocation lines inside a volume divided by the volume, and the justification of this interpretation depends on the angle of the dislocation lines to the etched surface. Thus in this case the measurement probably provides an underestimate. To achieve measurements of higher spatial resolution and to be able to study the dislocation structures in detail, the entire samples were photographed in an optical microscope with an automated xy-stage and image capture control. By this method images of magnification 80x were obtained.

All traces of the defect delineation had to be removed from the sample before the thermal treatment; this was done by mechanical polishing followed by chemical mechanical polishing.

The thermal treatment was performed at atmospheric pressure in an alumina tube furnace flushed with high purity argon (5.0), the samples resting horizontally on an alumina boat supporting the long edges of the sample. Two different furnaces were used. The furnace used for sample A was expected to be heavily contaminated by Titanium, whereas the second, used for sample B was expected to provide a cleaner atmosphere. No external stress was applied to the samples during the heat treatment. After the heat treatment, the samples were covered by a thick film, apparently thicker for the side facing towards the support. This film was removed by polishing, and then the samples were subjected to the same sample preparation and characterisation as before.

4. Results

Figure 3 shows the dislocation density measured by PVScan before heat treatment as well as lifetime measured before heat treatment for sample A. It is seen that apart from the top region, low dislocation density and high lifetime corresponds well and vice versa. After heat treatment, however the lifetime is reduced below measurable levels.

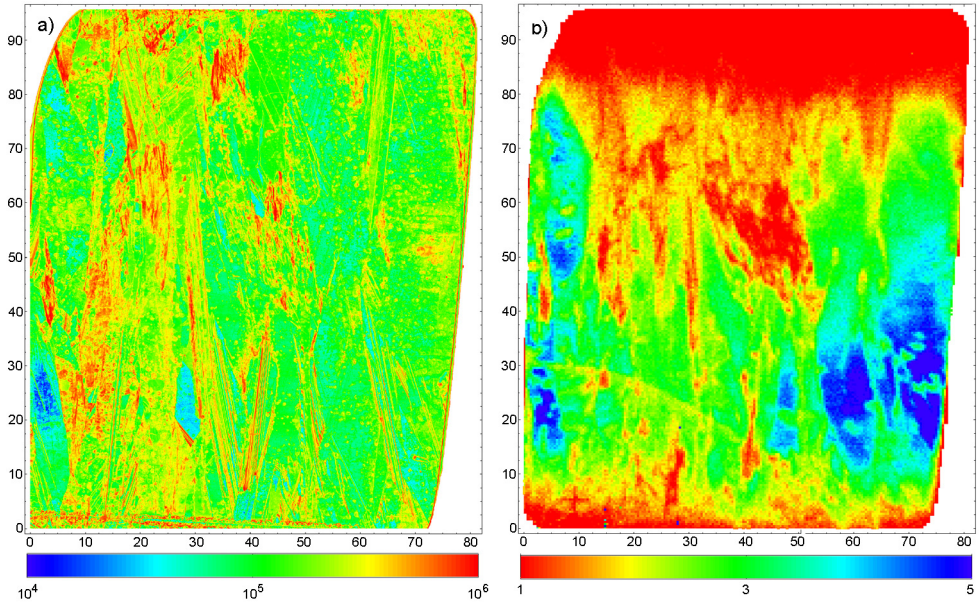

Fig. 3. Dislocation density (a) and lifetime (b) measured before heat treatment of sample A. The poor sample preparation leads to higher apparent values than realistic in low dislocation density areas, however high dislocation density areas are clearly visible. The lifetime measurements were performed on an unpassivated sample, thus the lifetime is not a true bulk lifetime. The scaling is in mm , and the colour bars are in cm^{-2} and microseconds for a) and b) respectively.

Optical microscopy shows that the general etch pit pattern is the same before and after annealing, and no particular dislocation patterns arose from the mechanical support. However some areas received an etch pit density reduction after the anneal (Berg et al. 2009). This effect was most profound in areas of initial high dislocation density. In order to investigate the nature of this effect, 50 % of the sample thickness was removed before it was polished and etched again. This procedure shows to which extent the interior of the sample was influenced by the heat treatment. A result from a high dislocation density area is shown in Figure 4. Since the grain structure changes considerably by moving 1 mm horizontally in the sample, it is not possible to compare dislocation density for small clusters. Therefore a general overview of the entire pictured area is considered, and it appears that the etch pit density is comparable to the situation before heat treatment. This is substantiated by quantitative measurements on five such areas, obtained by a combination of automatic and manual counting of etch pits, shown in Table 2. The area pictured in Figure 4 is area 1 in the table.

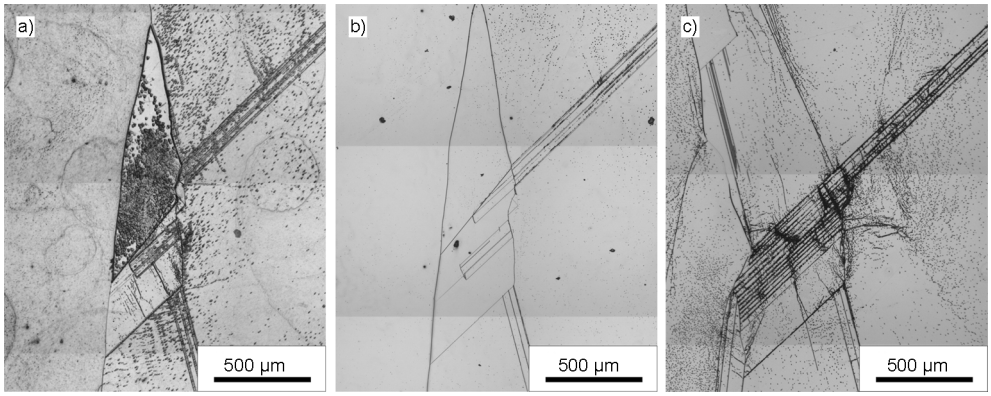

Fig. 4. Optical micrographs of defect etched areas. a) Surface before heat treatment. b) Surface after heat treatment. c) Interior, 1 mm below the surface parallel to the growth direction, after heat treatment.

		Dislocation density		
Area	Distance to ingot bottom (mm)	Before heat treatment	After heat treatment (surface)	After heat treatment (interior)
1	83	1.5×10^5	1×10^5	3.1×10^5
2	66	1.5×10^5	1.7×10^5	2.9×10^5
3	80	0.9×10^5	1×10^5	1.9×10^5
4	84	1.7×10^5	1.5×10^5	2.7×10^5
5	78	1.2×10^5	0.9×10^5	2.2×10^5

Table 2. Etch pit density measurements before and after heat treatment of 5 selected areas of initial high dislocation density in sample A

The density after heat treatment in the interior is a factor 2 higher than at the surface before heat treatment. This is probably explained by inferior etching conditions before heat treatment, which resulted in larger etch pits than normally expected; etch pits overlap when

the dislocation density becomes large and cannot be discriminated by the counting procedure, and these larger etch pits overlap at a lower dislocation density than normal. This may also explain the apparently slightly increasing etch pit density for two of the areas.

Even though these results show a clear etch pit density reduction close to the surface, but not in the interior, it became clear that the varying etching conditions made it difficult to quantify the changes accurately. The experiment was therefore repeated with sample B, this time in a different furnace. Quantitative results are shown in Table 3.

		Dislocation density		
Area	Distance to ingot bottom (mm)	Before heat treatment (cm^{-3})	After heat treatment (cm^{-3})	Remaining amount of etch pits (%)
1	96	2×10^5	1.9×10^5	95
2	82	4.6×10^5	4.5×10^5	97
3	56	6.1×10^5	5.6×10^5	91
4	96	2.6×10^5	2.4×10^5	90
5	82	1.4×10^5	0.7×10^5	54
6	56	7.7×10^5	4.7×10^5	61

Table 3. Etch pit density before and after high temperature treatment of sample B. Areas 1-3 are from the side facing downwards in the furnace whereas 4 - 6 face upwards.

It can be seen that the surface etch pit density is reduced similarly to sample A. It is also seen that the side facing towards the centre of the furnace receives a higher reduction than the side facing towards the support. The side with higher reduction in dislocation density also had a thinner film. The film was chemically analysed by EDS, which showed peaks corresponding to Silicon, Aluminium and Oxygen.

To investigate if an effect to the sample interior could be observed, a particular area showing initial high etch pit density both at the front and back surface was selected. This area was expected to consist of one large, relatively homogeneous dislocation cluster and was therefore ideal for comparisons of different faces. The sample was cut parallel to the growth direction so that the cut made a cross section through the cluster. The cross section was polished and etched and is shown in Figure 5 a. It shows a relatively homogeneous etch pit density, but a slight decrease in area of less than 50 μm from the edges (i.e. less than 50 μm depth) is observed. The etch pits were counted in four different areas, which are compared to the situation before and after heat treatment at the surface in Table 4.

The etch pit density in the interior is very similar to the density at the surfaces before heat treatment. This shows that we do not see any recovery effect of dislocations in the sample interior. The observed variations are probably caused by local variations in the crystal not related to the heat treatment.

Finally the ratio of round versus oval etch pits was investigated to study the angle at which the dislocations penetrate the surface. This was done in order to identify an effect from image forces, as dislocations that have aligned orthogonal to the surface (such as dislocation 2 in Figure 2) will change the etch pit shape from round to oval. The investigation was done

by automatic counting of particles using a roundness criterion and counting only areas outside of the dense clusters, and the results are shown in Table 5. The amount of oval etch pits is reduced for all but one area. The results for sample A indicated a larger reduction in oval etch pit density, but the different etch pit size before and after heat treatment for this sample makes this comparison less reliable.

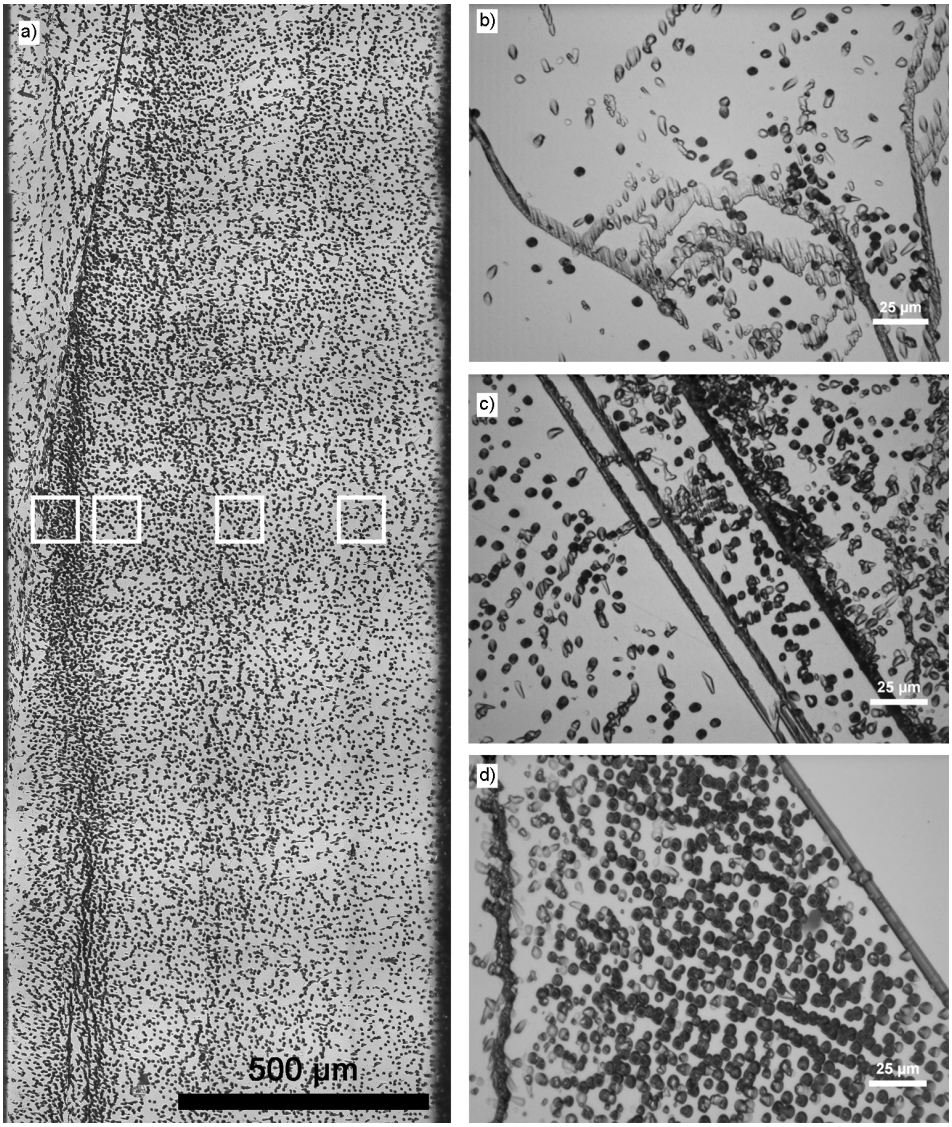

Fig. 5. a) Etch pit density of cross section through sample, normal to grain growth. Areas where etch pit density was counted are marked as white squares. The front surface is towards the left. b) Etch pits inside clusters in sample, Top. c) Middle. d) Bottom.

Area	Etch pit density
Front surface before annealing	$7.7x10^5$
Front surface after annealing	$4.7x10^5$
Area 1	$17.5x10^5$
Area 2	$11.2x10^5$
Area 3	$10.1x10^5$
Area 4	$7.3x10^5$
Back surface	Similar to front surface

Table 4. Etch pit density on cross section and front and back surface. The areas are marked in Figure 5 a.

		Portion oval etch pits (%)		
Area	Distance to ingot bottom (mm)	Before heat treatment	After heat treatment	Relative decrease (%)
1	96	22.3	22.6	-1.3
2	82	27.9	24.3	12.9
3	56	17.6	15.2	13.6
4	96	24.8	24.4	1.6
5	82	28.4	18.9	48.2
6	56	24.7	12.8	33.5

Table 5. Ratio of round vs. oval etch pits for sample B.

Interestingly, the amount of oval etch pits inside clusters seem to follow an increasing trend towards the top, as can be seen in Figure 5 b, c and d.

Fourier Transform Infrared Absorption analysis showed that the concentration of interstitial oxygen was of maximum 10-12 ppma for sample A and of maximum 6 ppma for sample B.

5. Discussion

Although a general trend towards the reduction in etch pit density at the surface is observed, our results show that this is not translated into a reduction in the interior. Rather, Figure 5 a indicates that only a small region close to the surface is affected. This indicates that the dislocations are affected by image forces caused by their proximity to the surface (Hirth and Lothe 1992). Since no apparent dislocation density reduction is achieved in the bulk of the samples, it appears that the driving force for reduction of stored energy by this process is too low at the temperature applied. This is probably connected to three factors: The low dislocation density in this material, which does not provide long ranging forces between the dislocations, the low stacking fault energy of silicon which creates high activation energy for the processes of climb and cross glide and finally the slow growth rate (10 – 20 mm/h) the silicon was produced at, which results in the material already having seen high temperatures for an extended period with the resulting rearrangement into low energy dislocation configurations.

The multicrystalline silicon investigated in this study has a relatively low dislocation density ranging from ~10^4 cm^{-3} in good areas to 10^8 cm^{-3} in the very dense clusters, whereas the dislocation density after cold working of metals is in the range 10^{10} to 10^{12} cm^{-3} (Nes 1995; Cahn et al. 1996). Since the force F_r between parallel dislocation segments is inversely proportional to their distance, e.g. given by

$$F_r = \frac{Gb^2}{2\pi r} \tag{1}$$

for a screw dislocation, where G is the shear modulus, b is the magnitude of the Burgers' vector and r is the distance between the segments, the driving force for network growth is expected to be much lower in the case of multicrystalline silicon. However, considering the observation in Figure 5 a) that image forces may operate down to a depth of ~50 μm, the forces in high dislocation areas (>10^6 cm^{-3}) should be adequate to generate motion in the slip planes. But although dislocations are highly mobile in the slip planes at the temperature applied in this experiment, not being restricted by the lattice resistance (Argon 2007), climb and cross glide are essential for network growth of dislocations and may be expected to be rate limiting.

Cross slip has indeed been observed in silicon at lower temperature than applied in this experiment by several authors (Möller et al. 1979; Jacques et al. 2000). Jacques et al. (Jacques et al. 2000) subjected silicon to stresses in the range of 10 MPa at temperatures between 975 and 1075 K. The force on the dislocations, calculated by

$$F_r = \tau b, \tag{2}$$

where τ is the applied stress, is F_r = 0.00384 Nm^{-1} for a force of 10 MPa and Burgers' vector of 0.384 nm, whereas the attractive force between parallel, opposite screw dislocations calculated from equation 1 is F_r = 0.0015 Nm^{-1} for a dislocation density of $\rho = 10^6$ cm^{-2}, using the elastic constants of (Burenkov and Nikanorov 1974) at 973 K. These numbers are of similar magnitude, therefore cross slip could be expected to occur, in spite of the high activation energy. Cross slip was also observed by Möller et al. (Möller et al. 1979) without applied load at a temperature of T>1170 K, the driving force in this case being image force from the sample surface.

Siethoff and Schröter (Schröter and Siethoff 1984; Siethoff 1984) argue that during dynamic recovery, stage III of the stress-strain curve, which corresponds to the first recovery stage at lower strains, the rate controlling mechanism is that of diffusion of vacancies connected to a climb process. The diffusion D constant is given by

$$D = D_0 e^{-\frac{U}{k_B T}}. \tag{3}$$

In silicon, analysis of the self diffusion parameters D_0 and U point to two different diffusion mechanisms being operative at different temperature: a vacancy mechanism below 1250°C and an interstitial mechanism above 1300°C (Siethoff 1984). For the low temperature regime D_0 = 0.35 cm^{2}s^{-1} and U = 3.9; for high temperature D_0 = 1460 cm^{2}s^{-1} and U = 5 eV . Using the latter, a diffusion constant D = 4.3*10^{-13} cm^2/s is calculated (it can be noted that the parameters calculated for the vacancy mechanism, if used in the calculation at 1350°C will give a value of D = 2.9*10^{-13}, not very different from the interstitial mechanism). The expression

$$L_d = \sqrt{Dt} \tag{4}$$

for diffusion length gives a value L_d = 0.8 μm for 4 hours annealing at 1350°C. The sources and sinks for point defects are grain boundaries and other dislocations which are a distance from 10 μm up to several mm away from the dislocation. This shows that diffusion of point defects to support climb may very well be a rate limiting process for this defect geometry, impeding the recovery by network growth.

It should be noted that in regions of very high dislocation density (~10^8 cm^{-3}), forces between dislocations will increase and distance between sources and sinks of point defects will decrease. Changes in such areas are not detectable by this experimental technique because of the overlapping etch pits. We may therefore not rule out the possibility of reduction of dislocation density in such regions by the observations and discussion above.

Interestingly, another element with low stacking fault energy, copper, shows very little response to recovery (Cahn et al. 1996; Martin et al. 1997) , as appears to be the case also for silicon in this experiment.

Migration towards the surfaces under the influence of image forces is not dependent on these rate limiting processes to the same extent if slip planes are favourably oriented, and it is therefore not surprising to see that this occurs, an effect observed both by the reduction in dislocation density in the proximity of the surface and in the transformation of oval etch pits to round. Different orientation of slip planes towards the surface may be a factor influencing the varying degree of reduction experienced in different areas.

For sample B there is a correlation between the amount of reduction of dislocation density, the change from oval to round etch pits and the amount of oval vs. round etch pits in clusters as a function of distance from the ingot bottom. This can be seen by comparing the data in Table 3, Table 5 and Figure 5. This again points to the image forces as the main driving force for dislocation density reduction near the surface.

Another factor influencing the efficacy of the surface in reducing dislocation density is the formation of a surface film during the heat treatment. After this film forms, the surface is no longer to be regarded as a free surface; the film may reduce the attraction to the surface, the governing factors being the elastic modulus and the thickness. For sample B a possible correlation was observed between the increased thickness of the layer and the reduced attraction of the surface for the two different sides, which can be explained by this influence. Another possible explanation is that the samples had to be polished different periods of time to remove the surface film, and this may also have influenced how much of the sample was polished away.

We do not find a simple correlation between the reduction in dislocation density and the oxygen values. For sample A a higher degree of reduction was experienced towards the top of the sample, whereas for sample B a trend towards a more efficient reduction towards the bottom is observed. The solubility of oxygen at 1350°C is 35 ppma (Pajot 1999), higher by a factor of 3 than the highest measured value in the samples studied here. Any oxygen precipitates on the dislocations should therefore be dissolved and not influence the mobility of the dislocations during the heat treatment.

6. Conclusion

We have shown that by performing an anneal of 4 h at 1350°C on bulk silicon samples, a quantifiable reduction in etch pit density is observed. This reduction is however only visible near the sample surface. A region in the range of less than 50 μm from the surface seems to be affected. No true bulk recovery is observed; the effect is attributed to image forces from the surface. The observations correspond well to theoretical predictions based on forces between dislocations at the given dislocation densities and restrictions to dislocation mobility by the process of climb and possibly also cross slip. These restrictions are caused by the low stacking fault energy of silicon which through the dissociation of dislocations into Shockley partials creates high activation energies for these processes.

It is very likely that the dislocations have already undergone recovery during the cooling of the ingot in the production process, at even higher temperatures than applied in this experiment. Thus the potential for lowering the total energy by dislocation migration is low in this material.

Since the image forces appear to be effective down to a thickness comparable to current wafer thickness, one can imagine a process where this force is utilised to reduce dislocation density of wafers. It is then important to take into account the orientation of the dislocation lines compared to the surface. Since dislocation clusters seem to follow the crystalline structure of directionally grown multicrystalline silicon, one may suggest that wafers cut parallel to the growth direction may be more receptive to such treatment than the current method of cutting parallel to the growth interface. This suggestion of course does not take into account other benefits of the currently preferred cutting direction. It should also be mentioned that if a diffusion barrier is applied to the surface to prevent contamination, the elastic modulus of this material may influence the magnitude of the image force.

7. Acknowledgements

This work was carried out in the projects “Crystalline Silicon Solar Cells – Cost Reduction” and “Defect Engineering in Crystalline Silicon Solar Cells” sponsored by The Norwegian Research Council, Elkem Solar and REC. Maulid Kivambe, Torunn Ervik, Birgit Ryningen and Ketill O. Pedersen are acknowledged for helpful discussions, and Eivind Øvrelid and Øyvind Mjøs for growing the crystals that were studied.

8. References

Argon, A. (2007). Strengthening Mechanisms in Crystal Plasticity. Oxford, Oxford University Press.

Bentzen, A., A. Holt, et al. (2006). "Gettering of transition metal impurities during phosphorous emitter diffusion in multicrystalline silicon solar cell processing." J. Appl. Phys. 99(9): 93509-93501.

Berg, M., G. Stokkan, et al. (2009). High temperature annealing of dislocations in silicon. Third International Workshop on Crystalline Silicon Solar Cells CSSC3, Trondheim.

Bertoni, M., C. Colin, et al. (2010). "Dislocation Engineering in Multicrystalline Silicon." Diffusion and Defect Data Part B (Solid State Phenomena) 156-8: 11-18.

Bertoni, M. I., D. M. Powell, et al. (2011). "Stress-enhanced dislocation density reduction in multicrystalline silicon." physica status solidi (RRL) – Rapid Research Letters 5(1): 28-30.

Burenkov, Y. A. and S. P. Nikanorov (1974). "Temperature dependence of the elastic constants of silicon." Soviet Physics - Solid State 16(5): 963-964.

Cahn, R. W., W. C. Robert, et al. (1996). Recovery and Recrystallization. Physical Metallurgy (Fourth Edition). Oxford, North-Holland: 2399-2500.

Fujiwara, K., W. Pan, et al. (2006). "Growth of structure-controlled polycrystalline silicon ingots for solar cells by casting." Acta Materialia 54(12): 3191-3197.

Green, M. A., K. Emery, et al. (2009). "Solar cell efficiency tables (version 33)." Progress in Photovoltaics: Research and Applications 17(1): 85-94.

Hartman, K., M. Bertoni, et al. (2008). "Dislocation density reduction in multicrystalline silicon solar cell material by high temperature annealing." Applied Physics Letters 93(12): 122108 (122103 pp.).

Hirth, J. P. and J. Lothe (1992). Theory of dislocations. Malabar, Fla., Krieger Publ. Co.

Hukin, D. Personal communication.

Isenberg, J., S. Riepe, et al. (2003). "Imaging method for laterally resolved measurement of minority carrier densities and lifetimes: Measurement principle and first applications." J. Appl. Phys. 93(7): 4268-4275.

Jacques, A., F. Vallino, et al. (2000). "Dislocation multiplication in silicon at the onset of plasticity observed by in situ synchrotron X-ray topography." J. Phys., Condens. Matter. (UK) 12: 10045-10058.

Kivambe, M., T. Ervik, et al. (2011). "The microstructure of dislocation clusters in industrial directionally solidified multicrystalline silicon." To be published.

Kuhlmann, D. (1951). "On the Theory of Plastic Deformation." Proceedings of the Physical Society. Section A 64(2): 140.

Kveder, V., M. Kittler, et al. (2001). "Recombination activity of contaminated dislocations in silicon: A model describing electron-beam-induced current contrast behavior." Physical Review B (Condensed Matter and Materials Physics) 63(11): 115208-115201.

Martin, J. W., R. D. Doherty, et al. (1997). Stability of microstructure in metallic systems. Cambridge, Cambridge University Press.

Möller, H. J., H. Ewaldt, et al. (1979). "Cross slip of single dissociated screw dislocations in silicon and germanium." Physica Status Solidi A 55(2): 469-478.

Nabarro, F. R. N. (1987). Theory of crystal dislocations. New York, Dover.

Nes, E. (1995). "Recovery revisited." Acta Metallurgica et Materialia 43(6): 2189-2207.

Pajot, B. (1999). Solubility of O in c-Si. Properties of crystalline silicon. R. Hull. London, INSPEC, the Institution of Electrical Engineers: 488-491.

Patel, J. R. (1958). "Arrangements of dislocations in plastically bent silicon crystals." Journal of Applied Physics 29(2): 170-176.

Rinio, M., S. Peters, et al. (2002). "Measurements of the normalized recombination strength of dislocations in multicrystalline silicon solar cells." Solid State Phenomena 82-84: 701-706.

Ryningen, B., G. Stokkan, et al. (2011). "Growth of dislocation clusters during directionally solidification of multicrystalline silicon ingots " To be published.

Ryningen, B., G. Stokkan, et al. (2008). Growth of Dislocation Clusters in Directionally Solidified Multicrystalline Silicon. 23rd European Photovoltaic Solar Energy Conference, Valencia, SPAIN, WIP - Munich.

Schröter, W. and H. Siethoff (1984). "New phenomena in the plasticity of semiconductors and fcc metals at high temperatures. Part II: Analysis of experimental data." Zeitschrift für Metallkunde 75(7): 482-491.

Schubert, M., J. Isenberg, et al. (2003). "Spatially resolved lifetime imaging of silicon wafers by measurement of infrared emission." J. Appl. Phys. 94(6): 4139-4143.

Schubert, M. C., S. Pingel, et al. (2007). "Quantitative carrier lifetime images optically measured on rough silicon wafers." Journal of Applied Physics 101(12).

Siethoff, H. (1984). "New phenomena in the plasticity of semiconductors and FCC metals at high temperatures. I. Theoretical models." Zeitschrift für Metallkunde 75(7): 475-481.

Siethoff, H., K. Ahlborn, et al. (1984). "Two independent mechanisms of dynamical recovery in the high-temperature deformation of silicon and germanium." Philosophical Magazine A (Physics of Condensed Matter, Defects and Mechanical Properties) 50(1): 1-6.

Siethoff, H., H. G. Brion, et al. (1986). "Dynamical recovery of 111 germanium." Physica Status Solidi A 97(1): 153-162.

Siethoff, H. and W. Schroter (1978). "Dynamical recovery and self-diffusion in silicon." Philosophical Magazine A (Physics of Condensed Matter, Defects and Mechanical Properties) 37(6): 711-718.

Siethoff, H. and W. Schroter (1983). "Work hardening and dynamical recovery in silicon and germanium at high temperatures and comparison with FCC metals." Scripta Metallurgica 17(3): 393-398.

Sopori, B., C. Li, et al. (2005). Efficiency limitations of multicrystalline silicon solar cells due to defect clusters, Warrendale, PA, USA, Materials Research Society.

Sopori, B., C. Wei, et al. (2000). "High-speed mapping of grown-in defects and their influence in large-area silicon photovoltaics." Journal of Crystal Growth 210: 346-350.

Sopori, B. L. (1984). "A new defect etch for polycrystalline silicon." Journal of the Electrochemical Society 131(3): 667-672.

Stoddard, N., W. Bei, et al. (2008). Casting single crystal silicon: novel defect profiles from BP solar's mono2 wafers, Erice, Italy, Trans Tech Publications Ltd.

Stokkan, G. (2010). "Relationship between dislocation density and nucleation of multicrystalline silicon." Acta Materialia 58(9): 3223-3229.

Stokkan, G., S. Riepe, et al. (2007). "Spatially resolved modeling of the combined effect of dislocations and grain boundaries on minority carrier lifetime." J. Appl. Phys.

Sumino, K. (1994). Mechanical behaviour of semiconductors. Handbook on Semiconductors, Materials, properties and preparation. S. Mahajan. Amsterdam, North-Holland. Vol. 3: 76-181.

Takahashi, I., N. Usami, et al. (2010). "Generation mechanism of dislocations during directional solidification of multicrystalline silicon using artificially designed seed." Journal of Crystal Growth 312(7): 897-901.

Usami, N., R. Yokoyama, et al. (2010). "Relationship between grain boundary structures in Si multicrystals and generation of dislocations during crystal growth." Journal of Applied Physics 107(1): 013511 (013515 pp.).

Zhang, X. G. (2001). Electrochemistry of silicon and its oxide. New York, Kluwer Academic/Plenum Publishers.

Part 4

Solar Bio-Technology

17

Photobiological Solar Energy Harvest

Ashley L. Powell and Halil Berberoglu*
The University of Texas at Austin, Mechanical Engineering Department
USA

1. Introduction

1.1 Background and motivation

In 2010, the United States consumed 36.96 quadrillion BTUs (39 quadrillion kJ) of liquid petroleum fuels (EIA, 2011). Even assuming the adoption of more stringent fuel economy standards and unconventional vehicle technologies, this number is expected to grow steadily with rising population and corresponding demand in the transportation sector. As the economies of developing countries strengthen, the global spread of industrialization and personal transportation will cause the demand for liquid fuel to rise dramatically in regions of historically low consumption. According to studies conducted by the Energy Information Administration, from 2007 to 2035, growth in the transportation sector accounts for 87 percent of the total increase in world liquid fuel consumption (EIA, 2010). Figure 1 displays this projected growth of liquid fuel consumption by various energy consuming sectors.

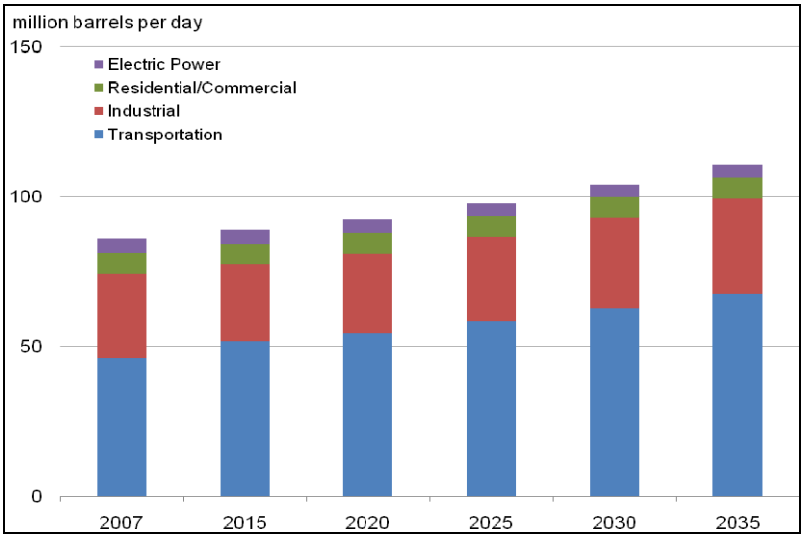

Fig. 1. World liquid fuels consumption by sector, 2007-2035 (EIA, 2010).

* Corresponding Author

The strength of the US economy depends heavily on its ability to transport goods and services from producers to consumers. The price of oil reached a record of $145/barrel in the summer of 2008 (EIA, 2011), crippling business activities and marking the beginning of a global recession. Similar price spikes during the energy crises of 1973, 1979, and 1990 were followed by periods of economic distress. Taking these events as a whole, the price volatility of petroleum fuels presents a clear threat to economic stability and American prosperity.

In addition, concerns over climate change have put reducing fossil fuel combustion emissions at the forefront of environmental policy. Since the industrial revolution, the concentration of carbon dioxide in the atmosphere has increased by 36% to approximately 390 ppm in early 2011 (Conway & Tans, 2011). Human activities outpace the planet's natural ability to remove the excess carbon, and the concentration of carbon dioxide continues to increase by approximately 1.9 ppmv each year. As atmospheric carbon dioxide concentration reaches its highest point in at least the last 650,000 years, it cannot be denied that industrialization has significantly altered the makeup of the Earth's atmosphere (Soloman, et al., 2007). The global focus on limiting Greenhouse Gas Emissions (GHG) suggests impending environmental regulation and possible carbon taxes on industries consuming fossil fuels. These forthcoming policies will serve to raise already steep fuel prices and put further strain on the global economy.

To meet the expected demand for energy without threatening national security, the economy, or the environment, a new portfolio of fuels must be adopted that can be produced inexpensively, domestically, and in extremely large quantities. The United States transportation sector alone consumed 26.7 x 10^{15} BTUs of liquid petroleum fuel in 2010, equivalent to over 4.6 billion barrels of crude oil (731 million m^3) (EIA, 2011). Based on energy content, over 205 billion gallons (776 million m3) of biodiesel must be produced each year to meet consumption. As most alternative fuels contain less combustible energy per unit volume, fuel from other unconventional sources would be required in even higher quantities. Figure 2 compares the most common alternative transportation fuels and their respective energy content as given by their higher heating value.

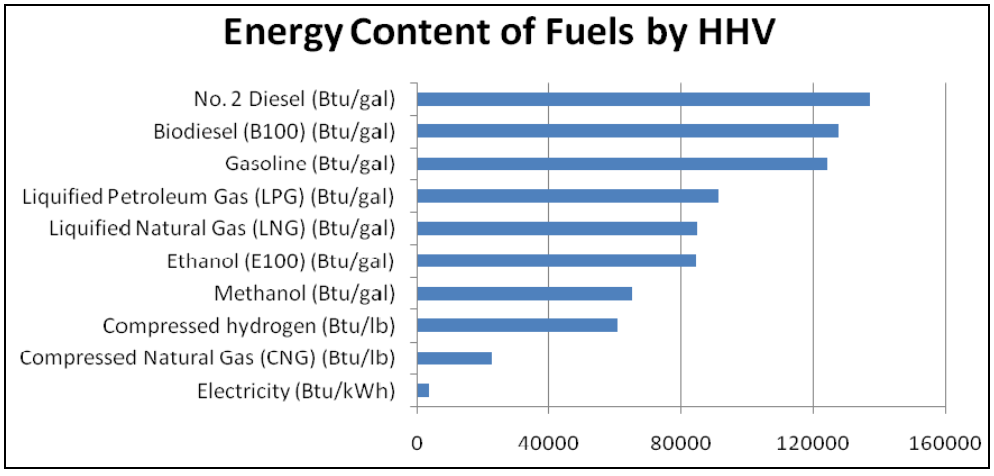

Fig. 2. Energy content of various fuels by Higher Heating Value (HHV) (EERE, 2011).

Recent innovations in electrically powered vehicles have led to a minority of drivers to consume less petroleum fuel. However, the low energy density of most batteries entails large battery packs, frequent recharging, and limited mileage. In addition, widespread adoption of this technology would put significant strain on the existing electric grid and potentially displace the demand for oil with that for the rare metals necessary for battery production, such as platinum, cadmium, and lithium (Hübner, 2010). Both the current infrastructure and the power requirements of heavy transportation, aviation, and maritime shipping necessitate a fuel that is both liquid and energy dense. Alternative fuels that meet these requirements include biodiesel, ethanol, methanol, and more recently, biobutanol, Fischer-Tropsch diesel, and hydrogenation-derived renewable diesel. However, the latter three fuels exist only in immature stages of development and will not likely be viable in the short to medium term (EERE, 2011).

The use of biodiesel in place of conventional petroleum diesel in compression ignition engines holds benefits for the economy, national security, and the environment. In 2000, biodiesel became the only commercially available alternative fuel to successfully pass the EPA-required Tier I and II health effects testing under the Clean Air Act. Burning biodiesel results in a significant reduction in the release of harmful emissions, such as sulfur oxides, carbon monoxide, and particulate matter. In addition, the US Department of Energy reported that replacing conventional diesel with biodiesel resulted in a 78.5% reduction in carbon dioxide emissions (National Biodiesel Board, 2009).

Biodiesel can be produced from any animal or vegetable oil, all of which are biodegradable, nontoxic, and renewable. Virgin soy bean oil and recycled cooking grease represent the most common domestic feedstock for biofuel production. However, current quantities of these readily available sources can provide only enough biodiesel to displace roughly 5% of the on-road diesel used in the United States (EERE, 2011). Increasing the cultivation of agricultural feedstock to meet the production of significantly more biodiesel would require unrealistic quantities of arable land, water, fertilizers, herbicides, and pesticides, all of which would be diverted from food production. To meet the current fuel demand, new feedstocks must be pursued.

1.2 Algal biofuel production history

In 1978, the National Renewable Energy Lab's landmark Aquatic Species Program began a twenty-five year investigation on the potential for microalgal biodiesel to solve the impending energy crisis. The program was motivated by the following: (i) lignocellulosic ethanol cannot substitute for energy dense diesel and aviation fuels; (ii) renewable oil sources are insufficient to meet the demand for diesel fuel; and (iii) the unprecedented environmental threat presented by global climate change. Over the course of twenty-five years, $25 million was spent to collect and screen microalgae, study the physiological and biochemical aspects of various species and the role of genetic engineering to optimize desired characteristics, refine the process engineering aspects of cultivation, harvesting, and extraction, and finally, to develop outdoor mass culture systems with the intention of large scale biofuel production. Although the program ended in 1996, the NREL's analysis and the progress made in the phycology field, particularly in the area of genetic modification of the algae's metabolic pathways, laid the groundwork for future research (Sheehan, et al., 1998). The study's conclusions revealed that the Southwest United States holds ample resources in

the form of land, water, and CO_2 for the production of more than 30 billion gallons of biodiesel. However, challenges remained as the relatively low price of oil in 1996 made the high capital cost of the production process hard to justify. Biological productivity remains the most important factor for determining the final fuel cost. While open ponds on low cost land were deemed the most viable option for growth facilities, their low productivities presented a significant hurdle. Areas for improvement were identified as the need to find a market for the biomass residue after oil extraction, water and nutrients should be recycled, research should continue to search for an ideal strain, and a lower cost, easily accessible source of supplementary CO_2 must be found (Jarvis E. E., 2008).

In 2006, 10,000 dry tons of algal biomass were produced worldwide (Schulz, 2006). Although commercial production of nutritional supplements comprised the vast majority, private companies and research organizations around the world have been working to build on the findings of the NREL's Aquatic Species Program to develop an economical method for the growth, harvesting, and processing of algae for fuel. In a significant strategy shift in 2009, ExxonMobil announced a partnership with Synthetic Genomics, a biotechnology company, that would allocate $600 million over the course of five to six years for the development of biofuel from algae (Howell K., 2009). This accelerated research initiative and a renewed global interest in developing a viable alternative fuel suggest that the many obstacles identified by the Aquatic Species Program may soon be overcome.

1.3 Algal biofuel production portfolio

Several methods exist for the production of fuel from algae: (i) generation of hydrogen during the growth stage, (ii) fermentation of carbohydrates and sugars into alcohols, (iii) transesterification of intracellular lipids into biodiesel, and (iv) gasification of the residual biomass. Figure 3 illustrates these various pathways and their constituent metabolic precursors.

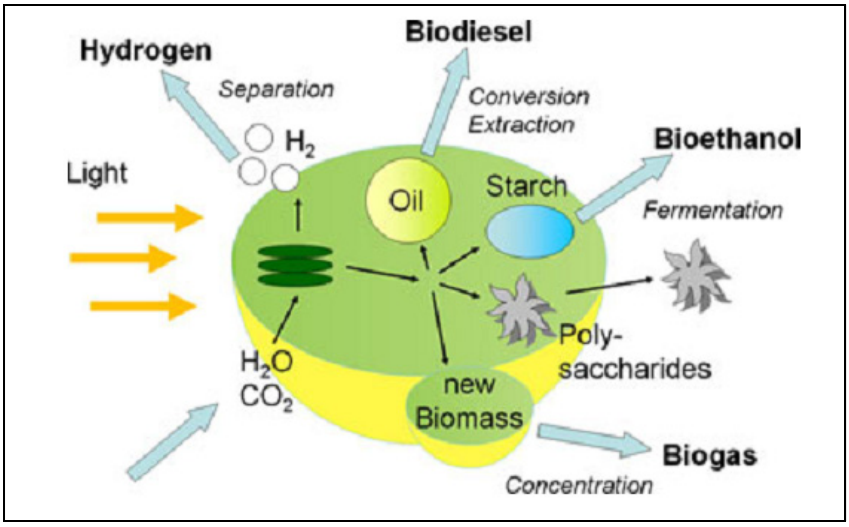

Fig. 3. Possible energy products from algae (Morweiser, et al., 2010).

1.3.1 Biohydrogen production

Biological hydrogen production has received attention in recent years as a safe and renewable energy source for a wide variety of applications, including the replacement of liquid fuel in the transportation sector. Remarkably, certain algal strains possess the ability to switch metabolic pathways and produce hydrogen during respiration. In a sealed, sulfur depleted environment, algae will stop oxidizing water, thus ending the supply of oxygen. When the remaining oxygen is consumed, the algae begin metabolizing stored compounds in an alternative respiration system from which hydrogen is evolved as the product (Melis & Melnicki, 2006). The catalysts for this reaction are either the hydrogenase or the nitrogenase enzymes, whose activities are inhibited by elevated oxygen levels in the environment. Moreover, the concentration of H^+ and electrons, which are obtained either directly from photosynthetic water splitting or indirectly through the degradation of starch, affects the productivity of this reaction (Kruse & Hankamer, 2010). While this process holds great promise for hydrogen production in general and fuel cell coupling in particular, research is still in its infancy and costs remain high.

1.3.2 Bioalcohol production

The Energy Policy Act of 2005 mandated an increase in the amount of biofuel blended into conventional gasoline, the vast majority of which has been met by corn ethanol (DOE, 2010). However, ethanol production from terrestrial plants such as corn, sugarcane, and lignocellulosic grasses requires large areas of arable land and huge volumes of potable water. Furthermore, the low energy density of ethanol cannot address the needs of the transportation sector in its entirety. Despite these issues, the market for ethanol remains large, as 23% of American the corn yield during the 2010/2011 growth season was diverted to ethanol production (USDA, 2011).

In the same way that carbohydrates generated by conventional ethanol feedstocks are broken down into sugar and fermented, the starches and cellulose in algae biomass can be used to produce ethanol. Depending on the strain of algae, the starch profile can include simple sugars or complex chains which must be broken before fermentation. The biomass can then be mixed with yeast or other fermentative microorganisms and fermented to produce alcohol (Bush & Hall, 2006). As the yeast consume sugar, they produce CO_2 which can be fed back into the growth system in a closed-loop process, as shown by Figure 4.

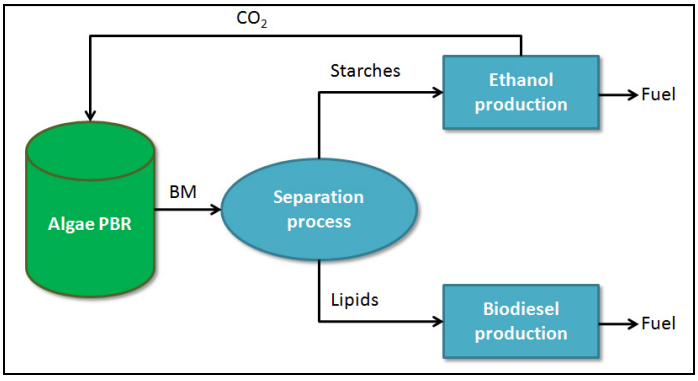

Fig. 4. Coproduction of ethanol and biodiesel from algae.

Although a combination biodiesel-ethanol plant is technically feasible, ethanol is a relatively inexpensive commodity and capital costs for such a facility are high. A more economically attractive approach to coproduction may be to convert the carbohydrate and protein dense biomass into a variety of high-value products, such as pigments, micronutrients, and omega-3 fatty acids in the form of EPA and DHA (Powell & Hill, 2009) (Singh & Gu, 2010). The chemical makeup of the algae biomass being cultivated dictates this co-product portfolio.

1.3.3 Biodiesel production

To produce biodiesel from algae, cell walls are ruptured and a solvent such as hexane is used to separate the intracellular lipids in the form of triacylglycerol (TAG) from the rest of the biomass. Methanol then acts as a catalyst to break these long TAG chains into smaller akyl ester chains, commonly known as biodiesel (Scott S. A., et al., 2010). In addition, this reaction produces glycerol as a byproduct.

While biodiesel represents the most volumetrically energy dense fuel derived from algae, the separation process of the TAG lipids from the residual biomass presents a costly and inefficient bottleneck. Large amounts of solvent are needed for current techniques, while contamination of the lipids from other cellular components remains an obstacle (Scott S. A., et al., 2010). Active research in this area has suggested the possibility of selective decomposition of the cell wall using enzymes, electromagnetic waves, and sonic vibration (Cooney, et al., 2009) (Andrade, et al., 2011). These novel methods seek to minimize the quantity of solvent required and result in more complete extraction of the lipids.

Regardless of these process engineering challenges, the rapid growth rate, high lipid content, and unique cultivation conditions of microalgae suggest it to be the only feedstock with the potential to completely displace liquid fuels derived from petroleum (Chisti, 2007). For the production of biodiesel, microalgal systems hold significant advantages over other crops, including their higher photon conversion efficiency, their ability to be harvested batch-wise nearly year-round, their utilization of salt and wastewater streams (Park, et al., 2011), and their potential for CO_2 sequestration via flue gas coupling (Schenk, et al., 2008). In terms of arable land usage, no other oil crop could provide the quantities needed for the widespread adoption of biofuels without drastically altering the world's current agricultural landscape, as shown by Table 1.

Plant source	Biodiesel (L/ha/year)	Area to produce global oil demand (hectares x 10^6)	Area required as percent global land mass	Area as percent global arable land
Soybean	446	10,932	73.4 %	551.6 %
Rapeseed/canola	1,190	4,097	27.5 %	206.7 %
Jatropha	1,892	2,577	17.3 %	130 %
Oil palm	5,950	819	5.5 %	41.3 %
Algae (10 g m^{-2} day^{-1} at 30 % TAG)	12,000	406	0.3 %	20.5 %
Algae (50 g m^{-2} day^{-1} at 50 % TAG)	98,500	49	0.3 %	2.5 %

Table 1. Comparison of crop-dependent biodiesel production from plant oils (Schenk, et al., 2008).

1.3.4 Biomethane production

Anaerobic digestion of organic waste produces a flammable gas mixture that can be burned for heat or used to power a gas engine. Once this biogas has been processed, it can be used in any conventional natural gas application. As the lipid fraction of algae ranges from 15-77% of total cell contents (Chisti, 2007), a large quantity of biomass remains after the extraction process. This organic biomass can be mixed with other forms of biowaste and anaerobically digested to produce biogas. In addition, the digested matter can be centrifuged and both the solid and liquid fraction used as fertilizers and soil conditioners. Figure 5 presents a basic schematic for a biogas production facility.

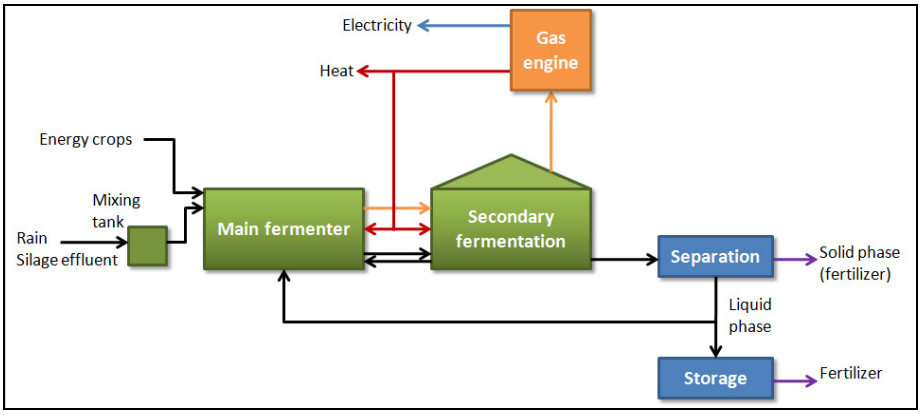

Fig. 5. Biogas production from energy crops, adapted from (Braun, et al., 2008).

The compaction of waste in landfills produces biogas naturally; however, if released freely into the atmosphere, this gas presents a significant pollution threat due to its methane content and combustibility when mixed with oxygen. Atmospheric methane is estimated to be more than twenty-one times as intense a greenhouse gas than carbon dioxide. However, when burned, biomethane is considered to be a relatively clean alternative fuel. Biomethane can be processed from biogas produced by the anaerobic digestion of animal waste, sewage, and crop waste from cellulosic and non-cellulosic plants. In the US, the potential annual production of biomethane from these sources could be equivalent to 10 billion gallons of gasoline. If this quantity of biomethane were substituted for conventional gasoline for fueling vehicles, greenhouse gas production could be reduced by 500 million metric tons of CO_2 per year (EERE, 2011). This reduction represents a 29% decrease in the rate of CO_2 emissions attributed to the American transportation sector in 2009 (EPA, 2011).

Despite this large breadth of activity seeking to realize algae's commercial potential, few comprehensive comparisons have been made to address the energetic and economic efficiency of these systems for biofuel production. The following sections analyze and compare methods for the cultivation, harvesting, and processing of microalgae for the production of biofuels. Particular emphasis is placed on the production of biodiesel due to its high energy density and compatibility with current transportation infrastructure and technology. A thermodynamic study identifies the most efficient production systems with regard to conversion of solar energy and utilization of auxiliary energy, and an economic

analysis highlights advantages of less efficient though potentially more profitable technologies. In this manner, current technology for algal biodiesel production can be assessed for its commercialization potential and utility to an energy consuming society.

2. Photobioreactor systems for biofuel production

Although the cultivation of algae began hundreds of years ago, only in recent decades have attempts been made to grow these organisms at an industrial scale. As with any agricultural system, as environmental control loosens, output becomes more erratic. Photobioreactors can be classified in two primary categories, closed and open systems. In closed systems, the algae are contained and culture conditions are highly regulated. In contrast, open systems dictate the algae grow exposed to the environment, permitting less control and increasing vulnerability to infection and invasion by predators. Although open systems present a higher risk of culture loss and generally produce less concentrated algae slurry, they are far less expensive to manufacture and operate than closed systems. Many have argued that open systems, particularly in the popular raceway pond configuration, currently represent the most economically viable method for producing algal biodiesel (Borowitzka, 2005) (Morweiser, et al., 2010) (Rodolfi, et al., 2009) (Stephens, et al., 2010). However, because these systems generate lower concentrations of biomass per liter, the concentration and extraction processes become more energy and cost intensive (Chisti, 2007). To analyze the photobioreactors both as singular units and part of the larger biofuel production system, this chapter examines closed and open reactors for their solar conversion and thermodynamic efficiencies with and without the inclusion of the harvesting and extraction processes.

2.1 Planktonic photobioreactors

Planktonic algae float or drift in a suspension of fresh or saline water. In the wild, these algae form large blooms at or near the surface and act as a vital food source for many fish and marine creatures. Planktonic photobioreactors serve to accommodate this type of algae by providing a slow moving current in which the culture can drift. As most cultivated algae strains exhibit this behavior, these photobioreactors have become extremely common while still assuming many different configurations.

2.1.1 Open pond raceways

Open pond systems generally consist of a lined or unlined shallow tank in which water is gently circulated via paddlewheels, as shown in Figure 6. The ponds are most commonly constructed out of earth, plastic, or concrete, and water depths range from 10-50 cm to optimize the absorption of light by the algae (Jorquera, et al., 2010). In the raceway configuration, algae inoculant is fed to the pond in front of a rotating paddlewheel. The algae mature as they circulate through the raceway and are harvested upon completing the path.

The relative technical simplicity and scalability compared to other PBR systems have made raceway ponds the most common method for commercial production of algae products. The largest algae growth system in the world utilizes this design, occupying over 440,000 m^2 in Southern California for the production of *Spirulina* sp., which is dried and sold as a nutritional supplement (Earthrise® Nutrional, LLC, 2009).

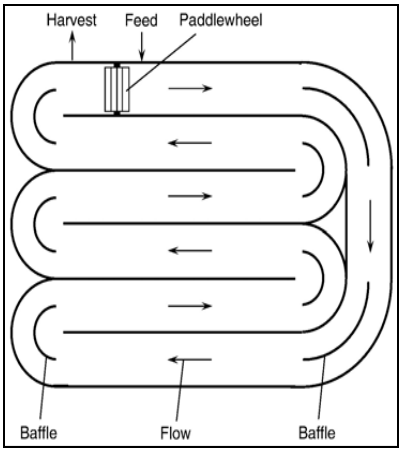

Fig. 6. Schematic of an open pond raceway system (Chisti, 2007).

Open ponds usually draw CO_2 from the atmosphere and receive unfiltered sunlight for photosynthesis. Because the pond is open to the ambient environment, evaporation off the surface helps to regulate its temperature. However, this evaporation also adds to the pond's high water consumption, and the exposure leaves the culture vulnerable to contamination and invasion by foreign species. In addition, because light conditions are not regulated, photoinhibition can be problematic. Finally, the large volumes of water required for these systems result in a much less concentrated product upon harvesting, requiring a more energy intensive dewatering processes. The cost of the final product ultimately depends on the amount of auxiliary energy required and the productivity of the photobioreactor, both of which are relatively low for open ponds in comparison to closed systems.

2.1.2 Tubular systems

Tubular systems can be oriented in horizontal, vertical, helical, or annular configurations and consist of series of small plastic or glass tubes through which planktonic algae gently circulate. In these systems, tubes are arranged parallel to each other and may be stacked to increase the yield per unit area. Highly turbulent flow is maintained by mechanical or airlift pumping to prevent algae sedimentation within the tubular array. Tubular photobioreactors operate as continuous culture systems in which a reservoir is used to remove dissolved oxygen and add CO_2 to the fluid before continuing the loop and repeating the process. Additional carbon dioxide may be supplied at intervals along the tubes to maintain a constant pH and ensure that photosynthesis is not interrupted by lack of carbon (Chisti, 2007). Figure 7 displays a basic schematic of a tubular photobioreactor.

Closed systems can achieve more than thirteen times the volumetric productivity than raceway ponds systems as they allow better capture of incident radiation, protection from contamination, more effective gas/liquid mass transfer, and a higher degree of control over pond conditions (Chisti, 2007) (Jorquera, et al., 2010). In addition, closed systems have much smaller areal footprints and require smaller volumes of water than open ponds, resulting in more productive facilities and higher biomass concentrations at harvest (Chisti, 2007). As

biomass concentration can be nearly 30 times greater than algae slurry harvested from raceway systems, biomass recovery from tubular systems is generally less labor intensive. However, tubular reactors can become expensive due to high power requirements for mixing and gas/liquid transfer. While open pond systems may consume as little as 4 W/m^3, horizontal tubular systems of similar scale have been reported to require as much as 2000-3000 W/m^3 (Jorquera, et al., 2010) (Sierra, et al., 2008). Depending on the cost of processing the harvested biomass and the market value of the final product, highly productive tubular systems may be economically justified (Chisti, 2007).

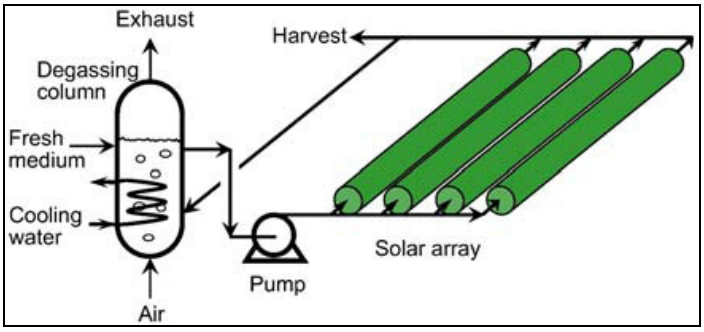

Fig. 7. Schematic of a tubular photobioreactor (Chisti, 2007).

2.1.3 Flat plate systems

Flat plate photobioreactors cultivate planktonic algae in vertical, translucent panels which are illuminated from both sides and mixed by aeration (Sierra, et al., 2008). As in all photobioreactors, these systems are developed in concert with the unique physiology of the algae species under cultivation. In particular, light regime, temperature regulation, and mass transfer represent important design parameters in the construction of these systems. Flat plate systems have been in use since the 1950's, and modern reactors have both reduced the areal footprint of the cultivation system (Pulz, et al., 1995) and facilitated the guidance of any desired light path through the use of laminated glass sheets (Hu & Richmond, 1996). Figure 8 displays a schematic for a flat plate photobioreactor system. Flat plate systems are usually constructed from glass or plastic panels held together by steel frames. Innovative systems have utilized plastic bags within a wire netting support system, resulting in a simpler construction than other designs (Tredici & Rodolfi, 2004).

In addition to the plate's material transmissivity, location and orientation of flat plate reactors largely determine the quantity and quality of incident solar radiation (Duffie & Beckman, 1980). For plates oriented in an East-West configuration at locations within 40° of the equator, the quantity of intercepted global radiation becomes similar to that of horizontal surfaces such as raceway ponds but with better homogenization of light reception over the course of a year (Sierra, et al., 2008). To minimize light saturation, panels can be placed in a North-South configuration to encourage a degree of mutual shading and dilute high intensity light during the afternoon, reducing photoinhibition (Morweiser, et al., 2010) (Carlozzi, 2003). Like tubular systems, the high surface area to volume ratio of flat plate systems results in shorter light paths, high photosynthetic efficiencies, and

consequently high productivities. Similar to their tubular counterparts, the energy requirements of flat plate photobioreactors makes them more expensive than the more technically crude open systems (Morweiser, et al., 2010).

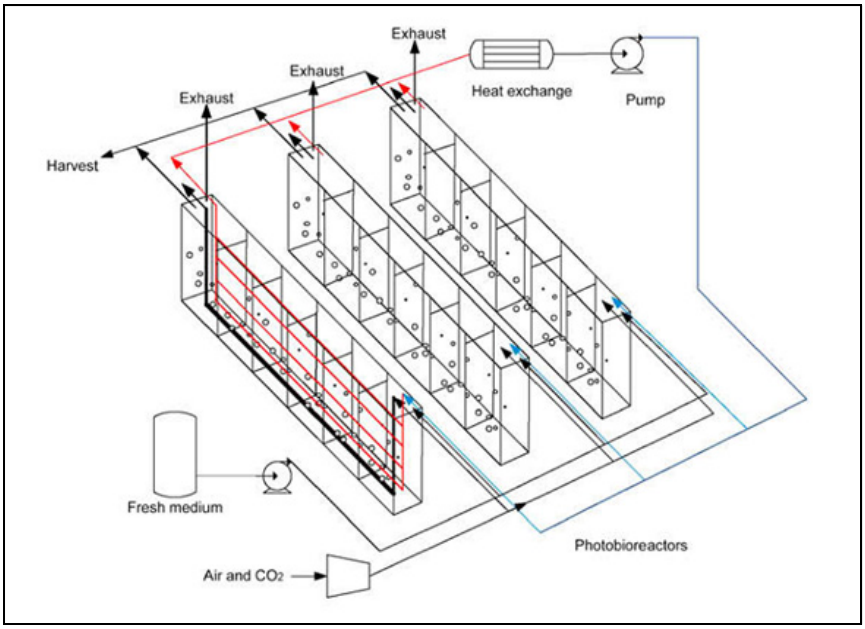

Fig. 8. Schematic of a flat plate photobioreactor (Jorquera, et al., 2010).

Flat plate reactors hold an advantage over tubular systems in that oxygen molecules generally have a much shorter distance to travel before reaching a degassing station. If the design of any closed system does not adequately account for this mass transfer, dissolved oxygen released during photosynthesis can accumulate and potentially damage the algae cells (Sierra, et al., 2008). Flat plate systems typically require approximately 40-50 W/m^3 for mixing, pumping, and mass transfer (Morweiser, et al., 2010). As discussed in the context of the open pond system, this consumption is orders of magnitude lower than that for tubular reactors of similar capacity, resulting in less costly operation. This lower power requirement for flat plate systems also becomes advantageous as many algae species are damaged by high levels of shear.

2.2 Benthic photobioreactors

Unlike planktonic organisms, benthic algae grow immobilized in a biofilm attached to a substrate. Benthic photobioreactors accommodate these species by providing a large surface upon which the algae can settle. These novel systems represent an alternative to the more commonly available planktonic photobioreactors and serve to expand culture options to include species that were once limited by cultivation method. Benthic photobioreactors have taken many different forms, all of which seek to maximize the substrate surface area and minimize water and auxiliary energy consumption and nutrient waste. In most systems,

water is gently circulated over the biofilm, and drip systems are employed to deliver nutrients. Figure 9 illustrates a novel benthic photobioreactor developed in The University of Texas' Solar Energy and Biofuels lab for the production of *Botryococcus braunii* sp. This lab scale system utilizes a carbonated concrete surface as the algae substrate and has demonstrated productivities of up to 30.73 kg/m^3 with a lipid content of 26.8%. In addition, this particular photobioreactor was shown to reduce the water requirement for cultivation by up to 42 times that of raceway pond systems (Ozkan, et al., 2011).

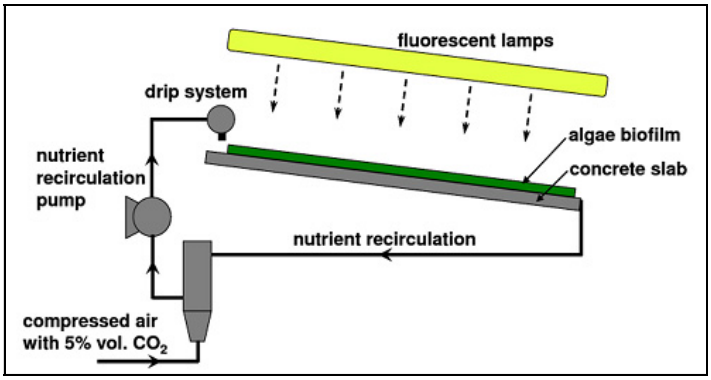

Fig. 9. Schematic of an algae biofilm photobioreactor (Ozkan, et al., 2011).

In addition to this carbonated concrete system, researchers have successfully immobilized benthic algae on a wide variety of substrates, including calcium alginate gels (Baillez, et al., 1985), agitated polystyrene foams (Johnson & Wen, 2010), and PVC bristle combs (Silva-Aciares & Riquelme, 2008). Membrane systems have been coupled with fossil-fired power plants in order to mitigate CO_2 emissions (Kremer, et al., 2006), and biofilms grown on corrugated raceways and algal turf scrubbers have been tested for the removal and recovery of nutrients from wastewater and animal waste effluent, respectively (Cragges, et al., 1997) (Kebede-Westhead, et al., 2006) (Mulbry, et al., 2008)(Park, et al., 2011). Many of these systems hold great promise for reducing the water, nutrient, and energy requirements of cultivation that plague planktonic photobioreactors. However, productivities vary widely between systems, and maximizing irradiance remains challenging. Further research will continue investigating these issues, especially with regard to the technology's potential coupling with waste stream treatment.

3. Algal biodiesel production and energy usage

3.1 Photobioreactors as solar energy conversion systems

When comparing the energy conversion efficiency of any technology, analyses must examine the utilization of freely available resources in addition to the auxiliary energy supplied by manmade systems. In this section, the relative merit of different methods for algal biodiesel production is determined based on their thermodynamic and solar energy conversion efficiencies. The overall efficiency of a system, η, can be defined as the net energy out of the system in kilowatts, P_{net}, relative to the energy input across the system boundary, P_{in}. Equation (1) illustrates this concept.

$$\eta = \frac{P_{net}}{P_{in}} \tag{1}$$

The sun represents the primary energy source provided to the algae cultivation systems and is supplemented by auxiliary power in the form of electricity for pumping and mixing. Energy utilization is examined during algae growth, harvesting, and extraction, i.e., during all processes up to the state known as "biocrude," at which the raw lipids can be refined into biodiesel. Figure 10 defines the system's control volume, with accompanying inputs and outputs. Unfortunately, reliable data could not be found for all consecutive stages of growth, harvesting, and processing for each photobioreactor system under study. Comprehensive energy input information could only be obtained for the open pond system. However, because the open pond demonstrated a lower biomass concentration in the harvested slurry, larger volumes must be processed for the same biomass yield. Thus, extraction and harvesting are expected to be more energy intensive. If the efficiency including harvesting and extraction for the open pond are positive, it can be assumed that the efficiencies of systems generating more highly concentrated slurries will be even more favorable.

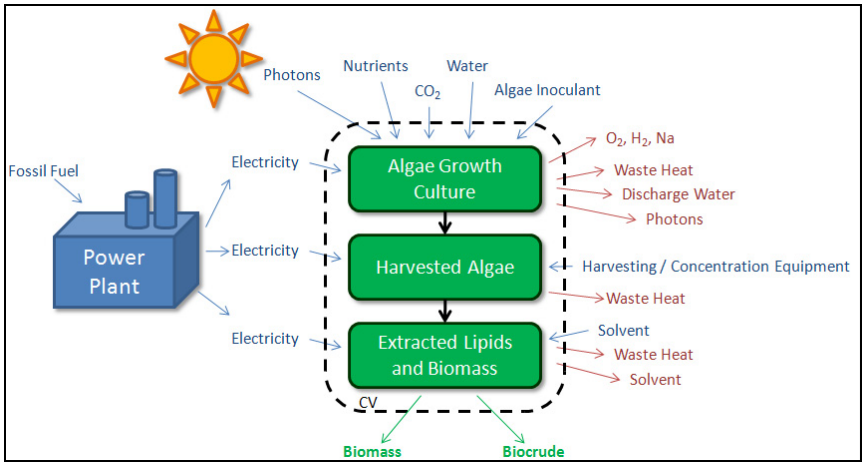

Fig. 10. Algae biofuel production process, adapted from (Beal, 2011).

P_{out} is defined as energy available within the biocrude produced by the system in kilowatts. This is calculated as:

$$P_{out} = x_{oil}\dot{m}_{algae}E_{oil} \tag{2}$$

Where $\dot{m}_{algae}$ represents the rate of algae production by mass in kilograms per second, x_{oil} is the mass fraction of lipids within the algae cell, and E_{oil} is the energy content of the produced lipid, equivalent to 37.6 megajoules per kilogram (Rebolloso-Fuentes, et al., 2001).

The net power produced by the system, P_{net}, considers only the useful energy that crosses the system boundary. Because the sun is widely available at no cost, P_{net} disregards this input, but takes into account auxiliary power, P_{aux}, supplied to the system in the form of electricity as:

$$P_{net} = P_{out} - P_{aux} \tag{3}$$

Furthermore, the closure bounds of what constitutes input power can be elaborated. To assess the solar energy conversion efficiency, P_{in} is equivalent to the full-spectrum of incident solar energy ($P_{solar,\,full}$). This enables a comparison to photovoltaic and solar thermal technologies in illustrating total solar resource utilization.

This efficiency will be markedly low, as green plants only utilize the photosynthetically active portion of the solar energy incident on Earth. Photosynthetically active radiation consists of light with a wavelength from 400 – 700 nm, a range which comprises approximately 46% of the full-spectrum (Larkum, 2003). Limiting the energy input to only that part of the solar spectrum which is photosynthetically active gives a more representative value of efficiency based on the organisms' natural abilities. Thus, a second calculation is considered with regard to the algae's utilization of only photosynthetically active radiation (*PAR*). In this calculation, P_{in} is redefined as $P_{solar,\,PAR}$ to represent only that fraction of the spectrum that is photosynthetically active (x_{PAR}), as:

$$P_{solar,PAR} = P_{solar,full} x_{PAR} \tag{4}$$

Moreover, the technology must be analyzed with sole regard to auxiliary inputs to the system. Because sunlight is free, abundant, and renewable, the production of fuel from this primary energy source can be merited as long as auxiliary inputs do not outweigh the net energy available in the final product. In this calculation, P_{in} is equivalent to P_{aux}. If this auxiliary power utilization effectiveness (ε_{aux}) is found to be less than unity, the system consumes more fuel than it produces and should not be implemented.

Finally, the thermodynamic efficiency is calculated based on the total energy input and useful energy output. In this calculation, input energy includes both the auxiliary energy supplied to the system and the full spectrum of incident solar energy. Table 2 summarizes these efficiencies.

Solar Energy Conversion Efficiency, Full Spectrum	$\eta_{solar} = \frac{P_{out}}{P_{solar,\,full}}$	(5)
Solar Energy Conversion Efficiency, PAR	$\eta_{PAR} = \frac{P_{out}}{P_{solar,PAR}}$	(6)
Auxiliary Power Utilization Effectiveness	$\varepsilon_{aux} = \frac{P_{out} - P_{aux}}{P_{aux}}$	(7)
Thermodynamic Efficiency	$\eta_{th} = \frac{P_{out} - P_{aux}}{P_{solar,\,full} + P_{aux}}$	(8)

Table 2. Energy conversion efficiency calculation methodology.

3.2 Parameters influencing energy output

To better understand the factors affecting photobioreactor productivity, a formulation was put forth by Weyer et al. to determine the theoretical maximum and best case productivity for open pond photobioreactors based on reactor design and the biochemical aspects of

photosynthesis (Weyer, et al., 2010). While their study does not provide clear information about energy consumption and thus cannot be used in a complete thermodynamic efficiency calculation, their breakdown of losses in the conversion of solar energy to chemical energy helps identify areas for potential design optimization. This section explains Weyer et al.'s eleven term formulation in order to clarify why biomass output varies with design choice and which factors limit productivity regardless of design.

3.2.1 Incident solar energy

The laws of thermodynamics represent the governing principles behind any efficiency analyses, stating that the energy flux into a system is at all times greater than or equal to that which can be stored within the system. Thus, for photobioreactor technologies, solar irradiance represents the primary limitation to the generation of algae biomass.

The energy available from the full spectrum of light incident on Earth's surface (E_{solar}) varies as a function of latitude and atmospheric conditions of the particular location under study. Weyer et al. employed the NREL's Blue Clear Sky Model (Bird & Hulstrom, 1981) to approximate atmospheric absorption assuming cloudless skies. Although this provided a theoretical maximum annual solar irradiance of 11,616 MJ/m^2, the model does not account for realistic climate conditions. For a more representative approximation of solar irradiance at a given location, historical meteorological data was collected. A survey of six sites with latitudes within 40 degrees of the equator gave values for annual solar irradience of 5,623-7,349 MJ/m^2 (Weyer, et al., 2010). For the purposes of this paper, the location of the photobioreactor was taken to be located in Eliat, Israel for better comparison to the experimental systems described in Section 3.3. The average annual solar irradiance for this location was found to be 7,301 MJ/m^2, as documented by US Department of Energy (EERE, 2011).

More than 99% of the radiation entering the atmosphere have a wavelength less than 4000 nm. However, photosynthesizing organisms can only utilize the portion of this spectrum commonly known as Photosynthetically Active Radiation (*PAR*), which ranges from approximately 400 – 700 nm (Szeicz, 1974). Figure 11 shows the incident solar radiation at the top of the atmosphere, at sea level , and at 10 m below ocean surface. To accurately determine the usable energy available to photosynthetic organisms, this reduction must be accounted for.

The second term in Weyer et al.'s study calculated the photosynthetically active fraction of the solar spectrum. Terrestrial solar energy as a function of wavelength, $E_{solar}(\lambda)$, is taken proportional to the full spectrum (approximated by zero to 4000 nm wavelengths) as:

$$x_{PAR} = \frac{\int_{400nm}^{700nm} E_{solar}(\lambda)\, d\lambda}{\int_{0}^{4000nm} E_{solar}(\lambda)\, d\lambda} \tag{9}$$

By this measure, the percentage of photosynthetically active radiation comes to approximately 45.8% of the full spectrum (E_{solar}). However, while this percentage is technically classified as photosynthetically active, chlorophyll better utilize the red and blue light on the far ends of the spectrum. Thus, treating the entire spectrum of visible light equally results in an overestimation of the energy input to the organic system (Larkum, 2003). A more accurate calculation can be made based on the light action spectra of the particular microalgae under study.

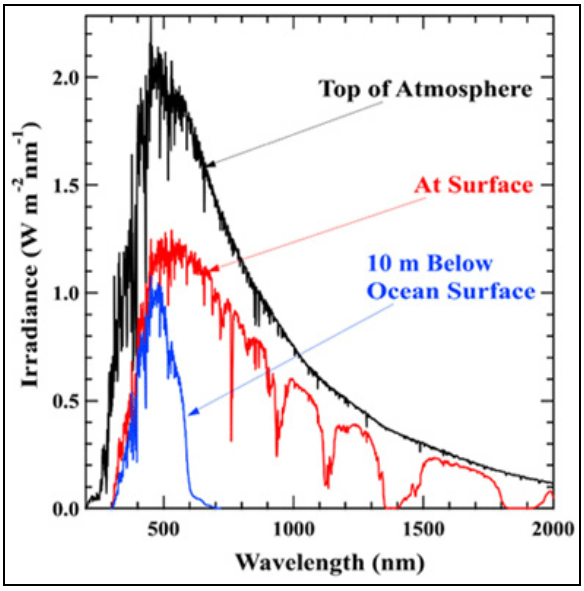

Fig. 11. Global solar irradiance (Spectral Irradience Monitor)

The usable incident radiation can then be analyzed for its energy density by examining the number of photons within the PAR range incident on the surface and their associated energy content. The wavelength-weighted average photon energy ($\overline{E}_{photon}$) can be found using the calculation of $E_{solar}(\lambda)$ and Planck's Law, which states that the energy associated with a wave is inversely proportional to its wavelength, given by Equation (10) where h represents Planck's constant (6.63 x 10^{-34} J/s) and c represents the speed of light (2.998 x 10^{8} m/s).

$$\overline{E}_{photon} = \frac{1}{3\times10^{-11}} \int_{400nm}^{700nm} \frac{hc}{\lambda} d\lambda \tag{10}$$

Using the wavelength-weighted average photon energy, the Photon Flux Density (PFD) incident on a surface can be calculated as:

$$PFD = \frac{E_{solar} x_{PAR}}{\overline{E}_{photon}} \tag{11}$$

3.2.2 Design specific losses

The first design-specific reduction in productive potential relates the losses in incident solar energy to the construction and geometry of the photobioreactor. The following two variables comprise this reduction: (i) reflection off the surface and (ii) the magnitude of radiation depending on the latitude, time of day, and day of the year. To determine this Photon Transmission Efficiency (η_{PT}), these two variables are multiplied and summed (Weyer, et al., 2010).

In the case of flat systems such as ponds or panels, the magnitude of radiation and the reflection off the surface of the photobioreactor can be calculated from the angle of incidence, which is based on the location of the surface and the solar time. These can be calculated based on the methodologies outlined by Duffie and Beckman (Duffie & Beckman, 1980).

Reflective losses take place when (i) there is an appreciable difference between the indices of refraction and (ii) the angle of incidence on the interface is large. Using the angle of incidence and Fresnel's equations for reflection of unpolarized radiation passing through a medium, the reflective losses can be calculated. By combining the magnitude of incident radiation with the reflected losses and integrating over the course of a day, the losses in photon transmission due to reflection can be found. Equation (12) illustrates this concept, where $r(t_s)$ represents reflectivity as a function of solar time in hours, and $G_r(t_s)$ represents the magnitude of global solar irradiance in MJ/m^2 per day.

$$\eta_{PT} = \frac{\int_0^{24hrs} r(t_s) G_r(t_s) dt_s}{\int_0^{24hrs} G_r(t_s) dt_s} \tag{12}$$

Figure 12 displays the reflected incident solar radiation for an open pond as it varies by latitude and time of year. For the best case scenario, losses due to reflection average about 5% of the total incident solar radiation, with increased losses during winter at locations far from the equator. If production is to continue year-round, losses due to reflection can be minimized by choosing an appropriate location nearer to the equator or inclining the systems with respect to the angle of the latitude. Although for pond systems this is not possible, for flat plate and benthic systems the angle of inclination can be adjusted to minimize reflection losses. The calculation for photon transmission efficiency becomes more complicated with flat plate, tubular, and bagged systems as the reflectivity and transmissivity of the container material must be accounted for.

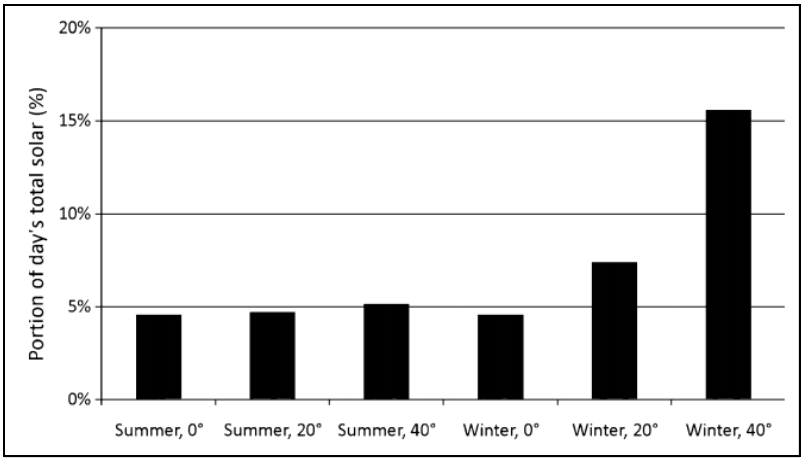

Fig. 12. Reflected solar radiation in an open pond by latitude and solstice (Weyer, et al., 2010).

The photon utilization efficiency (η_{PU}) represents the second photobioreactor design-specific reduction in energy output. Although an adequate quantity of photons may be incident upon the photobioreactor's surface, sub-optimal culture conditions will limit the cells' ability to utilize these photons. In particular, temperature and irradiance have significant effect on photosynthetic efficiency. Photoinhibition occurs under high irradience, slowing photosynthesis and potentially damaging cells. This can be particularly troublesome for horizontal systems exposed to unfiltered sunlight, such as in open ponds (Franklin, et al., 2003). Photon utilization efficiency can range from 50-90% under low light conditions; in a high light environment with photoinhibition occurring, efficiency drops to as low as 10-30% (Goldman, 1979). A median value of 50% was used by Weyer et al. to represent a best-case scenario for photon utilization efficiency. However, this may be high due to the almost unavoidable effects of photoinhibion in uncovered raceway systems (Weyer, et al., 2010).

3.2.3 Chemical conversion and biological process losses

Inevitable losses occur in the conversion of photons into chemical energy in the form of sugar. The overall chemical reaction for the photosynthetic conversion of carbon dioxide and water into sugar can be given as:

$$CO_2 + H_2O + 8 \text{ photons} \rightarrow CH_2O + O_2 \tag{13}$$

The eight photons needed for this reaction represent the "quantum requirement" (QR) for one mole of carbon dioxide and one mol of water to be converted into sugar and oxygen. This general formulation for photosynthesis represents the combination of two chemical reactions: light reactions where photons are converted to ATP and electron carriers in the two photosystems, and dark reactions where carbon dioxide is fixed in the Calvin cycle (Weyer, et al., 2010). Under ideal conditions, this process would require three photons at the lowest usable energy level (700 nm), as dictated by the energy requirement for the formation of sugar, CH_2O. However, due to the high energy levels required to split water molecules, plants have adapted two photosystems through which to transfer electrons. The combination of these systems divides the potential energy requirement, facilitating the conversion by using more photons at lower energies. In this process, commonly known as the Z-scheme for the characteristic shape of the electron transfer path, researchers have generally accepted that eight moles of photons are required per mole of CO_2 fixed. However, this may be conservative under realistic conditions. In Equation (13), CH_2O represents the simplest form of carbohydrate energy produced by photosynthesis, whose energy content of 482.5 kJ/mol is accounted for in the term E_{carb}.

The biomass accumulation efficiency (η_{BMA}) represents the loss in biomass production in exchange for other cellular functions. This "cost of living" efficiency varies drastically between different species and environments. Manipulating culture conditions to stress the cells has shown to increase lipid production in some species. In others, varying the nitrogen input and temperature have shown to affect biomass production. The general principles governing this phenomenon are not well understood, but a median value of 50% was estimated for a best-case scenario in which culture conditions are optimized to reduce the loss in biomass due to respiration (Weyer, et al., 2010).

Combining these terms with the energy content of the biomass produced (E_{BM}), which is taken as the heat of combustion as a weighted average based on the cellular composition, the biomass growth rate ($\dot{m}_{BM}$) can be obtained, as demonstrated in Equation (14). In Weyer et al.'s calculation, E_{BM} was taken to be 21.9 MJ/kg biomass to represent the median value of the energy content during the growth stage rather than in the oil laden state just before harvest. This may be an underestimate, as the biomass energy content for *Nannochloropsis* sp. has been reported to contain up to 33.5 MJ/kg biomass (Jorquera, et al., 2010). However, for this theoretical calculation, the algae species is not specified and 21.9 MJ/kg represents a conservative estimate.

$$\dot{m}_{BM} = \eta_{PT}\eta_{PU}\eta_{BMA}\frac{E_{carb}PFD}{E_{BM}QR} \tag{14}$$

The percent oil content of the cell is used to determine the rate of lipid production in the algae culture. A theoretical maximum for percentage oil has yet to be determined, with experimental values ranging from 15-77% of total cell contents (Chisti, 2007). However, the values were likely obtained using gravimetric analysis, which accounts for the total lipid quantity within the cell rather than that which is usable. Thus, these experimental values may be optimistic (Weyer, et al., 2010). In addition, cells which produce large quantities of lipids often grow at slower rates. Pursuit of a natural or genetically engineered algae strain must continue to balance these trade-offs. Using the lipid fraction (x_{oil}) and the algal oil's density (ρ_{oil}), the volumetric lipid production rate can be calculated as:

$$\dot{V}_{oil} = \frac{x_{oil}\dot{m}_{BM}}{\rho_{oil}} \tag{15}$$

The density of algal oil was taken to be similar to that of soybean oil, which is approximately 918 kg/m^3 (Weyer, et al., 2010).Using the mass rate of biomass production and the energy content of the oil, the energy output of the algal biofuel production system can be obtained. Equation (2) shows this calculation for P_{out}. This value can then be inserted into Equations (5) thru (8) to determine the system's solar conversion and thermodynamic efficiency. The energy content of lipids extracted from *Nannochloropsis* sp. was taken to contain 37.6 MJ/kg, which is assumed to be representative of oil from most algae strains (Rebolloso-Fuentes, et al., 2001).

$$P_{out} = x_{oil}\dot{m}_{BM}E_{oil} \tag{16}$$

Table 3 summarizes the assumptions made in the calculation of theoretical best case oil productivity for an open pond system.

3.3 Survey of actual energy output

To compare realistic productivity to the theoretical formulation proposed by Weyer et al., data was collected from three operating facilities. A 2010 study by Jorquera et al. compiled literature data from an open raceway pond (Richmond & Cheng-Wu, 2001), a vertical flat plate system (Cheng-Wu, et al., 2001) (Richmond & Cheng-Wu, 2001), and a horizontal tubular system (Chini Zittelli, et al., 1999). Baseline productivity was taken as uniform at 100,000 kg of

biomass per year to facilitate comparisons. Each photobioreactor cultivated the algal strain *Nannochloropsis* sp., whose oil content was assumed to be 29.6% dw, an average value based on reported ranges of 20-40% depending on culture conditions and maturity (Rodolfi, et al., 2009). Table 4 summarizes the relevant productivity data for each of these systems.

Term	Value	
1. Full-spectrum solar energy, E_{solar}	7301.13	MJ/m²-yr
2. Photosynthetic portion of spectrum, x_{PAR}	45.8%	
3. Average photon energy, E_{photon}	225.3E-3	MJ/mol
4. Photon transmission efficiency, η_{PT}	95%	
5. Photon utilization efficiency, η_{PU}	50%	
6. Quantum requirement, QR	8	
7. Carbohydrate energy content, E_{carb}	482.5	kJ/mol
8. Biomass accumulation efficiency, η_{BMA}	50%	
9. Biomass energy content, E_{BM}	21.9E-3	kJ/kg
10. Cell oil content, x_{oil}	29.6%	
11. Oil density, ρ_{oil}	918	kg/m³
Best case areal biomass productivity	97,078	kg/ha-yr
Best case areal oil productivity	31,302	L/ha-yr
Best-case areal energy production from lipids	1080.44	MJ/ha-yr
Area required to produce 100,000 kg biomass	10,301	m²

Table 3. Best case assumptions and productivities for a raceway pond (Weyer, et al., 2010).

	Open Raceway	Flat Plate	Tubular
Annual biomass productivity (kg/yr)	100,000	100,000	100,000
Areal footprint (m²)	25,988	10,147	10,763
Biomass concentration (g/l or kg/m³)	0.35	2.7	1.02
Areal biomass productivity (kg/ha-yr)	38,479	98,551	92,909
Areal oil productivity (L/ha-yr)	12,407	31,777	29,958
Areal energy productivity from lipids (MJ/ha-yr)	428.26	1,096.83	1,034.04

Table 4. Production data for photobioreactors (Jorquera, Kiperstock, Sales, Embirucu, & Ghirardi, 2010).

3.4 Solar energy input

The calculation for solar energy supplied to the systems was based on the respective location of each photobioreactor. These included Eilat, Israel for the raceway pond and flat plate photobioreactor and Florence, Italy for the tubular system. Historical meteorological averages for global solar radiation were used for the full spectrum solar power input ($P_{solar,}$

$_{full\ spectrum}$), which was then used to calculate the photosynthetically active portion of the incident radiation ($P_{solar,\ PAR}$), as discussed in Section 3.2.1. Global solar radiation includes both direct beam and diffuse radiation. Table 5 lists values for average global irradiance by location.

	Average global irradiance (full spectrum)	Average global irradiance (PAR)
Eilat, Israel (29°32′N, 34°57′E)	231.5 W/m² (7301 MJ/yr)	108.3 W/m² (3417 MJ/yr)
Florence, Italy (43°47′N, 11°11′E)	130.3 W/m² (4110 MJ/yr)	61.0 W/m² (1923 MJ/yr)

Table 5. Average global solar irradiance by photobioreactor location (EERE, 2011).

3.5 Auxiliary power inputs

Operational data was compiled for the systems under study by Jorquera et al. in order to compare each facility's Net Energy Ratio (NER) in its utilization of supplied auxiliary power. For this analysis, the data for total energy consumption for each system is used for P_{aux} in the calculation of auxiliary power utilization effectiveness and thermodynamic and solar efficiencies. Energy consumption data in the photobioreactor systems includes only that for air pumping, mixing, and liquid/gas mass transfer (Jorquera, et al., 2010). As consumption data for the tubular system was not reported by the operators, the power required for air pumping was assumed to be similar to that of other tubular facilities at 2500 W/m³ (Sierra, et al., 2008). Table 6 summarizes the auxiliary energy required on a volumetric and total annual consumption basis.

	Open Raceway	Flat Plate	Tubular
Volumetric energy consumption (W/m³)	3.72	53	2500
Total energy consumption (MJ/yr)	378,450	698,940	15,895,800

Table 6. Comparative energy consumption for photobioreactor systems (Jorquera, et al., 2010).

4. Efficiency results and other considerations

4.1 Solar conversion and thermodynamic efficiencies

Applying the data shown in Tables 4 thru 6 to Equations (5) thru (8), thermodynamic and solar efficiencies and auxiliary power utilization effectiveness for the systems can be found. The results of these calculations are summarized in Table 7.

	Raceway	Flat Plate	Tubular
Solar energy conversion efficiency, full spectrum	0.59%	1.50%	2.52%
Solar energy conversion efficiency, PAR	1.28%	3.28%	5.49%
Thermodynamic efficiency	0.39%	0.55%	-24.58%
Auxiliary power utilization effectiveness	1.94	0.59	-0.93

Table 7. Solar conversion and thermodynamic efficiencies and auxiliary power utilization effectiveness for photobioreactor systems.

The efficiency calculations presented in Table 7 assumed the energy out of the system only included that available in the extracted lipids. However, as was mentioned in Section 1.3's discussion of algal fuels, the residual biomass may be fermented into ethanol or processed as biogas. The total energy content of the generated biomass is taken to be 31.55 MJ/kg (Jorquera, et al., 2010). Table 8 recalculates the solar conversion and thermodynamic efficiencies and auxiliary energy utilization effectiveness to include the total energy available from the biomass and lipids generated by the system.

	Raceway	**Flat Plate**	**Tubular**
Solar conversion efficiency, full spectrum	1.66%	4.26%	7.13%
Solar conversion efficiency, PAR	3.63%	9.30%	15.57%
Thermodynamic efficiency	1.46%	3.28%	-21.19%
Auxiliary power utilization effectiveness	7.34	3.51	-0.80

Table 8. Solar conversion and thermodynamic efficiencies and auxiliary power utilization effectiveness including the total energy available in the biomass.

Of the three photobioreactors, the tubular system utilized incident solar energy most efficiently. As singular systems, perfectly efficient organisms can theoretically convert photosynthetically active solar energy into biomass at an efficiency of about 26.7% (Weyer, et al., 2010). However, due to losses also observed in the photobioreactor systems, photon transmission, photon utilization, and biomass accumulation reduce this photosynthetic conversion efficiency of solar energy into biomass to an approximate maximum of only 1-4% (Jorquera, et al., 2010). When including the total recoverable energy available in the biomass, the efficiency values in Table 8 are consistent with those for terrestrial plants, with distinctly higher efficiencies in the case of the flat plate reactor and tubular reactors.

The thermodynamic efficiency for each system was found to be low, and became highly negative in the case of the closed tubular reactor. However, as solar energy is assumed to be free, renewable, and abundant, a more economically important factor for the successful adoption of these technologies examines how well the facilities utilize auxiliary energy supplied to the system. Of the three photobioreactors, the energetic output from the raceway pond almost doubled the required auxiliary energy when solely accounting for lipid production, increasing to more than seven fold when including the energy available in the biomass. Though not as productive, the flat plate system had a positive thermodynamic efficiencies and high auxiliary energy utilization effectiveness as well. The tubular system, however, proved in both cases to require far too much auxiliary energy to justify large scale implementation.

The theoretical best case production for a raceway pond described in Section 3.2 would have the same efficiencies for the thermodynamic system if baseline production was taken to be 100,000 kg and similar auxiliary energy inputs were assumed. However, the areal productivity shown by the theoretical production calculation for a raceway pond was close to that of a flat plate or tubular system, as can be seen in Tables 3 and 4. This implies that raceway ponds can achieve productivities similar to that of closed systems, with better land utilization and potentially lower construction and operational costs. However, values used for photon utilization and biomass utilization efficiencies in the theoretical best case scenario

may be unrealistically high with regards to current technology for industrial production. Maintaining precise culture conditions in an open order to minimize losses in photon utilization and biomass accumulation efficiencies remains difficult.

4.2 Harvesting and processing energy costs

While the efficiency values for the raceway and flat plate systems appear encouraging, they account only for the growth phase of the biofuel production cycle, as was shown in Figure 11 in Section 3.1. Biomass harvest, lipid extraction, and processing require significant amounts of energy, which generally scales with the biomass concentration of the harvested liquid. The high volumes of water required by open raceway systems result in a significantly lower concentration of biomass in the harvested algae slurry than apparent in either of the closed systems, as shown in Table 4 of Section 3.3. Based on biomass concentration, the flat plate system produced the most favorable harvested product in terms of ease of extraction and processing. Although the data compiled for these systems did not include energy consumption during either of these phases, the energetic costs of harvesting and processing have been extensively documented for the more common cultivation method of raceway ponds. As the biomass concentration in the harvested slurry is reported to be lower for open ponds than for closed systems, raceway pond production can be judged as the most energetically and economically expensive method in terms of downstream processing.

Although many methods of harvesting and lipid separation exist, most can be classified as sedimentation or filtration based processes. Sedimentation processes depend on differences in the specific density of algae particles, while filtration methods exploit algae size and surface properties (Morweiser, et al., 2010). Centrifugation has proved popular for small scale algae cultivation operations and consumes roughly 5 kWh/m^3 at flow rates of 1 m^3/hr. Scaling up may reduce the energy consumption of centrifugation to approximately 1-3 kWh/m^3 (Morweiser, et al., 2010) (Molina Grima, et al., 2003). Although membrane filtration requires significantly less power than centrifugation methods, its success primarily relies on the algae strain's physiological properties and thus is not suitable in all algae cultivation scenarios (Schenk, et al., 2008). In addition, fouling of the membrane and pressure drops across the interface pose problems (Gregor & Gregor, 1978).

Data compiled for the energetic cost of harvesting and processing algae from a raceway pond cultivation system is listed in Table 9. The study in question was undertaken by Dr. Yusuf Chisti, and assumed a lipid fraction of 20% dw, biomass productivity of 0.025 kg/m^2-day, and biomass concentration of 1 kg/m^3. These energy costs can be applied to the open raceway pond system described in Section 3.3 to achieve a more comprehensive representation of the thermodynamic efficiency and auxiliary power utilization efficiency for the biofuel production process. However, it should be noted that Chisti's analysis assumes a much higher biomass concentration than that cited by Jorquera et al., and thus harvesting costs are likely underestimated when applied to the open pond production scenario. For construction, 80.4 MJ/m^2 was assumed for the facility area, divided by a 20 year productive life of the facility and by the mass of annual oil production. Energy costs of equipment, including that required for biogas production, were estimated to be 27.2 MJ/ton of machinery required, also divided by a 20 year lifespan and the mass of annual oil production. Table 10 displays these recalculated efficiencies including the energy

consumption of harvesting and processing, as well as the co-production of biogas from residual biomass.

Input	Energy (MJ/kg oil produced)
Harvesting	0.30
Oil recovery	3.17
Biogas production	0.88
Facility construction (including maintenance)	4.00
Energy embodied in equipment (including maintenance)	62.8×10^{-6}

Table 9. Harvesting and biofuel production energy costs (Chisti, 2008).

	Cultivation only	Complete process
Thermodynamic efficiency	1.46%	1.33%
Auxiliary power utilization	7.34	4.04

Table 10. Thermodynamic efficiency and auxiliary power utilization effectiveness for an open raceway pond during the growth stage compared to those for the complete biofuel production process.

While the inclusion of energy costs from downstream processing lowers the thermodynamic efficiency and auxiliary power utilization effectiveness, calculated values still suggest the process to be energetically positive. Energy consumption by harvesting and processing may be minimized by scaling the operation; however, increases in biomass concentration would have more dramatic effects on downstream costs (Stephens, et al., 2010). In the near term, the co-production of biogas or high value products from the residual biomass is likely as oil commodity prices remain low. With this in mind, biomass concentration plays an important role in both decreasing processing costs and increasing the production of profitable commodities more so than any substantial increase in the strain's lipid fraction (Stephens, et al., 2010). If auxiliary power requirements for closed system cultivation can be reduced, their generation of high concentration algal slurry could result in a commercially viable production process.

4.3 Water and nutrient usage

Facility and operation costs often scale with water and nutrient consumption. In an ideal system, water consumption would be kept to a minimum and losses due to evaporation would be negligible. However, open pond systems generally are located in hot, arid climates where incident solar energy levels are high and culture temperature can be maintained. Depending on pond composition, wind speed, ambient temperature, and relative humidity, evaporative losses in open ponds can reach levels of 1 cm/day (Sheehan, et al., 1998). For a large production facility, this daily loss in water depth would have to be compensated for by the continued addition of new culture medium. Fortunately, algae can utilize water that would not be suitable for human consumption or agriculture due to high salinity or waste contamination. However, these large volumes of water imply intensive pumping, which translates into higher costs. Table 11 reviews the biomass concentrations cited by Jorquera et

al.'s study and the corresponding water volume required by each facility, assuming no evaporation or water recycling.

	Raceway	Flat Plate	Tubular
Biomass concentration (kg/m^3)	0.035	0.27	0.56
Water required (m^3)	2,857,142	370,370	178,571
Water required (gal)	754,777,142	97,841,481	47,173,571

Table 11. Water requirements based on biomass concentration from each photobioreactor system (Jorquera, et al., 2010)

As shown in each photobioreactor system, water consumption scales directly with biomass concentration. The raceway pond demonstrates the lowest concentration and thus the highest corresponding water consumption. Although empirical data was not available, it can be assumed that water consumption in the open pond would be even greater due to high rates of evaporation. Closed systems hold a significant advantage in terms of water consumption and lower rates of evaporation, in addition to having the capability to recycle 70-80% of the water used in each growth cycle (Subhadra, 2010).

A study by Clarens et al. found that biodiesel production from microalgae in an open pond system consumed up to 12 times the water required by biodiesel production from canola on the same scale. However, by coupling production to wastewater treatment, the water consumed by the algal biodiesel production process can be reduced by 89% (Clarens, et al., 2010). In addition, coupling algae cultivation to wastewater treatment plants allows the algae to remove and recover nutrients that must otherwise be supplied via fertilizer.

Finally, the benthic photobioreactors discussed in Section 2.2 hold the potential to greatly reduce the water required for algae cultivation. As the algae are immobilized on a substrate, a relatively small volume of water circulates over the biofilm to enhance mass transfer of nutrients and CO_2. Lab scale operation of a carbonated concrete system has shown to consume up to 42 times less water than algae cultivation in conventional systems (Ozkan, et al., 2011).

4.4 Economics

A comprehensive study of the economic feasibility of the algal production process was conducted by Gao et al. in 2009. In this report, a formulation devised by Molina Grima in 2003 for cost estimation based on direct experience with a closed, tubular system and vendor quotes was refined and examined with a discount rate of 7% over ten years. Molina Grima's 100 hectare facility produced approximately 26.2 tons of biomass per hectare each year for the purpose of extracting a high value product. Using a conservative co-production estimate of 10% oil yield, costs of Molina Grima's tubular system were compared to those of a facility employing 192 hectares of open ponds on 384 hectares of land, as documented by the U.S. Department of Energy. The total cost breakdown included the capital and operating costs required to build a processing facility in which separation of lipids and transesterification of TAGs would transform the raw extracted material into biodiesel. While this study did not examine the energetic costs as documented by Jorquera's 2010 or Chisti's 2008 analyses, it provides a detailed representation of the economic costs of industrial scale biodiesel production operations. Table 12 contains a summary of this analysis.

	Closed System	Open System
Areal biomass production rate	26.2 tons/ha-yr	112 tons/ha-yr
Capital investment	> $3 million/ha	~$100,000/ha
Total annual operating cost	$933,995/yr	$147,769/yr
Biomass cost*	$35,649/ton	$1,319/ton
Biodiesel cost*	$49.39/gal	$5.46/gal

*Biomass and biodiesel costs accounts for expenditures associated with growth, harvesting, extraction, and refining.

Table 12. Cost comparison for a tubular and open pond system in 2003 dollars (Gao, et al., 2009, Molina Grima, et al., 2003).

With the cost of conventional diesel at approximately $1.51 for 2011/12, these numbers do not encourage potential investors to fund algae based operations (Radich, 2004). However, a closer examination can be made for advancements in closed and open cultivation system and processing technologies. Table 13 contains the recalculated production costs per gallon of biodiesel with oil yield improvements, reductions in the price of solvents and CO_2, and the application of existing U.S. tax credits made available by the American Recovery and Reinvestment Act of 2008.

System	Scenario	EE $/gal
Closed Tubular	Yield increased to 60%	$33.13
	Total capital + fixed cost of production reduced by 50%	$26.18
	60% yield; 50% capital/fixed cost reduction	$17.65
	50% hexane recovery	$49.28
	60% yield; 50% capital/fixed cost reduction; 50% hexane recovery	$17.54
	Tax credits; 60% yield; 50% Capital costs; 50% Hexane recovery	**$16.54**
Open Raceway	Yield increased to 20%	$4.24
	Yield increased to 30%	$3.02
	CO2 price of $0.2/kg (from $0.47/kg)	$3.29
	CO2 price of $0.035/kg (from $0.47/kg)	$1.96
	50% Hexane recovery	$5.34
	20% yield; $0.2/kg CO2 price	$2.61
	30% yield; $0.2 kg CO2 price	$1.94
	Tax credits; yield increased to 20%	$3.24
	Tax credits; yield increased to 30%	$2.02
	Tax credits; CO2 price of $0.2/kg (from $0.47/kg)	$2.29
	Tax credits; 20% yield; $0.2/kg CO2 price	$1.61
	Tax credits; 30% yield; $0.2 kg CO2 price	**$0.94**

Table 13. Costs for tubular and raceway systems with potential economic improvements and tax incentives (Gao, et al., 2009).

According to this study, cultivation of algae in closed tubular systems for biodiesel purposes is prohibitively expensive, and technical progress to lower the capital cost and/or increase oil yields, although making a significant difference, cannot come near competing economically with other biodiesel sources. However, similar advances in open pond technology can bring the costs of production down to only $1.94/gallon biodiesel.

Despite these challenges, provisions for research in the American Recovery and Reinvestment Act have strengthened the potential for commercialization of algal biodiesel. With the passage of this act, $61 billion were earmarked for energy generation, of which $800 million was specifically provided for biofuels (Voegele, 2009). In addition, existing tax credits for producers range from $1/gallon for "agro-diesel," $0.50/gallon for diesel made from recycled cooking oil, and an additional $0.10/gallon credit for small producers of biodiesel. An annual budget of $150 million has also been authorized for the FY2009 – FY2012 to be used for loan guarantees and grants for the construction of biorefineries. Import duties on ethanol also protect domestic producers of biofuels (Yacobucci, 2006). While all of this demonstrates the government is interested in protecting domestic producers of alternative fuels, none of the provisions specifically target to algal biofuels. If the "agri-biodiesel" tax credits are applied to the study conducted by Gao et al. for open ponds, the economic outlook becomes much more favorable.

5. Conclusions and outlook

The steady increase in liquid fuel consumption and the eventual depletion of petroleum reserves necessitates the adoption of alternative fuels. Biodiesel from algae feedstock holds a realistic potential to displace petroleum as the United States' transportation fuel due to algae's rapid growth rate and high oil content. Relative to other alternative fuels, biodiesel has a high energy density and can be used in a wide variety of transportation applications. Algae cultivation does not require the diversion of large portions of arable land from food production and can be grown without the consumption of potable water. Finally, algae cultivation with open pond and flat plate systems holds a positive energy balance in its favorable solar conversion and thermodynamic efficiencies. All of these facts have been recognized by industry and academia, and the research gaps identified by the NREL's historic Aquatic Species Program are quickly being filled. With this renewed interest, technical improvements and existing government incentives can make the production of biodiesel from algae economically justified.

By comparing Weyer et al.'s theoretical best case formulation with experimental data, the parameters causing the discrepancy in productivity for open pond systems can be identified. The land required by the best case scenario comes close to matching productivities achieved in the closed systems. By concentrating on incorporating the design advantages of each system, the best case scenario for open ponds described by Weyer et al. may be achieved. In particular, photon transmission efficiency and photon utilization efficiency represent important design parameters whose manipulation significantly affects the system's biomass output. Although photon transmission efficiency and photon utilization efficiency were taken to be 95% and 50% respectively, realistic values are likely much lower for open pond systems. Of the two parameters, photon utilization efficiency had a much more negative effect on the final biomass productivity, indicating the significance of maintaining optimal culture conditions. This control over the algae's

environment can also be translated into the losses in biomass accumulation efficiency, as biomass losses due to respiration may be mitigated in certain species by applying different environmental constraints. Both configurations of closed systems allow this variability, but the current auxiliary energy costs outweigh the potential benefits of this technical sophistication. Further research requires the development of a hybrid system in which aspects of both closed and open designs can be featured. Passive temperature control and use of atmospheric CO_2 must be combined with the lower water consumption and areal footprint of closed systems in order to generate an algae slurry with a high biomass concentration.

In addition to these design challenges, the theoretical study identified areas of biological constraint that could potentially be resolved through strain selection or genetic modification. In particular, expanding the portion of the solar spectrum usable for photosynthesis can increase the solar conversion efficiency while pigment reduction in the organisms can help reduce instances of photoinhibition, accelerating the biomass growth rate and resulting in a more productive culture. Likewise, reducing the quantum requirement through the modification of photosystems would allow for more efficient use of incident PAR energy. While the fraction of usable lipids remains important for the production of biodiesel from algae, biomass growth rate ultimately determines profitability, particularly when incorporating the production of a portfolio of high value products with a variety of algal fuels. In the short term, the coproduction of these high value products is necessary to overcome the economic and energetic obstacles of this relatively immature technology. However, as oil commodity prices continue to rise, the economics of algal biodiesel are expected to strengthen. Algae biodiesel's energy density and compatibility with infrastructure provide significant advantages to current alternative fuels. As research advances and production processes become less capital, energy, and water intensive, algae biodiesel will surpass its competitors as the most viable alternative to petroleum fuel.

6. References

Amin, S. (2009). Review on biofuel oil and gas production processes from microalgae. *Energy Conversion and Management, 50*, 1834-1840.

Andrade, J., Perez, A., Sebastien, P., & Eapen, D. (2011). A review of bio-diesel production processes. *Biomass and Bioenergy, 35*, 1008-1020.

Baillez, C., Largeau, C., & Casadevall, E. (1985). Growth and hydrocarbon production of Botryococcus braunii immobilized in calcium alginate gel. *Applied Microbiology and Biotechnology, 23* (2), 99-205.

Batan, L., Quinn, J., Wilson, B., & Bradley, T. (2010). Net erngy and greenhouse gas emission evaluation of biodisel derived from microalgae. *Environmental Science & Technology, 44*, 7975-7980.

Beal, C. (2011). First Principles: Thermodynamic Analysis of Algal Biocrude Production. *Constraints on Algal Biofuel Production*. The University of Texas at Austin, Mechanical Engineering.

Bird, R. E., & Hulstrom, R. L. (1981). *Simplified Clear Sky Model for Direct and Diffuse Insolation on Horizontal Surfaces.* Golden, CO: Solar Energy Research Institute.

Borowitzka, M. (2005). Culturing microalgae in outdoor ponds. In R. Anderson, *Algal Culturing Technologies* (pp. 205-218). London: Academic Press.

Braun, R., Weiland, P., & Wellinger, A. (2008). *Biogas from Energy Crop Digestion.* Task 37-Energy from Biogas and Landfill Gas. IEA Bioenergy.

Brune, D., Lundquist, T., & Benemann, J. (2009). Microalgal biomass for greenhouse gas reductions: Potential for replacement of fossil fuels and animal feeds. *Journal of Environmental Engineering, 135* (11), 1136-1144.

Bush, R. A., & Hall, K. M. (2006). *Patent No. 7135308.* United States of America.

Carlozzi, P. (2003). Dilution of solar radiation through culture lamination in photobioreactor rows facing South-North: A way to improve the efficiency of light utilization by cyanobacteria (Arthrospira platensis). *Biotechnology and Bioengineering, 81*, 305-315.

Cheng-Wu, Z., Zmora, O., Kopel, R., & Richmond, A. (2001). An industrial-size flate plate glass reactor for the production of Nannochloropsis sp. (Eustigmatophyceae). *Aquaculture, 195*, 35-49.

Chini Zittelli, G., Lavista, F., Bastiani, A., Rodolfi, L., Vincenzini, M., & Tredici, M. (1999). Production of eicosapentaenoic acid by *Nannochloropsis* sp. in outdoor tubular photobioreactors. *Journal of Biotechnology, 70*, 299-312.

Chisti, Y. (2007). Biodiesel from microalgae. *Biotechnology Advances, 25*, 294-306.

Chisti, Y. (2008). Biodiesel from microalgae beats ethanol. *Trends in Biotechnology, 26*, 126-131.

Chisti, Y. (2008). Response to Reijnders: Do biofuels from microalgae beat biofuels from terrestrial plants? *Trends in Biotechnology, 26*, 351-352.

Clarens, A., Resurrection, E., White, M., & Colosi, L. (2010). Environmental life cycle comparison of algae to other bioenergy feedstocks. *Environmental Science & Technology, 44* (5), 1813-1819.

Conway, T., & Tans, P. (2011). *Trends in Atmospheric Carbon Dioxide.* NOAA/ESRL.

Cooney, M., Young, G., & Nagle, N. (2009). Separation of Bio-oils from Microalgae. *Separation & Purification Reviews, 38*, 291-325.

Cooney, M., Young, G., & Pate, R. (2011). Bio-oil from photosynthetic microalgae: Case study. *Bioresource Technology*, *102*, 166-177.

Cragges, R., McAuley, P., & Smith, V. (1997). Wastewater nutrient removal by marine microalgae grown on a corrugated raceway. *Water Research, 31*, 1701-1707.

DOE. (2010). *Laws & Regulations, Energy Policy Act of 2005*. Retrieved March 30, 2011, from Federal Energy Management Program: http://www1.eere.energy.gov/femp/regulations/epact2005.html

Duffie, J. A., & Beckman, W. A. (1980). *Solar Engineering of Thermal Processes.* New York: Wiley-Interscience.

Earthrise® Nutrional, LLC. (2009). *About Earthrise: Our Farm*. Retrieved March 30, 2011, from Earthrise: http://www.earthrise.com/farm.html

EERE. (2011). Retrieved February 15, 2011, from Alternative & Advanced Vehicles Data Center: http://www.afdc.energy.gov/afdc/

EERE. (2011). *Biogas Production*. Retrieved April 14, 2011, from Alternative & Advanced Vehicles Data Center: http://www.afdc.energy.gov/afdc/fuels/emerging_biogas_production.html

EERE. (2011). *EnergyPlus Energy Simulation Software: Weather Data*. Retrieved April 10, 2011, from Building Technologies Program: http://apps1.eere.energy.gov/buildings/energyplus/weatherdata_about.cfm

EERE. (2011). *Fuel Properties Comparison Chart*. Retrieved April 12, 2011, from Alternative Fuels & Advanced Vehicles Data Center: http://www.afdc.energy.gov/afdc/progs/fuel_compare.php

EIA. (2011). *Annual Energy Outlook 2011 Early Release Overview*. U.S. Department of Energy.

EIA. (2010). *International Energy Outlook 2010, Transportation Sector Energy Consumption*. US Department of Energy.

EIA. (2011). *Spot Prices for Crude Oil and Petroleum Products*. Retrieved March 23, 2011, from Petroleum and Other Liquids: http://tonto.eia.doe.gov/dnav/pet/PET_PRI_SPT_S1_M.htm

EPA. (2011). *Inventory of U.S. Greenhouse Gas Emissions and Sinks: 1990-2009*. Washington D.C.: EPA.

Franklin, L. A., Osmond, B. C., & Larkum, A. W. (2003). Photoinhibition, UV-B and Algae Photosynthesis. In A. W. Larkum, S. E. Douglas, & J. A. Raven, *Photosynthesis in Algae* (pp. 351-384). Kluwer Academic Publishers.

Gao, Y., Gregor, C., Liang, Y., Tang, D., & Tweed, C. (2009). *Algae biodiesel: a feasibility report*. BPRO.

Goldman, J. C. (1979). Oudoor Algal Mass Cultures-- II. Photosynthetic Yield Limitations. *Water Research, 13*, 119-136.

Gregor, H. P., & Gregor, C. D. (1978). Synthetic membrane technology. *Scientific American, 239*, 112-128.

Grobbelaar, J. (2004). Algal nutrition. In A. Richmond, *Handbook of microalgal culture: biotechnology and applied phycology* (pp. 97-115). Blackwell.

Holm-Nielsen, J., Al Seadi, T., & Oleskowicz-Popiel, P. (2009). The future of anaerobic digestion and biogas utilization. *Bioresource Technology, 100*, 5478-5484.

Howell, K. (2009). Exxon Sinks $600M Into Algae-Based Biofuels in Major Strategy Shift. *New York Times* .

Hu, Q., & Richmond, A. (1996). Productivity and photosynthetic efficiency of Spirulina platensis as affected by light intensity, algal density and rate of mixing in a flat plate photobioreactor. *Journal of Applied Phycology, 18*, 139-145.

Hübner, Y. (2010). Electric-car developments raise grid questions. *Engineering & Technology, 5* (6), 15.

Jarvis, E. E. (2008). AFOSR Workshop. *Aquatic Species Program (ASP): Lessons Learned*. Washington, D.C.: National Renewable Energy Laboratory.

Johnson, M. B., & Wen, Z. (2010). Development of an attached microalgal growth system for biofuel production. *Applied Microbiology and Biotechnology, 85*, 525-534.

Jorquera, O., Kiperstock, A., Sales, E. A., Embirucu, M., & Ghirardi, M. L. (2010). Comparative energy life-cycle analysis of microalgal biomass production in open ponds and photobioreactors. *Bioresource Technology, 101*, 1406-1413.

Kebede-Westhead, E., Pizarro, C., & Wulbry, W. (2006). Treatment of swine manure effluent using freshwater algae: Production, nutrient recovery, and elemental composition of algal biomass at four effluent loading rates. *Journal of Applied Phycology, 18*, 41-46.

Knuckey, R., Brown, M., Robert, R., & Frampton, D. (2006). Production of microalgal concentrates by flocculation and their assessment as aquaculture feeds. *Aquacultural Engineering, 35* (3), 300-313.

Kremer, G., Bayless, D. J., Vis, M., Prudich, M., Cooksey, K., & Muhs, J. (2006). *Enhanced practical photosynthetic CO_2 mitigation*. DOE.

Kruse, O., & Hankamer, B. (2010). Microalgal hydrogen production. *Current Opinion in Biotechnology, 21*, 238-243.

Larkum, A. W. (2003). Light Harvesting Systems in Algae. In A. W. Larkum, S. E. Douglas, & J. A. Raven, *Photosynthesis in Algae* (pp. 277-304). Kluwer Academic Publishers.

Melis, A., & Melnicki, M. R. (2006). Integrated biological hydrogen production. *Journal of Hydrogen Energy, 31*, 1563-1573.

Molina Grima, E., Balarbi, E., Acien Fernandez, F., Robles Medina, A., & Chisti, Y. (2003). Recovery of microalgal biomass and metabolites: process options and economics. *Biotechnology Advances, 20*, 491-515.

Morweiser, M., Kruse, O., Hankamer, B., & Posten, C. (2010). Developments and perspectives of photobioreactors for biofuel production. *Applied Microbiology Biotechnology, 87*, 1291-1301.

Mulbry, W., Kondrad, S., Pizarro, C., & Kebede-Westhead, E. (2008). Treatment of dairy manure effluent using freshwater algae: Algal productivity and recovery of manure nutrients using pilot-scale algal turf scrubbers. *Bioresource Technology, 99*, 8137-8142.

National Biodiesel Board. (2009). *Benefits of Biodiesel.*

Ozkan, A., Kinney, K., & Katz, L. (2011). *Novel algae biofilm photobioreactor for reduced energy use and water usage.* The University of Texas at Austin, Cockrell School of Engineering. Austin: Unpublished.

Park, J., Craggs, R., & Shilton, A. (2011). Wastewater treatment high rate algal ponds for biofuel production. *Bioresource Technology , 102*, 35-42.

Powell, E., & Hill, G. (2009). Economic assessment of an integrated bioethanol-biodiesel-microbial fuel cell facility utilizing yeast and photosynthetic algae. *Chemical Engineering Research and Design, 87*, 1340-1348.

Pulz, O., Gerbsch, N., & Bacholz, R. (1995). Light energy supply in plate-type and light diffusing optical fiber bioreactors. *Journal of Applied Phycology, 7*, 145-149.

Radich, A. (2004). *Energy Information Administration*. Retrieved Nov. 25, 2010, from Biodiesel Performance, Costs, and Use: http://www.eia.doe.gov/oiaf/analysispaper/biodiesel/

Rebolloso-Fuentes, M. M., Navarro-Pérez, A., García-Camacho, F., Ramos-Miras, J. J., & Guil-Guerrero, J. L. (2001). Biomass nutrient profiles of the microalga Nannochloropsis. *Journal of Agricultural and Food Chemistry, 49*, 2966-2972.

Richmond, A., & Cheng-Wu, Z. (2001). Optimization of a plate glass reactor for mass production of Nannochloropsis sp. outdoors. *Journal of Biotechnology, 85*, 259-269.

Rodolfi, L., Chini Zitelli, G., Bassi, N., Padovani, G., Biondi, N., Bonini, G., et al. (2009). Microalgae for oil: strain selection, induction of lipid synthesis and outdoor mass cultivation in a low-cost photobioreactor. *Biotechnology Bioengineering, 102*, 100-112.

Schulz, T. (2006). *The economics of micro-algae production and processing into biofuel.* Farming Systems. Department of Agriculture of Western Australia.

Scott, S. A., Davey, M. P., Dennis, J. S., Horst, I., Howe, C. J., Lea-Smith, D. J., et al. (2010). Biodiesel from algae: challenges and prospects. *Current Opinion in Biotechnology, 21*, 277-286.

Scott, S., Davey, M., Dennis, J., Horst, I., Howe, C., Lea-Smith, D., et al. (2010). Biodiesel from algae: challenges and prospects. *Current Opinion in Biotechnology*, *21*, 277-286.

Sheehan, J., Dunahay, T., Benemann, J., & Roessler, P. (1998). *A Look Back at the U.S. Department of Energy's Aquatic Species Program--Biodiesel from Algae.* Office of Fuels Development. Golden, CO: NREL.

Schenk, P. M., Thomas-Hall, S. R., Stephens, E., Marx, U. C., Mussgnug, J. H., Posten, C., et al. (2008). Second generation biofuels: High-efficiency microalgae for biodiesel production. *Bioengineering Research, 1*, 20-43.

Sierra, E., Acién, F. G., Fernández, J. M., García, J. L., & González, C. M. (2008). Characterization of a flat plate photobioreactor for the production of microalgae. *Chemical Engineering Journal, 138*, 136-147.

Silva-Aciares, F. R., & Riquelme, C. E. (2008). Comparisons of the growth of six diatom species between two configurations of photobioreactors. *Aquacultural Engineering, 38*, 26-35.

Singh, J., & Gu, S. (2010). Commercialization potential of microalgae for biofuels production. *Renewable and Sustainable Energy Reviews, 14*, 2596-5610.

Soloman, S., Qin, D., Manning, M., Chen, Z., Marquis, M., Averyt, K., et al. (2007). *Contribution of Working Group I to the Fourth Assessment Report of the Intergovernmental Planel on Climate Change, 2007.* Intergovernmental Panel on Climate Change. Cambridge, UK and New York, NY, USA: Cambridge University Press.

Spectral Irradience Monitor. (n.d.). (NASA) Retrieved March 9, 2011, from Solar Radiation and Climate Experiment: http://lasp.colorado.edu/sorce/instruments/sim/sim_science.htm

Stephens, E., Ross, I., Mussnug, J., Wagner, L., Borowitzka, M., Posten, C., et al. (2010). Future prospects of microalgal biofuel production systems. *Trends in Plant Sciences, 15* (10), 554-564.

Subhadra, B. G. (2010). Comment on "Environmental life cycle comparison of algae to other bioenergy feedstocks". *Environmental Science & Technology, 44*, 3641-3642.

Szeicz, G. (1974). Solar radiation for plant growth. *Journal of Applied Ecology, 11* (2), 617-637.

Tredici, M., & Rodolfi, L. (2004). *Patent No. WO 2004/074423 A2*. International.

USDA. (2011). *Prospective Plantings (March 2011).* Washington, DC: National Agricultural Statistics Service.

Voegele, E. (2009). *President signs stimulus package*. Retrieved Nov. 30, 2010, from Biodiesel Magazine: http://www.biodieselmagazine.com/article.jsp?article_id=3252

Weyer, K. M., Bush, D. R., Darzins, A., & Wilson, B. D. (2010). Theoretical Maximum Algal Oil Production. *BioEnergy Research, 3*, 204-213.

Whipple, T. (2008). Peak oil. *Bulletin of the Atomic Scientists, 64* (5), 34-37.

Yacobucci, B. (2006). *Biofuels incentives: a summary of federal programs.* Washington, D.C.: Congressional Research Service, Library of Congress.

Zemke, P., Wood, B., Dye, D., Bayless, D., & Muhs, J., (2007). Economic analysis of a vertical sheet algal photobioreactor for biodiesel production. Energy Sustainability, 815-819.

18

Effect of Solar Concentrator System on Disinfection of Soil-Borne Pathogens and Tomato Seedling Growth

Sirichai Thepa[1], Jirasak Kongkiattikajorn[2]
and Roongrojana Songprakorp[1]
[1]*Energy Technology Division,*
School of Energy, Environment and Materials,
[2]*Biochemical Technology, School of Bioresources and Technology,*
King Mongkut's University of Technology Thonburi,
Thailand

1. Introduction

The development of non-imaging reflectors for circular-cylindrical solar energy receivers has consisted primarily of investigations on symmetrical V-trough and compound parabolic concentrator (CPC) designs, with the latter being favoured recently because of its superior optical collection. However, it has since been realised that asymmetrical versions of such reflectors may be developed and that they have their own limits of concentration and ideality. It was shown that ideal asymmetrical reflectors could achieve substantially greater peak concentration than symmetrical reflectors of the same acceptance angle (Mills and Giutronich, 1979). An important difference, however, is that the performance of the asymmetrical reflector is much higher at one solstice than another because the aperture is adjusted with respect to the acceptance angle envelope. With an asymmetrical collector, the possibility is presented of at least partial bias of the seasonal collector output toward the maximum load period. Such a bias would reduce dumped solar energy in low load periods, allowing a larger usable solar fraction of energy supplied. Phitthayarachasak (Phitthayaratchasak et al., 2005) upgraded the solarization system process to increase its efficiency by applying the asymmetrical compound parabolic concentrator (ACPC) to enable the concentration of more solar radiation by an average of up to 2.5 times. It is convenient to operate because there is no need to adjust the angle of the ACPC unit according to the movement of the sun. The result showed that the soil temperatures at various depths were high enough to inhibit the growth of microbes within a 5 day period. The solarization operating time was distinctly decreased. The solarization system is then a suitable process for destroying or inhibiting the growth of soil microbes which cause plant diseases (Burrafato, 1998; Le Bihan et al., 1997; Bell; 1998). Even though this system is easy to conduct, with less cost, and no pollution, it still needs 4–6 weeks to operate. Therefore, in this study, the CPC combined with an ACPC unit was developed in order to decrease the time for soil microbe inhibition to be closer to the time of traditional steaming methods.

2. Aim

The aim of this work is to study solar system treatments: solarization with ACPC, and CPC combined with ACPC and hot water. In addition, the effects on *Erwinia cartoverora* population in the soil and tomato seedling growth are also studied.

3. Methods

3.1 Design of the asymmetry compound parabolic concentrator (ACPC)

In general, a symmetrical compound parabolic concentrator (CPC), as shown in Fig. 1, comprises two identical parabolic reflectors which are usually oriented along an east-west axis while an axis of the CPC points toward the sun. For such a system to achieve maximum annual sunbeam on a focal plane, it requires an accurate sun tracking system and hence, additional cost. Moreover, a north-south tracking angle adjustment is also needed seasonally. With a modification of the traditional CPC, asymmetrical compound parabolic concentrator (ACPC), on the other hand, has different height of a parabola reflector on each side which allows for a longer time for incident solar irradiance beam on the reflectors without tracking, and hence, more heat would be absorbed on the focal area.

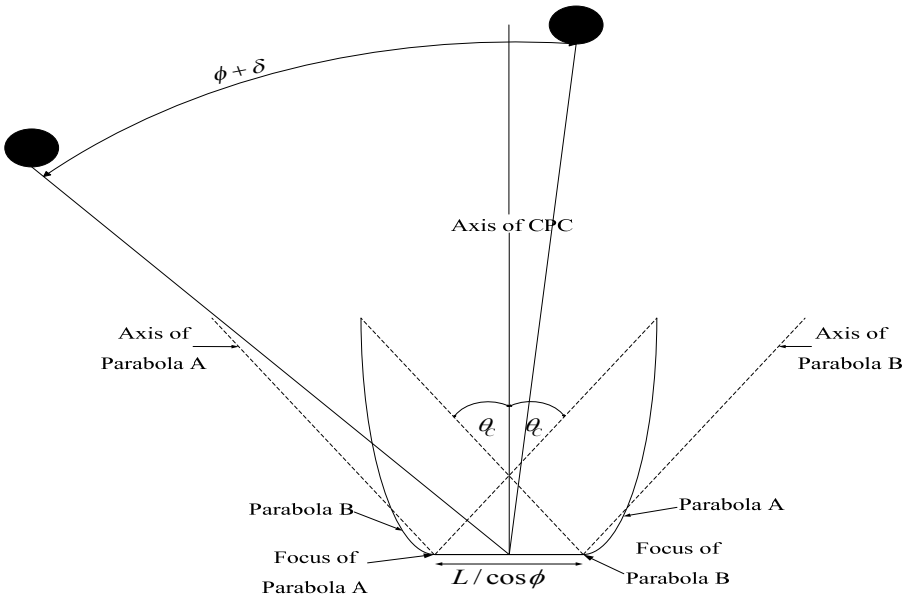

Fig. 1. Typical symmetrical compound concentrator and incident irradiance with its reflection beam on focal plane.

In this study, the ACPC is designed based on Bangkok location (latitude, ϕ = 14° N). Due to the rotational axis of the earth with 23.45° inclination respect to the orbital plane around the sun the angle of the sun above equatorial plane, declination angle, varies along with the day of the year and can be determined by

$$\delta = 23.45\sin\left[360\frac{(284+n)}{365}\right]$$

Where

δ = Declination (degree); $-23.45^{\circ} \le \delta \le 23.45^{\circ}$
n = Julian day (January 1, n = 1)

According to the setting position of ACPC and the declination axis, the sun position will be at an angle of $(\delta + \phi)$. Therefore, for Bangkok, the angle of incidence is in between -9.45° and 37.45°. In this research, the acceptance angle of APAC, θ_c = 21° is selected to obtain a solar incidence angle from -7° to 35° in the 2 periods: 13 Jan – 24 May and 22 June – 20 Dec without the axis adjustment.

Theoretically, there are 3 possible cases for the reflections of radiation beams on the CPC

1. $\theta < \theta_c$ Radiation reflection in between the two focal points of CPC
2. $\theta = \theta_c$ Radiation reflection at the focus of CPC
3. $\theta > \theta_c$ Radiation reflection off the focus outside CPC

In this design, the angle of radiation incident beam and the axis of the CPC, θ_c, are considered. As the angle of the radiation incident on one side of the CPC decreases ($\theta < \theta_c$) it will increase in the radiation on another side of the CPC. To gain more radiation reflection on the soil the axis of the CPC is pointed to the sun and the focal point of CPC is moved into the soil. The ACPC then has a large parabola on one side and a small one on the other side. The design and calculation of the ACPC is shown as below.

1. Large Collector Design

In this design, the CPC has a flat receiver as shown in Fig. 2 for which all parameters can be calculated using the following formula

$$H = \frac{a}{2}\left(\frac{1}{\tan\theta_c} + \frac{1}{\tan\theta_c \sin\theta_c}\right)$$

$$f = \frac{a}{2}(1+\sin\theta_c)$$

$$A_a = \frac{a}{\sin\theta_c}$$

With the given design parameters, the projected area of the solar radiation on the receiver, a = L/cosØ with L = 1 m and a latitude, Ø of Bangkok = 14 degrees one can obtain H=5.09 m, A_a = 2.88 m and f = 0.699 m. According to Fig. 2 (Duffie & Beckman, 1991), the relationship between a ratio of receiving height and aperture area, H/A_a, and a concentration ratio, CR with H/A_a = 1.77 results in CR = 2.80. Then, the edge of CPC was cut to fit the application by theoretically reducing H/A_a to 50%, which is 0.885, and this gives CR=2.4. Afterwards,

the CPC was tilted to Ø degree with a horizontal plane to obtain the focal point at Ltan = 0.25 m as depicted in Fig 3 (The CPC height reduced from 1.45 m to be 1.20 m with the acceptance aperture is 1 m).

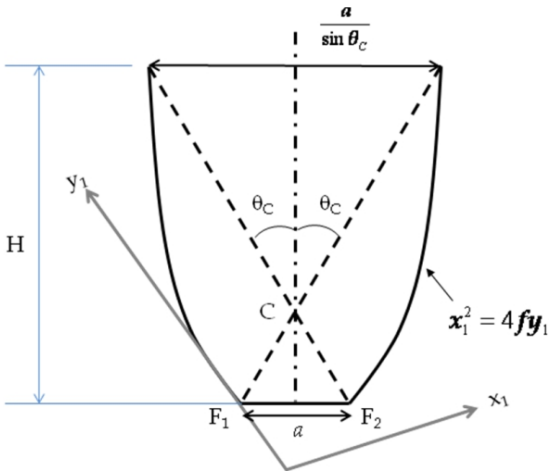

Fig. 2. Design parameters of Flat-Plate receiver CPC.

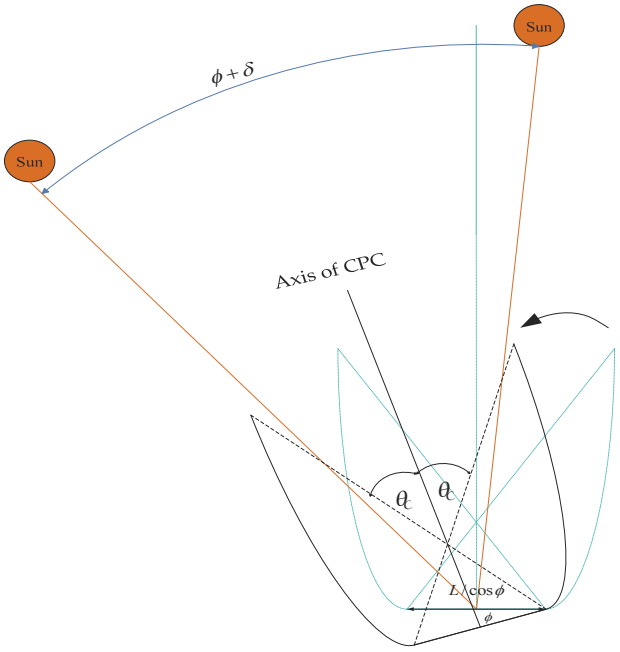

Fig. 3. An inclined CPC at angle Ø with horizontal plane to maximize the incident radiation.

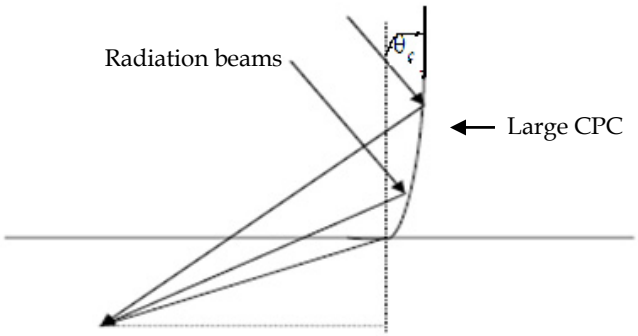

Fig. 4. A reflection of beams from CPC when the radiation beam is incident on a reflector.

2. Small CPC Design

The key point of the design is that the focal point of the small CPC must be the same as that of the large one while one of its curved sides is buried in soil angled at Ø with the ground level. The depth (L/cosØ) is 1 m. Consequently, the height of the small CPC reduces to 0.25 m. Then, the focus is horizontally adjusted until the edge of the large CPC reflector is onto the edge of the receiver or at a distance of L from that of the large one on the soil surface. The finished assembly of the ACPC, shown in Figs. 5 and 6 depicts the reflection path in ACPC.

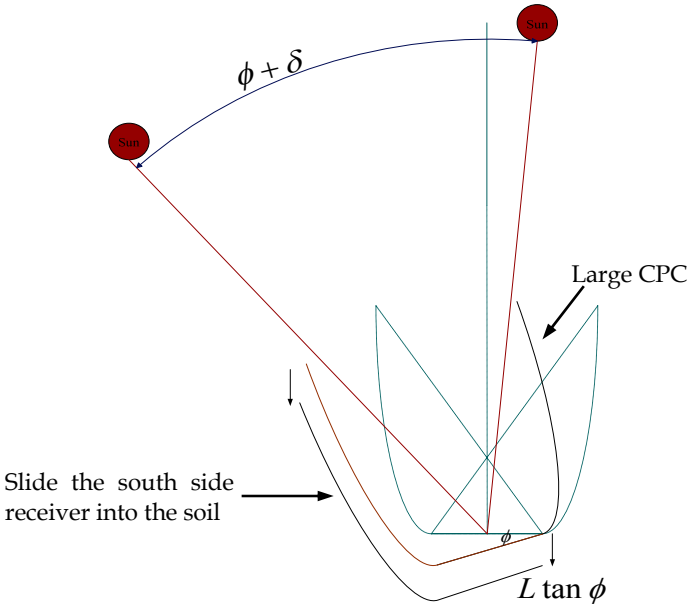

a) A South-side receiver is inclined and buried in the soil at the depth of Ltan Ø.

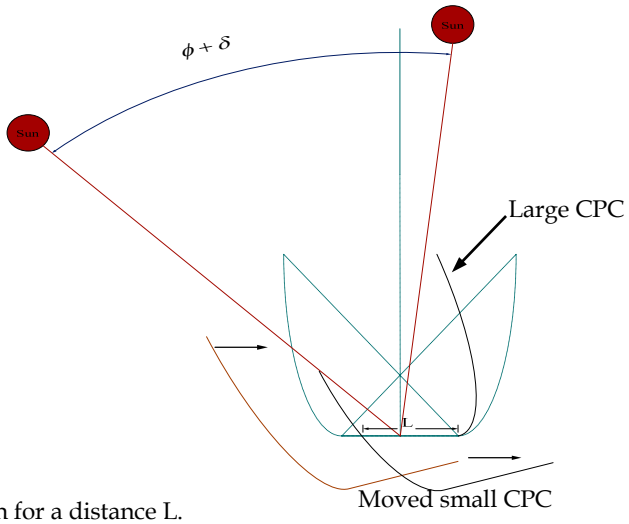

b) Move to the North for a distance L.

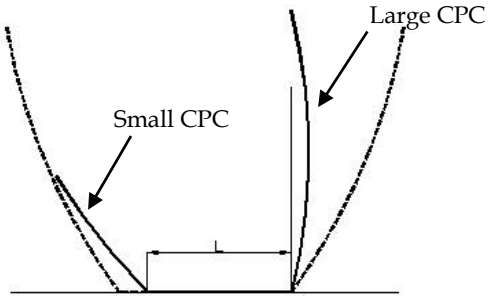

c) Asymmetrical compound parabolic concentrator (ACPC).

Fig. 5. Asymmetrical Compound Parabolic Concentrator (ACPC) assemble procedures.

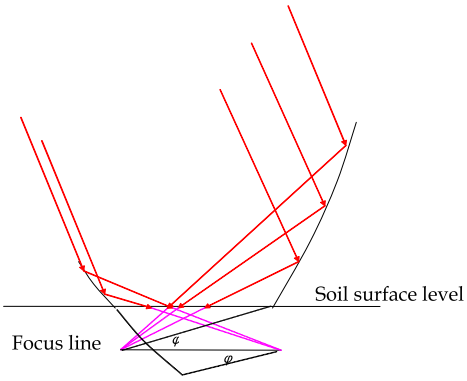

Fig. 6. Radiation beam and its reflections from asymmetrical CPC on soil surface.

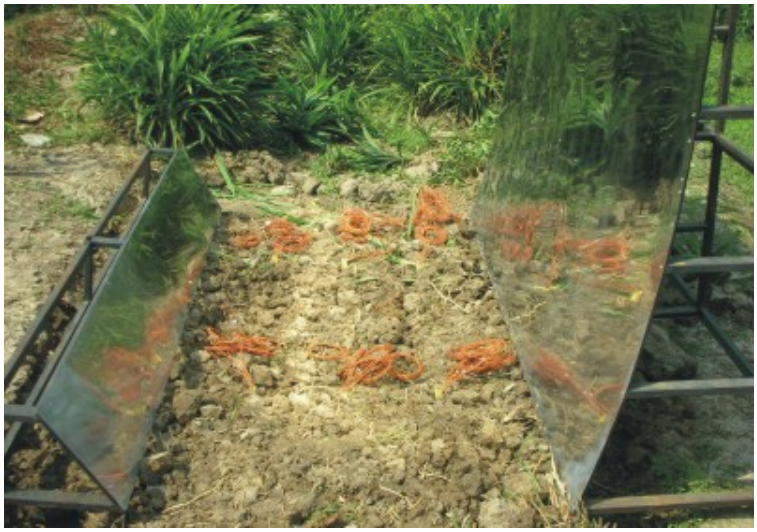

Fig. 7. Installation of ACPC.

3.2 Upgrading the ACPC unit with water boiler and CPC

The ACPC unit was capable of boiling water simultaneously while operating the disinfection process by using the heat from the ACPC panel because the surface has a high temperature. The process was operated by using copper tubes with the surface cut into a semicircle in order to increase larger spaces to absorb the heat, and fix them at the back side of the ACPC panel. A further step to increase the efficiency of the heating process, the hot water from ACPC panel in the copper tube was treated by CPC before the hot water outlet was fed into the soil plot.

When sunlight hits the ground it is partly reflected and partially absorbed by soil. The absorbed heat increases the soil temperature and is then transferred down into a deeper level. As soil has low heat conductivity the heat transfer is considerably poor. Increasing temperature of water droplets can obtain higher soil temperatures at the deeper level from the surface as water can diffuse through small pores and heat up the soil grains via conduction and convection processes.

The solarization process normally takes 4–6 weeks for the temperature to increase and induce lower levels of soil to be able to inhibit microbes which cause crop disease. In consequence, the ACPC unit is introduced to collect solar energy to provide higher temperature which can reduce the length of time of the solarization process down to 5 days. However, this time period is still not appropriate for industrial crops. Hence, the need for further improvement of the ACPC unit's capability to boil water simultaneously while operating the process. The hot water is then used to drip into the soil. It also gives moisture to the soil which absorbs the heat from the hot water to increase its own temperature. Furthermore, because the dripping water is hot, it is guaranteed not to have any microbes.

3.3 Experimental design and soil treatment

All the experiments were carried out under sunlight. For soil solarized plots, transparent polyethylene sheets 0.05 mm thick were used. Soil treatment was performed for 1 day starting from 8:30 am to 4:45 pm in April. Soil temperatures at depths of 0 cm, 10 cm, 20 cm, 30 cm and 50 cm were monitored by means of shielded copper-constantan thermocouples. The analog signals from the sensors were converted into digital signals. The output data were printed continuously (24 h) on an hourly basis using a computer connected on-line with the data acquisition system.

In this study, four vessels with diameters of 32 and 69 cm high were filled up with soil, which was then watered and left for 2 days to prepare the soil ready for planting. The thermocouples were set at the depth levels of 0, 5, 15, 30, and 50 cm in the centre of the vessels. The 100 watts of electric light to replace solar radiation (due to the lamp's heat is almost the same heat level of the solar radiation effected to the soil surface) was set at the height of 10 cm above the soil surface at the centre point of the vessels. The 60°C hot water from the boiler (its temperature is almost the same as its effect from ACPC) was then dropped at speeds of 12, 16 and 20 cc/min into the vessels number 2, 3, and 4, respectively for 5 h as shown in Fig. 8.

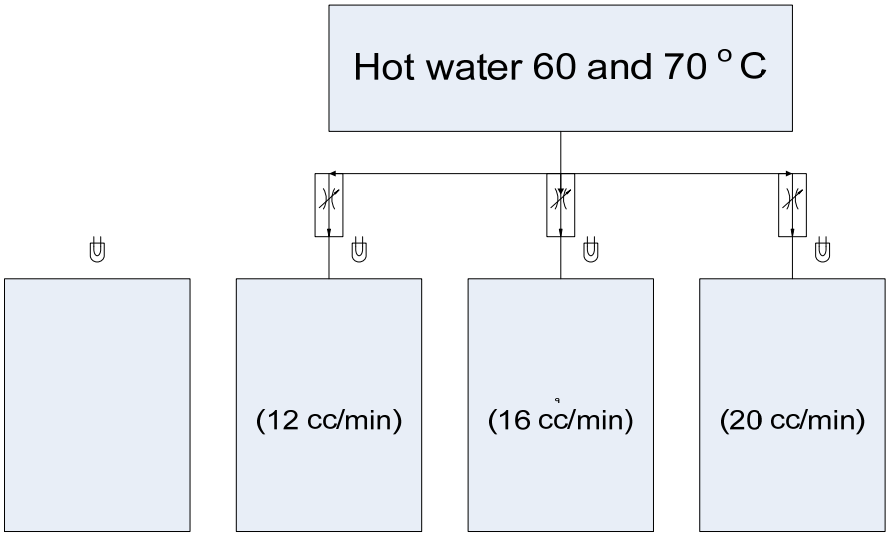

Fig. 8. Schematic diagram of hot water system for soil solarization (Phitthayaratchasak et al., 2009).

A further step to increase the efficiency of the heating process is to use copper tubes, with the surface cut into a semicircle in order to increase larger spaces to absorb the heat, and fix them at the back side of the ACPC panel as shown in Fig. 9. The temperature at various spots as shown in Figs. 10-11 was recorded every 5 min continuously for 5 h. There was no water dropping during the first 30 min and the last 90 min. The same water dropping process was repeated using the 70°C hot water (boiler).

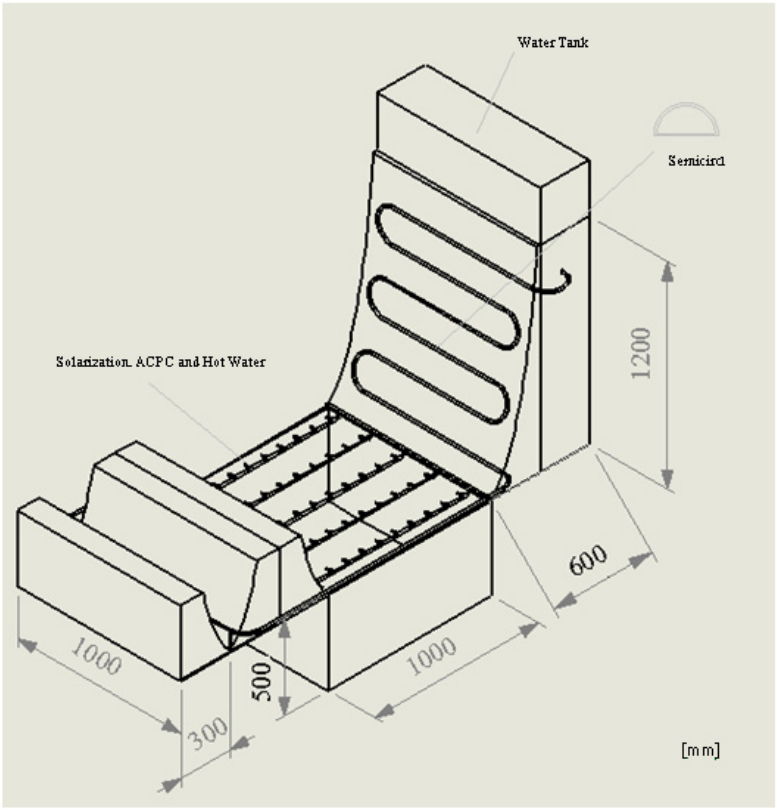

Fig. 9. Installation of combined CPC and ACPC soil solarization system.

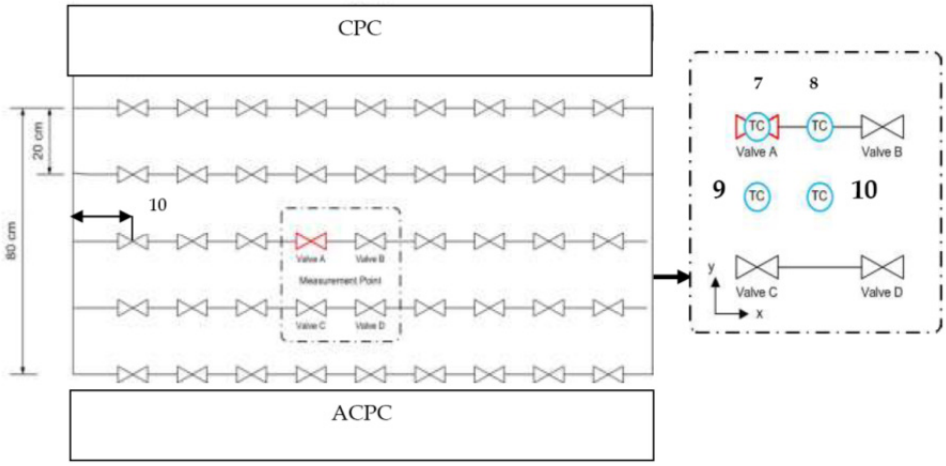

Fig. 10. Positioning of hot water nozzles and thermocouple

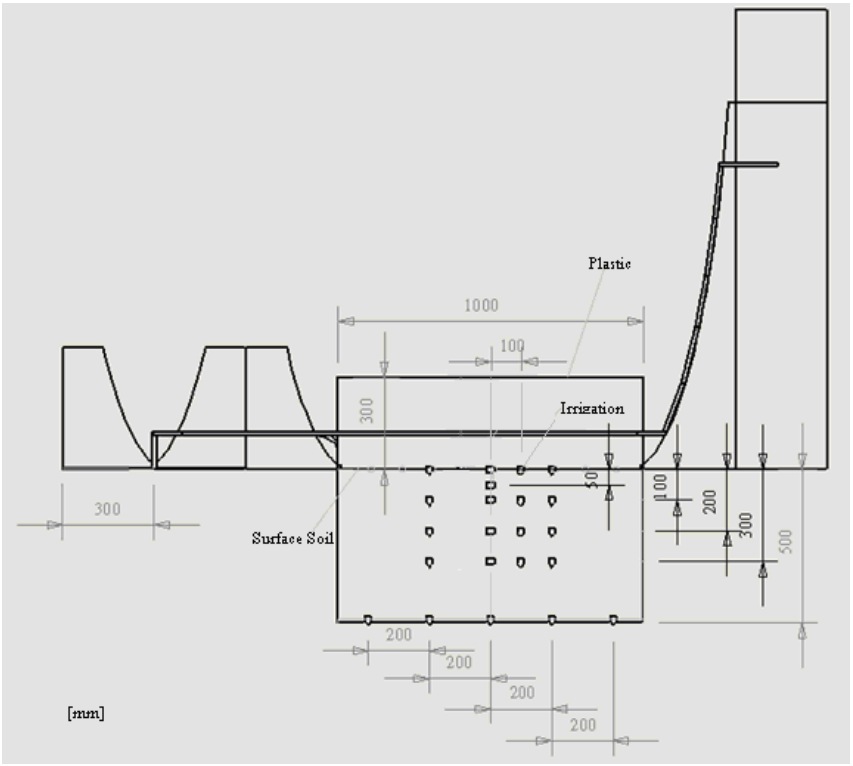

Fig. 11. Side-view of test apparatus setup showing positions of hot water nozzles and thermocouples

3.4 Effect of the treatments on soil microorganisms

Bacterial suspension containing $4x10^7$ cfu/ml prepared from culture of E. cartoverora strains were mixed thoroughly with sterile soil. After heat treatment by non-solarization, solarization, solarization with ACPC, solarization and CPC combined with ACPC and hot water during 12.30 to 16.30 hour for 0, 1, 2 and 4 h incubation at soil surface and the soil at 5-20 cm depth, the soils were counted for Erwinia spp. growing on culture medium compared to the control (non-solarization).

3.5 Bacterial treatment

Bacterial suspension of *E. cartoverora* strains were mixed thoroughly with soil. The first set where the sterile soil mixed with *E. cartoverora* suspension in sterile bags were placed at soil surface soil, soil 5 cm, 10 cm, and 20 cm depth in non-solarization plot. The second set where the soil was mixed with bacterial suspension of *E. cartoverora* strain and placed at soil surface, soil 5 cm, 10 cm, and 20 cm depth in solarization plot. The third set where the soil was mixed with bacterial suspension of *E. cartoverora* strain and placed at soil surface, soil 5 cm, 10 cm and 20 cm depth in solarization with ACPC plot. The fourth set where the soil

was mixed with bacterial suspension of *E. cartoverora* strain and placed at soil surface, soil 5 cm, 10 cm and 20 cm depth in solarization with ACPC and hot water plot.

3.6 Plant materials and growth conditions

Tomato seeds (L. esculentum Mill) were sterilized with 0.5% $HgCl_2$ for 5 min, soaked for 6 h in distilled water after being washed five times, then germinated at 25°C for 14 d in the soil containing E. cartoverora with the solarization with ACPC treatment and control in Erlenmeyer flask. Seeds of tomato were sown in sterile flasks, each containing sterile soil used for growth of seedlings, twenty seeds were sown in each flask at equal distances and watered as required to keep soil moist but not wet, all flasks were placed on a bench at room temperature.

3.7 Soil treatment

One millilitre bacterial suspension containing $4x10^7$ cfu prepared from an overnight culture of *E. cartoverora* strains were mixed thoroughly with each gram of soil. Four sets of flasks, each containing 4 bags, were used in this experiment. The first set where the sterile distilled water was mixed with sterile soil. The second and third sets where the soil was mixed with bacterial suspension of E. cartoverora strain and treated with solarization with ACPC and solarization with CPC combined with ACPC and hot water, respectively, before sowing. The forth set where the soil was mixed with bacterial suspension of *E. cartoverora* before sowing. Twenty seeds were sown in each bag, then watered with sterile water and maintained at room temperature. Two weeks after sowing, seedlings of each set were determined for weight and germination.

3.8 Determination of plant fresh weight and dry weight

After 14 days of planting, plant fresh weight was directly measured using an electronic scale and expressed as means of at least 20 tomato seedlings. For the determination of dry weight, samples were harvested, then dried at 105°C for 10 min, and kept at 80°C until dry weight remained constant. After cooling at room temperature, dry weights were weighed using an electronic scale.

4. Results

4.1 Thermal performances of CPC and ACPC

To evaluate the thermal performance of the concentrating system, the collectors were aligned with east-west axis. The large reflector of ACPC was oriented towards the south and a small reflector faced north. The CPC was placed next to the small reflector of the ACPC. Solar radiation at the middle point between the large and small reflectors of the ACPC, and on a normal plane outside the ACPC was measured. Fig. 12 shows the measured solar radiation.

As expected, the ACPC can increase the intensity of solar radiation within the range of 1.77 to 3.30 times during 9:30 a.m. – 5:30 p.m. and the average value is 2.5 times at 1:00 p.m. The maximum solar intensities at the measured points on a normal plane outside the ACPC and

between the ACPC reflectors were 938.50 W/m² and 3097.41 W/m² respectively. The inlet and outlet temperatures of the ACPC were measured after flowing water through the collectors from 1:00 – 5:00 p.m. The surface temperature of the ACPC reflector and the CPC fin were also measured.

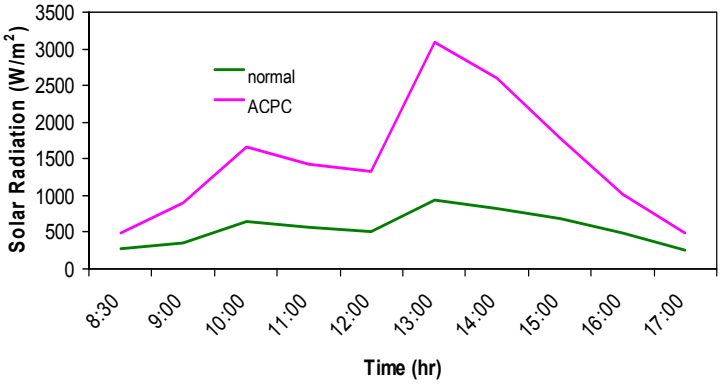

Fig. 12. Solar intensities measured at normal plane outside ACPC and between the reflectors.

Fig. 13 shows the measured inlet and outlet temperatures of ACPC and CPC during the test period in which the solar radiation was in the range of 253.99 – 938.50 W/m² with the average value of 643.8 W/m². As a result, the water temperature difference between the inlet and outlet of ACPC ranges from 4.6°C to 13°C. After passing the CPC, the water temperature was increased in the range of 1.9 - 8.4°C, additionally.

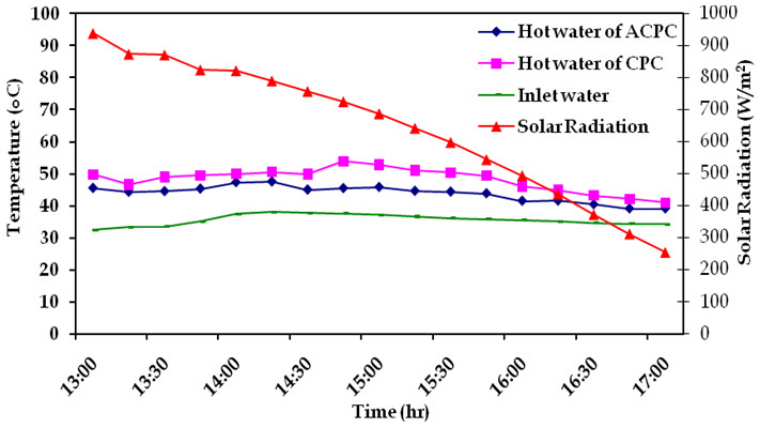

Fig. 13. Solar radiation and inlet/outlet temperature of ACPC and CPC.

Thermal efficiency of a solar thermal energy system is normally defined as the ratio of the useful heat and the incident solar energy. As shown in Fig. 13 the thermal efficiency of ACPC, based on the solar radiation in Fig. 14, is in the range of 46.42% - 51.58% (48% on

average) while that of CPC ranges from 42.63% to 58.60% with 51.30% on average. It is noted that efficiency of a solar thermal system varies according to solar radiation level and environments at the time. Wind velocity is one of the key factors that influence hot water production as it increases thermal loss while flows pass a collector.

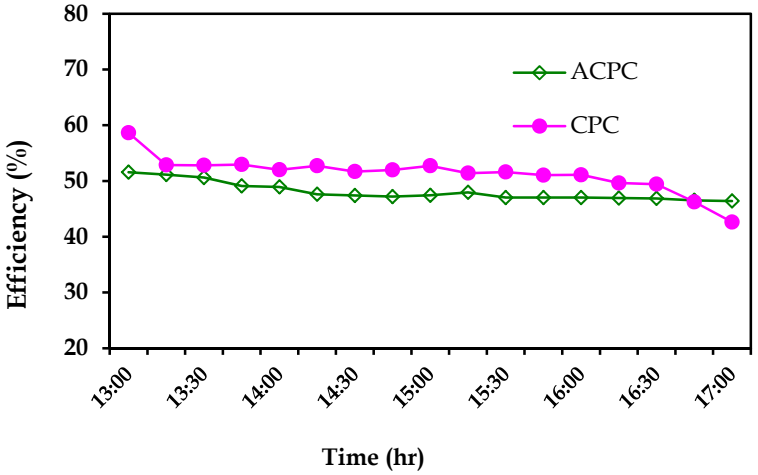

Fig. 14. Comparison of the efficiencies of CPC and ACPC.

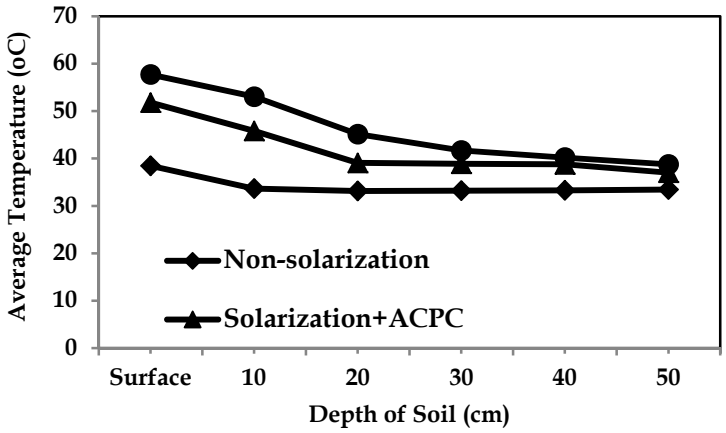

Fig. 15. Comparison of average soil temperature for all cases.

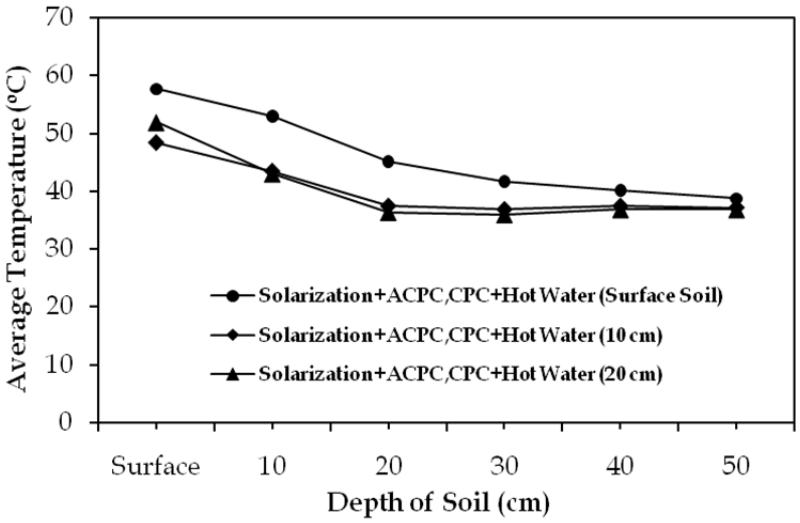

Fig. 16. Comparison of average soil temperature at various depths for the proposed case.

4.2 Application to reduce time to inhibit *Erwinia* in soil

4.2.1 Soil treatment

The maximum and average temperatures were always higher in solarized soil, solarized with ACPC treated soil and solarization with CPC combined with ACPC and hot water treated soil than bare soil during the experimental periods, regardless of the depth. The temperatures for non-solarized and solarized soil, solarized with ACPC treated soil and solarization with CPC combined with ACPC and hot water treated soil are shown in Fig. 17.

The temperatures for solarized ACPC treated soil and solarization with CPC combined with ACPC and hot water treated soil are shown in Fig. 17. The maximum and mean soil temperatures at 0 cm in the solarized ACPC treated soil were 60.3°C and 49.4°C, respectively. In the solarization with CPC combined with ACPC and hot water, the soil temperatures at 0 cm were 63.9°C and 52.3°C, respectively.

Table 1 shows effects of combined solar collector system of CPC and ACPC on soil surface temperature. On average, maximum surface temperature of solarized with ACPC treated soil and solarization with CPC combined with ACPC and hot water treated soil were higher than non-solarized soil. In the experiment, maximum temperature of solarized with ACPC treated soil and solarization with CPC combined with ACPC and hot water treated soil were 21°C and 24.8°C higher than non-solarized soil, respectively. The average temperature of solarized with ACPC treated soil and solarization with CPC combined with ACPC and hot water treated soil were 15.7°C and 18.9°C higher than non-solarized soil, respectively.

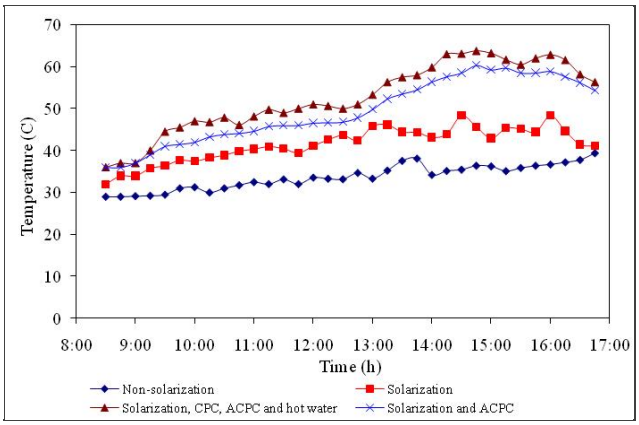
Temperature (C)
70
60
50
40
30
20
10
0
8:00
9:00
10:00
11:00
12:00
13:00
14:00
15:00
16:00
17:00
Time (h)
Non-solarization
Solarization
Solarization, CPC, ACPC and hot water
Solarization and ACPC

A

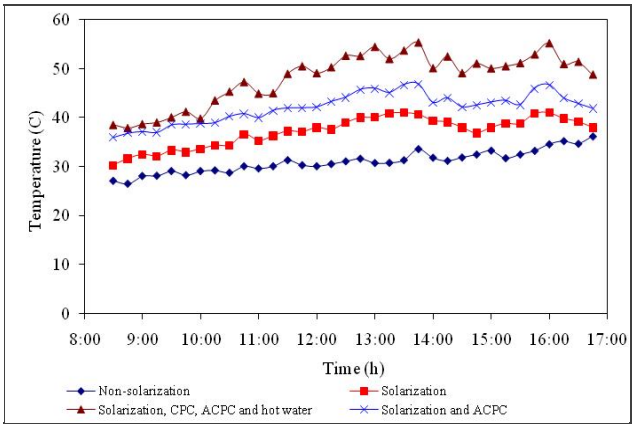
Temperature (C)
60
50
40
30
20
10
0
8:00
9:00
10:00
11:00
12:00
13:00
14:00
15:00
16:00
17:00
Time (h)
Non-solarization
Solarization
Solarization, CPC, ACPC and hot water
Solarization and ACPC

B

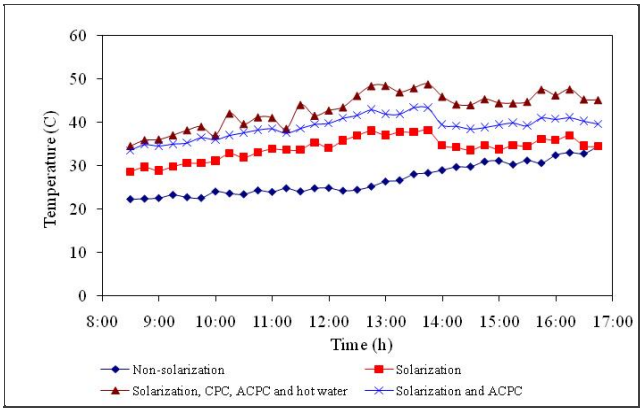
Temperature (C)
60
50
40
30
20
10
0
8:00
9:00
10:00
11:00
12:00
13:00
14:00
15:00
16:00
17:00
Time (h)
Non-solarization
Solarization
Solarization, CPC, ACPC and hot water
Solarization and ACPC

C

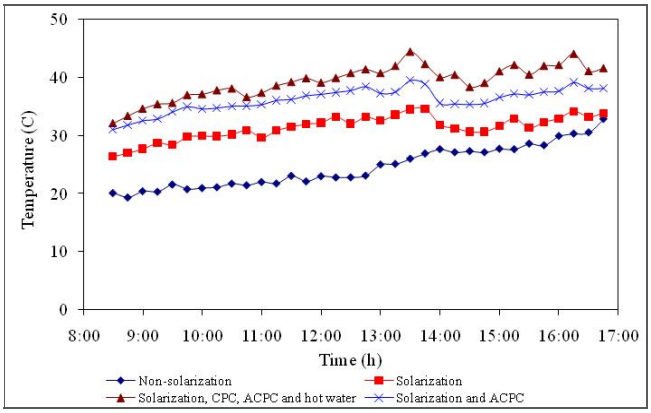

D

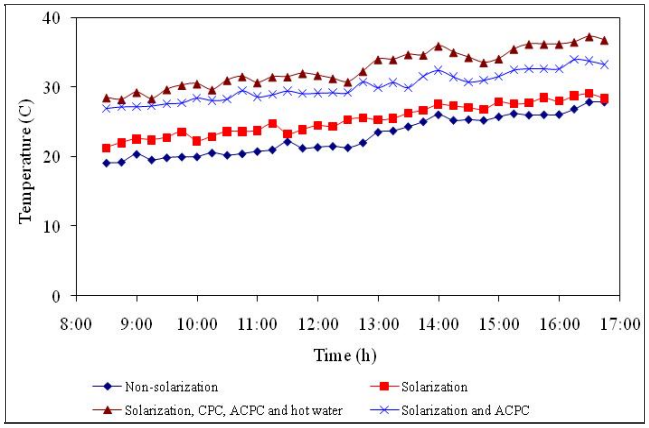

E

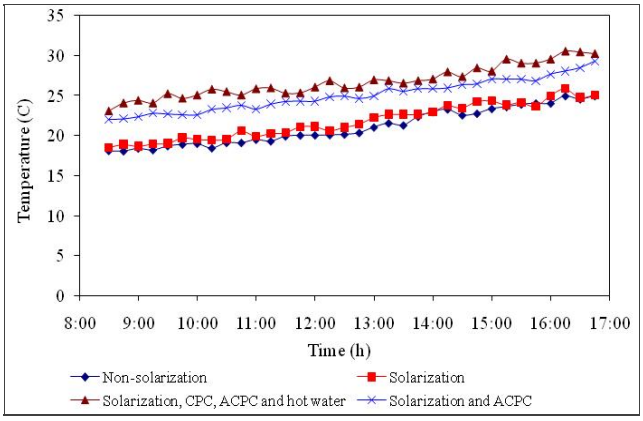

F

Fig. 17. The temperature profile for non-solarized, solarized, solarized with ACPC treated and solarization with CPC combined with ACPC and hot water treated soil of (A) surface soil, (B) soil at 5 cm, (C) soil at 10 cm, (D) soil at 20 cm, (E) soil at 30 cm, (F) soil at 50 cm.

Treatment	Maximum soil surface temperature (°C)	Average soil surface temperature (°C)
Non-solarization	39.1	33.4
Solarization	42.7	38.3
Solarization and ACPC	60.3	49.4
Solarization with CPC combined with ACPC and hot water	63.9	52.3
Air temperature	36.9	32.6

Table 1. The effects of combined solar collector system of CPC and ACPC of the intensity of light of 2044.4 W/m² on soil surface temperature (°C).

Treatment	Soil depth (cm)				
	5	10	20	30	50
Non-solarization	36.1	34.5	32.7	27.8	24.9
Solarization	41	38.1	34.5	29.1	25.8
Solarization and ACPC	46.9	43.4	39.4	34.0	29.2
solarization with CPC combined with ACPC and hot water	55.4	48.8	44.4	37.3	30.5

Table 2. The effects of solarization with the combined solar collector system of CPC and ACPC of the intensity of light of 2044.4 W/m² on maximum soil temperature (°C) at 5, 10, 20, 30 and 50 cm soil depths.

The temperatures for non-solarized soil, solarized soil, and the temperatures for ACPC with solarized treated soil and solarization with CPC combined with ACPC and hot water treated soil are shown in Fig. 17. The maximum and mean soil temperatures at different soil depth are shown in Table 2 and Table 3.

Maximum soil temperatures at 5, 10, 20 and 30 cm were higher in the solarized with ACPC treated soil and solarization with CPC combined with ACPC and hot water treated soil than the non-solarized soil. The maximum soil temperatures at 50 cm for solarized with ACPC treated soil and solarization with CPC combined with ACPC and hot water treated soil were also significantly different. The maximum temperature of solarized soil was higher than non-solarized soil. In the experiment, maximum temperature of solarized soil was 4.9, 3.6, 1.8, 1.3, 0.9°C higher than non-solarized soil at 5, 10, 20, 30 and 50 cm depth, respectively (Table 2). The maximum temperature at 5 with 10, 20, 30 and 50 cm in the solarized with ACPC treated plots differed by a maximum of 10.8, 8.9, 6.7, 6.2 and 4.3°C, respectively, on any one day. The maximum temperature at 5 with 10, 20, 30 and 50 cm in the solarization with CPC combined with ACPC and hot water treated plots differed by a maximum of 19.3, 14.3, 11.7, 9.5 and 5.6°C, respectively, on any one day.

Average soil temperatures at 5, 10, 20 and 30 cm were higher in the solarized with ACPC treated soil and solarization with CPC combined with ACPC and hot water treated soil than the non-solarized soil. The average soil temperature at 50 cm for solarized with ACPC treated soil and solarization with CPC combined with ACPC and hot water treated soil was

also significantly different. In the experiment, average temperature of solarized soil was 6.2, 7.2, 6.7, 2.3, 0.7°C higher than non-solarized soil at 5, 10, 20, 30 and 50 cm depth, respectively (Table 3). The average temperature at 5 with 10, 20, 30 and 50 cm in the solarized with ACPC treated plots differed by a average of 11.2, 12.2, 11.5, 7.2 and 4°C, respectively. The average temperature at 5 with 10, 20, 30 and 50 cm in the solarization with CPC combined with ACPC and hot water treated plots differed by a average of 17.2, 16.2, 14.7, 9.8 and 5.7°C, respectively.

Treatment	Soil depth (cm)				
	5	10	20	30	50
Non-solarization	30.9	26.8	24.5	23.0	21.0
Solarization	37.1	34.0	31.2	25.3	21.7
Solarization and ACPC	42.1	39.0	36.0	30.2	25.0
solarization with CPC combined with ACPC and hot water	48.1	43.0	39.2	32.8	26.7

Table 3. The effects of solarization with ACPC of the intensity of light of 2044.4 W/m^2 on average soil temperature (°C) at 5, 10, 20, 30 and 50 cm soil depths.

Soil solarization is a climate-dependent method and therefore its effectiveness in a specific region has to be assessed relative to the local climatological data. These studies that were carried out during day time showed that a combined solar system significantly increased soil temperature (Table 1-3).

Moreover, the highest increase was during when the highest temperatures were recorded, suggesting that climatological data can be used for predicting the effectiveness of combined solar collector system in a certain region. This might be related to soil temperature or the environmental factors such as the number of hours expose to sun light. Combining methods for improving pest control, especially when combining non-chemical methods, is the main objective of integrated pest management (Katan, 2000). In our studies, combining solarization with ACPC significantly improved the results in this experiment. This study thus shows that in general, the combined solar collector system of CPC and ACPC can increase soil temperature to reduce soil microbial population. However, the combined treatments of solarization and the combined solar collector system of CPC and ACPC showed a further improvement relative to the control, during which the highest temperatures were recorded. Combined methods have the potential to improve pest control but need to be optimized (Eshel et al., 2000). According to the results, the combinations increased the maximum soil temperature over the untreated control. Given the above considerations, the results illustrate the potential for combined application of ACPC with solarization, in enhancing soil surface temperature and at different soil depths for improving plant growth and in enhancing inhibition of soilborne pathogen yield. Temperature was greater at soil surface and at 5 cm depth and it gradually decreased as the soil depth increased. The maximum soil temperature treated with the combined solar collector system at 5 cm was never below 40°C after 2 hour treatment and for 5 hours it was close to 50°C.

Lower temperatures between 34.5 and 48.8°C were recorded at the 10-cm depth. At the 20-cm depth soil and 30-cm depth soil temperature fluctuated, between 29.3 and 36.4°C and between 28.5 and 37.3°C, respectively, for most of the period that soil was covered with the plastic sheets and ACPC. At the 50-cm depth soil temperature fluctuated, between 23 and 30.5°C. The temperature records in the experiment correspond to those reported by Lamberti et al. (1999). They reported that soil temperature was never below 35°C and did not exceed 40°C at 15 cm of depth of soil solarization during the summer while the following year soil temperature at the 15-cm depth was between 35 and 37°C. Higher temperature of soil solarization could be achieved by increasing the period of time exposed to the sun light considering that the temperature approaches 40°C for the treatment duration. However, in this experiment, the maximum soil temperatures treated the combined solar collector system at 5- and 10-cm depths were 48.8-55.4°C during 9 hours of the experimentation period. This level of temperature can be lethal for microorganism populations in soil. So, high temperatures during soil treated with the combined solar collector system were recorded in 5-10 –cm soil profile and these depths and therefore could inhibit soil microorganisms.

A significant observation arising from the field experiment was that the combined solar collector system for 9 hours provided satisfactory to increased high temperature. Soil solarization and the combined solar collector system resulted in high temperature at soil surface and at soil depth 5 cm over the control. In these results in combination of solarization with non-chemical control to enhance high temperature for control of microorganism wilts are in agreement with those reported for combination of solarization with non-chemical control by Giannakou (Giannakou et al., 2004), who reported that the combination of soil solarization with the bio-nematicide improved the parasite control. The parasite increased in plots compared to soil solarization and bio-nematicide plots by the end of the cropping season.

This could be partly due to the fact that soil solarization transforms soil physicochemical characteristics and partly because the combined solar collector system also has an impact on the soil microbial community. The combined solar collector system acts faster while soil solarization acts slowly, but for a prolonged period of time.

In general, it could be concluded that the novel use in the present study showed promising results by decreasing microorganism population. Soil solarization for longer time resulted in low microorganism numbers. However, more detailed field studies are required to establish the exact effects of soil solarization and on the microbial activity of soil and their impact on decreasing microorganism population efficacy.

Solarization could play a role in integrated control of different soilborne diseases but alone could not control the main soilborne diseases. Its adoption with the upgraded combined solar collector system treatment may be used to reduce the period of solarization. Solarization is mainly inconvenient by preventing use of the soil during the hot season, but possesses great potential as an alternative to fumigation for soil disinfestation. Solarization alone could control soilborne pathogens; however, the combination of soil solarization and the combined solar collector system was effective against microorganism wilts even though the solarization did not improve control of the individual pathogens. Moreover, at least in one case, the combined solar collector system increased potential of inhibition of soilborne pathogens of plants in plot area.

4.2.2 Effect of the treatments on soil microorganisms

The responses are that solarization with CPC combined with ACPC and hot water increased different temperature levels in the soil during the 4 hours in which the recorded temperatures went over 61°C, 55°C and 50°C, at 0 cm, 5 cm and 10 cm soil depth, respectively, affecting the *E. cartoverora* population (Table 4). The solarization with CPC combined with ACPC and hot water had significant effects on the microbiological population in the soil. Solarization slightly reduced the mean bacteria at 0 cm depth in 4 h about 15%. The populations of native *Erwinia* spp. in non-solarization plot at 0 cm soil treated for 4 h did not reduce significantly. After half an hour at 0-5 cm depth in the solarized with ACPC plots and solarization with CPC combined with ACPC and hot water plot the bacterial cells were reduced and after one hour the bacterial cell was undetectable. At 10 cm soil depth, the bacterial cells were reduced constantly and significantly reduced after 1 h in solarization with CPC combined with ACPC and hot water plot whereas at the 20 cm soil depth the bacterial cells were reduced constantly and significantly reduced after 2 h of treatment.

Time (h)	Population of *E. cartoverora* (cfu g^{-1})							
	Non-solarization plot (cm)				Solarization plot (cm)			
	0	5	10	20	0	5	10	20
½	2.3×10^7	1.1×10^7	3.4×10^7	2.6×10^7	1.4×10^7	2.3×10^7	2.2×10^7	2.6×10^7
1	2.1×10^7	6.4×10^7	2.3×10^7	3.2×10^7	1.6×10^6	5.2×10^7	4.7×10^7	4.4×10^7
2	3.5×10^7	1.7×10^7	4.2×10^7	5.1×10^7	1.2×10^5	2.3×10^6	5.3×10^7	2.7×10^7
4	6.4×10^7	2.2×10^7	1.6×10^7	2.4×10^7	1.4×10^5	1.6×10^6	1.9×10^7	2.9×10^7
Time (h)	Population of *E. cartoverora* (cfu g^{-1})							
	Solarization with ACPC plot (cm)				Solarization with CPC combined with ACPC and hot water plot (cm)			
	0	5	10	20	0	5	10	20
½	1.7×10^6	1.4×10^6	6.2×10^7	5.7×10^7	4.7×10^4	3.6×10^5	1.4×10^7	2.6×10^7
1	2.4×10^5	4.6×10^5	2.4×10^7	5.1×10^7	2.1×10^2	7.4×10^3	4.5×10^6	3.4×10^7
2	5.1×10^4	6.5×10^5	4.7×10^5	1.6×10^7	0	0	2.2×10^4	7.2×10^6
4	2.7×10^2	5.2×10^3	2.1×10^5	4.3×10^7	0	0	1.5×10^3	2.1×10^5

Table 4. Population of *E. cartoverora* at testing area, at varied time periods.

4.2.3 Effect of the treatments on seedling growth

There were significantly higher dry and fresh weights of tomato plants treated by solarization with CPC combined with ACPC and hot water compared with the untreated control. Treatment at soil surface with solarization with CPC combined with ACPC and hot water for 2 hours resulted in 97.74% and 85.89% increases in dry and fresh weights of tomato, respectively, compared to the untreated control. Treatment at soil 10 cm depth by solarization with CPC combined with ACPC and hot water for 2 hours resulted in 45.25% and 39.82% increases in dry and fresh weights of tomato, respectively, compared to the untreated control (Table 5).

As in the present study, the combined solar collector system was found to increase soil temperature, but not in toxic levels as reported in other disinfestation treatments, such as fumigation, steaming, autoclaving and irradiation (Chen et al., 1991). The reductions in microbial biomass and in the number of bacteria were expected, since the soil temperatures that prevailed during the solarization and the combined solar collector system treatment were high enough to cause the death of microorganisms. The data suggest that a significantly smaller microbial population in the solarized soil compared to the non-solarized plots. Soil disinfestations usually reduce the population of several species of microorganism, although thermotolerant and antagonistic species may survive the solarization treatment (Chen et al., 1991). Reductions of microorganism populations, however, have been reported in the rhizosphere and roots of solarized plants (Gamliel and Katan. 1992). Some bacteria are highly sensitive to soil solarization, which causes a reduction in their population, but they rapidly recolonize the soil again (Katan and DeVay, 1991). The results obtained regarding the effect of soil solarization with ACPC on weeds (Table 3) corroborate those of Elmore (Elmore, 1991) and Stapleton and DeVay (1995) who have included the species *Amaranthus* spp. and *E. indica* among the ones that are susceptible to soil solarization. In addition, it was also observed a reduction in infestation by *P. oleracea* after soil solarization. The weed infestation reduction observed in the present work was expected, considering the high soil temperatures that prevailed during soil solarization treated with the combined solar system, especially in the surface layers. Our studies that were carried out during day time showed that solarization treated with the combined solar system, their effectiveness, significantly increased soil temperature and increased harvest plant fresh weight (Table 2).

This study has demonstrated disease control and yield promotion by integrating solarization with the combined solar system. The inoculum density of *Erwinia* spp. was reduced after treatment by the combined solar system. This may be important in circumstances when soil solarization alone is not effective. The significant interactions between soil solarization and the combined solar collector system occurred probably because ACPC reduced the disease in solarized areas. Solarization alone was not effective for *Erwinia* at soil surface and soil 5 cm-depth for 4 hours. In the present work solarization with ACPC had a short-term effect in the control of *Erwinia* population. The present work showed that soil solarization with the combined solar collector system was suitable option for the control of *Erwinia* population, in the short time during the day. Other beneficial effects include a great reduction in weed infestation, especially in the soil surface layers, probably due to decreases in the soil microbial population. Soil solarization and the combined solar collector system enhance their economical viability and is an environmentally safe technology. Some authors have been discouraged with respect to the potential benefits of irradiation disinfection systems since they found that the efficient removal of pathogens required high energy levels (Mavrogianopoulos et al., 2000). Increases in soil temperature in the plot caused a decrease in *Erwinia* viability. *Erwinia* readily decayed and lost viability when exposed for short periods under solarization and the combined solar collector system at temperatures above 40°C. Among the solarization and the combined solar collector systems tested, treatment at soil surface with solarization and the combined solar collector system showed the most beneficial characteristics, as it consistently suppressed the *Erwinia cartoverora* and also promoted increased plant fresh and

dry weight compared to untreated control (Table 2). The use of treatment at solarization and the combined solar collector system for increasing yield and for crop protection is an attractive approach in the modern system in developing a sustainable agriculture.

Treatment		Dry weight (g)	Percent increase	Fresh weight (g)	Percent increase
Time (h)	Depth (cm)				
0	0	0.442	0.00	5.017	0.00
½	0	0.587	32.81	5.975	19.09
1	0	0.826	86.88	9.22	83.77
2	0	0.874	97.74	9.326	85.89
0	5	0.442	0.00	5.017	0.00
½	5	0.594	34.39	6.172	23.02
1	5	0.796	80.09	8.428	67.99
2	5	0.847	91.63	8.952	78.43
0	10	0.442	0.000	5.017	0.000
½	10	0.494	11.77	5.297	5.58
1	10	0.573	29.64	6.474	29.04
2	10	0.642	45.25	7.015	39.82

Table 5. Effect of solarization with CPC combined with ACPC and hot water treated soil on tomato growth response (as dry and fresh weight) as compared to untreated control.

The effects of high sub-lethal temperatures are influential in reducing *Erwinia*. During day time solarization and the combined solar collector system treatment were effective in reducing *Erwinia* viability as the *Erwinia* were subjected to sub-lethal temperatures. Soil solarization and the combined solar collector system reduced *Erwinia* viability by 49.74-89.22%. Reducing *Erwinia* viability in the top 5 cm of the soil would therefore ease disease pressure in tomato crops. This study thus shows that in general, solarization and the combined solar collector system can increase soil temperature to reduce *Erwinia* in the soil and increase dry and fresh weight of plant. While the effects would not be as great deeper in the soil, the *Erwinia* may still be weakened. The use of soil solarization to control crops will be most suited to the plant growing regions. Trials are now required to determine the actual reduction in plant afforded by this technique in the field. The combination of soil solarization with combined solar collector system may provide more effective control of crops than the use of soil solarization alone.

The present investigation confirmed the feasibility of controlling *E. cartoverora* in potato growth by heat treatment by combined solar collector system of propagation material. Critical time-temperature combinations were identified which resulted in a complete inactivation of the internal bacterial population. Therefore, the heat treatments by combined solar collector methods employed were chosen to provide a gentler form of heat to control growth of soilborne pathogen.

5. Conclusion

In the experimental approach it was attempted to use CPC combined with ACPC to increase water temperature for soil disinfection and disinfestation. The system had great effects on the microbiological population in the soil with higher heat transfer at deeper soil level and resulting high yield of plant growth, with the advantage that it is compatible for a more sustainable agriculture practice. The population of *E. cartoverora* was negative correlation of time course of solarization with CPC combined with ACPC and hot water treatment while increasing of tomato seedlings weight was positive correlation with the time course of the treatment. The experiments carried out in real scale showed that the system presents numerous advantages and pollution-free environment. Relatively high initial soil temperatures can be achieved. In this way, the use of the solar system for a short time to complement the CPC with ACPC application could reduce the energy required for soil disinfestation. Increase in the soil temperature by using low cost and environment friendly renewable energies for a short time period decrease the energy demand and could make the system economically affordable for soil disinfestation.

6. Acknowledgement

This work was supported by the Higher Education Research Promotion and National Research University Project of Thailand, Office of the Higher Education Commission.

7. References

Abdul-Jabbar, NK. & Salman, SA. (1998). Effect of Two-Axis Sun Tracking on the Performance of Compound Parabolic Concentrators, *Energy Conversion and Management,* Vol. 39, pp. 1073–10

Bell, CE. (1998). The economics of soil solarization compared to conventional agricultural production, *Proceedings of the Second Conference on Soil Solarization*. FAO Plant production and protection paper 147, pp. 506–16

Burrafato, GA. (1998). Device simulating the thermal regimes of soil solarization in laboratory experiments ''SUMMERTIME''. FAO, Vol. 109, pp.472–81.

Chen, Y., Gamliel, A., Stapleton, JJ. & Aviad, T. (1991). Chemical, physical, and microbial changes related to plant growth in disinfested soils. In: *Soil Solarization*, Katan, J. & DeVay, JE., pp. 103–129, CRC Press, Boca Raton, FL

Duffie, J.A. & Beckman, W.A. (1991). *Solar Engineering of Thermal Processes*, 2nd edition, John Wiley & Sons Inc, New York.

Elmore, CL. (1991). Weed control by solarization. In: *Soil Solarization*, Katan, J. & DeVay, JE., pp. 61–72, CRC Press, Boca Raton, FL

Eshel, D., Gamliel, A., Grinstein, A., Di Primo, P. & Katan, J. (2000). Combined soil treatments and sequence of application in improving the control of soilborne pathogens. *Phytopathology*, Vol. 90, pp. 751–757

Giannakou, IO., Karpouzas, DG. & Prophetou-Athanasiadou. D. (2004). A novel non-chemical nematicide for the control of root-knot nematodes. *Applied Soil Ecology*, Vol. 26, pp. 69–79

Gamliel, A. & Katan, J. (1992). Influence of seed and root exudates on fluorescent pseudomonads and fungi in solarized soil. *Phytopathology*, Vol. 82, pp. 320–327

Lamberti, F., D'Addabo, T., Greco, P., Carella, A. & DeCosmis, P. (1999). Management of root-knot nematodes by combination of soil solarization and fenamiphos in Southern Italy. In: Alternatives to Methyl Bromide for the Southern European Countries, Heraclion, Crete, Greece, pp. 89–96

Le Bihan, B., Soulas, ML., Camporota, P., Salerno, MI. & Perrin, R. (1997). Evaluation of soil solar heating for control of damping-off fungi in two forest nurseries in France. *Biological Fertilized Soils*, Vol. 25, pp. 189–95

Phitthayaratchasak, T., Thepa, S. & Kongkiattikajorn, J. (2005). Influence of asymmetry compound parabolic concentrator (ACPC) to underground temperature distribution. *Royal Project*, pp. 473–4

Phitthayarachasak, T., Thepa, S. & Kongkiattikajorn, J. (2009). Solar Energy System Reduces Time Taken to Inhibit Microbial Growth in Soil, *Renewable Energy*, Vol. 34, No. 11, pp. 2467-2473

Katan, J. (2000). Physical and cultural methods for the management of soil-borne pathogens. Crop Protections,Vol. 19, pp. 725–731

Katan, J. & DeVay, JE. (1991). Soil solarization: historical perspectives, principles, and uses, In: *Soil Solarization*, Katan, J. & DeVay, JE., pp. 23–37, CRC Press, Boca Raton, FL

Mavrogianopoulos, A., Frangoudakis, J. & Pandelakis, J. (2000). Energy efficient soil disinfestation by microwaves. *Agricultural Engineering Resources*, Vol. 75, pp. 149–153

Mills, DR. & Giutronich, JE. (1979). Symmetrical and asymmetrical ideal cylindrical radiation transformers and concentrators. *Optical Society of America*, Vol. 69, pp. 325-8

Stapleton, JJ. & DeVay, JE. (1995). Soil solarization: a natural mechanism of integrated pest management. In: *Novel approaches to integrated pest management*, Reuveni, R., pp. 309–350, CRC Press, Boca Raton, FL

19

Employing Cyanobacteria for Biofuel Synthesis and CCS

Christer Jansson
Lawrence Berkeley National Laboratory, Berkeley, CA USA

1. Introduction

Cyanobacteria are a large group of oxygenic photoautotrophic bacteria and, like plants and algae, can capture CO_2 via the Calvin-Benson cycle and convert it to a suite of organic compounds. They are important primary producers of organic material and play significant roles in biogeochemical cycles of carbon, nitrogen, and oxygen (Jansson and Northen 2010, Sharma et al. 2010). Through their photosynthetic capacity cyanobacteria have been tremendously important in shaping the course of evolution and ecological change throughout Earth's history, and they continue to contribute to a large share of the total photosynthetic harnessing of solar energy and assimilation of CO_2 to organic compounds. For example cyanobacteria account for 30% of the annual oxygen production on Earth (Sharma et al. 2010). Our oxygenic atmosphere was originally generated by numerous cyanobacteria during the Archaean and Proterozoic Eras. Many cyanobacteria are diazotrophs and can assimilate atmospheric N_2 and convert it to organic matter. Cyanobacteria occupy a wide array of terrestrial, marine, and freshwater habitats, including extreme environments such as hot springs, deserts, bare rocks, and permafrost zones. In their natural environments, some cyanobacteria are often exposed to the highest rates of UV irradiance known on our globe (Seckbach 2007). Cyanobacteria are Gram-negative bacteria but they combine properties of both Gram-negative and Gram-positive bacteria (Stewart et al. 2006); they contain an outer membrane and lipopolysaccharides (LPS), defining characteristics of Gram-negative bacteria, and a thick, highly cross-linked peptidoglycan layer similar to Gram-positive bacteria.

Cyanobacteria and eukaryotic microalgae exhibit a carbon-concentrating mechanism (CCM), a biochemical system that allows the cells to raise the concentration of CO_2 at the site of the carboxylating enzyme ribulose 1,5-bisphosphate carboxylase/oxygenase (Rubisco) up to 1000-fold over that in the surrounding medium (Fig. 1) (Badger and Price 2003, Jansson and Northen 2010, Price et al. 2008). Details of the CCM differ between cyanobacteria but the salient features include a series of bicarbonate (HCO_3^-) and CO_2 transporters and the carboxysome, a protein-enclosed micro-compartment that houses (most of) the Rubisco population and also contains the enzyme carbonic anhydrase (CA). Under low C_i (as CO_2 and HCO_3^-) conditions the CCM is induced and activated, supporting active transport of HCO_3^- across the outer and plasma membranes through HCO_3^-/Na^+ symports or ATP-driven uniports, as well as diffusion of CO_2, into the cytosol (Price et al. 2008). Uptake of

CO_2 is facilitated by CA-harboring NADPH dehydrogenase (NDH) complexes on the thylakoid and plasma membranes that converts the incoming CO_2 to HCO_3^- (reaction (1)).

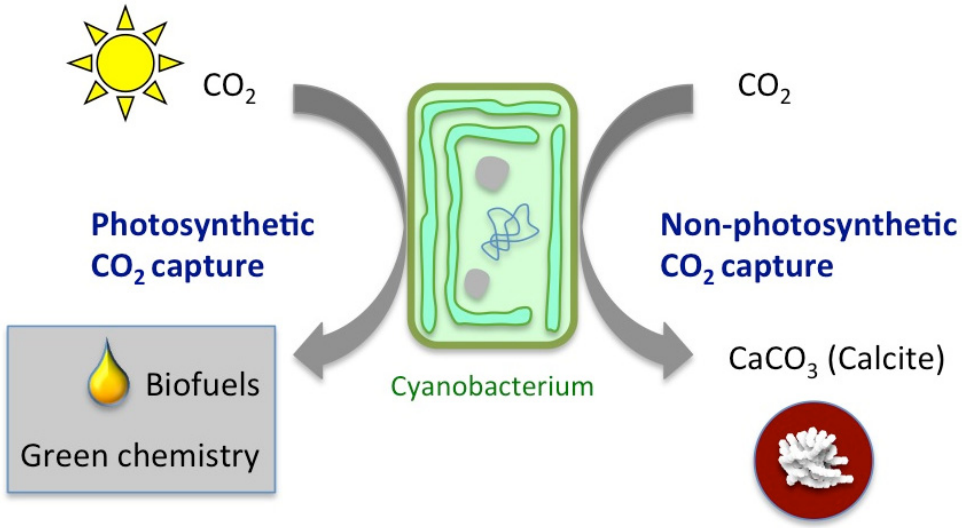

Fig. 1. The two modes of CO_2 uptake in cyanobacteria. Via photosynthesis, CO_2 is captured and converted to organic compounds, which can be exploited as biofuels or other industrial chemicals. In the calcification process, CO_2 is converted to inorganic $CaCO_3$, *e.g.* as calcite, which can be sequestered.

$$CO_2 + H_2O \leftrightarrows H^+ + HCO_3^- \quad (1)$$

Under these conditions, HCO_3^- is the predominant C_i species taken up by the cells. The cytosolic HCO_3^- subsequently enters the carboxysome where CA converts it to CO_2 for the Rubisco reaction (Jansson and Northen 2010, Price et al. 2008). At non-limiting C_i concentrations the CCM recedes to a basic, constitutive level, characterized by mainly CO_2 uptake (Price et al. 2008).

In addition to photosynthetic reduction of CO_2 to organic compounds, many cyanobacteria can take up CO_2 and mineralize it to recalcitrant calcium carbonate ($CaCO_3$) (see Section 3 below). Thus cyanobacteria present two different modes of CO_2 uptake, via photosynthesis and the Calvin-Benson cycle, and via biomineralization (calcification) (Fig. 1).

2. Cyanobacteria as photosynthetic bioreactors for direct conversion of CO_2 to hydrocarbon fuels

Cyanobacteria are well suited for synthetic biology and metabolic engineering approaches for the phototrophic production of various desirable biomolecules, including ethanol, butanol, alkylesters, and hydrocarbon biofuels. Phototrophic biosynthesis of high-density liquid biofuels in cyanobacteria would serve as a nice complement to the microbial

production of biodiesel and hydrocarbons in heterotrophic bacteria such as *E. coli*. Two biofuels that are being considered in microbial production systems are alkanes and isoprenoids. Alkanes of defined chain lengths can be used as injection fuel similar to gasoline and jet fuel. Many cyanobacteria synthesize alkanes, albeit at minute quantities. Optimizing the expression of the alkane biosynthesis genes and enhancing the carbon flux through the fatty acid and alkane biosynthesis pathways should lead to the accumulation and/or secretion of notable amounts of alkanes. It also becomes important to understand how to control the chain lengths of the produced alkane molecules. Isoprenoids, *e.g.* the monoterpene pinene and the sesquiterpene farnesene, are considered precursors for future biodiesel or next-generation jet fuel. Cyanobacteria produce carotenoids and extending the carotenoid biosynthetic pathways by introduction of constructs for appropriate terpene synthases should allow the biosynthesis of selected mono- and sesquiterpenes.

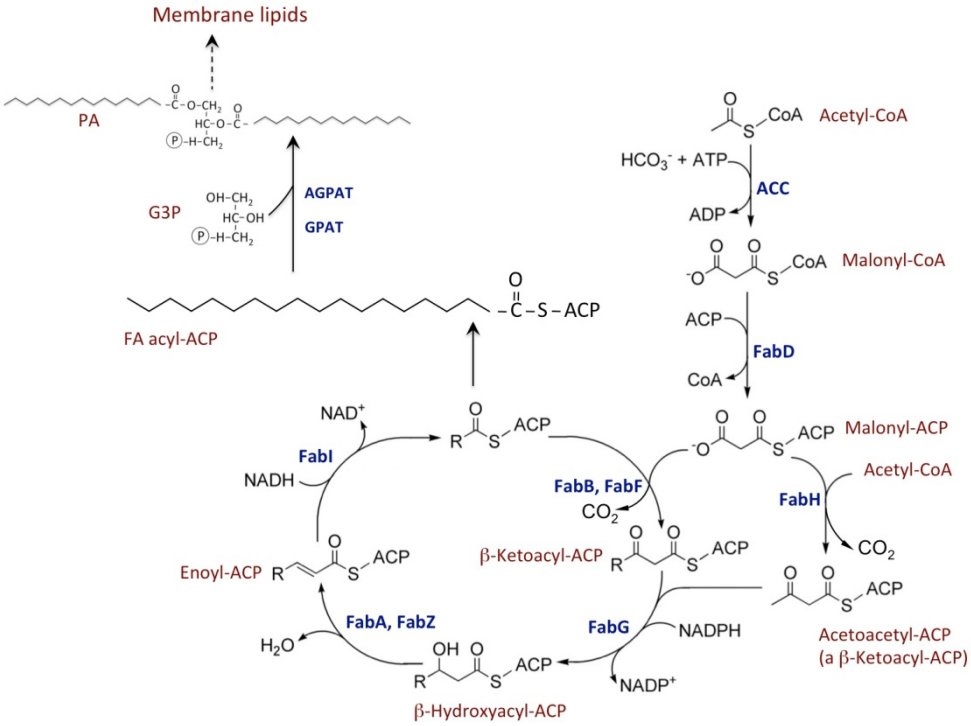

Fig. 2. Fatty acid and lipid biosynthesis in cyanobacteria. ACC, acetyl-coA carboxylase; ACP, acyl carrier protein; AGPAT, acylglycerol-3-phosphate acyltransferase; FabA/FabZ, ß-Hydroxyacyl-ACP dehydratase/isomerase; FabB ß-Ketoacyl-ACP synthase I; FabD, malonyl-CoA:ACP transacylase; FabF, ß-Ketoacyl-ACP synthase II; FabG, ß-Ketoacyl-ACP reductase; FabH, ß-Ketoacyl-ACP synthase III; FabI, enoyl-ACP reductase I; G3P, glycerol-3-PGPAT, glycerol-r-P acyltransferase; PA, phosphatidic acid.

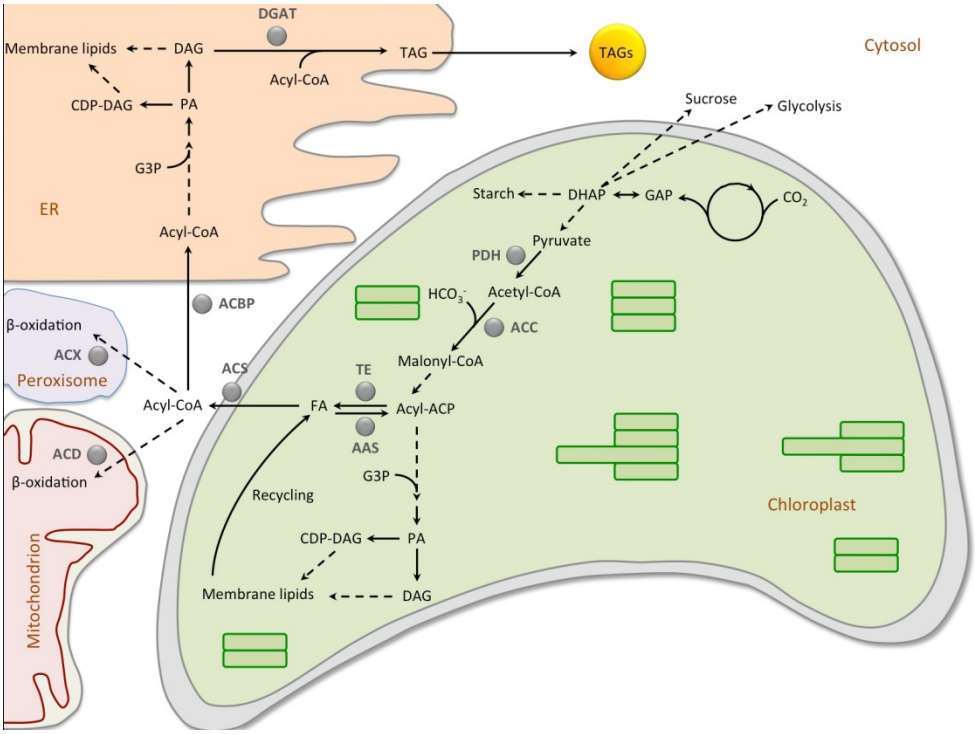

Fig. 3. Fatty acid and lipid biosynthesis in plants. AAS, acyl-ACP synthetase; ACC, acetyl-CoA carboxylase; ACP, acyl carrier protein; ACBP, acyl-CoA binding protein; ACS, acyl-CoA synthase; ACD, acyl-CoA dehydrogenase; ACX, acyl-CoA oxidase; CDP-DAG, cytidine diphosphate diacylglycerol; DAG, diacylglycerol; DGAT, diacylglycerol acyltransferase; DHAP, dyhydroxyacetone phosphate; ER, endoplasmatic reticulum; G3P, glycerol-3-P; GAP, glyceraldehyde 3-P; TAG, tryacylglyceride.

2.1 Biosynthesis of alkanes

The pathway for alkane synthesis in cyanobacteria is a two-step process downstream of fatty acid (FA) synthesis and seems to proceed via decarbonylation of fatty aldehydes (Schirmer et al. 2010), the major route for alkane synthesis in most organisms (Ladygina et al. 2006). FA synthesis in bacteria is accomplished by a type II FA synthase (FASII), a multienzyme system, utilizing a freely dissociable acyl carrier protein ACP. The products of FASII are released as acyl-ACPs and may be directly incorporated into membrane lipids by acyltransferases that attach a FA to the glycerol 3-phosphate backbone to form the key intermediate, phosphatidic acid. This is in contrast to FA synthesis in eukaryotes, where acyl-ACPs are either hydrolyzed by acyl-ACP thioesterases (TE; EC 3.1.2.14) to yield free FAs, or directly transferred to CoA for generation of acyl-CoA. For example, in plants and algae, where FA synthesis takes place on FASII complexes in the plastids, the release of free FAs are required for transport across the plastid envelope. Upon arrival at the outer plastid surface, the free FAs are re-activated by acyl-CoA synthetase (FadD; EC 6.2.1.3) to form acyl-

CoA. Acyl-CoA is the starting substrate for synthesis of TAGs but can also be used for ß-oxidation and for synthesis of membrane lipids.

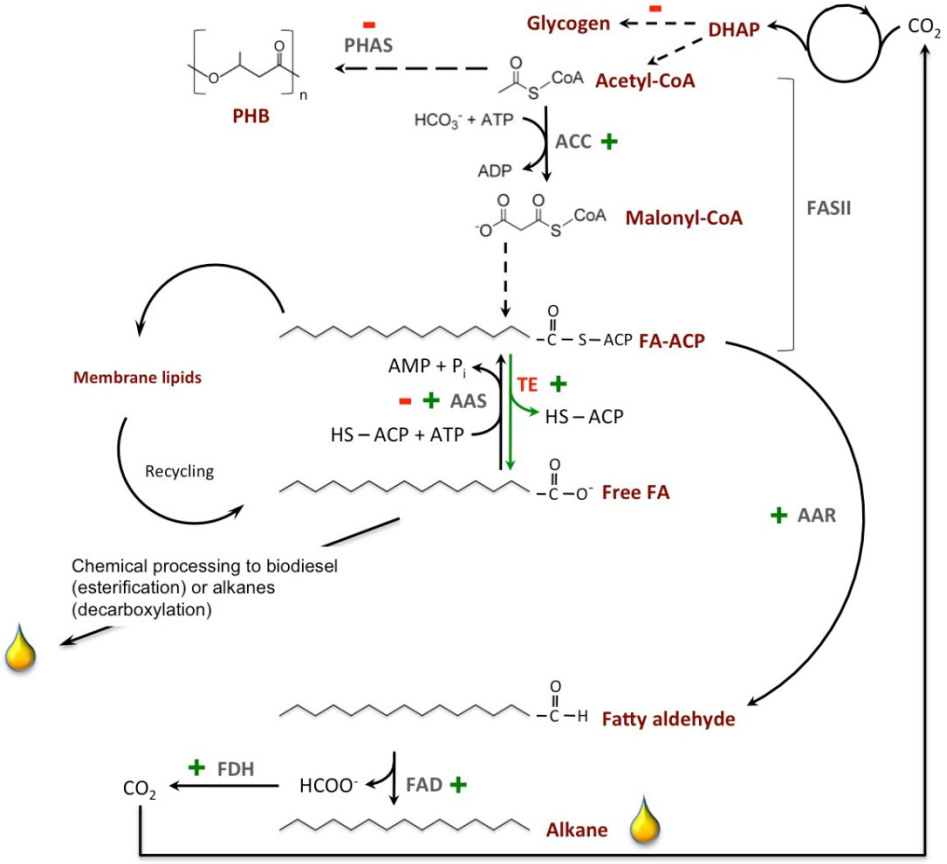

Fig. 4. Rationale for biosynthesis of alkane fuels in cyanobacteria. AAR; acyl-ACP reductase; AAS, acyl-ACP synthetase; ACC, acetyl-CoA carboxylase; ACP, acyl carrier protein; FAD, fatty acyl decarbonylase; FA, fatty acid; FASII, fatty acid synthase complex type II; FDH, formate dehydrogenase; PHAS, polyhydroxyalkanoate synthase; PHB, polyhydroxybutyrate; TE, thioesterase.

Most bacteria lack intracellular TEs that act on FA-ACPs, and the formation of free FAs mainly occurs during recycling of membrane lipids or degradation of acylated proteins. *E. coli* and other bacteria that can take up and metabolize exogenous FAs possess periplasmic TEs (*e.g.* TesA in *E. coli* (Cho and Cronan 1994)) that liberate FAs for import. Heterologous expression of TEs, primarily from plants, in bacteria has resulted in high production of free FAs (Jha et al. 2006, Jones et al. 1995, Steen et al. 2010, Voelker and Davies 1994, Yuan et al. 1995). The concomitant decrease in acyl-ACP levels also relieves the rigorous feedback inhibition of acetyl-CoA carboxylase (ACC; EC 6.4.1.2) (and other FA-biosynthesis enzymes) exerted by this end product. ACC catalyzes the rate-limiting step in FA synthesis and thus

expression of TEs in the cytosol of bacteria has the dual effect of producing free FAs and enhancing FA synthesis.

The decarbonylation pathway implies the involvement of the Fatty acyl-CoA or Fatty acyl-ACP reductase (FadR; EC 1.2.1.50), and Fatty aldehyde decarbonylase (FAD; EC 4.1.99.5) (Walsh et al. 1998; Ladygina et al. 2006) (Fig. 2). Gene sequences for *FadR* and *FAD* have recently been identified from several cyanobacteria (Schirmer et al. 2010). Interestingly, the decarbonylation step in cyanobacterial alkane biosynthesis may involve the release of formate ($HCOO^-$) rather than CO (Warui et al. 2011).

To generate alkanes of desired chain lengths (e.g., C_8, C_{10}, and C_{12} saturated species) for diesel, jet fuel or gasoline alternatives, cyanobacteria can be engineered to contain genes encoding TEs (Fig. 4) with different substrate specificities. For example, *FatB* from Arabidopsis (Accession NP_172327), *FatB2* from *Cuphea hookeriana* (GenBank: U39834.1), *FatB1* (pCGN3822) from *Umbellularia californica* (GenBank: M94159.1), and *FatB1* from *C. hookeriana* (GenBank: Q39513.1). Another potential TE is the mature TES enzyme from *E. coli* (Cho and Cronan 1994). In addition to inserting an appropriate TE, high-yield production of free FAs in cyanobacteria also require additional optimization by increasing the carbon flux towards FA synthesis. Such efforts can entail the insertion of extra copies of the gene for ACC, which catalyzes the rate-limiting step in FA-ACP synthesis. ACC is a heterotetramer consisting of AccA, AccB, AccC, and AccD. The genes for the different subunits are distributed in most, if not all, cyanobacterial genomes. For the sake of increasing ACC activity, an *ACC* operon can be constructed behind a strong promoter. Intuitively, another optimizing step would be to inactivate the *AAS* gene to prevent re-thioesterification of free FAs. However, since AAS rather than FadD may serve as the sole FA-activating enzyme in cyanobacteria, the yield of metabolites downstream of acyl-ACP, like alkanes, might benefit from increasing the copy number of *AAS* genes so as to speed up the activation of recycled FAs from the degradation of membrane lipids (Figs. 2, 4). With few exceptions, *AAS* exists as a single-copy gene in cyanobacteria, encoding an enzyme with broad substrate specificity (Kaczmarzyk and Fulda 2010). For the single purpose of free FA production, a simultaneous increase in AAC activity and inactivation of the gene for AAS is likely to improve the yield.

The physiological role(s) of alkanes in cyanobacteria is unknown. Not all cyanobacteria synthesize alkanes and in those that do, alkanes accumulate in very small amounts. It is possible that alkanes are required for proper membrane fluidity or function. Alternatively, they serve as carbon storage compounds under excess carbon and/or nutrient deficiency conditions. Although heptadecane (C_{17}) is the predominant *n*-alkane among cyanobacteria, many strains synthesize a wide array of linear, branched, and cyclic alkanes, some of which, e.g. branched methyl- and ethylalkanes, are only found in these microorganisms (Dembitsky et al. 2001, Jansson 2011). For example, the cyanobacterium *Microcoleus vaginatus* produces four *n*-alkanes and more than 60 different branched alkanes (Dembitsky et al. 2001). Another strain that merits emulation is *Anabaena cylindrica*, which was shown to form C_9-C_{16} *n*-alkanes under high NaCl stress conditions (Bhadauriya et al. 2008), presumably due to an increase in short-chain FA during salt stress. It should be noted that C_{12}-C_{16} *n*-alkanes are particularly well suited as jet fuel. Whether the difference in alkane composition observed between cyanobacterial strains and growth conditions reflect the existence of FAR and FAD enzymes with different chain length specificities, or whether alkane chain length is determined at the FA level, is not yet clear. In the latter case, FAR and FAD would be expected to exhibit broad substrate specificities.

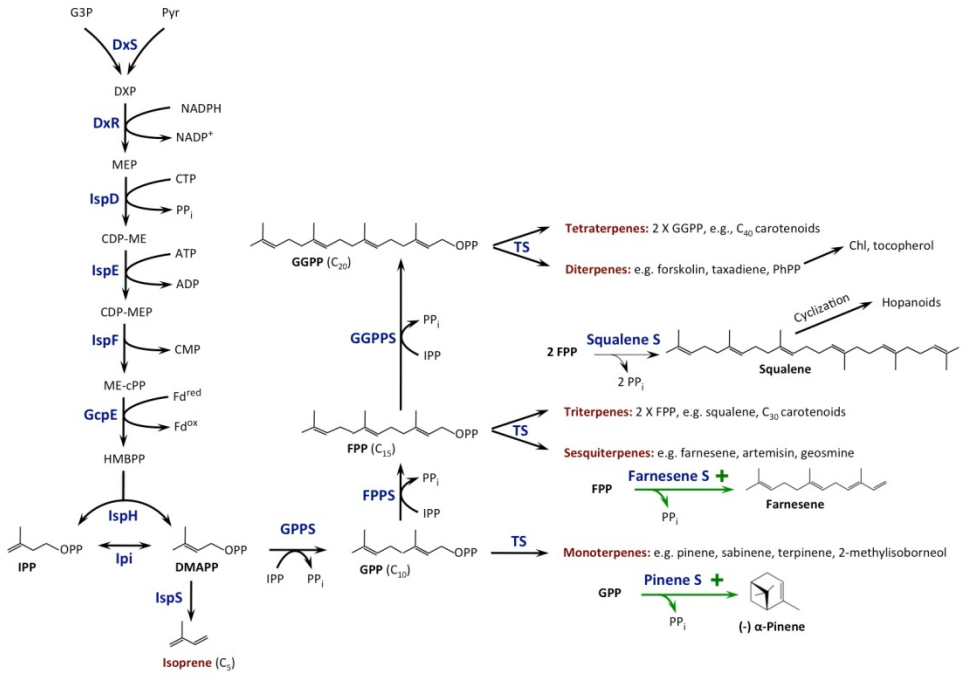

Fig. 5. Rationale for biosynthesis of isoprenoid fuels in cyanobacteria. CDP-ME diphosphocitidyl methylerythritol; CDP-MEP, diphosphocitidyl methylerythrotol 2-P; Chl, chlorophyll; DMAPP, dimethylallyl diphosphate; DXP, deoxyxylose 5-P; DxS, DXP synthase; DxR, DXP reductoisomerase; FPP, farnesyl diphosphate; G3P, Glyceraldehyde 3-P; Gcpe (IspG), HMBPP synthase; GPP, geranyl diphosphate; GGPP, geranylgeranyl diphosphate; GPPS, GPP synthase; GGPS, GGPP synthase; HMBPP, hydroxymethylbutenul; IspD, CDP-ME synthase; IspE, CDP-ME kinase; IspF, Me-cPP synthase; IspH, HMBPP reductase; IspS, isoprene synthase; Ipi, IPP isomerase; IPP, isopentenyl diphosphate; ME-cPP, methylerythritol 2,4-cyclodiphosphate; MEP, methylerythritol 4-P; Pyr, pyruvate; TS, terpene synthase.

2.2 Biosynthesis of isoprenoids

Branched hydrocarbons, which have higher octane rating than *n*-alkanes, can be produced by engineering the carotenoid pathway in cyanobacteria. While it is possible to use carotenoids themselves to make gasoline, e.g. via hydrocracking (Hillen et al. 1982), many carotenoids are solid at room temperature, complicating refining approaches. Cyanobacteria contain genes for carotenoid synthesis and thus synthesize geranyl pyrophosphate (GPP), farnesyl pyrophosphate (FPP), and geranylgeranyl pyrophosphate (GGPP), which are precursors for monoterpenes, sesqui- and triterpenes, and di- and tetraterpenes, respectively (Fig. 3). Most, if not all cyanobacteria produce sesquiterpenes such as geosmine, and monoterpenes such as 2-methylisoborneol (Agger et al. 2008) but synthesis of isoprene in naturally occurring cyanobacteria has not been reported. By introduction of an isoprene synthase (IspS) gene based on the mature enzyme from the Kudzu plant (*Pueraria montana*;

GenBank: AY316691), Lindberg *et al.*, (2010) demonstrated the production of volatile isoprene hydrocarbons in the cyanobacterium *S.* 6803 (Lindberg et al. 2010). The rationale for engineering cyanobacteria for isoprene, monoterpene, or sesquiterpene synthesis is straightforward as it involves the addition of a single gene, IspS or different terpene synthases (TS). A desirable objective will be to extend the carotenoid pathway for synthesis of pinene (a monoterpene), and farnesene (a sesquiterpene). Pinene is being considered for next-generation jet fuel, and farnesene is being developed as precursors to diesel fuels (Rude and Schirmer 2009). For example, synthetic gene constructs could be based on the mature proteins of (-)-α-pinene synthase from *Pinus taeda* (GenBank: AF543527.1), and α-farnesene synthase from *Pyrus communis* (GenBank: AY566286.1).

3. Cyanobacteria as catalysts for biomineralization of CO_2 to calcium carbonate

Biomineralization offers the potential to utilize photosynthetic microorganisms like cyanobacteria as solar-powered catalysts for the conversion of CO_2 to recalcitrant carbonates, primarily calcium carbonate ($CaCO_3$). If implemented at scale such calcifying systems could conceivably be deployed for biological carbon capture and storage (CCS) by sequestering point-source CO_2 (Jansson and Northen 2010). Microbial calcification, *i.e.* formation and precipitation of $CaCO_3$, is widespread in nature and among microorganisms, and of vast ecological and geological importance. Spectacular manifestations of cyanobacterial calcification are presented by stromatolites and whiting events (Jansson and Northen 2010). Another magnificent illustration of microbial calcification is the White Cliffs of Dover, which are mainly eukaryotic microalgal in origin.

Precipitation of $CaCO_3$ can proceed by either or both the following reactions:

$$Ca^{2+} + 2HCO_3^- \leftrightarrows CaCO_3 + CO_2 + H_2O \quad (2)$$

$$Ca^{2+} + CO_3^{2-} \leftrightarrows CaCO_3 \quad (3)$$

Bicarbonate (HCO_3^-) is ubiquitous in water and is formed via dissolution of gaseous CO_2 at pH values above about 6.0 at 25 ^oC:

$$CO_{2\,(aq)} + H_2O \leftrightarrows H_2CO_3 \quad (4)$$

$$H_2CO_3 \leftrightarrows HCO_3^- + H^+ \quad (5)$$

The concentration of carbonic acid (H_2CO_3) is small in circumneutral pH waters, so the dissolved CO_2 from reactions 3 and 4 occurs predominantly as HCO_3^-.

A fraction of HCO_3^- dissociates to form carbonate (CO_3^-):

$$HCO_3^- \leftrightarrows H^+ + CO_3^{2-} \quad (6)$$

Spontaneous calcification is often impeded by thermodynamic barriers, also in systems supersaturated with Ca^{2+} and CO_3^{2-} such as the oceans, (Berry et al. 2002). Cyanobacteria catalyze the calcification reaction(s) on their cell surface, the exopolysaccharide substances (EPS) layer, or the proteinaceous surface layer (S-layer), by one or both of two mechanisms (Jansson and Northen 2010). The photosynthetic electron transport and the CA activity in

the carboxysome (reaction (6)) both consume cytosolic H^+, resulting in a net increase of OH^- in the cytosol. Neutralization of this imbalance, *e.g.* by the activity of a Ca^{2+}/H^+ antiport, generates an alkaline microenvironment on the outer cell surface. The alkaline pH shifts the equilibrium of the bicarbonate buffer system (reactions (4) and (5)) to the right and promotes localized regions of increased CO_3^{2-} concentrations at the cell exterior (Fig. 1). A second means by which cyanobacteria can catalyze calcification is by the presence of Ca^{2+}-binding domains, *e.g.* glutamate and aspartate residues, or carboxylate and sulfonate groups, on the cell surface, which, together with the export of Ca^{2+} through the Ca^{2+}/H^+ translocator, raises the local Ca^{2+} concentration and serve as nucleation sites for $CaCO_3$ precipitation.

The physiological or biochemical function(s) of calcification in cyanobacteria are unclear, although some possibilities have been suggested (Jansson and Northen 2010). Since calcification will remove Ca^{2+} from chemical equilibria and may offer a means to sustain an active efflux of Ca^{2+} via the Ca^{2+}/H^+ translocator, which, in turn, generates a H^+ gradient that may enhance nutrient and HCO_3^- uptake (McConnaughey and Whelan 1997). A calcerous cell surface may also provide a protective layer against excessive light exposure.

In the context of evaluating the concept of cyanobacterial calcification for biological CCS, there are several outstanding issues that need to be addressed. First, it should be recognized that calcification as a natural phenomenon by marine or freshwater phytoplankton serves as a CO_2 source rather than a sink, i.e., calcification releases CO_2 to the atmosphere (Riebesell 2004). This can most easily be appreciated by looking at reaction (1) but, because of the HCO_3^- buffer system in oceans and lakes, it applies to reaction (2) as well (Frankignoulle 1994, Frankignoulle and Canon 1994). This global effect of calcification should not be confused with its potential use for biological CCS. In such a scenario, the comparison should be made between CO_2 in flue gas, *e.g.*, from a coal-fired power plant, being released to the atmosphere, or being partly captured by cyanobacteria and converted to $CaCO_3$ for precipitation. Second, assuming biocalcification as a means to mitigate CO_2 emissions, the question arises as to whether such a process can operate at a level that is industrially relevant. Combining observations from whiting events in the Great Bahama Bank and microcosm experiments with the marine *Synechococcus* 8806 (*S.* 8806), Lee *et al.* (Lee et al. 2006) suggested that *S.* 8806 is able to produce around 2.5 MT $CaCO_3$ per year, which would translate to a removal of half of the CO_2 emitted from a 500 MW coal-fired power plant. Although these data would tend to imply that cyanobacterial calcification is a viable CCS alternative, it is not immediately obvious from the calculations at what scale (*e.g.* the size of the culture pond) such a system would need to run. A third question concerns the diurnal fluctuations of the calcification process. If photosynthesis is required to maintain a necessary alkaline pH at the cell surface for calcification to occur, it is not clear to what extent the formed $CaCO_3$ is stable enough to prevent its dissolution during the night.

Another issue that also relates to the pH of the cyanobacterial culture is whether or not calcification can operate at high CO_2 levels, *e.g.*, in a pond infused with flue gas. In a high-CO_2 environment, the activity of the CCM is low and cells will preferentially take up CO_2 rather than HCO_3^-. The conversion of CO_2 during transport to the cytosol (Fig. 1) produces H^+ (reaction 6) that need to be neutralized, possibly via export to the medium (Price et al. 2008). This counterbalances the subsequent and opposite alkalinization reaction in the carboxysome. Also, rapid infusion of gaseous CO_2 into a cyanobacterial pond will likely lower the ambient pH, impeding alkalinization at the extracellular surface.

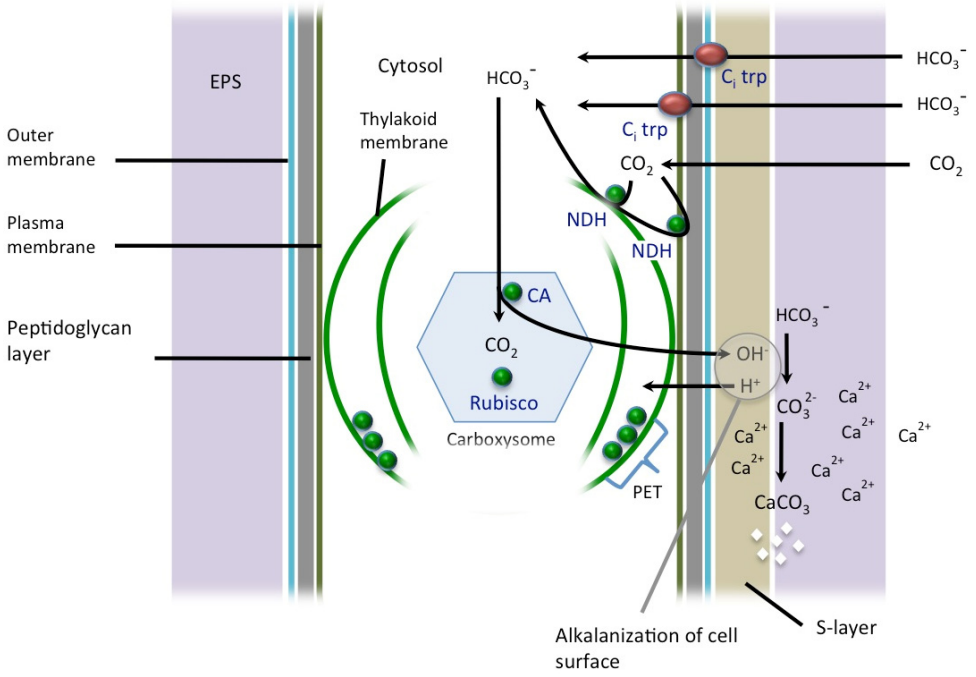

Fig. 6. Model of the carbon concentrating mechanism (CCM) and calcification in a cyanobacterial cell. CO_2 enters the cells mainly via active transport of HCO_3^- but also through diffusion of CO_2, which is converted to HCO_3^- during the uptake. Cytosolic HCO_3^- is subsequently imported to the carboxysome. CA, carbonic anhydrase; C_i, inorganic carbon; EPS, exopolysaccharide substances; NDH, NADPH dehydrogenase; PET photosynthetic electron transport. Modified from Jansson and Northen.

4. Conclusions

The employment of cyanobacteria as a biofuel platform offers great potential. Most of the attention in the algal biofuel space is currently devoted to eukaryotic microalgae, mainly because of their capacity to store large amounts of TAGs. However, recent demonstrations of FA ethylesters (FAEE; a biodiesel) and hydrocarbon fuels biosynthesis in *E. coli* (Kalscheuer et al. 2006; Beller et al. 2010; Schirmer et al. 2010; Steen et al. 2010) suggest that similar strategies in pathway engineering should prove achievable also in cyanobacteria, where photosynthesis, rather than organic feedstocks, will provide energy and carbon. Furthermore, cyanobacteria have previously been engineered to produce alcohol-based fuels such as ethanol and isobutanol (Deng and Coleman 1999; Atsumi et al. 2009).

The capacity of cyanobacteria to thrive in high CO_2 concentrations makes them an attractive system for beneficial recycling of CO_2 from point sources such as coal-fired power plants via biofuel synthesis, and for biological CCS via calcification. Since many cyanobacteria are halophilic, cultivation ponds can be sited away from agricultural land making use of seawater or various sources of saline wastewater.

Non-arguably, much research is needed to address challenges associated with utilization of cyanobacterial for biofuel synthesis or CCS. In addition to issues already discussed above, two more concerns are worth pointing out. Since algal cultivation requires measures for crop protection, it becomes important to learn how to construct robust consortia, or how to prevent or mitigate contamination and grazing of monocultures in open pond systems. Another hurdle in the algal biofuel industry is associated with harvesting and extraction, steps that account for 25-30% of the total biomass production cost; and strategies that facilitate, or obviate the need for, these steps need to be further developed. One solution is to use filamentous or self-flocculating strains to expedite harvesting. Another approach is to achieve release of the biofuel molecules to the medium, either through cell lysis or by secretion. An example of the former is an inducible lysis system reported for *S*. 6803 (Curtiss et al. 2011, Liu and Curtiss 2009). The feasibility of secretion was illustrated by the release of free FAs from *S*. 6803 and *Synechococcus elongatus* PCC 7942 cells to the medium after inactivation of the *AAS* gene (Kaczmarzyk and Fulda 2010).

5. Acknowledgements

This work was supported in part by U. S. Department of Energy Contract DE-AC02-05CH11231 with Lawrence Berkeley National Laboratory. Financial support from LDRD projects 366190 and 366188 are acknowledged.

6. References

Badger, M.R. & Price, G.D. (2003). CO_2 concentrating mechanisms in cyanobacteria: molecular components, their diversity and evolution, *Journal of Experimental Botany* 54, 609-622

Berry, L.; Taylor, A.R., Lucken, U., Ryan, K.P. & Brownlee C. (2002). Calcification and inorganic carbon acquisition in coccolithophores, *Functional Plant Biology* 29, 289-299

Bhadauriya, P.; Gupta, R. Singh, S. Bisen, P.S. (2008). *n*-Alkanes variability in the diazotrophic cyanobacterium *Anabaena cylindrica* in response to NaCl stress, *World Journal of Microbiology & Biotechnology* 24, 139-141

Cho, H.; Cronan, J.E. (1994). Protease-I of *Escherichia Coli* Functions as a Thioesterase *in Vivo*, *Journal of Bacteriology* 176, 1793-1795

Curtiss, R.; Liu, X.Y., Fallon, S., Sheng, J. (2011). CO_2-limitation-inducible Green Recovery of fatty acids from cyanobacterial biomass, *Proceedings of the National Academy of Sciences of the United States of America* 108, 6905-6908

Dembitsky, V.M.; Dor, I., Shkrob, I., Aki, M. (2001). Branched alkanes and other apolar compounds produced by the cyanobacterium from the Negev Desert, *Russian Journal of Bioorganic Chemistry* 27, 110-119

Frankignoulle, M. (1994). A Complete Set of Buffer Factors for Acid-Base CO_2 System in Seawater, *Journal of Marine Systems* 5, 111-118

Frankignoulle, M.; Canon, C. (1994). Marine Calcification as a Source of Carbon-Dioxide - Positive Feedback of Increasing Atmospheric CO_2, *Limnology and Oceanography* 39, 458-462

Jansson C. (2011). Metabolic Engineering of Cyanobacteria for Direct Conversion of CO_2 to Hydrocarbon Biofuels, *Progress in Botany* 73, In press

Jansson, C.; Northen, T. (2010). Calcifying cyanobacteria - the potential of biomineralization for carbon capture and storage, *Current Opinion in Biotechnology* 21, 365-371

Jha, J.K.; Maiti, M.K., Bhattacharjee, A., Basu, A., Sen, P.C., Sen, S.K. (2006). Cloning and functional expression of an acyl-ACP thioesterase FatB type from *Diploknema* (*Madhuca*) *butyracea* seeds in *Escherichia coli*, *Plant Physiology and Biochemistry* 44, 645-655

Jones, A.; Davies, H.M., Voelker, T.A. (1995). Palmitoyl-Acyl Carrier Protein (Acp) Thioesterase and the Evolutionary Origin of Plant Acyl-Acp Thioesterases, *Plant Cell* 7, 359-371

Lee, B.D.; Apel, W.A., Walton, M.R. (2006). Whitings as a Potential Mechanism for Controlling Atmospheric Carbon Dioxide Concentrations, *DOE, Final Project Report*, no. INL/EXT-06-01351

Liu, X. & Curtiss, R. (2009). Nickel-inducible lysis system in *Synechocystis* sp. PCC 6803, *Proceedings of the National Academy of Sciences of the United States of America* 106, 21550-21554

McConnaughey, T.A.; Whelan, J.F. (1997). Calcification generates protons for nutrient and bicarbonate uptake, *Earth-Science Reviews* 42, 95-117

Price, G.D.; Badger, M.R., Woodger, F.J., Long, B.M. (2008). Advances in understanding the cyanobacterial CO_2-concentrating-mechanism (CCM): functional components, Ci transporters, diversity, genetic regulation and prospects for engineering into plants, J*ournal of Experimental Botany* 59, 1441-1461

Riebesell, U. (2004). Effects of CO_2 enrichment on marine phytoplankton, *Journal of Oceanography* 60, 719-729

Seckbach, Je. (2007). *Algae and Cyanobacteria in Extreme Environments*. Dordrecht, The Netherlands: Springer.

Sharma, N.; Tiwari, S., Tripathi, K., Rai, A. (2010). Sustainability and cyanobacteria (blue-green algae): facts and challenges, *Journal of Applied Phycology*, 1-23

Steen, E.J.; Kang, Y.S., Bokinsk,y G., Hu, Z.H., Schirmer, A., McClure, A., del Cardayre, S.B., Keasling, J.D. (2010). Microbial production of fatty-acid-derived fuels and chemicals from plant biomass, *Nature* 463, 559-563

Stewart, I.; Schluter, P., Shaw, G. (2006). Cyanobacterial lipopolysaccharides and human health - a review, *Environmental Health: A Global Access Science Source* 5, 7

Voelker, T.A. & Davies, H.M. (1994). Alteration of the Specificity and Regulation of Fatty-Acid Synthesis of *Escherichia Coli* by Expression of a Plant Medium-Chain Acyl-Acyl Carrier Protein Thioesterase, *Journal of Bacteriology* 176, 7320-7327

Yuan, L.; Voelker, T.A., Hawkins, D.J. (1995). Modification of the Substrate-Specificity of an Acyl-Acyl Carrier Protein Thioesterase by Protein Engineering, *Proceedings of the National Academy of Sciences of the United States of America* 92, 10639-10643